Transactions of the ASME®

Editor, **T. H. OKIISHI (2003)**
Assistant to the Editor: **P. BUZZELL**
Associate Editors
Gas Turbine (Review Chair)
H. SIMMONS (2003)
Heat Transfer
T. ARTS (2005)
R. BUNKER (2006)
Structures and Dynamics
M. MIGNOLET (2005)
Turbomachinery
R. DAVIS (2005)
S. SJOLANDER (2005)

BOARD ON COMMUNICATIONS
Chair and Vice-President
OZDEN OCHOA

OFFICERS OF THE ASME
President, **REGINALD VACHON**

Executive Director, **VIRGIL R. CARTER**

Treasurer, **R. E. NICKELL**

PUBLISHING STAFF
Managing Director, Engineering
THOMAS G. LOUGHLIN
Director, Technical Publishing
PHILIP DI VIETRO
Manager, Journals
JOAN MERANZE
Production Coordinator
JUDITH SIERANT
Production Assistant
MARISOL ANDINO

Transactions of the ASME, Journal of Turbomachinery (ISSN 0889-504X) is published quarterly (Jan., Apr., July, Oct.) by The American Society of Mechanical Engineers, Three Park Avenue, New York, NY 10016. Periodicals postage paid at New York, NY and additional mailing offices. POSTMASTER: Send address changes to Transactions of the ASME, Journal of Turbomachinery, c/o THE AMERICAN SOCIETY OF MECHANICAL ENGINEERS, 22 Law Drive, Box 2300, Fairfield, NJ 07007-2300.
CHANGES OF ADDRESS must be received at Society headquarters seven weeks before they are to be effective. Please send old label and new address.
STATEMENT from By-Laws. The Society shall not be responsible for statements or opinions advanced in papers or ... printed in its publications (B7.1, Par. 3).
COPYRIGHT © 2003 by the American Society of Mechanical Engineers. For authorization to photocopy material for internal or personal use under those circumstances not falling within the fair use provisions of the Copyright Act, contact the Copyright Clearance Center (CCC), 222 Rosewood Drive, Danvers, MA 01923, tel: 978-750-8400, www.copyright.com. Request for special permission or bulk copying should be addressed to Reprints/Permission Department.
INDEXED by Applied Mechanics Reviews and Engineering Information, Inc. Canadian Goods & Services Tax Registration #126148048

Journal of Turbomachinery

Published Quarterly by The American Society of Mechanical Engineers

VOLUME 125 • NUMBER 3 • JULY 2003

TECHNICAL PAPERS

405 **Aerodynamic-Rotordynamic Interaction in Axial Compression Systems—Part I: Modeling and Analysis of Fluid-Induced Forces** (2002-GT-30488)
Ammar A. Al-Nahwi, James D. Paduano, and Samir A. Nayfeh

416 **Aerodynamic-Rotordynamic Interaction in Axial Compression Systems—Part II: Impact of Interaction on Overall System Stability** (2002-GT-30489)
Ammar A. Al-Nahwi, James D. Paduano, and Samir A. Nayfeh

425 **Assessing Viscous Body Forces for Unsteady Calculations** (2002-GT-30359)
L. Xu

433 **A Numerical Investigation on the Influence of Lateral Boundaries in Linear Vibrating Cascades** (2002-GT-30451)
Roque Corral and Fernando Gisbert

442 **Maximum Amplification of Blade Response due to Mistuning: Localization and Mode Shape Aspects of the Worst Disks** (2002-GT-30323)
Alejandro J. Rivas-Guerra and Marc P. Mignolet

455 **Predictions of Separated and Transitional Boundary Layers Under Low-Pressure Turbine Airfoil Conditions Using an Intermittency Transport Equation**
Y. B. Suzen, P. G. Huang, Lennart S. Hultgren, and David E. Ashpis

465 **Effect of Unsteady Stator Wake—Rotor Double-Leakage Tip Clearance Flow Interaction on Time-Average Compressor Performance** (2002-GT-30368)
Borislav Todorov Sirakov and Choon-Sooi Tan

475 **An Improved Streamline Curvature Approach for Off-Design Analysis of Transonic Axial Compression Systems** (2002-GT-30444)
Keith M. Boyer and Walter F. O'Brien

482 **Rolls Royce/Allison 501-K Gas Turbine Antifouling Compressor Coatings Evaluation** (2002-GT-30261)
Daniel E. Caguiat

489 **Thermodynamic Analyses of Wet Compression Process in the Compressor of Gas Turbine** (2002-GT-30590)
Qun Zheng, Yufeng Sun, Shuying Li, and Yunhui Wang

497 **Improving the Efficiency of the Trent 500-HP Turbine Using Nonaxisymmetric End Walls—Part 1: Turbine Design** (2001-GT-0444)
G. Brennan, N. W. Harvey, M. G. Rose, N. Fomison, and M. D. Taylor

505 **Measurement and Analysis of Ingestion Through a Turbine Rim Seal** (2002-GT-30481)
O. Gentilhomme, N. J. Hills, A. B. Turner, and J. W. Chew

513 **An Investigation on Turbine Tip and Shroud Heat Transfer** (2002-GT-30554)
Kam S. Chana and Terry V. Jones

521 **Local Mass/Heat Transfer on Turbine Blade Near-Tip Surfaces** (2002-GT-30556)
P. Jin and R. J. Goldstein

529 **A Novel Transient Heater-Foil Technique for Liquid Crystal Experiments on Film-Cooled Surfaces** (2002-GT-30552)
G. Vogel, A. B. A. Graf, J. von Wolfersdorf, and B. Weigand

(**Contents continued on inside back cover**)

This journal is printed on acid-free paper, which exceeds the ANSI Z39.48-1992 specification for permanence of paper and library materials. ♾™
♻ 85% recycled content, including 10% post-consumer fibers.

Downloaded 01 Jun 2010 to 171.66.16.52. Redistribution subject to ASME license or copyright; see http://www.asme.org/terms/Terms_Use.cfm

Journal of Turbomachinery **Volume 125, Number 3** **JULY 2003**

538 A Novel Transient Liquid Crystal Technique to Determine Heat Transfer Coefficient Distributions and Adiabatic Wall Temperature in a Three-Temperature Problem (2002-GT-30532)
Andrew C. Chambers, David R. H. Gillespie, Peter T. Ireland, and Geoffrey M. Dailey

547 Effect of Internal Coolant Crossflow on the Effectiveness of Shaped Film-Cooling Holes
Michael Gritsch, Achmed Schulz, and Sigmar Wittig

555 Heat Transfer in Rotating Rectangular Cooling Channels (AR=4) With Dimples (2002-GT-30220)
Todd S. Griffith, Luai Al-Hadhrami, and Je-Chin Han

564 Discussion of "Heat Transfer in Rotating Rectangular Cooling Channels (AR=4) With Dimples," by P. Ligrani

564 Closure to Discussion of "Heat Transfer in Rotating Rectangular Cooling Channels (AR=4) With Dimples," by the authors

565 Heat Transfer, Fluid Flow, and Pressure Measurements Inside a Rotating Two-Pass Duct With Detached 90-Deg Ribs (2002-GT-30201)
Tong-Miin Liou, Meng-Yu Chen, and Yu-Ming Wang

575 Spatially Resolved Heat Transfer and Friction Factors in a Rectangular Channel With 45-Deg Angled Crossed-Rib Turbulators
P. M. Ligrani and G. I. Mahmood

585 Comparisons of High-Reynolds-Number EVM and DSM Models in the Prediction of Heat and Fluid Flow of Turbine Blade Cooling Passages
Yoji Okita and Hector Iacovides

598 A Unified Approach for Designing a Radial Flow Gas Turbine (2002-GT-30578)
M. S. Y. Ebaid, F. S. Bhinder, and G. H. Khdairi

The ASME Journal of Turbomachinery is abstracted and indexed in the following:

Aluminum Industry Abstracts, Aquatic Science and Fisheries Abstracts, AMR Abstracts Database, Ceramics Abstracts, Chemical Abstracts, Civil Engineering Abstracts, Compendex (The electronic equivalent of Engineering Index), Corrosion Abstracts, Current Contents, Ei EncompassLit, Electronics & Communications Abstracts, Energy Information Abstracts, Engineered Materials Abstracts, Engineering Index, Environmental Science and Pollution Management, Excerpta Medica, Fluidex, Fuel and Energy Abstracts, INSPEC, Index to Scientific Reviews, Materials Science Citation Index, Mechanical & Transportation Engineering Abstracts, Mechanical Engineering Abstracts, METADEX (The electronic equivalent of Metals Abstracts and Alloys Index), Metals Abstracts, Oceanic Abstracts, Pollution Abstracts, Referativnyi Zhurnal, Shock & Vibration Digest, Steels Alert

Downloaded 01 Jun 2010 to 171.66.16.52. Redistribution subject to ASME license or copyright; see http://www.asme.org/terms/Terms_Use.cfm

Aerodynamic-Rotordynamic Interaction in Axial Compression Systems—Part I: Modeling and Analysis of Fluid-Induced Forces

Ammar A. Al-Nahwi
Consulting Services Department,
Saudi Arabian Oil Company (Saudi Aramco),
Dhahran 31311, Saudi Arabia

James D. Paduano
Department of Aeronautics and Astronautics,
Massachusetts Institute of Technology,
Cambridge, MA 02139

Samir A. Nayfeh
Department of Mechanical Engineering,
Massachusetts Institute of Technology,
Cambridge, MA 02139

This paper presents a first principles-based model of the fluid-induced forces acting on the rotor of an axial compressor. These forces are primarily associated with the presence of a nonuniform flow field around the rotor, such as that produced by a rotor tip clearance asymmetry. Simple, analytical expressions for the forces as functions of basic flow field quantities are obtained. These expressions allow an intuitive understanding of the nature of the forces and—when combined with a rudimentary model of an axial compressor flow field (the Moore-Greitzer model)—enable computation of the forces as a function of compressor geometry, torque and pressure-rise characteristics, and operating point. The forces predicted by the model are also compared to recently published measurements and more complex analytical models, and are found to be in reasonable agreement. The model elucidates that the fluid-induced forces comprise three main contributions: fluid turning in the rotor blades, pressure distribution around the rotor, and unsteady momentum storage within the rotor. The model also confirms recent efforts in that the orientation of fluid-induced forces is locked to the flow nonuniformity, not to tip clearance asymmetry as is traditionally assumed. The turning and pressure force contributions are shown to be of comparable magnitudes—and therefore of equal importance—for operating points between the design point and the peak of the compressor characteristic. Within this operating range, both "forward" and "backward" rotor whirl tendencies are shown to be possible. This work extends recent efforts by developing a more complete, yet compact, description of fluid-induced forces in that it accounts for all relevant force contributions, both tangential and radial, that may influence the dynamics of the rotor. Hence it constitutes an essential element of a consistent treatment of rotordynamic stability under the action of fluid-induced forces, which is the subject of Part II of this paper.
[DOI: 10.1115/1.1576430]

1 Introduction

The significant role of aerodynamic forces in producing rotordynamic whirl in turbomachines has long been recognized. Thomas [1] and Alford [2] were the first to suggest simple models that link the whirl-inducing tangential fluid force to a tip clearance asymmetry produced by a displaced rotor in an axial turbine. In such models, it is assumed that the tangential aerodynamic force depends linearly on the radial rotor offset, with a proportionality factor commonly referred to as the cross-coupled stiffness (Alford [2]; Ehrich [3]; Childs [4]). This stiffness is then adjusted for different turbomachines by a nondimensional correction factor, known as the β^{Al}-parameter, which may be viewed as the change of the turbomachine's thermodynamic efficiency per unit change in rotor displacement. As such, a fixed value of the β^{Al} parameter was initially used in checking the stability of turbine rotors during design. However, it later became clear that the aerodynamic forces and the stability of the rotor, especially for axial compressors, depend on many variables such as the operating point and machine's performance, and are therefore more complex than what may be captured by a constant β^{Al} parameter. As a result, this parameter has commonly become a nondimensional representation of the whirl-inducing force.

Following Thomas and Alford, there has been a substantial amount of work dedicated to understanding aerodynamic forces in different types of turbomachines. On the turbine side, Song and Martinez-Sanchez [5] developed and experimentally verified a first-principles based model to predict these forces in an axial turbine. In order to estimate the forces in an axial compressor, Colding-Jorgensen [6] adopted the actuator-disk-based model of Horlock and Greitzer [7], whereas Ehrich [8] used a parallel compressor model together with experimental flow field measurements at different clearance settings to calculate the β^{Al} parameter for three different compressors over a range of operating points. He showed that β^{Al} depends on the operating point and that its operating-point dependence varies from one compressor to another.

More recently, there has been a comprehensive study of aerodynamic forces that specifically addresses axial compressors. A two-part paper by Storace et al. [9] and Ehrich et al. [10] presents an experimental and analytical effort in which an offset rotor in a low-speed four-stage research compressor is considered. Detailed measurements of the pressure distribution on both sides of one of the rotor's blades were recorded and used to calculate the time-varying force on that blade as it travels through regions of different tip clearance. In a related work by Spakovszky [11] aerodynamic forces are calculated by implementing a blade-passage control volume analysis for which flow-field information is obtained from a separate calculation based on a high-order Moore-Greitzer-type model. Song and Cho [12] also presented an analytical calculation of these forces along the same lines of his earlier work on turbines, [5]. Examples of these results are compared to the results of this work later in this paper. These recent efforts have taken a new, more first-principles based approach that

Contributed by the International Gas Turbine Institute and presented at the International Gas Turbine and Aeroengine Congress and Exhibition, Amsterdam, The Netherlands, June 3–6, 2002. Manuscript received by the IGTI November 30, 2001. Paper No. 2002-GT-30488. Review Chair: E. Benvenuti.

 Copyright © 2003 by ASME

Downloaded 31 May 2010 to 171.66.16.27. Redistribution subject to ASME license or copyright; see http://www.asme.org/terms/Terms_Use.cfm

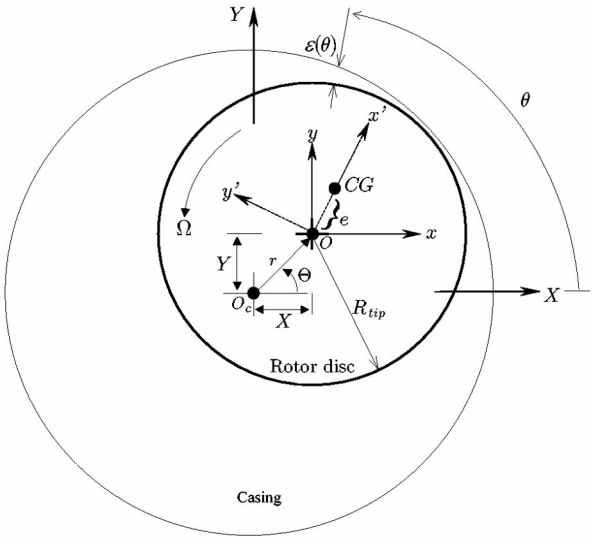

Fig. 1 Basic rotor-casing geometry (exaggerated proportions)

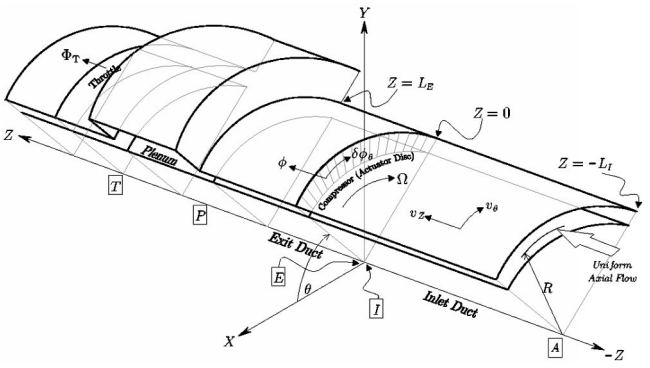

Fig. 2 Schematic of the compression system model

established a valuable foundation for understanding the nature of aerodynamic forces, and produced a useful set of measurements against which analytical calculations can be compared. This paper falls in this category, and is motivated by the need to build on these efforts in order to address the following:

- The configurations considered are usually static or steady in some sense (i.e., either the rotor is fixed or the flow field dynamics are excluded). The dynamic nature of the problem which ultimately decides the presence and form of instability (e.g., whirl) is not addressed, and is sometimes overlooked when making qualitative predictions about stability.
- Except for the recent efforts cited above, the force orientation has been traditionally assumed to be directly locked to the tip clearance distribution, ignoring the fact that the flow field velocity and pressure nonuniformity—which is the true source of the force—may be considerably out of phase with the geometric tip clearance distribution. The result is a possibly incorrect intuition about the direction of the net force.
- Except for the computational results of [11,12], the force contribution due to the hydrostatic pressure nonuniformity is usually not accounted for in the rotordynamic stability analysis, and has been overlooked in most previous treatments.
- Most of the previous efforts are specific to some configuration or compression system, restricted to a small range of operating conditions, or are computationally intensive. The result is an inability to extract general trends, establish dependency on parameters, or build an overall system dynamic model of a manageable complexity.

The objective of this work is to extend the current understanding of fluid-induced (aerodynamic) forces generated by asymmetric tip-clearance in axial compressors. In particular, to establish simple, first-principles-based relations between these forces and a given flow nonuniformity that account for all force contributions, that are valid over a wide range of compressor operating conditions, and that can easily be incorporated into a dynamic model of the compression system overall stability.

2 Modeling of Fluid-Induced Forces

2.1 Rotor-Casing Geometry. Figure 1 is a schematic of the simplified geometry considered here representing the (Jeffcott) rotor and depicting the main dimensions and displacements (with highly exaggerated proportions). In this figure, the position of the rotor relative to the casing is represented by the angle Θ and the radial displacement r (i.e., the distance between points O_c and O). The time derivative $\dot{\Theta}$ thus represents the frequency of rotor precessional motion, or whirl, ω^{wh}. Alternatively, the Cartesian coordinates of the rotor disk center X and Y and their time derivatives can also be used to describe the disc position and motion. The spin (or running) frequency of the disc about its axis (point O) is labeled Ω. The offset of the center of mass of the disk (point CG) from the geometric center is known as the amount of imbalance or eccentricity. Furthermore, the local tip clearance, $\varepsilon(\theta,\xi)$, is related to the rotor displacement, r, for small perturbations, as follows:

$$\varepsilon(\theta,\xi) = \bar{\varepsilon} - r(\xi)\cos(\theta - \Theta(\xi)) \tag{1}$$

where $\bar{\varepsilon}$ is the mean tip clearance when $r=0$, and $\xi = tU/R$ is nondimensional time.

2.2 Flow Field Description of an Axial Compression System. A suitable description of the flow field in an axial compression system is essential for calculating the forces generated by that flow field. Such a model gives as its output the fluid velocity and pressure fields around the rotor, which are used as inputs to the force model developed below. To that end, a high hub-to-tip ratio, low-speed axial compression system is considered in which the flow field may be assumed incompressible and two-dimensional (i.e., axial and circumferential). Such a compression system may be adequately described by a slightly modified version of the original Moore-Greitzer [13] model, which has been extensively utilized in numerous studies concerned with the stability of axial compression systems. The main modification in this development (as well as in that of Graf [14], Gordon [15], and Spakovszky [11]) is in allowing the pressure-rise characteristic of the compressor to depend linearly on the local tip-clearance.

A brief overview of the Moore-Greitzer model introduces the main equations, variables, and the nondimensionalization and rescaling needed for the development of the force model. Further details can be found in several references (e.g., Moore and Greitzer [13]), Longley [16], Al-Nahwi [17]. Figure 2 depicts an axial slice of the compression system being considered, showing the stationary coordinate system XYZ fixed to the casing as well as the system's main components, parameters, and flow field quantities. The axial stations A, I, E, P and T refer to the atmosphere, compressor inlet, compressor exit, plenum entrance, and throttle, respectively. Equations are written to describe the flow field in the upstream and downstream ducts, while flow quantities at the inlet and the exit of the compressor are linked through a few matching conditions based on mass and momentum conservation, blade geometry, and compressor pressure-rise characteristic. In this two-dimensional model, where all radial variations are neglected, the

Downloaded 31 May 2010 to 171.66.16.27. Redistribution subject to ASME license or copyright; see http://www.asme.org/terms/Terms_Use.cfm

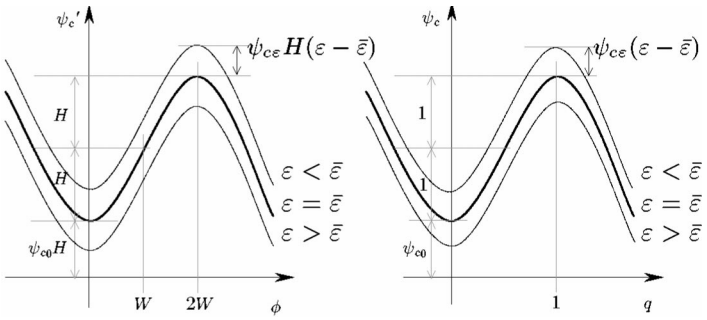

Fig. 3 General features of the compressor pressure-rise characteristic

flow is described by the nondimensional[1] velocity field $(v_Z(\theta,Z,\xi),v_\theta(\theta,Z,\xi))$, and the nondimensional pressure distribution $p(\theta,Z,\xi)/(\rho U^2)$. At the compressor inlet, point *I*, it is customary to use $\phi(\theta,\xi)=v_Z(\theta,0,\xi)$ to indicate the axial flow velocity into and throughout the compressor, also known as the flow coefficient. Further, ϕ can be split into two parts

$$\phi(\theta,\xi)=\Phi(\xi)+\delta\phi(\theta,\xi) \tag{2}$$

where $\Phi(\xi)$ is the annulus-averaged, axisymmetric axial flow coefficient, and $\delta\phi(\theta,\xi)$ is the circumferentially varying (not necessarily small) disturbance representing the angle-dependent flow nonuniformity.

A typical form of the pressure-rise characteristic (also adopted by Moore and Greitzer) is shown schematically on the left side of Fig. 3. A convenient rescaling[2] of flow field variables, however, produces the simpler characteristic shown on the right, where the two parameters *H* and *W* are absorbed into the pressure rise and flow coefficient, respectively. Such a rescaled characteristic is described by fewer parameters and has its peak at $q=1$. The rescaled flow variables are given by

$$q=\frac{\phi}{2W}\quad Q=\frac{\Phi}{2W}\quad \psi_c=\frac{\psi_c'}{H}\quad P=\frac{\Psi}{H} \tag{3}$$

Further, the rescaled pressure-rise characteristic is expressed in terms of the rescaled variables as

$$\psi_c(q,r,\Theta)=\psi_{c0}+1+3(q-0.5)-4(q-0.5)^3+\psi_{c\varepsilon}r\cos(\theta-\Theta) \tag{4}$$

where the last term on the RHS represents the linear dependence of the compressor pressure-rise on tip clearance mentioned earlier, with tighter tip-clearance associated with higher pressure-rise.

Expressions describing the flow field in each of the components of the compression system are now combined into one overall pressure balance between the inlet and the plenum. The result is a partial differential equation for which an approximate solution is sought by implementing a weighted-residual method known as the Galerkin approximation. In addition, by truncating the Fourier series used in this approximation at the first harmonic, three ODEs can be deduced from this one PDE which, together with the mass balance across the plenum, represent the simplest form of the Moore-Greitzer model (sometimes referred to as the four-state model). The first two equations describe surge dynamics, and are given by

$$\dot{Q}=\frac{S}{2\mathcal{L}}[\overline{\psi_c^C}(Q,a,b)-P] \tag{5}$$

$$\dot{P}=\frac{1}{2SB^2\mathcal{L}}[Q-Q_T(P)] \tag{6}$$

whereas the dynamics of the flow nonuniformity are given by

$$\dot{a}=\frac{1}{(2+\mu)}\left[\frac{S}{2}\overline{\psi_c^{Cc}}(Q,a,b,X)-\lambda b\right] \tag{7}$$

$$\dot{b}=\frac{1}{(2+\mu)}\left[\frac{S}{2}\overline{\psi_c^{Cs}}(Q,a,b,Y)+\lambda a\right] \tag{8}$$

in Cartesian form, and

$$\dot{A}=\frac{1}{(2+\mu)}\left[\frac{S}{2}\overline{\psi_c^{pc}}(Q,A,\eta,r,\Theta)\right] \tag{9}$$

$$\dot{\eta}=\frac{1}{(2+\mu)}\left[\lambda+\frac{S}{2A}\overline{\psi_c^{ps}}(\eta,r,\Theta)\right] \tag{10}$$

in polar form. The inertia parameters λ and μ are defined as follows

$$\lambda=\sum_{\substack{\text{rotors}\\ \text{only}}}\frac{l}{R\cos\gamma_r}\quad\text{and}\quad\mu=\sum_{\substack{\text{all}\\ \text{rows}}}\frac{l}{R\cos\gamma_r} \tag{11}$$

For similar rotor-stator pairs, i.e., N_{st} repeated stages, the λ and μ parameters may be approximated as

$$\lambda=\frac{N_{st}l}{R\cos\gamma_r}\quad\text{and}\quad\mu=\frac{(2N_{st}+1)l}{R\cos\gamma_r}\approx 2\lambda \tag{12}$$

Furthermore, the integrated characteristics appearing in the foregoing equations and resulting from the Galerkin approximation are defined as follows:

Cartesian version

[1]In general, these quantities are nondimensionalized as follows:

Velocity: $v=\tilde{v}/U=\tilde{v}/(R\Omega)$

Pressure: $p/(\rho U^2)=p/(\rho(R\Omega)^2)$

Lengths: For large, system-scale dimensions:

$Z=\tilde{Z}/R,\quad L_I=\tilde{L}_I/R,$

$\mathcal{L}=\tilde{\mathcal{L}}/R,\ldots$ and so on.

For small, blade-scale dimensions:

$r=\tilde{r}/l,\quad \varepsilon=\tilde{\varepsilon}/l,\ldots,$

and so on, where *l* is the blade chord.

Time: $\xi=t\Omega=tU/R$

[2]This rescaling scheme is similar, but not identical, to that used by McCaughan [18,19] in which nondimensional time was also rescaled by the factor $\mathcal{L}/S$ and the flow coefficient was shifted by 1. While the rescaling adopted by McCaughan best simplifies the flow field equations, its benefit is compromised once the rotordynamic model is added into the picture. The rescaling adopted here is more appropriate for the coupled model at hand.

Downloaded 31 May 2010 to 171.66.16.27. Redistribution subject to ASME license or copyright; see http://www.asme.org/terms/Terms_Use.cfm

$$\overline{\psi}_c^C=\frac{1}{2\pi}\int_0^{2\pi}\psi_c d\theta=\psi_{c0}+1+3(Q-0.5)-4(Q-0.5)^3$$
$$-6(a^2+b^2)(Q-0.5)$$
$$\overline{\psi}_c^{Cc}=\frac{1}{\pi}\int_0^{2\pi}\psi_c\cos\theta d\theta=-3a[4Q(Q-1)+(a^2+b^2)]+\psi_{c\varepsilon}X \quad (13)$$
$$\overline{\psi}_c^{Cs}=\frac{1}{\pi}\int_0^{2\pi}\psi_c\sin\theta d\theta=-3b[4Q(Q-1)+(a^2+b^2)]+\psi_{c\varepsilon}Y$$

Polar version

$$\overline{\psi}_c^p=\frac{1}{2\pi}\int_0^{2\pi}\psi_c d\theta=\psi_{c0}+1+3(Q-0.5)-4(Q-0.5)^3$$
$$-6A^2(Q-0.5)$$
$$\overline{\psi}_c^{pc}=\frac{1}{\pi}\int_0^{2\pi}\psi_c\cos(\theta-\eta)d\theta$$
$$=-3A[4Q(Q-1)+A^2]+\psi_{c\varepsilon}r\cos(\Theta-\eta) \quad (14)$$
$$\overline{\psi}_c^{ps}=\frac{1}{\pi}\int_0^{2\pi}\psi_c\sin(\theta-\eta)d\theta=\psi_{c\varepsilon}r\sin(\Theta-\eta)$$

Finally, the throttle characteristic is given by $Q_T=\psi_T^{-1}(P)=\gamma\sqrt{P}$.

Once these equations are solved, the total flow coefficient can easily be reconstructed as $q=Q+a\cos\theta+b\sin\theta=Q+A\cos(\theta-\eta)$. The above four-state model produces a solution for the compression system flow field provided that the system parameters, operating point and rotor position are all determined.

2.3 Description of Aerodynamic Forces

Force Contributions and Modeling Strategy. There are *three* effects that generate the total aerodynamic force on the rotor of an axial turbomachine, all of which can be traced to one source: the presence of a nonuniform flow field surrounding (and exchanging momentum with) the rotor[3]. The first contribution arises from the fact that a nonuniform flow field generates a circumferential distribution of flow velocity. As the flow passes through the rotor-blade rows, this nonuniform flow velocity results in various blades having to do unequal amounts of turning and thus being subject to nonuniform loading. The integrated effect of this uneven blade loading is a net force on the rotor called the turning force, F^{tu}. The second contribution is the unsteady momentum storage within the rotor which is called the unsteady force, F^{un}. The third and final contribution is due to the hydrostatic pressure distribution around the rotor which produces a net force called the pressure force, F^{pr}. All these forces must be taken into account for a reliable description of their effect on system stability.

To model these effects, a control volume (CV) enclosing the rotating assembly is considered such that the flow entering and leaving every rotor blade row also enters and leaves the control volume by crossing the control surface (CS) as shown in Fig. 4. Further, it is assumed that the control volume is translating but *non rotating*, and is fixed to the translating frame, xyz, which is in turn attached to the geometric center of the rotor, point *O*. It therefore has the same rectilinear acceleration as that point. This choice of control volume differentiates this model from that of [11]—also a momentum based model—and allows straightforward calculation of the momentum entering and leaving in terms of the flow field quantities available from the Moore-Greitzer model.

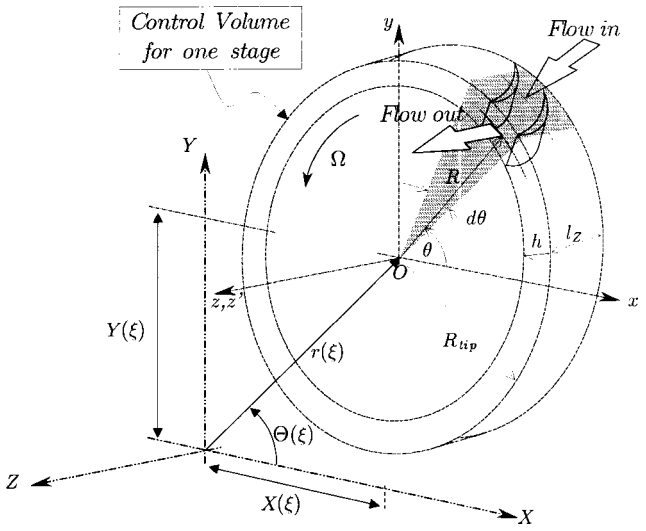

Fig. 4 A schematic of the control volume for one stage of the rotating assembly

Momentum Equation, Nondimensionalization, and General Force Expressions. The general vector form of the momentum equation applicable to this choice of control volume is arranged in the familiar form $M\mathbf{a}=\Sigma\mathbf{F}$, and is written in terms of dimensional quantities (marked by the tilde, e.g., $\tilde{F}$) as follows:

$$\int_{\text{CV,solid}}\tilde{\mathbf{a}}\rho_s d\mathcal{V}=-\int_{\text{CS}}\tilde{\mathbf{v}}_{xyz}\rho\tilde{\mathbf{v}}_{xyz}\cdot d\mathcal{A}$$
$$-\frac{\partial}{\partial t}\int_{\text{CV,fluid}}\tilde{\mathbf{v}}_{xyz}\rho d\mathcal{V}+\tilde{\mathbf{F}}^{pr}+\sum_{\substack{\text{CS \&}\\ \text{Body}}}\tilde{\mathbf{F}}^{other} \quad (15)$$

where the accelerations are measured in the inertial frame XYZ while the velocities are measured in the translating frame xyz, and the acceleration force acting on the fluid within the CV is neglected in comparison with that of the solid rotor due to the large difference in densities. Following a consistent nondimensionalization similar to that described in the foregoing for the flow field model, and expanding the acceleration term on the LHS to produce the imbalance force[4], $\mathbf{F}^{im}$, which is then moved to the RHS, the momentum equation becomes

$$\frac{d^2\mathbf{r}}{d\xi^2}=\chi\left[-\chi^{tu}\int_{\text{CS}}\mathbf{v}_{xyz}\mathbf{v}_{xyz}\frac{d\mathcal{A}}{\mathcal{A}^{tu}}-\chi^{un}\frac{\partial}{\partial\xi}\int_{\text{CV,fluid}}\mathbf{v}_{xyz}\frac{d\mathcal{V}}{\mathcal{V}^{un}}\right.$$
$$\left.-\chi^{pr}\int_{\text{CS}}\frac{p}{\rho R^2\Omega^2}\frac{d\mathcal{A}}{\mathcal{A}^{pr}}\right]+\mathbf{F}^{im}+\sum_{\substack{\text{CS \&}\\ \text{Body}}}\mathbf{F}^{other} \quad (16)$$

Several aspects of this equation deserve to be discussed. First, the first three terms on the RHS (between the large brackets) represent the turning, pressure, and unsteady force contributions, respectively. This is stated as

$$\mathbf{F}^{tu}=\chi(\mathbf{F}^{tu})_i=\chi\left[-\chi^{tu}\int_{\text{CS}}\mathbf{v}_{xyz}\mathbf{v}_{xyz}\cdot\frac{d\boldsymbol{\mathcal{A}}}{\mathcal{A}^{tu}}\right] \quad (17)$$

$$\mathbf{F}^{pr}=\chi(\mathbf{F}^{pr})_i=\chi\left[-\chi^{pr}\int_{\text{CS}}\frac{p}{\rho\Omega^2R^2}\frac{d\boldsymbol{\mathcal{A}}}{\mathcal{A}^{pr}}\right] \quad (18)$$

[3]Flow nonuniformity can be the result of several effects. When considering the rotordynamics of an axial turbomachine, however, the dominant effect is the tip clearance asymmetry, which we consider in this study.

[4]The details of deriving the dynamic terms, such as the imbalance force, are deferred to part II of this paper. For now, however, the emphasis is on the nondimensionalization of the complete equation which will lead to the proper definition and scaling of the aerodynamic forces.

Downloaded 31 May 2010 to 171.66.16.27. Redistribution subject to ASME license or copyright; see http://www.asme.org/terms/Terms_Use.cfm

$$\mathbf{F}^{un} = \chi(\mathbf{F}^{un})_i = \chi\left[-\chi^{un}\frac{\partial}{\partial \xi}\int_{\mathrm{CV,fluid}} \mathbf{v}_{xyz}\frac{d\mathcal{V}}{\mathcal{V}^{un}}\right] \tag{19}$$

where the quantities $(\mathbf{F}^{tu})_i$, $(\mathbf{F}^{pr})_i$ and $(\mathbf{F}^{un})_i$, may be viewed as the *average* aerodynamic force per stage of the compressor. For similar compressor stages, however, these quantities are the nondimensional force per stage. In addition, any of these forces, $(F)_i$, can also be viewed as a rescaled version of aerodynamic force, i.e., $(F)_i = F/\chi$.

Second, the nondimensional parameter, χ, which is defined by

$$\chi = \frac{N_{st}\rho(2\pi R h l_Z)}{N_{st}M_{st}} = \frac{\text{fluid mass within CV}}{\text{rotating assembly mass}} \tag{20}$$

is the main aerodynamic-rotordynamic *coupling* parameter with which all the aerodynamic forces scale, and is therefore expected to play a significant role in the dynamic coupling between the two domains. Note that as $\chi \to 0$ the basic Jeffcott rotordynamic model in its generalized form is recovered. Further, the χ-parameter as constructed in the foregoing may be viewed as the ratio of fluid mass within the control volume to mechanical mass of the rotating assembly (or the ratio of mass of fluid within one rotor blade row to the mechanical mass of that row). Since M_{st} is also roughly proportional to the dimensions R, h and l_Z, the χ-parameter may be viewed as the ratio of fluid to solid densities, ρ/ρ_s. Therefore, for the same turbomachine geometry, heavier fluid and/or lighter solid would lead to stronger influence of the aerodynamics on the rotordynamics.

Third, it can be seen that the turning, unsteady and pressure forces scale individually with the parameters χ^{tu}, χ^{un} and χ^{pr} respectively, which are defined as follows:

$$\chi^{tu} = \left(\frac{R}{l_Z}\right)^2 \cos\gamma_r = \frac{1}{(\mathrm{AR})_{br}^2}\cos\gamma_r \tag{21}$$

$$\chi^{pr} = 2\left(\frac{R}{l_Z}\right)^2\left(\frac{l}{h}\right)\cos^2\gamma_r = 2\,\frac{1}{(\mathrm{AR})_{br}^2}\,\frac{1}{(\mathrm{AR})_r}\cos^2\gamma_r \tag{22}$$

$$\chi^{un} = \left(\frac{R}{l_Z}\right)\cos\gamma_r\tan\gamma_r = \frac{1}{(\mathrm{AR})_{br}}\cos\gamma_r\tan\gamma_r \tag{23}$$

These parameters mainly depend on $(\mathrm{AR})_{br} = l_Z/R = \lambda\cos^2\gamma_r/N_{st}$ and $(\mathrm{AR})_r = (h/l)$, the stage and blade aspect ratios, respectively. For instance, smaller values of $(\mathrm{AR})_{br}$ (i.e., smaller axial blade chord and/or larger mean rotor radius) increase the influence of all three forces, more so for the turning and pressure forces than the unsteady force. On the other hand, smaller values $(\mathrm{AR})_r$ (e.g., shorter blade height) increase only the pressure force, leaving the other two contributions unchanged.

Fourth, other forces that may be considered in the summation of the last term on the RHS of Eq. (15) (e.g., gravity, stiffness and damping) will be relevant when the dynamics of the whole system are considered in Part II.

Fifth, the parameters $\mathcal{A}^{tu}$, $\mathcal{A}^{pr}$, and $\mathcal{V}^{un}$ introduced to complete the nondimensionalization are chosen to be proportional to the area through which the flow passes, the area upon which the pressure is acting, and the volume within which the momentum may be stored, respectively. Referring to Fig. 4, and taking into account the nondimensionalization of the overall equation, a suitable choice of these factors is given by

$$\mathcal{A}^{tu} = 2\pi N_{st} R h \tag{24}$$

$$\mathcal{A}^{pr} = 2\pi(2N_{st})R l_Z \tag{25}$$

$$\mathcal{V}^{un} = 2\pi N_{st} R h l_Z \tan\gamma_r \tag{26}$$

Further Simplifications. In order to go any further with the evaluation of the integrals appearing in the aerodynamic force expressions, the flow field $\mathbf{v}_{xyz}$ entering and leaving each rotor blade row, together with some form of average flow velocity to be used in evaluating the unsteady momentum need to be determined. In addition, the static pressure distribution around the CV needs to be determined. The velocity triangles of one stage are therefore considered as shown in Fig. 5, which depicts the plane containing a segment of the two-dimensional flow field (i.e., a plane parallel to Z and tangent to the rotor at some circumferential location θ). Figure 6 shows a three-dimensional view of one of the velocity triangles indicating the X and Y components, the angles involved, and other relevant dimensions.

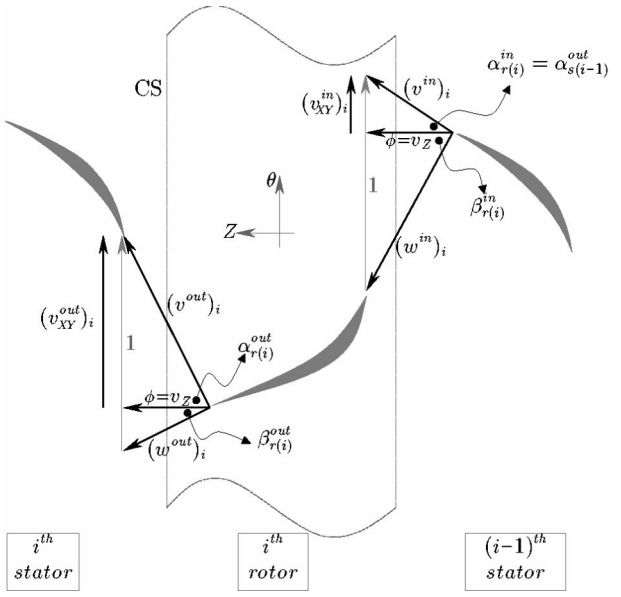

Fig. 5 Velocity triangles and terminology used in evaluating force expressions

It should be recognized that the flow velocity $\mathbf{v}_{xyz}$ appearing in the force expressions is measured in the relative frame xyz, while the velocity ϕ or q appearing in the Moore-Greitzer model is measured in the absolute frame. The relative and absolute velocities in these two frames are related through $\mathbf{v}_{xyz} = \mathbf{v}_{XYZ} - (l/R)(d\mathbf{r}/d\xi)$. However, it can be shown using straightforward order-of-magnitude estimates that the second term on the RHS is very small compared to the flow velocities and may thus be neglected.

Turning Force Expression. The required velocity vectors entering and leaving the ith rotor blade row can now be written in terms of the flow coefficient ϕ and the proper fluid-angle functions $\alpha^{\mathrm{out}}_{s(i-1)}(\phi)$ and $\beta^{\mathrm{out}}_{r(i)}(\phi)$. These two functions describe the angles at which the fluid leaves the stator and rotor blade row

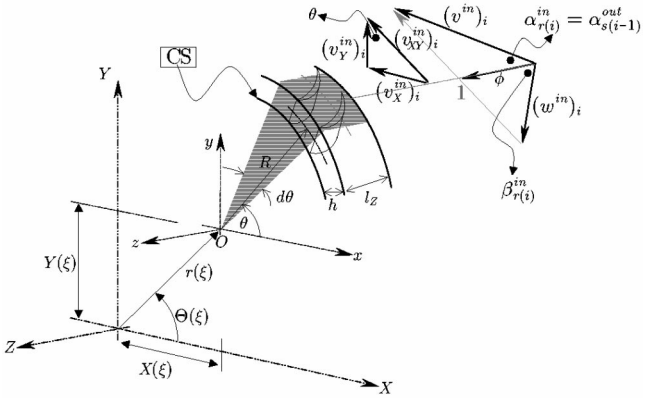

Fig. 6 Three-dimensional components of velocity triangle

Downloaded 31 May 2010 to 171.66.16.27. Redistribution subject to ASME license or copyright; see http://www.asme.org/terms/Terms_Use.cfm

respectively, and are typically different from the fixed-blade metal angles, with the difference (known as deviation) being a characteristic function of flow coefficient specific to the blade row being considered. The required flow velocity vectors are given in terms of these angles as

$$(\mathbf{v}^{\text{in}}_{XYZ})_i = \phi \tan \alpha^{\text{out}}_{s(i-1)}[-\sin\theta\mathbf{i}+\cos\theta\mathbf{j}]+\phi\mathbf{k}$$

$$(\mathbf{v}^{\text{out}}_{XYZ})_i = (1-\phi\tan\beta^{\text{out}}_{r(i)})[-\sin\theta\mathbf{i}+\cos\theta\mathbf{j}]+\phi\mathbf{k}$$

and,

$$(\mathbf{v}^{\text{out}}_{XYZ})_i-(\mathbf{v}^{\text{in}}_{XYZ})_i=(1-\phi(\tan\alpha^{\text{out}}_{s(i-1)}+\tan\beta^{\text{out}}_{r(i)})) \times[-\sin\theta\mathbf{i}+\cos\theta\mathbf{j}] \quad (27)$$

A convenient way to obtain a reasonable estimate of the foregoing angle functions is to extract them from another reasonably measurable and well-characterized quantity: the stage torque characteristic. The Euler turbine equation as applied to a steady, axisymmetric flow field, may be written in nondimensional form as

$$\frac{1}{2}(\tau_c)_i=\phi[(v^{\text{out}}_{XY})_i-(v^{\text{in}}_{XY})_i]=\phi[1-\phi(\tan\alpha^{\text{out}}_{s(i-1)}+\tan\beta^{\text{out}}_{r(i)})] \quad (28)$$

This directly gives a relation for the needed angle expression. Further, comparing the above Euler equation to Eq. (27), and considering similar stages, one finds that the average (i.e., per stage) turning force is exactly given by

$$(\mathbf{F}^{tu})_i=-\chi^{tu}\frac{1}{2\pi}\int_0^{2\pi}\frac{1}{2}(\tau_c)_i[-\sin\theta\mathbf{i}+\cos\theta\mathbf{j}]d\theta \quad (29)$$

For this purpose the following stage torque characteristic is adopted:

$$(\tau_c)_i=\frac{(\tilde{\tau}_c)_i}{\frac{1}{2}\rho\Omega^2R^3\mathcal{A}_c}=\tau_{c0}+\tau_{c1}q+\tau_{c2}q^2+\tau_{c3}q^3 \quad (30)$$

where $\mathcal{A}_c$ is the compressor flow through area, $\mathcal{A}_c\approx 2\pi Rh$, and the total compressor torque is simply $N_{st}(\tau_c)_i$. The coefficients of the above torque characteristic are determined for the compressor being considered such that the resulting characteristic has the usual S-shape, matches any available torque measurements over the stable and reversed-flow portions, and is interpolated using a cubic polynomial. Detailed measurements of an axial compressor torque over a wide range of operating conditions are reported by Day [20]; Gamache [21]; Gamache and Greitzer [22], and Lavrich [23], and can be utilized as a guide for the typical features of this characteristic.

Carrying out the integration in Eq. (29) yields the final expression of the average turning force required for the baseline model

$$(\mathbf{F}^{tu})_i=\frac{1}{4}\chi^{tu}\{[b\overline{F}^{tu}_c(Q,a,b)]\mathbf{i}+[-a\overline{F}^{tu}_c(Q,a,b)]\mathbf{j}\} \quad (31)$$

where the function $\overline{F}^{tu}_c(Q,a,b)$ is given by

$$\overline{F}^{tu}_c(Q,a,b)=\tau_{c1}+2\tau_{c2}Q+3\tau_{c3}\left[Q^2+\frac{1}{4}(a^2+b^2)\right] \quad (32)$$

Unlike earlier models (e.g., [1,2]), the foregoing expression agrees with recently published results (e.g., [10–12]) in that the force not only depends on the rotor eccentricity, but is also a function of flow field *variable* quantities Q, a and b. It can also be seen that this force contribution may in fact have a radial component which can play a role in the overall stability picture.

Unsteady Force Expression. To evaluate the unsteady momentum expression, an average velocity within the stage is defined as follows:

$$(\overline{\mathbf{v}}_{XYZ})_i=\frac{(\mathbf{v}^{\text{in}}_{XYZ})_i+(\mathbf{v}^{\text{out}}_{XYZ})_i}{2} =\left[1-\phi\left(\frac{1}{2}[\tan\beta^{\text{in}}_{r(i)}+\tan\beta^{\text{out}}_{r(i)}]\right)\right] \times[-\sin\theta\mathbf{i}+\cos\theta\mathbf{j}]+\phi\mathbf{k} \quad (33)$$

In order to avoid excessive complexity, it is noted that the foregoing angle combination $(1/2)[\tan\beta^{\text{in}}_{r(i)}+\tan\beta^{\text{out}}_{r(i)}]$ appearing is commonly used to define the angle of the average velocity within a blade passage. It is assumed here that this averaged angle remains, more or less, constant and is approximated by the blade stagger angle. That is

$$\frac{1}{2}[\tan\beta^{\text{in}}_{r(i)}+\tan\beta^{\text{out}}_{r(i)}]\approx\tan\gamma_r \quad (34)$$

Examination of detailed flow data, such as that given by Lavrich [23] suggests that this representation is adequate, especially in unstalled flow conditions.

The unsteady force contribution can be obtained after carrying out the integration to yield

$$(\mathbf{F}^{un})_i=\chi^{un}W\left[-\frac{db}{d\xi}\mathbf{i}+\frac{da}{d\xi}\mathbf{j}+\frac{1}{\tan\gamma_r}\frac{dQ}{d\xi}\mathbf{k}\right] \quad (35)$$

Pressure Force Expression. The static pressure distribution around the stage is now required. Since such detailed information is not directly available from the flow-field model adopted here, the following average pressure distribution for the ith stage is defined instead. That is, $\overline{p_i}=(p_i^{in}+p_i^{out})/2$, which is equivalent to assuming linear variation (increase for a compressor) of static pressure with the axial direction Z. This is a reasonable assumption supported by data such as that presented by Lavrich [23]. By combining the intermediate pressures of all stages, an overall pressure average is obtained and expressed in terms of the pressure at the compressor inlet and exit, p_I and p_E. This produces the convenient expression

$$(\mathbf{F}^{pr})_i=-\chi^{pr}\frac{1}{2\pi}\int_0^{2\pi}\frac{1}{2}\frac{p_I+p_E}{\rho\Omega^2R^2}[\cos\theta\mathbf{i}+\sin\theta\mathbf{j}]d\theta \quad (36)$$

The required overall pressure average can be constructed by manipulating the Moore-Greitzer model equations for the inlet and exit ducts, from which the pressure force reduces to the following simple expression:

$$(\mathbf{F}^{pr})_i=-\chi^{pr}\frac{1}{2\pi}\int_0^{2\pi}-\frac{1}{4}\phi^2[\cos\theta\mathbf{i}+\sin\theta\mathbf{j}]d\theta =\chi^{pr}W^2Q[a\mathbf{i}+b\mathbf{j}] \quad (37)$$

3 Analysis of Fluid-Induced Force

3.1 Qualitative Features of Aerodynamic Forces. The aerodynamic force expressions derived in the foregoing indicate that the forces are the direct result of the flow field nonuniformity, and that they depend on the operating point and compressor characteristic. Further, the compact form of these expressions allows establishment of clear relations between the forces and the quantities describing the flow nonuniformity.

A demonstration of these relations supported by a few numerical examples that are based on the MIT 3-stage experimental compressor[5] are now presented. Figure 7 depicts the pressure-rise and axisymmetric torque characteristics of this compressor.

[5]The parameters and performance of the MIT 3-stage compressor are very well documented by many authors such as Eastland [24], Gamache [21] and more recently by Van Schalkwy [25]. These documents are available upon request from the Gas Turbine Laboratory, 31-264, MIT.

Downloaded 31 May 2010 to 171.66.16.27. Redistribution subject to ASME license or copyright; see http://www.asme.org/terms/Terms_Use.cfm

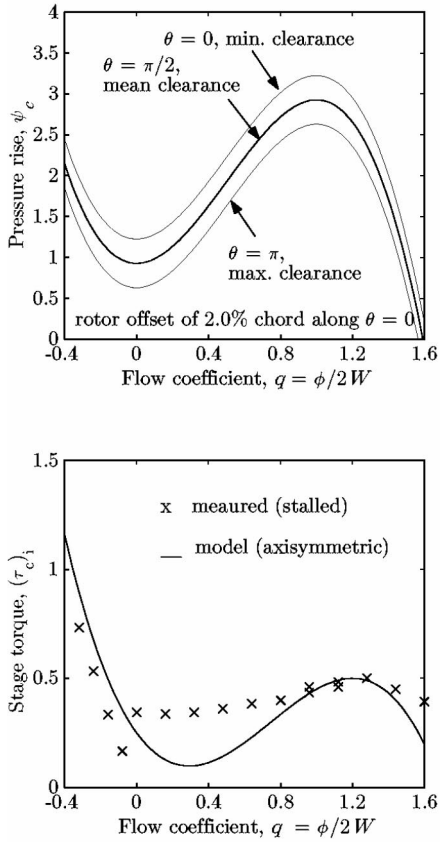

Fig. 7 Pressure-rise and torque characteristics for the MIT 3-stage axial compressor. (Measured performance reported by Gamache [21] and others.)

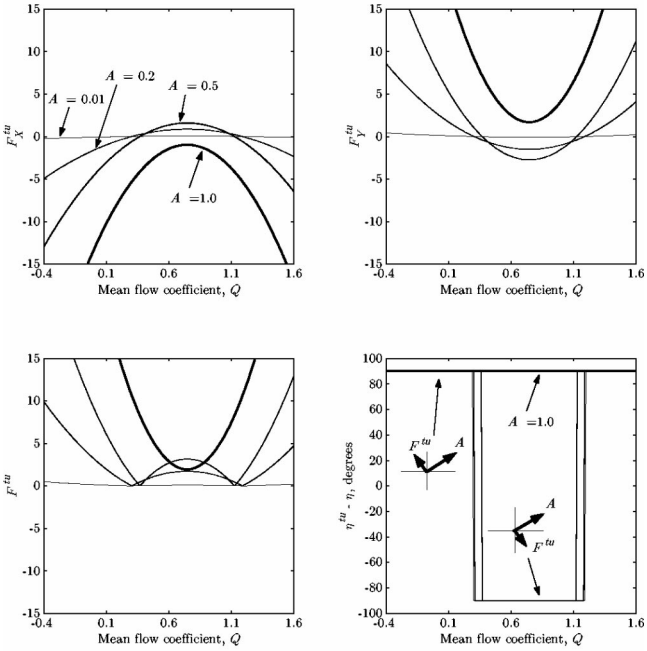

Fig. 8 Calculated amplitude of turning force F^{tu} for different values of flow nonuniformity amplitude

Turning Force. Recalling the expressions for the two components of the turning force, F_X^{tu} and F_Y^{tu}, the amplitude and phase of the turning force can be written as follows:

$$F^{tu}=\sqrt{(F_X^{tu})^2+(F_Y^{tu})^2}=\frac{1}{4}\chi^{tu}A\overline{F}_c^{tu}$$

$$=\frac{1}{4}\chi^{tu}A\left[\tau_{c1}+2\tau_{c2}Q+3\tau_{c3}\left(Q^2+\frac{1}{4}A^2\right)\right] \tag{38}$$

$$\eta^{tu}=-\tan^{-1}\frac{a}{b}=\eta\pm 90 \tag{39}$$

The foregoing phase relation indicates that, to the first harmonic approximation of the flow field, the line of action of the turning force contribution is perpendicular to the peak of the flow nonuniformity, and not to the tip clearance asymmetry. The amplitude of the turning force is a somewhat complicated expression that is cubic in A and quadratic in Q.

To illustrate the features of the foregoing relations, a flow field nonuniformity of amplitude A and some fixed phase η, say 30 deg, are assumed. Figure 8 shows a plot of the X and Y components of the turning force, together with its amplitude F^{tu}, and phase difference, $\eta^{tu}-\eta$, as a function of mean flow coefficient Q and for different values of flow nonuniformity amplitude A. It can be seen that for small values of A, and as the mean flow coefficient Q is decreased, the turning force reverses direction twice along the line perpendicular to A. That is, the phase difference $\eta^{tu}-\eta$ changes from 90 to -90 and then to 90 deg again. However, for a nonuniformity of large amplitude, e.g., $A=1.0$, the turning force maintains the same direction at $\eta^{tu}-\eta=90$ for all Q. Small values of A are representative of flow nonuniformities that are the result of a rotor offset, whereas the large value of $A=1$ represents a nonuniformity such as rotating stall.

Pressure Force. Using the X and Y components of the pressure force, an expression for the amplitude and phase of the pressure force contribution can also be written as

$$F^{pr}=\chi^{pr}W^2QA \tag{40}$$

$$\eta^{pr}=\tan^{-1}\frac{b}{a}=\eta\pm 0,180 \tag{41}$$

This indicates that the pressure force is exactly aligned with the flow nonuniformity (i.e., maximum flow coefficient). This is consistent with the simple Bernoulli relation between flow pressure and velocity, which requires the point on the circumference passing the minimum flow to have the maximum pressure. It should also be noted that, unlike the turning force, the pressure force is a simple function which is linear in both A and Q. Figure 9 shows a plot of the amplitude and phase difference of the pressure force and its X and Y components, as a function of Q and for different values of A.

Unsteady Force. Similarly, using the X and Y components of the unsteady force, expressions for the amplitude and phase of this force contribution can be written as follows:

$$F^{un}=\chi^{un}W\sqrt{\dot{A}^2+A^2\dot{\eta}^2} \tag{42}$$

$$\eta^{un}=-\tan^{-1}\frac{\dot{a}}{\dot{b}}=-\tan^{-1}\frac{\dot{A}\cos\eta-A\dot{\eta}\sin\eta}{\dot{A}\sin\eta+A\dot{\eta}\cos\eta} \tag{43}$$

The relations of the unsteady force are more complicated than the previous two. But some insight can be gained by considering the special case of pure rotating stall in which the flow nonuniformity has a constant amplitude, $A=A^{rs}$ (i.e., $\dot{A}=0$), and a constant rate of rotation, $\dot{\eta}=\nu^{rs}$. In such a case, the amplitude and phase of the unsteady force reduce to

$$(F^{un})^{rs}=\chi^{un}WA^{rs}\nu^{rs} \tag{44}$$

Downloaded 31 May 2010 to 171.66.16.27. Redistribution subject to ASME license or copyright; see http://www.asme.org/terms/Terms_Use.cfm

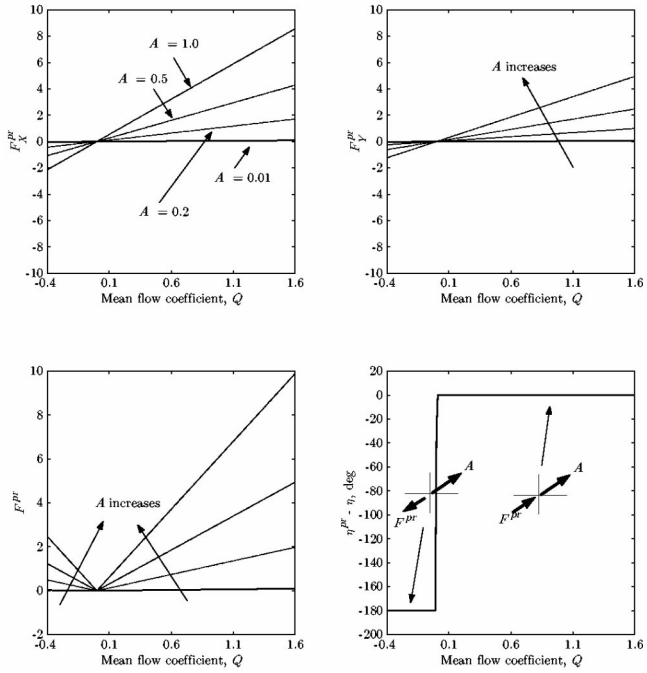

Fig. 9 Calculated amplitude of pressure force F^{pr} for different values of flow nonuniformity amplitude

$$(\eta^{un})^{rs} = \tan^{-1}\frac{\sin\eta}{\cos\eta} = \eta \pm 0,180 \tag{44}$$

which indicates that the unsteady force during rotating stall is also aligned with the flow nonuniformity (and hence rotating at the same frequency) and that the amplitude is a simple function that is linear in both A and ν^{rs}, but is independent of Q.

Figure 10 is a plot of the foregoing results showing the amplitude and phase difference of the unsteady force as a function of A for various values of ν^{rs}. It is noted that the amplitude of the unsteady force during rotating stall (i.e., $A \sim 1$) is in general very small compared to the turning and pressure force contributions at a similar value of A.

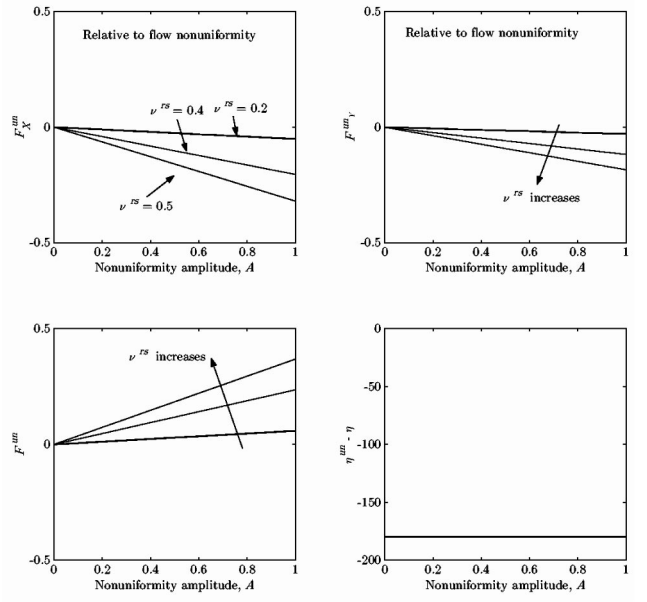

Fig. 10 Calculated amplitude of unsteady force F^{un} for different values of flow nonuniformity frequency

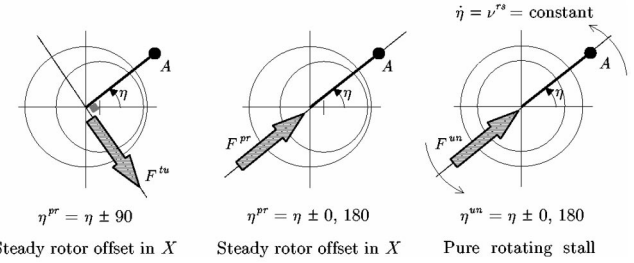

Fig. 11 Schematic of the phase relationship between the three aerodynamic forces and flow nonuniformity. Note that the flow nonuniformity, indicated by the large dot, is not in phase with the tip clearance asymmetry.

Finally, Fig. 11 is a schematic which summarizes the phase relations between the three force contributions and the flow field nonuniformity described in the foregoing.

3.2 Calculation of Aerodynamic Forces for a Fixed Rotor Offset. The relations described in the previous section do not take into account the link between the tip-clearance asymmetry and the flow field nonuniformity it generates. They simply give the aerodynamic forces resulting from a given, arbitrary flow nonuniformity without specifying how that nonuniformity is produced. As such, these relations develop the first level of understanding of the forces necessary for exploring more complicated situations. To that end, a more complete picture can be obtained by realizing that the flow nonuniformity as represented by (A, η) is not arbitrary, but is rather the result of a tip-clearance asymmetry, which in turn is produced by an offset of the rotor within the casing. So in order to further analyze these forces, the following strategy (similar to [11]) is adopted. A static rotor offset is chosen and the steady flow field equations for (A, η) are then solved. Based on this flow field, the aerodynamic forces are evaluated.

Solution of Steady-State Equations for the Flow Field. The steady flow field resulting from a stationary tip clearance asymmetry (e.g., due to static rotor deflection) is obtained by setting to zero the LHS of Eqs. (5), (6), (9), and (10) and solving the resulting set of simultaneous algebraic equations. Given the form of these equations, one can simplify this task by choosing the operating point (i.e., Q) of interest on the compressor map and the rotor deflection as inputs. Then, only the two equations, describing the flow nonuniformity (i.e., Eqs. (9) and (10))—which do not contain either P or γ—need to be solved for A and η. The first two equations (Eqs. (5), (6)) can then be used to find P and γ if needed. The result of the foregoing procedure together with some manipulation is the following two equations:

$$A^6 + [8Q(Q-1)]A^4 + \left[16Q^2(Q-1)^2 + \left(\frac{2}{3}\frac{\lambda}{S}\right)^2\right]A^2 - \left(\frac{1}{3}\psi_{c\varepsilon} r\right)^2 = 0 \tag{45}$$

$$\eta = \sin^{-1}\left(\frac{2A}{\psi_{c\varepsilon} r}\frac{\lambda}{S}\right) \tag{46}$$

A few comments are in order regarding the above two equations. It can be noted that r and $\psi_{c\varepsilon}$ play the same role in determining the flow nonuniformity amplitude A and the phase η. For instance, increasing the rotor offset r is equivalent to having higher compressor sensitivity to tip clearance $\psi_{c\varepsilon}$, either of which will increase the amplitude of the nonuniformity A. Further, it is observed that reducing the parameter ratio λ/S has a similar (yet weaker) effect on the steady state solution. For instance, higher

Downloaded 31 May 2010 to 171.66.16.27. Redistribution subject to ASME license or copyright; see http://www.asme.org/terms/Terms_Use.cfm

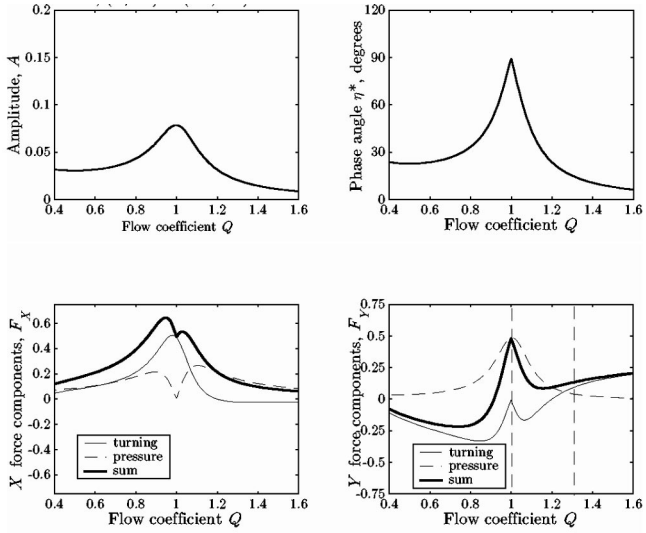

Fig. 12 Flow nonuniformity and aerodynamic forces for a fixed rotor offset of $r=1.0\%$ chord

values of the pressure-rise characteristic parameter $S=H/W$—corresponding to steeper characteristic—would (for the same λ) increase A and reduce η.

Evaluation of Flow Field Nonuniformity and Aerodynamic Forces. Figure 12 shows the flow field nonuniformity and the turning and pressure force contributions for a rotor offset of $r=1.0\%$ chord (about 35% of maximum possible deflection) in the X direction (i.e., $\Theta=0$). It can be seen that the flow nonuniformity amplitude A is of order 0.01 at very high mean flow coefficient Q; of order 0.05 at design flow of $Q=1.2$; and, of order 0.1 at $Q=1$ which corresponds to the peak pressure rise. The relatively high amplitude of the nonuniformity close to the peak of the characteristic is the result of the compressor's tendency to amplify distortions as it operates closer to its neutral stability point. In general, larger amplitudes of A are expected for higher tip-clearance sensitivity $\psi_{c\varepsilon}$ or for larger rotor deflections.

The phase η varies with Q in approximately the same way as A. The point of maximum flow is about 10° away from the minimum tip clearance point at very high Q. These two points move apart as the flow is reduced towards the peak, $Q=1$, at which point the flow nonuniformity is 90° out of phase with the tip-clearance asymmetry. The physical source of this phase difference can be linked to the fluid inertia in the rotor blade rows represented by λ. The larger this inertia, the more the flow nonuniformity lags behind the tip-clearance asymmetry. On the other hand, a steeper characteristic (larger S) tends to counter that effect.

Figure 12 also shows the X and Y components of the aerodynamic forces. For the given rotor deflection in the X direction, the X force component represents the restoring force while the Y component represents the whirl-inducing force. As Q is varied over the operating range, both these forces are seen to change sign. In particular, for $Q\gtrsim 0.4$ the X force component is shown to be in the same direction as the deflection. On the other hand, the Y component is shown to change sign more than once over the whole range of Q, hence providing both forward and backward whirl *tendencies*—as opposed to the ultimate direction of whirl which is decided by the dynamics of the system under the action of all relevant forces—depending on the operating point. It is worth noting that the pressure contribution, which has traditionally been neglected in studying compressor and turbine whirl phenomena, may have a strong influence on the net whirl tendency of the compressor. For example, it is noted that the Y component of the pressure force at around $Q=1$ is large enough to completely reverse the net effect from backward whirl (due to turning alone) to forward whirl.

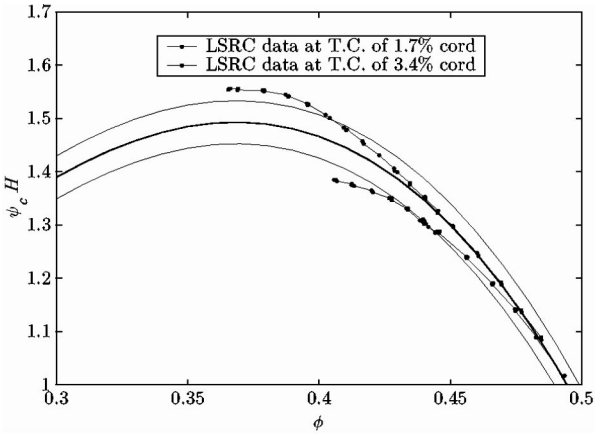

Fig. 13 Measured and assumed pressure-rise characteristics for the GE LSRC

The numerical results shown in Fig. 12 are specific to the compressor geometry and characteristic used in the calculation, and are thus expected to differ for other compressors of different geometries and characteristics.[6] Nevertheless, these results demonstrate the main features of aerodynamic forces, their principal components, and their dependence on relevant system parameters and flow variables.

3.3 Validation Against Available Experimental Data. The recently published data [9] and the accompanying numerical results [10] are utilized here for validating the calculations of the current model. These studies are based on the GE LSRC axial compressor: a 4-stage, low-speed experimental compressor at the GE Research Center. The results in these two references, and many others, are reported in terms of the known β^{Al} parameter. As mentioned briefly in the introduction, this parameter emerged from Alford's original analysis as a nondimensional "correction factor" that multiplies the cross-coupled stiffness relating the aerodynamic force, say $(\tilde{F}_Y)_i$, to the rotor displacement $\tilde{X}$. Mathematically, β^{Al} is expressed as follows:

$$(\tilde{F}_Y)_i=\underbrace{\beta_Y^{Al}\left(\frac{(\tilde{\tau}_c)_i}{2Rh}\right)}_{\text{cross-coupled stiffness}}\tilde{X} \quad \Rightarrow \quad \beta^{Al}=2Rh\,\frac{(\tilde{F}_Y)_i}{(\tilde{\tau}_c)_i\tilde{X}}$$

or, in terms of the current nondimensional quantities

$$\beta_Y^{Al}=\frac{4}{\cos\gamma_r}\left(\frac{l_Z}{R}\right)^2\left(\frac{h}{l}\right)\frac{(F_Y)_i}{(\tau_c)_i X} \tag{47}$$

where the aerodynamic force $(F_Y)_i$ can be either that due to turning, $(F_Y^{tu})_i$, which gives $(\beta_Y^{Al})^{tu}$, or that due to pressure, $(F_Y^{pr})_i$, which gives $(\beta_Y^{Al})^{pr}$. As mentioned earlier, until recently only the turning contribution in the direction of whirl (i.e., normal to rotor displacement) was addressed in the literature, and most mention of the Alford β-parameter refers to that component of the turning contribution. To the authors' knowledge, there is no published experimental or computational data against which the restoring forces, i.e., $(F_X^{tu})_i$ and $(F_X^{pr})_i$, can be compared.

The next step is to compare the pressure-rise characteristic used in the model to that obtained from measurements. Figure 13 shows two sets of characteristics. The first set consists of two pressure-rise measurements that correspond to two different mean tip-clearance settings of the compressor. The other set consists of three curves representing the modeled pressure-rise characteristic,

[6] A detailed comparison between four different generic compression systems, including an axial liquid pump, is given by [17].

Downloaded 31 May 2010 to 171.66.16.27. Redistribution subject to ASME license or copyright; see http://www.asme.org/terms/Terms_Use.cfm

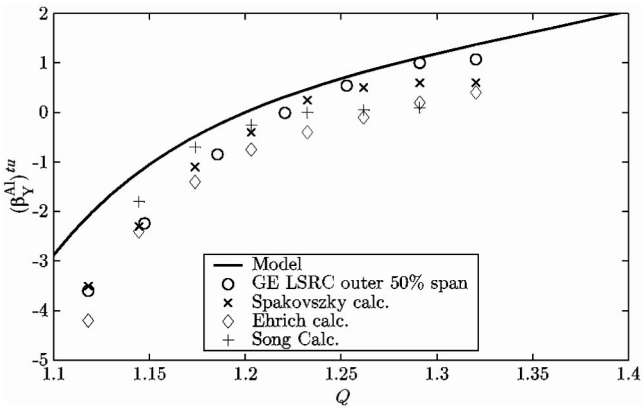

Fig. 14 Comparison between experiment, numerical results, and this model, for the GE LSRC compressor with $r=1.0\%$ chord

using a rotor offset that produces a tip clearance distribution whose maximum and minimum match the two experimental clearance settings. It can be seen from the figure that the measured characteristics are more sensitive to tip clearance around the peak than they are within the part of the operating range where the flow coefficient is highest. In addition, the peak of the characteristic shifts to the right for the larger tip clearance. Such variation in sensitivity and shift in the peak can not be captured using the simple linear dependence of the characteristic on tip clearance adopted in this paper. Although, a more sophisticated representation of the characteristic can capture such variation, it would produce dispensable mathematical complexity. To that end, the parameters (i.e., $S=H/W$ and $\psi_{c\varepsilon}$) of the current simple characteristic are tuned such that the modeled and measured loss in pressure rise are closest in the neighborhood of the design operating point, while underestimated at the peak and overestimated in the high flow region. It is shown below that the errors in this model predictions as compared to experimental data are predictably larger in those regions where the characteristics are furthers apart.

Figure 14 shows the calculation results of the current model against the data and computational results of [13,14]. The predictions of the current model are shown to compare well against the measurements, especially near the design point (i.e., $Q=1.2$ to 1.3), where the characteristics matched best. On the other hand, the error in predicted values of $(\beta_Y^{Al})^{tu}$ becomes expectedly larger as we move closer to the characteristic peak at $Q=1$ where the measured and modeled characteristics deviated the most. Additional calculations (not shown) performed with better characteristics matching at the peak bring $(\beta_Y^{Al})^{tu}$ prediction into a closer agreement with measurements in that region, but results in a larger deviation in the high flow region.

4 Conclusions

The model for the aerodynamic forces developed and analyzed in this paper reveals that there are three physical contributions to the total aerodynamic force on the rotor. In the presence of a flow nonuniformity, the three contributions arise from nonuniform turning done by the blades, nonuniform hydrostatic pressure acting on the hub (directly on the rotor), and the unsteady momentum storage within the rotor blade passages. Each of the three force contributions scales with a nondimensional parameter that depends only on blade and stage geometry.

In addition, simple analytical expressions for the aerodynamic forces were derived for a given compressor geometry, characteristics, operating point, and rotor deflection. These expressions give physical insights and establish a link between the direction of the three force contributions and the flow nonuniformity. Consequently, the aerodynamic forces are confirmed to be locked to the flow nonuniformity and not to the tip-clearance asymmetry, consistent with [10] and other related efforts. Using the analytical and numerical results of this force model, it is shown that in order to predict whether the rotor tends to whirl backward or forward, all force contributions as well as the compressor operating point have to be taken into account. This is especially true for operating points close to the design point where the pressure and turning contributions may be of comparable magnitudes but different signs. Finally, the force model compares well with recently published data of aerodynamic force measurements, as well as several more computationally-intensive efforts over the narrow range of operating conditions in which this data is available.

Acknowledgment

The authors would like to thank Professor Zoltan Spakovszky and Dr. Fredrich Ehrich for many useful ideas and discussions, and for making available their analytical and experimental expertise in the area of fluid-induced forces. The valuable guidance and support of Professors Kamal Youcef-Toumi and Alan H. Epstein are also acknowledged and appreciated.

This work was partially supported by the Saudi Arabian Oil Company (Saudi Aramco). It was also partially supported by AFOSR Grant F-49620-92-J-0409, Dr. Marc Jacobs, Technical Monitor.

Nomenclature

$\mathcal{A}, A$ = area, amplitude of flow nonuniformity
a, b = Cartesian components of flow nonuniformity
B = system stability B-parameter, $B=U/2a_s\sqrt{\mathcal{V}/\mathcal{A}\tilde{\mathcal{L}}}$
$(F)_i$ = per-stage, nondimensional aerodynamic force
H, W = pressure-rise characteristic parameters
h = blade radial span (height)
$\mathbf{i}, \mathbf{j}, \mathbf{k}$ = unit vectors
$L_I, L_E, \mathcal{L}$ = inlet, exit and total effective duct length
l, l_Z = blade chord, blade axial chord
N_{st} = no. of compressor stages
P = rescaled pressure-rise coefficient, $P=\Psi/H$
p, p_t = static, total pressure
Q, q = rescaled flow coefficient; $Q=\Phi/2W$, $q=\phi/2W$
R, r = mean annular radius, rotor radial displacement
S = pressure-rise characteristic aspect ratio, $S=H/W$
U = mean rotor speed
$\mathcal{V}, v$ = volume, flow field velocity
X, Y = Cartesian rotor displacements in inertial frame
α, β = absolute and relative flow angles
β^{Al} = Alford's β-parameter
γ = nondimensional throttle coefficient, or blade stagger angle
ε = tip clearance
η = phase angle of flow field nonuniformity
Θ, θ = angular (whirl) displacement of rotor center, circumferential coordinate
λ, μ = compressor inertia parameters
ξ = nondimensional time
ρ = density
$\tau_c, (\tau_c)_i$ = total, per-stage compressor torque
Φ, ϕ = annulus-averaged, total axial compressor flow coefficient
χ = aerodynamic-rotordynamic coupling parameter
Ψ = nondimensional plenum pressure, $\Psi=(p_P-p_{tA})/\rho\Omega^2R^2$
ψ_c = total-to-static pressure-rise characteristic
ψ_{c0} = shut-off value of ψ_c
$\psi_{c\varepsilon}$ = sensitivity of pressure-rise characteristic to tip-clearance, $\psi_{c\varepsilon}=-\partial\psi_c/\partial\varepsilon$
Ω = rotor rotational (spin) frequency ($\Omega=U/R$)

Downloaded 31 May 2010 to 171.66.16.27. Redistribution subject to ASME license or copyright; see http://www.asme.org/terms/Terms_Use.cfm

$(\cdot)^{tu,un,pr}$ = reference to turning, unsteady and pressure force contributions
$(\cdot)_{(i)}$ = reference to *i*th stage
$(\cdot)_r$, $(\cdot)_s$ = reference to rotor, stator blade rows
$\overline{(\cdot)}$ = averaged quantity
$\delta(\cdot)$ = disturbance or nonuniform component
$\tilde{(\cdot)}$ = dimensional quantity for which a nondimensional counterpart exists

References

[1] Thomas, H. J., 1958, ''Unstable Natural Vibration of Turbine Rotors Induced by the Clearance Flow in Glands and Blading,'' Bull. De l'A.I.M., **71**(11/12), pp. 1039–1063.
[2] Alford, J., 1965, ''Protecting Turbomachinery From Self-Excited Rotor Whirl,'' ASME J. Eng. Power, Oct., pp. 333–344.
[3] Ehrich. F. 1992, *Handbook of Rotordynamics*. McGraw-Hill Inc., New York.
[4] Childs, D., 1993, *Turbomachinery Rotordynamics, Phenomena, Modeling & Analysis*, John Wiley, New York.
[5] Song, S. J., and Martinez-Sanchez, M., 1997, ''Rotordynamic Forces Due to Turbine Tip Leakage, Parts I and II,'' ASME J. Turbomach., **119**, Oct., pp. 695–713.
[6] Colding-Jorgensen, J., 1992, ''Prediction of Rotor Dynamic Destabilizing Forces in Axial Flow Compressors,'' ASME J. Fluids Eng., **114**, Dec., 621–625.
[7] Horlock, J. H., and Greitzer, E. M., 1983, ''Non-Uniform Flows in Axial Compressors Due to Tip Clearance Variation,'' IMechE, Proc. Instn. Mech. Engrs., **197C**, 173–178.
[8] Ehrich, F., 1993, ''Rotor Whirl Forces Induced by the Tip Clearance Effect in Axial Flow Compressors,'' J. Vibr. Acoust., **115**, Oct., pp. 509–515.
[9] Storace, A. F., Wisler, D. C., Shin, H.-W., Beacher, B. F., Ehrich, F. F., Spakovszky, Z. S., Martinez-Sanchez, M., and Song, S. J., 2000, ''Unsteady Flow and Whirl-Inducing Forces in Axial-Flow Compressors,'' Part I—Experiment. ASME-IGTI Paper 2000-GT-0565.
[10] Ehrich, F. F., Spakovszky, Z. S., Martinez-Sanchez, M., Song, S. J., Wisler, D. C., Storace, A. F., Shin, H.-W., and Beacher, B. F., 2000, ''Unsteady Flow and Whirl-Inducing Forces in Axial-Flow Compressors,'' Part II—Analysis. ASME-IGTI Paper 2000-GT-0566.
[11] Spakovszky, Z. S., 2000, ''Analysis of Aerodynamically Induced Whirling Forces in Axial Flow Compressors,'' ASME-IGTI Paper 2000-GT-0418.
[12] Song, S. J., and Cho, S. H., 2000, ''Non-Uniform Flow in a Compressor Due to Asymmetric Tip Clearance,'' ASME-IGTI Paper 2000-GT-0416.
[13] Moore, F. K., and Greitzer, E. M., 1986, ''A Theory of Post-Stall Transients in Axial Compression Systems: Part I—Development of Equations,'' ASME J. Eng. Power, **108**, Jan., pp. 68–76.
[14] Graf, M. B., 1996, ''Effects of Asymmetric Tip Clearance on Compressor Stability,'' Master's thesis, Massachusetts Institute of Technology.
[15] Gordon, K., 1999, *Three-Dimensional Rotating Stall Inception and Effects of Rotating Tip Clearance Asymmetry in Axial Compressors*. Ph.D. thesis, Massachusetts Institute of Technology.
[16] Longley, J. P., 1993, ''A Review of Non-Steady Flow Models for Compressor Stability,'' ASME Paper 93-GT-17.
[17] Al-Nahwi, A. A., 2000, *Aerodynamic-Rotordynamic Interaction in Axial Compression Systems*. Ph.D. thesis, Massachusetts Institute of Technology.
[18] McCaughan, F., 1989, ''Application of Bifurcation Theory to Axial Flow Compressor Instability,'' ASME J. Turbomach., **111**, Oct., pp. 426–433.
[19] McCaughan, F., 1998, ''Numerical Results for Axial Flow Compressor Instability,'' ASME J. Turbomach., **111**, Oct., pp. 434–441.
[20] Day, I. J., 1976, *Axial Compressor Stall*. Ph.D. thesis, Cambridge University.
[21] Gamache, R. N., 1985, *Axial Compressor Reversed Flow Performance*. Ph.D. thesis, Massachusetts Institute of Technology.
[22] Gamache, R. N., and Greitzer, E. M., 1986, ''Reversed Flow in MultiStage Axial Compressors,'' AIAA J., AIAA-86-1747.
[23] Lavrich, P., 1988, *Time Resolved Measurements of Rotating Stall in Axial Compressors*. Ph.D. thesis, Massachusetts Institute of Technology.
[24] Eastland, A. H. J., 1982, ''Investigation of Compressor Performance in Rotating Stall: I-Facility Design and Construction and Initial Steady State Measurements,'' Technical Report 164, Massachusetts Institute of Technology, Gas Turbine Lab Report.
[25] Van Schalkwyk, C. M., 1996, *Active Control of Rotating Stall With Inlet Distortion*. Ph.D. thesis, Massachusetts Institute of Technology.

Downloaded 31 May 2010 to 171.66.16.27. Redistribution subject to ASME license or copyright; see http://www.asme.org/terms/Terms_Use.cfm

Aerodynamic-Rotordynamic Interaction in Axial Compression Systems—Part II: Impact of Interaction on Overall System Stability

Ammar A. Al-Nahwi
Abqaiq Plants,
Saudi Arabian Oil Company (Saudi Aramco),
Abqaiq, Saudi Arabia 31311

James D. Paduano
Department of Aeronautics and Astronautics,
Massachusetts Institute of Technology,
Cambridge, MA 02139

Samir A. Nayfeh
Department of Mechanical Engineering,
Massachusetts Institute of Technology,
Cambridge, MA 02139

This paper presents an integrated treatment of the dynamic coupling between the flow field (aerodynamics) and rotor structural vibration (rotordynamics) in axial compression systems. This work is motivated by documented observations of tip clearance effects on axial compressor flow field stability, the destabilizing effect of fluid-induced aerodynamic forces on rotordynamics, and their potential interaction. This investigation is aimed at identifying the main nondimensional design parameters governing this interaction, and assessing its impact on overall stability of the coupled system. The model developed in this work employs a reduced-order Moore-Greitzer model for the flow field, and a Jeffcott-type model for the rotordynamics. The coupling between the fluid and structural dynamics is captured by incorporating a compressor pressure rise sensitivity to tip clearance, together with a momentum based model for the aerodynamic forces on the rotor (presented in Part I of this paper). The resulting dynamic model suggests that the interaction is largely governed by two nondimensional parameters: the sensitivity of the compressor to tip clearance and the ratio of fluid mass to rotor mass. The aerodynamic-rotordynamic coupling is shown to generally have an adverse effect on system stability. For a supercritical rotor and a typical value of the coupling parameter, the stability margin to the left of the design point is shown to decrease by about 5% in flow coefficient (from 20% for the uncoupled case). Doubling the value of the coupling parameter not only produces a reduction of about 8% in the stability margin at low flow coefficients, but also gives rise to a rotordynamic instability at flow coefficients 7% higher than the design point.
[DOI: 10.1115/1.1576431]

1 Introduction

The design and operation of axial turbomachines are plagued by different types of aerodynamic and structural instabilities such as surge, rotating stall and shaft whirl, which may subject the machine components to stresses beyond their design limits. In addition to the possibility of costly and catastrophic mechanical failure, the mere interruption of operation may be at least as catastrophic (e.g., aircraft jet engines) or as costly (e.g., oil and gas production plants).

The aerodynamic performance and flow field stability of axial turbomachines (Greitzer [1]; Moore [2]; Moore and Greitzer [3]; Greitzer and Moore [4]; and Hynes and Greitzer [5]) are known to strongly depend on the clearance gap between the tips of the rotating blades and the stationary casing (Graf et al. [6]; Gordon [7]; Smith [8]; Baghdadi [9]; Storer and Cumpsty [10]; and Horlock and Greitzer [11]). The viscous losses associated with the leakage flow in the tip clearance region in an axial compressor, for instance, are manifested as a reduction in pressure rise capability and efficiency on one hand, and an increase in the stalling mass flow rate (i.e., loss of stability) on the other. Further, changes in either the mean tip clearance or its circumferential distribution may impact both performance and stability. In addition, asymmetric tip clearance distribution produces a nonuniform flow field which is ultimately responsible for generating aerodynamic forces on the rotor.[1]

One source of tip clearance change is the vibration of the rotor as governed by the structural dynamics of the rotor-bearings subsystem (i.e., rotordynamics) and by the fluid-induced forces acting on the rotor blades and hub. Under certain conditions, these forces can be of such magnitude and direction that they cause the rotor center to follow a fixed orbit, possibly of large amplitude, producing a self-excited instability known as rotor whirl—a phenomenon that has long been recognized and addressed in the rotordynamics literature (Thomas [12]; Alford [13]; Vance and Laudadio [14]; Colding-Jorgensen [15]; Ehrich [16]; Childs [17]; Litang et al. [18]; Spakovszky [19]; Song and Cho [20]; Storace et al. [21]; Ehrich et al. [22]; Akin et al. [23]; and Storace [24]).

Having recognized the dependence of the axial compressor flow field on tip clearance, the dependence of tip clearance on the compressor rotordynamics and, the rotordynamics dependency on fluid-induced forces, it follows that the dynamic behavior of the flow field and the rotordynamics in axial compression systems may be strongly coupled, Fig. 1.

There is evidence, both experimental and theoretical, that this interaction may be significant in that the rotordynamic behavior may potentially alter the aerodynamic stability, or vice versa. For instance, in the course of active control experiments of rotating stall, Weigl [25] reported on potential coupling between the rotordynamic and aerodynamic domains when he observed that the

Contributed by the International Gas Turbine Institute and presented at the International Gas Turbine and Aeroengine Congress and Exhibition, Amsterdam, The Netherlands, June 3–6, 2002. Manuscript received by the IGTI November 30, 2001. Paper No. 2002-GT-30489. Review Chair: E. Benvenuti.

[1] A comprehensive treatment of fluid-induced aerodynamic forces on axial compressor rotors is presented in a companion paper, Part I.

 Copyright © 2003 by ASME

Downloaded 31 May 2010 to 171.66.16.27. Redistribution subject to ASME license or copyright; see http://www.asme.org/terms/Terms_Use.cfm

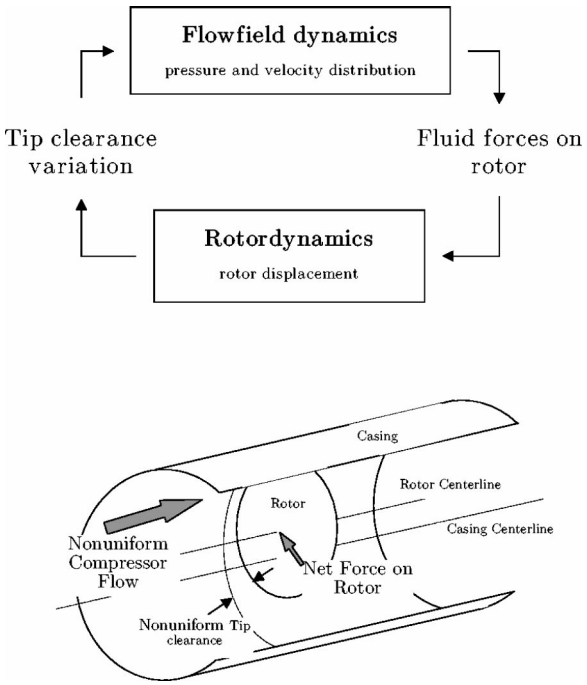

Fig. 1 Aerodynamic-rotordynamic coupling mechanism

frequency of rotor whirl (due to a deteriorating journal bearing) and that of rotating stall coincided when they were simultaneously present. He also observed that the first mode of circumferential flow disturbances had a much higher energy content prior to the onset of instability, as compared to runs with a healthy bearing. Another indication of possible coupling comes from a recent problem observed during the testing of a new engine which is still in the developmental stage, Ehrich [26]. The problem included the loss of aerodynamic stability (surge event) at the design point in the presence of a rotordynamic, subsyncronous, whirl-like behavior which has been identified as a subharmonic, nonlinear response to imbalance.

It is therefore of interest to understand the overall dynamic behavior of the coupled system. Further, such an understanding of the aerodynamic-rotordynamic interaction and its impact on stability should directly contribute to the advancement of several important areas of research—the active control of turbomachinery instabilities being a prime example—that may directly contribute to the design and operation of more stable and reliable compression systems. More specifically, the objectives of this work are to

- Determine the set of nondimensional parameters governing the coupling of aerodynamics and rotordynamics in an axial compression system, and relate these parameters, and how they scale, to a physical description of the mechanisms at work.
- In terms of these parameters, determine the conditions under which aerodynamic-rotordynamic coupling is important.
- Predict the potential impact of this coupling on the stability of the flow field and rotor structure. In particular, determine physical arguments and relative design parameter values that are potentially destabilizing and/or beneficial to overall stability.

An Overview of Previous Work. In addition to the aforementioned efforts, this work builds on a large body of published research in the areas of compression system aerodynamic and rotordynamic modeling and stability. For instance, the effect of tip clearance on aerodynamic stability of axial compression systems was addressed by Graf et al. [6] who used a modified version of the model by Hynes and Greitzer [5] to examine compression system stability, both theoretically and experimentally, under stationary tip clearance asymmetry (e.g., distorted casing). The study showed that the asymmetry has a destabilizing effect which is higher than that of a uniform clearance having the same mean. Gordon [7] generalized that treatment to include tip clearance asymmetries that may be rotating at any frequency. He showed that the inception of instability is adversely affected as this frequency becomes closer to a critical value in the neighborhood of the eigen-frequency of the rotating stall first mode.

One of the many extensions of the original Moore-Greitzer is of particular significance. The concept of active control of aerodynamic instabilities, first proposed by Epstein et al. Epstein et al. [27], has evolved to be a major area of interest in research and industry (a review of such concepts is given by Paduano et al. [28]). A relevant example from these active control efforts is the work by Spakovszky [29] in which a detailed experimental investigation of using magnetic bearings to stabilize rotating stall by means of actively moving the rotor and thus adjusting the tip clearance distribution is proposed and assessed. In addition, the nonlinear nature of the Moore-Greitzer-type models together with the fact that fully developed surge and rotating stall are ultimately nonlinear limit-cycle-type instabilities, have attracted attention from the nonlinear dynamics community. Abed et al. [30] addressed the bifurcation behavior of the simple, lumped parameter surge model. McCaughan [31] presented a detailed bifurcation analysis of the Moore-Greitzer third-order model and outlined the post-instability behavior—including both surge and rotating stall—of axial compression systems in the $B-\gamma$ parameter space (B and γ are the ratio of system compliance to inertia and the throttle coefficient respectively). Finally, several investigations (e.g., Nayfeh [32]) and Wang et al. [33]) have been conducted to apply nonlinear control concepts to alter the undesirable post-instability behavior of the system. This, in general, amounts to attempting to change the nature of the bifurcation from subcritical to supercritical. In order to achieve this, Wang et al. [33] theoretically examined the nonlinear aspects of actively controlling surge and rotating stall by means of tip-clearance actuation through magnetic bearings.

On the rotordynamic side of the problem, the Jeffcott rotor [34] proved to be a very useful tool for exploring fundamental rotordynamic phenomena such as the response to imbalance. The Jeffcott rotor is essentially stable since it is a damped vibratory system consisting of a mass, springs and dampers. The potential for instability arises from the interaction between centrifugal forces due to whirl-like rotation, and various internal and external forces acting on the rotor. Examples of such forces include different forms of fluid forces (such as those generated from tip clearance asymmetry, labyrinth seals flow, and oil flow in journal bearings) and forces due to internal rotor damping. A physical and concise description of basic rotordynamic phenomena can be found in Den Hartog [35]; Crandall [36]; Ehrich [37], and Childs [17]. As an example of the destabilizing effect of these forces on the rotordynamic stability of an actual engine, Akin et al. [23] reported on aerodynamically-induced rotor instability in the TF30 P111 engine. The authors accounted for different sources of destabilizing forces and concluded that, in that case, the Alford-type forces generated on the turbine side of the engine were responsible for the instability. Incorporating an oil-film damper at the bearing was proposed, analyzed and implemented, and was shown to eliminate the problem. The authors concluded, however, that the general determination of the source of instability is difficult and requires careful testing and analysis.

2 Overall System Model

To describe the aerodynamic-rotordynamic interaction at hand, the following sub-models are consolidated into one overall system model: the four-state Moore-Greitzer model which describes the flow field; the Jeffcott rotor model which describes the rotordynamics; a simple representation of compressor pressure rise char-

Downloaded 31 May 2010 to 171.66.16.27. Redistribution subject to ASME license or copyright; see http://www.asme.org/terms/Terms_Use.cfm

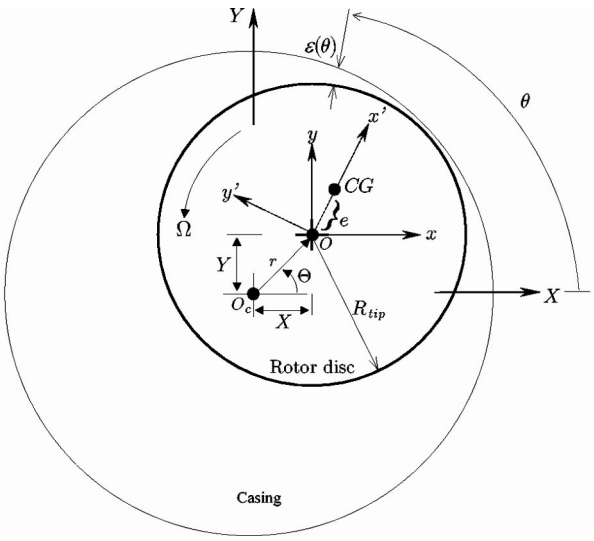

Fig. 2 Basic rotor-casing geometry (exaggerated proportions)

acteristic sensitivity to tip clearance, and, a description of aerodynamic forces generated by the flow field and acting on the rotor. With the exception of a few aspects of the rotordynamic model, all the other submodels have been developed and presented in a companion paper (Part I) to which the reader is referred for more details. In this part, however, the remaining components of the rotordynamic description[2] are presented, followed by a recapitulation of the main parts of the overall model.

2.1 Rotordynamic Description. Referring to Fig. 2, it may be noted that three important frequencies can be identified when discussing the Jeffcott rotor model: The first is Ω, the spinning frequency of the disk and shaft about their common geometric axis, O. The second is $\omega^{wh}=\dot{\Theta}$, the orbital frequency of point O about point O_c, called the whirl frequency. The third is ω, the natural vibration frequency of the rotating assembly, which is typically proportional to the ratio of mechanical stiffness to inertia.

To complete the description of the rotordynamic model, several important forces acting on the rotor need to be introduced. These forces were represented by the two terms $\mathbf{F}^{\text{im}}$ and $\Sigma\,\mathbf{F}^{\text{other}}$ in Eq. (16) of Part I. In what follows, only those forces relevant in the subsequent analysis presented in this paper are included here; namely aerodynamic, stiffness, damping and inertia forces. Several additional forces can also be considered depending on the focus of the analysis being pursued. To that end, the imbalance force, $\mathbf{F}^{\text{im}}$—which together with the term $d^2\mathbf{r}/d\xi^2$ emerge from the acceleration term on the LHS of Eq. (15) in Part I—is dropped by assuming that the imbalance e is equal to zero. Such a periodic forcing does not play a role in the stability analysis presented in this paper.

In addition to the aerodynamic forces which have been addressed in Part I, the two other essential forces (that were lumped under the summation $\Sigma\,\mathbf{F}^{\text{other}}$) are now introduced.

$$\sum_{\substack{\text{CS \&}\\ \text{Body}}} \mathbf{F}^{\text{other}}=\mathbf{F}^{da}+\mathbf{F}^{st}+\mathbf{F}^{ha} \tag{1}$$

In general, damping forces, (F^{da}), may include effects due to aerodynamic drag, internal shaft damping, oil-film damping in journal bearings, and squeeze-film damping used commonly with roller-element bearings. The internal shaft damping may (e.g., in the presence of material hysteresis) produce a force that contributes to whirl-like instabilities. In fact, this historically is the first effect to be recognized as a source of whirl-type, self-excited instabilities. However, in order to limit the sources of rotordynamic instability in this study, all damping effects are lumped into a single linear term of the viscous drag type, hence assuming no material hysteresis.

As for stiffness forces, (F^{st}), the basic Jeffcott rotor model traditionally makes a distinction between stiffness (restoring) forces due to shaft elasticity and those due to support bearing compliance. The simplest Jeffcott rotor, for instance, assumes an elastic shaft supported by rigid bearings. More sophisticated representations of stiffness forces have been included in the Jeffcott rotor model to account for several observed behaviors such as those resulting from stationary stiffness orthotropy in which the bearings stiffness in the X and Y directions are different. Such orthotropy tend to have a stabilizing effect in that it increases the critical spin frequency above which an instability may occur (see, for example, [1], Section 1.6]). Rotating stiffness orthotropy, on the other hand, is local to the shaft, and thus produces a rotating spring force which does not always act as a pure restoring force. Instead, a component of this spring force contributes to the whirling motion and may thus lead to what is known as a parametric instability. In addition, stiffness nonlinearity may also be included to represent hardening and softening spring effects, as well as the variation of stiffness over a cycle of the rotor whirl orbit due to rubbing (known as the normal-tight condition) or due to excessive bearing clearance (known as normal-loose condition). The rotordynamic response under such conditions can be very complicated and may even display chaotic behavior (an overview of this topic is given by Ehrich [39]). In this model, the stiffness effect of the shaft and bearings is combined into one lumped stiffness. Moreover, an additional nonlinear (cubic) term is included to represent a hardening system spring.

This allows the rotordynamic model to be written as

$$\frac{d^2\mathbf{r}}{d\xi^2}=\mathbf{F}^{da}+\mathbf{F}^{st}+\mathbf{F}^{ae} \tag{2}$$

where the nondimensional forces are given by

$$\mathbf{F}^{da}=-2\zeta\nu(\dot{X}\mathbf{i}+\dot{Y}\mathbf{j}) \tag{3}$$

$$\mathbf{F}^{st}=-(\nu^2X+\varpi X^3)\mathbf{i}-(\nu^2Y+\varpi Y^3)\mathbf{j} \tag{4}$$

$$\mathbf{F}^{ae}=\mathbf{F}^{tu}+\mathbf{F}^{pr}+\mathbf{F}^{un} \tag{5}$$

and where the aerodynamic force $\mathbf{F}^{ae}$ with its three contributions are as defined in Part I. Other quantities appearing above that have not been defined in Part I are given as

$$\zeta=\frac{c}{2M\omega}\qquad \nu=\frac{\omega}{\Omega}$$

$$\omega=\sqrt{\frac{k}{M}}\qquad \varpi=\left(\frac{l}{\Omega}\right)^2\frac{k^{ns}}{M}$$

The rotor's undamped natural frequency, ν, is worthy of special attention since rotors are commonly classified according to its value being above or below 1.0. Also, ν largely determines the response of the Jeffcott rotor to imbalance which has its maximum rotor deflection at the critical value $\nu=1.0$. Rotors normally operating at values of $\nu<1$ are referred to as supercritical rotors, reflecting the fact that the spin frequency Ω is larger the rotor's natural frequency. A subcritical rotor would thus have $\nu>1$. In general, most modern, high-speed turbomachines are in the range $0.1<\nu<0.5$ and are therefore supercritical at their typical running speeds.

As noted earlier, several other forces may be acting on rotors of axial compressors which are not included in this paper. Examples include Alford-type forces on the turbine (which may be on the

[2] A fully detailed development of the model including a discussion of all rotordynamic forces can be found in Al-Nahwi [38].

Downloaded 31 May 2010 to 171.66.16.27. Redistribution subject to ASME license or copyright; see http://www.asme.org/terms/Terms_Use.cfm

same rotor as the compressor) of a gas turbine engine, fluid forces from seals and journal bearings, actuation forces of magnetic bearings, gravity force on horizontal rotors, and several others. The *uncoupled* rotordynamic response to most of these forces have been addressed by many researchers. Although including these forces in an integrated model such as the one considered in this study is straightforward and may be useful, it can result in unwarranted complexity and prevent clear understanding of the basic coupling phenomena being in focus here. Including these forces may therefore be viewed as a useful extension to the current work that can be considered after the simplest, most basic coupling model has been explored.

2.2 Summary of Overall System Model. The flow field description was presented in some detail in Part I, wherein the surge dynamics were represented by Eqs. (5) and (6), the flow nonuniformity dynamics by Eqs. (7) and (8) in Cartesian from or (9) and (10) in polar form. Additional expressions needed to complete the flow field description include the compressor integrated characteristics given by (13) and (14), all in Part I.

As for the rotordynamic description, the X and Y components of Eq. (2) that include the additional forces described, in the foregoing can be written in Cartesian form as

$$\ddot{X}+2\zeta\nu\dot{X}=-\nu^2X-\varpi X^3+\chi\cdot(F_X^{ae})_i \tag{6}$$

$$\ddot{Y}+2\zeta\nu\dot{Y}=-\nu^2Y-\varpi Y^3+\chi\cdot(F_Y^{ae})_i \tag{7}$$

and in polar form as

$$\ddot{r}-r\dot{\Theta}^2+2\zeta\nu\dot{r}=-\nu^2r-[\cos^4\Theta+\sin^4\Theta]\varpi r^3+\chi\cdot(F_r^{ae})_i \tag{8}$$

$$r\ddot{\Theta}+2\dot{r}\dot{\Theta}+2\zeta\nu r\dot{\Theta}=[2\cos^2\Theta-1](\cos\Theta\sin\Theta)\varpi r^3+\chi\cdot(F_\Theta^{ae})_i \tag{9}$$

The foregoing expressions for the aerodynamic forces were given in Eqs. (31), (35) and (37), all in Part I, and can be written in terms of either the polar variables of the flow field (A and η); the polar variables of the rotordynamic model (r and Θ); or, a combination of these. This can be achieved using known relations such as $a=A\cos\eta$, $b=A\sin\eta$, $\dot{a}=\dot{A}\cos\eta-A\dot{\eta}\sin\eta$, and $\dot{b}=\dot{A}\sin\eta+A\dot{\eta}\cos\eta$. Finally the aerodynamic forces in the two coordinate systems are related through $F_r=F_X\cos\Theta+F_Y\sin\Theta$ and $F_\Theta=-F_X\sin\Theta+F_Y\cos\Theta$.

Examining the equations of the overall model, a few observations can be made regarding the nature of the aerodynamic-rotordynamic coupling and the main parameters governing it.

This model is an eighth order nonlinear dynamic description of the coupled compression system, which can be written in a state space form, with (Q,P) as the global compression system flow states; (a,b) or (A,η) as the compressor local flow nonuniformity states; and, $(X,\dot{X},Y,\dot{Y})$ or $(r,\dot{r},\Theta,\dot{\Theta})$ as the rotordynamic states. Furthermore, the functional dependency of the first compressor integrated characteristic, $\overline{\psi}_c^C(Q,a,b)$, and the throttle characteristic, $Q_T(P)$, on these state variables reveals that the surge dynamics are only indirectly coupled to the rotordynamics (X,Y) through the flow nonuniformity (a,b), Eqs. (5) and (6), Part I. On the other hand, the flow nonuniformity (a,b) is directly coupled to both the compression system operating point (Q,P) and the rotor position (X,Y), Eqs. (7) and (8), or (9) and (10), Part I. Finally, the dynamics of the rotor depend on both the flow nonuniformity (a,b) and the compression system operating point (Q,P) through the aerodynamic forces, $F^{ae}(Q,a,b,\dot{a},\dot{b})$, Eqs. (32), (35), and (37), Part I.

It is also recalled that two main governing parameters that emerged naturally from consistent nondimensionalization of system equations may also be identified. The influence of rotor position on the flow field is governed mainly by the nondimensional sensitivity parameter $\psi_{c\varepsilon}=-\partial\psi_c/\partial_\varepsilon$, while the influence of the flow field on the dynamics of the rotor is controlled by the nondimensional coupling parameters χ, which was defined in Eq. (20) of Part I as

$$\chi=\frac{N_{st}\rho(2\pi Rhl_Z)}{N_{st}M_{st}}=\frac{\text{fluid mass within CV}}{\text{rotating assembly mass}} \tag{10}$$

and which appeared as a weighting factor in front of the aerodynamic force terms in the rotordynamic equations. Typical values of χ are estimated for several low speed multistage axial compressors and found to range from 5×10^{-5} to 5×10^{-4}, while for a single stage axial liquid pump χ is found to be on the order of 10^{-2}.

3 Coupling Impact on Linear System Stability

3.1 Equilibrium Solutions. The linearized stability of the coupled system model about an equilibrium state is now examined for various values of coupling parameters (i.e., $\psi_{c\varepsilon}$, χ) as well as other system parameters (e.g., γ, B and ν). Such a stability investigation requires a linearization of the system equations which follows a standard Taylor series expansion about an equilibrium point (indicated by the subscript $_e$), and involves the evaluation of the Jacobian matrix of this model.

By examining the system equations, it can be seen that a simple equilibrium[3]—in which all the time derivative terms vanish—can exist only when the flow field is uniform and all forces on the rotor being balanced when it sits exactly in the center of the casing. This simply corresponds to an almost trivial equilibrium point where only (Q_e,P_e) are nonzero. In this case, determining (Q_e,P_e) that correspond to some throttling coefficient γ_e requires the solution of the following two simultaneous algebraic equations:

$$0=\overline{\psi}_c^C(Q_e,a_e=0,b_e=0)-P_e \tag{11}$$

$$0=Q_e-\gamma_e\sqrt{P_e} \tag{12}$$

It should be noted that even for more complicated equilibrium points (e.g., off-centered rotor) it is far more convenient and intuitive to use the equilibrium point flow coefficient Q_e as a control parameter instead of the throttling coefficient γ_e. For instance, $Q_e=1.0$ is the point of peak pressure rise on the compressor characteristic, while $Q_e=1.2$ is a good choice for a typical design operating point, allowing a 20% nominal stability margin. The equilibrium point for a centered rotor are then determined as follows. The desired compressor operating point about which the stability is to be assessed is chosen by selecting a value of Q_e. Equation (11) then gives P_e by direct substitution, while Eq. (12) can be easily solved for $\gamma_e=Q_e/\sqrt{P_e}$.

3.2 Stability Bounds of the Coupled System. Having determined the equilibrium, the stability of the coupled system may now be examined by computing the eigenvalues and eigenvectors of the linearized model in order to determine the stable and unstable regions in its multi-dimensional parameter space defined by the nondimensional parameters Q_e, χ, $\psi_{c\varepsilon}$ and ν. It should be noted first that varying the system stability parameter, B, has no effect on the stability boundary of the coupled system presented below. The reason is that the B-parameter is known to be mostly influential in determining the post-instability behavior of the system. In particular, large values of the B-parameter ($B\sim1$) are typically associated with surge while small values ($B\sim0.1$) are associated with rotating stall.

General Features of Stability Bounds. Figure 3 depicts the stability boundary in the (Q_e,χ) parameter space for a hypotheti-

[3]Another type of equilibrium points that is not presented here corresponds to the case where the rotor is not centered in the casing, but rather is deflected under the effect of some additional constant force (e.g., gravity). Finding the fixed points in such a case is more involved as it requires (in principle) the solution of eight simultaneous nonlinear algebraic equations.

Downloaded 31 May 2010 to 171.66.16.27. Redistribution subject to ASME license or copyright; see http://www.asme.org/terms/Terms_Use.cfm

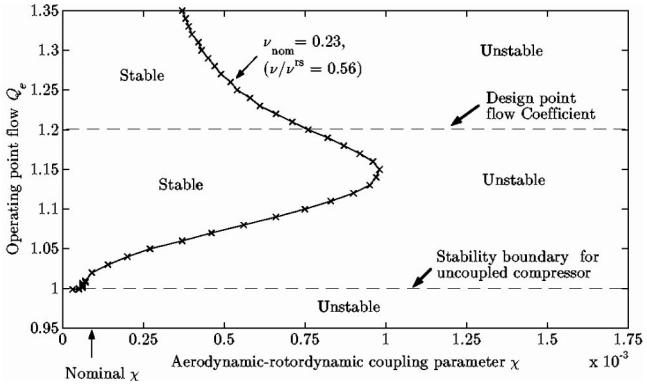

Fig. 3 Coupled system linear stability boundary in the $Q_e-\chi$ parameter space for a centered rotor equilibrium, all parameters at nominal values

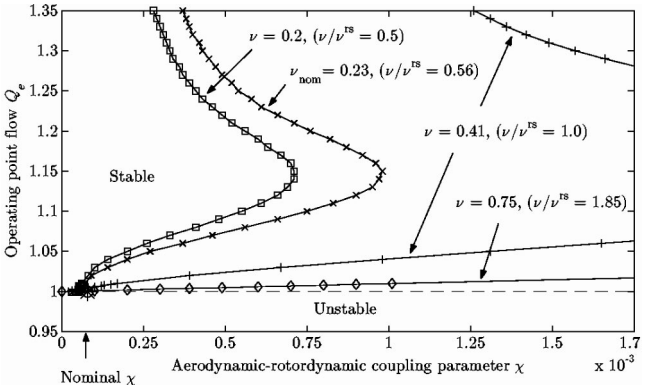

Fig. 4 Effect of rotor's natural frequency (ν) on the coupled system linear stability boundary for a centered rotor equilibrium, all other parameters at nominal values

cal 9-stage low speed compressor,[4] referred to here as C2. The unstable region in this case is that below and to the right of the solid line. In contrast to the uncoupled compressor which, according to the Moore-Greitzer model, loses stability (typically in the form of rotating stall) at the peak of the characteristic ($Q_e \leqslant 1$), the stability of the coupled system is shown to be degraded in that the onset of instability is encountered at operating points with a higher flow coefficient Q_e. This means that on a compressor map, the stability boundary of this coupled system would lie to the right of the peak of the characteristic, hence, reducing the stability margin. For instance, for values of $\chi = 2.5\times10^{-4}$ and 5×10^{-4}, a reduction of the flow coefficient by throttling, say from the design point at $Q_e = 1.2$, takes the system into instability at $Q_e = 1.05$ and 1.08, respectively, a reduction of 5 and 8% in the stability margin predicted for the uncoupled compressor. For higher values of χ, the stability margin is further reduced until a critical value is reached around $\chi = 1\times10^{-3}$, at which the system becomes unstable for all operating points Q_e. Furthermore, it is observed that there exists a range of values of χ below the critical (in the range $3\times10^{-4} < \chi < 1\times10^{-3}$), for which instability may be encountered at flow coefficients *higher* than the design point. For example, at a value of $\chi = 5\times10^{-4}$, instability is encountered at $Q_e = 1.27$, giving a stability margin of only 7% in flow coefficient to the right of the design point on the compressor map.

Effect of Rotor's Natural Frequency, ν. The effect of the rotor's natural frequency ν on this stability boundary is depicted in Fig. 4 which shows the boundaries corresponding to three values of ν in addition to that shown in the previous figure. These values are selected as follows: $\nu = 0.2$ represents the highly supercritical rotor; $\nu = \nu^{rs}$ represents the case where the aerodynamic and rotordynamic uncoupled and undamped natural frequencies match; $\nu = 0.75$ represents the case of moderately supercritical rotor; and, finally, $\nu = \nu_{nom}$ is the nominal case. In all these cases, the unstable region remains below and to the right of any of the solid lines. It can be seen from the figure that higher values of ν (e.g., corresponding to a stiffer rotor) have a larger stable region. For the cases with high enough ν (usually in subcritical range), the adverse effect of coupling is greatly reduced and the stability is closer to the uncoupled system. The stability boundary in such a case has only one branch that can be observed within this realistic range of flow coefficients. Also shown in the figure are the ratio of ν to ν^{rs} from which the closeness of these two frequencies can be inferred; a ratio which determines some aspects of the stability of this coupled system.

Effect of Tip Clearance Sensitivity, $\psi_{c\varepsilon}$. The effect of the second coupling parameter, namely the compressor sensitivity to tip clearance $\psi_{c\varepsilon}$, is depicted in Fig. 5 which shows the stability boundary for three different values of $\psi_{c\varepsilon}$. The less sensitive the compressor is to tip clearance the larger the stability margin for any given χ. This points towards the similar effect that the two coupling parameters $\psi_{c\varepsilon}$ and χ have, which is later exploited by combining the two coupling parameters into one.

3.3 Stability in the Design Parameter Space. An alternative way to view the stability results is to consider the parameter space χ versus ν. In such a space, a stability boundary may be constructed for each value of equilibrium flow coefficient Q_e, which splits the space into a stable and unstable parameter combinations (χ,ν). This view serves to elucidate how the stability of the system is affected as these two design parameters are changed.

Recalling that the effect of compressor sensitivity to tip clearance on stability, shown in Fig. 5, suggests that the two coupling parameters $\psi_{c\varepsilon}$ and χ influence the stability of the coupled system in a similar manner, and looking back at the system equations, it may be noted that a rescaling can be adopted such that only the product of these two parameters appear. In particular, rescaling the

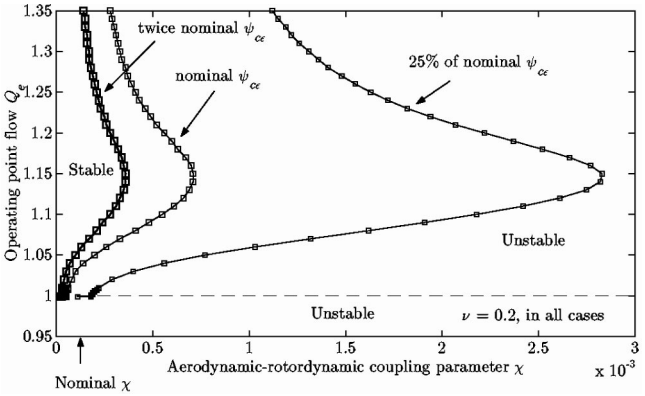

Fig. 5 Effect of compressor tip clearance sensitivity on linear stability boundary of the coupled system for a centered rotor equilibrium, three values of $\psi_{c\varepsilon}$, ν=0.2, all other parameters at nominal values

[4]This hypothetical compressor may be thought of as being the same as the MIT 3-stage compressor (introduced in Part I), except with more identical stages stacked together to represent a high pressure ratio compressor. Important parameters, namely S, λ and μ, are three times those of the MIT 3-stage compressor, and so is the effective total duct length, $\mathcal{L}$. As a result, the rotor axial span is now roughly three times as long yielding a supercritical rotor with ν=0.23. The consideration of such a compressor is motivated by the findings of Graf et al. [6]) who suggested that the higher curvature of the compressor pressure-rise characteristic can exacerbate the destabilizing effect of tip-clearance asymmetry. In addition, the high pressure-rise compressor and the supercritical rotor make this system a closer representation of a modern compressor.

Downloaded 31 May 2010 to 171.66.16.27. Redistribution subject to ASME license or copyright; see http://www.asme.org/terms/Terms_Use.cfm

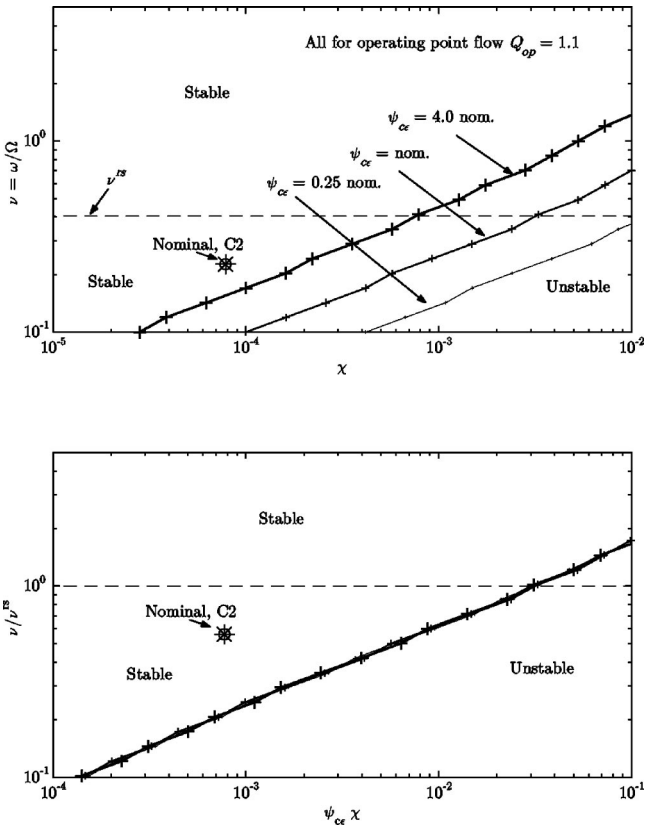

Fig. 6 Linear stability in the design parameter space: combining the two coupling parameters as $\psi_{c\varepsilon}\chi$, for compressor C2, all other parameters are at nominal values

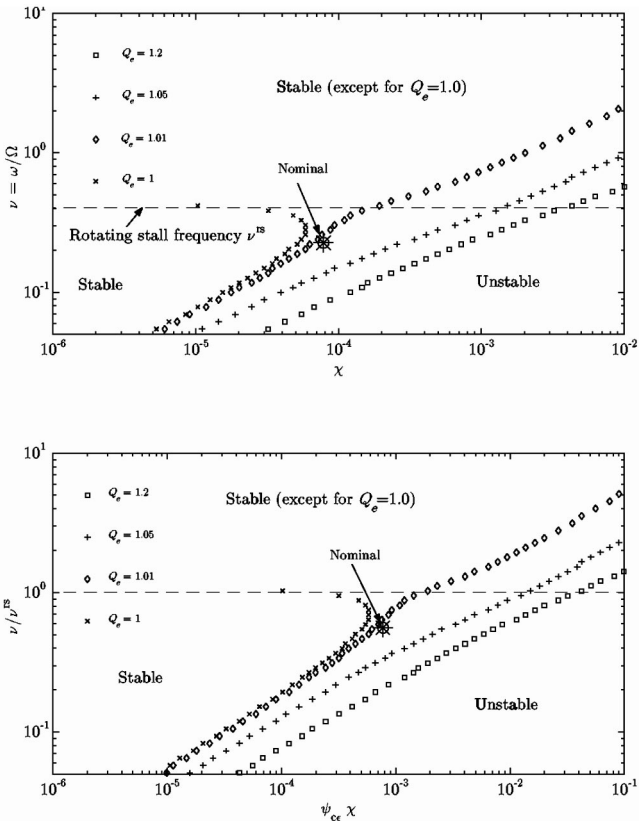

Fig. 7 Linear stability in the design parameter space: compressor C2, for four different operating flow coefficients. All other parameters are at their nominal values

rotor displacement variables X and Y with χ causes the latter to disappear from the rotordynamic equations and appear instead in the equations of $\dot{a}$ and $\dot{b}$ as the product $\psi_{c\varepsilon}\chi$. This reduction in coupling parameters is captured in Fig. 6, where the stability boundaries due to different values of tip clearance sensitivity in the top sub-plot (all corresponding to one value of Q_e) collapse onto one boundary in the reduced parameter space in the bottom subplot.

Figure 7 depicts the stability results for the same 9-stage compressor in the design parameter space (χ,ν), for different values of Q_e and nominal $\psi_{c\varepsilon}$. Each line in these figures corresponds to an operating point flow coefficient Q_e and divides the plane into a stable and unstable regions; the unstable region being that below and to the right of these lines (except for $Q_e=1.0$ where the stable region is confined to the lower left corner of the plane). The use of the ratio $\nu/\nu^{rs}=\omega/\omega^{rs}$—which does not depend on the rotor spinning speed Ω—as the other parameter combination in the bottom sub-plots of these figures is motivated by the following observation. In the two figures above, as well as in similar calculations for additional compression systems [38], it is observed that, except for $Q_e=1$, the stability boundary changes monotonically with ν for all flow coefficients $Q_e>1$ (i.e., to the right of the characteristic peak). For $Q_e=1$, on the other hand, the boundary for rotors with $\nu/\nu^{rs}>1$ is different that for those with $\nu/\nu^{rs}<1$. The difference is that the former type are unstable at $Q_e=1$ regardless of the value χ, while the later may be stable or unstable depending on χ. Further, this difference in the stability at $Q_e=1.0$ does not amount to a significant gain in overall stability margin, but it may be shown to reflect whether the aerodynamic or the rotordynamic mode becomes unstable first as the peak of the compressor characteristic ($Q_e=1.0$) is crossed.

A Note on Modes of Instability. For an uncoupled compressor with a low B parameter, the dominant mode of instability encountered as the compressor is throttled to flow coefficients $Q_e<1$ is known to be rotating stall. It is of interest to determine whether the dominant mode of instability for the coupled system is different as it loses stability at either end of the stability margin. To answer this question, the mode of instability may be predicted by identifying the first pair of eigenvalues to cross the imaginary axis as the coupled system loses stability. The structure of the corresponding eigenmode can then shed some light on whether the instability originates as an aerodynamic, a rotordynamic or a mixed type. Carrying out such an exercise for the compressor at hand reveals that the type of instability first encountered at both bounds is mostly rotordynamic. However, when crossing the bound to the left of the design point, the aerodynamic (rotating stall) mode is only marginally stable, and is therefore expected to develop into full rotating stall soon after the inception of any instability. The eventual mode of instability as the response grow beyond the linear approximation can not be determined except through examining the original nonlinear model as presented in the forthcoming.

3.4 Summary of Coupled System Linear Stability. The parametric studies presented conducted using this model establish the significance of the interaction between aerodynamics and rotordynamic in determining the overall coupled system stability. The main results are summarized in the following points, and are shown schematically in Fig. 8.

- The coupling changes the nature of overall stability picture in that it creates a stability margin with two bounds, one on each side of the design operating point.

Downloaded 31 May 2010 to 171.66.16.27. Redistribution subject to ASME license or copyright; see http://www.asme.org/terms/Terms_Use.cfm

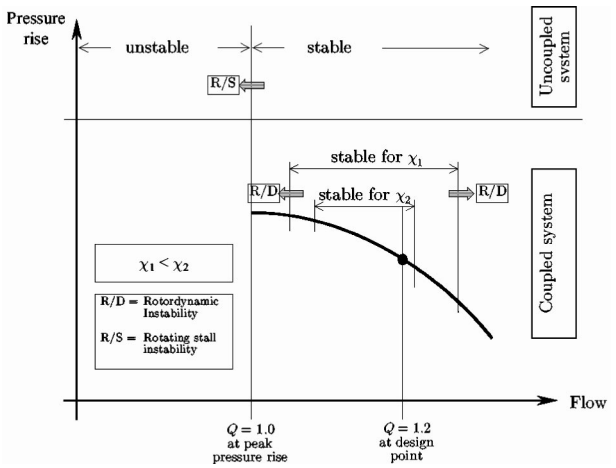

Fig. 8 Schematic depiction of stability boundaries on the compressor map

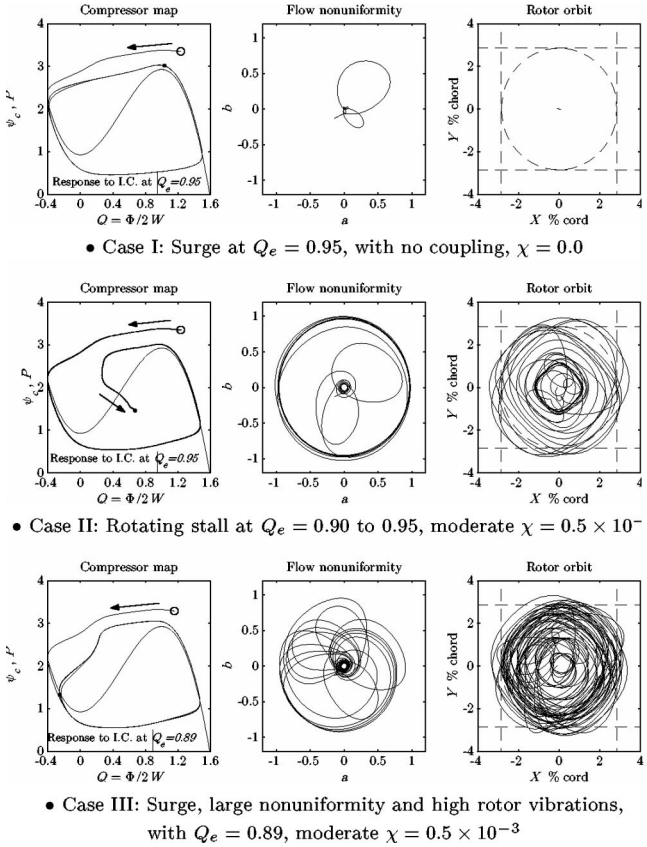

Fig. 9 Demonstration of how coupling alters post-instability behavior: response to initial conditions, ν=0.44 (25% of nominal), and B=1.0

- As the coupling is increased, these two bounds move closer to the design point resulting in a smaller stable operating range.
- Locally, the mode that loses stability upon crossing either of the two boundaries is mostly rotordynamic (except when the rotor's natural frequency is very high and the coupling impact is minimal). Nevertheless, rotating stall is still expected to appear soon after crossing the low flow boundary as the growing rotordynamic instability promotes larger flow nonuniformity. This, however, cannot be shown from the linearized analysis, and requires examining the post-instability behavior of the system.
- Highly supercritical rotors tend to be more susceptible to fluid-induced instabilities. This is confirmed by the above results and is consistent with common observations. Further, a variation of the rotor's natural frequency from supercritical to subcritical stabilizes the rotor and thus reduces the overall destabilizing effect of the coupling. This variation takes place gradually except in the neighborhood of the rotating stall frequency and for operating points close to the peak of the characteristic. In such cases, rotors with $\nu/\nu^{rs}<1$ tend to retain their stability only for a very small further reduction in flow coefficient.
- For the class of compression systems that are well described by the current model, a design parameter space is identified in which the effects of all the relevant system parameters are captured, and in which the stability boundaries for any compressor in this class are roughly the same. This parameter space is defined by the ratio of rotordynamic to aerodynamic uncoupled frequencies, ν/ν^{rs} on one hand and the product of the two coupling parameters, $\psi_{c\varepsilon}\chi$, on the other, with the operating point Q_e as the third parameter.

4 Post-Instability Nonlinear Behavior

A numerical survey of the nonlinear post-instability behavior of the coupled system model is conducted in order to explore and demonstrate the different post-instability behavior as the stability bound identified above are crossed. It is confirmed by means of numerous numerical simulations (not shown) that the instability is mostly rotordynamic (forward whirl in the cases simulated) right after the bounds are crossed. However, for the bound to the left of the design point (i.e., at low Q_e), aerodynamic instability soon takes over upon any further throttling.

The B-parameter dependence of the nonlinear behavior is generally the same as the uncoupled case: rotating stall and surge are encountered for low and high values of B, respectively; but in contrast to the uncoupled compression system, the simulations show that the coupling may favor rotating stall over surge even with large values of B that are known to be associated with surge only. For instance, a set of three simulations (each occupying one row of subplots) is shown in Fig. 9 depicting the response of the MIT 3-stage compressor to initial conditions. The rotor natural frequency is taken to be in the supercritical range (ν=0.44, 25% of the nominal value) and a large value of $B=1.0$ is used such that the dominant mode of instability for an uncoupled system would be surge. The first simulation assumes no coupling (i.e., χ=0.0) and is at $Q_e=0.95$; an operating point to the left of the characteristic peak, where the system is known to be unstable. As expected, the system displays a surge instability with sustained oscillations in axisymmetric flow and pressure dominanting. The second simulation shows the system response in an identical situation except for the introduction of coupling by setting $\chi=0.5\times10^{-3}$. In this case, the system response exhibits one surge-like cycle (due to the large initial conditions) but goes into rotating stall as the ultimate form of post-instability behavior. Equilibrium points further to the left show the same change in behavior until the point $Q_e=0.9$ is reached. Any further throttling, as shown in the third simulation at $Q_e=0.89$, gives rise to sustained surge oscillations that are slightly modified due to the interaction with the flow nonuniformity and rotor vibrations, both of which are present and large in this case. This tendency to favor rotating stall in regions typically dominated by surge may be due to the large rotordynamic oscillations, which directly produce rotating stall-like circumferential flow nonuniformities. The existence of such large nonuniformities in the flow field prior to the full development of the aerodynamic instability seems to expand the domain of attraction of rotating stall as the dominant mode of instability over a wider range of operating conditions.

Another impact of the coupling on the post-instability behavior

Downloaded 31 May 2010 to 171.66.16.27. Redistribution subject to ASME license or copyright; see http://www.asme.org/terms/Terms_Use.cfm

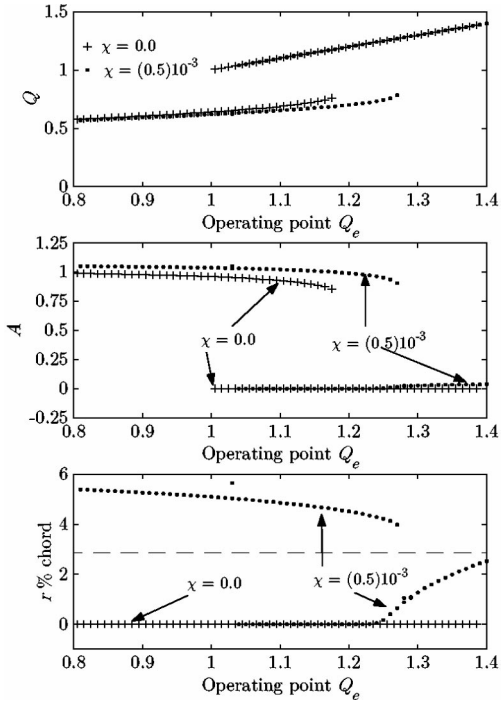

Fig. 10 Bifurcation map comparing χ=0.0 and 0.5×10^{-3}, with nominal ν=0.23, and low B=0.1

may be demonstrated by constructing a bifurcation map for the 9-stage compression system (C2) introduced earlier, with low $B=0.1$ and nominal $\nu=0.23$. Figure 10 shows a set of such maps in terms of Q, A, and r, for two cases: one with no coupling ($\chi=0.0$) and one with moderate coupling ($\chi=0.5\times10^{-3}$). It can be seen from the figure that the bifurcation in both cases is of the same subcritical type, which is considered more harmful due to the hysteresis in recovering from the limit cycle as the compressor throttling is decreased (operating point moved to the right). Comparing the two cases in the figure also reveals that not only does the coupling reduces the stability margin (as predicted by the linearized analysis), but it also increases the hysteresis of the subcritical bifurcation by about 2% as compared to the hysteresis of the uncoupled system. Furthermore, for large enough disturbances the coupling renders this compression system unstable over the whole operating range. In other words, because a limit cycle exists for every value of Q_e (most clearly seen in the third subplot of r), it is conceivable that one could enter either rotating stall or whirl due to a large disturbance, and not be able to recover the system to a nonoscillating equilibrium by choice of mass flow. This severe condition could indeed be detrimental to the operation of the compressor.

5 Conclusions

A first-principles, reduced-order integrated model of aerodynamic-rotordynamic interactions in axial compression systems has been developed by consolidating a single-harmonic, two-dimensional version of the Moore-Greitzer model that describes the flow field and a simple, mass-spring-damper Jeffcott-type model of the rotor that describes the rotordynamics. The coupling between the fluid and structural dynamics is captured by a linear compressor sensitivity to tip clearance, and a momentum-based model of the aerodynamic forces on the rotor. Careful nondimensionalization of the overall model gave rise to a set of parameters that govern the system behavior. Two main coupling parameters, each of which governs the influence of one domain on the other, are the nondimensional sensitivity of the compressor pressure-rise characteristic to tip clearance, which describes the rotordynamic influence on aerodynamics, and the ratio of fluid mass to the rotor solid mass, which describes the aerodynamic influence on rotordynamics.

Using a linearized version of the model, the stability of the coupled system was examined through a comprehensive set of parametric studies. In doing so, the regions in the parameter space where coupling has the most effect were determined. Light was also shed on the nature of the different types of instabilities that may be encountered as the stability boundaries are crossed. To that end, it was found that for moderate values of the main coupling parameters, the coupling generally has an adverse effect in that the stability margin for the coupled system is smaller (by 5% to 10%) than that of the uncoupled compressor, with this adverse effect being most pronounced for supercritical rotors. In addition, the system displays another instability of the rotordynamic type (forward whirl in cases examined here) at operating points higher than design point.

Highlights from a numerical survey of the nonlinear post-instability behavior of the coupled system were presented including important effects such as the domination of rotating stall for operating conditions where surge would normally be dominant for an uncoupled compressor, and the possible loss of stability over the whole operating range for large disturbances. These aspects of the post-instability behavior suggest a rich dynamic character and can thus be the basis for future research.

Acknowledgment

The authors would like to thank Professor Zoltan Spakovszky and Dr. Fredrich Ehrich for many useful ideas and discussions, and for making available their analytical and experimental expertise in the area of fluid-induced forces. The valuable guidance and support of Professors Kamal Youcef-Toumi and Alan H. Epstein are also acknowledged and appreciated.

This work was partially supported by the Saudi Arabian Oil Company (Saudi Aramco). It was also partially supported by AFOSR Grant F-49620-92-J-0409, Dr. Marc Jacobs, Technical Monitor.

Nomenclature

$\mathcal{A}$, A = area, amplitude of flow nonuniformity
a, b = Cartesian components of flow nonuniformity
B = system stability parameter, $B=U/2a_s\sqrt{\mathcal{V}/\mathcal{AL}}$
C2 = hypothetical 9-stage low-speed axial compression system
c = rotordynamic damping coefficient
e = rotor's center of mass eccentricity
F, $(F)_i$ = force, per-stage force
H, W = pressure-rise characteristic parameters
$\mathbf{i}$, $\mathbf{j}$, $\mathbf{k}$ = unit vectors
k = rotordynamic stiffness constant
$\mathcal{L}$ = total effective duct length
M, M_{st} = total, per-stage rotor mass
N_{st} = no. of compressor stages
P = rescaled pressure-rise coefficient, $P=\Psi/H$
Q, q = rescaled flow coefficient; $Q=\Phi/2W$, $q=\phi/2W$
R, r = mean annular radius, rotor radial displacement
S = pressure-rise characteristic aspect ratio, $S=H/W$
U = mean rotor speed
X, Y = Cartesian rotor displacements in inertial frame
α, β = absolute and relative flow angles
γ = nondimensional throttle coefficient
ε = tip clearance
ζ = damping coefficient
η = phase angle of flow field nonuniformity
Θ, θ = angular (whirl) displacement of rotor center, circumferential coordinate
λ, μ = compressor inertia parameters
ν = rotor natural frequency, fraction of Ω, ($\nu=\omega/\Omega$)

Downloaded 31 May 2010 to 171.66.16.27. Redistribution subject to ASME license or copyright; see http://www.asme.org/terms/Terms_Use.cfm

$\nu^{rs,wh}$ = rotating stall, whirl frequencies, all fraction of Ω
ξ = nondimensional time
ϖ = nonlinear rotor stiffness coefficient (nondim.)
Φ, ϕ = annulus-averaged, total axial compressor flow coefficient
χ = aerodynamic-rotordynamic coupling parameter
ψ_c = total-to-static pressure-rise characteristic
$\psi_{c\varepsilon}$ = sensitivity of pressure-rise characteristic to tip-clearance, $\psi_{c\varepsilon} = -\partial\psi_c/\partial\varepsilon$
Ω = rotor rotational (spin) frequency ($\Omega = U/R$)
$(\cdot)^{da,st,ns}$ = reference to damping, linear stiffness, and nonlinear stiffness forces
$(\cdot)^{rs}$ = reference to rotating stall
$(\cdot)^{tu,un,pr}$ = reference to turning, unsteady and pressure force contributions
$(\cdot)_e$ = value of quantity at an equilibrium point
$\overline{(\cdot)}$ = averaged quantity

References

[1] Greitzer, E. M., 1976, "Surge and Rotating Stall in Axial Flow Compressors, Part I. Theoretical Compression System Model, Part II. Experimental Results and Comparison With Theory," ASME Eng. Power, **98**(2), Apr., pp. 190–217.
[2] Moore, F. K., 1984, "A Theory of Rotating Stall of Multistage Axial Compressors: Part I. Small Disturbances; Part II. Finite Disturbances; Part III. Limit Cycles," ASME J. Eng. Gas Turbines Power, **106**, pp. 313–336.
[3] Moore, F. K., and Greitzer, E. M., 1986, "A Theory of Post-Stall Transients in Axial Compression Systems: Part I—Development of Equations," ASME J. Eng. Gas Turbines Power, **108**, Jan., pp. 68–76.
[4] Greitzer, E. M., and Moore, F. K., 1986, "A Theory of Post-Stall Transients in Axial Compression Systems: Part II—Application," ASME J. Eng. Gas Turbines Power, **108**, April, pp. 231–239.
[5] Hynes, T. P., and Greitzer, E. M., 1987, "A Method for Assessing Effects of Circumferential Flow Distortion on Compressor Stability," ASME J. Turbomach., **109**, July, pp. 371–379.
[6] Graf, M. B., Wong, T. S., Greitzer, E. M., Marble, F. E., Tan, C. S., Shin, H.-W., and Wisler, D. C., 1997, "Effects of Nonaxisymmetric Tip Clearance on Axial Compressor Performance and Stability," Technical Report 228, Massachusetts Institute of Technology, Gas Turbine Lab Report.
[7] Gordon, K., 1999, *Three-Dimensional Rotating Stall Inception and Effects of Rotating Tip Clearance Asymmetry in Axial Compressors*, Ph.D. thesis, Massachusetts Institute of Technology.
[8] Smith, L. H., 1958, "The Effect of Tip Clearance on the Peak Pressure Rise of Axial-Flow Fans and Compressors," *ASME Symposium on Stall*, pages 149–152.
[9] Baghdadi, S., 1995, "Modeling Tip Clearance Effects in Multi-Stage Axial Compressors," ASME Paper 95-GT-291.
[10] Storer, J. A., and Cumpsty, N. A., 1993, "An Approximate Analysis and Prediction Method for Tip Clearance Loss in Axial Compressors," ASME Paper 93-GT-140.
[11] Horlock, J. H., and Greitzer, E. M., 1983, "Non-Uniform Flows in Axial Compressors Due to Tip Clearance Variation," IMechE, Proc. Mech. Instr. Engrs., **197C**, pp. 173–178.
[12] Thomas, H. J., 1958, "Unstable Natural Vibration of Turbine Rotors Induced by the Clearance Flow in Glands and Blading," Bull. De l'A.I.M., **71**(11/12), pp. 1039–1063.
[13] Alford, J., 1965, "Protecting Turbomachinery From Self-Excited Rotor Whirl," ASME J. Eng. Power, Oct., pp. 333–344.
[14] Vance, J. M., and Laudadio, F. J., 1984, "Experimental Measurements of Alford's Force in Axial Flow Turbomachinery," ASME J. Eng. Gas Turbines Power, **106**, July, pp. 585–590.
[15] Colding-Jorgensen, J., 1992, "Prediction of Rotor Dynamic Destabilizing Forces in Axial Flow Compressors," ASME J. Fluids Eng., **114**, Dec., pp. 621–625.
[16] Ehrich, F., 1993, "Rotor Whirl Forces Induced by the Tip Clearance Effect in Axial Flow Compressors," J. Vibr. Acoust., **115**, October, pp. 509–515.
[17] Childs, D., 1993, *Turbomachinery Rotordynamics, Phenomena, Modeling & Analysis*, John Wiley, New York.
[18] Litang, Y., Jie, H., Qihan, L., Zigen, Z., and Fuan, Z., 1994, "Blade Tip Destabilizing Forces and Instability Analysis for Axial Rotors of Compressor," Proc. Asian-Pacific Conference on Aerospace Technology and Science, 1st, Hangzhou, China, Accession No. A95-40315, Oct.
[19] Spakovszky, Z. S., 2000, "Analysis of Aerodynamically Induced Whirling Forces in Axial Flow Compressors," ASME-IGTI Paper 2000-GT-0418.
[20] Song, S. J., and Cho, S. H., 2000, "Non-Uniform Flow in a Compressor Due to Asymmetric Tip Clearance," ASME-IGTI Paper 2000-GT-0416.
[21] Storace, A. F., Wisler, D. C., Shin, H.-W., Beacher, B. F., Ehrich, F. F., Spakovszky, Z. S., Martinez-Sanchez, M., and Song, S. J., 2000, "Unsteady Flow and Whirl-Inducing Forces in Axial-Flow Compressors. Part I—Experiment," ASME-IGTI Paper 2000-GT-0565.
[22] Ehrich, F. F., Spakovszky, Z. S., Martinez-Sanchez, M., Song, S. J., Wisler, D. C., Storace, A. F., Shin, H.-W., and Beacher, B. F., 2000, "Unsteady Flow and Whirl-Inducing Forces in Axial-Flow Compressors. Part II—Analysis," ASME-IGTI Paper 2000-GT-0566.
[23] Akin, J. T., Fehr, V. S., and Evans, D. L., 1988, "Analysis and Solution of the Rotor Instability Problem in the Advanced Model TF30 P111+Engine," AIAA J.
[24] Storace, A. F., 1990, "A Simplified Method of Predicting the Stability of Aerodynamically Excited Turbomachinery," Proc. 6th workshop on rotordynamic instability problems in high performance turbomachinery, Texas A&M.
[25] Weigl, H. J., 1997, *Active Stabilization of Rotating Stall and Surge in a Transonic Single Stage Axial Compressor*, Ph.D. thesis, Massachusetts Institute of Technology.
[26] Ehrich, F., 1997–2000, Massachusetts Institute of Technology, Gas Turbine Lab, personal communication.
[27] Epstein, A. H., Ffowcs Williams, J. E., and Greitzer, E. M., 1989, "Active Suppression of Aerodynamic Instabilities in Turbomachines," Am. J. Hum. Genet., **5**, pp. 204–211.
[28] Paduano, J. D., Greitzer, E. M., Epstein, A. H., Guenette, G. R., Gysling, D. L., Haynes, J., Hendricks, G. J., Simon, J. S., and Valvani, L., 1993, "Smart Engines: Concepts and Application," *Integrated Computer-Aided Engineering*, pp. 3–28.
[29] Spakovszky, Z. S., 2000, *Applications of Axial and Radial Compressor Dynamic System Modeling*, Ph.D. thesis, Massachusetts Institute of Technology.
[30] Abed, E., Houpt, P. K., and Hosny, W. M., 1993, "Bifurcation Analysis of Surge and Otating Stall in Axial Flow Compressors," ASME J. Turbomach., **115**, Oct., pp. 817–824.
[31] McCaughan, F., 1989, "Application of Bifurcation Theory to Axial Flow Compressor Instability," ASME J. Turbomach., **111**, Oct., pp. 426–433.
[32] Nayfeh, M., 1999, *Bifurcation Control of Stall and Surge in Aeroengine Compression Systems*, Ph.D. thesis, University of Maryland.
[33] Wang, Y., Paduano, J. D., and Murray, R. M., 1999, "Nonlinear Control Design for Rotating Stall With Magnetic Bearing Actuators," Conference on Control Applications, Honolulu.
[34] Jeffcott, H., 1919, "The Lateral Vibration of Loaded Shafts in the Neighborhood of a Whirling Speed—The Effect of Want of Balance," Philosophical Mag. J. Science, pp. 304–314.
[35] Den Hartog, J. P., 1985, *Mechanical Vibration*, Dover Publications Inc.
[36] Crandall, S., 1983, "The Physical Nature of Rotor Instability Mechanisms," *Applied Mechanics Division, ASME*, 55:1–18, June. The Applied Mechanics, Bioengineering, and Fluids Engineering Conference, Houston, TX.
[37] Ehrich, F., 1992, *Handbook of Rotordynamics*, McGraw-Hill Inc., New York.
[38] Al-Nahwi, A. A., 2000, *Aerodynamic-Rotordynamic Interaction in Axial Compression Systems*, Ph.D. thesis, Massachusetts Institute of Technology.
[39] Ehrich, F., 1995, "Nonlinear Phenomena in Dynamic Response of Rotors in Anisotropic Mounting Systems," *Special 50th Anniversary Design Issue*, Trans. ASME, **117**, June, pp. 154–161.

Downloaded 31 May 2010 to 171.66.16.27. Redistribution subject to ASME license or copyright; see http://www.asme.org/terms/Terms_Use.cfm

Assessing Viscous Body Forces for Unsteady Calculations

L. Xu
Whittle Laboratory,
University of Cambridge,
Cambridge, UK

A strategy has been developed to model the three-dimensional unsteady flows through turbomachines subject to nonaxisymmetric flow/geometrical conditions such as low order distortions with relatively long length-scale unsteadiness, by modeling the viscous effects as local source terms for a coarse computational mesh, but not calculating them directly. In general full annulus multi-row calculations are required for such flows, but currently the computational resources are devoted to resolving detailed viscous flow very close to the walls, which in some cases is not the center of concern. By avoiding resolving detailed viscous effects the model can accelerate the calculation by at least two orders of magnitude. The method has been illustrated to be able to resolve disturbances down to the blade passing frequency and give good estimates of overall unsteady blade forces due to blade row interactions. Obviously, the correct modeling of the viscous body force as source terms in the governing equations is the key for accuracy of such calculations. Different ways of constructing/approximating the viscous body force term are discussed and their adequacy in unsteady flow calculations is assessed. It is found that in general the viscous force is relatively small compared to the total blade force, even smaller the unsteady fluctuation of the viscous force and a simple drag coefficient model is quite adequate to model both time mean and dynamic viscous effects. However, for the cases when separations are present variations in the drag coefficient may become large and more detailed modeling may be required. [DOI: 10.1115/1.1574823]

Keywords: Unsteady Flow Model, Viscous Body Force

Introduction

Time accurate numerical simulations of flows in turbomachinery face a fundamental dilemma that originates from the wide span of length (as well as time) scales of the fluid dynamics. On one hand, long length scale unsteadiness such as those caused by low order distortions or by nonaxisymmetrical structures, requires the CFD to be able to resolve engine order (once per revolution) scales, in the order of meters. Yet on the other extreme the CFD also needs to resolve small scales down to sub-boundary layer scale in order to correctly estimate the viscous effects, the length scale can be particularly small, down to the order of tens of microns for high Reynolds numbers. During its transient operation various time and length scale disturbances would also be present in a turbomachine. However, it is the need of resolving the smallest scale that sets the practical limits on the mesh size, time step length thus overall computer resources, and this is particularly true for an explicit CFD scheme. Typically, an explicit Reynolds-averaged N-S (RANS) calculation would have no problem in resolving any unsteadiness up to 10 MHz due to the fine mesh used in near wall regions; but this also means for disturbances with time scales five to six orders of magnitude higher, the high demand on the computer resources is not only for the memory but also for the CPU time. For example, recent work by Unno et al. [1] on a simulation of fan-OGV-pylon configuration used about 50 million grid points on a massively parallel (166 CPUs) computer. Certainly such calculations cannot be run routinely for design purposes. By implementing phase-lagged boundary conditions (e.g., Giles [2], He [3], and Li and He [4,5]), it is possible to avoid full annulus multi-passage unsteady calculation, instead, only a single passage calculation is needed. This can save up to two orders of magnitude of the computer resources, mainly in memory; but with problems where a large range of disturbance scales are present, or as the number of blade rows increases, massive computational resource is still required.

Historically lower dimension models, which rely heavily upon empiricism, have been used for problems with long length scale disturbances such as those associated with inlet distortion, e.g., Davis [6], Williams [7], Hynes and Greitzer [8], O'Brien [9], Escuret and Garnier [10], and Longley [11]. A common feature of those lower dimension models is that the blade row response to the unsteady flow is modeled in an over simplistic way such that dynamic response of the flow in a blade passage cannot be modeled. Short length scale phenomena are categorically included in STEADY characteristics set a priori.

Adamcyzk [12] formally proposed a representation of the blade effects with both inviscid and viscous body forces for his passage-averaged multistage flow model, which can be implemented in actuator/semi-actuator model or passage averaged body force model. Three dimensional models for long length scale problems based on an actuator disk model (Joo and Hynes [13]) or passage averaged body force model (Gong et al. [14]) account for the three dimensionality of the flow. However, they still need to infer the blade row performance under unsteady disturbances from the steady axisymmetric characteristics. An advantage of the passage-averaged body force model over the actuator disc model is that the source terms can be distributed both radially and axially; therefore, it is possible for it to account for at least some of the dynamic responses, e.g., due to inertial and/or convection. The body force model is also considered numerically superior for being rid of the stiff artificial boundaries of actuator disks, which reflect waves in unsteady flows. Nevertheless, it remains a big problem to distribute the body force source terms in space based upon steady axisymmetric characteristics, especially at off design operations. For example, when near stall, blade loading and blockage would experience a large chordwise as well as radial redistribution that is dependent upon individual design and is almost impossible to generalize.

Putting the solution of the unsteady flow problem in a wider scope, Xu et al. [15] proposed a generic flow model with a hier-

Contributed by the International Gas Turbine Institute and presented at the International Gas Turbine and Aeroengine Congress and Exhibition, Amsterdam, The Netherlands, June 3–6, 2002. Manuscript received by the IGTI January 2002; revised manuscript received November 12, 2002. Paper No. 2002-GT-30359. Review Chair: E. Benvenuti.

 Copyright © 2003 by ASME

Downloaded 31 May 2010 to 171.66.16.27. Redistribution subject to ASME license or copyright; see http://www.asme.org/terms/Terms_Use.cfm

archy of the body force models for multi-scale unsteady flows. The methodology unifies the highly simplified empirical model to empiricism-free LES and/or direct numerical simulation (DNS) into a single solution framework and compromises between the empiricism and computer resources would be made while choosing an appropriate model for a particular application. The framework is rather like a generalization of large eddy simulation (LES), in the sense that large scales of unsteadiness above a preset threshold are directly calculated by the governing conservation equations of the flow. But all subscale disturbances will be modeled through different levels of modeling, which can be derived from an empirical, numerical or analytical source, or a combination of those sources. Sitting in the middle range of the model spectrum is the viscous body force model, which has advantages of having relatively low dependence on empiricism and low computer resource demand. In that paper computational results of an axial turbine and a transonic fan using the proposed viscous body force model with coarse meshes were compared in details with fine mesh RANS solutions, and very good agreement between two sets of calculations was demonstrated. The key to the success of the viscous body force model is obviously the construction of the source term itself. This is addressed in this paper. Unsteady RANS solutions are used as baselines for the evaluation of the viscous body force terms to be used as sources in the model and relative merits and model validity are discussed.

Generic Body Force Model

The governing equations for flow in turbomachinery can be written in conservative form in cylindrical coordinates in a general form with unsteady and convective terms on the left-hand side and viscous terms on the right-hand side in the form of body force as source terms. It should be noted that if the blade surface boundary is not included in the boundary conditions, the right-hand source terms would also include the effects of the inviscid blade force

$$\frac{\partial \rho}{\partial t}+\frac{\partial(r\rho u)}{r\partial r}+\frac{\partial(\rho v)}{r\partial\theta}+\frac{\partial(\rho w)}{\partial z}=0$$

$$\frac{\partial}{\partial t}\begin{vmatrix}\rho u\\ \rho v\\ \rho w\end{vmatrix}+\frac{\partial}{r\partial r}\begin{vmatrix}r(\rho u^2+p)\\ r\rho uv\\ r\rho uw\end{vmatrix}+\frac{\partial}{r\partial\theta}\begin{vmatrix}\rho uv\\ \rho v^2+p\\ \rho vw\end{vmatrix}+\frac{\partial}{\partial z}\begin{vmatrix}\rho wu\\ \rho wv\\ \rho w^2+p\end{vmatrix}-\frac{1}{r}\begin{vmatrix}\rho v^2+p\\ -\rho uv\\ 0\end{vmatrix}=\begin{vmatrix}F_r\\ F_\theta\\ F_z\end{vmatrix} \tag{1}$$

$$\frac{\partial(\rho e)}{\partial t}+\frac{\partial(ru(\rho e+p))}{r\partial r}+\frac{\partial(v(\rho e+p))}{r\partial\theta}+\frac{\partial(w(\rho e+p))}{\partial z}=W_f$$

here symbols have their usual meaning. The source terms on RHS of the momentum equations are the body force terms and the work done by the forces appears on the RHS of the energy equation. It should be emphasized that for adiabatic flow, the set of equations is nominally exact as long as the RHS sources are exact. The RHS can be the viscous terms in a DNS on one extreme, and, taking spanwise or/and circumferential averages on the LHS, stage characteristics in 1 or 2-dimensional models on the other. Figure 1 illustrates schematically the demand on the computer resources versus the demand of the empiricism in forming the RHS for different levels of modeling. The attraction of the viscous body force model is obvious in that it can be relatively independent of the empiricism while at the same time demands much less computer resources than the fine mesh RANS model.

The advantage on saving computer resources comes from the possibility of using a very coarse computational mesh, thus large time step length. Less empiricism is based on the fact that the source terms can be derived from one or a series of stand alone fine mesh *steady* RANS calculations, which have become routine in design practice and indeed can be very fast as well as accurate.

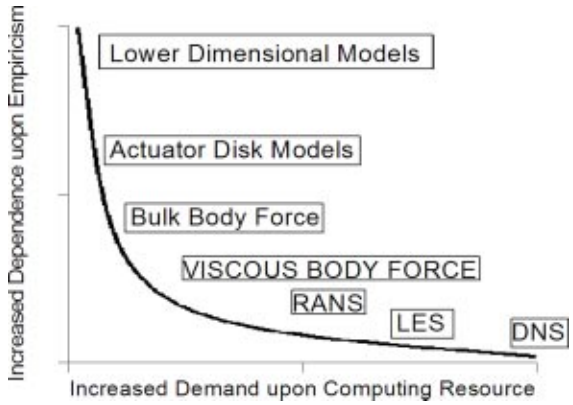

Fig. 1 Demands of model hierarchy on computing resources and empiricism

Viscous Body Force Versus Bulk Body Force

In contrast to the viscous body force model which models the viscous effects but directly solves the Euler equations through blade passages, a bulk body force model only solves the flow in a duct and models blade inviscid force as well as that due to viscous effects. Gong's [14] body force model falls into this category. Because only passage-averaged flow is solved in the duct and no attempt is made to take blade geometry into account (which can be grossly packed into the source terms), it can be an order of magnitude more efficient than the viscous body force model. Gong et al. [14] derived the source terms from the known compressor characteristics and their distributions along the chord are based on empirical assumptions. An improvement to this can be made by extracting the source terms from single passage RANS solutions thus its dependency on empiricism can be virtually removed, at relatively low cost of computer resources. However, by performing passage averaging, information regarding the dynamics of flow inside the blade passage is lost and it is not possible to study the blade response to unsteady disturbances, which, in many cases, actually is just the center of the problem to be addressed. From this point of view, although the bulk body force model is much faster, and could be numerically more accurate (due to the possibility of using a very regular mesh), than the viscous body force model, the latter is a step improvement over the bulk body force model. Because it solves the inviscid flow inside blade passages, it is capable of resolving the unsteady flow in the blade passage and of providing blade unsteady force with good accuracy.

The biggest problem in deriving the viscous source terms from steady RANS solutions is to work out the dynamic part of the sources from a series of steady solutions. Nominally, one can always write down the expression for body force as

$$\mathbf{F}(r,\theta,z,t)=\mathbf{F}(r,\theta,z)+\mathbf{F}'(r,\theta,z,t) \tag{2}$$

In cases when the second term is negligibly small compared to the first term, the dynamics of the viscous effect may be ignored and only the time mean viscous effects are accounted for in the calculation. However, in general one cannot ignore the dynamics of the viscous body force; thus, the second term has to be modeled. This can be approached in the following ways depending on the relative amplitude of unsteadiness imposed:

1. For very large imposed unsteadiness, each blade passage is likely to experience large excursions in the steady characteristics, then the body force terms have to be extracted from a series of solutions of the RANS at the corresponding flow conditions. This works effectively with a low reduced frequency when for each blade passage a quasi-steady reference flow condition may be established. Obvious difficulty

Downloaded 31 May 2010 to 171.66.16.27. Redistribution subject to ASME license or copyright; see http://www.asme.org/terms/Terms_Use.cfm

will emerge when the reduced frequency becomes high, as a reference condition will be difficult to define.

2. For the cases when the flow in the blade passages experiences small excursions, the dynamic part of the body force can be expressed as

$$\mathbf{F}'(r,\theta,z,t) = \frac{\partial \mathbf{F}}{\partial t}(r,\theta,z,\varphi(t))dt = \frac{\partial \mathbf{F}}{\partial \varphi}(r,\theta,z,\varphi)\frac{\partial \varphi}{\partial t}(r,\theta,t)dt \tag{3}$$

i.e., as a function of the change of local flow rate. Where the flow coefficient ϕ is defined as passage averaged Va/U (axial velocity/blade speed). The partial derivative of the force with respect to the flow coefficient can be estimated from the steady flow calculations. This again will have problems when the reduced frequency is high, as well as for the transonic fans when operating on the vertical part of the characteristics.

3. An alternative for formulating the viscous body force for a high reduced frequency is to view the viscous body force as viscous drag and derive drag coefficients from the fine mesh RANS calculations

$$C_d = |\mathbf{F}| / \left(\frac{1}{2}\rho u^2 \mathrm{Vol}\right) \quad \text{from fine mesh RANS}$$
$$\mathbf{F} = -C_d \frac{1}{2}\rho |u| \overline{u} \quad \text{Vol to coarse mesh calc.} \tag{4}$$

Here Vol is the volume of the mesh cell in CFD calculation and ρ and u are local density and velocity, respectively. The viscous force is seen proportional to the local dynamic head which varies with time under unsteady disturbances, while for small excursions from a reference point, the drag coefficient distribution in a blade passage can be assumed as unchanged. For boundary layer flow it is a very good assumption.

In the following sections fine mesh unsteady RANS solutions are used to evaluate the time mean and unsteady viscous body forces. The program used is the unsteady version of Denton's multistage turbomachinery solver with a mixing length turbulence model (c.f. Marshall et al. [16]). The program solves the five governing equations in finite volume form, using explicit integration schemes in both space and time. Because in the program the viscous stresses are integrated over the surfaces of a discretised volume to derive an equivalent body force source, it is particularly convenient to extract these source terms from the calculation for the purpose of the assessment. Three typical cases are chosen for the assessment. A turbine rotor/stator interaction case for viscous body force of relatively high frequency under mostly favorable pressure gradient, a fan rotor/vane interaction case for adverse pressure gradient, and a fan rotor experiencing an engine order inlet distortion to assess the effects of large amplitude low frequency unsteady disturbances. It is expected that when the variation of viscous force or drag coefficient is relatively small, a time mean force term or a time mean drag coefficient from a single steady RANS calculation can be a good approximation. However, if the variation is large, a series RANS calculations have to be performed to provide time-dependent viscous force terms.

Embedded Turbine Stator Case

The second stator of a two stage high pressure turbine has been studied. The turbine is of low reaction ($R=0.3$), moderate loading ($\Delta H/U^2=1.5$) and repeating stage design representative of those used in high pressure steam turbines, and was designed and tested in three stages at the Whittle Laboratory by Kachel [17]. The number of blades for the stator is 32 and 40 for the rotor, so it is convenient to use the blade count 4 and 5 for the stators and rotors, respectively, so the calculation only needs to cover a segment of $\pi/4$ to save the computing efforts. However, because the turbine was tested at very low speed, it is felt still too large a task to do unsteady calculations for the whole three-stage version; thus, for the calculation the number of stages is cut to two. The second stator sees the unsteady disturbances from both up- and downstream rotors, and indeed those from the upstream stator. The computational mesh used in the calculation is $37\times85\times37$ for each of 18 blade passages (in pitchwise, streamwise and spanwise directions respectively, the same notation for all cases below in this paper). It typically takes more than two weeks of CPU time to obtain an unsteady solution on a PIII 500 machine. This is largely due to the combination of low convective speed and long flow path.

Fig. 2 Instantaneous entropy at turbine midspan

Figure 2 shows a snapshot of the entropy function ($e^{-\Delta s/R}$) at midspan, one would expect to see high unsteady activities around the leading edge and trailing edge, as well as on the blade surfaces where wakes interact with the boundary layer. Away from wall regions, viscous effects will be small, mainly due to mixing of the wake/vortex. To illustrate this, the calculated total viscous specific body force (unit volume force, in N/m^3) distributions across the stator are plotted in Fig. 3.

The wall boundary layer development, especially that on the suction surface, is dominant throughout the passage, the effects of secondary flow start to show up about half way through the blade. It is clear that for coarse mesh calculations only the viscous forces in the cells adjacent to walls need to be modeled for the most part of the passage, and at most 20% of the passage towards the trailing edge.

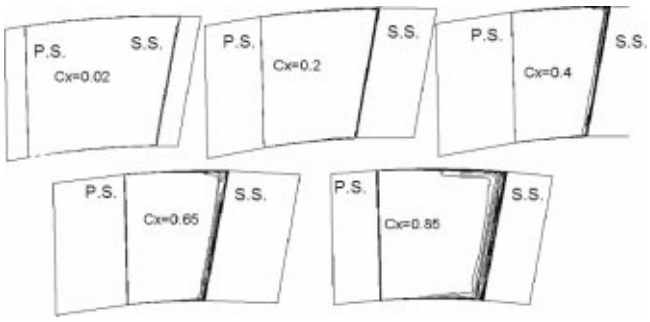

Fig. 3 Contours of viscous body force showing its development along the blade passage

Downloaded 31 May 2010 to 171.66.16.27. Redistribution subject to ASME license or copyright; see http://www.asme.org/terms/Terms_Use.cfm

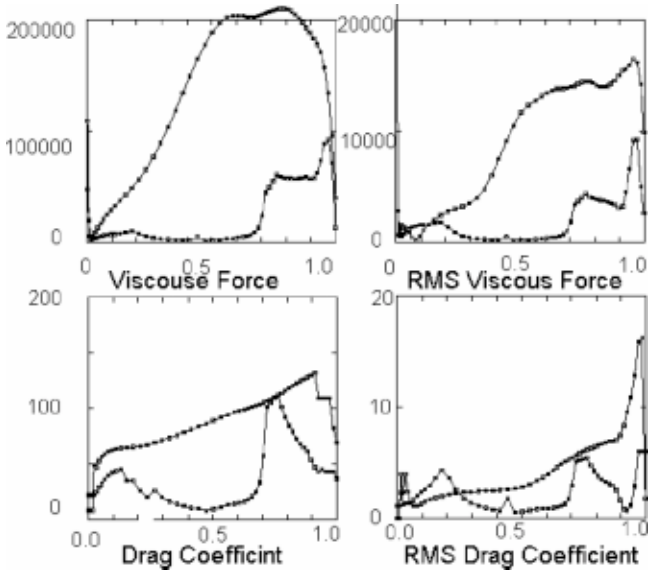

Fig. 4 Viscous force and drag coefficient near blade surfaces at midspan along axial chord

Figure 4 shows cycle averaged viscous force and the drag coefficient defined as the specific viscous force normalized by the LOCAL dynamic head, and their RMS evaluated from the variations through a cycle. It is seen in general that the RMS variation for both force and drag coefficient is less than 10% of the mean value. However the variation of the force has much larger dynamic range as well as larger variations while the mean force term is large. This would introduce larger errors if the viscous effect is only modeled by the time mean term. The RMS variation of drag coefficient is mostly only about 5% of the mean level but has a large peak towards the trailing edge, most likely the result of the potential interaction from the downstream rotor. Figure 5 shows the contours of the mean viscous force and its RMS variation on the top and the time mean drag coefficient and its RMS variation on the bottom, near the suction surface. Clearly apart from the edges and secondary flow the overall dynamics are small compared with the mean value. If the mean drag coefficient is used to model the unsteady viscous effects, it has the advantage that it will respond to the local dynamic head variation, while if the mean viscous force is used directly there will be no variation in the viscous terms due to flow unsteadiness.

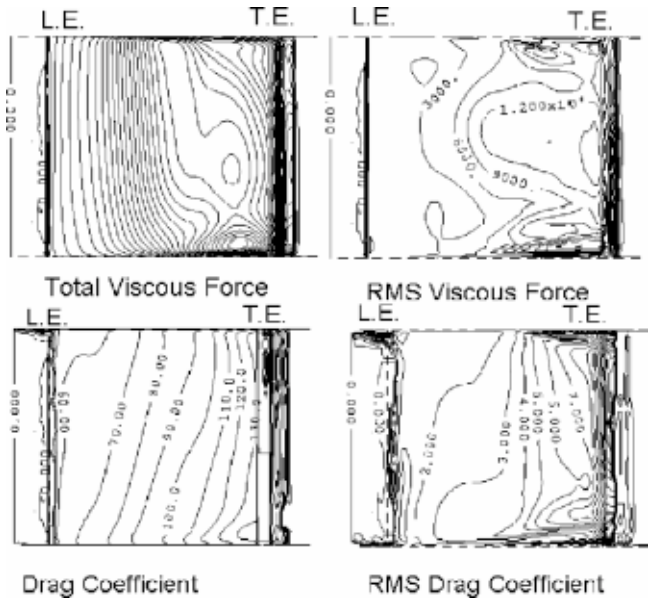

Fig. 5 Contour plots of the drag coefficient and RMS drag coefficient near suction surface

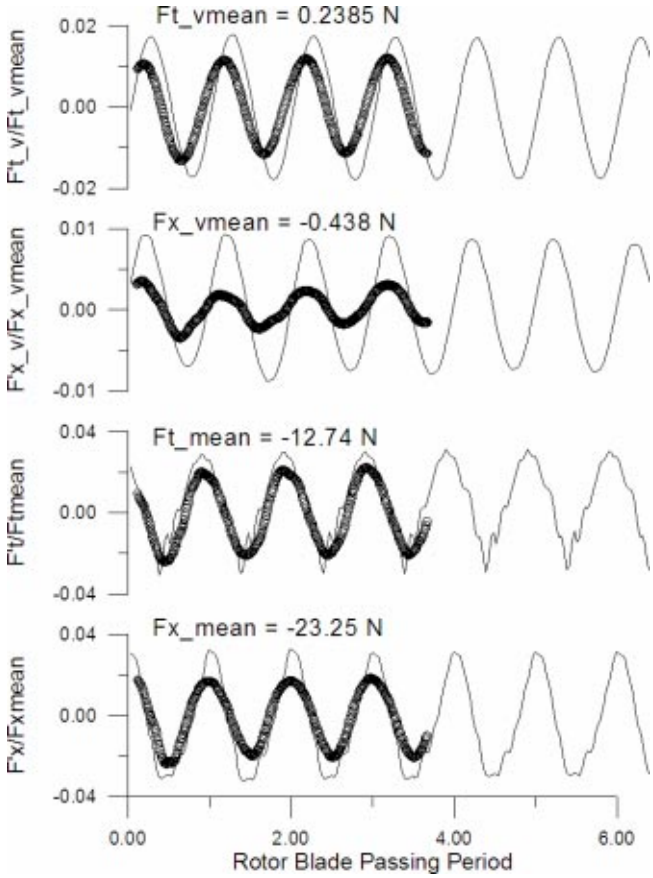

Fig. 6 Variation of total blade force and viscous body force with time

The correlation between drag coefficient based upon the local dynamic head and viscous force can be traced back to Denton's U^3 method for estimating viscous loss in steady flows (Denton [18]). Ikeda [19] used a commercial code (Star-CD with $\kappa-\varepsilon$ turbulence model) to assess the loss generation inside turbine stages against the U^3 method, and found extremely good agreement even with a constant value of drag coefficient. Because in unsteady calculations the physical time step used is far smaller than the time scale of the unsteadiness, it would be not unreasonable to assume that the viscous force responds to the local velocity variation in a quasi-steady manner. A time mean drag coefficient can then be used as a first approximation. Figure 6 compares the blade forces calculated from a RANS solution and a coarse mesh ($10\times24\times10$ within each blade passage) solution using a constant drag coefficient for each of four solid walls. The values of the drag coefficient have been adjusted to the mean value from the RANS solution, and to produce similar stage efficiency. In the graph the top two lines are the viscous forces in the tangential and axial directions and the bottom two are the total blade forces integrated over the blade surfaces in the tangential and axial directions. The thin lines are from the coarse mesh solution and the circles denote the RANS solution. It is interesting to notice that for this case, the mean viscous force is only about 2% of the total blade force, and the unsteady amplitude of the viscous force is only about 1% of that of the total blade force. This highlights the relative importance of inviscid unsteady force whilst errors in estimating the viscous force may be tolerated in such applications.

Downloaded 31 May 2010 to 171.66.16.27. Redistribution subject to ASME license or copyright; see http://www.asme.org/terms/Terms_Use.cfm

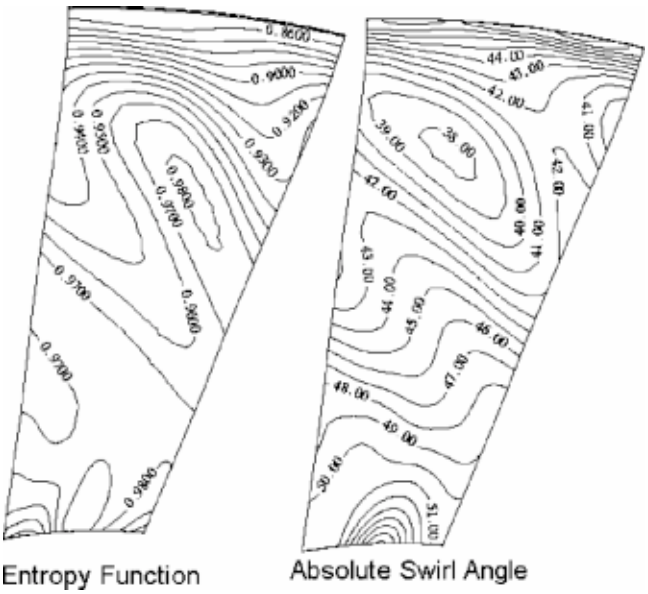

Fig. 7 Contours of entropy function and swirl at OGV inlet in quasi-orthogonal view

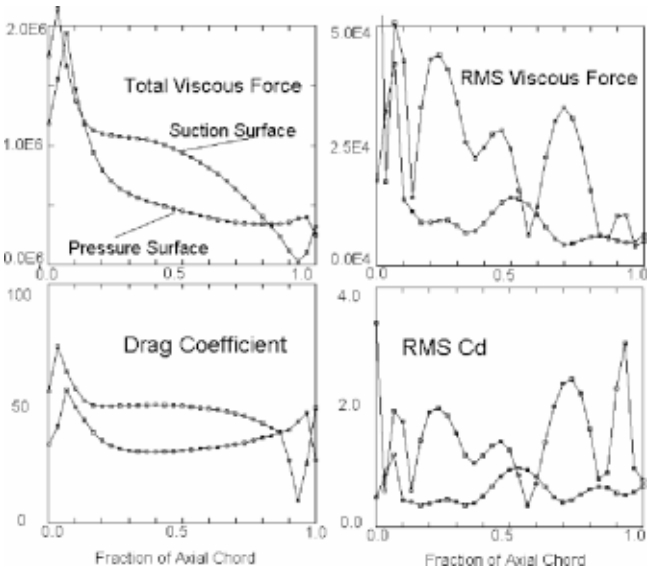

Fig. 9 Surface distributions of total drag force, RMS force variation, *Cd* and RMS *Cd* variation at midspan

The coarse mesh calculation resulted in only slightly higher fluctuation amplitudes for total blade force and the tangential component of the viscous force, but for the axial component of the viscous force it is more than doubled. There is also a small phase shift in viscous body force between the two calculations, but that for the total blade force agrees well. The discrepancy is thought insignificant considering the fact that the mean values are predicted well and the unsteady fluctuations are only about 1% of the mean. However, it should be emphasized that the forces presented here are integrated over the whole blade passage and larger variations at the edges and in secondary flow regions have been outweighed by the majority part of the blade where the unsteady fluctuation is small. To compare the computing costs, the coarse mesh calculation running in full annulus takes only about 1/25th of the CPU time compared with that for the fine mesh RANS calculation running in only 1/8 of annulus.

Fan Outlet Guide Vane Case

A fan OGV in a civil fan stage is used to examine the unsteady viscous force subject to a high adverse pressure gradient and with trailing edge separation, whilst under moderate frequency disturbances. The stage design is representative of a modern high bypass civil fan with pressure ratio of 1.8 and rotor/OGV count ratio of 1:3. The case is running at 90% of the design speed. The mesh for the rotor passage is 37×186×40 and 37×96×40 for the vane. Relatively large amounts of grid (330,000 in total) have been used in the duct between the rotor and the vane to ensure the proper capturing of the rotor wake and its propagation in the duct.

Figure 7 shows the entropy and flow swirl angle contours in a cross section just upstream of the vane. In reaching the OGV the rotor wake is highly tilted in the tangential direction and smeared. There are two spanwise locations where the vanes will have relatively large unsteadiness, near the hub and at about 75% span. Figure 8 plots the entropy function contours of these two sections at one time instance. While the suction surface boundary layer at the hub section has clearly separated, that at 75% span remains attached.

Similar to Fig. 4, Fig. 9 plots the force, Cd and their RMS variation distributions on the OGV surfaces at midspan. The drag coefficient shows a flat distribution along most of the chord and, as expected for this part of the blade, the unsteadiness is small. The RMS variation of Cd is only about 3% of the mean value on the suction surface and slightly over 1% on the pressure surface. Also, as shown in Fig. 10 the distributions of the Cd and its RMS variation are fairly constant over most of the suction surface, including 75% span where initially a high fluctuation was expected; but significant large-amplitude unsteadiness is seen appearing in the hub corner stall region. In this region both the drag coefficient

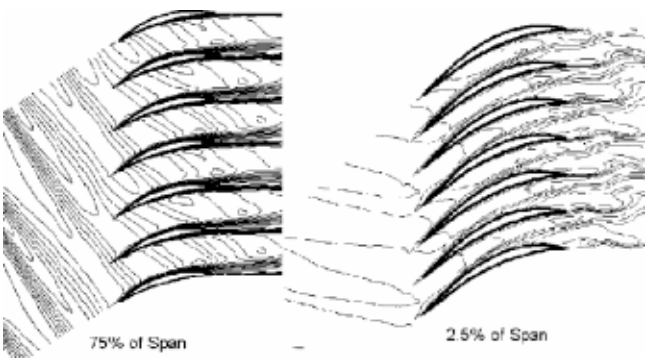

Fig. 8 Entropy contours at 75 and 2.5% spans

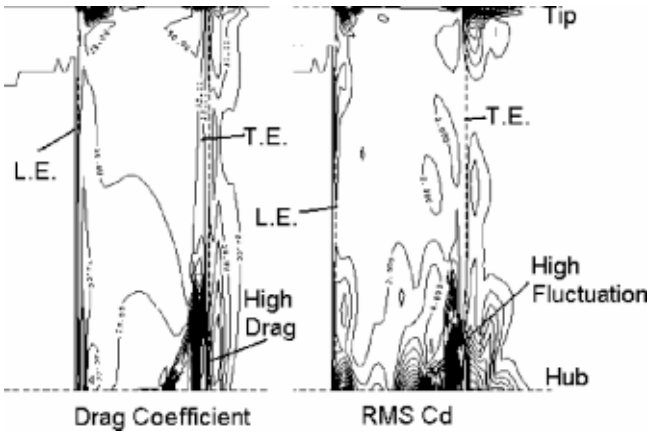

Fig. 10 Contours of *Cd* and RMS Cd on OGV suction surface

Downloaded 31 May 2010 to 171.66.16.27. Redistribution subject to ASME license or copyright; see http://www.asme.org/terms/Terms_Use.cfm

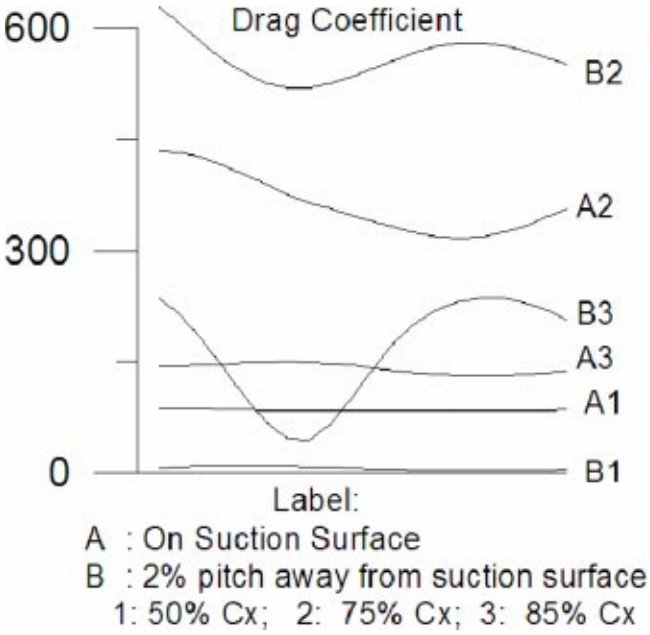

Fig. 11 Variation of drag coefficient over one rotor passing period

and its fluctuation are orders of magnitude higher than those on the rest of the surface, as shown in the time history of the drag coefficient in Fig. 11. In the graph Points A1, A2, and A3 are located on the blade surface and B1, B2, and B3 are 2% pitch away from the blade surface. Points A1 and B1 are located at 50% of axial chord where the boundary layer is still attached, points A2 and B2 at 75% of axial chord are in the separating region and points A3 and B3 at 85% axial chord are in the separated region. Points A1 and B1 have low level of drag and activity as expected. Point A3 has high drag level but low activity for being at the bottom of the separation. While points A2, B2, and B3 show not only large drag and high activity but also irregular wave form, indicating complicated interactions in the separating and separated regions. The fact that the drag coefficients at locations A2 and B2 lack periodicity indicates that the unsteadiness in the separation is possibly not entirely driven by the incoming wake.

Fan Rotor Distortion Case

To assess the effects of large-amplitude low-frequency disturbances, the ADLARF transonic fan under an engine order inlet stagnation pressure distortion is studied. More information about the fan can be found from Hah et al. [20]. The distortion is imposed as a single circumferential sine wave variation, with a radial profile of amplitude, which peaks at about 83% span, of 13% of inlet stagnation pressure while the rotor is running at 98% design speed. A mesh of 41×178×49 per passage is used for the RANS calculation. For the whole annulus of 16 blades, the total mesh size is over 5.7 million.

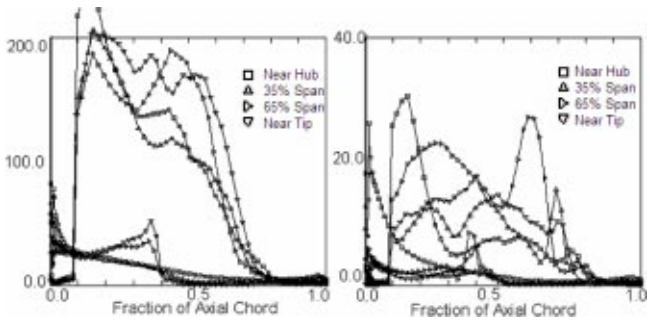

Fig. 12 Surface distributions of *Cd* and its RMS variation along span

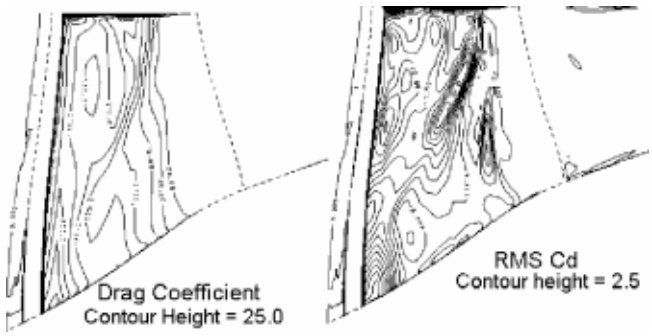

Fig. 13 Contours of *Cd* and its RMS variation on fan suction surface

Figures 12 and 13 show the surface distributions and suction surface contours of the time mean drag coefficient and its RMS variation, respectively. The viscous force is dominantly on the suction surface; both the time mean level and RMS variation are small on the pressure surface despite large amplitude disturbances. Most unsteady activity of the viscous force comes from three regions; leading edge, in particular near the hub section where local incidence is high, shock region where the shock/boundary layer interaction is unsteady due to the shock movement, and the tip leakage flow region. The last shows by far the largest unsteadiness. It is also worth noticing that for the whole blade span, the rear 20% of axial chord on suction surface and 50% of the chord pressure surface there is little unsteady activities in the viscous force. It is observed that apart from the tip clearance flow region, the relative RMS variation of Cd level is not larger than that on the OGV surface. An integration of the total forces acting on the blade shows that the magnitude of the time mean viscous force is about 1% of that of total blade force, with 15% peak-to-peak variation. Considering the disturbance in this case is much larger it is a vindication that the viscous drag force does to a certain degree scale with the local dynamic head.

Figure 14 illustrates the variation of total viscous force and drag coefficient on six points on the rotor suction surface over one rotor revolution. Points A, B, and C are just downstream of the leading edge, at hub, midspan and tip, respectively, while points D, E, and F are the corresponding hub, midspan and tip points located on mid chord. The viscous force and its variation are extremely high at the blade tip (points C and F). The waveforms also contain significant high-frequency components, indicating high-intensity nonlinear interactions. At hub leading edge, both the force and its variation are large, at comparable level of those at blade tip but show little sign of nonlinearity, indicating that the unsteadiness of the viscous force is largely driven by the incoming flow distortion.

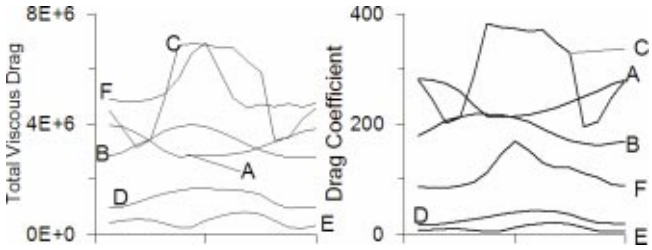

Fig. 14 Variations of total viscous force and drag coefficient over one rotor revolution

Downloaded 31 May 2010 to 171.66.16.27. Redistribution subject to ASME license or copyright; see http://www.asme.org/terms/Terms_Use.cfm

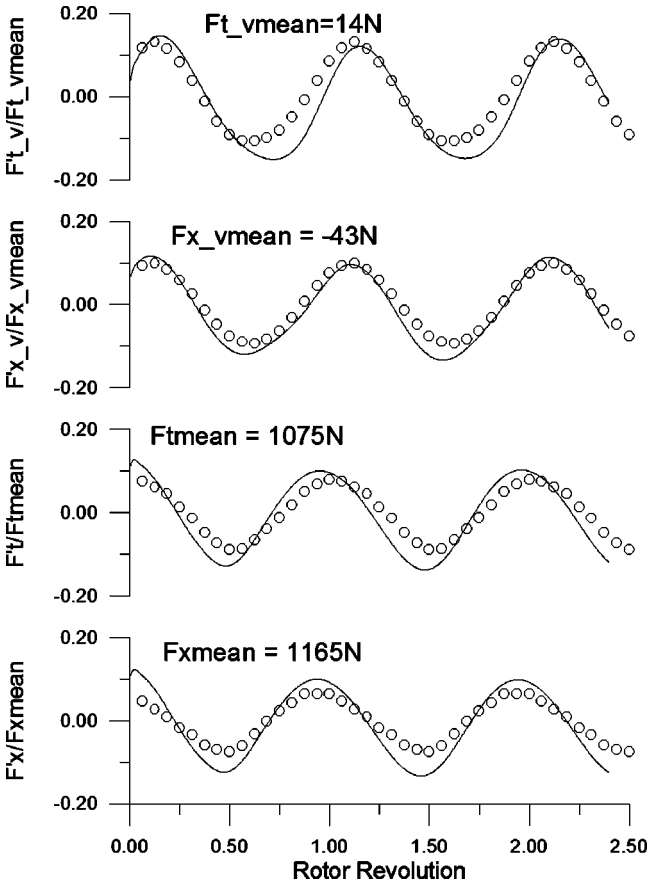

Fig. 15 Variation of total blade force and viscous body force with time, ADLARF fan

In the same format as in Fig 6, in Fig. 15 a comparison of the blade forces calculated from both fine mesh RANS and coarse mesh viscous body force model is presented. Solid lines are the coarse mesh viscous body force model results and open circles the fine mesh RANS results. The coarse mesh calculation was done using a $10\times25\times10$ mesh inside each blade passage, and a total of 128,000 mesh points for the whole calculation including extended up and downstream annulus ducts. Again a single constant Cd is used for each surface to check the dynamic response of the viscous body force model against the RANS calculation. The calculation shows very similar total blade forces, both the mean values and the amplitude of the variation. A small phase lag is seen in the tangential force. For the viscous forces, the relative variations are very well predicted. The mean level for the viscous force, however, is about three times lower in the fine mesh RANS calculation, i.e., the RANS solution predicts -16 N and 3.2 N for axial and tangential forces respectively but the coarse mesh calculation predicts -43 N and 14 N, respectively. This is hardly surprising because the RANS calculation indicates a large spatial variation of Cd near the blade surface and a single value cannot be a proper representation of the distribution. Despite of this, the dynamic response of the viscous body force model shows an extremely encouraging agreement with the RANS calculation.

Discussions and Concluding Remarks

Three unsteady flow cases, two with low-amplitude high-frequency disturbances subject to favorable and adverse pressure gradients respectively due to blade row interactions and one with high-amplitude low-frequency disturbance due to inlet flow distortion have been examined using an unsteady RANS for the purpose of assessing viscous body force terms in unsteady flows. It is found that even for the case with large amplitude inlet distortion, both unsteady viscous body force and its peak-to-peak amplitude are only few percent of the total unsteady blade force. This means that the overall effect of any error in modeling the total blade force would be much more significant than that due to the viscous effect alone. In other words, a much larger error in modelling could be tolerated for the viscous body force model than that for the bulk body force model, which has to model the inviscid blade force.

As expected, in general viscous forces are concentrated in boundary layer regions, except in the locations where there is separation. Therefore, to model the distribution of the viscous force terms for a coarse mesh calculation only the cells adjacent to solid walls are important. Although the viscous body force is relatively small compared to the inviscid blade force, the dynamics of the viscous body force has a similar range of relative variation to its time average value as that of the total blade force, thus needs to be modeled in unsteady calculations.

The drag coefficient defined as the specific viscous force normalized by the local dynamic head has smaller dynamic range in space and time compared with the viscous body force term itself. In most part of the unsteady flows investigated in this paper the RMS variation of drag coefficient is less than ten percent of the corresponding drag coefficient level. In these cases if a drag coefficient distribution which is constant in time but varies in space is used to model the viscous effect, it will not only correctly model the time-mean viscous effects such as viscous loss, and, more important for compressors, viscous blockage, but also their dynamic responses. Unlike the time constant viscous force, the time constant drag coefficient responds to the unsteady disturbances by generating unsteady viscous force proportional to the local dynamic head. Within the assumptions of numerical time resolution being sufficiently higher than the time scale to be resolved, which is typically the blade passing frequency in the viscous body force model, and of attached boundary layer flows, this model yields satisfactory results.

It is observed that there are a few locations where the RMS variation of drag coefficient is high, indicating high dynamic activities, which are largely unaccounted for by the unsteady dynamic head and may require more sophisticated modeling such as outlined in Eq. (3). The first of such locations is the leading edge. However it should be realized that the leading edge flow is largely inviscid in the sense that boundary layer on the blade is just started. The specific viscous drag calculated is scaled by the unit volume so is indirectly to mass flow. The amount of mass flow involved in viscous effect at the leading edge is extremely small therefore it is regarded as insignificant even if its relative variation is large.

Tip clearance flow and the separated flow near the trailing edge are two other locations where the RMS variation of the drag coefficient can be very large. The complication not only comes from the fact that U^3 analogy for viscous loss is likely invalid in those regions, but also due to that the unsteadiness in those regions may not only result from the outside unsteady disturbances. There is no simple way of modelling these variations. But one may just afford not to model them if the mass flow involved is relatively small, which is actually true for these cases.

In conclusion, the results of this study show that the drag coefficient model can reproduce overall correct dynamic response of the viscous effect for a range of flows from high-frequency small-amplitude blade row interaction to engine order large amplitude distortion. In general, only one reference fine mesh steady RANS calculation is needed for the construction of the spatial drag coefficient distribution. This study also illustrates that the viscous body force model coupled with coarse mesh calculation is able to resolve unsteadiness up to blade passing frequency. The results compare very favourably with proper unsteady RANS results, only at a CPU cost usually less than 1% of that of the latter.

Downloaded 31 May 2010 to 171.66.16.27. Redistribution subject to ASME license or copyright; see http://www.asme.org/terms/Terms_Use.cfm

Acknowledgment

The author would like to thank Prof. J. D. Denton and Dr. T. P. Hynes for their continuous interest and support. Thanks are also due to anonymous reviewers for their constructive comments on the manuscript.

References

[1] Unno, M. et al., 2001. ''Unsteady Three Dimensional Navier-Stokes Simulations of Fan-OGV-Strut-Pylon Interaction,'' ISABE-2001-1197.
[2] Giles, M. B., 1990, ''Stator/rotor Interaction in a Transonic Turbine,'' J. Propul. Power, **6**(5), pp. 621–627.
[3] He, L., 1992, ''Method of Simulating Unsteady Turbomachinery Flows with Multiple Perturbations,'' AIAA J., **30**(11), pp. 2730–2735.
[4] Li, H. D., and He, L., 2001, ''Single-Passage Solution of Three Dimensional Unsteady Flows in a Transonic Fan Rotor,'' Proc. I Mech E, Part A Power Energy, **123**(3), Sept., pp. 680–685.
[5] Li., H. D., and He, L., 2001, ''Prediction of Flutter and Inlet Distortion Driven Response of a Transonic Fan Rotor Using Phase-Lagged Boundary Conditions,'' ASME 2001-GT-0272.
[6] Davis, M. W., Jr., 1982, ''A Stage-by-Stage Dual Spool Compression System Modelling Technique,'' ASME Paper 82-GT-189.
[7] Williams, D. D., 1986, ''Review of Current Engine Response to Distorted Inflow Conditions,'' AGARD Conf. Proc., AGARD CP-400.
[8] Hynes, T. P., and Greitzer, E. M., 1987, ''A Method for Assessing Effects of Inlet Flow Distortion on Compressor Instability,'' ASME J. Turbomach., **109**, pp. 371–379.
[9] O'Brien, W. F., 1992, ''Dynamic Simulation of Compressor and Gas Turbine Performance,'' AGARD Conf. Proc., AGARD-LS-183.
[10] Escuret, J. F., and Garnier, V., 1994, ''Numerical Simulations of Surge and Rotating Stall in Multistage Axial Compressors,'' AIAA Pap., No. 94-3202.
[11] Longley, J. P., 1997, ''Calculating the Flow Field Behavior of High Speed Multistage Compressors,'' ASME Paper 97-GT-468.
[12] Adamczyk, J. J., 1985, ''Model Equation for Simulating Flows in Multistage Turbomachinery,'' ASME Paper 85-GT-226.
[13] Joo, W. G., and Hynes, T. P., 1997, ''The Simulation of Turbomachinery Blade Rows in Asymmetric Flow Using Actuator Disks,'' ASME J. Turbomach., **119**, Oct. 2002.
[14] Gong, Y. F. et al., 1999, ''A Computational Model for Short Wavelength Stall Inception and Development in Multi-Stage Compressors,'' ASME J. Turbomach., **121**, Oct., pp. 726–734.
[15] Xu, L., Hynes, T. P., and Denton, J. D., 2002, ''Towards Long Length Scale Unsteady Modeling,'' Proc. Turbomachines, I Mech E, Vol. 216, Part A: J. Power Energy, **216**.
[16] Marshal, J., Xu, L., Denton, J. D., and Chew, J., 2000, ''Prediction of Low Engine Order Inlet Distortion Driven Resonance in a Low Aspect Ratio Fan,'' ASME Paper, 2000-GT-374.
[17] Kachel, C., 2001, private communication, details in 2002, Cambridge University Ph.D. thesis.
[18] Denton, J. D., 1993, ''Loss Mechanisms in Turbomachines.'' IGTI Gas Turbine Scholar Lecture 1994 ASME J. Turbomach., **115**(4), Oct..
[19] Ikeda, T., 1999, ''Performance Estimation Method for Axial Turbine Stages,'' Proc. Int. Gas Turbine Congress, Kobe, Japan.
[20] Hah, C., Rabe, D. C., Sullivan, T. J., and Wadia, A. R., 1998, ''Effect of Inlet Distortion on the Flow Field in a Transonic Compressor Rotor,'' ASME J. Turbomach., **120**, Apr., pp. 233–246.

Downloaded 31 May 2010 to 171.66.16.27. Redistribution subject to ASME license or copyright; see http://www.asme.org/terms/Terms_Use.cfm

A Numerical Investigation on the Influence of Lateral Boundaries in Linear Vibrating Cascades

Roque Corral[1]
Industria de TurboPropulsores S.A.,
28830 Madrid, Spain
e-mail: Roque.Corral@itp.es

Fernando Gisbert
School of Aeronautics, UPM,
28040 Madrid, Spain

The effect of the finite extent of linear cascades on the unsteady pressure distribution of vibrating blades is assessed by means of a numerical study. The span of a reference cascade made up of flat plates has been changed to investigate its influence on the computed influence coefficients. It is concluded that the number of passages required to match a solution obtained with a traveling-wave mode strongly depends on the interblade phase angle under consideration and that existing linear vibrating cascade facilities have a marginal resolution to accurately match CFD analysis that assume that the blade is vibrating in a traveling-wave mode. [DOI: 10.1115/1.1575255]

Introduction

Matching experimental data and analytical results is always a long and iterative process. More often than not the agreement between experiments and simulations does not meet the expectations since the uncertainties in both sides are either not negligible or simply not fully understood by the counterpart. The situation is aggravated by the use of simplified models that do not match all the nondimensional parameters of the problem or contain geometric simplifications to accommodate the blade to the existing facility.

Experimental aeroelasticity in turbomachinery is a particularly tough field and a clear example where all the aforementioned limitations are present. Vibrating cascades have been used in the past (Bolcs [1]), Buffum and Fleeter [2] among others) as a standard vehicle to validate CFD models since, on the contrary than rotating compressor or turbine rigs, provide a unique capability to control the displacement of the blade. Most of the documented cases correspond to two-dimensional configurations (see Fransson and Verdon [3] for a detailed review), but recently three-dimensional experiments have been performed (Bell and He [4]). Another attractiveness of this type of installations is its low cost compared to rig testing, however still cost limitations impose severe restrictions in the mass flows and pressure ratios that may be obtained in them. These constrains directly translate in a limitation on the maximum number of passages of the installation.

Most of the existing vibrating cascade facilities are of the linear type (e.g., [2]) and a few of them fall under the category of annular cascades (e.g., [5]). The main advantage of annular cascades over the linear ones is that the periodicity of the flow is automatically ensured and the blade motion may be prescribed either as a traveling-wave or an individual blade mode. The individual blade mode data (i.e. the influence coefficients) may be expanded in traveling-wave modes assuming that the unsteady perturbations behave in a linear way in first approximation, which is believed to be true for a wide range of reduced frequencies and Mach numbers if the blade displacements are small compared to the blade chord [5]. Linear cascades are usually formed by a limited number of passages and therefore only a reduced number of influence coefficients may be measured, drastically reducing the number of interblade phase angles that may be reconstructed.

However the hypothesis of linearity of the unsteady perturbations and the reduced number of influence coefficients that may be measured are not the most limiting factors of a linear or sector cascade. Bölcs et al. [5] demonstrated in its annular cascade wind tunnel that in most of the cases it was enough to consider two blades at each side of the reference blade to obtain reasonably accurate data, although they admitted that in a linear cascade it would be probably necessary to include more blades to avoid reflections from the lateral walls of the wind tunnel. Actually, the number of required passages for a given geometry and operating conditions may only be determined either in an annular cascade or by successive modifications of a linear cascade increasing its number of passages. This problem was acknowledged by Buffum and Fleeter [2] when abandoned the standard practice of vibrating nine blades in linear cascades, to conduct an experiment with a low solidity configuration representative of a propfan application where just five blades were vibrated in a traveling-wave mode. Actually, a review of linear cascade data reported for the *Standard Aeroelastic Configurations* [3] shows that they were obtained with not less than nine blades. Recently, a redesign of the NASA Glenn oscillating cascade facility has been conducted using advanced numerical tools (Chima et al. [6]) and the degree of spatial periodicity obtained in the facility reported (Lepicovsy et al. [7]). This is an indication that the problem is a concern, however nothing is commented on the quality of the unsteady flow that may be expected. Ott et al. [8] conducted a similar study in the EPFL (Ecole Polytechnique Fédérale Lausanne) linear cascade and concluded that even in the presence of a reasonable spatially periodic flow, the quality of the unsteady flow had to be examined with extreme care.

The objective of the paper is to numerically investigate the effect of the lateral boundaries on a linear cascade to assess the degree of accuracy of the unsteady data that may be expected for a given number of blades. Hall [9] conducted a set of numerical experiments of the Buffum cascade to assess the degree of matching of a numerical tool with the experiments. He first concluded that the nominal inlet flow angle needed to be corrected to reproduce the steady loading of the airfoil, then computed the influence coefficients and showed that probably the number of airfoils of the cascade was not enough to achieve an unsteady periodic solution. This fact is unfortunate since one of the main purposes of linear vibrating cascades is to obtain accurate data for code validation that are usually taken as a reference for further improvement of the numerical tools.

To separate the influence of the lack of periodicity of the steady field from the one of the finite span of the cascade we have based the study on the inviscid computation of a cascade of flat plates, for which there is no doubt about the periodicity of the steady uniform base flow, and an asymptotic quasi-analytical solution exist.

[1]Also Associate Professor at the School of Aeronautics, UPM, Madrid.

Contributed by the International Gas Turbine Institute and presented at the International Gas Turbine and Aeroengine Congress and Exhibition, Amsterdam, The Netherlands, June 3–6, 2002. Manuscript received by the IGTI June 11, 2001. Paper No. 2002-GT-30451. Review Chair: E. Benvenuti.

 Copyright © 2003 by ASME

Downloaded 31 May 2010 to 171.66.16.27. Redistribution subject to ASME license or copyright; see http://www.asme.org/terms/Terms_Use.cfm

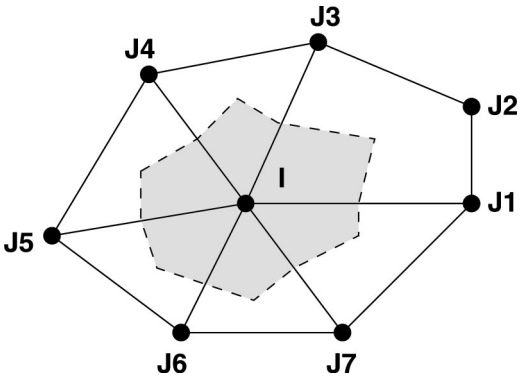

Fig. 1 Typical hybrid-cell grid and associated dual mesh

Numerical Methodology

Spatial Discretization. The code solves the two-dimensional Euler equations in conservative form

$$\frac{d}{dt}\int_{\Omega}\mathbf{U}d\Omega+\int_{\Gamma}\{(\mathbf{f},\mathbf{g})-\mathbf{U}\mathbf{v}\}\cdot\mathbf{n}dA=0 \tag{1}$$

where **U** is the vector of conservative variables, **f** and **g** the inviscid fluxes, Ω the flow domain, Γ its boundary, **n** the unit outward normal to the boundary, and **v** the velocity of the boundary.

The spatial domain is discretized using hybrid unstructured grids that may contain cells with an arbitrary number of faces and the solution vector is stored at the vertices of the cells. The code uses an edge-based data structure, a typical grid is discretized by connecting the median dual of the cells surrounding an internal node (Fig. 1). For the node *i* the semi-discrete form of Eq. (1) can be written as

$$\frac{d(\Omega_i\mathbf{U}_i)}{dt}+\sum_{j=1}^{n_{\text{edges}}}\frac{1}{2}S_{ij}(\mathbf{F}_i+\mathbf{F}_j)-\mathbf{D}_{ij}=0 \tag{2}$$

where S_{ij} is the area associated to the edge ij, n_{edges} the number of edges that surround node *j*. The resulting numerical scheme is cell-centered in the dual mesh and second-order accurate. It may be shown that for triangular grids the scheme is equivalent to a cell vertex finite volume scheme. A blend of second and fourth-order artificial dissipation terms, $\mathbf{D}_{ij}$, is added to capture shock waves and prevent the appearance of high frequency modes in smooth flow regions, respectively. The second order terms are activated in the vecinity of shock waves by means of a pressure-based sensor and locally the scheme reverts to first order in these regions. The artificial dissipation terms can be written as

$$\mathbf{D}_{ij}=|A_{ij}|S_{ij}[\mu_{ij}^{(2)}(\mathbf{U}_j-\mathbf{U}_i)-\mu_{ij}^{(4)}(L_j-L_i)] \tag{3}$$

where $\mu_{ij}^{(2)}=0.5(\mu_i^{(2)}+\mu_j^{(2)})$ and $\mu_{ij}^{(4)}=0.5(\mu_i^{(4)}+\mu_j^{(4)})$ are the average of the artificial viscosity coefficients in the nodes *i* and *j* which are given by

$$\mu_i^{(2)}=\min(\varepsilon_2,k_2\delta_i),\quad \mu_i^{(4)}=\max(0,\varepsilon_4-k_4\delta_i) \tag{4}$$

where δ_i is a pressure-based sensor

$$\delta_i=\frac{|\Sigma_{j=1}^{n_{\text{edges}}}(p_j-p_i)|}{\Sigma_{j=1}^{n_{\text{edges}}}(p_j+p_i)} \tag{5}$$

and ε_2, k_2, ε_4 and k_4 are constants. Typically, $\varepsilon_2=0.5$ and $\varepsilon_4=1/128$. L is a pseudo-Laplacian operator

$$\mathrm{L}(\mathbf{U}_i)=\sum_{j=1}^{n_{\text{edges}}}(\mathbf{U}_j-\mathbf{U}_i)\simeq\frac{n_{\text{edges}}}{4}(\Delta x^2\mathbf{U}_{xx}+\Delta y^2\mathbf{U}_{yy})_i \tag{6}$$

where the last approximation is only valid in regular grids. $|A_{ij}|$ is a 4×4 matrix that plays the role of a scaling factor. If $|A_{ij}|=(|u|+c)_{ij}I$, where I is the identity matrix, the standard scalar formulation of the numerical dissipation terms (Jameson et al., [10]) is recovered. When $|A_{ij}|$ is chosen as the Roe [11] matrix the matricial form of the artificial viscosity (Swanson and Turkel [12]) is obtained. Some simple validation cases and the importance of using the matricial form of the artificial viscosity for unsteady problems have been previously discussed (Corral et al. [13]). The scalar version of the numerical diffusion terms has been used in this work since for the Mach numbers of interest the differences between both approaches are negligible.

Temporal Discretization. Equation (2) can be expressed in the form

$$\frac{d(\Omega_i\mathbf{U}_i)}{dt}=\mathbf{R}(\mathbf{U},t)=\mathbf{C}(\mathbf{U},t)+\mathbf{D}(\mathbf{U}) \tag{7}$$

The main difference with respect the nonvibrating case is that the residual, **R**, depends explicitly on *t* since all the geometric factors (e.g., the volume area, Γ, the boundary velocity, **v**, etc.) depend explicitly on *t*. The residual has been split in the convective, **C**, and numerical diffusion, **D**, parts. The integration in time is performed using an explicit five stage Runge-Kutta scheme, where the artificial viscosity terms are evaluated only in three stages of the Runge-Kutta. In this case each stage, *k*, of the Runge-Kutta scheme can be written as

$$(\Omega\mathbf{U})^{(k)}=(\Omega\mathbf{U})^n+\alpha_k\Delta t(\mathbf{C}(\mathbf{U}^{(k-1)},t_n+\alpha_{k-1}\Delta t)+\beta_k\mathbf{D}(\mathbf{U}^{(k-1)})+(1-\beta_k)\mathbf{D}(\mathbf{U}^{(k-2)})) \tag{8}$$

where $\alpha_1=1/4$, $\alpha_2=1/6$, $\alpha_3=3/8$, $\alpha_4=1/2$, $\alpha_5=1$, $\beta_1=1$, $\beta_2=0$, $\beta_3=0.56$, $\beta_4=0$ and $\beta_5=0.44$. The scheme is second order accurate in time. Implicit residual smoothing may be used to increase the stability limit of the scheme although this technique has not been employed in this work.

Boundary Conditions. The second-order approximation of the 2-D, unsteady, nonreflecting boundary conditions (Giles [14]) has been used at the inlet and outlet.

The code uses phase-lagged boundary conditions in the periodic boundaries to compute in a single passage arbitrary interblade phase-angles. The standard periodicity condition is substituted by

$$\mathbf{U}(x,y=y_0,t=t_0)=\mathbf{U}(x,y=y_0+s,t=t_0+\Delta T) \tag{9}$$

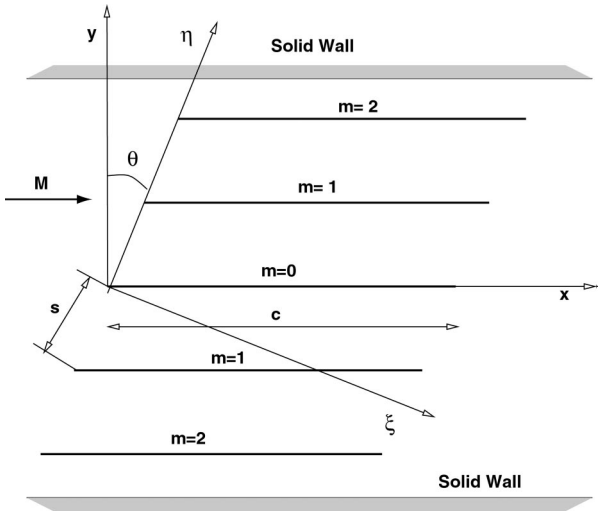

Fig. 2 Scheme and nomenclature of a linear flat plate cascade with five passages

Downloaded 31 May 2010 to 171.66.16.27. Redistribution subject to ASME license or copyright; see http://www.asme.org/terms/Terms_Use.cfm

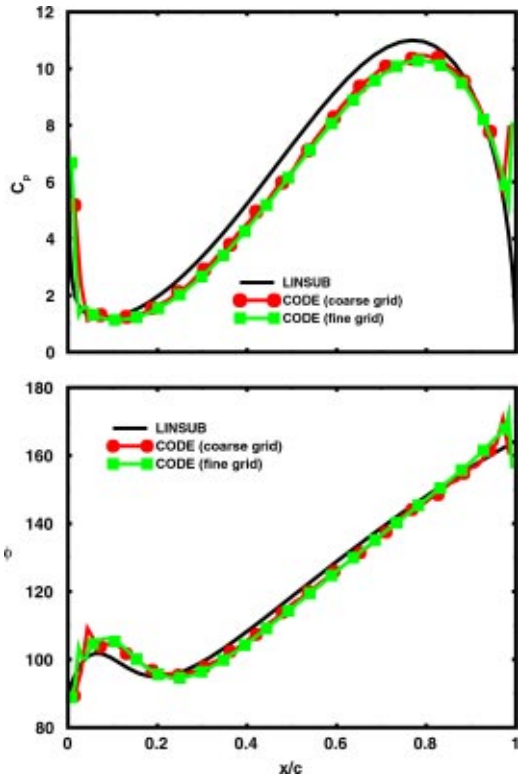

Fig. 3 Comparison with LINSUB (solid line) of the unsteady pressure amplitude (top) and phase (bottom) obtained with the current method for the baseline case ($M=0.5$, $St=5$, $s/c=0.5$, $\theta=30$ deg, $\sigma=0$ deg) with two different grids.

where $\Delta T=\sigma/\omega$ and s is the cascade pitch. The capability of the code to reproduce full annulus simulations for blade-row interactions and vibrating blades, as well as the details of this technique, may be found in Burgos and Corral [15].

Mesh Generation. Hybrid unstructured grids are generated using an internal package (G2D) where viscous layers are generated by means of an advancing-front algorithm and the inviscid field is filled with triangles using a Delaunay approach (Corral and Fernández-Castañeda [16]). Moving grids are computed in a preprocessing step. The information of the wall displacements is used to derive the boundary velocities which are transferred to the inner nodes in a smoothing step. When the blade movement is harmonic the grid displacements are filtered out using a Fourier decomposition to avoid the potential presence of nonharmonic components associated to the grid displacements.

Results

Baseline Case Description. A cascade of vibrating flat plates has been chosen as the vehicle to test the effect of the finite span of the wind tunnel on the solution. The advantage of the flat plate cascade is that the unsteady solution on the plate may be obtained in quasi-analytical form using the LINSUB code (Whitehead [17]). Figure 2 shows the layout and nomenclature of the cascade. LINSUB provides the solution in form of traveling-waves but these may be readily translated into the corresponding *exact* influence coefficients. To investigate numerically the effect of the boundaries we compare the influence coefficients obtained with the Mu^2s^2T code in the traveling-wave mode with the ones obtained vibrating the middle blade ($m=0$).

Figure 3 shows the level of accuracy that may be expected from the code using the traveling-wave formulation. As baseline case we have chosen a flat plate vibrating in torsion about the leading-edge with $M=0.5$, $\theta=30$ deg, $s/c=0.5$ and $St=5$ and a maximum amplitude of 1 deg for which the resonant conditions correspond to $\sigma_1=-62.2$ deg and $\sigma_2=109.5$ deg. The inlet and outlet boundaries are located one chord upstream and downstream of the leading and trailing edges, respectively. The $\sigma=0$ deg interblade phase angle has been reproduced and the effect of the grid density investigated. The solutions for two unstructured grids made up of about 3900 and 12,900 nodes have been compared, the differences between both solutions are considered small and the coarse grid

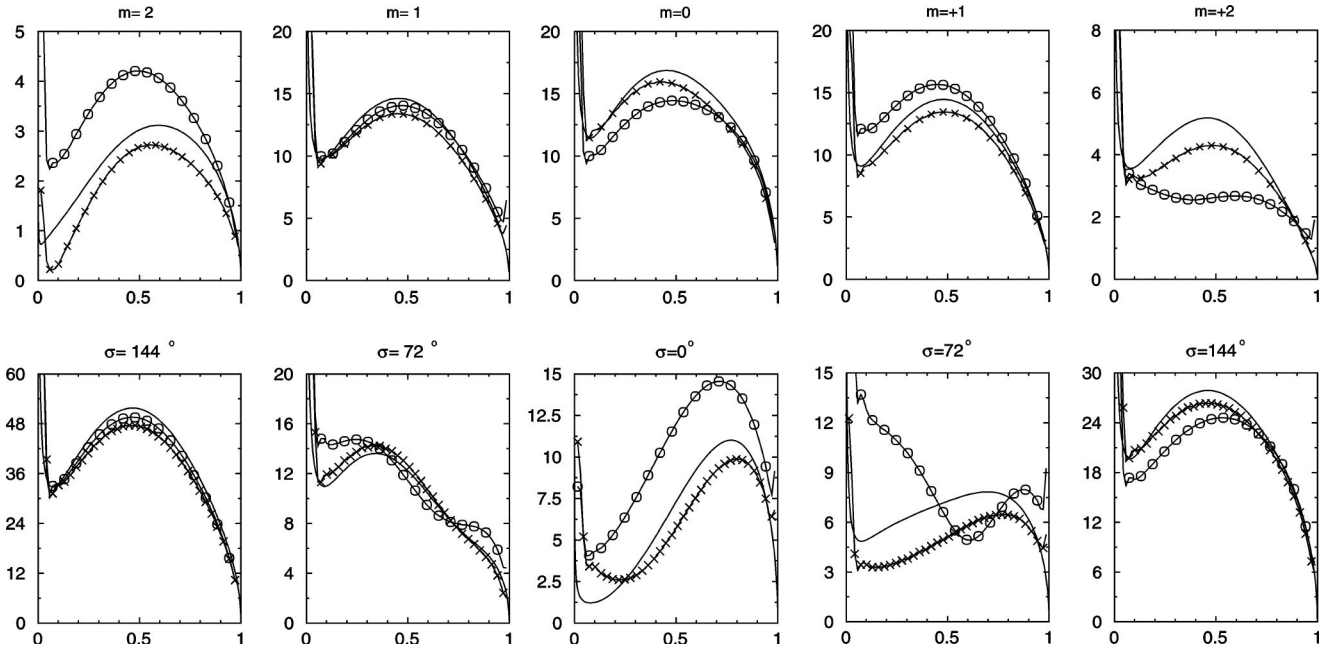

Fig. 4 Comparison against LINSUB (solid line) of the unsteady pressure amplitude in the influence coefficient (top) and traveling-wave (bottom) forms of a cascade of five flat plates vibrating in a blade alone mode computed using periodic (×) and inviscid wall (○) boundary conditions in the lateral walls

Downloaded 31 May 2010 to 171.66.16.27. Redistribution subject to ASME license or copyright; see http://www.asme.org/terms/Terms_Use.cfm

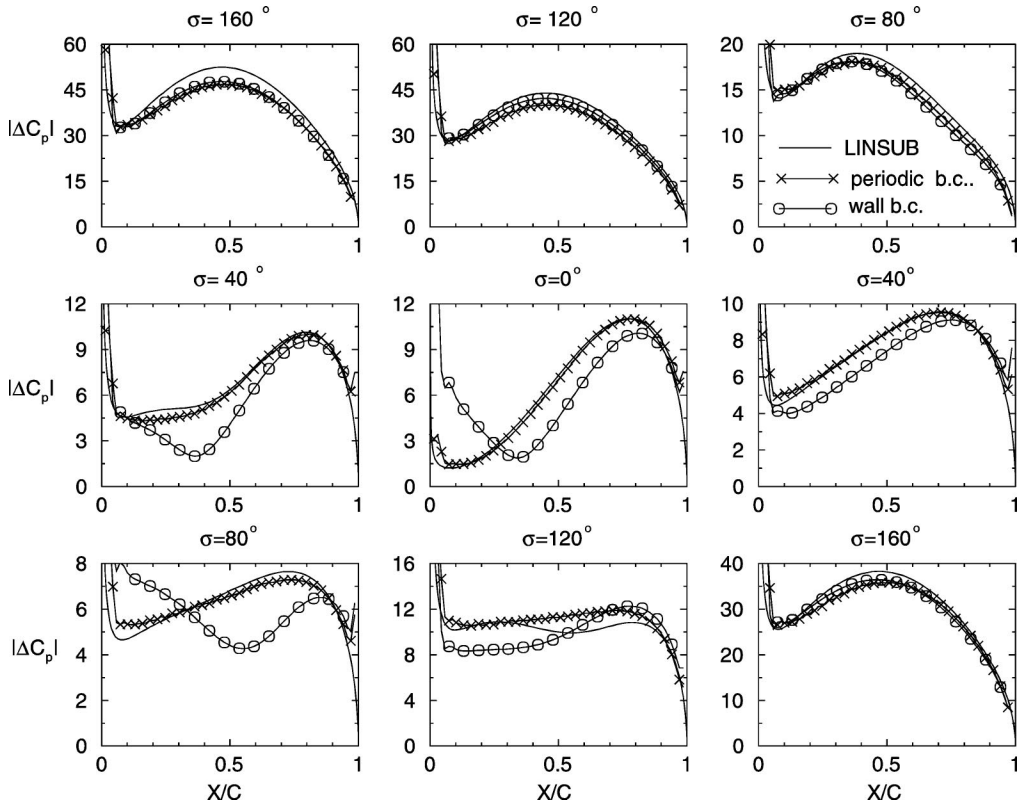

Fig. 5 Comparison against LINSUB (solid line) of the unsteady pressure amplitude expressed in form of traveling-waves of a cascade of nine flat plates vibrating in blade alone mode computed using periodic (×) and inviscid wall (○) boundary conditions in the lateral walls

has been used in the following studies to reduce the computational time. Still some discrepancies may be appreciated between the present method and LINSUB.

Individual Blade Vibration Mode. Figure 4 (top) compares the exact influence coefficients obtained by LINSUB with the ones computed with the present method vibrating the middle plate in a numerical cascade consisting of five passages and *measuring* the unsteady pressure in all the blades. Spatially periodic and solid wall boundary conditions were imposed in the lateral walls. It may be observed that the agreement in the middle blade is clearly better than the one in the blades located in the outer part of the numerical cascade ($m=\pm 2$). Qualitatively, the behavior is the same for both types of boundary conditions, but the reflection caused by the solid walls is significantly larger than the one produced by the assumption that the flow is spatially periodic. This means that the main source of error is associated to the presence of the lateral walls, independently of the type of boundary condition imposed in them.

The same comparison expressed in terms of traveling-waves is displayed at the bottom of the Fig. 4. The super resonant interblade phase angles ($\sigma=0$ deg and $\sigma=72$ deg) contain the largest errors and differ significantly from the analytical solution. The unsteady pressure distributions of the subresonant interblade phase angles are qualitatively correct, but the discrepancies with respect the analytical uncontaminated solution would hinder the validation process if the equivalent experiment were carried out. The conclusion is that five passages are insufficient to conduct validation cases against a cascade unless the whole facility were modeled. The study demonstrates that the effect of changing the boundary conditions is larger than any other and thus the discrepancies must be associated to the finite extent of the lateral boundary rather than to any other numerical error.

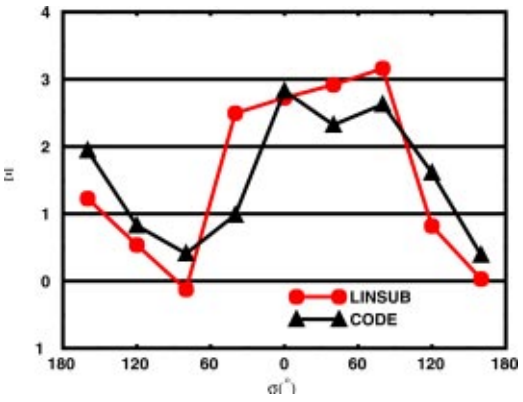

Fig. 6 Nondimensional work-per-cycle obtained from LINSUB (○) and from a cascade of nine flat plates vibrating in blade alone mode computed using solid lateral walls

Convergence of the Influence Coefficient Approach. Due to the lack of agreement between the finite span computation and the analytical results we have repeated the same exercise for $N=9$ and 21 to determine whether the process is convergent or not and dissipate any doubt about the correctness of the implementation of the influence coefficient technique in the code. The solution for $N=9$ is displayed in Fig. 5 and the work per cycle in Fig. 6. The trends are the same as the ones encountered with five blades. The solutions at the outer blades are contaminated also due to the influence of the lateral walls, and although the relative value of the unsteady pressure in these plates with respect to the one of the middle plate is small, their contribution to the construction of the traveling wave-mode is still relevant, mainly to the modes with

Downloaded 31 May 2010 to 171.66.16.27. Redistribution subject to ASME license or copyright; see http://www.asme.org/terms/Terms_Use.cfm

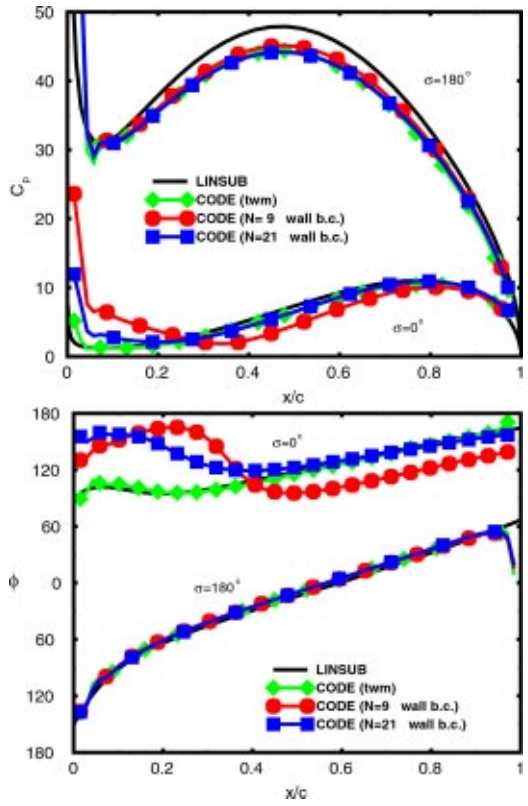

Fig. 7 Comparison with LINSUB (solid line) of the unsteady pressure amplitude (top) and phase (bottom) obtained with the current method for the baseline case ($M=0.5$, $St=5$, $s/c=0.5$, $\theta=30$ deg) and two different interblade phase angles ($\sigma=0$ deg and $\sigma=\pi$)

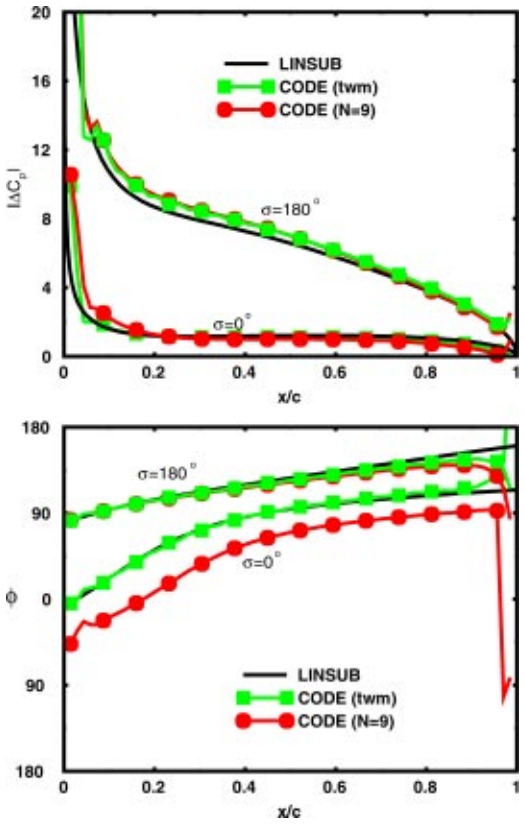

Fig. 9 Comparison with LINSUB (solid line) of the unsteady pressure amplitude (top) and phase (bottom) obtained with the current method using nine blades ($M=0.5$, $St=1$, $s/c=0.5$, $\theta=30$ deg, $\sigma=0$ deg)

small interblade phase-angles. This behavior may be easily understood by looking at the relation between the unsteady pressure coefficient and the influence coefficients

$$\mathrm{Re}(\Delta\tilde{C}_p^{\sigma}) = \sum_{m=-\infty}^{m=+\infty} \mathrm{Re}(C_m)\cos(m\sigma) - \mathrm{Im}(C_m)\sin(m\sigma) \quad (10)$$

with a similar expression for the imaginary part. Let us concentrate in the interblade phase angle $\sigma=0$ deg, in this case, Eq. (10) reduces to $\mathrm{Re}(\Delta\tilde{C}_p^{\sigma})=\Sigma_m \mathrm{Re}(C_m)$ and all the small queues of the influence coefficients contribute to the sum. The opposite limit corresponds to $\sigma=180$ deg, in this case Eq. (10) takes the form $\mathrm{Re}(\Delta\tilde{C}_p^{\sigma})=\Sigma_m(-1)^m \mathrm{Re}(C_m)$ and the influence coefficients of the queue tend to calcel out by pairs, and therefore the sensitivity of the pressure distribution to the number of elements of the series is much less than in the previous case.

It may be appreciated also that the matching of the periodic boundary conditions with the analytical solution is much better than the one obtained using inviscid walls. This means that the influence coefficient technique compares better with the traveling-wave solution in an annular cascade than in a linear cascade and that conclusions about the minimum number of blades required to

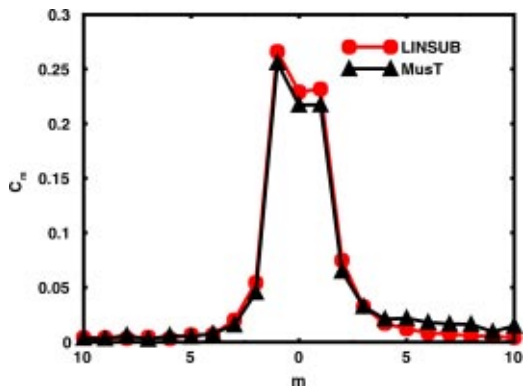

Fig. 8 Comparison with LINSUB (○) of the influence coefficients obtained with the current method (×) for the baseline case ($M=0.5$, $St=5$, $s/c=0.5$, $\theta=30$ deg) and $N=21$

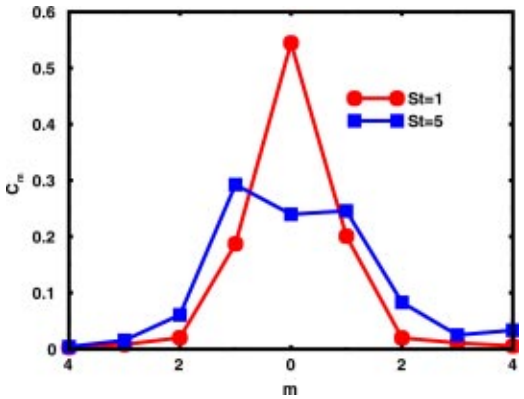

Fig. 10 Influence coefficients obtained with the LINSUB with nine blades ($N=9$) for the baseline case ($M=0.5$, $s/c=0.5$, $\theta=30$ deg) and two reduced frequencies $St=1$ and $St=5$

Downloaded 31 May 2010 to 171.66.16.27. Redistribution subject to ASME license or copyright; see http://www.asme.org/terms/Terms_Use.cfm

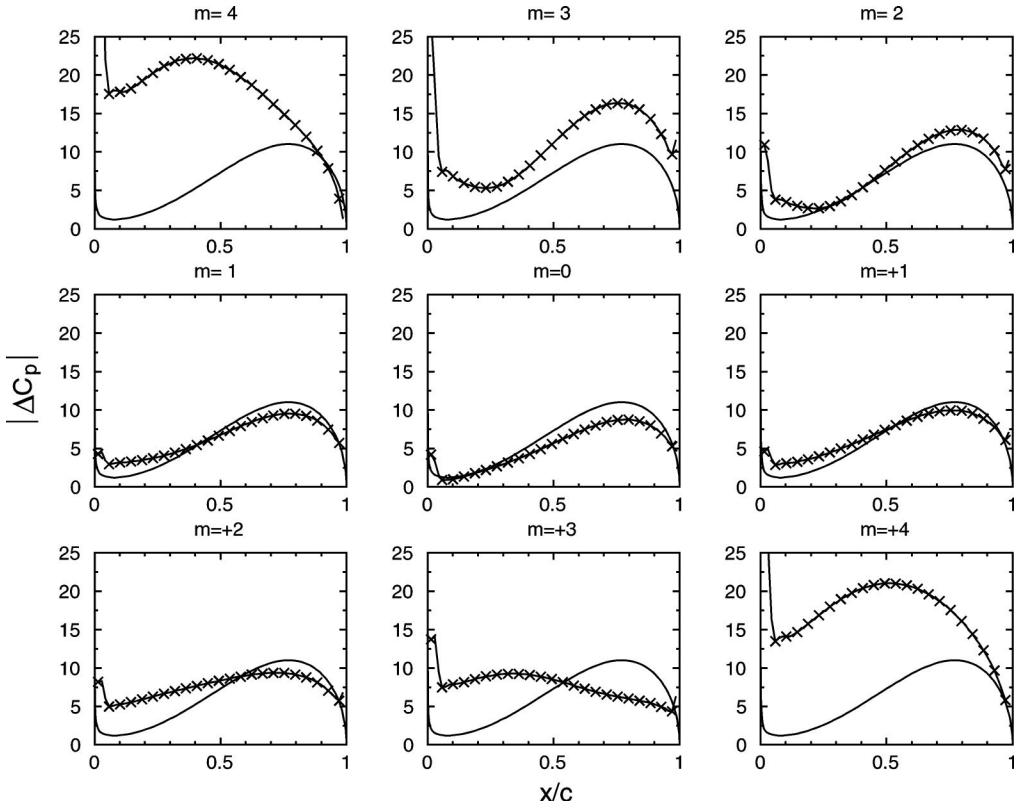

Fig. 11 Comparison against LINSUB (solid line) of the unsteady pressure amplitude of the different airfoils (×) of a cascade of nine flat plates vibrating in traveling-wave mode (σ=0 deg)

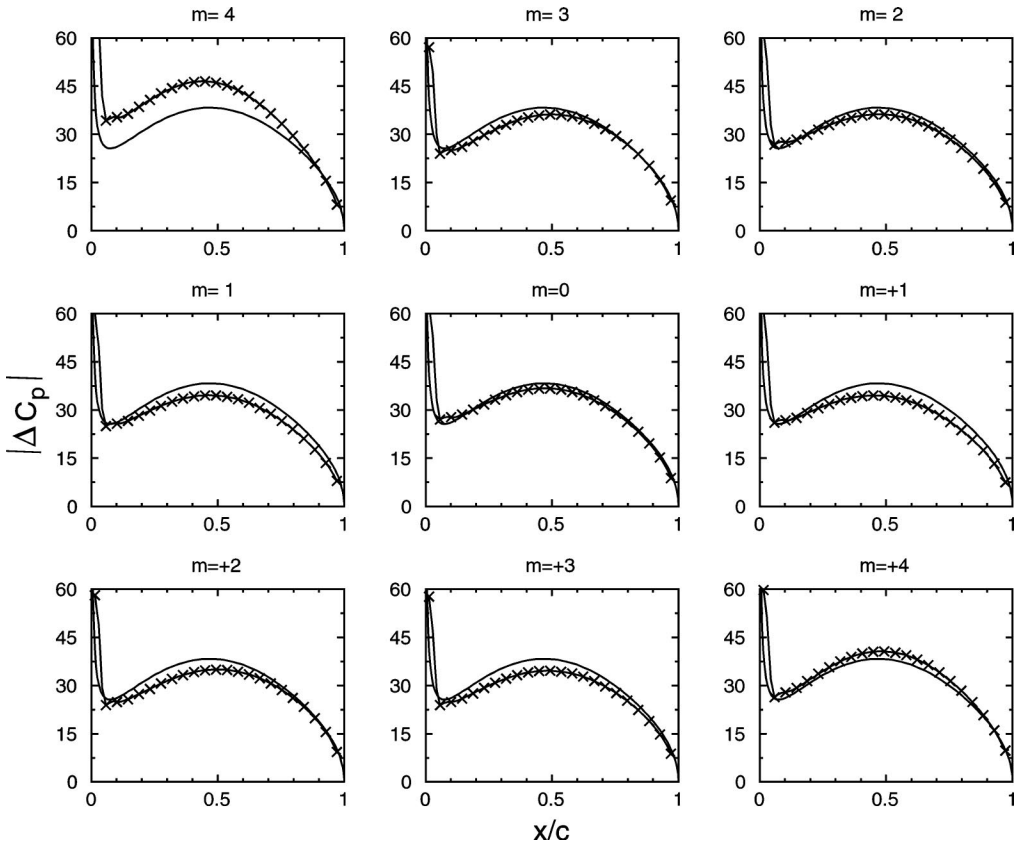

Fig. 12 Comparison against LINSUB (solid line) of the unsteady pressure amplitude of the different airfoils (×) of a cascade of nine flat plates vibrating in traveling-wave mode (σ=160 deg)

Downloaded 31 May 2010 to 171.66.16.27. Redistribution subject to ASME license or copyright; see http://www.asme.org/terms/Terms_Use.cfm

match the traveling-wave solution obtained from an annular cascade may not be directly extrapolated to a linear or sector facility.

Figure 7 displays the convergence of the influence coefficient technique for large number of blades to the solution obtained in the form of traveling-waves using the phase-lagged boundary conditions for two different interblade phase angles. The crosses ($\times$) represent the solution obtained with the traveling-wave formulation of the problem which compares well with the solution obtained by LINSUB, except for the amplitude of the $\sigma=180$ deg case which is slightly off the quasi-analytical value. This error is consistent and a good matching of the influence coefficient technique with the traveling-wave formulation is obtained even with nine blades. The convergence of the $\sigma=0$ deg case is slower and although the unsteady pressure amplitude may be considered converged for 21 blades, still large discrepancies may be appreciated in the phase. We associate this phenomenon to the influence of the lateral walls since the matching of the traveling-wave formulation of the problem with LINSUB is quite good. Figure 7 is a proof of the correct implementation of the influence coefficient technique since the solutions obtained with this approach converge to the ones obtained in form of traveling-waves using the phase-lagged boundary conditions when the number of blades of the numerical cascade is large enough.

Figure 8 compares the influence coefficients (IC) obtained by means of a simulation with 21 passages and solid lateral walls with the LINSUB solution translated to IC form that are considered as the *exact* solution. The influence coefficients have been renormalized in this case in the following way:

$$\bar{C}_m = \frac{C_m}{\Sigma_{i=-M}^{M} C_i}, \tag{11}$$

where $m=(N-1)/2$. The agreement between both curves is fairly good and demonstrates that in spite of the small amplitude of the influence coefficients for $|m|>4$, the part of the solution that is not computed in the $N=9$ case is still not negligible and may contaminate the solution for some interblade phase angles. This is seen in Fig. 7 where two interblade phase angles have been reconstructed using 9 and 21 influence coefficients and differences in the solution may be clearly appreciated, specially in the phase of $\sigma=0$ deg case.

Reduced Frequency Sensitivity. To assess the effect of the reduced frequency on the sidewall contamination we have repeated the simulation for the $N=9$ case setting $St=1$, which is more representative for a flutter problem. The unsteady pressure distributions for the reconstruction of $\sigma=0$ deg and $\sigma=180$ deg may be seen in Fig. 9. In general the agreement is better than for the $St=5$ case. This is due to the fact that the influence coefficient decay much faster with the distance when the reduced frequency is smaller (see Fig. 10), and therefore, for a given number of blades, the accuracy of the influence coefficient approach increases when the vibration frequency is reduced.

Traveling-Wave Vibration Mode. Up to now, two strategies for vibrating the blades have been compared, namely, the influence coefficient technique, which is a widely used method in linear cascades, and the traveling-wave approach, that is usually used in annular cascades. Some times however, the latter is used as well in linear cascades, as it has been the case of the NASA oscillatting cascade facility. We have compared this technique to the standard influence coefficient technique where just one of the blades is vibrated. The same cascade consisting of nine flat plates has been vibrated in two traveling-wave modes ($\sigma=0$ and 160 deg) using solid wall boundary conditions at the wind tunnel lateral boundaries. The results are displayed in Figs. 11 and 12. It may be seen that for the $\sigma=0$ deg case only the three central plates have similar unsteady pressure distributions. Airfoils $m=\pm 4$ have similar pressure distributions, but these resemble the $\sigma=160$ deg case instead the $\sigma=0$ deg one due to sidewall contamination. The practical difficulties to obtain an accurate representation of superresonant cases in linear cascades were reported by Buffum and Fleeter [2]. The unsteady periodicity in the $\sigma=160$ deg is better, as may be appreciated in Fig. 12, where the unsteady pressure distribution in all the blades is comparable and only the plate $m=-4$ differs significantly from the rest. However, no improvement is appreciated with regard the results obtained by vibrating just the middle blade.

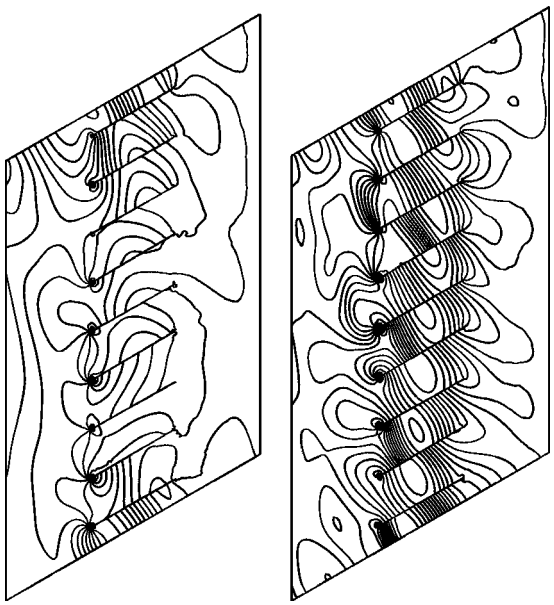

Fig. 13 Instantaneous isocontour lines of static pressure of a linear cascade of nine flat plates vibrating in traveling-wave mode; left: $\sigma=0$ deg, right: $\sigma=160$ deg

Figure 13 shows the pressure isocontours in a generic instant of the aforementioned case. It may be seen that the solution for $\sigma=0$ deg is fully contaminated by the influence of the lateral walls. The solution at any instant should be the same for all the blades; however, it is obvious that every passage contains a different instantaneous solution which is an indication of the degree of perturbation induced by the walls. It is worth noting how the solution in the lateral passages looks like the one of the $\sigma=160$ deg represented in the right hand side of the same figure. The solution of the $\sigma=160$ deg case contains several minimal flow units constituted by pairs of plates which is an indication that the solution is periodic and consistent with the rest of the results. This should be the case if the interblade phase-angle were exactly 180 deg.

Geometric Effects. To assess the effect of sidewall contamination on realistic blades we have repeated the same exercise with two cascades representative of a compressor and a turbine blade consisting of seven and nine blades respectively. The compressor blade correspond to the 10th standard configuration [3] with an exit isentropic Mach number, $M_{is}=0.7$ and an inlet angle $\alpha=55$ deg. The lateral walls of the cascade have been defined shifting the mid-line of the airfoil. The comparison between the solutions obtained vibrating the blade in traveling-wave mode and using the IC technique using seven blades and solid lateral walls may be seen in Fig. 14. The trends are very similar to the ones encountered in the baseline case as could be expected since the compressor blade may be seen in first approximation as a flat plate. Figure 15 shows that although the sidewalls have been chosen with care it would be necessary a redesign of them to minimize the influence of the nonperiodicity of the mean field into the unsteady field. The unsteady pressure obtained from the lower airfoil of the cascade has not been used to reconstruct the traveling-wave solution.

Downloaded 31 May 2010 to 171.66.16.27. Redistribution subject to ASME license or copyright; see http://www.asme.org/terms/Terms_Use.cfm

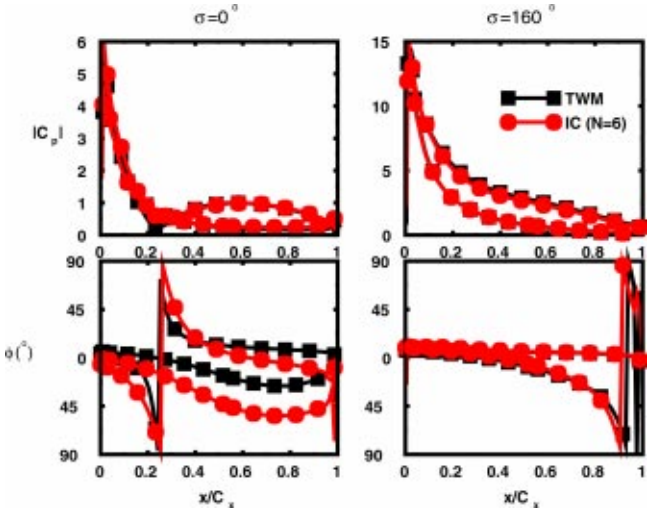

Fig. 14 Comparison of the unsteady pressure amplitude (top) and phase (bottom) obtained with the current method using the twm mode and a cascade of nine blades with solid lateral walls for the 10th standard configuration and two interblade phase angles σ=0 deg (left) and σ=160 deg (right)

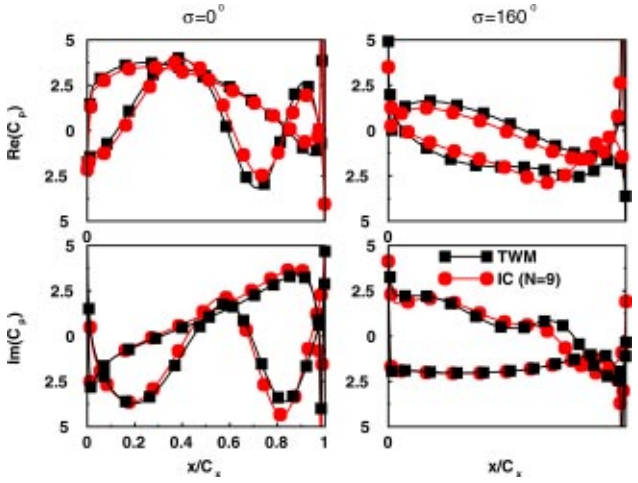

Fig. 16 Comparison of the unsteady pressure amplitude (top) and phase (bottom) obtained with the current method using the twm mode and a cascade of nine blades with solid lateral walls for the T106 blade and two interblade phase angles σ=0 deg (left) and σ=160 deg (right)

The turbine blade corresponds to the well known T106 section (Wood et al. [18]). The exit isentropic Mach number is $M_{is}=0.59$ and the inlet angle $\alpha=37.7$ deg. The center of torsion of the airfoil has been chosen at the airfoil mid-line at the half-axial chord and the reduced frequency based on the exit velocity $St=5$. The lateral walls of the cascade are streamlines obtained from a simulation of a single passage with periodic boundary conditions and therefore it may be ensured that the mean flow is identical in all the passages. The comparison between the unsteady pressures obtained in the traveling-wave mode and the influence coefficient technique using nine blades and solid lateral walls may be seen in Fig. 16. In this case the agreement between both simulations is higher than expected from the previous simulations. It is speculated that this is due to the particular shape of the blade and not to the better quality of the mean flow, however this point needs further investigation.

Concluding Remarks

A cascade of flat plates has been chosen as a limit case for the investigation of the unsteady periodicity in linear cascades. The attractiveness of this case is twofold, firstly it may be ensured that the steady solution is fully periodic and secondly a quasi-analytic solution exists which allows direct comparison between the computed and the nominal solution. The conclusions may be summarized in the following way:

1. The linearity of the flow is not a sufficient condition to guarantee that experimental data may be readily translated from the influence coefficient to the traveling-wave form due to the interference of the lateral walls.
2. The conclusions obtained in annular cascades about the minimum number of passages required to avoid the influence of the lateral walls of the wind tunnel may not be directly extrapolated to linear cascades.
3. It is expected that the matching between experimental data obtained from linear cascades and CFD results presents an asymptotic limit due to the finite extent of the cascade. The situation is aggravated for small interblade phase angles and certainly, although this point has not been investigated in this work, for transonic cases.
4. Vibrating a linear cascade in traveling-wave mode does not seem to present any advantage over the single mode technique, except probably for cases that behave in a nonlinear way, since it avoids the use of the hypothesis of the linearity to reconstruct solutions in form of influence coefficients into traveling-wave ones.
5. The blade shape seems to play an important role and it seems that the conclusions obtained from compressor blading may not be extrapolated to turbines blades although this point requires further investigation.

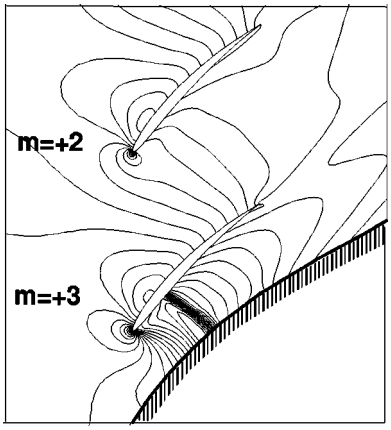

Fig. 15 Isomach lines of the 10th standard configuration computation in the sidewall region

Acknowledgments

The authors wish to thank ITP for the permission to publish this paper and for its support during the project. This work has been partially funded by ITP under Contract No. DT-ITP-00-0010 to the School of Aeronautics. The second author wants to thank ITP for allowing him the use of its facilities during the development of this work.

Nomenclature

- $\mathbf{f}, \mathbf{g}$ = convective fluxes
- m = airfoil number
- $\mathbf{n}$ = normal
- N = no. of blades
- St = $\omega c/V_{inlet}$ reduced frequency

Downloaded 31 May 2010 to 171.66.16.27. Redistribution subject to ASME license or copyright; see http://www.asme.org/terms/Terms_Use.cfm

twm = traveling-wave mode
$\mathbf{U}$ = conservative variables
Ω = control volume
α = torsion angle
ϕ = phase angle
σ = interblade phase angle
ω = angular frequency
θ = cascade stagger angle
Ξ = nondimensional work-per-cycle
$\Delta\tilde{C}_p = p^+ - p^-/\rho_\infty U_\infty^2 \alpha$, unsteady pressure coefficient

References

[1] Bölcs, A., 1983, "A Test Facility for the Investigation of the Steady and Unsteady Transonic Flows in Annular Cascades," ASME Paper 83-GT-34.

[2] Buffum, D. H., and Fleeter, S., 1991, "Linear Oscillating Cascade Unsteady Aerodynamic Experiments," in the 6th International Symposium on Unsteady Aerodynamics, Aeroelasticity and Aeroacoustics of Turbomachines, Ed. Atassi, September 15–19.

[3] Fransson, T. H., and Verdon, J. M., 1992, "Standard Configurations for Unsteady Flow Through Vibrating Axial-Flow Turbomachine-Cascades," KTH Technical Report TRITA/KRV/92-009.

[4] Bell, D. L., and He, L., 2000, "Three-Dimensional Unsteady Flow for an Oscilatting Turbine Blade and the Influence of the Tip-Clearance," ASME J. Turbomach., **122**(1), Jan., pp. 93–101.

[5] Bölcs, A., Fransson, T. H., and Schlafli, D., 1989, "Aerodynamic Superposition Principle in Vibrating Turbine Cascades," AGARD, 74th Specialists' Meeting of the Propulsion and Energetics Panel on Unsteady Aerodynamic Phenomena in Turbomachines, Luxembourg, August 28–September 1.

[6] Chima, R. V., McFarland, E. R., Wood, J. R., and Lepicovsky, J., 2000, "On Flowfield Periodicity in the NASA Transonic Flutter Cascade, Part II-Numerical Study," ASME Paper 2000-GT-0573.

[7] Lepicovsky, J., McFarland, E. R., Chima, R. V., and Wood, J. R., 2000, "On Flowfield Periodicity in the NASA Transonic Flutter Cascade, Part I—Experimental Study," ASME Paper 2000-GT-0572.

[8] Ott, P., Norryd, M., and Bölcs, A., 1998, "The Influence of Tailboards on Unsteady Measurements in a Linear Cascade," ASME Paper 98-GT-0572.

[9] Hall, K. C., 1999, "Linearized Unsteady Aerodynamics," in Aeroelasticity in Axial Flow Turbomachines VKI Lecture Series 1999-05.

[10] Jameson, A., Schmidt, W., and Turkel, E., 1981, "Numerical Solution of the Euler Equations by Finite Volume Techniques Using Runge-Kutta Time Stepping Schemes," AIAA Pap. No. 81–1259.

[11] Roe, P., 1981, "Approximate Riemman Solvers, Parameters, Vectors and Difference Schemes," J. Comput. Phys. **43**, pp. 357–372.

[12] Swanson, R. C., and Turkel, E., 1992, "On Central-Difference and Upwinding Schemes," J. Comput. Phys. **101**, pp. 292–306.

[13] Corral, R., Burgos, M. A., and García, A., 2000, "Influence of the Artificial Dissipation Model on the Propagation of Acoustic and Entropy Waves," ASME Paper 2000-GT-563.

[14] Giles, M. B., 1990, "Non-Reflecting Boundary Conditions for Euler Equation Calculations," AIAA J., **28**(12), pp. 2050–2057.

[15] Burgos, M. A., and Corral, R. 2001, "Application of the Phase-Laged Boundary Conditions to Rotor/Stator Interaction," ASME Paper 2001-GT-586.

[16] Corral, R., and Fernández-Castañeda, J., 2001, "Surface Mesh Generation by Means of Steiner Triangulations," AIAA J., **39**(1), Jan., pp. 176–180.

[17] Whitehead, D. S., 1987, "Classical Two-Dimensional Methods," Chapt. 2, AGARD Manual on Aeroelasticity in Axial Flow Turbomachines: Unsteady Turbomachinery Aerodynamics, Vol. 1, eds., M. F. Platzer and F. O. Carta, AGARD-AG-298.

[18] Wood, J. R., Strasizar, T., and Hathaway, M., 1990, "Test Case E/CA-6 Subsonic Turbine Cascade T106," Test Cases for Computation of Internal Flows in Aero Engine Components, AGARD-AR-275, July.

Downloaded 31 May 2010 to 171.66.16.27. Redistribution subject to ASME license or copyright; see http://www.asme.org/terms/Terms_Use.cfm

Maximum Amplification of Blade Response due to Mistuning: Localization and Mode Shape Aspects of the Worst Disks

Alejandro J. Rivas-Guerra
Assoc. Mem. ASME
e-mail: alejandro.rivas@asu.edu

Marc P. Mignolet
Fellow ASME
e-mail: marc.mignolet@asu.edu

Arizona State University,
Department of Mechanical and
Aerospace Engineering,
Tempe, AZ 85287-6106

This paper focuses on the determination and study of the maximum amplification of the steady state forced response of bladed disks due to mistuning. First, an optimization strategy is proposed in which partially mistuned bladed disks are considered as physical approximations of the worst case disk and the mistuned properties are sought to maximize the response of a specific blade. This approach is exemplified on both a reduced order model of a blisk and a single-degree-of-freedom per blade disk model an extensive parametric study of which is conducted with respect to blade-to-blade coupling, damping, and engine order. A mode shape-based formulation of the amplification factor is then developed to clarify the findings of the parametric study in the strong coupling/small damping limit. In this process, the upper bound of Whitehead is recovered for all engine orders and number of blades and the conditions under which this limit is exactly achieved or closely approached are clarified. This process also uncovers a simple yet reliable approximation of the resonant mode shapes and natural frequencies of the worst disk.
[DOI: 10.1115/1.1506958]

Keywords: Mistuning, Blade Vibration, Maximum Amplitude, Optimization, Mode Shape

Introduction

The blades of any given disk do not exhibit geometrical and/or material properties that are perfectly identical to each other. Rather, they each have their own characteristics (e.g., natural frequencies, mode shapes, etc.) that differ slightly from the design requirements because of finite manufacturing tolerances, in-service wear, foreign object damage, etc. Surprisingly, it has been demonstrated that these small variations, collectively referred to as mistuning, strongly influence the dynamic response of bladed disks (see for example references [1–14]). In particular, it has often been observed that the amplitudes of vibration of mistuned bladed disks can exceed, sometimes significantly, the corresponding forced responses of their tuned counterparts. These increased response levels are typically associated with potentially sharp decreases of the fatigue life of the blades and thus represent a very important design/analysis consideration.

To quantify the increase in response and to allow comparison between different bladed disk models, the "amplification factor" has been introduced as the ratio of the largest amplitude of blade response on a mistuned disk obtained in a frequency sweep divided by the corresponding tuned resonant amplitude. Among the noteworthy amplification factors available in the literature are the values of 2.43 (72-blade disk) and 5 (92-blade disk) obtained by Basu and Griffin [4] and Petrov and Ewins [15] in computational efforts and the experimental factor of 5.28 (max to min, 52-blade disk) observed by Kaiser et al. [16]. These large magnification factors and the significant decrease of the blade fatigue life they incur have led to the search for the maximum amplification factor that can be achieved and, to a smaller degree, for the pattern of mistuning yielding this forced response.

This issue was first addressed by Whitehead [1,17,18] who obtained the remarkably simple upper bound of $(1+\sqrt{N})/2$ for the magnification factor that can be observed when the natural frequencies of the N-blade tuned and mistuned disks are well separated, i.e. when each blade can be modeled as a single-degree-of-freedom system. He further demonstrated that this upper bound can indeed be achieved, e.g., in the limit of a zero damping and for engine orders 0 and $N/2$ (if N is even). While the optimization efforts of Petrov and Ewins [15] have yielded an amplification factor close to $(1+\sqrt{N})/2$ for a full finite element model of a turbine disk (5 versus 5.3), most other optimization efforts, such as those of [13,19–21] have yielded lower or much lower values than Whitehead's limit. These lower estimates and the lack of influence of damping and engine order in the upper bound $(1+\sqrt{N})/2$ have left the issue without a full solution.

In this light, the goal of this investigation is to revisit the prediction of the maximum amplification factor, both quantitatively and qualitatively, focusing in particular on the effects of damping and varying engine orders. Special emphasis will also be placed on the properties of the worst disk, e.g., mistuning pattern, mode shapes and natural frequencies, that lead to the maximum amplification factor.

In keeping with the phenomenological focus of the present investigation, the simple bladed disk model shown in Fig. 1 will be considered for most of the analysis but the applicability of the

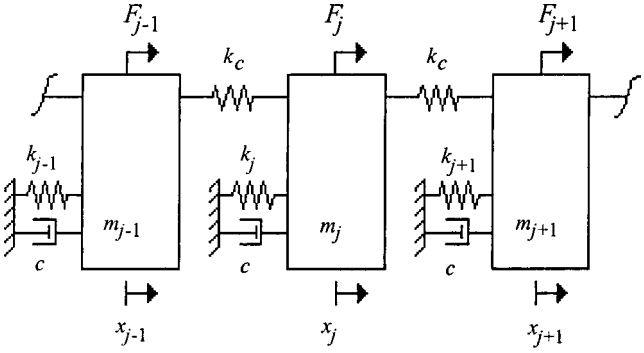

Fig. 1 Single-degree-of-freedom per blade bladed disk model (all m_j are equal)

Contributed by the International Gas Turbine Institute and presented at the International Gas Turbine and Aeroengine Congress and Exhibition, Amsterdam, The Netherlands, June 3–6, 2002. Manuscript received by the IGTI, March 4, 2002. Paper No. 2002-GT-30323. Review Chair: E. Benvenuti.

 Copyright © 2003 by ASME

Downloaded 31 May 2010 to 171.66.16.27. Redistribution subject to ASME license or copyright; see http://www.asme.org/terms/Terms_Use.cfm

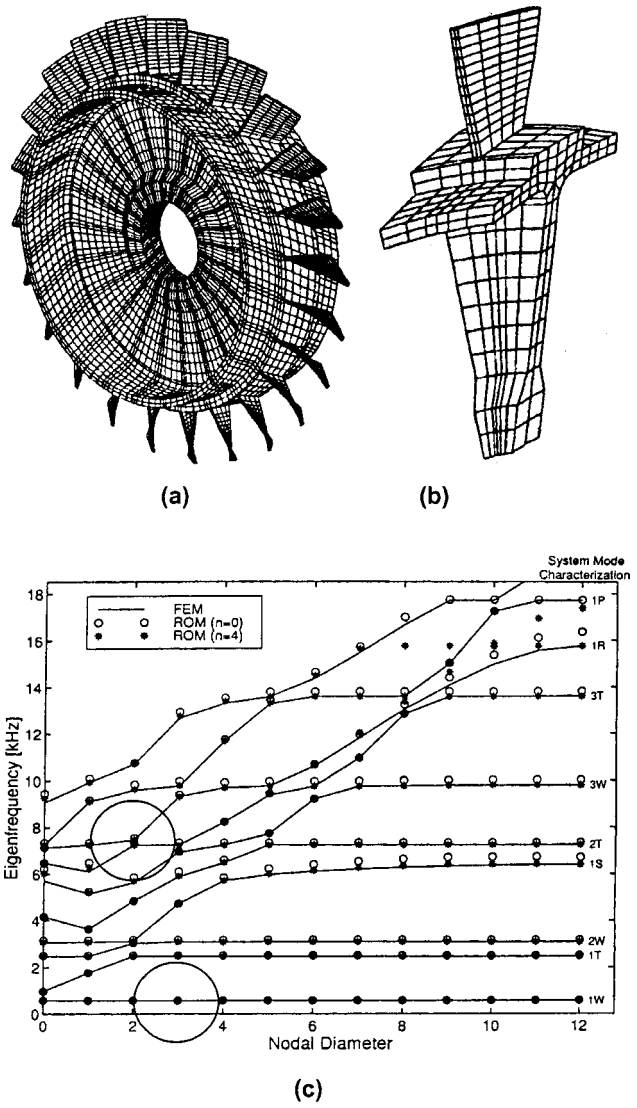

Fig. 2 Blisk example: (*a*) blisk view, (*b*) blade sector finite element mesh, and (*c*) natural frequency versus nodal diameter plot

concepts will also be demonstrated on the reduced order model (see Castanier et al. [22]) of the blisk shown in Fig. 2 (see Bladh et al. [23]).

Localization-Based Optimization and Partial Mistuning Modeling

The determination of the maximum amplification factor is achieved by finding the mistuned blade properties (stiffnesses, masses, natural frequencies, . . .) that lead to the largest response of a specified blade, blade 1 say. This problem may appear straightforward at first but the number of variables present in this optimization effort equals the number of degrees-of-freedom on the disk and may thus be exceedingly large in connection with a full finite element model of the bladed disk. To reduce the complexity of this problem, Petrov and Ewins [15] introduced mistuning only in selected degrees-of-freedom while considering the response of the full finite element model. The optimization scheme used here is somewhat of a dual of theirs: it relies on a reduced order model (REDUCE, see [22]) of the bladed disk, but could include mistuning on all degrees-of-freedom.

As will be shown later, there can be a rather large number of local maxima of the amplification factor and thus a well designed search procedure must be used to capture the global optimum. While genetic algorithms have recently been found to be quite successful in connection with blade mistuning optimization (see [13], [24]), a different approach was followed here. Specifically, it has been shown [25] that the dynamic behavior of the highest responding blade in a population of disks is dictated by local interactions only, even for very high coupling levels. It was then shown that the amplitude of vibration of such a blade can be well estimated by assuming a ''partial mistuning'' model [11] in which only the few surrounding blades are mistuned. In the present context, this finding indicates that the dominant influence on the amplification factor arises from the mistuned properties of the s-blade sector $j \in [1,p+1] \cup [N-p+1,N]$ with $s=2p+1$ typically much less than N.

These observations are the basis for the proposed localization-based optimization algorithm which can be summarized as follows:

i. For a given set of tuned blade parameters, a 3-blade mistuned sector (blades N, 1, and 2) is first considered and the mistuned properties of these 3 blades are varied as to maximize the amplitude of the steady state response of blade 1.

ii. Using the optimum 3-blade mistuning pattern as initial guess, a 5-blade mistuned sector is then considered and the optimization effort is reconducted yielding a new (higher) amplification factor.

iii. The process is repeated with 7, 9,.. blade mistuned sectors until convergence of the amplification factor is obtained.

Some of the advantages of this approach are:

a. the number of variables, i.e. the mistuned blade properties, involved in the optimization effort is as small as possible

b. the likelihood to converge to a *local* maximum of the amplification factor appears to be dramatically reduced as opposed to a full optimization effort of the entire set of mistuned blade properties.

The above procedure has performed particularly well for moderate damping ratios, i.e., of the order of one or several percent. For smaller damping ratios, it is suggested to initiate the procedure at a damping level of 1% or so and to proceed with cascaded decreases in damping and increases in partial mistuning width.

In regards to computational issues, it should also be noted that the determination of the forced response of a partially mistuned disk can be achieved in a particularly efficient manner by partitioning the degrees-of-freedom into those directly affected by mistuning (subscript d) and those only indirectly subjected to it (subscript i). Specifically, it can be shown (see [11] and [25]) that the response $\underline{x}_d$ of the n_m degrees-of-freedom that are directly affected by the mistuning can be determined from the $n_m \times n_m$ system of equation

$$H_{pm}\underline{x}_d = \underline{x}_d^{(t)} . \tag{1}$$

In this equation, the subscript pm refers to partial mistuning, $\underline{x}_d^{(t)}$ is the tuned response of the d degrees-of-freedom, and the element kl of the matrix H_{pm} is

$$(H_{pm})_{kl} = \delta_{kl} + \sum_{j=1}^{n_m} (\Delta H_{dd})_{jl} (\underline{h}_d^{(j)})_k \tag{2}$$

in which δ_{kl} denotes the Kronecker symbol. Further, ΔH_{dd} denotes the $n_m \times n_m$ partition of the impedance matrix associated with mistuning and $\underline{h}_d^{(j)}$ is the response of the *tuned* system on the degrees-of-freedom d to a single, unit force acting on the degree-of-freedom j of the set $\underline{x}_d$. Once the response $\underline{x}_d$ of the degrees-of-freedom that are directly affected by the mistuning has been determined from Eq. (1), the motion of the remaining degrees-of-freedom can be determined as

Downloaded 31 May 2010 to 171.66.16.27. Redistribution subject to ASME license or copyright; see http://www.asme.org/terms/Terms_Use.cfm

$$\underline{x}_i = \underline{x}_i^{(t)} - \sum_{j=1}^{n_m} \left[\sum_{k=1}^{n_m} (\Delta H_{dd})_{jk} (\underline{x}_d)_k \right] \underline{h}_i^{(j)} \tag{3}$$

where $\underline{h}_i^{(j)}$ is defined similarly to $\underline{x}_d^{(j)}$ but for the degrees-of-freedom i.

Parametric Study of the Single Degree-of-Freedom per Blade Bladed Disk Model

Before addressing complex models, it is desired to first proceed with a comprehensive parametric study of the single-degree-of-freedom per blade bladed disk model shown in Fig. 1 to provide an initial perspective on the determination of the mistuned properties leading to the maximum amplification factor and the properties of the corresponding worst disk.

Dimensionless Equations of Motion and Parameters. The desired parametric study of the maximum amplification factor is most easily performed in terms of dimensionless variables and parameters. To accomplish such a formulation, denote first by $X_j(t)$ the response of blade j of the bladed disk model of Fig. 1. From the equations of motion, it is found that

$$m\ddot{X}_j + c\dot{X}_j + (k_j + 2k_C)X_j - k_C X_{j-1} - k_C X_{j+1} = F_j(t) \tag{4}$$

where $F_j(t)$ is the time-varying force acting on blade j. Of particular importance in the present context is the engine order excitation of the form

$$F_j(t) = F_0 e^{i(\omega t + (j-1)\Delta\varphi)} \tag{5}$$

where $\Delta\varphi = 2\pi r/N$ is the interblade phase angle and r is the engine order.

Assuming a steady state solution of Eqs. (4) and (5) of the form $X_j(t) = x_j e^{i\omega t}$ where x_j is a complex amplitude yields the linear system of equations

$$(k_j + 2k_C - m\omega^2 + i\omega c)x_j - k_C x_{j-1} - k_C x_{j+1} = F_0 e^{i(j-1)\Delta\varphi} \tag{6}$$

When the system is tuned, i.e. $k_j = k_t$ for all j, the natural frequency corresponding to the rth engine order is

$$\omega_r = \sqrt{\frac{k_t + 4k_C \sin^2(\pi r/N)}{m}} \tag{7}$$

and the amplitude of response x_j of each blade at that frequency is equal to $F_0/(ic\omega_r)$. Note that this ratio also closely approximates the peak response of the system as long as the damping ratio ζ, or equivalently $c\omega_r/k_t$, is much smaller than 1. Accordingly, it is proposed here to introduce the amplification factor of blade j as $|\overline{A_j}|$ where $\overline{A_j}$ is the ratio of the mistuned and largest tuned complex amplitudes, i.e.

$$\overline{A_j} = \frac{x_j}{(F_0/c\omega_r)} = \frac{c\omega_r x_j}{F_0} \tag{8}$$

With this notation, Eq. (6) can be rewritten in dimensionless form

$$(\overline{k_j}\overline{k_C} + i)\overline{A_j} - \overline{k_C}\overline{A_{j-1}} - \overline{k_C}\overline{A_{j+1}} = \frac{\omega_r}{\omega} e^{i(j-1)\Delta\varphi} \tag{9}$$

where

$$\overline{k_j} = \frac{k_j + 2k_C - m\omega^2}{k_C} \tag{10}$$

and

$$\overline{k_C} = \frac{k_C}{c\omega} \tag{11}$$

Introducing finally $A_j = \omega/\omega_r \overline{A_j}$, it is seen that

$$(\overline{k_j}\overline{k_C} + i)A_j - \overline{k_C}A_{j-1} - \overline{k_C}A_{j+1} = e^{i(j-1)\Delta\varphi} \tag{12}$$

In view of the above relation, the present study can be restated as the following optimization problem.

Given the value of the parameter $\overline{k_C}$, it is desired to find the mistuning pattern $\overline{k_j}$, $j = 1, \ldots, N$ that yields the largest possible amplification factor of a specific blade, blade 1 say, i.e. $|A_1|$.

From Eq. (12), it can be concluded that the maximum amplification factor $|A_1|$ is a function of only three dimensionless parameters, the ratio of coupling stiffness to damping $\overline{k_C}$, the engine order r (or the interblade phase angle $\Delta\varphi$), and the number of blades N. Then, considering the relation $A_j = \omega_r/\omega A_j$, it would seem that the amplification factor could be made arbitrarily large by exciting the system at arbitrarily low frequencies. In fact, this increase in response would be accomplished by changing uniformly the blade stiffnesses by $m(\omega^2 - \omega_r^2)$. This effect is not associated with mistuning per se as it is also observed in the tuned system. Indeed, it is characterized by an overall decrease of the natural frequencies of the disk and thus implies an increase of the forced response levels at a fixed value of the excitation F_0. To avoid the contamination of the mistuning analysis by this overall (tuned) trend, the frequency of the excitation will be held constant, equal to ω_r so that $\overline{A_j} = A_j$.

For convenience, a last transformation of Eq. (9) will be performed that involves the response y_j of the bladed disk in the rotating frame. Specifically, assuming $A_j = y_j e^{i(j-1)\Delta\varphi}$ it is found for $\omega = \omega_r$ that

$$(\overline{k_j}\overline{k_C} + i)y_j - \overline{k_C}e^{-i\Delta\varphi}y_{j-1} - \overline{k_C}e^{i\Delta\varphi}y_{j+1} = 1. \tag{13}$$

Note finally that $|y_1| = |A_1|$ is the amplification factor to be maximized.

Partial Mistuning Formulation. In the present single-degree-of-freedom per blade study, the vector $\underline{x}_d$ contains the responses y_j of the blades in the sector $j \in [1, p+1] \cup [N-p+1, N]$. Then, from Eq. (13), the partial mistuning matrix H_{pm} of Eqs. (1) and (2) can be rewritten in the form

$$H_{pm} = \begin{bmatrix} 1+\delta k_{N-p+1}\tilde{h}_0 & \cdot & \delta k_N \tilde{h}_{N-p+1} & \delta k_1 \tilde{h}_{N-p} & \cdot & \delta k_{p+1}\tilde{h}_{N-2p} \\ \cdot & \cdot & \cdot & \cdot & \cdot & \\ \delta k_{N-p+1}\tilde{h}_{p-1} & \cdot & 1+\delta k_N \tilde{h}_0 & \delta k_1 \tilde{h}_{N-1} & \cdot & \delta k_{p+1}\tilde{h}_{N-p-1} \\ \delta k_{N-p+1}\tilde{h}_p & \cdot & \delta k_N \tilde{h}_1 & 1+\delta k_1 \tilde{h}_0 & \cdot & \delta k_{p+1}\tilde{h}_{N-p} \\ \delta k_{N-p+1}\tilde{h}_{p+1} & \cdot & \delta k_N \tilde{h}_2 & \delta k_1 \tilde{h}_1 & \cdot & \delta k_{p+1}\tilde{h}_{N-p+1} \\ \cdot & \cdot & \cdot & \cdot & \cdot & \cdot \\ \delta k_{N-p+1}\tilde{h}_{2p} & \cdot & \delta k_N \tilde{h}_{p+1} & \delta k_1 \tilde{h}_p & \cdot & 1+\delta k_{p+1}\tilde{h}_0 \end{bmatrix} \tag{14}$$

Downloaded 31 May 2010 to 171.66.16.27. Redistribution subject to ASME license or copyright; see http://www.asme.org/terms/Terms_Use.cfm

where $\delta k_j = k_j - k_t$ is the mistuned stiffness of blade j. Further, the corresponding vector $x_d^{(t)}$ is simply

$$\underline{x}_d^{(t)} = [1 \ \cdot \ 1 \ 1 \ \cdot \ 1]^T \tag{15}$$

To complete the formulation of the problem, it remains to compute the coefficients $\tilde{h}_j$ which represent the *tuned* response of blade $j+1$ due to a harmonic force of unit magnitude and frequency $\omega = \omega_r$ acting on blade 1. These parameters can in general be computed by a modal expansion, but in the case of the single-degree-of-freedom per blade model of Fig. 1 a closed-form solution can be obtained (see [10]). Specifically, given the cyclosymmetric nature of the tuned system, $\tilde{h}_j$ can always be expressed as the sum of terms of the form $\alpha_i \lambda_i^{j-1}$ for specific values of λ_i. Introducing such an assumed solution in the tuned set of equations (13) with a force acting only on blade 1, it is shown that there are only two possible values of λ_i, i.e., $\lambda_i = z_0$ and $\lambda_i = 1/z_0$ where z_0 is any of the two complex solutions of the quadratic equation

$$z_0^2 - \left(2 \cos \Delta\varphi + \frac{i}{\overline{k_C}} \right) z_0 + 1 = 0 \tag{16}$$

that is

$$z_0 = \left(\cos \Delta\varphi + \frac{i}{2\overline{k_C}} \right) \pm \sqrt{\left(\cos \Delta\varphi + \frac{i}{2\overline{k_C}} \right)^2 - 1}. \tag{17}$$

Besides its mathematical definition, the parameter z_0 is an important property of the tuned system. Specifically, it characterizes the spatial (around the disk) decay of the blade responses to a perturbation on blade 1, i.e., it is the corresponding decay of the traveling waves. In that sense, z_0 is a spatial analogue of the log decrement of the impulse response of a single-degree-of-freedom system. In fact, one can demonstrate that $\gamma_{td} = -\ln|z_0|$ is the localization factor of the tuned damped chain of single-degree-of-freedom systems. In this perspective, $|z_0|$ could be viewed as an overall measure of the blade-to-blade coupling in the system, combining both the physical interaction between blades (the springs of stiffness k_C) and the damping. As expected, in the limit of a zero damping, z_0 and its inverse converge to $e^{i\Delta\varphi}$ and $e^{-i\Delta\varphi}$, respectively. In accordance with the above physical description, it is necessary to take the root in Eq. (17) that yields $|z_0| < 1$.

From the value of z_0, the coefficients $\tilde{h}_j$ can then be determined as (see [10] for details)

$$\tilde{h}_{j-1} = \frac{e^{-i(j-1)\Delta\varphi} z_0}{k_C (1 - z_0^2)(1 - z_0^N)} [z_0^{j-1} + z_0^{N-j+1}]. \tag{18}$$

Note from Eq. (18) that the coefficients $\tilde{h}_j$ are inversely proportional to k_C and thus that the optimized values of $\delta k_j / k_C$ and $|y_1| = |A_1|$ from Eqs. (1), (2), (14), and (15) are only functions of N and z_0.

Parametric Study Results. The optimization effort was conducted as described above. That is, given the values of the parameters $\overline{k_C}$, r, and N, the mistuning width s was first set to three and the corresponding stiffnesses (δk_N, δk_1, and δk_2) maximizing the amplification factor $|A_1|$ were obtained by the MATLAB function fminsearch. These three stiffnesses were then used to form the initial guess of a five-blade ($s=5$) mistuned disk and so on until the amplification factor had converged. In fact, the amplification factor obtained with $s=5$ was found in all cases to be within 2–3% of the converged estimate so that only 5 of the 24 ($=N$) stiffnesses needed to be considered in the optimization effort.

The results were analyzed in terms of both pairs of variables $(\overline{k_C}, r)$ and $(|z_0|, r)$ but it is in terms of the latter parameters that the behavior is simplest, see Fig. 3 and 4. Also indicated in these plots is the value of Whitehead's limit, i.e. $0.5 + 0.5\sqrt{24} = 2.95$.

An inspection of Fig. 3 and 4 reveals for low values of $|z_0|$ (small $\overline{k_C}$) that the amplification factor is almost independent of the engine order and follows very closely the straight line $1 + |z_0|$. Around $|z_0| = 0.6$, this uniformity of behavior starts breaking down but the growth of the amplification factor with increasing $|z_0|$ accelerates for all engine orders. At high values of $|z_0|$ (i.e. $|z_0| \approx 1$), the amplification factor is maximum at $r=0$ and $N/2$ ($=12$) where it matches Whitehead's limit ($=2.95$) and minimum for $r = N/4$ ($=6$) where it is only slightly below this upper bound, i.e., it equals 2.77.

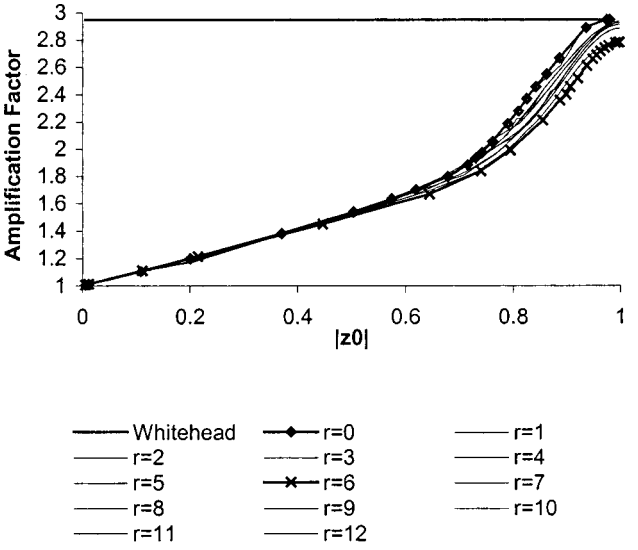

Fig. 3 Amplification factor as a function of $|z_0|$ for different engine orders r

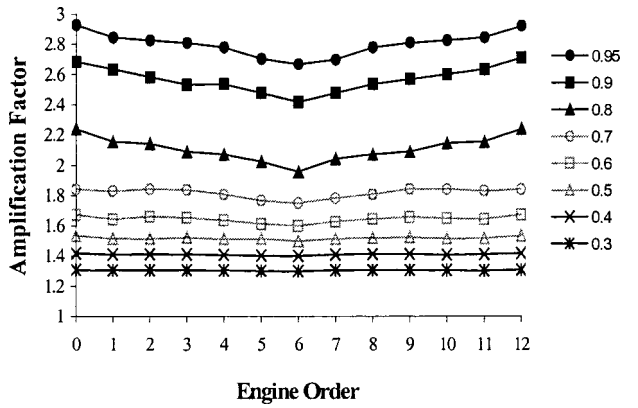

Fig. 4 Amplification factor as a function of the engine order r for different values of $|z_0|$

Multiplicity of Optimal Solutions. The search for the largest amplification of blade response requires not only the determination of a maximum of this function but also the confirmation that the value obtained is the overall maximum if any other extrema are found. The assessment of the existence, or lack thereof, of multiple maxima is thus particularly important. In the three-blade partial mistuning model, the optimization effort can be accomplished analytically and results in up to six different optimum mistuning patterns. For small values of $|z_0|$, two of these solutions are real while the four others are complex valued. As $|z_0|$ increases however, the number of optima also increases through a root "splitting" process as seen in Fig. 5 for $r=6$. A similar observation was also drawn in connection with larger mistuned sectors, e.g., five and seven blades.

It is worth noting that the new solution appearing in the splitting process (root 1 in Fig. 5) tends to exhibit both a larger am-

Downloaded 31 May 2010 to 171.66.16.27. Redistribution subject to ASME license or copyright; see http://www.asme.org/terms/Terms_Use.cfm

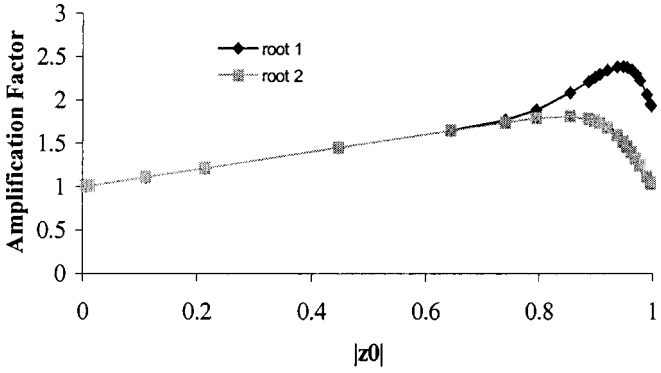

Fig. 5 Amplification factor for the three-blade partial mistuning with wall as a function of $|z_0|$, $r=6=N/4$

plification factor and larger mistuned stiffnesses than the old one (root 2 in Fig. 5). Further, it was also observed that the amplification factor of each solution (or branch) peaks at some intermediate value, i.e., in $0<|z_0|<1$, see Fig. 5 for example. These findings may shed some light on a classic issue related to the maximum amplification factor. Specifically, it has long been argued (see for example [9]) that the maximum amplification factor achieves a maximum at some intermediate blade-to-blade coupling level. The present results (see also the discussion of [25]) indicate on the contrary that the maximum amplification factor is a monotonic function of $|z_0|$ and thus of the blade-to-blade coupling. However, as observed above, the solution jumps from one curve to another and each of these jumps corresponds to an increase in the overall blade mistuning. Since Monte Carlo simulations studies generally focus on small mistuning levels, it is not expected that optimal mistuned disks with very large deviations from the tuned system would be captured. Equivalently, it can be expected that the Monte Carlo simulations would converge to curves of the maximum amplification factor corresponding to solutions with small mistuning levels which, as seen in Fig. 5, display a peak at some intermediate coupling level.

In summary, it is suggested that Monte Carlo studies yield only a *local* maximum of the amplification factor, one that is characterized by a small mistuning level, for blade-to-blade coupling level exceeding the location of the peak amplification factor.

Clarification of the Behavior for Small $|z_0|$

The behavior for small values of $|z_0|$ is surprisingly common for all engine orders, i.e., the amplification factor is almost exactly $1+|z_0|$ for $|z_0|<0.6$ independently of the engine order. To clarify this behavior, the values of the stiffnesses yielding this amplification factor were first analyzed. As might be expected, it was first noticed that the 3-blade partial mistuning model centered around blade 1 was sufficient to obtain a very close approximation of the maximum amplification factor. Further, for all engine orders except $r=0$ and $r=N/2$ when N is even, it was observed that the optimum mistuned stiffness of one of the two neighbors of blade 1, i.e., blade N or blade 2, was extremely large, several orders of magnitude larger than the stiffnesses of the other two blades. Accordingly, the optimum solution exhibits on one side of blade 1 a "wall" for which $\delta k_j\to\infty$, $y_j\to 0$ and $\delta k_j y_j\to$finite. On the contrary, for $r=0$ and $r=N/2$ when N is even, the symmetry of the coefficients $\tilde{h}_j$ around $j=0$, i.e. $\tilde{h}_{N-1}=\tilde{h}_1$, etc., see Eq. (18), implies a similarly symmetric optimum distribution of stiffnesses and $\delta k_N=\delta k_2$. In both situations, these observations can be used to reduce the number of unknowns from 3 to 2 for a three-blade partial mistuning and thus, allow for the derivation of closed form expression for the stiffnesses δk_1 and δk_2.

Consider first the engine orders $r\neq 0$ and $r\neq N/2$ for which the optimum solution exhibits a wall on blade N. With $\delta k_N\tilde{h}_0\gg 1$, Eqs. (1), (2), (14), (15) for $s=3$ can be rewritten as

$$\begin{bmatrix} \delta k_N\tilde{h}_0 & \delta k_1\tilde{h}_{N-1} & \delta k_2\tilde{h}_{N-2} \\ \delta k_N\tilde{h}_1 & 1+\delta k_1\tilde{h}_0 & \delta k_2\tilde{h}_{N-1} \\ \delta k_N\tilde{h}_2 & \delta k_1\tilde{h}_1 & 1+\delta k_2\tilde{h}_0 \end{bmatrix}\begin{bmatrix} y_N \\ y_1 \\ y_2 \end{bmatrix}=\begin{bmatrix} 1 \\ 1 \\ 1 \end{bmatrix} \tag{19}$$

Then, eliminating the large stiffness δk_N from the above three equations yields

$$\begin{bmatrix} \tilde{h}_0+\delta k_1(\tilde{h}_0^2-\tilde{h}_{N-1}\tilde{h}_1) & \delta k_2(\tilde{h}_0\tilde{h}_{N-1}-\tilde{h}_1\tilde{h}_{N-2}) \\ \delta k_1(\tilde{h}_0\tilde{h}_1-\tilde{h}_2\tilde{h}_{N-1}) & \tilde{h}_0+\delta k_2(\tilde{h}_0^2-\tilde{h}_{N-2}\tilde{h}_2) \end{bmatrix}\begin{bmatrix} y_1 \\ y_2 \end{bmatrix}$$
$$=\begin{bmatrix} \tilde{h}_0-\tilde{h}_1 \\ \tilde{h}_0-\tilde{h}_2 \end{bmatrix} \tag{20}$$

Finally, the solution of Eq. (20) yields the response of blade 1, y_1, and the stiffnesses δk_1 and δk_2 can be selected to maximize $|y_1|^2$. These computations yield polynomial equations in the unknown stiffnesses which admit a straightforward, but in general complicated, solution.

The noteworthy exception is the case $r=N/4$ for which the parameter z_0 and the coefficients $\tilde{h}_j$ are all purely imaginary. With this property, one finds that a set of optimal stiffnesses is simply $\delta k_1=\delta k_2=0$ so that the worst mistuned disk (the one yielding the largest amplification of the forced response) is tuned, except for blade N which exhibits a large stiffness. For small values of $|z_0|$, this simple solution is indeed the only one yielding a maximum amplification factor and, from Eq. (20),

$$y_1=1-\frac{\tilde{h}_1}{\tilde{h}_0} \tag{21}$$

Introducing the expressions of the coefficients $\tilde{h}_0$ and $\tilde{h}_1$ from Eq. (18) yields after some algebraic manipulations

$$|y_1|=\frac{1+|z_0|-|z_0|^{N-1}+|z_0|^N}{1+|z_0|^N}=1+|z_0|+O(|z_0|^{N-1}) \tag{22}$$

For all other engine orders with repeated natural frequencies, i.e., $r\neq 0$, $N/2$, and $N/4$, it is necessary to proceed under the assumption that $|z_0|$ is small enough to neglect its second and higher-order contributions. This limiting behavior yields

$$\delta k_1\approx-\frac{\mathrm{Re}(\tilde{h}_0)}{|\tilde{h}_0|^2} \tag{23}$$

and

$$\delta k_2\approx\frac{\mathrm{Im}(\tilde{h}_{N-1})+|\tilde{h}_{N-1}|}{\mathrm{Re}(\tilde{h}_{N-1})\mathrm{Im}(\tilde{h}_0)}, \tag{24}$$

where $\mathrm{Re}(z)$ and $\mathrm{Im}(z)$ denote the real and imaginary part of an arbitrary complex number z, and

$$|y_1|\approx 1+\frac{|\tilde{h}_1|}{|\tilde{h}_0|}\approx 1+|z_0| \tag{25}$$

Consider now the cases $r=0$ and $r=N/2$ for which the optimum distribution of stiffnesses is symmetric. With $\delta k_N=\delta k_2$ and $y_N=y_2$, Eqs. (1), (2), (14), (15) for $s=3$ become

$$\begin{bmatrix} 1+\delta k_1\tilde{h}_0 & 2\,\delta k_2\tilde{h}_1 \\ \delta k_1\tilde{h}_1 & 1+\delta k_2(\tilde{h}_0+\tilde{h}_2) \end{bmatrix}\begin{bmatrix} y_1 \\ y_2 \end{bmatrix}=\begin{bmatrix} 1 \\ 1 \end{bmatrix} \tag{26}$$

It is again found that the maximization of $|y_1|$ with respect to the stiffnesses δk_1 and δk_2 leads to polynomial equations in these variables which admit a complicated closed form solution. In the limit of $|z_0|\to 0$, the solution simplifies to

Downloaded 31 May 2010 to 171.66.16.27. Redistribution subject to ASME license or copyright; see http://www.asme.org/terms/Terms_Use.cfm

$$\delta k_1 \approx -\frac{\mathrm{Re}(\tilde{h}_0)}{|\tilde{h}_0|^2} \tag{27}$$

and

$$\delta k_2 \approx -\frac{1}{\mathrm{Im}(\tilde{h}_0)} \tag{28}$$

for which

$$|y_1| \approx 1 + \frac{|\tilde{h}_1|}{|\tilde{h}_0|} \approx 1 + |z_0| \tag{29}$$

It is thus concluded from the above derivations that the behavior of the maximum amplification factor is identical for all engine orders in the limit $|z_0| \to 0$. However, the nature of the solution, i.e. the form the mistuning distribution is quite different if $r=0$ or $r=N/2$, i.e., for nonrepeated modes, or if $r \neq 0$ and $r \neq N/2$, i.e. for repeated modes. In the former case, the distribution of the stiffnesses is symmetric with respect to the highest responding blade while, in the latter case, there is a ''wall'' (very stiff blade) on one side of this highest responding blade.

Clarification of the Behavior for $|z_0| \approx 1$ and Modal Aspects of the Worst Disks

Having clarified the behavior of the maximum amplification factor for small values of $|z_0|$, it is now desired to address the other limit, i.e., $|z_0| \approx 1$. Of particular importance here will be the correlation of the present findings with the limit of Whitehead [1]. In this regard, it should first be noted that Whitehead's analysis proceeds in the limit of a negligible damping, which corresponds exactly to $|z_0| \to 1$.

If the damping was zero, the tuned response would be infinite and a non-zero amplification factor for the optimal mistuned disk would require that its response also be infinite. That is, when the damping is zero, at least one of the natural frequencies of the worst disk is equal to the excitation frequency, i.e., to the tuned natural frequency corresponding to the rth engine order. Further, since the damping is zero, the contributions of the non-resonant modes to the response are negligible; they are finite as opposed to the infinite amplitude of the resonant mode.

These simple observations suggest that the best framework for the prediction of the maximum amplification factor in the small damping limit is actually in terms of the modes of the worst disk.

Single Frequency Modes, $r=0$ or $N/2$ (N Even). Consider first the cases $r=0$ and $r=N/2$ for which the tuned system exhibits a single natural frequency and assume similarly that the worst disk will also have only one mode at resonance. Denote by $\underline{\psi}$ and $\underline{\varphi}$ the mass normalized resonant modes of the worst mistuned and tuned disks, respectively, and let $\underline{E}_1$ be the N-component vector the first element of which is 1 and all others 0. Then, considering only the resonant mode, the response of blade 1 of the worst disk is

$$x_1 = \left[\frac{\underline{\psi}^T \underline{F}}{(\overline{\omega}_r^2 - \omega_r^2) + i c_r \omega_r}\right] \underline{\psi}^T \underline{E}_1 \tag{30}$$

In the above expression, $\underline{\psi}^T \underline{E}_1$ is the component of the mode on blade 1 while the term in brackets represents the steady state modal amplitude of response to the force $\underline{F} e^{i\omega_r t}$. Moreover, $\overline{\omega}_r$ is the natural frequency of the resonant mode of the worst disk and c_r is the modal damping coefficient. Note that $\overline{\omega}_r$ should approach ω_r as c_r goes to zero as discussed above.

Further simplifications of Eq. (30) are possible. First, the vector $\underline{F}$ of the magnitudes of the forces applied to the blades is the same as the one applied to the tuned disk, i.e., $\underline{F} = F_0 \underline{\varphi}$, so that

$$\underline{\psi}^T \underline{F} = F_0 \underline{\psi}^T \underline{\varphi}. \tag{31}$$

Next, note that the modal damping coefficient c_r is given by

$$c_r = \underline{\psi}^T C \underline{\psi} = \frac{c}{m} \underline{\psi}^T M \underline{\psi} = \frac{c}{m} \tag{32}$$

since the damping matrix is proportional to the mass matrix and the modes are normalized with respect to that same mass matrix.

With these results, Eq. (30) can be written as

$$x_1 = \frac{m F_0}{i c \omega_r}\left[\frac{\underline{\psi}^T \underline{\varphi}}{1 - i\Delta}\right] \underline{\psi}^T \underline{E}_1 \tag{33}$$

where

$$\Delta = \frac{\overline{\omega}_r^2 - \omega_r^2}{c_r \omega_r} \tag{34}$$

In fact, Eq. (33) is also valid for the tuned disk with $\underline{\psi} = \underline{\varphi}$. Since $r=0$ or $r=N/2$, the mass normalized tuned mode shape is

$$\underline{\varphi} = \frac{1}{\sqrt{Nm}}[1 \quad \pm 1 \quad 1 \quad \pm 1 \quad \cdots]^T \tag{35}$$

with the + and − signs corresponding to $r=0$ and $r=N/2$, respectively. Then,

$$\underline{\varphi}^T \underline{\varphi} = \frac{1}{m} \text{ and } \underline{\varphi}^T \underline{E}_1 = \frac{1}{\sqrt{Nm}} \tag{36}$$

and the tuned amplitude of blade 1 can be expressed as

$$x_{1t} = \frac{F_0}{i c \omega_r} \frac{1}{\sqrt{Nm}}. \tag{37}$$

Thus, the amplification factor of blade 1 is

$$A_1 = \frac{x_1}{x_{1t}} = \sqrt{Nm^3}\left[\frac{\underline{\psi}^T \underline{\varphi}}{1 - i\Delta}\right] \underline{\psi}^T \underline{E}_1 \tag{38}$$

It is interesting to note that the amplification factor is solely a function of the mode shape and natural frequency of the mistuned disk. Thus, it would be most convenient if the maximization of A_1 could be sought by varying directly the mode shape $\underline{\psi}$ and the natural frequency $\overline{\omega}_r$, or equivalently the parameter Δ, as opposed to the blade stiffnesses δk_j.

In fact, this approach is appropriate because the mapping δk_j to ($\underline{\psi}$, Δ) is one-to-one. To show this correspondence, note first that, given a set of stiffnesses δk_j, the mode shapes and natural frequencies are uniquely determined from an eigenvalue/eigenvector analysis. Further, to demonstrate the reverse proposition, note that the stiffnesses, mode shape, and natural frequency of the worst disk are all related by

$$(K_t + \Delta K)\underline{\psi} = \overline{\omega}_r^2 M \underline{\psi} \tag{39}$$

where K_t and ΔK are the tuned and mistuned stiffness matrices. Moreover, ΔK is diagonal with elements $\delta k_1, \ \delta k_2, \ldots, \delta k_N$. Thus, from Eq. (39),

$$\delta k_j = \frac{[(\overline{\omega}_r^2 M - K_t)\underline{\psi}]_j}{[\underline{\psi}]_j} \tag{40}$$

where the notation $[\underline{U}]_j$ denotes the jth component of an arbitrary vector $\underline{U}$. Equation (40) demonstrates that to a given a mode shape $\underline{\psi}$ and a natural frequency $\overline{\omega}_r$, (or deviation Δ), corresponds a unique set of stiffnesses $\delta k_1, \ \delta k_2, \ldots, \delta k_N$ provided that none of the components of the mode shape vanish. In view of the above results, the mapping δk_j to ($\underline{\psi}$, Δ) is one-to-one and the maximization of Eq. (38) can be sought directly by varying $\underline{\psi}$ and Δ.

Downloaded 31 May 2010 to 171.66.16.27. Redistribution subject to ASME license or copyright; see http://www.asme.org/terms/Terms_Use.cfm

Note that the derivation of Eq. (38) was based on mass normalized mode shapes. It is thus required to add the constraint

$$\underline{\psi}^T M \underline{\psi} = 1 \tag{41}$$

to the maximization process. Considering first the role of Δ, it is readily seen that $|A_1|$ is maximum when $\Delta = 0$. Next, to proceed with the maximization with respect to $\underline{\psi}$, introduce the representation

$$\underline{\psi} = \alpha \underline{\varphi} + \gamma \underline{E}_1 + \underline{\psi}_\perp \tag{42}$$

where $\underline{\psi}_\perp$ is a vector perpendicular to both $\underline{\varphi}$ and $\underline{E}_1$. With the results of Eq. (36), it is found that the amplification factor is

$$A_1 = \sqrt{Nm^3}\left(\frac{\alpha}{m} + \frac{\gamma}{\sqrt{Nm}}\right)\left(\gamma + \frac{\alpha}{\sqrt{Nm}}\right) \tag{43}$$

while the normalization constraint, Eq. (41), can be expressed as

$$\alpha^2 + \frac{2\alpha\gamma m}{\sqrt{Nm}} + m\gamma^2 = 1 - \underline{\psi}_\perp^T M \underline{\psi}. \tag{44}$$

It can be concluded from the above equation that the parameters α and γ are proportional to $\sqrt{1 - \underline{\psi}_\perp^T M \underline{\psi}}$ for a given perpendicular component $\underline{\psi}_\perp$ and, consequently, that the amplification factor A_1 should be proportional to $1 - \underline{\psi}_\perp^T M \underline{\psi}$. Thus, the optimal selection of $\underline{\psi}_\perp$ is $\underline{\psi}_\perp = \underline{0}$ and the normalization constraint reduces to

$$\alpha^2 + \frac{2\alpha\gamma m}{\sqrt{Nm}} + m\gamma^2 = 1. \tag{45}$$

The maximization of A_1, Eq. (43), given the constraint of Eq. (45) is a standard optimization problem that can be solved for example by Lagrange multipliers and yields

$$\alpha^2 = \frac{N}{2(N + \sqrt{N})} \tag{46}$$

and

$$\gamma = \frac{1}{\sqrt{m}}\alpha \tag{47}$$

for which A_1 is purely imaginary and

$$|A_1|_{\max} = \frac{1}{2}(1 + \sqrt{N}) \tag{48}$$

The upper bound of Whitehead [1] is thus recovered. As the above proof demonstrates, this bound is indeed achieved and the corresponding stiffnesses δk_1, δk_2, ..., δk_N can be obtained from Eq. (40). Specifically, with $\Delta = 0$ and the modal representation $\underline{\psi} = \alpha \underline{\varphi} + \gamma \underline{E}_1$, it is found that

$$\delta k_j = \frac{\gamma[(\omega_r^2 M - K_t)\underline{E}_1]_j}{[\alpha \underline{\varphi} + \gamma \underline{E}_1]_j} \tag{49}$$

In particular, for the single-degree-of-freedom system shown in Fig. 1, it is found that

$$\delta k_1 = \frac{\gamma(\omega_r^2 m - k_t - 2k_C)}{\alpha/\sqrt{Nm} + \gamma} \tag{50}$$

$$\delta k_2 = \delta k_N = \frac{\gamma k_C}{\alpha[\underline{\varphi}]_2} \tag{51}$$

and all other stiffnesses δk_j are zero. Noting finally that $m\omega_r^2 = k_t$ and $[\underline{\varphi}]_2 = 1/\sqrt{Nm}$ for $r = 0$ and $m\omega_r^2 = k_t + 4k_C$ and $[\underline{\varphi}]_2 = -1/\sqrt{Nm}$ for $r = N/2$, it is found that

$$\delta k_1 = \mp 2k_C \frac{\sqrt{N}}{\sqrt{N} + 1} \tag{52}$$

$$\delta k_2 = \delta k_N = \pm \sqrt{N} k_C \tag{53}$$

where the upper sign is for $r = 0$ and the lower one for $r = N/2$.

Repeated Frequency Modes, $r \neq 0$ and $N/2$ (N Even). It is now desired to turn to the estimation of the amplification factor for $r \neq 0$ and $r \neq N/2$. In such cases, it might be expected that two mode shapes $\underline{\psi}_1$ and $\underline{\psi}_2$ of natural frequencies $\overline{\omega}_{r,1}$ and $\overline{\omega}_{r,2}$ will be contributing to the response of the worst disk, so that

$$x_1 = \left[\frac{\underline{\psi}_1^T \underline{F}}{(\overline{\omega}_{r,1}^2 - \omega_r^2) + ic_{r,1}\omega_r}\right]\underline{\psi}_1^T \underline{E}_1 + \left[\frac{\underline{\psi}_2^T \underline{F}}{(\overline{\omega}_{r,2}^2 - \omega_r^2) + ic_{r,2}\omega_r}\right]\underline{\psi}_2^T \underline{E}_1 \tag{54}$$

The mode shapes $\underline{\psi}_1$ and $\underline{\psi}_2$ will be orthogonal to the (tuned) mass matrix since there is no mistuning in mass and will also be assumed to be normalized with respect to that matrix so that

$$\underline{\psi}_1^T M \underline{\psi}_1 = 1 \quad \underline{\psi}_2^T M \underline{\psi}_2 = 1 \text{ and } \underline{\psi}_1^T M \underline{\psi}_2 = 0 \tag{55}$$

For an r^{th} engine order excitation, see Eq. (5), the complex force exerted on the j^{th} blade is given by

$$F_j = F_0 e^{i[\omega t - (j-1)\Delta\varphi]} = F_0 e^{i\omega t}[\cos(j-1)\Delta\varphi + i\sin(j-1)\Delta\varphi] \tag{56}$$

and the complex force vector $\underline{F}$ can thus be expressed in the form

$$\underline{F} = F_0 \sqrt{\frac{Nm}{2}}(\underline{\varphi}_1 + i\underline{\varphi}_2) \tag{57}$$

where $\underline{\varphi}_1$ and $\underline{\varphi}_2$ are the mass normalized tuned mode shapes of the disk, i.e.,

$$\underline{\varphi}_1 = \sqrt{\frac{2}{Nm}}[1 \quad \cos\Delta\varphi \quad \cos 2\Delta\varphi \quad \cdots]^T \tag{58}$$

and

$$\underline{\varphi}_2 = \sqrt{\frac{2}{Nm}}[0 \quad \sin\Delta\varphi \quad \sin 2\Delta\varphi \quad \cdots]^T \tag{59}$$

Finally, since the damping matrix C is proportional to the mass matrix, the normalization constraints of Eq. (55) imply, as in the one mode case, that

$$c_{r,1} = c_{r,2} = \frac{c}{m} \tag{60}$$

Then, the forced response of blade 1 can be written as

$$x_1 = \frac{mF_0}{ic\omega_r}\sqrt{\frac{Nm}{2}}\left\{\left[\frac{\underline{\psi}_1^T(\underline{\varphi}_1 + i\underline{\varphi}_2)}{1 - i\Delta_1}\right]\underline{\psi}_1^T \underline{E}_1 + \left[\frac{\underline{\psi}_2^T(\underline{\varphi}_1 + i\underline{\varphi}_2)}{1 - i\Delta_2}\right]\underline{\psi}_2^T \underline{E}_1\right\} \tag{61}$$

where the parameters Δ_1 and Δ_2 are defined as in Eq. (34) with the mistuned frequencies $\overline{\omega}_{r,1}$ and $\overline{\omega}_{r,2}$.

Equation (61) is also applicable for the tuned case provided that $\underline{\psi}_1 = \underline{\varphi}_1$, $\underline{\psi}_2 = \underline{\varphi}_2$, and $\Delta_1 = \Delta_2 = 0$, and it is found that

$$x_{1t} = \frac{F_0}{ic\omega_r} \tag{62}$$

Accordingly, the amplification factor for blade 1 is

$$A_1 = \frac{x_1}{x_{1t}} = \sqrt{\frac{Nm^3}{2}}\left\{\left[\frac{\underline{\psi}_1^T(\underline{\varphi}_1 + i\underline{\varphi}_2)}{1 - i\Delta_1}\right]\underline{\psi}_1^T \underline{E}_1 + \left[\frac{\underline{\psi}_2^T(\underline{\varphi}_1 + i\underline{\varphi}_2)}{1 - i\Delta_2}\right]\underline{\psi}_2^T \underline{E}_1\right\} \tag{63}$$

Downloaded 31 May 2010 to 171.66.16.27. Redistribution subject to ASME license or copyright; see http://www.asme.org/terms/Terms_Use.cfm

As accomplished in connection with the nonrepeated modes, $r=0$ or $N/2$ see Eq. (38), one can seek the maximization of $|A_1|$ directly in terms of the mode shapes $\underline{\psi}_1$ and $\underline{\psi}_2$ and the parameters Δ_1 and Δ_2. In doing so, it should be recognized that $\underline{\psi}_1$, $\underline{\psi}_2$, Δ_1, and Δ_2 are not independent of each other: they represent a set of $2N$ variables while in fact the optimization is intended with respect to only the N unknown stiffnesses δk_j. Thus, the maximization of $|A_1|$ with respect to $\underline{\psi}_1$, $\underline{\psi}_2$, Δ_1, and Δ_2 should be achieved under the constraint that the stiffnesses δk_j recovered from the first and second mode shapes and natural frequencies be identical. That is, from Eq. (40)

$$\delta k_j=\frac{[(\bar{\omega}_{r,1}^2M-K_t)\underline{\psi}_1]_j}{[\underline{\psi}_1]_j}=\frac{[(\bar{\omega}_{r,2}^2M-K_t)\underline{\psi}_2]_j}{[\underline{\psi}_2]_j} \tag{64}$$

for $j=1,2,3,\ldots,N$. However, the consideration of this set of constraints renders the optimization of Eq. (63) quite challenging, it yields $3N$ nonlinear equations in the $2N$ unknowns of $\underline{\psi}_1$, $\underline{\psi}_2$, Δ_1, and Δ_2 and the N Lagrange multipliers associated with Eq. (64). Accordingly, to obtain a first estimate of the maximum amplification factor, the constraints of Eq. (64) will be ignored but the modes will be required to satisfy the orthonormalization conditions of Eq. (55). This process will yield an upper bound of the maximum amplification factor.

Proceeding in parallel with the derivations of Eqs. (42)–(45), it can be shown that the maximization of Eq. (63) with the normalization constraints of Eq. (55) (but without Eq. (64)) is achieved when the mode shapes admit the representation

$$\underline{\psi}_1=\alpha_1\underline{\varphi}_1+\beta_1\underline{\varphi}_2+\gamma_1\underline{E}_1 \tag{65}$$

and

$$\underline{\psi}_2=\alpha_2\underline{\varphi}_1+\beta_2\underline{\varphi}_2+\gamma_2\underline{E}_1 \tag{66}$$

This first observation reduces the maximization of $|A_1|$ to an optimization problem with only eight variables, α_1, β_1, γ_1, α_2, β_2, γ_2, Δ_1, and Δ_2. Among the few solutions of this problem that were numerically obtained, one of particular importance is

$$\alpha_1=\alpha_2=-\sqrt{\frac{N}{6N+8\sqrt{N}}} \tag{67}$$

$$\beta_1=-\beta_2=-\frac{\sqrt{2}}{2} \tag{68}$$

$$\gamma_1=\gamma_2=\sqrt{\frac{2}{m}}\,\alpha_1 \tag{69}$$

$$\Delta_1=-\Delta_2=\sqrt{2}\alpha_1=-\sqrt{\frac{N}{3N+4\sqrt{N}}} \tag{70}$$

to which corresponds a purely imaginary value of A_1 with amplification factor

$$|A|_{1\ \max}=\frac{1}{2}(1+\sqrt{N}). \tag{71}$$

That is, this optimization process has recovered the Whitehead upper limit.

Note that other optimum solutions do exist. For example, with the values of β_1 and β_2 given by Eq. (68), there is also a local maximum of the amplification factor for

$$\alpha_1=\alpha_2=-\sqrt{\frac{N}{6N-8\sqrt{N}}} \tag{72}$$

$$\gamma_1=\gamma_2=-\sqrt{\frac{2}{m}}\,\alpha_1 \tag{73}$$

and

$$\Delta_1=-\Delta_2=\sqrt{2}\alpha_1=-\sqrt{\frac{N}{3N-4\sqrt{N}}} \tag{74}$$

for which

$$A_{1\ \max}=\frac{1}{2}(\sqrt{N}-1) \tag{75}$$

which is the Whitehead upper limit minus one. It is thus concluded that the presence of local maxima is not an artifice of the partial mistuning modeling but rather is a genuine characteristic of the amplification factor.

Before focusing more specifically on the solution yielding Eq. (71), it is worth nothing that the optimal value of Δ_1 and Δ_2 were never found to be zero, i.e., that the two resonant modes of the worst disk are split while the 2 frequencies converge to each other in the limit $c\to 0$, they remain separated with respect to the bandwidth, i.e., $\lim_{c\to 0}(\Delta_2-\Delta_1)/c$ is finite nonzero. The splitting of repeated modes by mistuning has been well established and its importance has recently been well discussed [20]. Accordingly, it would be desirable to evaluate the effects of the frequency shifts Δ_1 and Δ_2 on the maximum amplification factor. To this end, the optimization process was repeated with the values of Δ_1 and Δ_2 fixed to zero. Multiple solutions of the optimization problem were again obtained but the highest was found to be the ''lower'' Whitehead limit of reference [17], i.e.

$$|A|_{1\max,\Delta_1=\Delta_2=0}=\frac{1}{2}\left(1+\sqrt{\frac{N}{2}}\right) \tag{76}$$

and corresponding to

$$\alpha_1=\alpha_2=-\frac{1}{2}\sqrt{\frac{\sqrt{N}}{\sqrt{2}+\sqrt{N}}} \tag{77}$$

$$\beta_1=-\beta_2=-\frac{\sqrt{2}}{2} \tag{78}$$

and

$$\gamma_1=\gamma_2=\sqrt{\frac{1}{m}}\,a_1 \tag{79}$$

Note that the two mistuned modes of Eqs. (65) and (66) are not uniquely defined; since the two corresponding natural frequencies are equal, any linear combination of the modes of Eqs. (65), (66), and (77)–(79) is also a bonafide mode. Then, the ''lower'' Whitehead limit of Eq. (76) ([17]) is obtained in the presence of a *single* resonating mode which is an appropriate linear combination of Eqs. (65), (66), and (77)–(79). Thus, if frequency splitting is not allowed, only a single mode is present in the response and the lower Whitehead limit is obtained as observed in [26].

The foregoing derivation demonstrates that the Whitehead upper limit of $\frac{1}{2}(1+\sqrt{N})$ cannot be achieved unless the constraints of Eq. (64) are satisfied exactly. To assess if and how these conditions could be met, note first in the limit of $|z_0|\to 1$ that $\bar{\omega}_r=\omega_r$, see Eq. (34). Further, since $\underline{\varphi}_1$ and $\underline{\varphi}_2$ are the corresponding two tuned mode shapes, they satisfy the relations

$$(K_t-M\omega_r^2)\underline{\varphi}_1=(K_t-M\omega_r^2)\underline{\varphi}_2=\underline{0} \tag{80}$$

so that Eq. (64) reduces to

$$\delta k_j=\frac{\gamma_1[(\omega_r^2M-K_t)\underline{E}_1]_j}{[\underline{\psi}_1]_j}=\frac{\gamma_2[(\omega_r^2M-K_t)\underline{E}_1]_j}{[\underline{\psi}_2]_j} \tag{81}$$

Noting that $\gamma_1=\gamma_2$, see Eq. (69), it is concluded from the foregoing relation that the stiffness constraint on blade j is satisfied if either

Downloaded 31 May 2010 to 171.66.16.27. Redistribution subject to ASME license or copyright; see http://www.asme.org/terms/Terms_Use.cfm

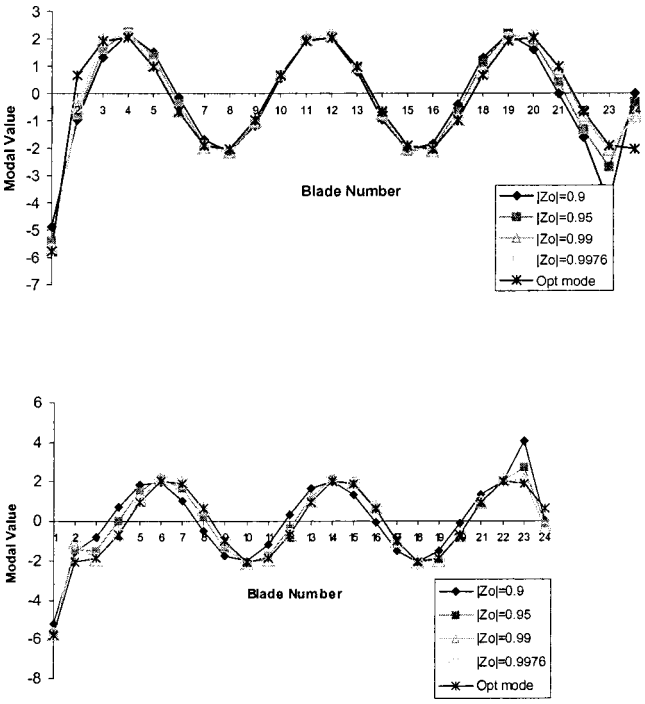

Fig. 6 Convergence of the two resonant mode shapes of the worst disk, as optimized by the localization-based approach, to those given by Eqs. (65)–(70) as $|z_0|\to 1$, $r=3$

$$\lfloor \underline{\psi}_1 \rfloor_j = \lfloor \underline{\psi}_2 \rfloor_j \quad \text{or} \quad [(K_t - M\omega_r^2)\underline{E}_1]_j = 0 \tag{82}$$

These two conditions can in turn be further simplified. Specifically, given the expressions of the two modes $\underline{\psi}_1$ and $\underline{\psi}_2$, Eq. (65) and (66), and the equalities $\alpha_1=\alpha_2$ and $\gamma_1=\gamma_2$, it is found that $\lfloor \underline{\psi}_1 \rfloor_j = \lfloor \underline{\psi}_2 \rfloor_j$ occurs when $\lfloor \underline{\varphi}_2 \rfloor_j = 0$ which is always true for $j=1$. In regards to the second condition of Eq. (78), note that the tuned stiffness matrix K_t can be expressed as the sum of the diagonal matrix of the blade alone stiffnesses and of a cyclosymmetric coupling matrix $K^{(c)}$. Thus, the condition $[(K_t - M\omega_r^2)\underline{E}_1]_j = 0$ reduces to $K_{j1}^{(c)} = 0$ for $j>1$.

It is thus concluded from the foregoing derivations that the stiffness constraints of Eq. (64) will be satisfied exactly (and thus the Whitehead upper limit will be achieved) if and only if the stiffness coupling occurs only between blades of indices j and l for which $\lfloor \underline{\varphi}_2 \rfloor_{|j-l|+1} = 0$. For example, for $N=24$ and $s=2$, the tuned mode $\underline{\varphi}_2$ vanishes on blades 1, 7, 13, and 19 and thus the Whitehead upper limit holds if the stiffness coupling occurs only between blades 1 and 7, 2 and 8, 3 and 9, . . . , but also possibly between 1 and 13, 2 and 14, etc., irrespectively of the magnitude of this coupling.

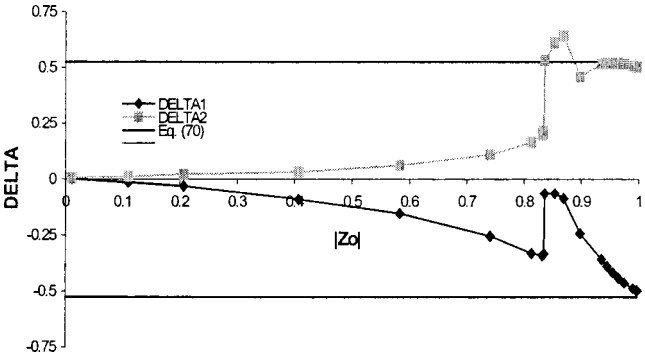

Fig. 7 Convergence of the parameter Δ for the two natural frequencies of the worst disk, as optimized by the localization based approach, to those given by Eq. (70) as $|z_0|\to 1$, $r=3$

The unusual form of this blade-to-blade coupling suggests that the Whitehead upper limit would not be achieved for simple models of physical bladed disks. However, the numerical results of Fig. 3 and 4 demonstrate that the true maximum amplification factor, i.e. obtained with enforcing the constraints of Eq. (64), would be quite close to this bound. The observed closeness between the Whitehead upper limit and the exact maximum amplification factor would suggest that the modal characteristics of the worst disks, i.e., mode shapes and natural frequencies, should be well approximated by Eqs. (65)–(70). This expectation is indeed correct as can be seen from the mode shape comparison of Fig. 6 and the natural frequencies of Fig. 7. It is quite interesting to observe from Fig. 6 that a wall continues to exist in the optimum solution until $|z_0|\approx 0.9$ as it did at very low values of this parameter.

In regards to the natural frequencies, it can be seen from Fig. 7 that they equal the excitation frequency only when $|z_0|=0$ (as $k_C\to 0$) or $|z_0|=1$ (as $c\to 0$). Nevertheless, for all values of $|z_0|$, this frequency is approximately symmetrically placed with respect to the two natural frequencies and lies within their bands, at a distance approximately equal to $\Delta\zeta_r\omega_r$ where ζ_r is the damping ratio of the tuned bladed disk of the r^{th} engine order mode. It was generally observed that the two natural frequencies of the optimized system were between the $r-1$st and $r+1$st tuned natural frequencies, so that $\Delta\to 0$ as $k_C\to 0$ (i.e. $|z_0|\to 0$) as seen in Fig. 7.

Two additional comments should be made in connection with Fig. 7. First, the jump which occurs for $|z_0|\approx 0.83$ is associated with a change of solution in the optimization effort, as seen in Fig. 5. Second, note the nonsymmetrical convergence to the limit values of Eq. (70). This behavior appears to be associated with the closeness of the $r-1$st and $r+1$st engine order tuned natural frequencies from the rth ones. For $r=3$, the frequency difference between the 4th and 3rd engine order natural frequencies is larger than for the 3rd and 2nd. Accordingly, the highest of the two resonant natural frequencies of the optimized system converges faster to its asymptotic behavior (Eq. (70)) than the lowest one does. For $r=6=N/4$, a symmetric behavior of these two natural frequencies is observed reflecting the symmetry of the 5th and 7th engine order natural frequencies with respect to the 6th ones.

The foregoing findings demonstrate that the modal optimization effort conducted in the foregoing without the stiffness constraints of Eq. (64) provides a good approximation of the behavior of a 24-blade disk. Additional results, e.g., see the forthcoming, suggest in fact that the difference between the maximum amplification factor obtained by the localization-based optimization approach and the Whitehead upper bound is monotonically decreasing as $N\to\infty$, e.g. it is 5.7% for $N=24$ and 2.3% for $N=168$ for $s=N/4$. Accordingly, the results of the modal optimization, Eqs. (65)–(70), are expected to become more and more accurate as $N\to\infty$.

A First-Order Perturbation. Notwithstanding the simplicity of the Whitehead upper bound, it would be desirable to obtain an improved estimate of the true maximum amplification factor that would reveal the engine order and blade number effects described in the foregoing. Such an approximation can be obtained in a perturbation type format by considering the effect of the stiffness constraints as the small quantity and the expressions of Eqs. (65), (66), and (70) as the zeroth-order approximation of the mode shapes $\underline{\psi}_1$, and $\underline{\psi}_2$ and the natural frequencies $\bar{\omega}_{r,1}$ and $\bar{\omega}_{r,2}$. Then, first order corrections $\underline{u}$, $\underline{v}$, σ_1, and σ_2 of these terms were sought by linearizing the full (including the stiffness constraints) optimization problem around the zeroth-order approximation. To this end, both linear and quadratic terms in $\underline{u}$, $\underline{v}$, σ_1, and σ_2 were retained in the expression of the amplification factor of Eq. (63) and in the mass orthogonality constraints of Eq. (55), while only

Downloaded 31 May 2010 to 171.66.16.27. Redistribution subject to ASME license or copyright; see http://www.asme.org/terms/Terms_Use.cfm

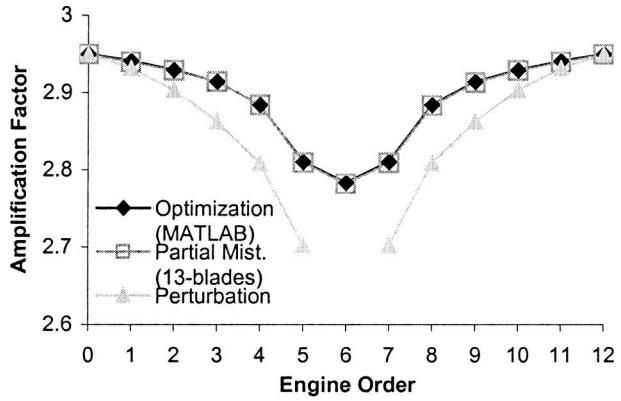

Fig. 8 Amplification factor as a function of engine order r for $|z_0|=1$ as computed by partial mistuning, perturbation, and a full optimization

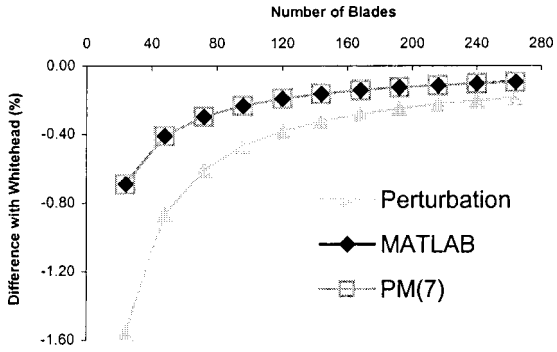

Fig. 9 Relative difference between the Whitehead upper limit and the amplification factors obtained for $|z_0|=1$ and $r=N/12$ with the perturbation approach, a full optimization, and partial mistuning with five and seven-blade sectors (PM (5) and PM (7), $N=24$ only)

the linear ones were kept in the stiffness constraints of Eq. (64). The details of this derivation are omitted here for brevity.

In fact, this process leads to a well posed problem for all engine orders $r \neq N/4$ and provides a basis for studying the engine order and number of blades effects in the maximum amplification factor. Shown in Fig. 8 are the estimates of the amplification factor that were obtained by this perturbation scheme as a function of the engine order for the 24-blade disk considered before (see Figs. 3 and 4). While these values underestimate somewhat the amplification factor obtained by partial mistuning, the trend with respect to engine order is clearly accurate. This finding suggested that the perturbation-based mode shapes and natural frequencies could be used as initial guesses in a full nonlinear optimization of Eq. (63) with the constraints of Eqs. (55) and (64). This modal-based optimization effort was carried out, as its localization-based counterpart, in the MATLAB environment (function fmincon). It was found to converge extremely quickly, in a just a few iterations, to amplification factors that closely match the 7 and 9-blade partial mistuning results, see Fig. 8. Since this convergence occurred without obtaining any local maxima, it is suggested that this perturbation with subsequent optimization, if necessary, may provide a particularly efficient computational scheme for the determination of the maximum amplification factor for $|z_0| \approx 1$.

In the special case of the engine order $r=N/4$, it was found that the quadratic form of the amplification factor did not represent well Eq. (63). Thus, higher-order terms should have been included which would have rendered nonlinear the perturbation problem. In view of the complexity, this approach was not undertaken.

The behavior as $N \to \infty$ of both the exact maximum amplification factor and the solution of the modal optimization problem (with or without the stiffness constraints of Eq. (64)) is of particular interest as the number of blades on some stages can be quite large. From Eqs. (67), (69), and (70) it is readily found that

$$\alpha_1 = \alpha_2 \to -\sqrt{\frac{1}{6}}; \quad \Delta_1 = -\Delta_2 \to -\sqrt{\frac{1}{3}}$$

$$\text{and} \quad \gamma_1 = \gamma_2 \to -\sqrt{\frac{1}{3m}} \tag{83}$$

Since each of the components of the tuned vectors $\underline{\varphi}_1$ and $\underline{\varphi}_2$ are inversely proportional to $\sqrt{N}$, it can be argued that the two mistuned mode shapes $\underline{\psi}_1$ and $\underline{\psi}_2$ converge in shape to a purely localized mode on the worst responding blade, i.e., the sole $\underline{E}_1$ term in Eq. (65) and (66). This perspective is not always appropriate, for example not in connection with energies where a sum of a large number of small terms adds up to a nonzero number. In fact, it can be seen that the fraction of the total kinetic energy (or modal mass) stored in blade 1 is

$$\mathrm{KE}_1 = m\left(\gamma_1 + \sqrt{\frac{1}{mN}}\,\alpha_1\right)^2 = \left(1 + \frac{1}{\sqrt{N}}\right)^2 \alpha_1^2 \quad r = 0, N/2 \tag{84}$$

$$\mathrm{KE}_1 = m\left(\gamma_1 + \sqrt{\frac{2}{mN}}\,\alpha_1\right)^2 = 2\left(1 + \frac{1}{\sqrt{N}}\right)^2 \alpha_1^2 \quad r \neq 0, N/2 \tag{85}$$

which converges to 1/2 (for $r=0$ or $N/2$) or 1/3 (for all other engine orders) as $N \to \infty$.

In regards to the mistuning pattern in the limit $N \to \infty$, it can be seen from Eq. (64) that the stiffness of the worst blade stays finite but the other blades are either tuned (if there is no coupling between the blade and the worst blade) or infinitely stiff (if there is a coupling between the blade and the worst blade).

The above discussion is technically applicable only to the solution, Eqs. (65)–(70), of the modal optimization problem *without* the stiffness constraints of Eq. (64). Fortunately, however, it has been observed that the solutions of the stiffness constrained and unconstrained optimization problems approached each other as the number of blades tends to infinity. This observation is substantiated for example by the amplification factor plot of Fig. 9 which clearly shows that the exact maximum amplification factor (resulting from the MATLAB modal-based optimization) approaches the Whitehead upper bound.

The correct behavior exhibited by the solution of the perturbation problem (see Fig. 9) allows for an estimation of the convergence rate of the maximum amplification factor to the Whitehead limit. Indeed, it was found for the blade-to-blade coupling shown in Fig. 1 that the only nonhomogenous terms in the linear system of equations for the perturbations in mode shapes and natural frequencies arose from the stiffness constraints associated with the blades 2 and N. Further, the corresponding terms are opposite of each other and proportional to $1/\sqrt{N}$. Since the matrix of the system of equation admits a finite limit as $N \to \infty$, it is then concluded that the perturbations in mode shapes and natural frequencies exhibit a limiting $1/\sqrt{N}$ behavior. Thus, the maximum amplification factor should converge to the Whitehead upper bound as $1/N$ as seen in Fig. 9. Relying on the similarity of the perturbation and MATLAB modal-based optimization curves, it is finally concluded that the exact maximum amplification factor should also display the $1/N$ asymptotic character.

Application to a Blisk Reduced Order Model

As a final example of application, the blisk shown in Fig. 2 (see Bladh et al. [23]) was considered and its analysis was very efficiently carried out using the reduced order modeling strategy of Castanier et al. [22] with the code REDUCE (v. 2.3b6). The maxi-

Downloaded 31 May 2010 to 171.66.16.27. Redistribution subject to ASME license or copyright; see http://www.asme.org/terms/Terms_Use.cfm

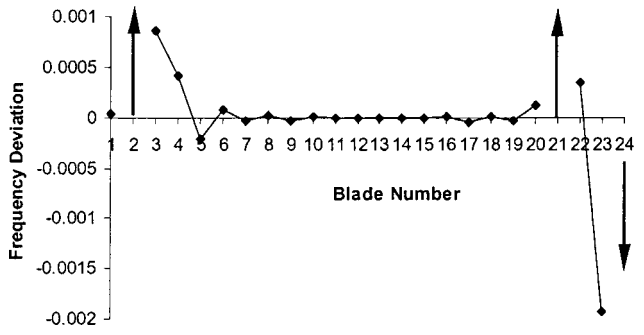

Fig. 10 Optimum mistuning pattern, i.e., frequency deviations δ_j, Eq. (82), for the blisk of Fig. 2, case 1. The arrows indicate deviations out of the range shown, $\delta_2 = 177.6$, $\delta_{21} = 21.65$, and $\delta_{24} = -0.967$.

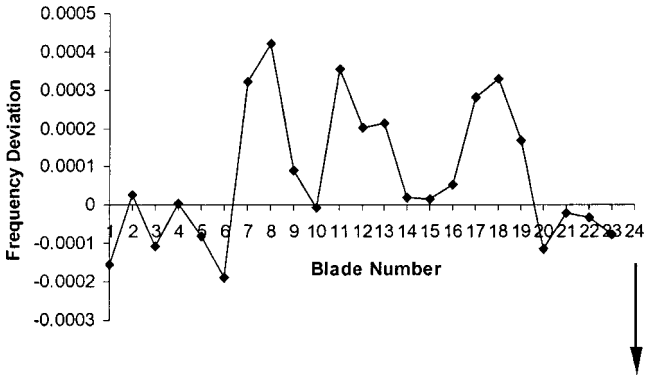

Fig. 11 Optimum mistuning pattern, i.e. frequency deviations δ_j, Eq. (82), for the blisk of Fig. 2, case 2. The arrow indicates a deviation out of the range shown, $\delta_{24} = -0.179$.

mum amplification factor was sought for the two frequency and engine order combinations circled in Fig. 2(*b*), i.e., $r = 3$, $\omega = 577.1486$ Hz (case 1) and $r = 2$, $\omega = 7334.7369$ Hz (case 2). It was in particular desired to determine if the features of the mistuning pattern and the mode shapes and natural frequencies of the worst disk observed in connection with the single-degree-of-freedom model were also reproduced for this more complex system. To this end, the damping ratios of the disk and blades were selected to be very low, 5×10^{-7} (case 1) and 5×10^{-8} (case 2), to match at best the limiting case $|z_0| \to 1$ of the single-degree-of-freedom system. For simplicity, it was assumed that the relative

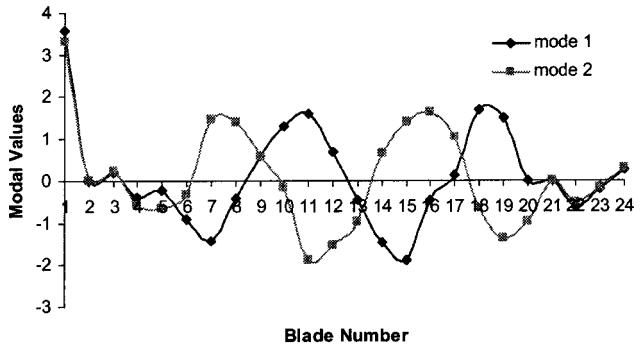

Fig. 12 Resonant mode shapes of the worst disk for the blisk of Fig. 2, case 1.

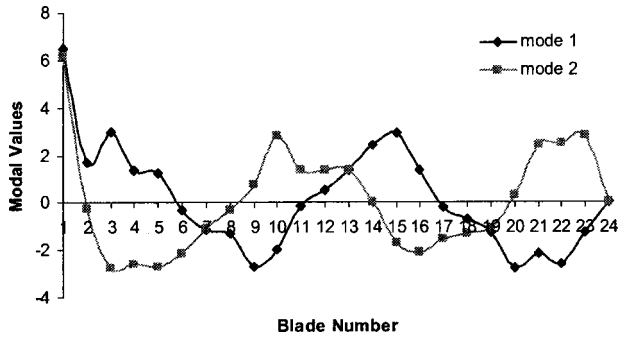

Fig. 13 Resonant mode shapes of the worst disk for the blisk of Fig. 2, case 2

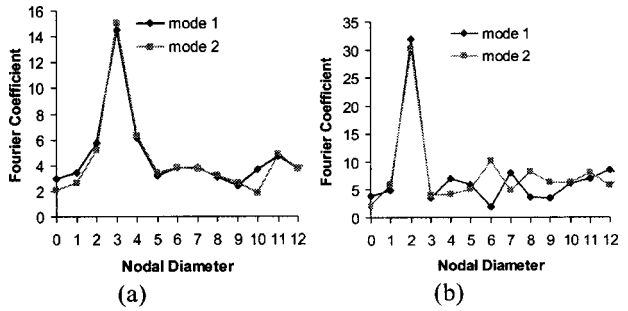

Fig. 14 Fourier transforms of the resonant mode shapes of the worst disks for the blisk of Fig. 2, (*a*) case 1, (*b*) case 2

variations of the different blade alone natural frequencies were the same for any given blade, thereby reducing the number of mistuning parameters to one per blade, i.e., to

$$\delta_j = \frac{(\omega_{i,j}^2)_{\text{mist}} - (\omega_{i,j}^2)_{\text{tun}}}{(\omega_{i,j}^2)_{\text{tun}}} \quad \text{for any } i \text{ and } j = 1, \ldots, N. \tag{86}$$

In the foregoing equation, $(\omega_{i,j})_{\text{tun}}$ and $(\omega_{i,j})_{\text{mist}}$ denote the ith tuned and mistuned blade alone natural frequencies of blade j. Note finally that the optimization process focused on maximizing the norm of the response of blade 1 at the prescribed frequencies.

The localization-based algorithm described earlier led to amplification factors of 2.68 and 2.78 for cases 1 and 2, respectively, which compare quite well with the Whitehead upper bound of 2.95 and the single-degree-of-freedom results of 2.93 ($r = 2$) and 2.91 ($r = 3$). The mistuning patterns, i.e., the values of δ_j, shown in Figs. 10 and 11 are clearly reminiscent of the partially mistuned disks obtained in connection with the single-degree-of-freedom model. Specifically, one or a few of the blades surrounding the largest responding one exhibit a fairly large mistuning level while all others are close to their tuned conditions. This observation is somewhat in line as well with the results of Petrov and Ewins [15].

A model analysis of this worst disks revealed that there exist only two natural frequencies very close to the excitation frequency yielding values $\Delta_1 = -0.250$ and $\Delta_2 = 0.442$ (case 1), and $\Delta_1 = -0.546$ and $\Delta_2 = 0.546$ (case 2). Most of these results are quite close to the coefficients -0.511 and 0.511 obtained in the single-degree-of-freedom analysis, Eq. (70), and are nevertheless indicative that the excitation frequency is placed well within the half-power bands of the two modes (which would correspond to $\Delta = \pm 1$).

To provide a perspective on the 3-D mode shapes corresponding to these two sets of frequencies, the node and direction of

Downloaded 31 May 2010 to 171.66.16.27. Redistribution subject to ASME license or copyright; see http://www.asme.org/terms/Terms_Use.cfm

maximum displacement on blade 1 was identified for both cases and the corresponding displacement of the remaining 23 blades were noted. This data was then plotted versus blade number, see Figs. 12 and 13. Note in all cases the strong peak on the highest responding blade (blade 1), and that the response of this blade in the two modes is almost exactly the same, both in agreement with Eqs. (65) and (66). Clearly, these two modes are not perfect linear combinations of the two tuned modes and the localized component E_1, but these three terms are clearly the dominant contributions to the modes as can be seen from the Fourier plots of Fig. 14. The two peaks are associated with the tuned modes, at 3 and 2 nodal diameters, respectively, while the almost constant "floor" is indicative of a response on blade 1 only, i.e., E_1. Note finally that the Fourier transforms of the two modes are almost equal in complete agreement with Eqs. (65) and (66).

Summary

This paper addressed the determination of the largest amplification of the forced response of bladed disks due to mistuning. The contributions of the present effort can be summarized as follows.

1. A novel optimization approach was proposed that relies on a recent finding that the disk behavior is very localized around the highest responding blade, even in the presence of a strong blade-to-blade coupling and/or small damping. On this basis, it was argued that the effects of the mistuning of the blades far from the highest responding one would be smaller than those of the blades close to it. Accordingly, the mistuned blade properties were sought through an incremental process in which 3, 5, 7,.. blade partially mistuned disks were successively optimized. This approach was often found to converge to the global maximum of the amplification factor thus avoiding the many local maxima that were also shown to exist.

2. The special case of the single-degree-of-freedom per blade disk model shown in Fig. 1 was first considered to conduct a comprehensive parametric study of the maximum amplification factor with respect to the damping, blade-to-blade coupling, engine order, and blade number. A nondimensionalization of the equations of motion demonstrated first that the amplification factor must be sought at a fixed frequency (e.g., the tuned natural frequency) and does not depend separately on the blade-to-blade coupling and the damping term but rather on their ratio, see Eq. (9). This dependency is most pronounced through the complex tuned parameter z_0, see Eqs. (16) and (17), which depends on this ratio and the engine order.

3. The application of these concepts to a 24-blade disk first confirmed the fundamental importance of the parameter z_0: the amplification factor due to mistuning depends almost exclusively on the magnitude $|z_0|$ of this complex number for a fixed number of blades, see Figs. 3 and 4. Further, in the limit of $|z_0|\to 0$ (actually $|z_0|<0.6$), which corresponds to a very small blade-to-blade coupling, it was found that the amplification factor is very well approximated by the straight line $1+|z_0|$. In the other extreme of a very large blade-to-blade coupling and/or very small damping, i.e., $|z_0|\to 1$, Whitehead's upper bound of $(1+\sqrt{N})/2$ is exactly (for $r=0$ or $N/2$) or approximately (for $r=1,\ldots,N/2-1$) recovered.

For small values of $|z_0|$, the response of the blades is governed only by short-range interactions and a partially mistuned disk with a very small mistuned sector provides a very accurate model. In fact, the behavior of the amplification factor in the domain $0<|z_0|<0.6$ was justified from a three-blade partial mistuning model that either is symmetric (for $r=0$ or $N/2$) or exhibits a wall on one side (for $r\neq 0$ and $N/2$).

A clarification of the behavior of the amplification factor for $|z_0|\to 1$, e.g., its convergence to a value close to the Whitehead upper limit, was also accomplished but through a modal perspective of the amplification factor. In this process, it was also shown that

4. The resonant mode shape(s) of the worst disk for all engine orders is (are) exactly (for $r=0$ or $N/2$) or approximately (for all other engine orders) a combination of the tuned mode shape(s) and of a purely local component, i.e., the vector $\underline{E}_1$. That is, the resonant modes of this disk are perfect (for $r=0$ or $N/2$) or near perfect (for all other engine orders) combinations of a local and a global component. Further, the coefficients of the linear combination are not function of the engine order (two groups of coefficients exist, one for the single natural frequencies, $r=0$ or $N/2$, and one for the repeated ones).

5. The resonant mode shape(s) of the worst disk is (are) exactly (for $r=0$ or $N/2$) or approximately (for all other engine orders) independent of the blade-to-blade coupling magnitude (i.e., the value of k_C) and type (i.e. interaction of one blade with the direct neighbors, as in Fig. 1, or longer range interaction), but the distribution of mistuned stiffnesses does depend on these characteristics.

6. As the number of blades becomes large, i.e. as $N\to\infty$, the relative difference between the exact maximum amplification factor and the Whitehead upper bound decreases as $1/N$. Further, the resonant mode shape(s) of the worst disk for any engine order converge(s) in shape to a purely local component, i.e., only the maximum responding blade exhibits a nonzero motion, again independently of the blade-to-blade magnitude and type. Further, the total kinetic energy in the maximum responding blade equals half (for $r=0$ and $r=N/2$) or one third (for all other engine orders) of the total kinetic energy of the entire bladed disk.

7. The REDUCE reduced order model of the blisk shown in Fig. 2 was finally considered to assess the validity of the foregoing comments to more complex bladed disk models. The results of this preliminary comparison indicate, for the two excitation conditions considered, that the features of the worst disks are very reminiscent of the observations drawn in connection with the single-degree-of-freedom system. Specifically, the mistuning patterns closely resemble partially mistuned disks as in the single-degree-of-freedom analysis. Further, two natural frequencies of the mistuned disks are placed approximately symmetrically with respect to the excitation frequency. Finally, it is found that the mode shapes of the worst disks strongly involve the corresponding two tuned modes and a purely local effect on the highest responding blade, in perfect agreement with the single-degree-of-freedom findings.

Acknowledgments

The support of this work by the grant NAG-1-2233 from NASA is gratefully acknowledged. In addition, the authors wish to express their gratitude to the University of Michigan group, Professor C. Pierre and Drs M. P. Castanier and R. Bladh, for the use of both REDUCE and the blisk example geometry.

References

[1] Whitehead, D. S., 1966, "Effect of Mistuning on the Vibration of Turbomachine Blades Induced by Wakes," J. Mech. Eng. Sci., **8**, pp. 15–21.
[2] Ewins, D. J., 1969, "The Effects of Detuning Upon the Forced Vibrations of Bladed Disks," J. Sound Vib., **9**, pp. 65–79.
[3] Kielb, R. E., and Kaza, K. R. V., 1984, "Effects of Structural Coupling on Mistuned Cascade Flutter and Response," ASME J. Eng. Gas Turbines Power, **106**, pp. 17–24.
[4] Basu, P., and Griffin, J. H., 1986, "The Effect of Limiting Aerodynamic and Structural Coupling in Models of Mistuned Bladed Disk Vibration," ASME J. Vib., Acoust., Stress, Reliab. Des., **108**, pp. 132–139.
[5] Wei, S. T., and Pierre, C., 1988, "Localization Phenomena in Mistuned Assemblies with Cyclic Symmetry—Part I: Free Vibrations," ASME J. Vib., Acoust., Stress, Reliab. Des., **110**, No. 4, pp. 429–438.
[6] Wei, S. T., and Pierre, C., 1988, "Localization Phenomena in Mistuned Assemblies with Cyclic Symmetry—Part II: Forced Vibrations," ASME J. Vib., Acoust., Stress, Reliab. Des., **110**, No. 4, pp. 439–449.
[7] Sinha, A., and Chen, S., 1989, "A Higher Order Technique to Compute the Statistics of Forced Response of a Mistuned Bladed Disk," J. Sound Vib., **130**, pp. 207–221.
[8] Lin, C. C., and Mignolet, M. P., 1997, "An Adaptive Perturbation Scheme for the Analysis of Mistuned Bladed Disks," ASME J. Eng. Gas Turbines Power, **119**, pp. 153–160.

Downloaded 31 May 2010 to 171.66.16.27. Redistribution subject to ASME license or copyright; see http://www.asme.org/terms/Terms_Use.cfm

[9] Wei, S.-T., and Pierre, C., 1990, ''Statistical Analysis of the Forced Response of Mistuned Cyclic Assemblies,'' AIAA J., **28**, No. 5, pp. 861–868.
[10] Mignolet, M. P., Hu, W., and Jadic, I., 1998, ''On the Forced Response of Harmonically and Partially Mistuned Bladed Disks. Part I: Harmonic Mistuning,'' Proc., ISROMAC-7 Symposium, Honolulu, Hawaii, Feb. 22–26, **Vol. B**, pp. 591–602; also, Int. J. Rotating Mach., **6**, No. 1, pp. 29–41, 2000.
[11] Mignolet, M. P., Hu, W., and Jadic, I., 1998, ''On the Forced Response of Harmonically and Partially Mistuned Bladed Disks. Part II: Partial Mistuning and Applications,'' Proc., ISROMAC-7 Symposium, Honolulu, Hawaii, Feb. 22–26, **Vol. B**, pp. 603–613; also, Int. J. Rotating Mach., **6**, No. 1, pp. 43–56, 2000.
[12] Yang, M.-T., and Griffin, J. H., 2001, ''A Reduced Order Model of Mistuning Using a Subset of Nominal System Modes,'' ASME J. Eng. Gas Turbine Power, **123**(4), pp. 893–900.
[13] Petrov, E.P., Vitali, R., and Haftka, R., 2000, ''Optimization of Mistuned Bladed Discs Using Gradient-Based Response Surface Approximations,'' *Proc., 41st AIAA/ASME/ASCE/AHS/ASC Structures, Structural Dynamics and Materials Conference and Exhibit*, Atlanta, GA, April, Paper AIAA-2000-1522.
[14] Petrov, E., Sanliturk, K., Ewins, D. J., and Elliott, R., 2000, ''Quantitative Prediction of the Effects of Mistuning Arrangement on Resonant Response of a Practical Turbine Bladed Disc,'' 5th National Turbine Engine High Cycle Fatigue (HCF) Conference, Chandler, AZ, March 7–9.
[15] Petrov, E. P., and Ewins, D. J., 2001, ''Analysis of the Worst Mistuning Patterns in Bladed Disc Assemblies,'' Presented at the Turbo Expo 2001, New Orleans, LA, Jun. 4–7, Paper 2001-GT-0292.
[16] Kaiser, T., Hansen, R. S., Nguyen, N., Hampton, R. W., Muzzio, D., Chargin, M. K., Guist, R., Hamm, K., and Walker, L., 1994, ''Experimental/Analytical Approach to Understanding Mistuning in a Transonic Wind Tunnel Compressor,'' NASA Technical Memorandum, No. 108833, pp. 1–13.
[17] Whitehead, D. S., 1976, ''Effect of Mistuning on Forced Vibration of Blades with Mechanical Coupling,'' J. Mech. Eng. Sci., **18**, pp. 306–307.
[18] Whitehead, D. S., 1998, ''The Maximum Factor by Which Forced Vibration of Blades Can Increase Due to Mistuning,'' ASME J. Eng. Gas Turbines Power, **120**, pp. 115–119.
[19] Sinha, A., 1997, ''Computation of the Maximum Amplitude of a Mistuned Bladed Disk Assembly Via Infinity Norm,'' Proc., ASME International Mechanical Engineering Congress and Exposition, Dallas, TX, November 16–21, **AD-55**, pp. 427–432.
[20] Kenyon, J. A., and Griffin, J. H., 2001, ''Forced Response of Turbine Engine Bladed Disks and Sensitivity to Harmonic Mistuning,'' presented at the Turbo Expo 2001, New Orleans, LA, June 4–7, Paper 2001-GT-0274.
[21] Petrov, E. P., and Iglin, S. P., 1999, ''Search of the Worst and Best Mistuning Patterns for Vibration Amplitudes of Bladed Disks by the Optimization Methods Using Sensitivity Coefficients,'' *Proc. 1st ASSMO UK Conference 'Engineering Design Optimization'*, July 8–9, Ilkley, UK, pp. 303–310.
[22] Castanier, M. P., Ottarson, G., and Pierre, C., 1997, ''A Reduced Order Modeling Technique for Mistuned Bladed Disks,'' J. Vibr. Acoust., **119**, pp. 439–447.
[23] Bladh, R., Castanier, M. P., and Pierre, C., 2001, ''Component-Mode-Based Reduced Order Modeling Techniques for Mistuned Bladed Disks—Part II: Application,'' ASME J. Eng. Gas Turbines Power, **123** (1), pp. 100–108.
[24] Choi, B.-K., Lentz, J., Rivas-Guera, A. J., and Mignolet, M. P., 2003, ''Optimization of Intentional Mistuning Patterns for the Reduction of the Forced Response Effects of Unintentional Mistuning,'' ASME J. Eng. Gas Turbines Power, **125**(1), pp. 131–140.
[25] Rivas-Guerra, A. J., and Mignolet, M. P., 2003, ''Local/Global Effects of Mistuning on the Forced Response of Bladed Disks,'' J. Eng. Gas Turbines Power, to be published.
[26] Kenyon, J. A., Griffin, J. H., and Feiner, D. M., 2002, ''Maximum Bladed Disk Forced Response From Distortion of a Structural Mode,'' ASME J. Turbomach., **125**(2), pp. 352–363.

Downloaded 31 May 2010 to 171.66.16.27. Redistribution subject to ASME license or copyright; see http://www.asme.org/terms/Terms_Use.cfm

Predictions of Separated and Transitional Boundary Layers Under Low-Pressure Turbine Airfoil Conditions Using an Intermittency Transport Equation

Y. B. Suzen
Senior Engineer Associate

P. G. Huang
Professor

Department of Mechanical Engineering,
University of Kentucky,
Lexington, KY 40506-0503

Lennart S. Hultgren
Aerospace Engineer
Mem. ASME

David E. Ashpis
Aerospace Engineer

National Aeronautics and Space Administration,
Glenn Research Center at Lewis Field,
Cleveland, OH 44135

A new transport equation for the intermittency factor was proposed to predict separated and transitional boundary layers under low-pressure turbine airfoil conditions. The intermittent behavior of the transitional flows is taken into account and incorporated into computations by modifying the eddy viscosity, μ_t, with the intermittency factor, γ. Turbulent quantities are predicted by using Menter's two-equation turbulence model (SST). The intermittency factor is obtained from a transport equation model, which not only can reproduce the experimentally observed streamwise variation of the intermittency in the transition zone, but also can provide a realistic cross-stream variation of the intermittency profile. In this paper, the intermittency model is used to predict a recent separated and transitional boundary layer experiment under low pressure turbine airfoil conditions. The experiment provides detailed measurements of velocity, turbulent kinetic energy and intermittency profiles for a number of Reynolds numbers and freestream turbulent intensity conditions and is suitable for validation purposes. Detailed comparisons of computational results with experimental data are presented and good agreements between the experiments and predictions are obtained. [DOI: 10.1115/1.1580159]

1 Introduction

Flow transition plays an important role in turbomachinery applications. Majority of boundary layer flows in turbomachines involve flow transition under the effects of freestream turbulence, diverse pressure gradients, wide range of Reynolds numbers, flow separation, and unsteady wake-boundary layer interactions.

Prediction of this type of complex flows is an important element in analysis and performance evaluation of gas turbine engine components and ultimately in the design of more efficient jet engines. Especially, in low-pressure turbine applications prediction of transition behavior is even more important for reasons of design efficiency. For low-pressure turbines the flow is mostly turbulent at the high Reynolds number conditions encountered at take-off and the efficiency is at its design maximum. However, due to decrease of Reynolds number caused by high altitude conditions at cruise speeds, design based on the sea level conditions tends to underpredict losses and thus leads to substantial drops in efficiency [1–3]. These losses are attributed to flow separation on the suction surface of the turbine blades. At low Reynolds numbers with low freestream turbulence, the boundary layers on the airfoil surface have a tendency to remain laminar and hence the flow may separate before it becomes turbulent. This may cause a drop in efficiency and result in increase of fuel consumption. The impact of such losses is directly felt on the operation costs. It has been estimated that a 1% improvement in the efficiency of a low pressure turbine would result in a saving of $52,000 per year on a typical airliner [4].

In order to calculate the losses and heat transfer on various components of gas turbine engines, and to be able to improve component efficiencies and reduce losses through better designs, accurate prediction of development of transitional boundary layers is essential [1]. For an accurate prediction of transitional flows under the diverse conditions encountered in turbomachinery applications, the aim is to find a model providing the following properties:

- Physically accurate and versatile: The model should be capable of accurately predicting transitional flows under the diverse conditions encountered in turbomachinery applications, such as pressure gradients, freestream turbulence, wide range of Reynolds numbers, unsteady wake-boundary layer interactions and flow separation.
- Computationally efficient and inexpensive: The model should not involve extensive computational effort and should be relatively cheap to compute.
- Compatible with current CFD methods: The model should be easy to implement into existing CFD codes without requiring extensive changes in computational strategy.

One of the current methods for predicting flow transition is to use the stability theory. In this method, stability equations are solved at streamwise stations in order to predict the onset of transition. This method requires prior solution of the mean flow field and returns only the onset point of transition without any information on the turbulent part of the flow. Another method is using empirical correlations in the form of e^n. This type of methods also require prior solution of the mean flow field. These two methods are not compatible with current CFD methods.

One method compatible with current CFD methods is the use of low-Reynolds number turbulence models. Savill [5,6], has organized a number of workshops to assess the capability of current turbulence models in predicting flow transition. The comparisons showed that none of the existing models was adequate to predict flow transition for a range of flow conditions. Westin and Henkes [7] have also tested a large variety of turbulence models and compared models' performances in predicting a few of the T3-series transition flow experiments [5]. They indicated that none of the models could predict both onset location and length of transition

Contributed by the International Gas Turbine Institute for publication in the JOURNAL OF TURBOMACHINERY. Manuscript received by the IGTI July 9, 2001; revised manuscript received March 10, 2003. Associate Editor: S. Sjolander.

 Copyright © 2003 by ASME

Downloaded 31 May 2010 to 171.66.16.27. Redistribution subject to ASME license or copyright; see http://www.asme.org/terms/Terms_Use.cfm

for a range of flow conditions. This outcome is not at all surprising since most of the current turbulence models are not designed to predict flow transition.

An alternative method to this approach is to use the concept of intermittency to blend the flow from the laminar to the turbulent regions. This approach, although highly empirical, has shown some successes in predicting transition behavior. Dhawan and Narasimha [8] correlated the experimental data and proposed a generalized intermittency distribution function across flow transition. The correlation was later improved by Gostelow et al. [9] for flows with pressure gradients subject to a range of freestream turbulence intensities.

Solomon et al. [10], following the work of Chen and Thyson [11], developed an improved method to predict transitional flows involving changes in pressure gradients. In this model, the effects of changing streamwise pressure gradient on the breakdown physics and spot spreading rates are taken into account. This is accomplished by varying the spot spreading angle and propagation parameter through the transition zone according to the local pressure gradient parameter.

Steelant and Dick [12] proposed a transport equation for intermittency, in which the source term of the equation is developed such that the γ distribution of Dhawan and Narasimha [8] across the transition region can be reproduced. Steelant and Dick used their model, coupled with two sets of conditioned Navier-Stokes equations, to predict transitional flows with zero, favorable, and adverse pressure gradients. However, since their technique involved the solution of two sets of strongly coupled equations, the method is not compatible with existing CFD codes, in which only one set of Navier-Stokes equations is involved. Moreover, the model was designed to provide a realistic streamwise γ behavior but with no consideration of the variation of γ in the cross-stream direction.

Cho and Chung [13] developed a $k-\epsilon-\gamma$ turbulence model for free shear flows. Their turbulence model explicitly incorporates the intermittency effect into the conventional $k-\epsilon$ model equations by introducing an additional transport equation for γ. They applied this model to compute a plane jet, a round jet, a plane far wake, and a plane mixing layer with good agreements. Although this method was not designed to reproduce flow transition, it provided a realistic profile of γ in the cross-stream direction.

Suzen and Huang [14] improved the intermittency transport equation by combining the best properties of Steelant and Dick's model and Cho and Chung's model. Their model reproduces the streamwise intermittency distribution of Dhawan and Narasimha [8] and also produces a realistic variation of intermittency in the cross-stream direction. The model is capable of predicting flow transition under diverse conditions. The predicting capabilities of this model have been validated against T3-series experiments of Savill [5,6] and low-pressure turbine experiments of Simon et al. [15] with good success [14,16,17].

In the current research we focus on further validation of the intermittency transport model of Suzen and Huang [14] against the experiments of Hultgren and Volino [18]. Hultgren and Volino's experiments investigated the effects of freestream turbulence and Reynolds number on separated and transitional boundary layers under low-pressure turbine airfoil conditions. In their experiments, a flat plate boundary layer subject to a streamwise pressure gradient was studied. The superimposed pressure gradients were produced by attaching a two-dimensional contoured shape to the wall opposite to the test surface and by applying suction on the contoured wall. The resultant pressure profile represents that on the suction side of the Pak-B airfoil. The experiments covered a range of flow conditions including Reynolds numbers between 50,000 and 300,000 and freestream turbulence intensities between 0.2 and 7%. These cases cover a realistic range of operating conditions from take-off to cruise. On the test wall, velocity, turbulent kinetic energy and intermittency profiles were measured at 14 streamwise stations. In the measurements, quantities such as skin friction coefficients, transition start and end locations, and the locations of separation and reattachment were also determined. Further details of the measurements and experimental data were given by Volino and Hultgren [19].

The experiments of Hultgren and Volino [18] provide a good set of data for the development and validation of the models for flow transition. In the next section, the intermittency transport model is presented and implementation of the model is described along with the empirical correlations employed for the onset of transition. In Section 3, the numerical details of the prediction process are given. In Section 4, the predictions of the new intermittency model are compared against the experimental data. Finally, conclusions are provided in Section 5.

2 Transport Model for the Intermittency

In this section, the transport model for intermittency is presented. The model combines the transport equation models of Steelant and Dick [12] and Cho and Chung [13]. Details of the development and implementation of the transport model are given in Suzen and Huang [14,16], Suzen et al. [17].

The model equation is given by

$$\frac{\partial \rho\gamma}{\partial t}+\frac{\partial \rho u_j\gamma}{\partial x_j}=(1-\gamma)\Bigg[(1-F)2C_0\rho\sqrt{u_k u_k}\,f(s)f'(s)+F\Bigg(\frac{C_1\gamma}{k}\tau_{ij}\frac{\partial u_i}{\partial x_j}-C_2\gamma\rho\frac{k^{3/2}}{\epsilon}\times\frac{u_i}{(u_k u_k)^{1/2}}\frac{\partial u_i}{\partial x_j}\frac{\partial\gamma}{\partial x_j}\Bigg)\Bigg]+C_3\rho\frac{k^2}{\epsilon}\frac{\partial\gamma}{\partial x_j}\frac{\partial\gamma}{\partial x_j}+\frac{\partial}{\partial x_j}\times\Bigg(((1-\gamma)\gamma\sigma_{\gamma l}\mu+(1-\gamma)\sigma_{\gamma t}\mu_t)\frac{\partial\gamma}{\partial x_j}\Bigg) \quad (1)$$

The distributed breakdown function, $f(s)$ has the form

$$f(s)=\frac{as'^4+bs'^3+cs'^2+ds'+e}{gs'^3+h} \quad (2)$$

where $s'=s-s_t$, s is the distance along the streamline coordinate, and s_t is the transition location. The coefficients are

$$a=50\sqrt{\frac{n\sigma}{U}}\quad b=-0.4906\quad c=0.204\Bigg(\frac{n\sigma}{U}\Bigg)^{-0.5}$$
$$d=0.0\quad e=0.04444\Bigg(\frac{n\sigma}{U}\Bigg)^{-1.5} \quad (3)$$
$$h=10e\quad\text{and}\quad g=50$$

The shear stresses are defined as

$$\tau_{ij}=\mu_t\Bigg[\frac{\partial u_i}{\partial x_j}+\frac{\partial u_j}{\partial x_i}-\frac{2}{3}\frac{\partial u_k}{\partial x_k}\delta_{ij}\Bigg]-\frac{2}{3}\rho k\delta_{ij} \quad (4)$$

The blending function F is constructed using a nondimensional parameter, $k/W\nu$, where k is the turbulent kinetic energy and W is the magnitude of the vorticity. The blending function has the form

$$F=\tanh^4\Bigg[\frac{k/W\nu}{200(1-\gamma^{0.1})^{0.3}}\Bigg] \quad (5)$$

The model constants used in Eq. (1) are

$$\sigma_{\gamma l}=\sigma_{\gamma t}=1.0\quad C_0=1.0\quad C_1=1.6$$
$$C_2=0.16\quad\text{and}\quad C_3=0.15$$

The intermittency is incorporated into the computations simply by multiplying the eddy viscosity obtained from a turbulence model, μ_t, by the intermittency factor, γ. Simon and Stephens [20] showed that by combining the two sets of conditioned

Downloaded 31 May 2010 to 171.66.16.27. Redistribution subject to ASME license or copyright; see http://www.asme.org/terms/Terms_Use.cfm

Navier-Stokes equations and making the assumption that the Reynolds stresses in the nonturbulent part are negligible, the intermittency can be incorporated into the computations by using the eddy viscosity, μ_t^*, which is obtained by multiplying the eddy viscosity from a turbulence model, μ_t, with the intermittency factor, γ; that is,

$$\mu_t^* = \gamma \mu_t \tag{6}$$

is used in the mean flow equations. It must be noted that γ does not appear in the generation term of the turbulent kinetic energy equations.

The intermittency model had been implemented into TURCOM code developed by Huang and Coakley [21] and validated against low-pressure turbine experiments of Simon et al. [15] in Suzen et al. [17].

It is essential that the turbulence model selected to obtain μ_t must produce fully turbulent features before transition location in order to allow the intermittency to have full control of the transitional behavior. Menter's [22] SST model satisfies this requirement. It produces almost fully turbulent flow in the leading edge of the boundary layer and therefore it is used as a baseline model to compute μ_t and other turbulent quantities in the computations [17].

The value of $n\sigma$ used in evaluating the constants given by Eq. (3) is provided by the following correlation for zero pressure gradient flows [17]:

$$\hat{n}\sigma = (n\nu^2/U^3)\sigma = 1.8\times 10^{-11}\mathrm{Tu}^{7/4} \tag{7}$$

When flows are subject to pressure gradients, the following correlation is used:

$$\frac{\hat{n}\sigma}{(\hat{n}\sigma)_{ZPG}} = \begin{cases} M^{(1-\exp(0.75\times 10^6 K_t \mathrm{Tu}^{-0.7}))}, & K_t < 0 \\ 10^{-3227 K_t^{0.5985}}, & K_t > 0 \end{cases} \tag{8}$$

with M defined as:

$$M = (850\mathrm{Tu}^{-3} - 100\mathrm{Tu}^{-0.5} + 120)$$

where $(\hat{n}\sigma)_{ZPG}$ is the value for flow at zero pressure gradient and can be obtained from Eq. (7) and $K_t = (\nu/U_t^2)(dU/dx)_t$ is the flow acceleration parameter. The favorable pressure gradient part of the foregoing correlation (for $K_t > 0$) is from Steelant and Dick [12]. The portion of the correlation for adverse pressure gradient flows, $K_t < 0$, is formulated using the transition data of Gostelow et al. [9] and Simon et al. [15] in Suzen et al. [17].

The current approach uses the intermittency transport model to obtain the intermittency distribution for the transitional flows, while the onset of transition is defined by the correlations discussed in the next section.

Attached-Flow Transition. Abu-Ghannam and Shaw [23] suggested that the onset of transition for attached flows can be obtained by correlating the boundary layer momentum thickness Reynolds number to the freestream turbulence intensity according to

$$\mathrm{Re}_{\theta t} = 163 + \exp\left[F(\lambda_\theta) - \frac{F(\lambda_\theta)}{6.91}\mathrm{Tu}\right] \tag{9}$$

where

$$F(\lambda_\theta) = 6.91 + 12.75\lambda_\theta + 63.64\lambda_\theta^2 \quad \text{for } \lambda_\theta < 0, \text{ or}$$

$$F(\lambda_\theta) = 6.91 + 2.48\lambda_\theta - 12.27\lambda_\theta^2 \quad \text{for } \lambda_\theta > 0$$

Although Abu-Ghannam and Shaw correlation shows good agreement with experimental data for flows with zero and adverse pressure gradients, the model is not very sensitive to flows subject to strong favorable pressure gradients, in which one would expect the transition to be delayed as a result of flow acceleration [17].

To allow for a more sensitive response to strong favorable pressure gradients while maintaining the good features of Abu-Ghannam and Shaw in adverse pressure gradient region, the transition criterion was re-correlated to the freestream turbulence intensity, Tu, and the acceleration parameter, K_t,

$$\mathrm{Re}_{\theta t} = (120 + 150\mathrm{Tu}^{-2/3})\coth[4(0.3 - K_t\times 10^5)] \tag{10}$$

where K_t was chosen as the maximum absolute value of that parameter in the downstream deceleration region [17]. Equation (10) was designed to have a better fit of the available experimental data: while the correlation fits the transition data well for flows under adverse pressure gradients, it was purposely designed to rise rapidly as K_t becomes positive. This measure is to reflect the fact that the flow becomes less likely to have transition when subject to favorable pressure gradients.

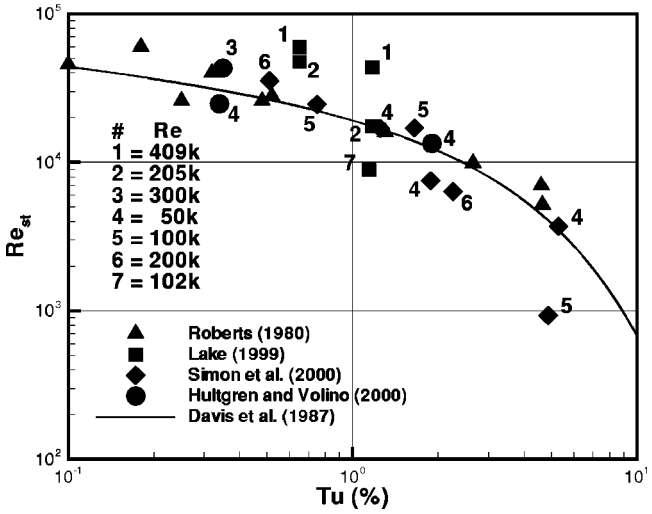

Fig. 1 Onset of separated flow transition

Separated-Flow Transition. Roberts [24] proposed a semi-empirical theory to predict onset of transition within a laminar separation bubble over the airfoil suction surface. The transition Reynolds number, Re_{st}, which is based on the length defined between the onset location of separation and that of transition, is correlated as a function of a turbulent factor representing effects of the external turbulence level and its disturbance spectrum. The model was simplified by Davis et al. [25] to only a function of turbulence intensity,

$$\mathrm{Re}_{st} = 2.5\times 10^4 \log_{10}\coth(0.1732\mathrm{Tu}) \tag{11}$$

where Tu is the freestream turbulence intensity value at the onset of separation. Although this model was originally proposed for swept wing flows, it had been used widely for predicting onset of transition in a variety of separated flows. However, comparisons of recently available data for onset of transition in separated flows suggest that the correlation for the onset of transition is better represented by a function of more than one parameter.

In Fig. 1, Davis et al. [25] correlation is given along with the data of Roberts [24] (the original data used to develop Davis' correlation), Simon et al. [15], Hultgren and Volino [18] and Lake [26]. Each point (except for the data of Roberts [24]) is numbered to indicate the Reynolds numbers of the cases based on exit velocity and suction surface length. There is some scatter in the data especially for high Reynolds number cases of Lake [26]. In order to capture the scatter of the data, we incorporated the effect of Reynolds number into the correlation for Re_{st}. The new correlation expresses Re_{st} in terms of the turbulence intensity (Tu) and the momentum thickness Reynolds number at the point of separation ($\mathrm{Re}_{\theta s}$) and is given as;

$$\mathrm{Re}_{st} = 874\,\mathrm{Re}_{\theta s}^{0.71}\exp[-0.4\mathrm{Tu}] \tag{12}$$

Downloaded 31 May 2010 to 171.66.16.27. Redistribution subject to ASME license or copyright; see http://www.asme.org/terms/Terms_Use.cfm

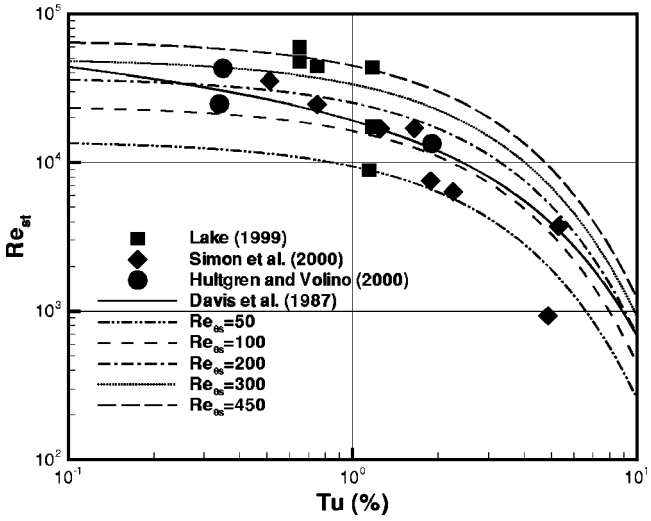

Fig. 2 Onset of separated flow transition with new correlation (Eq. 12)

In Fig. 2, the new correlation is compared with the experimental data for different values of $Re_{\theta s}$. In contrast to Davis et al. [25] correlation, the current formula seems to provide a better representation of the data scattering. In the present paper Eq. (12) is used as a replacement of Davis et al. correlation to predict the onset of separated-flow transition.

3 Numerical Details

As mentioned earlier, the experiments made use of a flow suction on the upper (contoured) surface to arrive at the desired pressure distribution. Although the shape of the upper contoured surface is known, no information is available for the conditions of the suction on this surface. This somewhat makes the computation of the problem ill-posed. In order to provide the upper boundary of the computational domain, we defined a prescribed streamline, obtainable by integrating the experimental measured velocity profiles, as the upper boundary. Once the streamline is defined as the upper computational boundary, a slip boundary condition can be applied at the upper surface.

For example, in Fig. 3 the streamlines obtained by using different values of

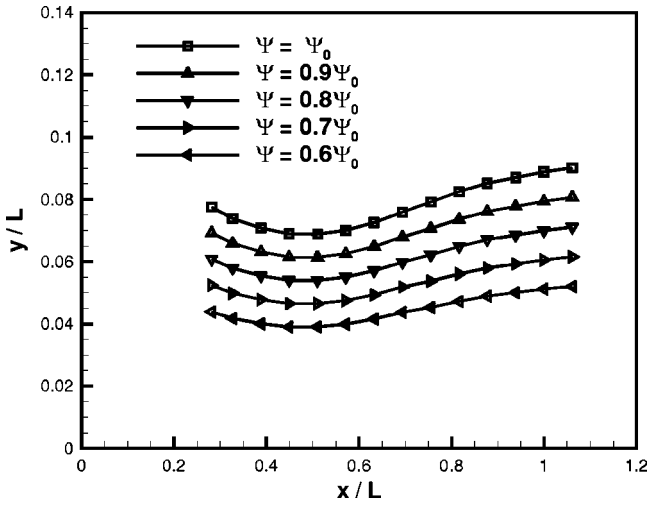

Fig. 3 Streamlines from experimental data, Re=300,000, FSTI=7%

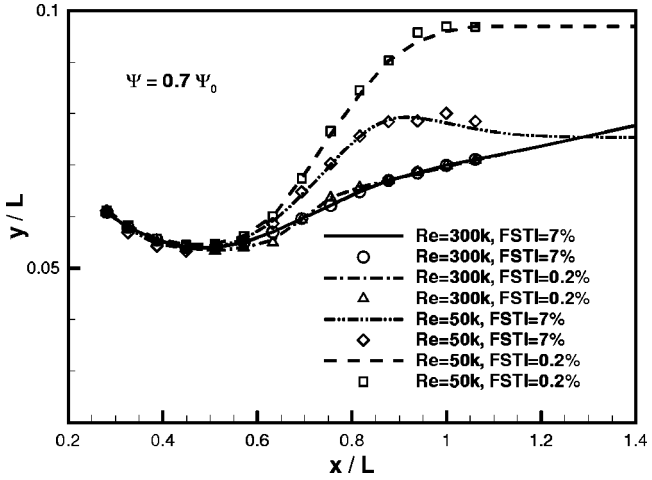

Fig. 4 Outer boundary shapes for all cases

$$\Psi = \int_0^h u\,dy, \tag{13}$$

are presented for the case with Re=300,000 and FSTI=7%. In this figure Ψ_0 is the Ψ obtained from Eq. (13) at the first station taking h as the maximum height of the measured y position. To define the streamlines, we performed the integration of measured velocity profiles based on Eq. (13) in all x stations such that Ψ is a constant. Any one of the streamlines shown in Fig. 3 can be used as the outer boundary of the computational domain, as long as they are well outside the boundary layer. Similar streamline curves can be generated for other cases.

In the computations, we selected a streamline corresponding to $\Psi=0.7\Psi_0$ as the upper boundary of the computational domain. The shapes of the upper streamlines are presented in Fig. 4 for all of the cases considered. In this figure the symbols show the points obtained from integration of the experimental velocity profiles and the lines indicate the boundary shapes used in the computations. By varying different streamline positions, we have found the streamline corresponding to $\Psi=0.7\Psi_0$ is sufficiently remote from the boundary layer to be considered as freestream. The boundary layer edge at each axial station is taken to be the location where the velocity is 99% of the maximum streamwise velocity at that station. Nonuniform meshes consisting of 140×60 grid points are used for all calculations. All grids have first y^+ values less than 0.5. A grid refinement study for the case with Re=50,000 and FSTI=7% (using a 250×100 mesh) has revealed that the solution obtained by the current mesh can be accepted as a grid independent solution.

Although the last experimental station is located at $x/L=1.06$, the computational domain is extended to $x/L=1.4$ in the streamwise direction to allow the outflow boundary condition to be applied in the computations. We have extended the upper streamline boundary up to $x/L=1.25$ and a constant pressure outflow boundary conditions is applied downstream of that station. Although this extension of the domain may appear to be arbitrary, it is necessary to avoid having reversed flow close to the exit boundary. Since no reverse flow was encountered for all cases after $x/L\approx1.25$, the extension of the domain up to $x/L=1.4$ seems reasonable. The plate surface is assumed to be an adiabatic wall and a constant-pressure outflow boundary condition is applied on the exit plane for all cases.

In order to obtain accurate inlet profiles for the computations, a laminar computation over a flat plate is performed. From this computation, the profile matching the momentum thickness the first experimental station is extracted as the inlet condition for the computations.

Downloaded 31 May 2010 to 171.66.16.27. Redistribution subject to ASME license or copyright; see http://www.asme.org/terms/Terms_Use.cfm

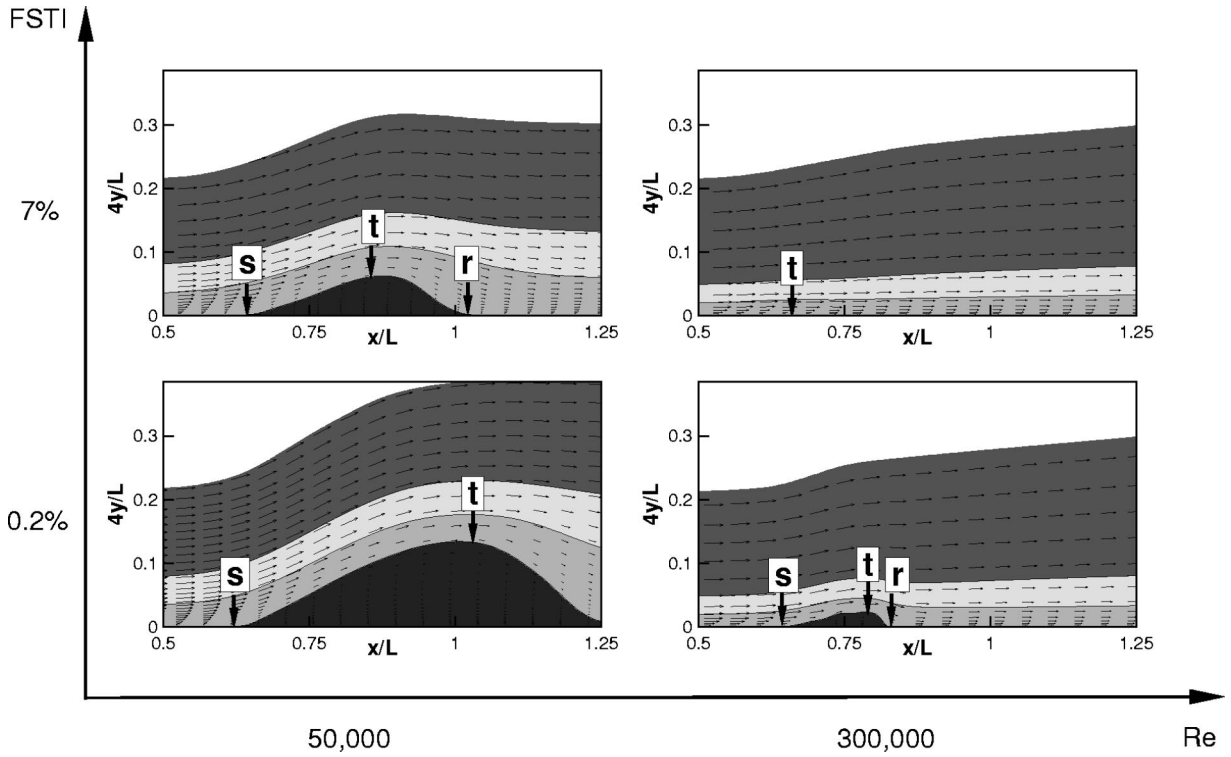

Fig. 5 Overall view of effects of Reynolds number and freestream turbulence intensity

4 Results and Discussion

In this section the comparison of the predictions with experimental data of Hultgren and Volino [18] are presented.

The experiment considered in this study involves two different Reynolds numbers, Re=300,000 and Re=50,000 (based on nominal exit velocity, U_{ref}, and wetted plate length, $L=0.208$ m) and two freestream turbulence intensities, FSTI=7% and FSTI=0.2%. Figure 5 depicts the dynamic interplay between transition and separation when subject to variations in Reynolds number and freestream turbulence effects. In this figure the insets **s** and **t** denote the onset of separation and transition, respectively, and the inset **r** denotes the reattachment point. The first case considered is with Re=300,000 and FSTI=7%. For this case, the transition position is at $x/L=0.66$ and only a tiny flow separation is observed near $x/L\approx0.7$. As the Reynolds number is decreased from 300,000 to 50,000 while keeping the freestream turbulence intensity the same, the onset of transition is delayed until $x/L=0.85$. As a result of the delay of the transition, a sizable flow separation is encountered between $x/L\approx0.65$ and ≈1.0. On the other hand, when the turbulence intensity is decreased from 7 to 0.2% while the Reynolds number is maintained at 300,000, the transition onset is delayed until $x/L\approx0.79$. As a result, a small but visible separation bubble is observed in the vicinity of $x/L\approx0.75$. The last case involved a simultaneous decrease of Reynolds number and freestream turbulence intensity, from 300,000 to 50,000 and from 7 to 0.2%, respectively. In this case the onset of transition is delayed to $x/L\approx1.03$ and a massive separation extending from $x/L\approx0.65$ to ≈1.25 is observed. The current prediction is an attempt to mimic the aforementioned dynamic behavior of the interaction between transition and separation when subject to changes in Reynolds number and freestream turbulence intensity conditions.

For the case involving Re=300,000 and FSTI=7%, experimental onset point of transition is at $\mathrm{Re}_\theta=336$ which corresponds to a location $x/L=0.66$. However, the onset point of transition for this case seems to be higher than other experimental data trend compiled by Mayle [1] and Savill [5] and also higher than the value given by the correlation of Abu-Ghannam and Shaw [23]. For example, the freestream turbulence intensity at the point of transition is Tu=1.7% and the acceleration parameter is, $K_t=-2.5\times10^{-6}$, by applying Eq. (10), the predicted onset location is much earlier (at $\mathrm{Re}_\theta=230$, corresponding to $x/L=0.55$). To show the effect of the transition positions, we have performed two different computations for this case: one using the experimental onset point of transition and the other using the onset point obtained from the correlation, Eq. (10).

The predicted pressure coefficient distribution along the surface is compared with experimental data, as shown in Fig. 6(*a*). In this figure, the results of the computation using the experimental onset of transition point is titled as "Computation 1" and the one obtained by utilizing Eq. (10) is denoted as "Computation 2." Both results show very good agreements with experimental data and only slight differences in the distributions near $x/L\approx0.65$ are observed between the two computations.

The velocity profiles for the two computations are compared with experimental data in Figs. 6(*b*) and (*c*). In the experiment, the flow remains laminar before station $x/L=0.69$. At station $x/L=0.69$ the velocity profile indicates that the flow is on the verge of separation. At the next station ($x/L=0.75$), the boundary layer is attached and the flow continues to develop as an attached turbulent boundary layer. Although it is not seen from the measured velocity profiles, it was reported experimentally that a very small separation region exists between the two measured stations, $x/L=0.69$ and 0.75. In contrast, no separation was observed in both computations although the comparison of the velocity profiles shows the predictions agree very well with experimental data. Both computations produce similar results except in the region $x/L\approx0.7$. Due to the fact that the onset point of transition of computation 2 is slightly upstream, the result of computation 2 is fuller and is less likely to separate than that of computation 1; otherwise, the differences between the two profiles are small.

The intermittency profiles of the two computations are compared with experimental data in Figs. 7(*a*) and (*b*). As can be seen from Fig. 7*a*, the flow is laminar at the first seven stations. In both

Downloaded 31 May 2010 to 171.66.16.27. Redistribution subject to ASME license or copyright; see http://www.asme.org/terms/Terms_Use.cfm

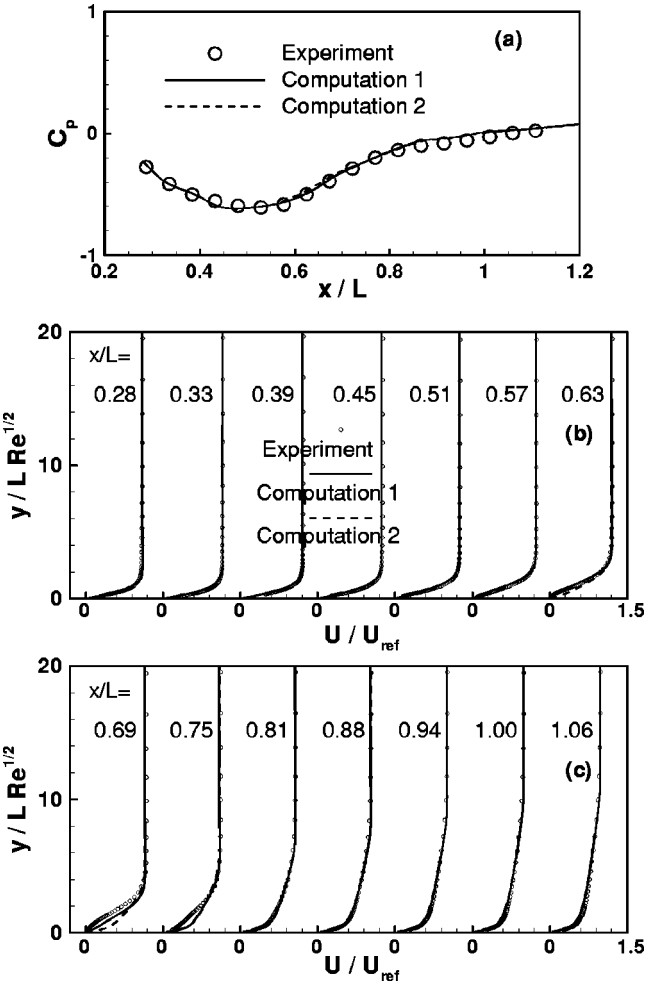

Fig. 6 Prediction of experiment of Hultgren and Volino [18]—Re=300,000, FSTI=7%

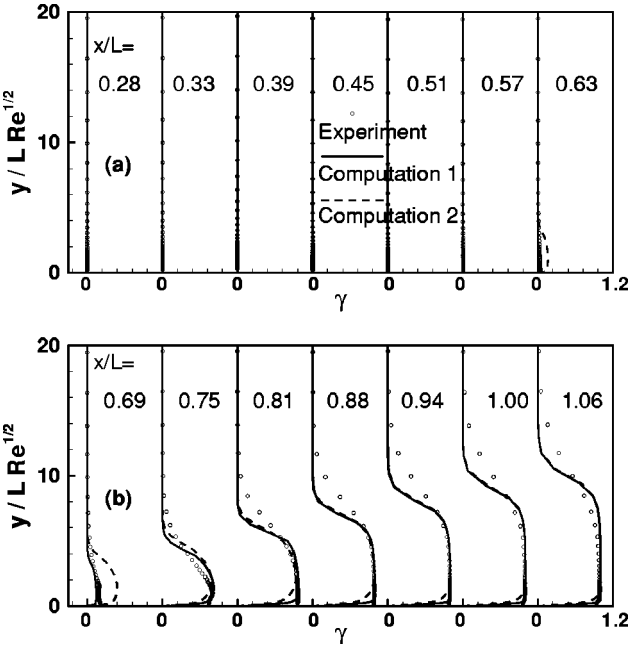

Fig. 7 Comparison of intermittency profiles along the surface—Re=300,000, FSTI=7%

the experiment and the computation 1, transition begins at station $x/L=0.66$ and in computation 2 the transition starts at $x/L=0.55$. While the transition of the computation 2 is ahead of the computation 1, the length of transition is somewhat longer due to the fact that a small value of spot generation rate, $n\sigma$, is calculated. The maximum value of the intermittency in the profiles of computation 1 reaches unity near station $x/L=0.81$ whereas in computation 2, the intermittency reaches unity only after $x/L=0.88$. Overall, computation 1 shows slightly better agreement with experiments than computation 2 even though the differences of the two results are mainly limited to the near wall region.

In Figs. 8(*a*) and (*b*), comparisons of the turbulent kinetic energy profiles are made. As can be seen from these figures, the freestream decay of turbulent kinetic energy throughout the plate is made to match the decay of freestream turbulence. This match provides the initial conditions for dissipation of the turbulent kinetic energy (see Suzen and Huang [14], for details). The predicted profiles of the turbulent kinetic energy seem to follow the experimental trend well even though the values are slightly larger before $x/L=0.7$ and smaller after that. Again, the differences of the two computations were only limited to region near $x/L=0.7$.

The next case considered involves the same freestream turbulence intensity (FSTI=7%) while Reynolds number is reduced from 300,000 to 50,000. In the experiment, the flow separated at $x/L=0.63$ and the onset of transition was observed at $x/L=0.85$. In the computations, separation took place at $x/L=0.66$ and the onset point of transition calculated from Eq. (12) was at $x/L=0.88$. The pressure coefficient distribution is compared with experimental data, as shown in Fig. 9(*a*). The agreement with the experimental data is good except in the region after $x/L=0.95$, where it can be seen that the pressure coefficient is slightly underpredicted indicating that the streamwise velocity distribution is slightly overpredicted.

The comparisons of the velocity profiles are given in Figs. 9(*b*) and (*c*). The profiles are in good agreement with the experiment up to $x/L=0.88$. The experimental data shows that the flow attaches after $x/L=0.94$ whereas the predictions indicate that the separation is extended up to $x/L=1.0$.

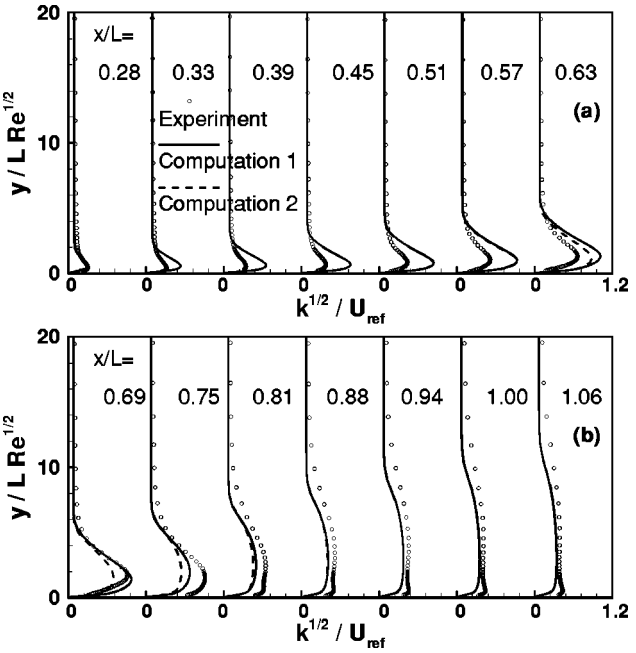

Fig. 8 Comparison of turbulence intensity profiles along the surface—Re=300,000, FSTI=7%

Downloaded 31 May 2010 to 171.66.16.27. Redistribution subject to ASME license or copyright; see http://www.asme.org/terms/Terms_Use.cfm

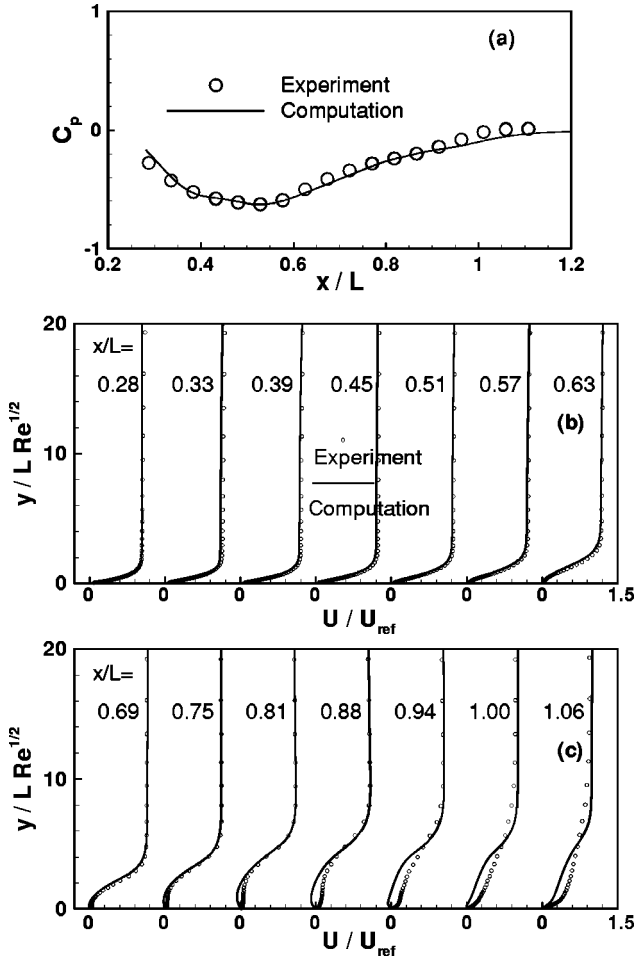

Fig. 9 Prediction of experiment of Hultgren and Volino [18]—Re=50,000, FSTI=7%

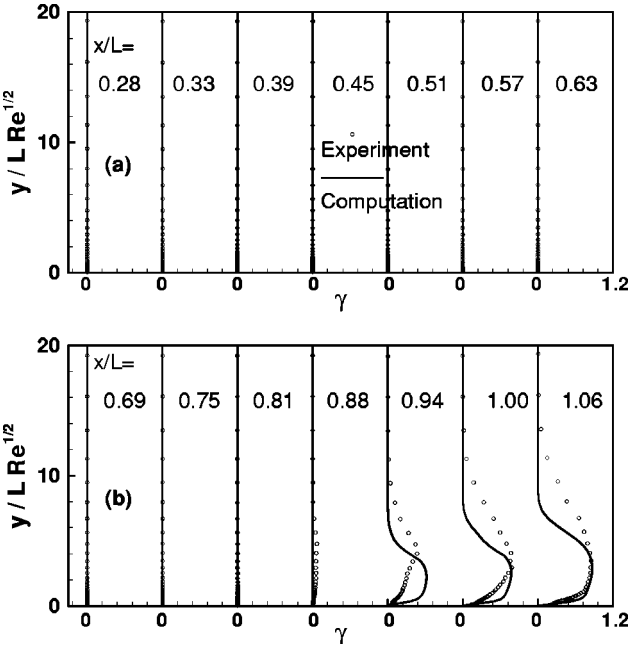

Fig. 10 Comparison of intermittency profiles along the surface—Re=50,000, FSTI=7%

The intermittency profiles are compared to experimental data in Figs. 10(*a*) and (*b*). The general profile trend is well predicted even though the exact profile shapes are not well captured. In Figs. 11(*a*) and (*b*), comparisons of turbulence intensity profiles are shown. It can be seen that the comparisons between the predictions and experimental data are favorable.

The next case involves FSTI=0.2% and Re=300,000. In the experiment, the flow separated at $x/L=0.67$, and the transition onset was observed between stations $x/L=0.75$ and $x/L=0.81$. The prediction shows that separation was at $x/L=0.66$ and the onset of transition (obtained from Eq. (12)) was at $x/L=0.79$. The comparison of the pressure coefficient distribution is presented in Fig. 12(*a*). The computed profile shows very good agreement with the experimental data.

The comparison of the velocity profiles are given in Figs. 12(*b*) and (*c*). The agreement between the predictions and experimental data is very good. It should be noted that there seems to be some discrepancies between the prediction and the measurement in the near-wall region near the flow separation region ($x/L\approx0.8$), this difference is caused by the failure of the hot wire measurement for the flow reversal.

The intermittency profiles are compared to experimental data in Figs. 13(*a*) and (*b*). The trend for the streamwise development of the intermittency factors seems to be well predicted, even though the model predicts a less diffusive behavior of the intermittency profiles near the freestream region.

The turbulence intensity profiles along the surface are compared to experimental data in Figs. 14(*a*) and (*b*). Although the general trend of the turbulent kinetic energy profiles is captured, it can be seen that the prediction gives rise to larger values of the turbulence kinetic energy for flow up to $x/L\approx0.85$.

Finally, both Reynolds number and the freestream turbulence intensity are decreased to 50,000 and to 0.2%, respectively. For this case, flow separation was observed at $x/L=0.63$ and the onset of transition was observed between stations $x/L=1.0$ and 1.06 in the experiment. The flow did not reattach at the last measured station ($x/L=1.06$). The predictions indicate that the flow separation is at $x/L=0.64$ and the onset of transition calculated from Eq. (12) is at $x/L=1.03$. The predicted pressure coefficient distri-

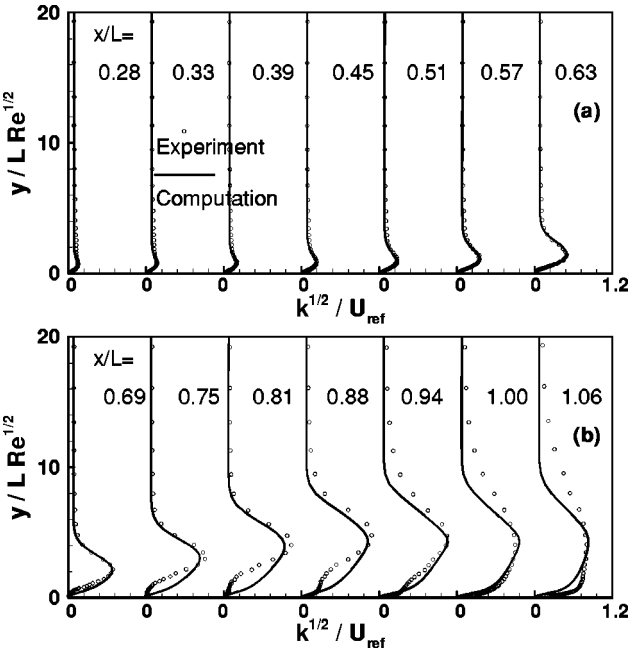

Fig. 11 Comparison of turbulence intensity profiles along the surface—Re=50,000, FSTI=7%

Downloaded 31 May 2010 to 171.66.16.27. Redistribution subject to ASME license or copyright; see http://www.asme.org/terms/Terms_Use.cfm

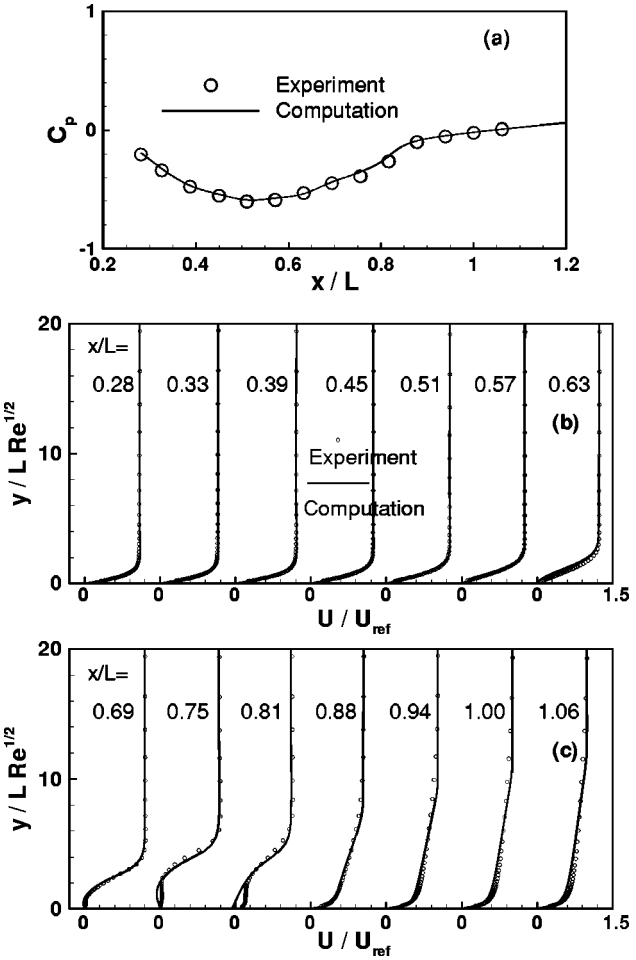

Fig. 12 Prediction of experiment of Hultgren and Volino [18]—Re=300,000, FSTI=0.2%

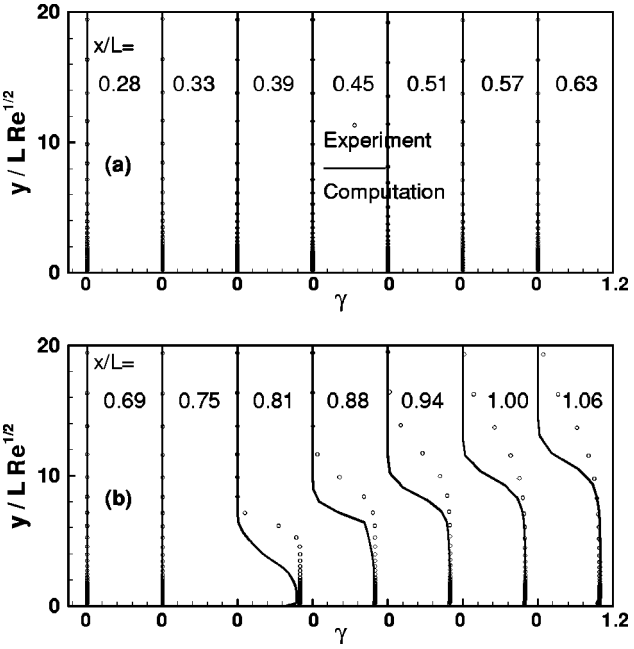

Fig. 13 Comparison of intermittency profiles along the surface—Re=300,000, FSTI=0.2%

bution is compared with experimental data, shown in Fig. 15(*a*). The agreement between the prediction and experimental data is very good.

The comparisons of the velocity profiles are shown in Figs. 15(*b*) and (*c*). As can be seen from the figures, good agreement is also observed for the velocity profiles. Once again, the discrepancy between the prediction and experiments near the wall is caused by the failure of the hot wire measurement in the separation region.

The intermittency profiles are compared to experimental data in Figs. 16(*a*) and (*b*). As can be seen from the figures, the flow remains laminar up to station $x/L=1.0$. At the last measurement station, $x/L=1.06$, the predicted intermittency factors show a larger magnitude than the experiments.

The turbulence intensity profiles are compared to experimental data in Figs. 17(*a*) and (*b*). It can be seen that the prediction gives rise to larger values of the turbulent kinetic energy profiles for region $x/L>0.65$. Even though the agreement is not that good, due to the fact that the transition only occurs at $x/L=1.03$ its impact to the velocity profiles is not that pronounced.

5 Concluding Remarks

A new transport equation for the intermittency factor is employed to predict a recent transitional boundary layer flow experiment under low pressure turbine airfoil conditions. The intermittent behavior of the transitional flows is taken into account by modifying the eddy viscosity with the intermittency factor. The new transport model not only can reproduce the experimentally observed streamwise variation of the intermittency in the transition zone, but also provides a realistic cross-stream variation of the intermittency profile. Computations are performed for two different Reynolds numbers and two different values of free stream turbulence intensities. Detailed comparisons with experiments are made for pressure coefficients, velocity, intermittency and turbulent kinetic energy profiles. Overall, good agreement with the experimental data is obtained. It has been demonstrated that the predictions accurately mimic the dynamic behavior of the inter-

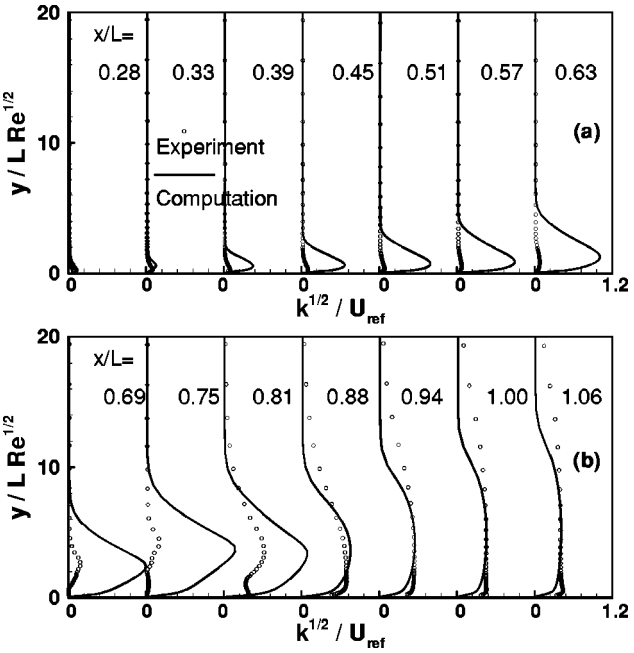

Fig. 14 Comparison of turbulence intensity profiles along the surface—Re=300,000, FSTI=0.2%

Downloaded 31 May 2010 to 171.66.16.27. Redistribution subject to ASME license or copyright; see http://www.asme.org/terms/Terms_Use.cfm

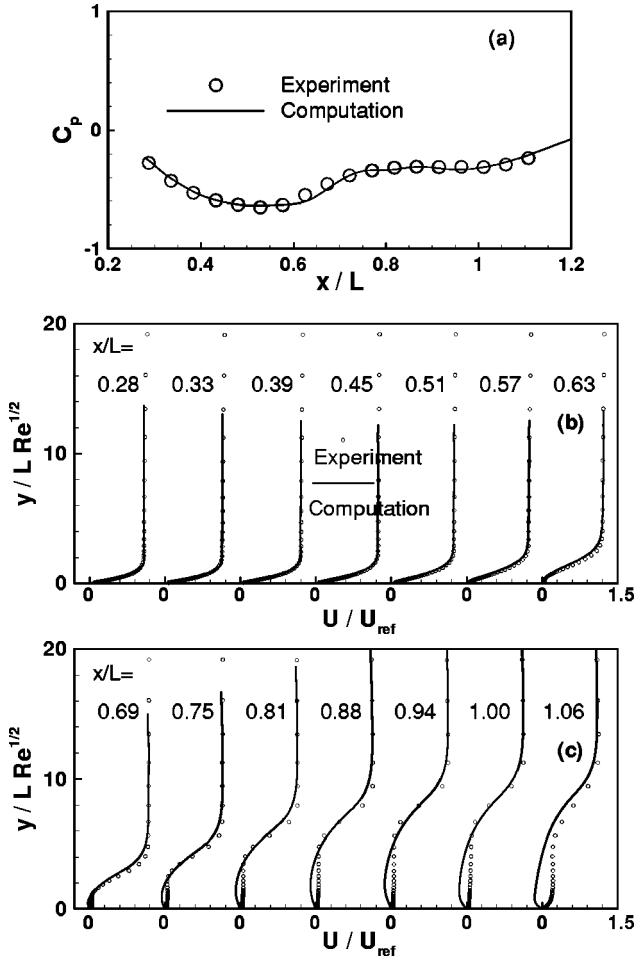

Fig. 15 Prediction of experiment of Hultgren and Volino [18]—Re=50,000, FSTI=0.2%

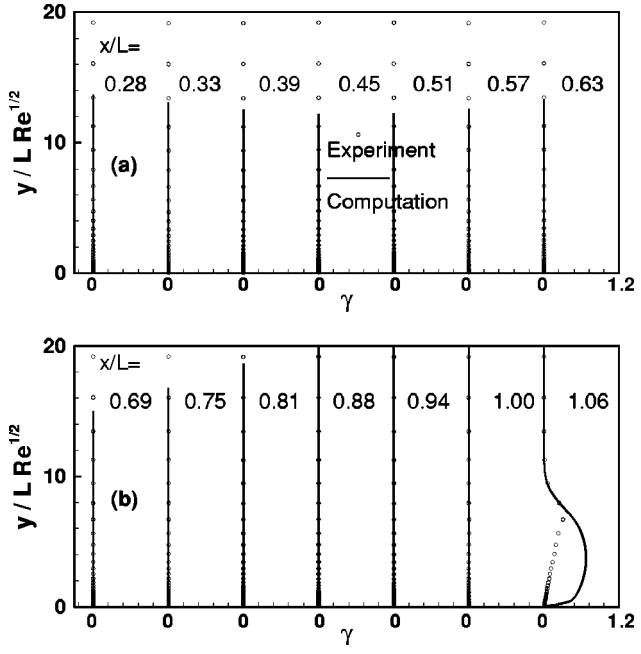

Fig. 16 Comparison of intermittency profiles along the surface—Re=50,000, FSTI=0.2%

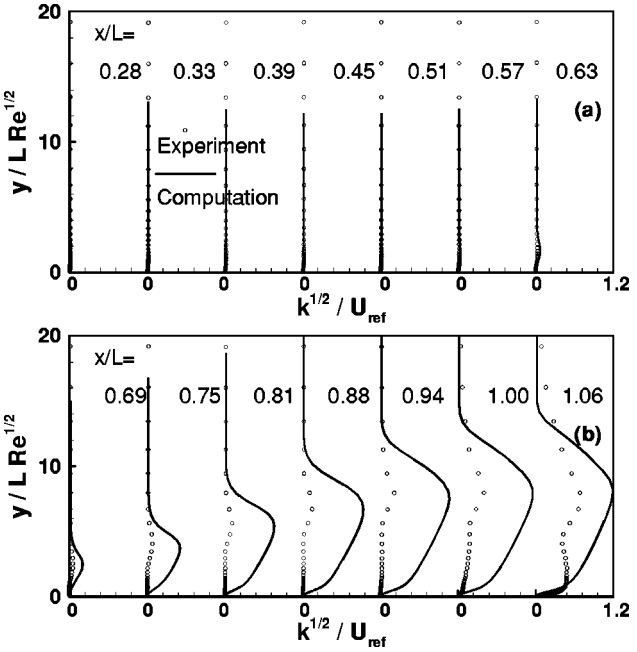

Fig. 17 Comparison of turbulence intensity profiles along the surface—Re=50,000, FSTI=0.2%

play between the transition and separation when subject to variations of Reynolds number and freestream turbulence intensity conditions.

Acknowledgments

This work is supported by NASA Glenn Research Center under grant NCC3-590. The project is part of the Low Pressure Turbine Flow Physics program of NASA-Glenn. This paper was originally published as AIAA Paper 2001-0446.

Nomenclature

C_p = pressure coefficient, $1-(U_e/U_{ref})^2$
FSTI = freestream turbulence intensity (%)
K_t = flow acceleration parameter, $(\nu/U^2)(dU/ds)$
k = turbulent kinetic energy
L = nominal suction surface wetted length
N = nondimensional spot breakdown rate parameter, $n\sigma\theta_t^3/\nu$
n = spot generation rate
p = static pressure
Re = Reynolds no., LU_{ref}/ν
Re_{st} = $(s_t-s_s)U_e/\nu$
$\mathrm{Re}_{\theta t}$ = $\theta_t U_e/\nu$
s = distance along streamwise coordinate
Tu = local turbulence intensity (%), u'/U
U = boundary layer streamwise velocity
U_e = local freestream velocity
U_{ref} = nominal exit freestream velocity
u_τ = friction velocity
W = magnitude of vorticity
x = wetted streamwise distance along suction surface
y_n = distance normal to wall
y^+ = $y_n u_\tau/\nu$
γ = intermittency factor
θ = momentum thickness
λ_θ = pressure gradient parameter, $(\theta^2/\nu)(dU/ds)$
μ = molecular viscosity
μ_t = eddy viscosity
ν = μ/ρ

Downloaded 31 May 2010 to 171.66.16.27. Redistribution subject to ASME license or copyright; see http://www.asme.org/terms/Terms_Use.cfm

ν_t = μ_t/ρ
ρ = density
σ = spot propagation parameter

Subscripts

e = freestream
s = onset of separation
t = onset of transition

References

[1] Mayle, R. E., 1991, "The Role of Laminar-Turbulent Transition in Gas Turbine Engines," ASME J. Turbomach., **113**, pp. 509–537.
[2] Rivir, R. B., 1996, "Transition on Turbine Blades and Cascades at Low Reynolds Numbers," AIAA Pap., AIAA-96-2079.
[3] Lake, J. P., King, P. I., and Rivir, R. B., 2000, "Low Reynolds Number Loss Reduction on Turbine Blades With Dimples and V-Grooves," AIAA Pap., AIAA-00-0738.
[4] Wisler, D. C., 1998, "The Technical and Economic Relevance of Understanding Boundary Layer Transition in Gas Turbine Engines," *Minnowbrook II-1997 Workshop on Boundary Layer Transition in Turbomachines*, eds., J. E. LaGraff and D. E. Ashpis, NASA CP-1998-206958, pp. 53–64.
[5] Savill, A. M., 1993, "Some Recent Progress in the Turbulence Modeling of By-pass Transition," *Near-Wall Turbulent Flows*, eds., R. M. C. So, C. G. Speziale, and B. E. Launder, Elsevier Science Publishers B. V., pp. 829–848.
[6] Savill, A. M., 1993, "Further Progress in The Turbulence Modeling of By-pass Transition," *Engineering Turbulence Modeling and Experiments 2*, eds., W. Rodi and F. Martelli, Elsevier Science Publishers B. V., pp. 583–592.
[7] Westin, K. J. A., and Henkes, R. A. W. M., 1997, "Application of Turbulence Models to Bypass Transition," ASME J. Fluids Eng., **119**, pp. 859–866.
[8] Dhawan, S., and Narasimha, R., 1958, "Some Properties of Boundary Layer During the Transition From Laminar to Turbulent Flow Motion," J. Fluid Mech., **3**, pp. 418–436.
[9] Gostelow, J. P., Blunden, A. R., and Walker, G. J., 1994, "Effects of Free-Stream Turbulence and Adverse Pressure Gradients on Boundary Layer Transition," ASME J. Turbomach., **116**, pp. 392–404.
[10] Solomon, W. J., Walker, G. J., and Gostelow, J. P., 1995, "Transition Length Prediction for Flows With Rapidly Changing Pressure Gradients," ASME Paper ASME-95-GT-241.
[11] Chen, K. K., and Thyson, N. A., 1971, "Extension of Emmons' Spot Theory to Flows on Blunt Bodies," AIAA J., **9**(5), pp. 821–825.
[12] Steelant, J., and Dick, E., 1996, "Modelling of Bypass Transition With Conditioned Navier-Stokes Equations Coupled to an Intermittency Transport Equation," Int. J. Numer. Methods Fluids, **23**, pp. 193–220.
[13] Cho, J. R., and Chung, M. K., 1992, "A $k-\epsilon-\gamma$ Equation Turbulence Model," J. Fluid Mech., **237**, pp. 301–322.
[14] Suzen, Y. B., and Huang, P. G., 1999, "Modelling of Flow Transition Using an Intermittency Transport Equation," NASA Contractor Report NASA-CR-1999-209313.
[15] Simon, T. W., Qiu, S., and Yuan, K., 2000, "Measurements in a Transitional Boundary Layer Under Low-Pressure Turbine Airfoil Conditions," NASA Contractor Report NASA-CR-2000-209957.
[16] Suzen, Y. B., and Huang, P. G., 2000, "Modelling of Flow Transition Using an Intermittency Transport Equation," ASME J. Fluids Eng., **122**, pp. 273–284.
[17] Suzen, Y. B., Xiong, G., and Huang, P. G., 2002, "Predictions of Transitional Flows in Low-Pressure Turbines Using an Intermittency Transport Equation," AIAA J., **40**(2), pp. 254–266.
[18] Hultgren, L. S., and Volino, R. J., 2000, "Separated and Transitional Boundary Layers Under Low-Pressure Turbine Airfoil Conditions," NASA TM, in preparation.
[19] Volino, R. J., and Hultgren, L. S., 2000, "Measurements in Separated and Transitional Boundary Layers Under Low-Pressure Turbine Airfoil Conditions," ASME/IGTI Paper 2000-GT-0260.
[20] Simon, F. F., and Stephens, C. A., 1991, "Modeling of the Heat Transfer in Bypass Transitional Boundary-Layer Flows," NASA Technical Paper 3170.
[21] Huang, P. G., and Coakley, T. J., 1992, "An Implicit Navier-Stokes Code for Turbulent Flow Modeling," AIAA Pap., AIAA-92-0547.
[22] Menter, F. R., 1994, "Two-Equation Eddy-Viscosity Turbulence Models for Engineering Applications," AIAA J., **32**(8), pp. 1598–1605.
[23] Abu-Ghannam, B. J., and Shaw, R., 1980, "Natural Transition of Boundary Layers-The Effects of Turbulence, Pressure Gradient, and Flow History," J. Mech. Eng. Sci., **22**(5), pp. 213–228.
[24] Roberts, W. B., 1980, "Calculation of Laminar Separation Bubbles and Their Effect on Airfoil Performance," AIAA J., **18**(1), pp. 25–31.
[25] Davis, R. L., Carter, J. E., and Reshotko, E., 1987, "Analysis of Transitional Separation Bubbles on Infinite Swept Wings," AIAA J., **25**(3), pp. 421–428.
[26] Lake, J. P., 1999, "Flow Separation Prevention on a Turbine Blade at Low Reynolds Number," Ph.D. dissertation, Air Force Institute of Technology, Dayton, OH.

Downloaded 31 May 2010 to 171.66.16.27. Redistribution subject to ASME license or copyright; see http://www.asme.org/terms/Terms_Use.cfm

Effect of Unsteady Stator Wake—Rotor Double-Leakage Tip Clearance Flow Interaction on Time-Average Compressor Performance

Borislav Todorov Sirakov

Choon-Sooi Tan

MIT Gas Turbine Laboratory,
Cambridge, MA 02139

A study has been conducted, using unsteady three-dimensional Reynolds-averaged Navier-Stokes simulations to determine the impact on rotor performance of the interaction between upstream (steady defect and time-varying defect) stator wakes and rotor tip clearance flow. The key effects of the interaction between steady stator wakes and rotor tip clearance flow are: 1) a decrease in loss and blockage associated with tip clearance flow; 2) an increase in passage static pressure rise. Performance benefit is seen in the operability range from near design to high loading. The benefit is modest near design and increases with loading. Significant beneficial changes due to the stator-rotor interaction occur when the phenomenon of tip clearance flow double-leakage is present. Double-leakage occurs when the tip clearance flow passes through the tip gap of the adjacent blade. It is detrimental for compressor performance. The effect of strong stator-rotor interaction is to suppress double-leakage on a time-average basis. Double-leakage typically takes place at high loading but can be present at design condition as well, for modern highly loaded compressor. A benefit due to unsteady interaction is also observed in the operability range of the rotor. A new generic causal mechanism is proposed to explain the observed changes in performance. It identifies the interaction between the tip clearance flow and the pressure pulses, induced on the rotor blade pressure surface by the upstream wakes, as the cause for the observed effects. The direct effect of the interaction is a decrease in the time-average double-leakage flow through the tip clearance gap so that the stream-wise defect of the exiting tip flow is lower with respect to the main flow. A lower defect leads to a decrease in loss and blockage generation and hence an enhanced performance compared to that in the steady situation. The performance benefits increase monotonically with loading and scale linearly with upstream wake velocity defect. With oscillating defect stator wakes, rotor performance shows dependence on oscillation frequency. Changes in the tip region occur at a particular reduced frequency leading to (1) decrease in blockage, and (2) increase in passage loss. The changes in rotor performance at a particular reduced frequency are hypothesized to be associated with the inherent unsteadiness of the tip clearance vortex and its resonance behavior excited by the oscillating wakes. [DOI: 10.1115/1.1574822]

Introduction and Technical Background

Tip clearance flow has been a topic of interest due to its profound effects on compressor performance and stability (Wisler [1], Smith [2], Koch [3], among others). A brief overview of relevant previous work on tip clearance flow and unsteady flow in compressors is given to motivate the present work.

The structure and physics of tip clearance flow have been investigated by Rains [4], Hunter and Cumpsty [5], Chen et al. [6], Storer and Cumpsty [7], Khalid [8], and Nikolaoue et al. [9] among others. Rains [4] proposed an inviscid model for the leakage flow velocity by relating the tip leakage flow to the blade static pressure difference. He assumed that the kinetic energy of the leakage flow velocity component normal to the chord cannot be recovered and he calculated the loss in efficiency, based on this assumption. Storer and Cumpsty [7] developed a simple control volume analysis model for calculation of tip clearance flow loss using ideas from Rains' model. They view the mixing process of the leakage jet and the main stream as the major loss mechanism. Khalid [8] provided a rational methodology for quantifying the flow blockage associated with tip clearance flow. He also developed a simple model using a description of the growth of a two-dimensional wake in an adverse pressure gradient, which provides insights to the important processes associated with blockage growth. Khalsa et al. (Appendix of reference [8]) reported the phenomenon of **double-leakage** (the passage of tip clearance fluid through the neighboring tip clearance gap). He stated that double-leakage reduces the relative stagnation pressure of the tip clearance flow (thus making Storer's assumption invalid when double-leakage is present) and causes an increase in passage blockage. Khalsa [10] discusses double leakage and, based on his computations, concludes that double-leakage increases both passage loss and blockage. Smith [11] experimentally investigated the effect of changing the axial spacing between blade rows on compressor performance changes. He obtained a one-point efficiency gain and a two to four percent stage pressure rise increase in a low-speed research compressor, by reducing blade row spacing from 0.37 to 0.07 chords. Mikolajczak [12] reported similar results. Hetherington and Moritz [13], however, achieved a two-point efficiency

Contributed by the International Gas Turbine Institute and presented at the International Gas Turbine and Aeroengine Congress and Exhibition, Amsterdam, The Netherlands, June 3–6, 2002. Manuscript received by the IGTI January 2002; revised manuscript received January 31, 2003. Paper No. 2002-GT-30368. Review Chair: E. Benvenuti.

 Copyright © 2003 by ASME

Downloaded 31 May 2010 to 171.66.16.27. Redistribution subject to ASME license or copyright; see http://www.asme.org/terms/Terms_Use.cfm

gain by increasing the spacing between the blade rows in a multistage compressor. Such findings suggest the existence of more than one mechanism affecting compressor performance. Valkov [14] investigated the effect of upstream wakes and tip clearance vortices on stator time-average performance. He identified two generic causal mechanisms with significant impact on performance. These are reversible recovery of energy in the disturbances (beneficial) (in accord with Smith's results [11]) and non-transitional boundary layer response (detrimental). The net effect is beneficial. Valkov reports 0.2 points efficiency gain for rotor-stator axial spacing of 0.37 chords compared to infinite spacing and 0.6 points efficiency gain for the close spacing (0.07 chords) case with stronger unsteadiness. Graf [15] and Tzeng [16] investigated the effects of the downstream stator pressure field on the time-average performance of the upstream rotor. Graf found that the back pressure fluctuations are important for blade passage performance and tip clearance flow development. He reported a decrease in tip clearance loss and an increase in overall loss for strong interaction case. Graf's computed results show that the motion of the tip vortex can be at frequency different from the blade passing frequency. Presently, it is suggested that this may be somewhat related to the unsteadiness observed in the tip region by Bae [17] and Mailach [18] in experiments, and by Vo [19] in his calculations. Bae hypothesized that the observed vortex unsteadiness could be analogous to Crow instability observed in wing trailing vortex pairs and showed that the frequency of the instability scales with the passage flow-through time. In a more recent study, Tzeng [16] deduced that the effect of backpressure on upstream rotor time-average performance may be negligible. Thus far, there are two remaining aspects of unsteadiness on low-speed axial compressor performance that have not been addressed: 1) constant/time-invariant defect stator wake-rotor tip vortex interaction; and 2) oscillating defect stator wake-rotor tip vortex interaction. These form the focus of the paper. The paper is arranged as follows: The first section presents the overall approach to the problem and information about the numerical tools employed. A description of the stator wakes is also included. A section presenting the methodology for isolating the effects of unsteadiness on performance follows. The main results are presented in the Results and Observations section. An explanation of the observed changes is offered in the Mechanistic Explanation section and the paper ends with a Summary and Conclusions section.

Approach

The approach consists of implementing a set of numerical experiments for quantifying the performance change and for identifying the cause-and-effect associated with the interaction between upstream wakes and rotor tip clearance flow. Time-accurate, Reynolds-averaged, Navier-Stokes simulations are carried out to obtain unsteady solutions at different operating conditions. For the **steady** amplitude wake cases, averaged boundary conditions are extracted from the unsteady calculations and steady solutions are obtained at the same mass flow, with the same boundary conditions, for a consistent back-to-back comparison. Iterations on the backpressure boundary condition are required to match mass flow between unsteady and steady solution at each operating condition. Detailed description of a consistent back-to-back method for assessing time-average effects of unsteady flow against an equivalent steady flow is presented in the next section. Four important cases are selected for delineating the parametric dependence of the effect of unsteadiness on blade row axial spacing and rotor blade loading. The four cases are strong wakes (50% velocity defect in stator frame, corresponding to reduced spacing between the blade rows) at high loading and design conditions and typical wakes (27% velocity defect in stator frame, corresponding to nominal spacing between the blade rows) at high loading and design conditions. For the cases with **oscillating** defect stator wakes an oscillatory upstream stagnation pressure profile was introduced. The defect of the wakes is varied in the range (30 $\pm$20)% velocity defects at different frequencies. For both steady and oscillating defect wake cases shear stresses are turned-off on the casing wall, hub wall, and blade surfaces (i.e., solving the Reynolds Average Navier-Stokes Equations with inviscid wall boundary conditions allowing slip velocity) to exclude the effects of wake-blade boundary layer interaction reported by Valkov [14]; The goal of this study is to assess the effect of the stator wakes on rotor tip clearance flow and a full stator-rotor calculation is deemed unnecessary. The substitution of the stator row with stator wakes prescribed upstream of the rotor is an approximation that will capture the important aspects of the interaction between a stator and rotor in terms of accompanying changes in rotor time-average performance.

Numerical Tools. The Computational Fluid Dynamics code selected for this investigation is Denton's UNSTREST solver [20]. It is a 3-D, unsteady, viscous code employing an explicit, second-order-accurate scheme to solve the unsteady Reynolds-averaged Navier-Stokes equations. The code uses Prandtl's mixing-length turbulence model for eddy viscosity. UNSTREST requires a simple H-mesh grid and is able to run both multiple blade-row and multiple blade-passage calculations [20].

The grid for this study consists of two computational domains. The first domain is a stationary duct (36 axial $\times$49 circumferential $\times$37 radial). A moving rotor domain follows it (126 axial $\times$49 circumferential $\times$37 radial). Performance is calculated from averaged values in the inlet plane of the rotor domain and in the blade trailing edge plane. The purpose of the finite length duct upstream of the rotor is to release wakes in the stationary frame so as to simulate the presence of an upstream stator wake. The wakes are rotating with respect to the rotor domain. The generated grid is such as to mitigate the numerical dispersion of the wakes traveling through the rotor domain. The current grid has a resolution of 293,706 points, following a recommendation by Denton [21], the author of the code. Results are calculated for several different cycles from a converged periodic solution. When the computed pressure rise, loss, and blockage results from the different cycles are compared, they show uncertainty in the fourth significant figure. Results are reported to within this accuracy. There are five grid points in the tip clearance region, which is deemed adequate to capture the key relevant features of tip clearance flow (Dawes [22]). As the tip flow exits the tip clearance and meets with the main flow a shear layer is formed between them and the tip clearance flow evolves in a physically consistent manner.

Wake Description for Constant Defect Wakes. The wake at the inlet of the duct is prescribed as a total pressure defect. The defect is constructed as a Gaussian profile because the objective here is to elucidate the key role of the relative defect [14]. The wake is characterized with a peak velocity defect A_v and a 99% velocity defect thickness, T_v. The strongest wake achieved for this study is a wake with $A_v = 50\%$. The corresponding thickness for such a wake strength should be $T_v = 0.12$ chords based on measurements in a low speed axial compressor (Stauter [23]). However, too strong and too thin a wake would dissipate and disperse before reaching the rotor unless an unreasonably high-resolution grid is used. For this reason the peak defect is set to the original maximum of 50% but the thickness is increased by 2.8 times the measured value to alleviate this problem. Because the increase in thickness is the same for the strong and typical wake cases the relative changes between the two cases remain the same and the performance trend is preserved. Figure 1 describes the wakes chosen for the strong and nominal design interaction cases.

Method for Designing a Steady Calculation

The issue of designing equivalent steady flow from given unsteady flow field to achieve a consistent back-to-back comparison is conceptually non-trivial. For example, if each variable of interest is averaged separately in the unsteady flow field, the resulting averaged steady flow field is inconsistent. The average total pres-

Downloaded 31 May 2010 to 171.66.16.27. Redistribution subject to ASME license or copyright; see http://www.asme.org/terms/Terms_Use.cfm

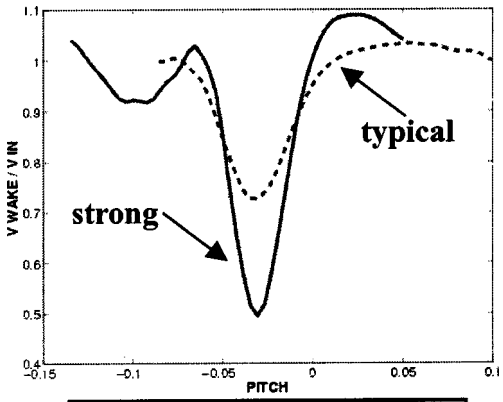

UPSTREAM WAKE DESCRIPTION		
	Av (%)	Tv (chords)
TYPICAL	27	0.56
STRONG	50	0.34

Fig. 1 Stator wakes description

sure from the unsteady solution will be different from the total pressure calculated from the averaged Mach number and averaged static pressure. Therefore, the unsteady solution should be brought to a steady state through a physically consistent process, despite the changes in the thermodynamic state of the fluid that will inevitably occur. To obtain consistent steady solution only five quantities can be conserved because this is the number of the primitive variables (pressure, density, and three velocities) in the flow field. Only five equations can be used to solve for five unknowns. Therefore, five averaged quantities, which will remain the same from the unsteady to the steady solution, must be selected.

A physically consistent situation is to allow the flow to mix-out completely before reaching the rotor (the use of mixing plane between the blade rows has been a common practice). The flow is brought to a steady (or circumferentially uniform) state through conservation of axial impulse, angular and radial momentum, mass and energy. Thus these are the quantities selected for conservation.

Methodology. The following method is used to design steady calculations for comparison with the unsteady solutions:

1. Obtain a time accurate solution for a given operating condition.
2. Time average in a cycle the five selected quantities at each grid point: mass, energy, axial impulse, angular momentum, radial momentum.
3. Construct the steady flow field at a chosen inlet plane by solving the following equations for pressure, density, and three velocities:

$$A=\overline{\rho u}=\frac{1}{T}\int_0^T \rho u dt \tag{1}$$

$$B=\overline{p}+\overline{\rho u^2}=\frac{1}{T}\int_0^T (p+\rho u^2)dt \tag{2}$$

$$C=\overline{\rho uv}=\frac{1}{T}\int_0^T \rho uv dt \tag{3}$$

$$D=\overline{\rho uw}=\frac{1}{T}\int_0^T \rho uw dt \tag{4}$$

$$E=\left(\overline{\rho e}+\overline{p}+\overline{\rho}\frac{\overline{u^2}+\overline{v^2}+\overline{w^2}}{2}\right)\overline{u}$$
$$=\frac{1}{T}\int_0^T\left(\rho e+p+\rho\left(\frac{u^2+v^2+w^2}{2}\right)\right)u dt \tag{5}$$

and

$$\overline{p}=\overline{\rho e}(\gamma-1) \tag{6}$$

By substituting the remaining equations into the energy equation, a quadratic equation in P can be obtained

$$\left(\frac{-1}{\gamma-1}-\frac{1}{2}\right)\overline{p}^2+B\left(\frac{1}{\gamma-1}\right)\overline{p}+\frac{1}{2}(B^2+C^2+D^2)-EA=0 \tag{7}$$

The root corresponding to an increase in entropy is selected.

4. Extract the inlet averaged boundary conditions (P_t, T_t, and absolute angle) required as input to the CFD code from the foregoing averaged flow field.
5. Obtain the steady solution without upstream wakes with the extracted boundary conditions and at the same time-average mass flow. Iterations on the exit pressure boundary condition are required to match the mass flow in both cases. Obtain the solution using the same time-accurate code, same grid, and same post-processors.
6. Construct the steady flow fields at the selected inlet and exit planes in the rotor domain, as described in step 3, for both the unsteady and steady solutions. Since the steady solution is also obtained in a time accurate mode for consistency, it is subjected to the same averaging procedure.
7. Once both cases are brought to steady state, perform the appropriate spatial averages at the inlet and exit planes to obtain one-dimensional figures of merit, such as area-average static pressure and mass-average total pressure.
8. Compare the unsteady performance of the rotor to the steady one. The ''steady'' flow in this study is a flow field obtained at the same time averaged mass flow with the same circumferentially mixed-out inlet boundary conditions as the unsteady one.

Results and Observations

Constant Defect Wakes. The rotor simulated in this study is from the last stage of a three stage, low speed axial compressor with overall pressure ratio of 1.6 and tip clearance of 2% of blade height. The overall effect of upstream unsteadiness on rotor total-to-static pressure rise can be seen in Fig. 2. The two speed-lines show that upstream unsteadiness has a beneficial effect on rotor

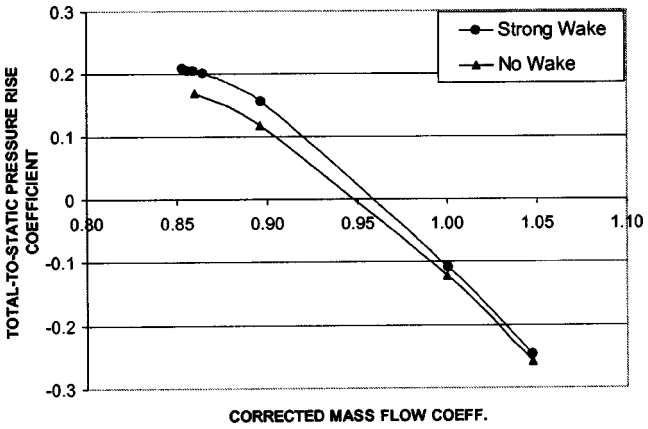

Fig. 2 Effect of upstream wake on rotor total-to-static pressure rise coefficient showing the benefit of upstream stator wake-rotor tip clearance flow interaction on time-average performance

Downloaded 31 May 2010 to 171.66.16.27. Redistribution subject to ASME license or copyright; see http://www.asme.org/terms/Terms_Use.cfm

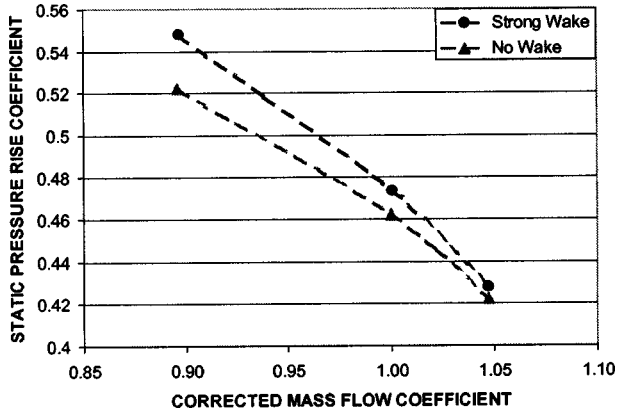

Fig. 3 Beneficial effect of strong upstream stator wake—rotor tip clearance flow interaction on rotor static pressure rise coefficient

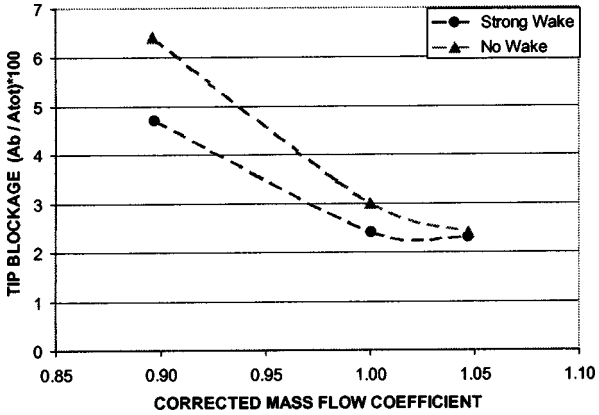

Fig. 5 Beneficial effect of strong upstream stator wake—rotor tip clearance flow interaction on tip region blockage generation

performance. It can be inferred from the results that the effect on total-to-static pressure rise coefficient is modest close to design but becomes significant at high-loading (0.17 steady versus 0.20 time-average unsteady).

The leftmost points in Fig. 2 correspond to the lowest mass flow for which a steady state or a time-periodic solution is achievable. If these are taken to be the operability limit [19], then the results in Fig. 2 would imply that there could be benefit in the operability range of the rotor due to the unsteady interaction. Smith [11] has observed such a benefit in his experiments. A discussion of this issue will follow later. The performance benefit caused by the typical wake unsteady interaction with the rotor tip clearance flow is less than the performance benefit in the strong unsteady interaction case.

Figures 3 through 5 present the effect of upstream wakes on rotor static pressure rise, tip region loss, and blockage. Figure 3 shows the calculated benefit from the unsteady interaction between upstream wakes and rotor tip clearance flow on rotor static pressure rise. The computed trend is in qualitative agreement with measured trend reported by Smith [11] (However, such an agreement between the results in the two studies is fortuitous as discussed in the next section). Changes in static pressure rise are caused by both changes in blade passage loss and blockage. Therefore, the effect on static pressure rise can be viewed as the net effect on performance. To check the consistency of the solution, the change in static pressure rise is estimated from the changes in loss and blockage and compared to the computed change. Influence coefficients as derived in Shapiro [24] provide a convenient way to perform such a comparison. The results from the CFD calculation and the estimated results based on the method of influence coefficients are in good agreement (within 4% from the CFD results).

Figures 4 and 5 show the effects of upstream wakes on tip region loss and blockage generation. Loss is calculated from the difference between blade inlet and exit time averaged entropy flux and blockage is calculated using Khalid's procedure [8]. The benefit in blockage is up to a 27% decrease from the computed value in the steady case (0.064 steady versus 0.047 time-average unsteady) and the benefit in loss coefficient is up to a 40% decrease from the computed value in the steady case (0.174 steady versus 0.103 time-average unsteady).[1] The beneficial effects increase with loading and with upstream wake velocity defect.

Figure 6(*a*) shows that the beneficial effect from the unsteady interaction scales linearly with the upstream wake velocity defect. Thus, when the observed changes in static pressure rise are normalized by the wake velocity defect, the data collapses on the same linear curve, as shown in Fig. 6(*b*). This information will allow the designer to estimate the aerodynamic benefit from closing the spacing between the blade rows and correct any results obtained with a mixing-plane steady approximation.

From the results it can be inferred that the benefit in blade passage static pressure rise, tip region loss generation, and tip region blockage generation increases with loading and with upstream stator wake velocity defect.

Comparison to Previous Results. Smith's experiment in 1970 on a low-speed axial compressor demonstrated a measured benefit in both pressure rise and efficiency by reducing the spacing between the blade rows from 0.37 to 0.07 blade chords. The effect that he measured has been attributed to the increased unsteadiness in the blade rows.

Some of the effect is attributed to wake recovery through inviscid stretching based on Kelvin's theorem [11]. Valkov [14] performed a numerical study and quantified the effect of upstream wakes and tip vortices on stator performance. As mentioned earlier, he identified two causal mechanisms (reversible recovery of wake energy and non-transitional boundary layer response) leading to changes in performance and quantified the net benefit. The results in the current study exclude the effects of upstream wakes on blade surface boundary layers, the effect of wake stretching downstream of the blade row and to a large extent the effect of wake stretching inside the passage (the effect of wake stretching outside the tip region is excluded by reporting changes in the tip region only). The focus of the present work is on the effect of unsteadiness in the tip region. The design characteristics of the

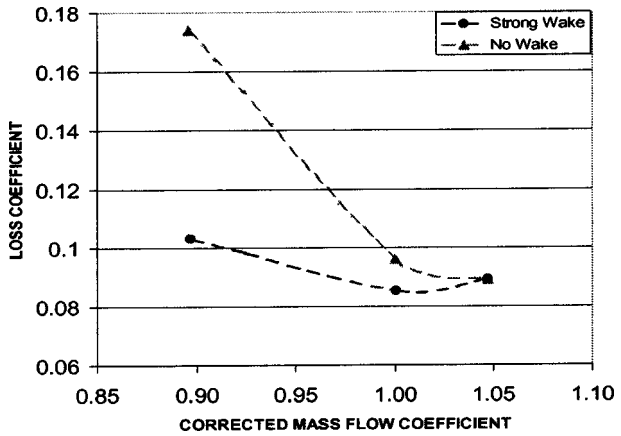

Fig. 4 Beneficial effect of strong upstream stator wake—rotor tip clearance flow interaction on tip region loss generation

[1]Loss coefficient is calculated in the tip region only, where loss is significant. Loss coefficient $= T(\bar{s}_e^{\bar{m}} - \bar{s}_{in}^{\bar{m}})/1/2U_{tip}^2$.

Downloaded 31 May 2010 to 171.66.16.27. Redistribution subject to ASME license or copyright; see http://www.asme.org/terms/Terms_Use.cfm

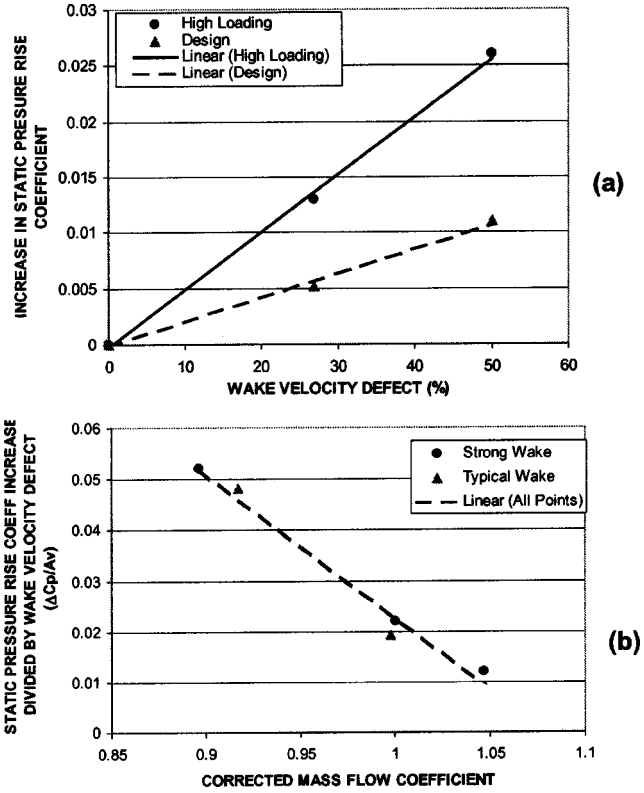

Fig. 6 Beneficial effect of upstream unsteadiness increases monotonically with upstream wake defect. (Static pressure rise coefficient is normalized by wake velocity defect to obtain a single linear dependence on operating condition for all wakes.)

blade geometry used in the previous work done by Smith [11] and Valkov [14] and the blade geometry used in the present study are not the same. However, some of the important geometric and flow parameters are similar (Table 1). Based on the observation that the design characteristics of these three blade rows are similar on an approximate basis, the results from the current study are combined with Valkov's findings to assess against Smith's experimental data on the relative importance of the new mechanism to the measured beneficial changes. Table 2 presents the comparison.

The results in Table 2 show that the beneficial effect observed in the current study is comparable to the net beneficial effect calculated by Valkov [14] and Deregel [26]. Taken together they could account for Smith's experimental findings. However, recent discussions with Smith [27] indicated that such a comparison might not be appropriate. Based on the blade geometry, stagger, and loading, Smith estimated that the compressor from his experiment did not experience any double tip leakage flow. Therefore, as will be explained in the following section, the observed benefits in the two studies have different origins.

Table 1 Rotor geometry for the LAR rotor by Smith [11], GE E^3 blade geometry by Wisler [25], and rotor blade geometry in present investigation

	LAR rotor (Smith)	E3 stator (Valkov)	Rotor in present Study
Mach no.	N/A	0.55	0.5
Reynolds no.	178,000	247,000	355,000
Aspect ratio	1.96	1.37	0.96
Tip solidity	0.93	1.4	1.08
Tip stagger	43.4	44	47.1
Inlet tip vel. diagram included angle	92°	N/A	90°

Table 2 Upstream stator wake-rotor tip clearance flow interaction benefit, reversible recovery of wake energy and nontransitional boundary layer response benefit, and their net to compare with Smith's experimental findings

Benefit from increasing upstream unsteadiness on stage performance (reduction of blade row axial spacing from 0.37 to 0.07 chords)		
	Pressure rise	Efficiency
Valkov/Deregel (net effect from reversible recovery of wake energy and non-transitional boundary layer response)	1–3% +	0.40 pts +
Present study-stage (effect of stator wake—rotor tip clearance flow interaction)	2.2% +	0.76 pts +
Net effect (Valkov+present study)	3.2–5.2% +	1.16 pts +
SMITH (experimental data)	2~4% +	1.00 pts +

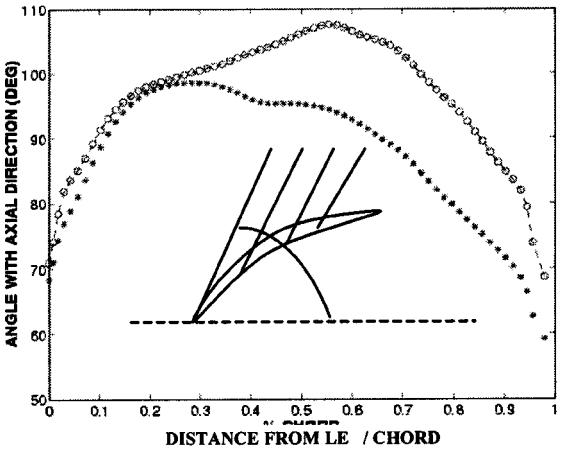

Fig. 7 Angle between tip clearance flow exit direction and axial direction in the relative frame

Interface Angle Between Main Flow and Tip Flow. It was observed that the angle of the interface between the incoming flow and the tip clearance flow was different in the steady and time-average unsteady cases. For the strong interaction case the average interface angle in the unsteady case is 3° lower than the interface angle in the steady case. This is a consequence of the difference in the tip clearance flow exit stream-wise velocity. This difference leads to a difference in the tip clearance fluid exit angle (Fig 7), which consequently causes a difference in the interface angle between the time averaged unsteady and steady cases. Possible benefit of up to 2.8% in corrected mass flow coefficient due to this change may be expected in the operability range of the rotor. The estimation of the benefit is based on the criteria for tip region flow breakdown developed by Vo [19]; this occurs when the interface angle between the tip flow and the main flow reaches 90° from the axial direction.

Mechanistic Explanation

It is of interest to determine the mixed-out loss for the tip region. The mixed-out loss from the unsteady flow situation is 27% lower than the value calculated from the steady flow situation.

Downloaded 31 May 2010 to 171.66.16.27. Redistribution subject to ASME license or copyright; see http://www.asme.org/terms/Terms_Use.cfm

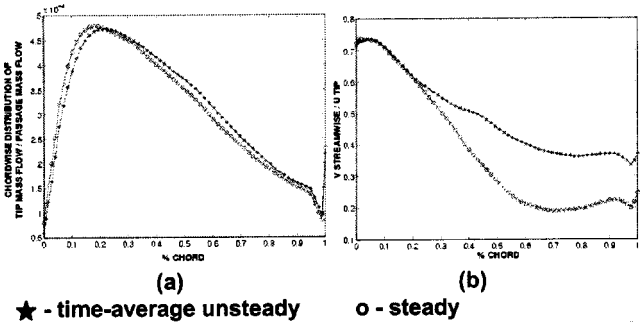

Fig. 8 Chordwise distribution of tip clearance mass flow and stream wise velocity (in direction of main flow relative to blade) for steady and unsteady cases. (Total tip clearance mass flow is 2% of blade passage mass flow.)

This implies that the tip flow in situations that involve unsteady interactions with upstream wakes would exit the tip clearance region with significantly smaller defect with respect to the main flow, than the tip flow under conditions when interactions with upstream wakes are absent.

The average normal components of velocity through the tip clearance flow (which determine the mass flow) are the same for the steady and unsteady flow situations (Fig. 8(*a*)). However, the stream-wise components of the tip flow exit velocity are different between the time-average of the unsteady calculation and the steady calculation. This is the reason for the difference in the exit defect of the tip flow in the steady and time-average unsteady cases.

The average stream-wise component of the tip flow exit velocity normalized by the rotor tip velocity in the unsteady case is 0.50, which is 25% higher than that in the steady case, 0.40 (Fig. 8(*b*)). To examine further this change in tip clearance flow behavior the relative stagnation pressure in the tip clearance gap is calculated and shown in Fig. 9. Relative stagnation pressure is chosen because it can show where the tip clearance fluid is coming from. The main flow and the wakes have high relative stagnation pressure while the tip clearance flow has a relative total pressure defect. It can be clearly seen from the figure that on a time-average basis the tip flow exiting the tip gap in the steady case has much higher relative stagnation pressure defect than the one in the unsteady case.

The reason for this behavior can be seen in Fig. 10. The tip clearance flow in the steady case double-leaks (passes through the tip gap of the adjacent blade) through a significant portion of the

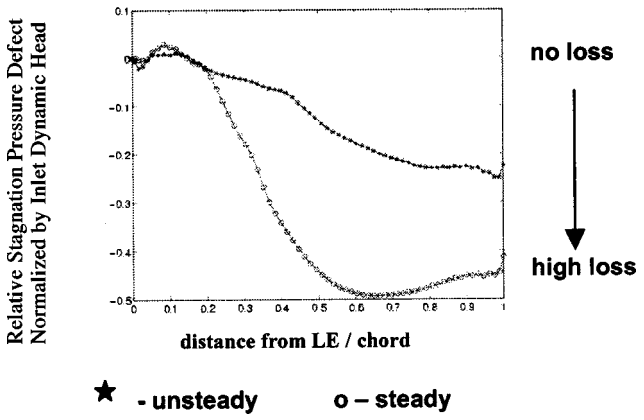

Fig. 9 Relative stagnation pressure of tip clearance fluid exiting the tip gap. On a time-average basis unsteady tip clearance flow exits the tip gap with less relative stagnation pressure defect.

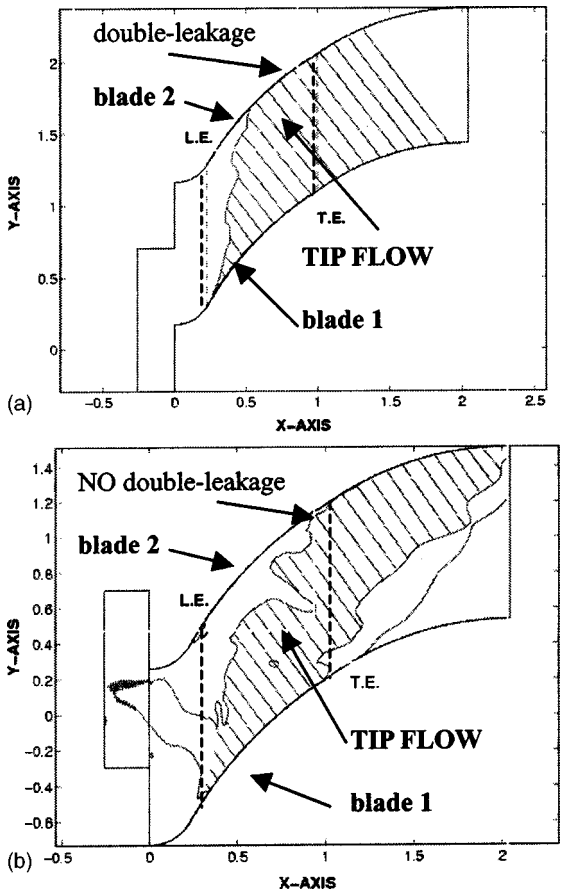

Fig. 10 Tip clearance flow behavior in steady and unsteady environment (98% cut); *x*-axis is in the axial direction and *y*-axis is in the circumferential direction—(*a*) steady (tip clearance fluid from blade 1 passes through tip gap of blade 2), (*b*) instantaneous unsteady (no tip clearance fluid from blade 1 passes through tip gap of blade 2)

next blade. Double-leakage means that the pressure difference across the blade drives through the tip gap the low stagnation pressure fluid originating from the previous tip clearance instead of the high total pressure fluid from the main flow and the wakes (Wakes in the relative frame have higher stagnation pressure than the main flow when the main flow inlet velocity triangle has an included angle $\geqslant$90 deg, which is typically the case in the tip region at high loading).

The low stagnation pressure tip fluid exits the tip gap with low stream-wise velocity component. In the unsteady case, however, double-leakage occurs only at certain selected instants of time. Figure 10(*b*) shows instant of time when there is absolutely no double-leakage in the unsteady case. Therefore, only some of the fluid that exits the tip clearance gap in the unsteady case comes from the previous tip clearance and has high loss and low stagnation pressure. Thus, on a time average basis, the relative stagnation pressure of the fluid exiting the tip clearance is higher in the unsteady case. Consequently, the streamwise velocity component of the exiting tip flow is higher in the unsteady case and the defect with respect to the main flow is smaller. The smaller defect generates less loss and blockage in the blade passage.

To address the question on why at high loading the tip clearance flow double-leaks in a steady environment and double-leaks only at certain instants of time in an unsteady environment, the effect of the upstream wakes needs to be examined. In the rotor relative frame the upstream wakes appear as jets normal to the blade chord directed away from the blade suction surface. This behavior is sketched in Fig. 11.

Downloaded 31 May 2010 to 171.66.16.27. Redistribution subject to ASME license or copyright; see http://www.asme.org/terms/Terms_Use.cfm

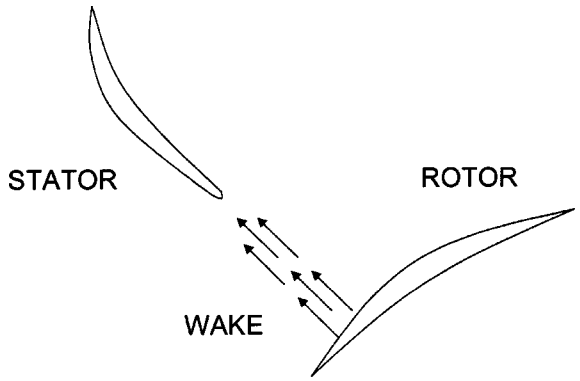

Fig. 11 Upstream wakes appear as normal jets directed away from the rotor suction side in the rotor relative frame

The normal jet in the rotor frame impinges on the pressure surface of the blades and a local stagnation point appears (Fig. 12). This stagnation of the fluid produces strong pressure pulses on the blades (Fig. 13). The strength of these pressure pulses reaches values of up to 50% of the inlet relative dynamic head, which is significant. Such pressure pulses have been previously reported by Valkov [14].

Figure 14 elucidates the effect of the pressure pulses on the rotor tip clearance flow. Figure 14(*a*) identifies the location of a pressure pulse using a single pressure contour at a given instant of time. Figure 14(*b*) shows that at this exact location at the same instant of time, the tip clearance fluid is directed away from the pressure pulse, and blocked from passing into the clearance gap.

The pressure pulse creates a locally strong pressure gradient, which tends to deflect the clearance fluid away, thus reducing the amount of double-leakage flow. Therefore, whenever a pressure pulse passes through the region of double-leakage, it turns the tip clearance fluid away from the blade and prevents double-leakage. Another way to think about this phenomenon is that high relative stagnation pressure wake fluid passes through the tip clearance instead of the low relative stagnation pressure tip clearance fluid from the previous blade thus blocking instantaneously the double-leakage phenomena. A quasi-steady argument and physical model based on this idea is given further in the section. It is important to note that when wakes and the associated wake jets pass along the tip gap there is more fluid driven through the tip clearance gap but on time average basis, the same amount of fluid passes through the tip gap in the steady and unsteady cases. The effect of the wake jets ***is not*** to prevent tip clearance flow from taking place (in fact, they drive more), but ***is*** to suppress double-leakage of tip flow. Since the upstream wakes causing the pressure pulses pass periodically through the rotor domain, the result is a tip clearance flow, which oscillates back and forth between double-leakage and no double-leakage.

This mechanism is described in Fig. 15. The oscillatory change in the direction of the tip clearance flow leads to a significant reduction of the time-average double-leakage flow in the unsteady case. This explains the smaller extent of the defect with which the tip clearance flow exits the tip gap in the unsteady case and consequently, the improvement in performance.

To confirm the periodic changes in the direction of the tip clearance flow and the resulting periodic changes of the relative stag-

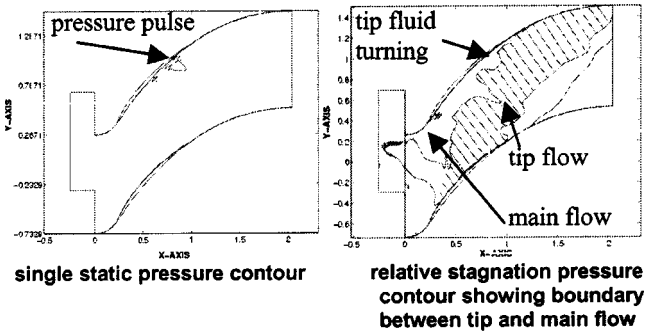

Fig. 14 Location of isolated pressure pulse and its turning effect on tip clearance flow (98% span cuts)

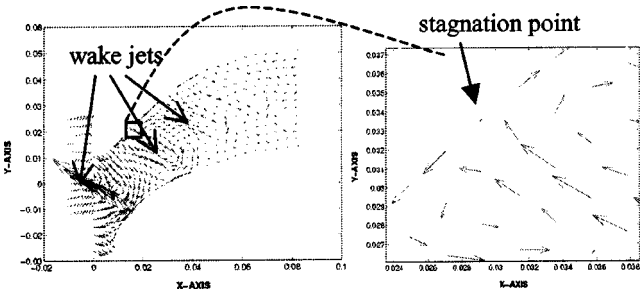

Fig. 12 Instantaneous disturbance velocity field in the rotor (50% cut). The upstream wakes impinge on the pressure side and stagnation points appear; *x*-axis is in the axial direction and *y*-axis is in the circumferential direction.

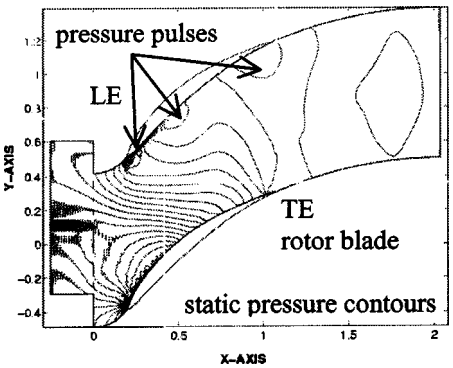

Fig. 13 Instantaneous position of pressure pulses in the rotor passage (50% Cut). Pressure pulses appear as a result of the wake jet stagnation on the pressure surface.

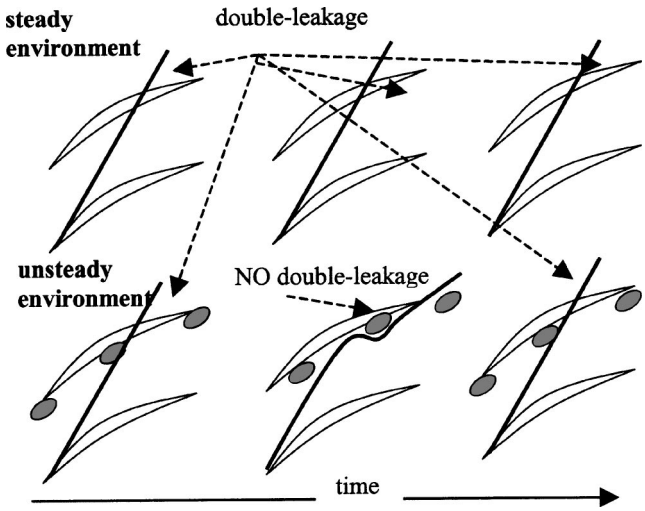

Fig. 15 Fluid scenario to explain the reduction of tip clearance fluid double-leakage and enhancement of performance. Pressure pulses prevent double-leakage during selected instants of time in a cycle.

Downloaded 31 May 2010 to 171.66.16.27. Redistribution subject to ASME license or copyright; see http://www.asme.org/terms/Terms_Use.cfm

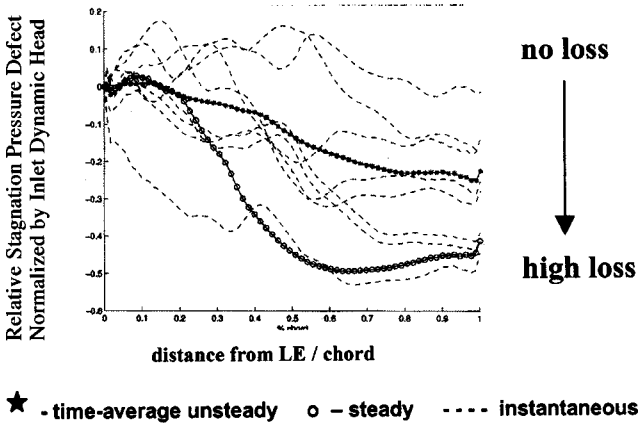

Fig. 16 Relative stagnation pressure defect is shown with dotted lines in the tip gap for different instants of time in a cycle. Average steady and unsteady values are shown with solid lines.

nation pressure of the fluid passing through the tip gap, Fig. 16 is presented. It shows the relative stagnation pressure defect at different instants of time and the average values for the unsteady and steady cases. It can be observed that in the unsteady case both low stagnation pressure tip fluid and high stagnation pressure main flow and wake fluid pass through the tip gap at different times.

An alternative quasi-steady perspective on this flow phenomenon may provide additional understanding. The wake jets in the rotor passage transport wake fluid towards the pressure side of the blade. Therefore, on a time average basis wake fluid accumulates on the pressure side of the blade. The wake fluid is high-energy fluid in the frame of the rotating rotor. Its relative stagnation pressure and temperature are higher than the stagnation pressure of the main flow and especially higher than the stagnation pressure of the tip clearance flow. Therefore, the tip clearance appears as an area contraction and three different flows compete to pass through it. This situation can be modeled in the following simple way, as suggested by Gong[2] (Fig. 17).

Two streams, a high stagnation pressure (wakes) and a low stagnation pressure (tip flow) stream pass through a nozzle. More high stagnation pressure fluid will pass through the throat of the nozzle. For a given high ratio of the stagnation pressures of the high energy to the low energy flow the high-energy flow will block completely the low energy flow from passing through the nozzle. In the same way, the high-energy wake fluid, which accumulates on the pressure side of the rotor blades, restricts the amount of tip clearance flow that double leaks through the neighboring tip clearance.

Relevance of Proposed Mechanism to Observed Performance Changes. To evaluate and quantify the relevance of the proposed mechanism to the observed performance changes a

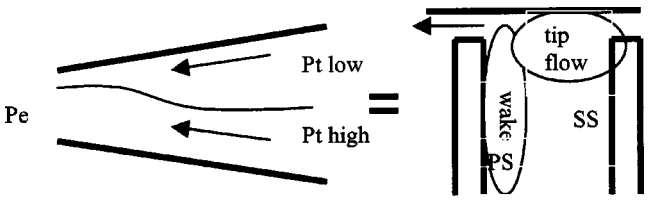

Fig. 17 Compound nozzle flow for two streams

[2]The authors are grateful to Dr. Yifang Gong from MIT Gas Turbine Lab for providing this physical interpretation.

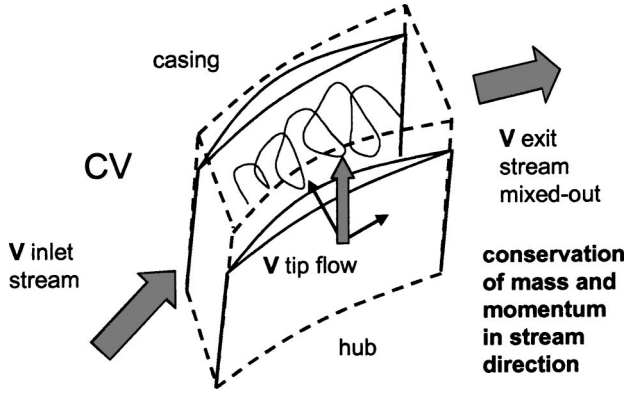

Fig. 18 Control volume mixing analysis for prediction of tip clearance loss

simple control volume mixing analysis is performed. The analysis uses Storer and Cumpsty's [7] idea, but all necessary input parameters are extracted from the computed solutions instead of being estimated with the assumptions in the original model. The inlet and exit area, density, and the inlet stream-wise velocity of the tip fluid and the main fluid are needed for the control volume calculation to obtain a mixed-out loss. The analysis uses conservation of mass and momentum in the stream-wise direction and assumes mixing at constant pressure. A schematic of the control volume is shown in Fig. 18.

The assumption of Storer and Cumpsty in their original model that the tip fluid stagnation pressure is equal to the stagnation pressure of the upstream main flow breaks down as soon as double-leakage occurs. Double-leakage changes significantly the tip clearance fluid stagnation pressure as shown in the previous figure (Fig. 16). This fact was previously reported by Khalsa [8]. Therefore, the original model cannot be applied to situations with double-leakage. It will underestimate the losses by up to 60% as shown in Table 3, which compares the loss generated in a steady environment to the one generated in an unsteady environment with wake interaction. Loss is estimated using the original model in the first row, the model using input parameters extracted from the solution in the second row, and the CFD results in the third row.

The foregoing results show that when Storer and Cumpsty's model is corrected for the stagnation pressure of the tip clearance flow it gives a reasonable estimate for the tip clearance loss for both steady and unsteady configurations. As soon as double-leakage occurs, the relative stagnation pressure of the tip clearance fluid for both steady and unsteady cases has to be adjusted accordingly. It will not be the same with the stagnation pressure of the main flow.

Wakes With Time-Periodic Variation in Strength. Up to now we have approximated the stator wakes as steady. In this section we examine the effect of stator wake unsteadiness. Specifically the response of rotor performance to upstream stator wakes with oscillating velocity defect is investigated. To amplify the unsteadiness of the tip vortex the tip clearance gap is increased

Table 3 Estimated loss using original storer's mixing model and modified storer's mixing model to compare against computed values

LOSS (TtΔS/0.5Utip^2)			
	No Wake	Strong Wake	Difference
Storer's Mixing Model	5.06 e-3	5.06 e-3	0%
Storer's Model (Corrected Pt Tip Fluid)	11.89 e-3	9.09 e-3	23.50%
CFD Calculation	12.06 e-3	7.87 e-3	34.70%

Downloaded 31 May 2010 to 171.66.16.27. Redistribution subject to ASME license or copyright; see http://www.asme.org/terms/Terms_Use.cfm

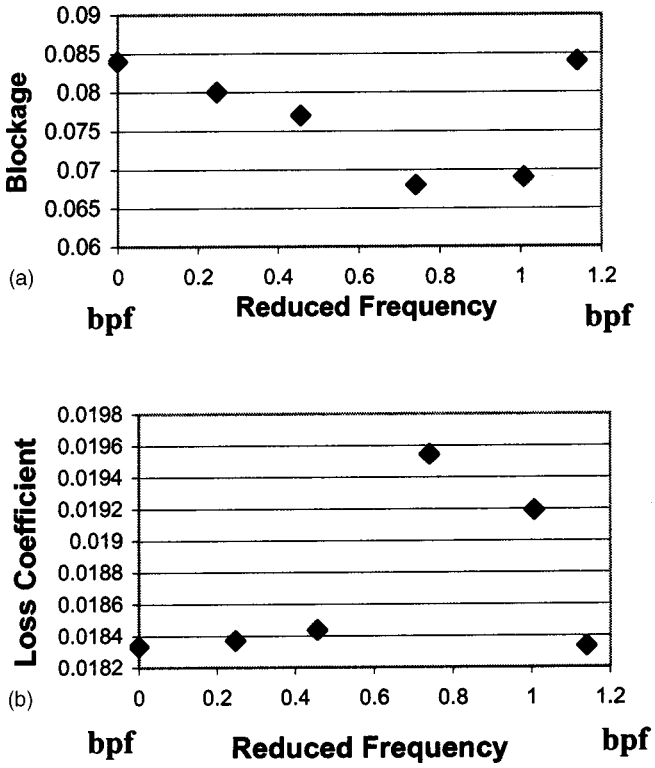

Fig. 19 Passage blockage and loss coefficient dependence on stator wake amplitude oscillation frequency (bpf denotes blade passing frequency)

to 3% of blade height. Calculations are performed at high loading condition. The response of the tip flow to different stator wake oscillation frequencies is shown in Figs. 19(*a*) and (*b*).

It can be inferred from the above figures that tip clearance flow is sensitive to forcing at reduced frequency (based on blade chord and passage flow-through time, as defined by Bae[3] [17]) of about 0.74. The effect on performance at this condition, based on the current numerical results, is a 19% reduction in blockage and 7% increase in passage loss compared to forcing at reduced frequencies away from 0.74. Bae observed similar trends in his experiments [17]. He hypothesized that the reason for the performance changes observed when forcing the tip clearance vortex at reduced frequency of 0.75 is enhanced mixing at resonance conditions in the tip region. The tip clearance fluid mixes earlier in the blade passage with the main flow thus alleviating the growth of a velocity defect region in an adverse pressure gradient. The blade passage loss increases because of the enhanced mixing. The experiments performed by Bae involved oscillating synthetic jets situated above the tip clearance vortex and directed normal to the flow. It is interesting to note that, even without external actuation, the inherent unsteadiness of the upstream wakes can bring about similar effects on performance through tip clearance vortex excitation. The reduced frequency at which this phenomenon occurs in the present study (0.74) is in accord with the one measured in Bae's experiments (0.75), although it does not constitute a back-to-back comparison. Therefore, the manipulation of the frequency contents in a compressor blade row environment may possibly lead to performance changes[4].

Summary and Conclusions

This study investigated the effect of interaction between upstream steady and oscillating defect wakes and rotor tip clearance flow in terms of time-average performance. Based on the present numerical studies it was found for the steady defect wakes case that strong interaction can decrease the tip region loss coefficient by up to 40% with respect to the steady case value (0.174 steady versus 0.103 time-average unsteady), decrease tip region blockage by up to 27% with respect to the steady case value (0.064 steady versus 0.047 time-average unsteady), and increase rotor passage static pressure rise coefficient by up to 5% with respect to the steady case value (0.52 steady versus 0.55 time-average unsteady). For the oscillating defect wakes case it was found that excitation of the tip clearance vortex at reduced frequency of 0.74 leads to a 19% decrease in blockage (from 0.084 to 0.068) and a 7% increase in passage loss (from 0.0183 to 0.0195). The following conclusions are inferred:

1. Interaction with steady upstream wakes has a beneficial effect on rotor tip flow behavior resulting in enhanced rotor performance. At high loading the effect becomes significant. Significant beneficial changes occur only when double-leakage of tip clearance fluid is present. The beneficial effect of steady upstream wake—tip flow interaction is of comparable importance to the net beneficial effect of isentropic wake recovery and non-transitional boundary layer response. The beneficial effect increases monotonically with loading and scales linearly with upstream wake amplitude measured in terms of velocity defect.
2. The cause for the observed performance changes is the ***wake induced pressure pulse—tip flow*** interaction. It decreases the amount of double-leakage on a time-average basis and thus, decreases the stream-wise velocity defect of the tip clearance fluid exiting the tip gap.
3. Double-leakage of tip clearance flow is an important phenomenon in compressors representative of modern design [27]. It typically occurs at high loading but can be present at design condition. Double-leakage is detrimental for performance (blockage and loss); however, the effect of interaction between upstream stator wakes and rotor tip flow is to decrease double-leakage and thus to improve performance.
4. The effect on loss can be reasonably estimated with Storer and Cumpsty's model if the correct tip clearance fluid relative stagnation pressure is used. The original model tends to underestimate loss by up to 60% of the calculated value, when tip clearance flow double-leakage is present.
5. A design with reduced spacing between the blade rows can benefit from the higher upstream unsteadiness. The beneficial response of the rotor tip leakage flow to steady upstream stator wakes implies that a more aggressive rotor blade design in terms of loading can be sought. The effect of unsteadiness from upstream wakes should be included in design and performance prediction tools.
6. Tip clearance vortex behavior can be sensitive to frequency content. At reduced frequency of 0.74, resonance conditions appear to be established and enhanced mixing in the tip region takes place as described by Bae. This leads to a 19% reduction in blade passage blockage and a 7% increase in blade passage loss compared to forcing at frequencies away from 0.74.

Acknowledgments

Support for this work was provided by Rolls Royce through the Sir Frank Whittle Fellowship, Mitsubishi Heavy Industries with Dr. Aoki, Dr. Yukata, and Dr. Tashiro as contract monitors, and Advanced Gas Turbine Systems Research with Dr. Fant and Dr. Wenglarz as contract monitors, contract # DE-FC21-92MC24061. We would also like to thank E. M. Greitzer, F. E. Marble, J. D. Denton, W. N. Dawes, D. H. Vo and Y. Gong for helpful comments and discussions. In particular we would like to acknowledge the continuous interest of Dr. Yifang Gong in this project and his valuable ideas. We would also like to thank Dr. Leroy Smith for the useful discussions and suggestions leading to improvements in the technical aspects of the manuscript. The constructive comments from the reviewers are also gratefully acknowledged.

[3]reduced_frequency=(frequency*blade chord)/(blade passage through-flow velocity)

[4]Bae reports measurements that imply **improved** performance.

Downloaded 31 May 2010 to 171.66.16.27. Redistribution subject to ASME license or copyright; see http://www.asme.org/terms/Terms_Use.cfm

Nomenclature

A_b = blocked area
A_{tot} = total area
A_v = peak velocity defects for wakes
B = blockage
bpf = blade passing frequency
C_p = static pressure rise coefficient
CV = control volume
e = energy
_e = referring to rotor trailing edge exit plane
_in = referring to rotor domain inlet plane
LE = blade leading edge
P_e = exit stalic pressure
PS = blade pressure surface
P_t = stagnation pressure
s = specific entropy
SS = blade suction surface
t = time
T = time period
TE = blade trailing edge
tip = rotor tip region
T_p = total pressure 99% defect thickness
T_t = total temperature
T_v = velocity 99% defect thickness
u = axial velocity
U_{tip} = rotor tip velocity
v = circumferential velocity
$V_{streamwise}$ = velocity in streamwise direction
w = radial velocity

References

[1] Wisler, D. C., 1985, ''Loss Reduction in Axial-Flow Compressors Through Low-Speed Model Testing,'' ASME J. Eng. Gas Turbines Power, **107**, pp. 354–363.
[2] Smith, L. H., Jr., 1958, ''The Effect of Tip Clearance on Peak Pressure Rise of Axial-Flow Fans and Compressors,'' ASME Symposium on Stall, pp. 149–152.
[3] Koch, C. C., and Smith, L. H., 1976, ''Loss Sources and Magnitudes in Axial-Flow Compressors,'' ASME J. Eng. Power, **98**, pp. 411–424 (July).
[4] Rains, D. A., 1954, ''Tip Clearance Flows in Axial Flow Compressors and Pumps,'' California Institute of Technology, Hydrodynamics and Mechanical Engineering Laboratories, Report No. 5.
[5] Hunter, I. H., and Cumpsty, N. A., 1982, ''Casing Wall Boundary-Layer Development Through an Isolated Compressor Rotor,'' ASME J. Turbomach., **104**, pp. 805–817.
[6] Chen, G. T., Greitzer, E. M., Tan, C. S., and Marble, F. E., ''Similarity Analysis of Compressor Tip Clearance Flow Structure,'' ASME Paper No. 90-GT-153.
[7] Storer, J. A., and Cumpsty, N. A., ''An Approximate Analysis and Prediction Method for Tip Clearance Loss in Axial Compressors,'' ASME Paper No. 93-GT-140.
[8] Khalid, S. A., Khalsa, A. S., Waitz, I. A., Tan, C. S., Greitzer, E. M., Cumpsty, N. A., Adamczyk, J. J., and Marble, F. E., 1999, ''Endwall Blockage in Axial Compressors,'' ASME J. Turbomach., **121**, July.
[9] Nikolaou, I. G., Giannakoglou K. C., and Papailiou K. D., ''Study of a Radial Tip Clearance Effects in a Low-Speed Axial Compressor Rotor,'' ASME Paper No. 96-GT-37.
[10] Khalsa, A. S., 1996, ''Endwall Blockage in Axial Compressors,'' Ph.D. thesis, MIT, June.
[11] Smith, L. H., Jr., 1970, ''Casing Boundary Layers in Multistage Axial Flow Compressors,'' *Flow Research on Blading*, L. S. Dzung, ed., Elsevier Publishing Company.
[12] Mikolajczack, A. A., 1977, ''The Practical Importance of Unsteady Flow,'' AGARD Conf. Proc., AGARD CP-144, North Atlantic Treaty Organization.
[13] Hetherington, R., and Morritz, R. R., 1977, ''The Influence of Unsteady Flow Phenomena on the Design and Operation of Aero Engines,'' AGARD Conf. Proc., AGARD CP-144, North Atlantic Treaty Organization.
[14] Valkov, T. V., and Tan, C. S., 1999, ''Effect of Upstream Rotor Vortical Disturbances on the Time-Averaged Performance of Axial Compressor Stators: Framework of Technical Approach and Wake-Stator Blade Interactions,'' ASME J. Turbomach., **121**, July.
[15] Graf, M. B., 1996, ''Effects of Stator Pressure Field on Upstream Rotor Performance,'' Ph.D. thesis, MIT, June.
[16] Tzeng, Y. S., 2000, ''The Effect of Rotor-Stator Interaction on Rotor Performance', GTL Report (unpublished), MIT Gas Turbine Laboratory, Dec.
[17] Bae, J., 2003, ''Active Control of Tip Clearance Flow in Axial Compressors,'' ASME Paper No. GT-2003-38661.
[18] Mailach, R., Sauer, H., and Vogeler, K., ''The Periodical Interaction of the Tip Clearance Flow in the Blade Rows of Axial Compressors,'' ASME Paper No. 2001-GT-299.
[19] Vo, H. D., 2001, ''Role of Tip Clearance Flow on Compressor Stability,'' Ph.D. thesis, MIT, Sept.
[20] Denton, J. D., PROGRAM UNSTREST, Version UNSTSS13, June 2000.
[21] Denton, J. D., 2000, personal communication.
[22] Denton, J. D., and Dawes, W. N., 1999, ''Computational Fluid Dynamics for Turbomachinery Design,'' IMechE Conf. Trans., **213**, Part C.
[23] Stauter, R. C., Dring, R. P., and Carta, F. O., 1991, ''Temporally and Spatially Resolved Flow in a Two-Stage Axial Flow Compressor,'' ASME J. Turbomach., **113**, Apr.
[24] Shapiro, A., 1953, *The Dynamics and Thermodynamics of Compressible Fluid Flow*. The Ronald Press Company, New York.
[25] Wisler, D. C., 1981, ''Core Compressor Exit Stage Study,'' Volume IV—Data and Performance Report for the Best Stage Configuration, NASA CR-165357, NASA LEWIS Research Center. NASA Tech. Memo.
[26] Deregel, P, and Tan, C. S., ''Impact of Rotor Wakes on Steady-State Axial Compressor Performance,'' ASME Paper No. 96-GT-253.
[27] Smith, L. H., Jr, 2002, personal communication.

Downloaded 31 May 2010 to 171.66.16.27. Redistribution subject to ASME license or copyright; see http://www.asme.org/terms/Terms_Use.cfm

An Improved Streamline Curvature Approach for Off-Design Analysis of Transonic Axial Compression Systems

Keith M. Boyer
Mem. ASME,
Assistant Professor,
Department of Aeronautics,
USAF Academy, CO 80840-6222
e-mail: keith.boyer@usafa.af.mil

Walter F. O'Brien
Fellow ASME,
J. Bernard Jones Professor and Head,
Mechanical Engineering Department,
Virginia Tech,
Blacksburg, VA 24061-0238
e-mail: walto@vt.edu

A streamline curvature throughflow numerical approach is assessed and modified to better approximate the flow fields of transonic axial compression systems. Improvements in total pressure loss modeling are implemented, central to which is a physics-based shock model, to ensure accurate and reliable off-design performance prediction. The new model accounts for shock geometry changes, with shock loss estimated as a function of inlet relative Mach number, blade section loading (flow turning), solidity, leading edge radius, and suction surface profile. Data from a single-stage, isolated rotor provide the basis for experimental comparisons. Improved performance prediction is shown. The importance of properly accounting for shock geometry and loss changes with operating conditions is demonstrated. [DOI: 10.1115/1.1565085]

Keywords: Transonic, Compressor, Streamline Curvature, Loss, Deviation

Introduction

Accurate and robust turbomachinery off-design performance prediction remains elusive. The numerical representation of transonic compression systems, most notably high-speed fans, is especially challenging. The difficulties are due in large part to highly three-dimensional blade design and the resulting flow field which includes complex shock structure and subsequent interactions (with blade boundary layers, endwalls, etc.).

Engine-inlet integration issues contribute to the difficulties associated with fan off-design analysis. The use of serpentine inlet ducts and fighter supermaneuvers further complicate the issue. Advanced military systems have experienced distortion levels—intensity and dynamics—exceeding the current operational experience. Consequences from these unprecedented levels are evidenced into the second stage of modern military fans. Current ground test methods do not adequately simulate these complex flow patterns. One of the key issues being addressed by the fighter engine high-cycle fatigue (HCF) initiative established in December 1994 is how to characterize and simulate these complex flow fields [1].

It is clear that analytical methods are essential for understanding high-speed fan issues. While fully, 3-D, unsteady Reynolds-averaged Navier-Stokes (RANS) approximations offer the greatest potential for faithfully representing flow details at the smallest length scales, physics-based improvements to ''simpler'' methods are needed. The mesh sizes required to resolve flow details (resulting in large computational requirements), and modeling issues associated with turbulence and transition continue to present significant challenges to RANS approaches. Regarding the calculation of 3-D, unsteady, full annulus flow through multiple blade rows, Denton and Dawes [2] noted recently that the accuracy would '' . . . be limited by the limitations of turbulence and transition modeling for many years to come, if not for ever.''

The goal of the current work is the development of an improved streamline curvature (SLC) method for approximating important flow phenomena in modern compression systems subjected to *off-design operating conditions*. Solutions were sought that retain essential global features of the flow. These solutions could provide accurate boundary conditions for higher-order models (i.e., at the inlet and exit of a blade row being represented by an unsteady RANS approximation). Further, the particular SLC approach chosen here is the same as that used in the Turbine Engine Analysis Compressor Code-TEACC by Hale et al. [3]. The TEACC was developed specifically as an efficient alternative to 3-D, fully viscous, turbomachinery CFD approaches to investigate complex engine-inlet integration issues [3–5].

The present paper highlights some of the improvements in loss modeling made to an existing SLC code, and demonstrates the importance of an accurate shock loss model. The use of the improved code for analyzing the off-design performance of a modern fan, multistage design is presented by Boyer and O'Brien [6].

Streamline Curvature Assessment

Throughflow methods, of which streamline curvature is the dominant numerical approach, still remain an important tool for turbomachinery design. Recently, Denton and Dawes [2] reviewed the SLC approach, suggesting that ''little has changed'' since the review of Hirsch and Denton in 1981. This is likely due to the focus on (and success of) full CFD methods. The development, improvement, and application of RANS approaches dominate the literature.

It is generally accepted that any streamline curvature solution technique will yield satisfactory flow solutions as long as the deviation, losses, and blockages are accurately predicted. The majority of recent improvements in SLC methods seem to have occurred in the representation of endwall boundary layer and secondary loss and spanwise loss mixing procedures; see for example, Dunham [7] and Gallimore [8]. The current SLC approach was assessed relative to these improvements and key transonic flow field phenomena.

A significant consideration in the design of transonic fan blades is the control of shock location and strength to minimize aerodynamic losses without limiting flow. Recent works by König et al. [9] and Bloch et al. [10–12] have demonstrated that the efficiency characteristic of transonic machines is largely determined by the shock loss (i.e., the profile loss is relatively independent of Mach number). Additionally, Bloch's investigation [11] showed that much of the increase in loss with increasing flow angle was due to

Contributed by the International Gas Turbine Institute and presented at the International Gas Turbine and Aeroengine Congress and Exhibition, Amsterdam, The Netherlands, June 3–6, 2002. Manuscript received by the IGTI October 22, 2001. Paper No. 2002-GT-30444. Review Chair: E. Benvenuti.

Downloaded 31 May 2010 to 171.66.16.27. Redistribution subject to ASME license or copyright; see http://www.asme.org/terms/Terms_Use.cfm

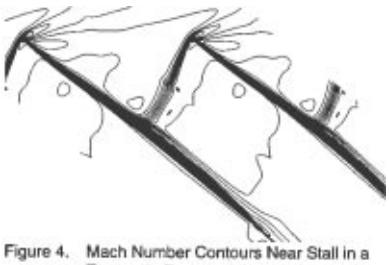

Figure 4. Mach Number Contours Near Stall in a Transonic Fan.

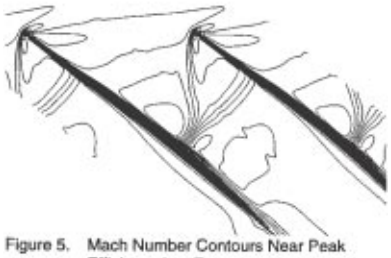

Figure 5. Mach Number Contours Near Peak Efficiency in a Transonic Fan.

Figure 6. Mach Number Contours for Back Pressure Slightly Below the Maximum Choked Value.

Figure 7. Mach Number Contours for Lowest Back Pressure Operating Point.

Fig. 1 Shock structure of high tip-speed fans $-M_{1rel}>1.4$ (from [11])

a detached bow shock. Indeed, as illustrated in Fig. 1, the trend for highly transonic fans ($M_{1rel}>1.4$) seems to be to design for an oblique leading edge shock through high loading conditions (flow turning) up through peak efficiency. Any numerical approximation attempting to faithfully predict off-design performance must take into account the changes in shock geometry with aerodynamic loading exemplified in Fig. 1.

The streamline curvature code (SLCC) used in the present work was developed by Hearsey [13]. Hearsey's approach uses the well-known SP-36 correlations in NASA SP-36 [14], to determine low-speed ''reference'' deviation and loss, then ''corrects'' these values for various real-flow effects, including those from annulus wall boundary layer, spanwise mixing, and secondary flows. Because the current application was outside the database used to develop some of the empirical/semi-empirical models, a detailed assessment of the loss and deviation correlations was performed. Results from the assessment provided the basis for improvements to selected models/correlations, central to which was a physics-based shock loss model presented in the next section.

Determination of Deviation Angle. Blade section exit *deviation* angle was determined using Eq. (1)

$$\delta = \delta_{\text{ref}} + \delta_{3D} + \delta_M + \delta_{va} + \delta_i \tag{1}$$

The low-speed, minimum loss deviation angle, δ_{ref}, is determined using the Lieblein correlation (Cumpsty [15]), a modification to the widely used Carter's rule relating deviation to blade section camber and solidity. The remainder of the terms attempt to account for the effects of various real-flow phenomena previously mentioned. The δ_i, deviation due to actual incidence angle, is most suspect as it is determined from a four-piece curve using NACA-65 series cascade data as its basis.

The method for determining exit flow deviation angle, Eq. (1), was assessed relative to that recommended by Çetin et al. [16]. For the following reasons, it was decided to remain with the current approach:

- Çetin et al. recommended a modification to Carter's rule to account for transonic and 3-D effects. The current method is exactly that.
- The off-design correlation they recommended (Creveling and Carmody [17]) contained minimal data at high Mach numbers.

A detailed assessment of off-design deviation estimation for highly transonic bladings is needed, beyond the scope of this work.

Determination of Losses. Equation (2) identifies the components used in determining the relative total pressure *loss* coefficient

$$\varpi = (\varpi_{\text{min}} + \varpi_{\text{M}} + \varpi_{\text{tip}} + \varpi_{\text{hub}})\left[1 + \left(\frac{i - i_{\text{min}}}{W}\right)^2\right] \tag{2}$$

Profile loss (blade section boundary layer and wake) is contained in the ϖ_{min} term, determined using the method of Koch and Smith [18]. Their approach is still regarded as one of the most complete, as it accounts for actual momentum thickness and shape factor assuming a fully turbulent boundary layer. The ϖ_{M} term contains an estimate of the shock loss, while the last two terms (in parentheses) account for the effects of secondary loss. All of these (with the exception of ϖ_{min}) are discussed in the next section.

The increment in loss at off-design is accounted for through the parabolic term in brackets in Eq. (2). This is a common approach taken in streamline curvature methods to achieve a more realistic loss ''bucket'' shape. The W is a ''width'' which effectively specifies the working range of the section (as a function of inlet metal angle, camber, maximum t/c, $M_{1\text{rel}}$, and incidence). As discussed in the next section, this off-design ''correction'' was not used for supersonic blade sections as a result of the improved shock loss model.

Finally, aerodynamic *blockage* estimates were used to account for the effects of both annulus wall boundary layer (AWBL) and tip leakage flow. An estimate for displacement thickness was used to adjust the actual casing to account for the mass flow deficit due to endwall boundary layer (Boyer [19]). Additional area reduction in the outermost streamtube at rotor exit was used to account for tip leakage effects. The total blockage due to tip endwall boundary layer losses was kept at approximately 10%, quite reasonable as discussed by Rabe [20].

Summary of Loss Model Improvements

The relative magnitudes of loss components in highly transonic fans, broken down into three broad categories—profile, shock, and secondary—are shown schematically in Fig. 2. Consistent with the earlier discussion, shock loss dominates and can be an order of magnitude greater than the profile loss. This is substantiated by Denton [21], as well as recent experience by the authors. The secondary loss includes endwall interactions between annulus boundary layers and blade rows, most notably tip gap flows. The

Downloaded 31 May 2010 to 171.66.16.27. Redistribution subject to ASME license or copyright; see http://www.asme.org/terms/Terms_Use.cfm

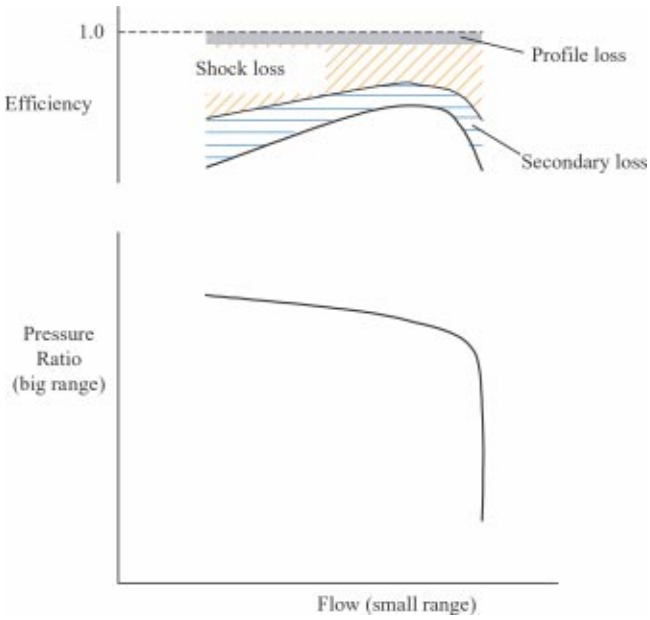

Fig. 2 Approximate loss source distribution in highly transonic fan blade section ($M_{1rel}>1.4$)

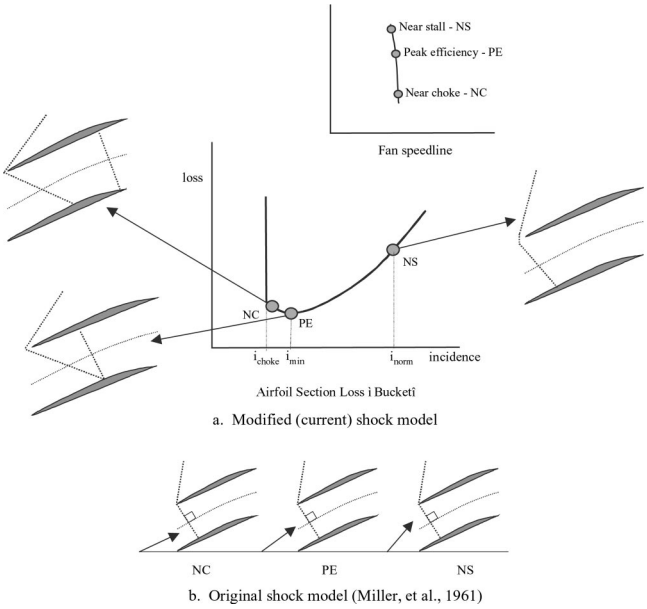

Fig. 3 Assumed shock structure at different operating conditions—(*a*) modified (current) shock model (*b*) original shock model [22]

three loss categories depicted in Fig. 2 offer an alternative representation of loss mechanisms in highly transonic designs to the traditional breakdown of loss into ''profile,'' ''endwall,'' and ''tip leakage'' [21].

Shock Loss. Improving the shock system representation and subsequent loss estimation was central to the current work. Hearsey [13] used the method of Miller et al. [22] to approximate the shock loss as that resulting from a single, attached shock normal to the blade passage mean camber line. For application to modern, transonic fan designs employing precompression airfoils, this simple approximation is inadequate. An improved, physics-based model, based on the method of Bloch et al. [12], was implemented.

Figure 3 shows the assumed shock structure, consistent with recent observations already discussed. For reference, the original shock model is also included. The method of Moeckel [23] is used to determine the shape of the *detached* leading edge shock and detachment distance. The method requires specification of M_{1rel} and blade leading edge radius, and application of continuity between the shock vertex and sonic point.

As suggested in Fig. 3, shock structure is assumed known at the three blade section operating conditions indicated. A dual-shock structure was assumed at the peak efficiency (i_{min}) operating point. At this condition, the leading edge detached shock is at its maximum obliqueness, followed immediately by a normal passage shock (if so dictated by the downstream M).

At near-choke (i_{choke}), the method of König et al. [9] is used to estimate the Mach number directly upstream of the second shock (assumed to be at the trailing edge of the passage). Substitute contours replace the actual flow path in the blade passage and the following exit-to-entrance area ratio equation is used:

$$\frac{A_{exit}}{A_{inlet}} = 0.499M_{2s} + 0.501 + C_{ar} \tag{3}$$

König et al. established the constants in Eq. (3) by comparing computed and measured data obtained on eight cascades with MCA, wedge, and precompression airfoils. The value for C_{ar} was determined by them to be 0.0774 for MCA or wedge sections, and 0.0351 for precompression sections.

A single, detached normal shock is assumed at the near-stall condition (i_{norm}). While the mechanism for changing from a dual-shock to single shock is understood—second shock moves upstream due to increasing backpressure, eventually coalescing with the first—the incidence angle at which this transition takes place, i_{norm}, is not known. Note that the current SLC method supplies estimates for i_{choke}, i_{stall}, and i_{min}. The following simple representation for i_{norm} is used:

$$i_{norm} = i_{stall} - 1.0 \quad (\text{deg}) \tag{4}$$

Equation (4) merely provides a convenient and consistent way to locate i_{norm}. The ''correct'' value would be a complex function of section geometry, operating conditions, and secondary flow interactions.

Precise shock loss estimation requires integration of the loss along the shock to account for Mach number and flow angle variations. To be consistent with the general SLC approach, shock loss was estimated from single-point calculations (with the exception of the bow shock portion). The choice of suitable ''averages'' was made by considering the flow physics.

The angle at the shock sonic point is taken as the ''average'' shock angle (Fig. 4). The location of the sonic point is known through application of the Moeckel method for approximating the shock hyperbola. As Fig. 4 demonstrates, this simple approximation captures the physical trends and appears quite suitable. At elevated Mach number (Fig. 4(*b*)), the shock is more swept back

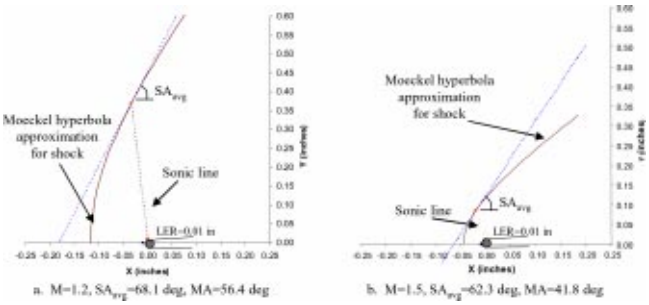

Fig. 4 Use of shock angle at sonic point for loss estimation—(*a*) M=1.2, SA_{avg}=68.1 deg, MA=56.4 deg, (*b*) M=1.5, SA_{avg}=62.3 deg, MA=41.8 deg

Downloaded 31 May 2010 to 171.66.16.27. Redistribution subject to ASME license or copyright; see http://www.asme.org/terms/Terms_Use.cfm

relative to the upstream flow—the average shock angle decreases. Note also the decreased detachment distance at increased M. Finally, Fig. 4 provides the isentropic Mach angle (MA), further verifying the choice for SA_{avg}. The angle must be between the Mach angle and 90 deg.

Approximation of the elevated Mach number at the shock entrance was obtained using the existing approach of Miller et al. [22]—the average of M_{1rel} and the peak suction surface Mach number obtained from Prandtl-Meyer analysis. A DCA profile and leading edge thickness of 5% of $(t/c)_{max}$ was used to estimate the suction surface turning. For precompression sections, M_{1rel} is used at the outermost tip section, and the Mach number is smoothly increased (linearly) to an elevated M determined as described above where the precompression geometry ends.

At i_{min}, the leading edge shock is at its maximum obliqueness. The average total pressure loss across the first shock is computed from oblique shock theory. If the M computed behind the first shock is greater than 1.0, then a second normal shock is assumed.

As the blade section loading increases ($i > i_{min}$), the passage shock moves upstream subjecting the incoming flow to a stronger shock system, increasing the loss. This effect is modeled through a smooth increase in shock angle given by Eq. (5)

$$SA = SA_{sonic} + \frac{(90 - i_{min})}{(i_{norm} - i_{min})^4}(i - i_{min})^4 \tag{5}$$

Further, for operation at incidence angles greater than i_{min}, *detached* bow shock loss is estimated using the method described by Bloch et al. [12] applied to the Moeckel hyperbola

$$\frac{P_{0bow}}{P_{01}} = 1 - \frac{\int_0^\infty (1 - P_{02rel}/P_{01rel})dy}{\int_0^s dy} \tag{6}$$

where P_{02rel}/P_{01rel} is obtained from oblique shock theory applied locally as the integration proceeds. The increment and upper bound of the numerical integration were selected to ensure that they did not bias the loss estimation accuracy [19].

Because more flow passes through the strong portion of the shock as it moves upstream, an increment of bow shock loss "due to increased incidence" is approximated as

$$\varpi_{bow} = \varpi_{bow} + \frac{0.015}{(i_{norm} - i_{min})^3}(i - i_{min})^3 \tag{7}$$

The constant and exponent in Eq. (7) were estimated from the results of Bloch [10] and are not meant to be universal. With this representation, the impact on adiabatic efficiency when operating at near-stall versus peak efficiency is about 3%. It should be noted that the *overall bow shock loss* contributed 10–30% of the total loss at near-stall, dependent on section geometry and loading.

Finally, with conditions represented by $i < i_{min}$, the effect of the increased strength of the second shock as it moves downstream is approximated by

$$\varpi_M = \varpi_{M,min} + \frac{\varpi_{M,choke} - \varpi_{M,min}}{(i_{choke} - i_{min})^4}(i - i_{min})^4 \tag{8}$$

The choice of "4" for the exponent in Eqs. (5) and (8) was based on the shape of the loss characteristic curves from the data on nine transonic designs (Çetin et al. [16]; Law and Puterbaugh [24]). Further, for Eq. (8), the choice produced the desired rapid rise in loss with incidence angles less than i_{choke} (see Fig. 3). By definition, the incidence cannot be less than the choking incidence. The SLC method does not represent the physical mechanism for leading edge choke determined by the first captured Mach wave set by flow conditions and flow induction surface. An approximation was required.

Secondary Loss and Other Modifications. Hearsey [13] used a relatively simple correlation to estimate losses arising from secondary flows. His representation included effects of spanwise mixing. In the current work, a method was implemented to include the well known effects of increased tip losses with loading (i.e., see Lakshminarayana et al. [25]). As indicated by Eq. (9), a parabolic increase with incidence angle was used as a modifier (in brackets) to the original tip loss model

$$\varpi_{tip} = \varpi_{min} TLOSS\left(2\frac{r - r_{hub}}{r_{tip} - r_{hub}} - 1\right)^3 \left[1 + \frac{(i - i_{min})^2}{(i_{stall} - i_{min})^2}\right] \tag{9}$$

Using the modified form above, tip section loss coefficients approximately doubled (over those predicted by the original representation) when operating at near-stall versus peak efficiency. While admittedly oversimplified, Eq. (9) does appear to offer a reasonable accounting for the physical phenomena.

Finally, two changes were made in regard to off-design loss estimation that help make the correlations more generally applicable to modern, transonic designs. First, the well-known decrease in blade section working range with Mach number was incorporated in the new shock model just described. Thus, for any section with $M_{1rel} > M_{crit}$, the parabolic term of Eq. (2) was not used.

Second, as observed by the current authors and others [7], the NASA SP-36 prediction of minimum-loss incidence is poor. The increase in i_{min} with increasing Mach number was too large (minimum incidences as high as 15 deg in hub sections). Consequently, the i_{min} correlation was modified to include a factor, *imnfac*, as follows:

$$i_{min} = i_{ref} + \theta f(M_{1rel}) imnfac \tag{10}$$

The $f(M_{1rel})$ is a three-part curve obtained from NACA 65-series and DCA blade section data [13].

A value of 0.5 for imnfac results in more realistic estimates for the minimum-loss incidence angle (imnfac = 1.0 is the original correlation). Note that the modification has a greater impact on the hub section prediction (due to higher camber, θ) than the tip.

Verification of Improvements—Application to an Isolated Rotor

The focus here is verification of the improved *shock loss model*. Answers to the questions below were sought:

- Do results make sense relative to the original shock model [22]?
- Do results represent flow physics? Is the model an improvement?

Additional verification of all the improvements is provided by Boyer and O'Brien [6]. The application described in that work is representative of the designs for which the present work is intended.

For two reasons, NASA Rotor 1B (R1B) was the primary vehicle used to verify the SLC improvements: 1) experimental data were readily available, and 2) the unmodified SLC approach used here had been previously applied to this design by Hale [3]. Table 1 summarizes key geometric and design point parameters for this single transonic blade row (Seyler and Gestolow [26]).

Rig test data at 100% *Nc* provided the basis for comparison. An increment to the predicted deviation was required to match the measured rotor mass-averaged total temperature ratio at each of seven operating conditions. The same additional deviation was applied to each of eleven streamlines specified in the simulation. This procedure provided a common basis for loss prediction comparisons between the two shock models. Both overall and radial performance comparisons are made at operating conditions ranging from choke to stall.

Figure 5 shows the overall performance comparison at 100% *Nc*. Following the procedure just outlined, the three temperature characteristics overlap. Improvements from the modifications are

Downloaded 31 May 2010 to 171.66.16.27. Redistribution subject to ASME license or copyright; see http://www.asme.org/terms/Terms_Use.cfm

Table 1 NASA Rotor 1B design parameters

Number blades	44
Blade section profile	DCA—bottom 60% MCA—top 40%
Inlet hub-to-tip ratio	0.5
Diameter	92.71 cm (36.5 in)
Tip solidity	1.3
Tip speed	426.7 m/s (1400 ft/s) (M_{1rel} approx. 1.4)
Design corrected mass flow rate	97.75 kg/s (215.5 lbm/s)
Design pressure ratio	1.6
Design efficiency	0.858

demonstrated, most notably in the efficiency characteristic. Also shown are the additional deviation curves required to match overall TR at each operating condition.

Figure 6 compares original and modified predicted shock loss at two different blade tip sections over the range of overall operating conditions indicated in Fig. 5. The difference is significant, but not surprising, given the simplified original approach. Note the opposite trends predicted by the two methods as the blade sections approach stall. The decreasing trend that is predicted by the original model is not physical, but expected. As the blade ''loads up'' (increased incidence), the inlet relative Mach number decreases slightly, as indicated in Fig. 6. With an attached, normal shock assumption, the entropy creation would decrease roughly as the cube of (M^2-1) [21], consistent with the trend evidenced by the

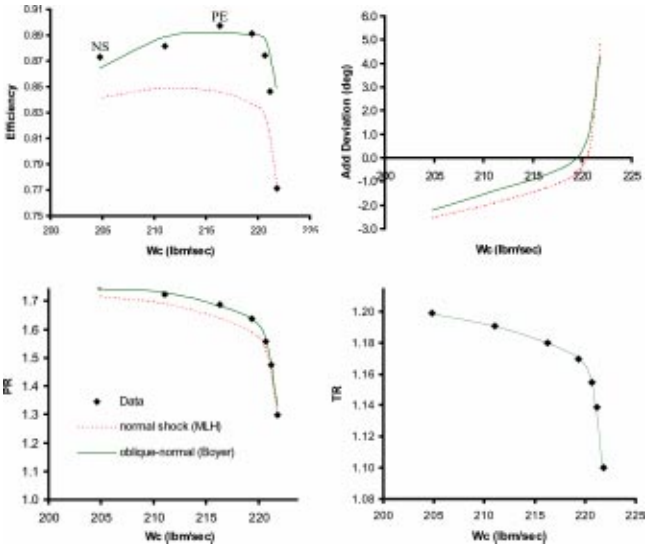

Fig. 5 R1B overall performance comparison at 100% Nc

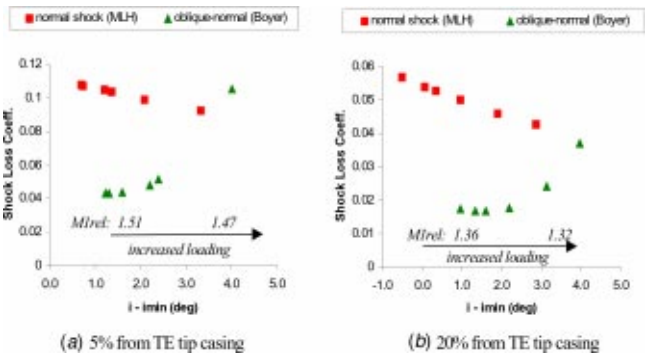

Fig. 6 Blade section shock loss comparison at different loadings—(*a*) 5% from TE tip casing, (*b*) 20% from TE tip casing

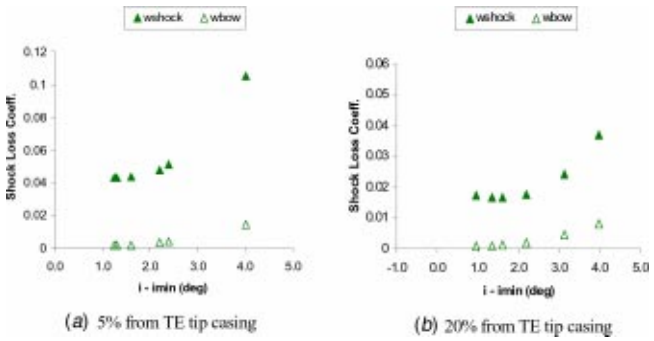

Fig. 7 Prediction of loss attributed to detached bow shock—(*a*) 5% from TE tip casing, (*b*) 20% from TE tip casing

original model. With the new model, the shock is at some oblique angle to the flow at low loading conditions, and becomes more normal and further detached as stall is approached, more than offsetting the effect of slightly decreased Mach number. The correct trend is predicted by the new model, which indeed displays the well-known ''bucket'' shape. Note further that at high incidence angles (i.e., near stall), the new model predicts higher loss than the original-this due to the inclusion of bow shock loss.

An evaluation of the detached bow shock portion of the loss characteristic is provided in Fig. 7 (same two blade sections as Fig. 6). The solid triangles represent the shock loss; the open symbols, the bow shock portion of that loss. In Fig. 7(*a*), the bow shock accounts for approximately 13% of the shock loss as the section approaches stall, while further down the span from the tip (Fig. 7(*b*)), it is responsible for over 20%. Admittedly, the bow shock model is crude and requires additional validation, especially the representation of increased bow shock loss with incidence angle, Eq. (7); however, the predicted trend is quite reasonable.

Figure 8 shows the radial distribution of total loss coefficient (profile, shock, and secondary) at the peak efficiency and near-stall operating conditions. Predictions from both the original and modified codes are provided along with those determined from the R1B data. Improved prediction from the modified method is evidenced in the spanwise comparisons shown in Fig. 8, most notably in the outer span blade region affected by the improved shock model.

It should be noted that R1B had a part-span shroud located at a radius of 37.3 cm (14.7 in), the effects of which are evidenced in the test data of Fig. 8. No attempt was made to account for the influence of the shroud in the current effort which could explain the overprediction of loss in the near-hub region. Inclusion of the

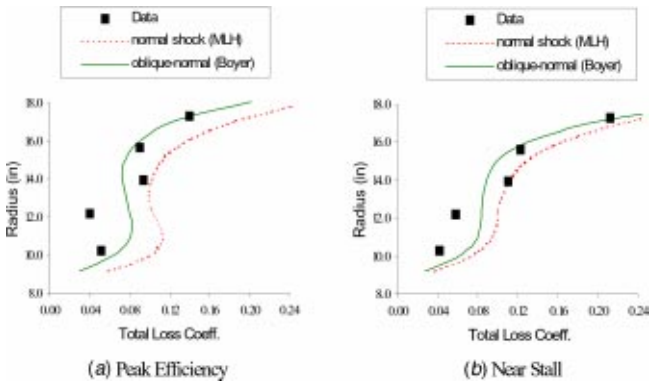

Fig. 8 Rotor 1B radial loss prediction

Downloaded 31 May 2010 to 171.66.16.27. Redistribution subject to ASME license or copyright; see http://www.asme.org/terms/Terms_Use.cfm

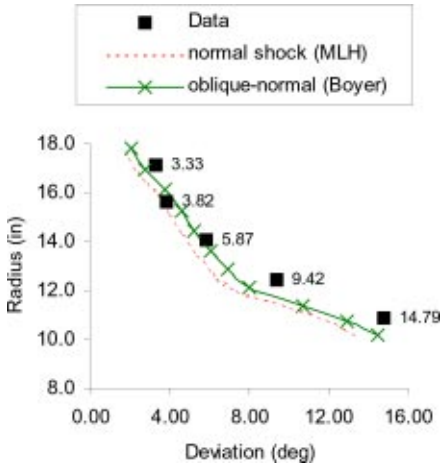

Fig. 9 R1B radial deviation at peak efficiency

shroud effects, either though additional loss or radial blockage, would alter the meridional velocity estimation and hence, the important incidence angle prediction.

Discussion

While the single application just presented does not completely verify the adequacy of the modifications, results do provide evidence of an improved representation. Overall and radial performance predictions compare favorably with those determined from the R1B experiments. The predicted performance appears to be right for the right reasons—more of the flow physics is captured. The multistage application presented by Boyer and O'Brien [6] lends additional credence to these observations.

The questions posed at the start of the previous section can be answered. The modified shock loss model offers an improved representation of the flow physics. An attached, single, normal shock model, commonly assumed in streamline curvature methods, is inadequate for capturing the correct trends. Attempts to compensate for these inadequacies often involve use of an off-design loss "correction" (parabolic term of Eq. 2), also common with SLC approaches. The problems associated with such methods are the issues that arise when an application is outside the database used to develop the corrections. A fine example is evident in the current work, discussed below.

The need to adjust the predicted deviation to match the overall total temperature (see Fig. 5) is a direct result of the present application being outside the correlation database. While any adjustment is undesirable, the approach used here represents a significant reduction from previous model "calibrations." Previous applications of the original SLC code required specification of radial distributions of deviation, loss, and blockage as functions of speed and mass flow rate to achieve similar results [4,5]. Note that the deviation curves shown in Fig. 5 represent *additional* deviation included in the estimate at each of eleven blade sections (i.e., a δ_{add} included in Eq. 1). For example, Fig. 9 shows *total* deviation at various radial locations ($\times$'s indicate streamline locations at the rotor exit) for the peak efficiency operating point. The SLC estimates include -0.70 deg additional deviation at each of the 11 streamline locations for this condition.

Finally, while a fair amount of latitude is involved in the modeling choices here, it is emphasized that the improved shock loss model is based upon sound physical principles. The basic assumptions contained in the method [23] are: 1) hyperbolic shock shape which asymptotically approaches the freestream Mach lines, and 2) a straight sonic line between the shock and sonic body point. The sonic point on the shock is determined via application of the continuity equation between the shock vertex and sonic point. With the assumptions, shock location becomes a single-valued function of upstream Mach number, with shock shape uniquely determined from blade LER and Mach number. While the choices of exponent 4 over 2 or 3 in Eqs. (5) and (8), or the selection of i_{norm} based on Eq. (4) are arguable, the basis of the improved model is physically grounded.

Conclusions

The modifications to an existing streamline curvature throughflow solver have resulted in an improved approximation for representing compression system flow fields. Most notably, incorporation of an improved shock model has produced a unique throughflow analysis tool in its thorough, physics-based treatment of shock losses. Basic principles are used to predict the detached, hyperbolic shock shape dictated by Mach number and blade section leading edge radius. The new model accounts for shock geometry changes with blade section operating condition (and hence, associated total pressure loss changes), making it most suitable for off-design performance prediction of modern fan designs (with $M_{1\text{rel}}$ in excess of 1.6).

It appears that the new model offers potential for more accurate off-design analysis of transonic designs. Further, incorporation of the model into novel approaches using streamline curvature methods (like the TEACC mentioned in the Introduction) could result in a significantly improved tool for analyzing complex engine-inlet integration issues. Additional verification through application to highly transonic, multistage fans and comparison with results from experimental data and/or CFD solvers is needed. One such application is presented in [6].

Acknowledgments

The authors wish to acknowledge the United States Air Force, Virginia Tech, and General Electric Aircraft Engines (GEAE) for permission to publish this work. Special thanks to the Arnold Engineering Development Center at Arnold AFB, TN for allowing us access to the streamline curvature source code. Finally, much thanks to Peter King, Wing Ng, Milt Davis, Alan Hale, and Doug Rabe—members of the Ph.D. committee who reviewed this work.

Nomenclature

A = area (blade section passage)
DCA = double circular arc
i = incidence angle (deg)
LER = leading edge radius
M = Mach no.
MA = Mach angle (deg)
MCA = multiple circular arc
MLH = Miller, Lewis, Hartmann
NC = near choke
Nc = rotor corrected speed
NS = near stall
PE = peak efficiency
PR = total pressure ratio
r = radius (from machine centerline)
R1B = Rotor 1B (NASA)
SA = shock angle (deg)
SLC = streamline curvature
t/c = blade section thickness-to-chord ratio
TE = trailing edge
TLOSS = tip loss factor-Eq. (9)
TR = total temperature ratio
W = width of loss "bucket"-Eq. (2)
Wc = corrected mass flow rate
δ = exit flow deviation angle (deg)
θ = blade section camber angle (deg)
ϖ or w = relative total pressure loss coefficient $\varpi = (P_{02,\text{deal}} - P_{02})_{\text{rel}} / P_{01,\text{rel}} - P_1$

Downloaded 31 May 2010 to 171.66.16.27. Redistribution subject to ASME license or copyright; see http://www.asme.org/terms/Terms_Use.cfm

Subscripts

1 = upstream (of blade row or shock)
2 = downstream (of blade row or shock)
add = additional
avg = average
crit = critical
i = incidence
M = Mach no.
max = maximum
min = minimum
norm = normal
ref = reference (low speed)
rel = relative
s = shock
va = axial velocity ratio

References

[1] AFRL-PR-WP-TM-1998-2148, 1999, *High Cycle Fatigue (HCF) Science and Technology Program 1998 Annual Report*, prepared by Universal Technology Corporation, Dayton, OH, Jan.

[2] Denton, J. D., and Dawes, W. N., 1999, ''Computational fluid dynamics for turbomachinery design,'' Proc., Institution of Mechanical Engineers, J. Mechanical Eng. Sci., Part C, **213**(C2).

[3] Hale, A. A., Davis, M. W., Jr., and Kneile, K. R., 1994, ''Turbine Engine Analysis Compressor Code: TEACC—Part I: Technical Approach and Steady Results,'' AIAA-94-0148, 32nd Aerospace Sciences Meeting, Reno, NV, Jan.

[4] Hale, A., and O'Brien, W., 1998, ''A Three-Dimensional Turbine Engine Analysis Compressor Code (TEACC) for Steady-State Inlet Distortion,'' ASME J. Turbomach., **120**, July, pp. 422–430.

[5] Hale, A., Chalk, J., Klepper, J., and Kneile, K., 1999, ''Turbine Engine Analysis Compressor Code: TEACC—Part II: Multi-Stage Compressors and Inlet Distortion,'' AIAA-99-3214, 17th AIAA Applied Aerodynamics Conference, Norfolk, VA, June 28–July 1.

[6] Boyer, K. M., and O'Brien, W. F., 2002, ''Application of an Improved Streamline Curvature Approach to a Modern, Two-Stage Transonic Fan: Comparison with Data and CFD,'' ASME Paper GT-2002-30383, June.

[7] Dunham, J., 1996, ''Compressor Off-Design Performance Prediction Using an Endwall Model,'' ASME Paper No. 96-GT-62, presented at the International Gas Turbine and Aeroengine Congress & Exhibition, Birmingham, UK, June 10–13.

[8] Gallimore, S. J., 1997, ''Viscous Throughflow Modeling of Axial Compressor Bladerows using a Tangential Blade Force Hypothesis,'' ASME Paper No. 97-GT-415, presented at the International Gas Turbine and Aeroengine Congress & Exhibition, Orlando, FL, June 2–5.

[9] König, W. M., Hennecke, D. K., and Fottner, L., 1996, ''Improved Blade Profile Loss and Deviation Angel Models for Advanced Transonic Compressor Bladings: Part II—A Model for Supersonic Flow,'' ASME J. Turbomach., **117**, Jan., pp. 81–87.

[10] Bloch, G. S., ''Flow Losses in Supersonic Compressor Cascades,'' Ph.D. dissertation, Mechanical Engineering Dept., Virginia Polytechnic Institute and State University, Blacksburg, VA, July 1996.

[11] Bloch, G. S., Copenhaver, W. W., and O'Brien, W. F., 1996, ''Development of an Off-Design Loss Model for Transonic Compressor Design,'' AGARD Conf. Proc., Jan., pp. 16-1–16-14.

[12] Bloch, G. S., Copenhaver, W. W., and O'Brien, W. F., 1999, ''A Shock Loss Model for Supersonic Compressor Cascades,'' ASME J. Turbomach., **121**, Jan., pp. 28–35.

[13] Hearsey, R. M., ''Program HT0300 NASA 1994 Version,'' Doc. No. D6-81569TN, Volumes 1 and 2, The Boeing Company, 1994.

[14] NASA SP-36, 1965, *Aerodynamic Design of Axial-Flow Compressors*, eds., I. A. Johnsen and R. O. Bullock.

[15] Cumpsty, N. F., *Compressor Aerodynamics*, Department of Engineering, University of Cambridge, Longman Scientific & Technical, Longman Group UK, Limited Essex CM20 2JE, England, co-published in the United States with John Wiley & Sons, Inc., New York, NY, 1989.

[16] Çetin, M., Üçer, A. Ş., Hirsch, CH., and Serovy, G. K., 1987, ''*Application of Modified Loss and Deviation Correlations to Transonic Axial Compressors*,'' AGARD Conf. Proc. .

[17] Creveling, H. F. and Carmody, ''Axial-Flow Compressor Computer Program for Calculating Off-Design Performance,'' NASA-CR-72472, 1968.

[18] Koch, C. C., and Smith, Jr., L. H., 1976, ''Loss Sources and Magnitudes in Axial-Flow Compressors,'' ASME J. Eng. Power, July, pp. 411–424.

[19] Boyer, K. M., ''An Improved Streamline Curvature Approach for Off-Design Analysis of Transonic Compression Systems,'' Ph.D. dissertation, Mechanical Engineering Dept., Virginia Polytechnic Institute and State University, Blacksburg, VA, April 2001.

[20] Rabe, D. C., ''Shock Wave End Wall Boundary Layer Interaction in a Transonic Compressor Rotor,'' Ph.D. dissertation, Mechanical Engineering Dept., Virginia Polytechnic Institute and State University, Blacksburg, VA, May 1987.

[21] Denton, J. D., 1993, ''Loss Mechanisms in Turbomachines,'' ASME J. Turbomach., **115**, Oct., pp. 621–656.

[22] Miller, G. R., Lewis, Jr., G. W., and Hartmann, M. J., 1961, ''Shock Losses in Transonic Compressor Blade Rows,'' ASME J. Eng. Power, July, pp. 235–242

[23] Moeckel, W. E., 1949, ''Approximate Method for Predicting Form and Location of Detached Shock Waves Ahead of Plane or Axially Symmetric Bodies,'' NACA TN 1921.

[24] Law, C. H., and Puterbaugh, S. L., 1988, ''Parametric Blade Study Test Report Rotor Configuration No. 4,'' AFWAL-TR-88-2110, Wright-Patterson AFB, OH, Nov.

[25] Lakshminarayana, B., Sitaram, N., and Zhang, J., 1985, ''End-Wall and Profile Losses in a Low-Speed Axial Flow Compressor Rotor,'' ASME Paper No. 85-GT-174.

[26] Seyler, D. R., and Gestolow, J. P., 1967, ''Single Stage Experimental Evaluation of High Mach Number Compressor Rotor Blading Part 2-Performance of Rotor 1B,'' NASA-CR-54582, Sept.

Downloaded 31 May 2010 to 171.66.16.27. Redistribution subject to ASME license or copyright; see http://www.asme.org/terms/Terms_Use.cfm

Rolls Royce/Allison 501-K Gas Turbine Antifouling Compressor Coatings Evaluation

Daniel E. Caguiat
Naval Surface Warfare Center,
Carderock Division,
Gas Turbine Emerging Technologies, Code 9334,
Phildelphia, PA 19112

The Naval Surface Warfare Center, Carderock Division (NSWCCD) Gas Turbine Emerging Technologies Code 9334 was tasked by NSWCCD Shipboard Energy Office Code 859 to research and evaluate fouling resistant compressor coatings for Rolls Royce Allison 501-K Series gas turbines. The objective of these tests was to investigate the feasibility of reducing the rate of compressor fouling degradation and associated rate of specific fuel consumption (SFC) increase through the application of anti-fouling coatings. Code 9334 conducted a market investigation and selected coatings that best fit the test objective. The coatings selected were Sermalon for compressor stages 1 and 2 and Sermaflow S4000 for the inlet guide vanes and remaining 12 compressor stages. Both coatings are manufactured by Sermatech International, are intended to substantially decrease blade surface roughness, have inert top layers, and contain an anti-corrosive aluminum-ceramic base coat. Sermalon contains a Polytetrafluoroethylene (PTFE) topcoat, a substance similar to Teflon, for added fouling resistance. Tests were conducted at the Philadelphia Land Based Engineering Site (LBES). Testing was first performed on the existing LBES 501-K17 gas turbine, which had an uncoated compressor. The compressor was then replaced by a coated compressor and the test was repeated. The test plan consisted of injecting a known amount of salt solution into the gas turbine inlet while gathering compressor performance degradation and fuel economy data for 0, 500, 1000, and 1250 KW generator load levels. This method facilitated a direct comparison of compressor degradation trends for the coated and uncoated compressors operating with the same turbine section, thereby reducing the number of variables involved. The collected data for turbine inlet, temperature, compressor efficiency, and fuel consumption were plotted as a percentage of the baseline conditions for each compressor. The results of each plot show a decrease in the rates of compressor degradation and SFC increase for the coated compressor compared to the uncoated compressor. Overall test results show that it is feasible to utilize antifouling compressor coatings to reduce the rate of specific fuel consumption increase associated with compressor performance degradation. [DOI: 10.1115/1.1573665]

Introduction

Salt ingestion testing, conducted at the Philadelphia Land Based Engineering Site (LBES) has shown that the Allison 501-K17 gas turbine's specific fuel consumption clearly increases as its compressor becomes fouled. Fouling is the process of dirt, soot, salt, and other contaminants adhering to the blades of the compressor. Fouling reduces aerodynamic performance by restricting airflow and increasing blade surface roughness and associated frictional losses.

The U.S. Navy's Preventative Maintenance System (PMS) contains the procedures for performing internal detergent crank wash on the Allison 501-K17 Gas Turbine. Detergent crank wash is the process of motoring the gas turbine, using the turbine's starter, while spraying a detergent solution into the compressor to wash the blades. Crank washing, which is currently performed after every 500 h of gas turbine operation, cleans the compressor blades and restores compressor performance to a certain level. However, during each 500-h interval, gas turbine compressor performance continues to degrade, resulting in an increased specific fuel consumption and increased operational cost.

One method of potentially decreasing the rate at which fouling occurs is to apply a fouling-resistant coating to the compressor blade surfaces. Fouling resistant coatings typically have surface finishes that are several times smoother than the underlying compressor blade material. In addition, these coatings are normally un-reactive with dirt, salt and other foulants. These two properties result in a decrease in the ability of a foulant particle to adhere to a given blade.

Test Objective

The Naval Surface Warfare Center, Carderock Division (NSWCCD) Gas Turbine Emerging Technologies Code 9334 was tasked by NSWCCD Shipboard Energy Office Code 859 to research and evaluate fouling resistant compressor coatings for Rolls Royce Allison 501-K Series gas turbines. The objective of these tests was to investigate the feasibility of reducing the rate of compressor fouling degradation and associated rate of specific fuel consumption (SFC) increase through the application of anti-fouling coatings. The results from these tests will indicate the benefits of conducting actual shipboard fuel economy tests with a coated compressor.

Preliminary Research

The preliminary research phase began with a study of the effects of fouling on gas turbine compressor operation. It also included examining 501-K gas turbine operation in order to determine the best method for conducting coatings tests on this engine. Possible foulants were selected and an injection system was developed for the gas turbine. Finally, reports from previous Naval Surface Warfare Center fouling-related tests were examined, and data was used to formulate the test plan.

Contributed by the International Gas Turbine Institute and presented at the International Gas Turbine and Aeroengine Congress and Exhibition, Amsterdam, The Netherlands, June 3–6, 2002. Manuscript received by the IGTI October 31, 2001. Paper No. 2002-GT-30261. Review Chair: E. Benvenuti.

 Copyright © 2003 by ASME

Downloaded 31 May 2010 to 171.66.16.27. Redistribution subject to ASME license or copyright; see http://www.asme.org/terms/Terms_Use.cfm

Table 1 Calculations for initial salt injection rate

Inlet air flow rate (kg air/s)	17	X
Typical Salt Concentration Downstream of Air Fllters (kg salt/kg air)	1.00E-08	/
Fraction of salt in saltwater (kg salt/kg saltwater)	5.00E-02	/
Salt water density (kg saltwater/mˆ3 saltwater)	1026	X
Conversion factor qal/mˆ3	264	X
Conversion factor (sec/h)	3600	X
Ratio: (pesired test hours/actual fleet hours)	1000	=
Required saltwater flow rate (gal/h)	**3.0**	**GPM**

Determination of Fouling Method. Fouling/coatings tests were conducted at the DDG-51 Land Based Engineering Site (LBES) rather than in an actual shipboard environment. Since cost and time were limiting factors at LBES, it was necessary to determine a method of simulating a typical shipboard fouling cycle in an accelerated manner. Such a simulation involves consideration of the following factors.

Shipboard Foulants. It was necessary to determine what different types of foulants might be present in a shipboard environment. Sand, sea salt, soot from re-ingested exhaust and airborne dirt are all possible foulants. However, for a DDG-51 class ship, sand is most likely not a major issue since operations are not primarily near the shoreline. Soot, dirt, and salt are therefore the most likely foulants present in such an environment.

Method of Cleaning Gas Turbine After Test Completion. In developing a system to inject foulants, it was necessary to consider not only system effectiveness but also a method of cleaning the gas turbine and removing foulants after test completion. It was determined that soot and dirt might be extremely difficult and costly to remove from both the gas turbine internal components as well as the inlet plenum. Therefore, a decision was made to use only sea salt as a foulant.

Salt Ingestion Rate. The goal of these tests was not to make a direct correlation between test site and shipboard data, but to determine the effect of fouling on performance parameters in general. Therefore, the focus was placed on ensuring that a sufficient amount of fouling occurred during the test duration. In selecting an initial salt injection rate, the following information was considered:

1. The typical salt-in-air concentration ingested into fleet gas turbines. This was chosen to be 0.01 parts per million based upon filter specifications and reference [1].
2. The average mass flow rate for the gas turbine. This was determined, based upon engine data, to be 17 kg/s or 38 lb/sec.
3. The length of time that a fleet gas turbine must operate before a clearly visible fouling trend is evident. This was arbitrarily chosen to be 2000 h (or approximately 1 year of operation).
4. Using the information from steps 1–3, and using a salt solution concentration of 5%, a calculation was performed to determine the flow rate that would be needed for a clear fouling trend to be evident after a 4-h maximum test duration. This calculation is shown in Table 1.
5. Nozzles were selected to produce the necessary 3.0 GPH flow rate.
6. Once the fouling tests began, performance data trends were analyzed and the salt solution concentrations were adjusted accordingly.

The final salt ingestion parameters are shown in Table 2.

Table 2

Solution concentration	Flow rate	Fouling interval
0.50%	3 GPM	0.25 h

Salt Injection System Arrangement. The salt injection systems developed for these tests consisted of an air-pressurized tank holding salt solution, two gas turbine inlet-mounted air-atomized spray nozzles, associated tubing and instrumentation.

Saltwater Droplet Size. The salt spray system was capable of injecting a salt spray solution at a flow rate of 3 gal per hour. The salt spray system had two nozzles and each of them was operated at 1.5 gal per hour. As shown in Fig. 1 below, there are a number of water pressure/air pressure combinations that will produce a flow rate of 1.5 gal per hour. For these tests, pressures of 60 psi and 40 psi were chosen for water and air respectively.

As shown in Fig. 2 at a water pressure of 60 psi and an air pressure of 40 psi, median droplet volume diameter is approximately 50 micron. Table 3 (taken from Reference [1] for gas turbine engines), shows that at an average inlet salt concentration of 0.01 parts per million (which is within the range of the filter specification for the 501-K17), at least 45% of particles should be under 13 micron. The salt nozzles selected for these tests primarily produced droplets larger than 13 micron. Since the larger droplets will have more momentum, they should not be redirected by the airstream as easily as smaller droplets. Therefore, larger

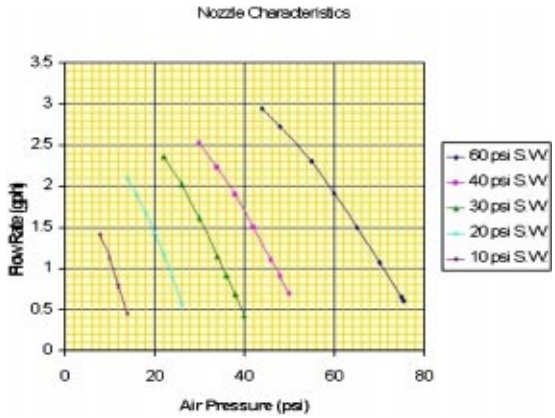

Fig. 1 Salt spray nozzle flow rate versus air and water pressures

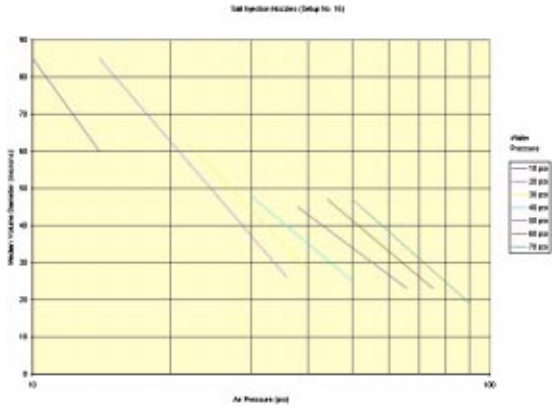

Fig. 2 Median volume diameter versus air pressure for salt nozzles

Downloaded 31 May 2010 to 171.66.16.27. Redistribution subject to ASME license or copyright; see http://www.asme.org/terms/Terms_Use.cfm

Table 3 Inlet salt requirements from MIL-E-17341C

Inlet salt concentration	Maximum particles greater than 13 Micron
0.003	25%
0.007	45%
0.016	45%
0.03	50%

droplets will tend to impinge on the compressor blades more often than smaller droplets [2]. Thus, the selection of these nozzles further accelerated fouling.

Salt Deposit Geometry. It was assumed that in the LBES accelerated test environment, salt would have a propensity to deposit in the same locations on the compressor blading as it would in a nonaccelerated shipboard environment. This assumption should be valid since as the airstream carries salt through the compressor, salt tends to adhere to stagnation points on the compressor blading. These stagnation points are independent of time frame and therefore salt deposition geometry is independent of time frame.

Effects of Fouling on Compressor Performance. Foulants adhering to the compressor blades increase blade surface roughness which produce more turbulent flow through the compressor [3]. This increases the amount of energy required to obtain a given pressure ratio by moving compressor operation further from an isentropic operating condition and more toward an operating point at which frictional losses must be overcome. Furthermore, as a compressor becomes fouled, the mass flow of air through each stage of the compressor will be reduced due to the increased thickness of the now turbulent boundary layer [3]. This will further decrease pressure ratio and increase the effective angle of attack of each compressor blade. As fouling continues, in the extreme case, this angle of attack can increase until compressor stall occurs [4].

501-K Gas Turbine Engine Operation and the Specific Effects of Fouling. The Rolls Royce/Allison 501-K gas turbine generator consists of a gas turbine that is mechanically coupled to a generator through a reduction gearbox. The 501-K governor maintains its speed, Ngg, at around 13,820 RPM at all times. Therefore, for a ''clean,'' new engine operating under standard day conditions, there is a certain compressor discharge pressure (CDP), compressor discharge temperature (CDT), fuel flow rate, and turbine inlet temperature (TIT) associated with each electrical load.

As fouling occurs under such constant Ngg and electrical load conditions, CDP will decrease. Since the energy of the air stream is dependent on the fuel/air mixture, fuel flow rate will need to increase in order to maintain the load. In addition, CDT and TIT will increase since the increased surface roughness associated with fouling leads to increased frictional losses.

Market Research. Market research was conducted in order to select the proper anti-fouling coatings for use on the 501-K17. There were a number of companies identified which manufacture compressor coatings including Standard Acro Inc, MDS-PRAD (a joint Russian-Canadian venture), and Sermatech International. However, Sermatech was the most prominent supplier of these coatings and had a variety of coatings in use on commercial gas turbines.

NSWCCD Code 9334 met with a Sermatech representative and a metallurgist from Limerick, PA. The representative from Sermatech inspected a decommissioned Navy-owned Allison 501-K17 gas turbine compressor and determined the best Sermatech coatings for providing fouling resistance. The coatings recommended were Sermalon on the first two compressor stages and Sermaflow S-4000 for the remaining 12 stages and inlet guide vanes. Sermalon contains a Polytetrafluoroethylene (PTFE) (A substance similar to Teflon) topcoat and is therefore more fouling resistant than Sermaflow S-4000. However, the Sermalon coating system is thicker than Sermaflow S-4000 and would restrict the airflow through latter compressor stages to the point where its application may be detrimental to performance. Sermaflow S-4000 is a smooth, inert coating and provides fouling resistance along with a thin coating thickness for latter compressor stages.

Under contract to NSWCCD Code 9334, John J. McMullen Associates (JJMA) performed additional research related to coating properties and possible methods of comparing coated versus uncoated compressors. In this report, JJMA recommended testing the Sermatech coatings. In addition, JJMA recommended that Aeroblue AF, manufactured by Standard Aero, also be tested. NSWCCD Code 9334 considered testing Aeroblue AF, but since Aeroblue is similar to Sermalon and due to the additional funding required for a third antifoulant coating evaluation, a decision was made to test only the two Sermatech coatings.

Antifouling Compressor Coating Properties

Surface Roughness. A major factor in fouling resistance of compressor coatings is surface finish roughness. Foulants will tend to more easily adhere to a rougher, more frictional surface. For this test, surface roughness was measured using the method outlined in reference [5]. The apparatus used for this method consists of a stylus, which is stroked along the surface of the compressor blade and induces an electrical signal that is proportional to its vertical velocity. The stylus moves a distance (referred to as the cut-off) of either 0.01 or 0.03 in. as a reading is taken. The stroke length must be at least five times the cut-off length. The five readings obtained are then averaged and the resulting value is converted into actual surface height variation (i.e., surface roughness), which is measured in micro-inches or Ra.

Typical uncoated, new compressor blades can have Ra values of 35–40 micro-in. These Ra values will increase substantially as fouling or corrosion pitting occurs while a compressor is in service. The surface roughness for the blades of the 501-K compressor coated for this test was between 60–70 Ra. Ra values for both coatings applied by Sermatech were measured using a 0.03 cut-off. The average roughness was 14 Ra with many of the values between 9–11 Ra.

Properties of Coatings Applied. The antifouling compressor coatings tested were Sermatech's Sermalon 962/1140 and Sermaflow S-4000. The Sermalon structure is shown in Fig. 3. As shown, it consists of three layers. The Al/ceramic basecoat bonds

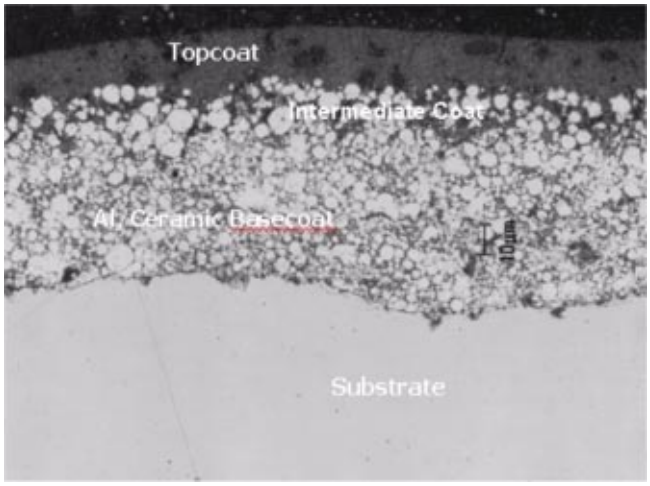

Fig. 3 Sermalon coating cross section

Downloaded 31 May 2010 to 171.66.16.27. Redistribution subject to ASME license or copyright; see http://www.asme.org/terms/Terms_Use.cfm

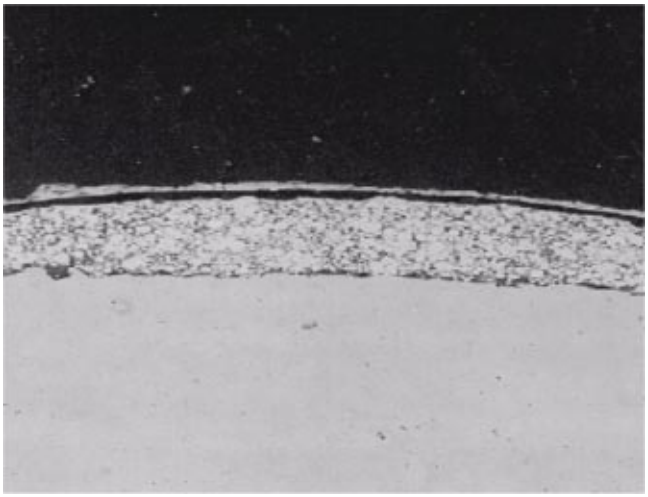

Fig. 4 Sermaflow S-4000 cross section

to the substrate and provides protection against corrosion. The Al-filled intermediate coat further prevents corrosion, and the PTFE-filled topcoat resists fouling.

The Sermaflow S-4000 structure, shown in Fig. 4, is a single layer coating consisting of an aluminum ceramic base coat and a thin chemically inert top coat which prevents corrosion of the substrate and decreases surface roughness to prevent fouling. Sermaflow S-4000 topcoat, like the Sermalon topcoat, is highly inert to prevent salt or other foulants from chemically bonding with it. The chemical bonding, which occurred on noncoated blades, tended to corrode the blade and increase surface roughness, thereby increasing the fouling rate of the compressor.

Test Methodology

The test plan conducted for both coated and uncoated compressor fouling tests was as follows:

1. Collect data at selected operating points within the gas turbine's range. This was to be done by varying generator load from 0 to 1250 KW (0, 500, 1000, and 1250 KW).
2. Inject a known quantity of salt into the gas turbine inlet. The quantity calculated was 0.0158 lb of salt to be sprayed over the course of 15 min.
3. Repeat steps 1 and 2 until a clear data trend is evident.

Performance parameters monitored included compressor inlet and discharge temperatures and pressures, engine vibration, fuel volumetric flow rate, turbine inlet temperature, and generator load. Salt was then sprayed at a rate of 3 gall per min with a concentration of 0.5% for the 15-min injection period. This process of data point collection between 15-min salt spray intervals would allow ''snapshots'' of compressor health during the course of a fouling cycle. The equation used to calculate compressor efficiency for the 501-K is given in Eq. (1).

$$[(Pt3/\mathrm{Pt2})^{\gamma-1/\gamma}-1]/[(Tt3/Tt2)-1] \tag{1}$$

where state 2 is defined as the total pressure $(Pt2)$ and temperature $(Tt2)$ at the compressor inlet, and state 3 is defined as the total pressure $(Pt3)$ and temperature $(Tt3)$ at the compressor exit, and where γ is the ratio of specific heats for air in these respective states.

Test Results

Compressor Coating Application Results. The compressor tested was a decommissioned asset from USS Compte De Grasse and required overhaul prior to coating application. After overhaul completion, the compressor was disassembled and shipped to

Fig. 5 Compressor casing coated with Sermatel 6F-1

Fig. 6 Stages 1 and 2 coated with 962/1140

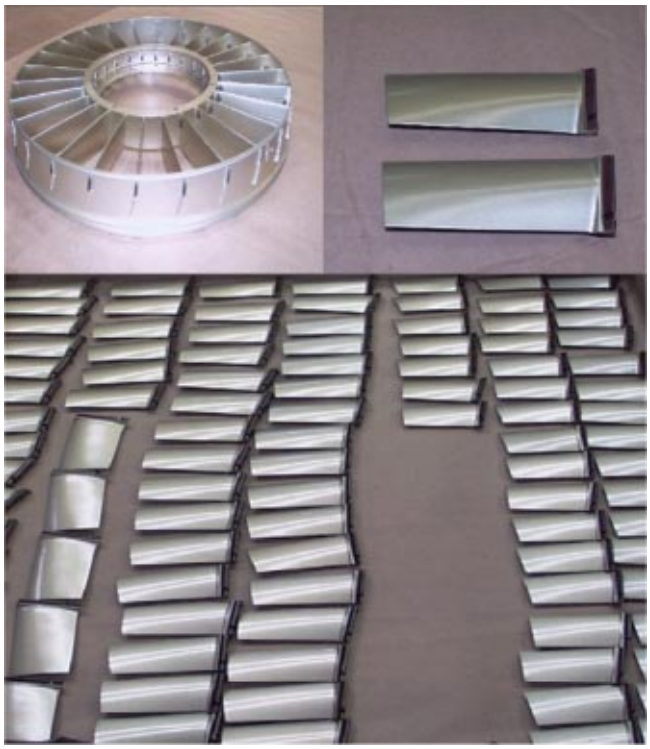

Fig. 7 Inlet guide vanes and compressor blades coated with Sermaflow S-4000

Downloaded 31 May 2010 to 171.66.16.27. Redistribution subject to ASME license or copyright; see http://www.asme.org/terms/Terms_Use.cfm

Sermatech in Limerick, PA for application of the two coatings. Figures 5 through 7 show the coated compressor components prior to reassembly. Figure 5 shows the compressor and diffuser casing coated with Sermatel 6F-1. Figure 6 shows stages 1 and 2 stators and blades coated 962/1140, a Sermalon variation. Figure 7 shows the air inlet guide vane assembly and various blades coated with Sermaflow S-4000. After being coated, the compressor was then shipped back to Standard Aero for reassembly. The complete, reassembled compressor was installed in place of the existing LBES 501-K17 compressor for testing.

Data Trends. Data from the fouling test on the uncoated Allison 501-K17 gas turbine shows a nearly linear upward trend in fuel flow rate, a nearly linear upward trend in CDT and a nearly linear downward trend in CDP (see Figs. 8–10) as the salt intake increases. This equates to a downward trend in compressor adiabatic efficiency. Note that the amount of salt required to reduce CDP by 7% and increase fuel flow and CDT by 3% was only 0.065 lb.

In addition, compressor adiabatic efficiency was calculated using Eq. (1). As can be seen in Fig. 11, a 6.5% efficiency loss was realized after less than 0.08 lb of salt were ingested by the gas turbine. The baseline test was repeated to verify these results.

As shown in Fig. 12, turbine inlet temperature also indicated compressor degradation. This was expected for a fouled compressor, as more energy is required to produce a given pressure ratio than for a ''clean'' compressor. This energy is used to compensate for the increase in friction and turbulence associated with salt deposits on the compressor blades. Therefore, to obtain this additional energy, more fuel must be burned, causing combustor discharge temperatures, and hence, turbine inlet temperatures, to increase.

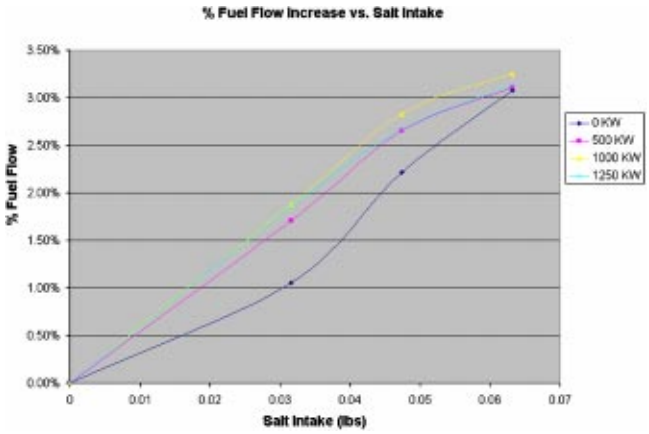

Fig. 8 Fuel flow versus salt intake

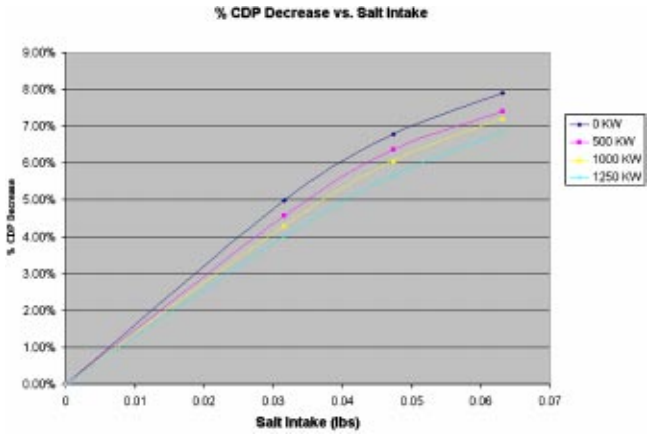

Fig. 9 CDP versus salt intake

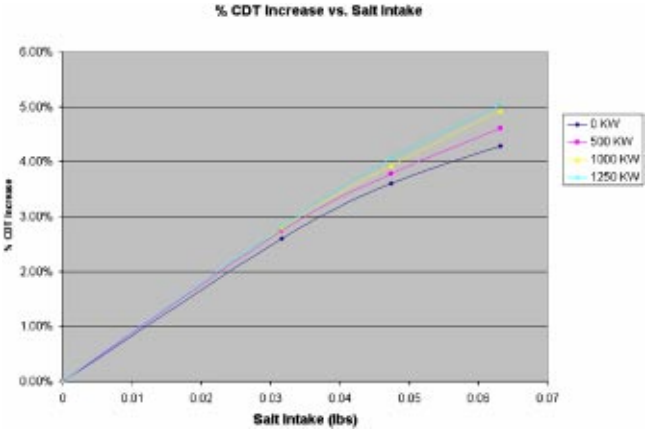

Fig. 10 CDT versus salt intake

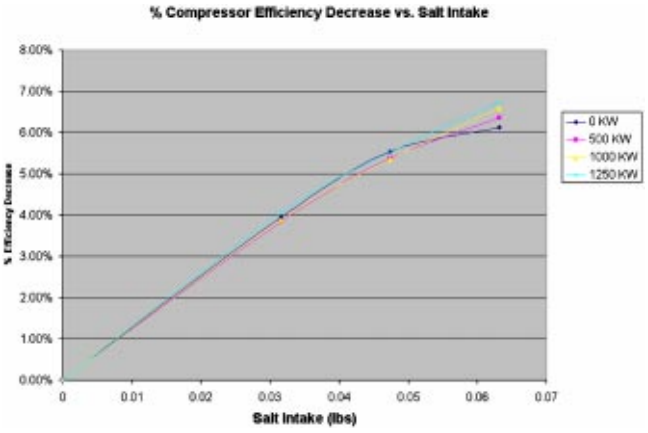

Fig. 11 Adiabatic efficiency change versus salt intake

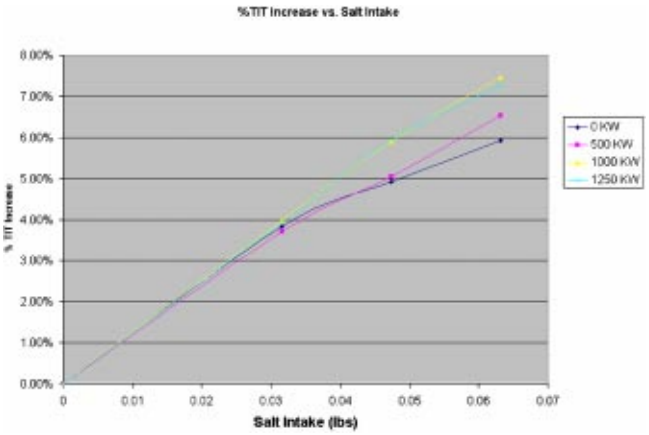

Fig. 12 TIT versus salt intake

Coated Versus Uncoated Comparison. Graphs, similar to Figs. 8 through 12, compared coated and uncoated compressor performance. These results are shown in Figs. 13 through 17. As shown, there are clear decreases in degradation for each parameter associated with the coated compressor. The results are further verified at each load level. In addition, repeat tests were conducted on each compressor to further verify results.

Downloaded 31 May 2010 to 171.66.16.27. Redistribution subject to ASME license or copyright; see http://www.asme.org/terms/Terms_Use.cfm

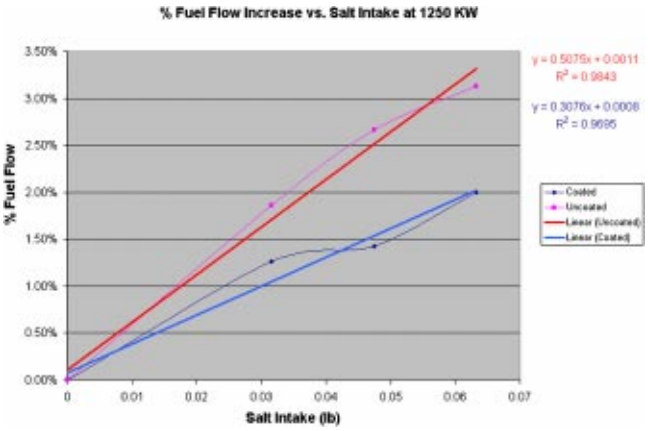

Fig. 13 Fuel flow comparison

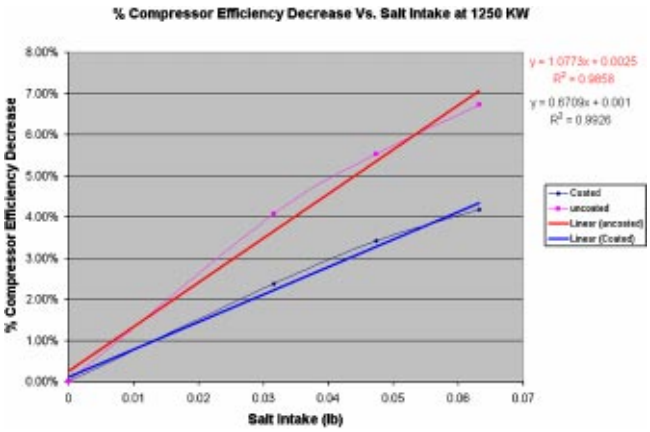

Fig. 16 Compressor efficiency comparison

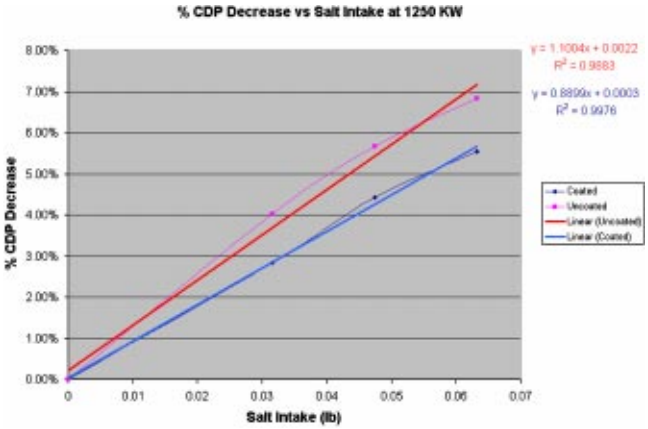

Fig. 14 CDP comparison

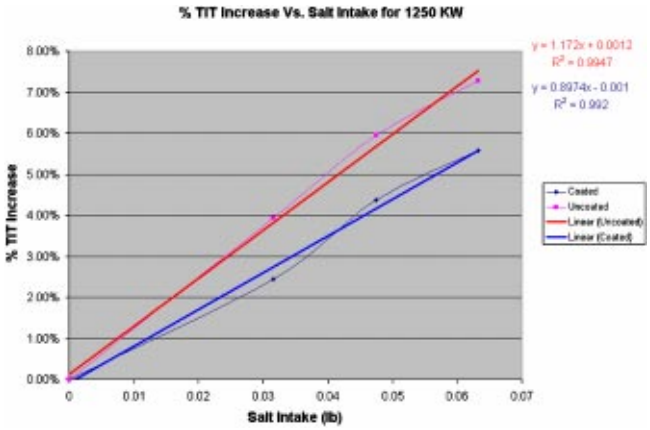

Fig. 17 TIT comparison

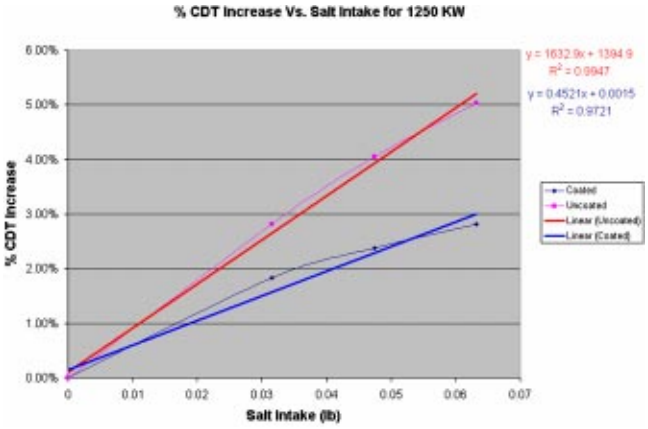

Fig. 15 CDT comparison

Conclusions and Recommendations

The Rolls-Royce/Allison 501-K17 was sensitive enough to fouling to yield clearly visible trends in all operational parameters that were measured. In addition, it is feasible to quantify fuel economy losses associated with fouling of the 501-K17 in a shipboard environment provided shipboard foulants adhere in a similar manner as in the LBES test. This will facilitate a shipboard fuel economy comparisons for a coated versus uncoated compressor.

A direct numerical correlation between degradation rates during this accelerated test versus an actual shipboard environment would be questionable due to the larger saltwater droplet sizes used for the test. However, results from these tests show that the application of the compressor coatings significantly improved the compressor's resistance to fouling. This improvement to fouling resistance can be seen in pressure ratio, TIT, overall compressor efficiency, and fuel consumption slopes during the fouling cycle. Based upon these results, it is recommended that a coated compressor be evaluated in a shipboard environment in order to further quantify fuel economy gains associated with a coating application.

Acknowledgments

The author wishes to thank Brian Rampolla, John J. McMullen and Associates.

Nomenclature

Ngg = gas generator speed
CDP = compressor discharge pressure
CDT = compressor discharge temperature
TIT = turbine inlet temperature
SFC = specific fuel consumption

References

[1] MIL-E-17341C, *Military Specification: Engines, Gas Turbine, Propulsion and Auxiliary Naval Shipboard,* Section 4.3.2.3.

Downloaded 31 May 2010 to 171.66.16.27. Redistribution subject to ASME license or copyright; see http://www.asme.org/terms/Terms_Use.cfm

[2] Weinert, E. P., and Carlton, G. A., *Salt-Water Problems in Marine Gas Turbines*.
[3] Kurz, R., and Brun, K., 2000, ''Degradation in Gas Turbine Systems,'' ASME Paper No. 2000-GT-345.
[4] Mezheritsky, A. D., and Sudarev, A. V., 1990, ''The Mechanism of Fouling and the Cleaning Technique in Application to Flow Parts of the Power Generation Plant Compressors,'' ASME Paper No. 90-GT-103.
[5] McMordie, B. G., 1994, ''Measuring Surface Finish of Compressor Airfoils Protected by Environmentally Resistant Coatings,'' Aerospace/Airline Plating and Metal Finishing Forum, Apr.

Downloaded 31 May 2010 to 171.66.16.27. Redistribution subject to ASME license or copyright; see http://www.asme.org/terms/Terms_Use.cfm

Qun Zheng
e-mail: zhengqun@hrbeu.edu.cn

Yufeng Sun

Shuying Li

Yunhui Wang

Harbin Engineering University,
Harbin 150001, China

Thermodynamic Analyses of Wet Compression Process in the Compressor of Gas Turbine

Thermodynamic model of wet compression process is established in this paper. The topics of ideal wet compression process, actual wet compression process, water droplet evaporative rate, wet compression work, inlet evaporative cooling, concept of wet compression efficiency, aerodynamic breaking of water droplets etc. are investigated and discussed in this paper. [DOI: 10.1115/1.1575254]

Keywords: Thermodynamic Analyses, Wet Compression, Compressor, Gas Turbine

Introduction

One of the most effective way to increase the gas turbine output power is reducing the amount of compression work of its compressor, if we take into account that the compressor consumes about 1/3–1/2 work produced by turbine. Intercooling in the compression process or between two parts of compressor can reduce the compression work effectively. But the heat absorbed by the coolant is rejected from the cycle. So general intercooling techniques will increase the gas turbine output, but will decrease the cycle efficiency sometimes. The large amount of latent heat of water when it evaporates from liquid to vapor arises the idea that mixing water with the compressed hot air to cool the air. By this way, it will reduce the compression work, and the evaporated water (vapor) will produce more work in turbine as an ingredient of working fluid mixture. Inlet evaporative cooling has been used to increase the gas turbine output power and to improve thermal efficiency in recent years. This is a cost-effective way to enhance the performance of the gas turbine directly; but the effect of this technique is restricted greatly by environmental air temperature and humidity when applying. There are many inlet evaporative coolers, or spray chiller providers appeared around the world these years; and also, many gas turbine manufacturers have tested and applied this technique or provide similar equipment as accessories [1–5]. The hotter and drier the inlet air is, the more effective of the equipment.

According to the operating results that a 1% water injection to air mass flow will increase the gas turbine output up to 10% and efficiency up to a relative 3% [6–9]. The other benefits are reduced NOx emissions.

In this paper, we try to introduce the concept of continuously evaporating internal cooling of the compressor—wet compression, or say, humid air compressor (HAC) as we called it in reference [10]. It is sophisticated to some extent, but more effective and prospective.

Thermodynamic investigations of wet compression process are carried out. The results indicate that this technique has great potential to improve the compressor performance.

The wet compression process differs fundamentally from dry air compression process. How to calculate the variation of thermodynamic parameters of wet compression process is important for evaluating wet compression itself and for analyzing gas turbine performance. Several aspects about wet compression process are discussed in the followings.

Contributed by the International Gas Turbine Institute and presented at the International Gas Turbine and Aeroengine Congress and Exhibition, Amsterdam, The Netherlands, June 3–6, 2002. Manuscript received by the IGTI January 10, 2002. Paper No. 2002-GT-30590. Review Chair: E. Benvenuti.

Ideal Wet Compression Process

Ideal Wet Compression Process Equation. According to Gibbs equation

$$Tds = dh - \frac{dp}{\rho} \tag{1}$$

For ideal wet compression, assume the evaporative heat equals to fictitious reversible heat

$$Tds = -Ldw \tag{2}$$

So the Gibbs equation becomes

$$-Ldw = dh - dp/\rho \tag{3}$$

From thermally and calorically perfect gas expressions, Eq. (3) is rewritten as

$$-Ldw = \frac{\gamma R}{\gamma - 1} dT - \frac{dp}{p} RT \tag{4}$$

Then, we got the equation of compression process

$$\frac{dp}{p} = \left(\frac{\gamma}{\gamma - 1} + \frac{L}{R} \frac{dw}{dT} \right) \frac{dT}{T} \tag{5}$$

It can be seen from Eq. (5) that for wet compression process, the evaporative rate dw/dT plays an important role. It is just this term that makes the wet compression different from dry compression.

Isentropic Index of Wet Compression Process. To get the isentropic index of wet compression process, integrating Eq. (5) from inlet to outlet of compressor. Assume evaporative rate varies with temperature linearly, that is $dw/dT = \text{const}$; we have

$$\left(\frac{p}{p_1} \right) = \left(\frac{T}{T_1} \right)^{k/k-1} = \left(\frac{T}{T_1} \right)^{\sigma} \tag{6}$$

From Eqs. (5) and (6), we know that

$$\frac{\gamma}{\gamma - 1} + \frac{L}{R} \frac{dw}{dT} = \frac{k}{k-1} = \sigma \tag{7}$$

After evaporative rate being given or under condition of saturated wet compression, isentropic index of wet compression can be calculated from Eq. (7).

If evaporative rate is $dw/dT = 7.5 \times 10^{-4}$, the calculated isentropic index of wet compression is $k = 1.122$. Such a result reminds us that it is similar to the insentropic index of wet steam expansion process in steam turbine.

 Copyright © 2003 by ASME

Downloaded 31 May 2010 to 171.66.16.27. Redistribution subject to ASME license or copyright; see http://www.asme.org/terms/Terms_Use.cfm

Actual Wet Compression Process

For actual wet compression, the process index depends on both entropy increase of air $\Delta S=(1/\gamma-1)(n-\gamma/n-1)R\ln T_2/T_1$ and water evaporative rate dw/dT. From Gibbs equation, we have

$$-Ldw+\frac{1}{\gamma-1}\frac{n-\gamma}{n-1}RdT=\frac{\gamma R}{\gamma-1}dT-\frac{dp}{\rho} \tag{8}$$

Substituting thermally and calorically perfect gas expressions into Eq. (8),

$$\frac{dp}{p}RT=\frac{\gamma R}{\gamma-1}dT+Ldw-\frac{1}{\gamma-1}\frac{n-\gamma}{n-1}RdT \tag{9}$$

Dividing RT from left and right sides of Eq. (9), we obtain,

$$\frac{dp}{p}=\left(\frac{\gamma}{\gamma-1}+\frac{L}{R}\frac{dw}{dT}-\frac{1}{\gamma-1}\frac{n-\gamma}{n-1}\right)\frac{dT}{T} \tag{10}$$

Integration of Eq. (10) gives

$$\frac{p}{p_1}=\left(\frac{T}{T_1}\right)^{m/m-1} \tag{11}$$

where

$$\frac{m}{m-1}=\frac{\gamma}{\gamma-1}+\frac{L}{R}\frac{dw}{dT}-\frac{1}{\gamma-1}\frac{n-\gamma}{n-1} \tag{12}$$

m is the polytropic index of actual wet compression process.

Comparing indices of k, m, n, we have the following results:

$$k<m<n \tag{13}$$

Exit Temperature of Wet Compression

Because of the Internal cooling of wet compression, the compressor exit temperature of wet compression drops greatly.

The exit temperature of ideal wet compression process can be obtained in following ways:

1. From Eq. (6), the exit temperature is

$$\frac{T_2}{T_1}=\left(\frac{p_2}{p_1}\right)^{k-1/k} \tag{14}$$

2. Or, if specific heat is not constant, according to isentropic condition

$$\Delta s=0 \tag{15}$$

For wet air, Eq. (15) means

$$s_{a2}+w_2s_{w2}+f_2s_{f2}=s_{a1}+w_1s_{w1}+f_1s_{f1} \tag{16}$$

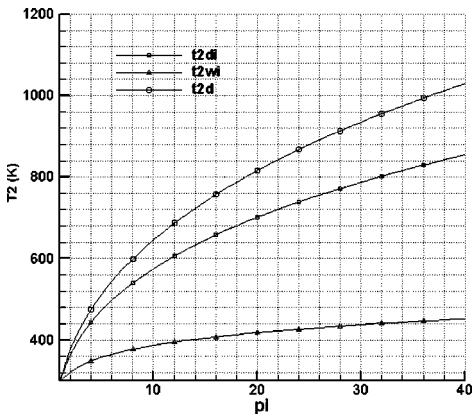

Fig. 1 Exit temperatures of ideal wet compression and dry air compression processes

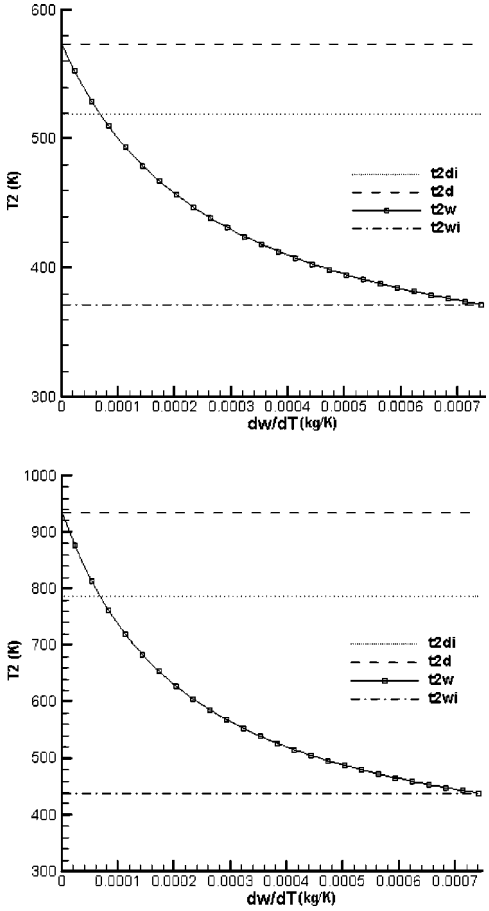

Fig. 2 t2di, t2d, t2w, t2wi are compressor exit temperatures of ideal dry air compression, dry air compression, wet compression, and ideal wet compression, respectively

Iteration is needed to get the compressor exit temperature through the balance of Eq. (16). If compression ratio is $pi=7$ as in the foregoing, inlet temperature is $t_1=25$, evaporative rate $dw/dT=7.5\times10^{-4}$ kg/K, then compressor exit temperature of saturated wet compression is $T_{21}=368$ K. While the exit temperature of dry air compression is $T_2=520$ K for the same compression ratio and inlet temperature. The drop of compressor exit temperature due to the internal cooling of wet compression is $\Delta T_2=152$ K.

The higher the compression ratio is, the greater is the difference between T2 and T21. That results in more compression works being reduced. And that means more output power of gas turbine can be delivered. The compressor exit temperatures under different pressure ratios are shown in Fig. 1. Here, t2d, t2di and t2wi are exit temperatures of actual dry, ideal dry compression, and ideal wet compression processes, respectively.

The exit temperature of actual wet compression depends on both the compression ratio and the evaporative rates. As shown in Fig. 2, when the evaporative rate is greater than about 0.8e-5 kg/K, the wet exit temperature can even be lower than that of ideal dry air compression. The higher is the evaporative rate, the lower is the compressor exit temperature. The exit temperature can be as low as 368 K when compression ratio is 7.

Compression Work of Wet Compression Process

The compression work decreases because of the internal evaporative cooling. However, the evaporating during the compression process makes the calculation of the compression work complicated. The enthalpy of mixed working fluids (wet air) is

Downloaded 31 May 2010 to 171.66.16.27. Redistribution subject to ASME license or copyright; see http://www.asme.org/terms/Terms_Use.cfm

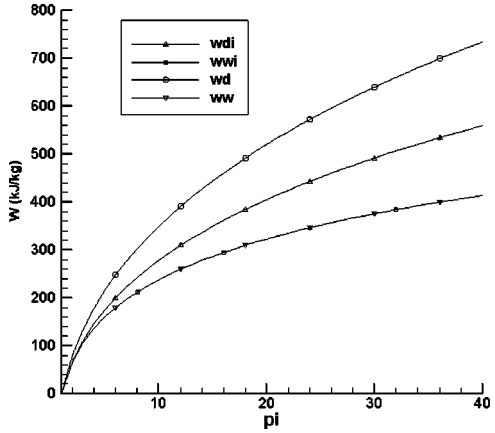

Fig. 3 Actual and isentropic compression works of dry air and wet compression (evaporative rate is $dw/dt=7.5e\text{-}4$)

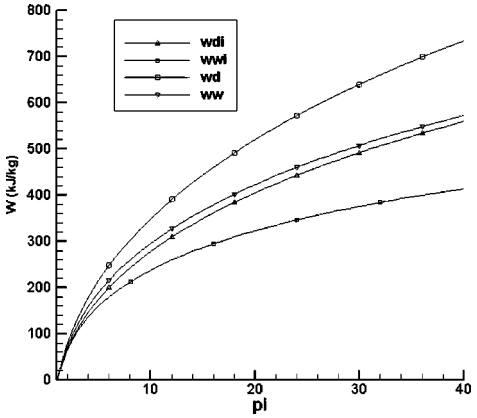

Fig. 5 Actual and isentropic compression works of dry air and wet compression (evaporative rate is $dw/dt=1.5e\text{-}4$)

$$h=h_a+wh_w+fh_f \tag{17}$$

From Eq. (17), we have

$$dh=dh_a+d(wh_w)+d(fh_f)=dh_a+wdh_w+h_wdw+fdh_f+h_fdf \tag{18}$$

During compression process, it can take $dh_f\approx 0$.

Because $dw=-df$, Eq. (18) is rewritten as

$$dh=dh_a+wdh_w+h_wdw-h_fdw=dh_a+wdh_w+dw(h_w-h_f)$$
$$=dh_a+wdh_w+dw(h_w-h_g+h_{fg}) \tag{19}$$

where h_{fg} is latent heat.

From the view of droplet evaporation, Eq. (18) is

$$dh=dh_a+wdh_w-h_wdf+h_fdf$$
$$=dh_a+wdh_w-df(h_w-h_g+h_{fg}) \tag{20}$$

Then the work of wet compression process is

$$W_c=h_{a2}-h_{a1}+w_2h_{w2}-w_1h_{w1}+f_2h_{f2}-f_1h_{f1} \tag{21}$$

If we take $w_2-w_1=\Delta w$, $f_1-f_2=\Delta f$, $\Delta w=\Delta f$ then the wet compression work is

$$W_c=h_{a2}-h_{a1}+w_1(h_{w2}-h_{w1})+\Delta wh_{w2}+f_2(h_{f2}-h_{f1})-\Delta fh_{f1} \tag{22}$$

If water evaporates completely at the exit of compressor, then we have $f_2=0$. In such a case, wet compression work is

$$W_c=h_{a2}-h_{a1}+w_1(h_{w2}-h_{w1})+\Delta wh_{w2}-\Delta fh_{f1}$$
$$=h_{a2}-h_{a1}+w_1(h_{w2}-h_{w1})+\Delta w(h_{w2}-h_{f1}) \tag{23}$$

where $\Delta w=\Delta f$ is evaporative amount from inlet to outlet.

The compression work can also be written as

$$W_c=(h_{a2}+w_2h_{w2})-(h_{a1}+w_1h_{w1})-\Delta fh_{f1} \tag{24}$$

If $w_1=0$, means the compression process begins from dry air, then compression work is

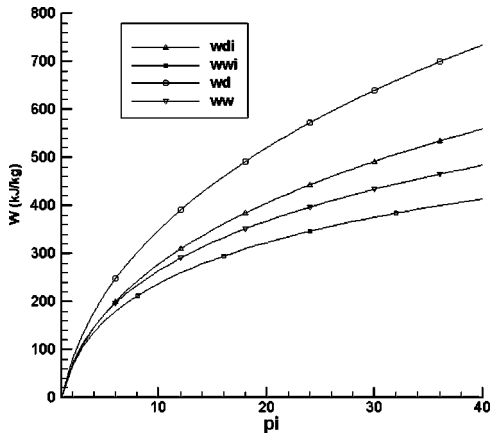

Fig. 4 Actual and isentropic compression works of dry air and wet compression (evaporative rate is $dw/dt=3.5e\text{-}4$)

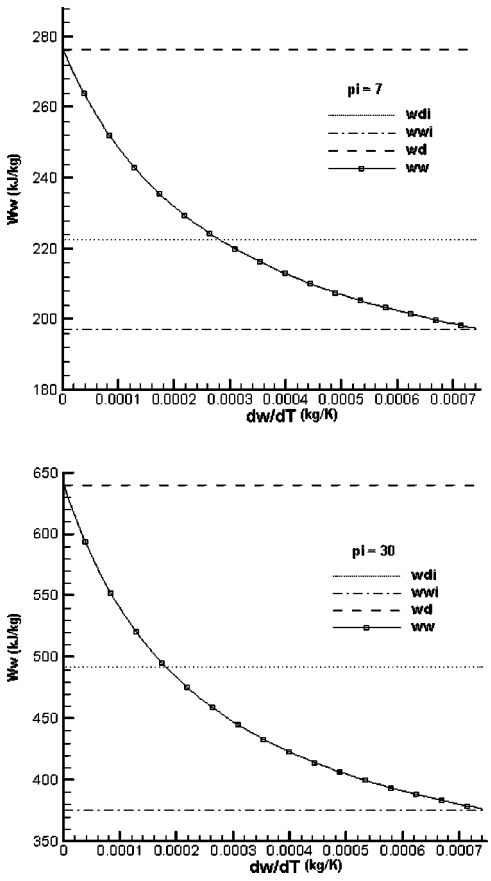

Fig. 6 Wet compression work variation with evaporative rates—(*a*) compression ratio $pi=7$, (*b*) compression ratio $pi=30$

Downloaded 31 May 2010 to 171.66.16.27. Redistribution subject to ASME license or copyright; see http://www.asme.org/terms/Terms_Use.cfm

$$W_c=(h_{a2}+w_2h_{w2})-h_{a1}-\Delta fh_{f1} \tag{25}$$

Because, in this case, $w_2=\Delta f$; therefore

$$W_c=h_{a2}-h_{a1}+\Delta f(h_{w2}-h_{f1}) \tag{26}$$

Generally speaking, $w_1\neq 0$. That implies compressor inlet air is humid air or some kinds of evaporative cooling techniques adopted before the inlet of compressor.

The compression works under different pressure ratios and different evaporative rates are shown in Figs. 3–5. The evaporative rates are 7.5e-4, 3.5e-4 and 1.5e-4, respectively. Here, Wd and Wdi are actual and isentropic dry air compression works; Ww and Wwi are actual and isentropic wet compression works. It can be seen from the figures that the wet compression works are much lower than those of dry air compressions. The higher is the pressure ratio, the more saving is the compression work. When pressure ratio is 40, the wet compression work is only about half of the dry air compression work. These results indicate the great potential of the wet compression. When evaporative rate reaches about 1.8e-4 or more, the wet compression work will be lower than that of isentropic dry air compression. The wet compression work is higher than the dry air isentropic work, if evaporative rate is less than 1.5e-4 (see Fig. 5), but that is still much lower than actual dry air compression work. So, it is also a great improvement for dry air compression.

Figure 6 is the variation of wet compression works with evaporative rates. In these two cases, the compression ratios are 7 and 30, respectively. The dry air compression work and isentropic work are also drawn in these figures with slash or dot lines for comparison. The wet compression work Ww decreases along with the increasing of evaporative rate dw/dt. It starts from actual dry air compression work Wd and decreases till approaching to isentropic wet compression work Wwi. The wet compression work Ww can be lower than dry air isentropic compression work Wdi, which will be illustrated further in later section.

Compressor Inlet Evaporative Cooling

Evaporative cooling before compressor inlet can be taken as a part of wet compression techniques. When inlet air is humidified, its temperature will decrease. As the air reaches saturation, its temperature gets to the lowest level. The temperature drop depends on the environmental temperature and relative humidity. The smaller is the humidity, the more drop of the temperature.

If the atmosphere relative humidity is φ, then moisture content or steam-to-air ratio is

$$w_0=\frac{M_v}{M_a}\frac{p_v}{p_a}=0.622\frac{\varphi p_{sv}}{p-\varphi p_{sv}} \tag{27}$$

where M_v, p_v are mass and pressure of vapor, M_a, p_a are mass and pressure of air, respectively. Subscript sv represents saturation state.

When the inlet air is humidified, the change of enthalpy is

$$h_1-h_0=(w_1-w_0)h_{f0} \tag{28}$$

Taking the specific heat and latent heat as constants in this process

$$[1.005t_1+w_1(2501+1.859t_1)]-[1.005t_0+w_0(2501+1.859t_0)]$$
$$=(w_1-w_0)h_{f0} \tag{29}$$

where $G_{pa}=1.005$ KJ/Kg·K, $C_{ps}=1.859$ KJ/Kg·K, $L_{0H_2o}=2501$ KJ/Kg are specific heat of air, vapor at constant pressure, and latent heat.

Based on Eq. (29), we can get the temperature after air humidifying. When the air reaches saturation,

$$w_1=0.622\frac{p_{sv}}{p-p_{sv}}.$$

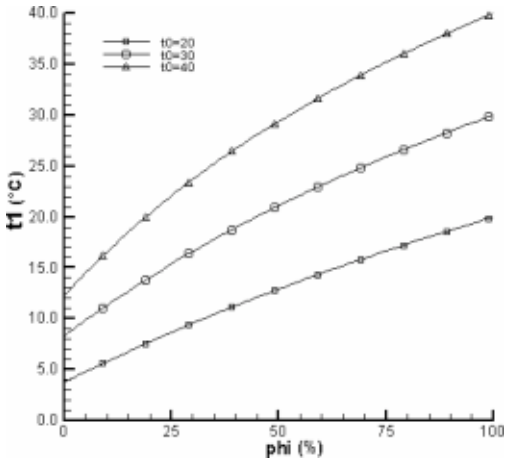

Fig. 7 Compressor inlet temperature after inlet evaporative cooling

Solving Eq. (29) through iteration $t_1\rightarrow p_{sv}(t_1)\rightarrow w_1\rightarrow t_1'$. The temperature and pressure of saturated vapor is related by the expression $\log_{10}p_{sv}=5.55-2061/T_{sv}$ for the convenience of computation.

For example, when environment temperature is $t_0=20$ relative humidity is $\varphi=30\%$, moisture contents are $w_0=0.0045$ kg/kgDA, $w_1=0.0081$ kg/kgDA respectively. The water amount injected is $\Delta w=3.6$e-3 kg/kgDA, and the inlet wet air temperature drops to $t_1=10.8$.

When environment temperature is $t_0=20$, relative humidity increases to $\varphi=50\%$, moisture contents are $w_0=0.0075$ kg/kgDA, $w_1=0.0108$ kg/kgDA. The water amount injected is $\Delta w=w_1-w_0=3.3$e-3 kg/kgDA, and the inlet wet air temperature drops to $t_1=13.8$.

When environment temperature is $t_0=20$, relative humidity increases to $\varphi=70\%$, moisture contents are $w_0=0.01060$ kg/kgDA, $w_1=0.01190$ kg/kgDA, respectively. The water amount injected is $\Delta w=w_1-w_0=1.3$e-3 kg/kgDA, then the inlet wet air temperature drops to $t_1=16.5$.

Figures 7 and 8 are inlet temperature and evaporative amount for inlet evaporative cooling from environmental state to saturation state at different environmental temperature and different relative humidity. The higher is the environmental temperature and the lower is the relative humidity, the more effective is the inlet evaporative cooling. When the environmental humidity is high, for example, $\varphi>75\%$, the inlet evaporative cooling will not

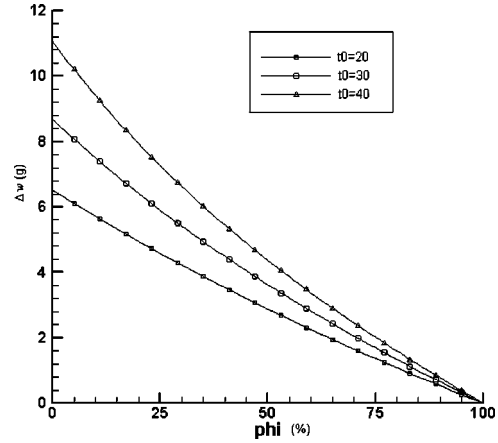

Fig. 8 Evaporative amount of water (g/kgDA) need for inlet cooling

Downloaded 31 May 2010 to 171.66.16.27. Redistribution subject to ASME license or copyright; see http://www.asme.org/terms/Terms_Use.cfm

very effective. The amount of compression work saving depends on environmental temperature, relative humidity and the effectiveness of inlet evaporative cooling.

Internal evaporative cooling of wet compression can achieve much the same effect as that of inlet evaporative cooling, but does not restricted so much by the environmental conditions. Through evaporative cooling, the compressor mass rate and compression ratio will increase. The increased mass rate comes from the added steam, high-density air and the through flow increase of turbine due to the higher compression ratio. If the compression ratio remains the same, the compression work will be reduced, so the gas turbine will deliver more output power if considering the compressor consumes 1/2–2/3 of the total work generated by turbine. Moreover, for wet compression, besides achieving internal cooling effect, the heat of compressed air is not rejected as those of general inter cooling, such as in the case of ICR engine, but is recovered by the evaporated water.

Efficiency of Wet Compression Process

Because of the change of isentropic process of wet compression and the reducing of compression work, the compression efficiency must be redefined. Otherwise, if we take the isentropic compression work of dry air as a basis to evaluate wet compression, then the efficiency, ''equivalent adiabatic efficiency'' as we called it, may be greater than 1.0.

Three kinds of efficiency of wet compression are discussed in the following.

Equivalent Adiabatic Efficiency. The equivalent adiabatic efficiency of wet compression process is defined as

$$\eta_{ec}=\frac{W_{di}}{W_w}=\frac{\eta_d W_d}{W_w} \tag{30}$$

For ideal compression process or isentropic wet compression process, we have $W_w=W_{wi}$. In this case, equivalent adiabatic efficiency is

$$\eta_{eic}=\frac{W_{di}}{W_{wi}} \tag{31}$$

Generally speaking, the isentropic work of wet compression is less or equal to the isentropic work of dry air compression, which means the equivalent adiabatic efficiency will be $\eta_{eic}\geqslant 1$.

Wet Isentropic Compression Efficiency. If we take wet isentropic compression work as comparing basis to evaluate the actual wet compression process, the compression effectiveness can be determined by the following wet isentropic efficiency:

$$\eta_w=\frac{W_{Wi}}{W_W} \tag{32}$$

Such efficiency reflects the extent of actual wet compression process approaching to the ideal wet compression process. Generally, the wet isentropic compression efficiency has $\eta_w<1.0$.

Efficiency of Wet Compression. The effectiveness of wet compression process can also be judged with ''efficiency of wet compression'' defined as

$$\eta_{wd}=\frac{W_d-W_w}{W_d-W_{wi}} \tag{33}$$

where, W_d is dry air actual compression work.

This kind of efficiency reflects the ratio of deviation of actual wet compression process from dry air actual compression process and the deviation of ideal wet compression process from dry air actual compression process. It can also be utilized to evaluate the actual wet compression.

If we compared the dry air compression with wet air compression using the ''equivalent adiabatic efficiency,'' generally we have

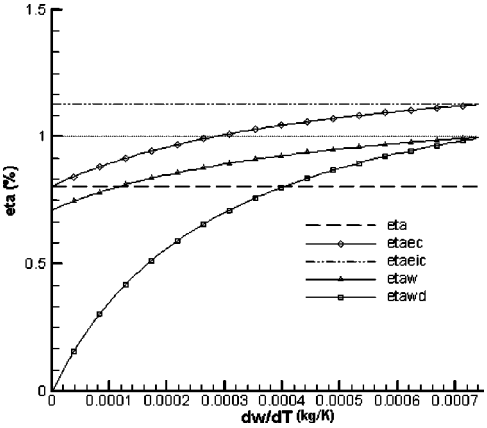

Fig. 9 Efficiencies of wet compression process

$$\eta_d\left(=\frac{W_{di}}{W_d}\right)<\eta_{ec}\left(=\frac{W_{di}}{W_w}\right)<\eta_{eci}\left(=\frac{W_{di}}{W_{wi}}\right) \tag{34}$$

Actually, because the wet compression process may have some additional losses for the wet compressor shrouds, friction between different phases, breaking water droplets and the flow coefficient deviation from its optimal value of present compressor, etc., the equivalent adiabatic efficiency η_{ec} may not be greater than 1.0. However, it will be surely greater than dry adiabatic efficiency.

Figure 9 shows the efficiencies of wet compression that defined above. Here the dry air polytropic efficiency is $\eta_p=0.85$. The ''equivalent adiabatic efficiency'' will greater than 1.0 even when evaporative rate is not very high. That indicates the great potential we can improve the compressor performance by wet compression techniques. For the evaluation of wet compression itself, the wet isentropic compression efficiency ($etaw$) and efficiency of wet compression ($etawd$) may be more convenient because of the maximum values of them is 1.0. Which one is used depends on how to evaluate the wet compression.

Discussion on the Diagram of Wet Compression Process

Representing Wet Compression Process on the p-v and T-S Diagrams of Dry Air Compression Process. If we represent the wet compression process on the p-v and T-S diagrams of dry air compression process, it is as shown in Figs. 10 and 11. The diagrams can be used to compare the wet compression process with other dry air compression processes, i.e., isentropic process, isothermal process, and polytropic process.

In these figures, $1-2k$ represents the wet compression process.

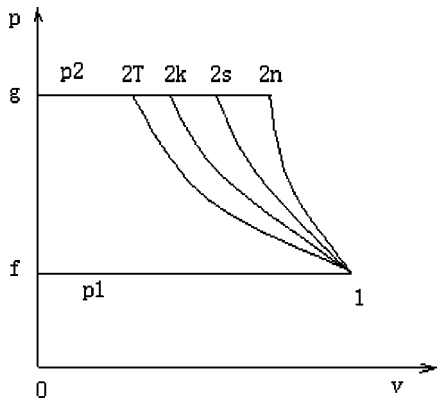

Fig. 10 p-v diagram of compression processes

Downloaded 31 May 2010 to 171.66.16.27. Redistribution subject to ASME license or copyright; see http://www.asme.org/terms/Terms_Use.cfm

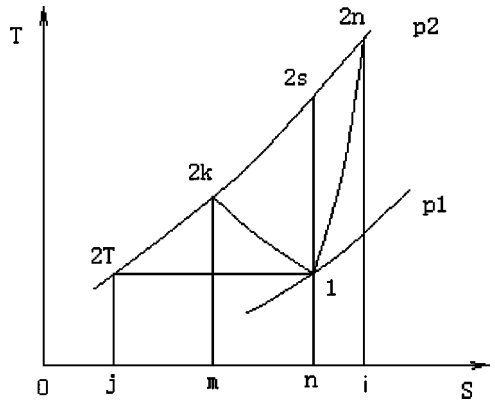

Fig. 11 *T-S* diagram of compression processes

Based on the p-v diagram, the compression works of the compression processes are the following areas:

$$W_{CT}=f-1-2_T-g-f \quad \text{(Isothermal)}$$

$$W_{CK}=f-1-2_k-g-f \quad \text{(Wet compression)}$$

$$W_{CS}=f-1-2_S-g-f \quad \text{(Isentropic)}$$

$$W_{CN}=f-1-2_n-g-f \quad \text{(Polytropic)}$$

Comparing the areas of these processes, we get the conclusions

$$W_{CT}<W_{CK}<W_{CS}<W_{CN}$$

From the T-S diagram, the compression work of these processes can be taken as the areas

$$W_{CT}=n-1-2_T-j-n \quad \text{(Isothermal)}$$

$$W_{CK}=n-1-2_k-2_T-j-n \quad \text{(Wet compression)}$$

$$W_{CS}=n-2_s-2_T-j-n \quad \text{(Isentropic)}$$

$$W_{CN}=i-2_n-2_T-j-i \quad \text{(Polytropic)}$$

The work difference between wet compression process and dry air isentropic compression process is

$$\Delta W=W_{CS}-W_{CK}=1-2_S-2_K-1 \quad \text{(Area)}$$

The heat released by hot compressed air is $\Delta Q=n-1-2_K-m-n$, which is absorbed and utilized by the evaporating water droplet in the wet compression process. A part of extra heat in area $n-2_s-2_k-m-n$ has to be added for heating the wet and low temperature air. However, such a heat partly comes from released heat $n-1-2_K-m-n$ and the remaining part is equivalent to the energy saving of compression work $1-2_S-2_K-1$.

The work saving is more considerable, if we compare the wet compression works with the dry air actual compression process

$$\Delta W=W_{CN}-W_{CK}=n-1-2_K-2_n-i-n \quad \text{(area)}$$

As previously discussed, for the same compression pressure ratio $\pi=p_2/p_1$, the exit temperature of wet isentropic compression process is lower than that of dry air isentropic compression process. From the point of wet air, the isentropic process is $1-2k$ on the T-S diagram (Fig. 12). If we draw the dry air isentropic process in the same chart, it is along the line $1-2s$. For wet compression, it is something like isobar line shifts to the dash line position.

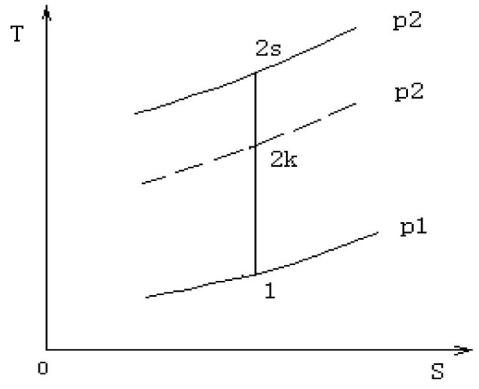

Fig. 12 *T-S* diagram of isentropic wet compression process—1–2*s* dry air isentropic compression process, 1–2*k* wet air isentropic compression process

Evaporative Rate of Water Droplet

The evaporative rate of water droplet is very important to the wet compression process. According to Langmuir-Maxwell method [11]

$$\frac{dw}{dt}=-\frac{df}{dt}=-\frac{2\pi D_v d_p}{RG_a}\left(\frac{P_L}{T_L}-\frac{P_G}{T_G}\right) \tag{35}$$

Here $dw/dt=(dw/dT)(dT/dt)$. p_L, T_L are pressure and temperature on the surface of droplet, they can be taken as saturated pressure and temperature. p_G, T_G are environmental pressure and temperature. D_v is diffusive coefficient.

Equation (35) is rewritten as

$$\frac{df}{dt}=\frac{2\pi D_v d_p}{RG_a}\left(\frac{p_s}{T_s}-\frac{P_G}{T_G}\right) \tag{36}$$

If we take $T_S=T_G$, Eq. (36) is simplified as

$$\frac{df}{dt}=\frac{2\pi D_v d_p}{RG_a T_G}(p_s-p_G) \tag{37}$$

That is the evaporative rate.

If the droplet is very small, Kelvin effect has to be taken into account [12]. Because free energy function is

$$F=h-Ts=u+pv-Ts \tag{38}$$

Then we have

$$dF=du+pdv+vdp-Tds-sdT \tag{39}$$

According to the first law of thermodynamics

$$Tds=du+pdv \tag{40}$$

Equation (39) is

$$dF=vdp-sdT \tag{41}$$

In evaporating process

$$dF=vdp \tag{42}$$

$$\Delta F=\int_{P_L}^{P_S} v\,dp=RT\int_{P_L}^{P_S}\frac{dp}{p}=RT\ln\frac{p_s}{p_L} \tag{43}$$

and

$$\Delta F=v\int dp=v\Delta p=v4\sigma/d_p=\frac{4\sigma}{d_p\rho_L}$$

Therefore, we get

$$\ln\frac{p_s}{p_L}=\frac{4\sigma}{d_p\rho_L RT} \tag{44}$$

If the water droplet is so small that close to zero, Fuchs effect has to be considered [11]. Then the evaporative rate is revised as

Downloaded 31 May 2010 to 171.66.16.27. Redistribution subject to ASME license or copyright; see http://www.asme.org/terms/Terms_Use.cfm

$$\frac{df}{dt}=\frac{2\pi D_v d_p}{RG_a}\left(\frac{p_L}{T_L}-\frac{P_G}{T_G}\right)\left[\frac{2\lambda+d_p}{d_p+5.33(\lambda^2/d_p)+3.42\lambda}\right] \quad (45)$$

where, λ is average free length of gaseous molecule.

Evaporation Time of Water Droplet

The water droplet injected into the airflow of compressor must be evaporated in a short time. So the droplet should be small enough to fulfill such an evaporation requirement.

The liquid mass change is

$$dM=d(fG_a)=4\pi r^2 dr\rho_L=\frac{\pi d_p^2}{2}dd_p\rho_L \quad (46)$$

Considering Eq. (35), we get the water droplet diameter-reducing rate

$$\frac{dd_p}{dt}=\frac{4D_v}{R\rho_L d_p}\left(\frac{p_G}{T_G}-\frac{P_L}{T_L}\right) \quad (47)$$

Integration of Eq. (47) from d_1 to d_2 gives

$$\int_{d_1}^{d_2} d_p dd_p=\int_0^t \frac{4D_v}{R\rho_L}\left(\frac{P_G}{T_G}-\frac{P_L}{T_L}\right)dt \quad (48)$$

That is

$$d_2^2-d_1^2=\frac{8D_v t}{R\rho_L}\left(\frac{P_G}{T_G}-\frac{P_L}{T_L}\right)_M \quad (49)$$

where subscript M means average value at the evaporation process. Therefore, the drying ($d_2\rightarrow 0$) time of droplet with initial diameter $d_1=d_p$ is

$$t=\frac{R\rho_L d_p^2}{8D_v\left(\frac{P_L}{T_L}-\frac{P_G}{T_G}\right)_M} \quad (50)$$

For modern gas turbine, the axial velocity in compressor is in order of 10^2 m/s, so the maximum staying time of droplet is generally in order of 0.01 s, from Eq. (50), the calculated diameter of droplet should smaller than 20 μm.

The foregoing result is the minimum requirement. In fact, the smaller is the droplet diameter, the better evaporative effect can be achieved. Where the injection position is nearer to the inlet, the finer is required for injected mist. If the droplet diameter is $d_p \leqslant 5$ μm, it can move along the streamlines; and if the droplet has smallest diameter, it is not only good for evaporating, but also has higher flow efficiency due to the least disturbance to airflow.

Aerodynamic Breaking of Water Droplet in High-Speed Airflow

The diameter of water droplet, which just leaves the nozzle, depends on the nozzle diameter of sprayer and the injection pressure. The nozzle diameter cannot be too small in considering the machining difficulty and contaminates blocking problem. If the injecting pressure is in the range of 1.0 to 10.0 MPa, the diameter of water droplet will be in the order of 10^1 to 10^2 μm [11]. Water heating can reduce the diameter, but it will not prevent for further breaking. The air or steam-driven sprayer can refine the droplets, however, that demands higher-pressure driving air or steam.

The high-speed airflow in compressor is of the ability to break water droplet in itself. For this reason, the final diameter d_p of droplet injected into the airflow is not only depending on the performance of injection nozzle, but also depending on the aerodynamic breaking ability of high-speed airflow. That is to say, the final diameter of water droplet depends on the ratio of aerodynamic force of airflow and the droplet surface tension, namely Weber number or Weber criterion.

After aerodynamic breaking, the diameter of droplet is

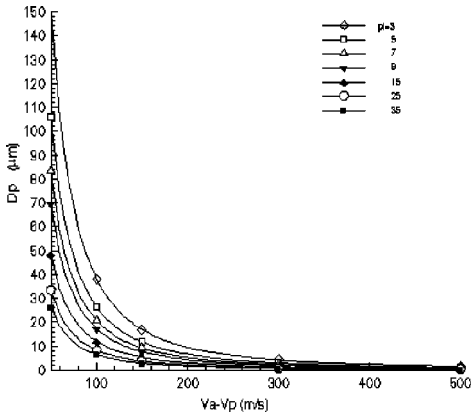

Fig. 13 Droplet diameter under different environmental pressure

$$d_p=\mathrm{We}_{\mathrm{cr}}\frac{2\sigma}{\rho_a(V_a-V_p)^2} \quad (52)$$

where V_p is the speed of water droplet. $\mathrm{We}_{\mathrm{cr}}$ is critical Weber number.

Under different environmental pressures and velocity gradients, the final droplet diameters are shown in Fig. 13. When the velocity gradient is above 150 m/s, the droplet diameters are less than 20 μm in any case. Such a diameter can satisfy the evaporative requirement. It can also be seen that the higher is the environmental pressure, the finer is the diameter of droplet.

The breaking time is also a very important factor to be considered for injected water droplets. Figure 14 is the breaking time of droplets with diameters 200 and 1000 μm. According to the figure that the breaking time is in the order of 10^{-4}–10^{-5} s. That means the water droplet can be broken very quickly.

Conclusion

Thermodynamic model of wet compression process is established in this paper. Ideal wet compression process, actual wet compression process, water droplet evaporation rate, wet compression work, inlet evaporative cooling, concept of wet compression efficiency and aerodynamic breaking of water drop etc., are discussed. The results indicate that:

• Effective cooling can be achieved through wet compression. Such a cooling brings the reducing of compression work. The wet compression work can even be lower than that of dry air isentropic compression work. If we take the increase of turbine output

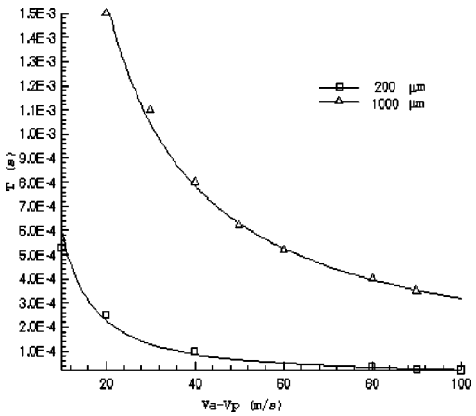

Fig. 14 Breaking time of water droplets in high-speed airflow and velocity gradient

Downloaded 31 May 2010 to 171.66.16.27. Redistribution subject to ASME license or copyright; see http://www.asme.org/terms/Terms_Use.cfm

power into account, we can say that wet compression technique has great potential to enhance the performance of gas turbine.

• Because the decrease of compression work, the 'equivalent adiabatic efficiency' can be greater than 1.0, a new wet compression isentropic efficiency as defined in our paper is necessary for evaluating the wet compression process.

• The evaporation in wet compression process makes the index of process and compression works differ from dry air compression process fundamentally. A new system for that is given in this paper.

• Evaporative rate, time and aerodynamic breaking and breaking time of water are also very important for wet compression. Some more detailed investigation will be carried for these problems.

• The decrease of compressor exit temperature arise the idea of WCR (wet cooling and regenerative) gas turbine, which will greatly increase the cycle efficiency.

Nomenclature

L = latent heat
w, f = steam-to-air ratio and water-to-air ratio, respectively
dw/dT = evaporative rate
k = isentropic index of wet compression
γ = isentropic index of dry air compression
n = polytropic exponent of dry air compression process
m = polytropic index of actual wet compression process
$h_a\ h_w\ h_f$ = enthalpies of air, steam and water
d_p = diameter of water droplet
G_a = air mass flow rate
σ = surface tension of water droplet

Subscripts

0, 1, 2 = environment, inlet, and outlet
a, w, f = air, steam (or wet), water
g = saturated steam
d = dry
i = ideal

References

[1] "LM6000 Spring Design Enhanced to Increase Power and Efficiency," 2000, Gas Turbine World, July–Aug., pp. 16–19.
[2] Rising, B., and Hitzel, R., 2000, "Wet Compression Upgrade Technology: Operating Experience," Power-Gen Europe Conference.
[3] Aagren, N. D., Cavani, A., and Westermark, M. O., 1997, "New Humidifier Concept in Evaporative Gas Turbine Cycles," Proc., TAIES'97, pp. 270–276.
[4] De Lucia, M., Bronconi, R., and Carnevale, E., 1994, "Performance and Economic Enhancement of Cogeneration Gas Turbines Through Compressor Inlet Air Cooling," ASME J. Eng. Gas Turbines Power, **116**, pp. 360–365.
[5] El-Awad, M. M., 2000, "A Thermodynamic Comparison of Gas-turbine Power Augmentation by Inlet-air Cooling and Steam Injection," Proc., Int. Conference on Fluid and Thermal Energy Conversion, Bandung, Indonesia.
[6] De Lucia, M., and Carnevale, E., 2001, "Gas Turbine Inlet Air Cooling System Increases Performance of a Natural Gas Injection Station," Energy-Tech.
[7] Nagoya, K. K., 1997, "Guidance & Propulsion Systems Works," Mitsubishi Heavy Industries Technical Review.
[8] De Lucia, M., Lanfranchi, C., and Boggio, V., 1995, "Benefits of Compressor Inlet Air Cooling for Gas Turbine Cogeneration Plants," 95-GT-311.
[9] Takizawa, M., Ohara, H., and Morikawa, K., 1993, "Repowering of Thermal Power Plants as Fully-Fired Combined Cycle Generating Plants," 93-GT-473.
[10] Zheng, Q., Sun, Y., et al., 1997, "Experiments on Water Spraying Internal Cooling in Compressor of Gas Turbine," 97-GT-158.
[11] Chai, Y., 1995, *Two-Phase Flows in Steam Turbine*, Xi'an Jiaotong University Press.
[12] Hinds, W. C., 1999, *Aerosol Technology: Properties, Behavior, and Measurement of Airborne Particles*, Wiley, John & Sons Inc., New York, NY.

Downloaded 31 May 2010 to 171.66.16.27. Redistribution subject to ASME license or copyright; see http://www.asme.org/terms/Terms_Use.cfm

G. Brennan
e-mail: graham.brennan@rolls-royce.com

N. W. Harvey

M. G. Rose

N. Fomison

M. D. Taylor

Turbine Systems,
Rolls-Royce plc,
Derby, UK

Improving the Efficiency of the Trent 500-HP Turbine Using Nonaxisymmetric End Walls—Part I: Turbine Design

This paper describes the redesign of the HP turbine of the Rolls-Royce Trent 500 engine, making use of nonaxisymmetric end walls. The original, datum turbine used conventional axisymmetric end walls, while the vane and (shrouded) rotor aerofoil profiles were nominally the same for the two designs. Previous research on the large-scale, low-speed linear cascade at Durham University (see Hartland et al. Compositor: complete ref. in Abstract), had already demonstrated significant potential for reducing turbine secondary losses using nonaxisymmetric end walls-by about one third. This paper shows how a methodology was derived from the results of this research and applied to the design of the single-stage Trent 500-HP turbine (model rig). In particular, the application of a new linear design system for the parametric definition of these end wall shapes (described in Harvey et al. Compositor: complete ref. in Abstract) is discussed in detail.
[DOI: 10.1115/1.1450766]

Introduction

Few successful attempts have been made to reduce secondary loss through application of end-wall profiling to a blade row. One successful application of profiling has been demonstrated in the Linear Cascade at Durham University by Hartland et al. [1]. The end wall investigated at Durham demonstrated the advantages of end-wall profiling in a low-speed linear cascade which showed a 34% reduction in secondary loss. In addition to this, profiling of the end-wall has the advantage of reducing exit whirl angle deviations which in turn would reduce incidence loss for the downstream blade row. However, this benefit has not been quantified in the linear cascade.

The objective of this work is to validate the potential implied by the Durham Cascade results in an engine representative environment. The Trent 500 model test rig is selected as the basis for the experiment. This cold flow rig is a 75% scale model of the Trent 500-HP turbine. The objective of the test is to compare the efficiency of the profiled end-wall turbine with that for the existing axisymmetric turbine at the same specific work output. The design is constrained to have the same aerofoil geometry as the axisymmetric turbine.

Nonaxisymmetric end-wall profiling is applied to the HP NGV and rotor hub and casing end walls. The design process and predicted benefit in performance are described in Part 1; Part 2 of this paper describes the model test rig results.

Secondary Loss in Turbomachinery

Secondary loss is a term which is generally used to describe all other losses, excluding overtip leakage and aerofoil profile loss occurring within a turbine stage. It is the least understood loss mechanism and typically it accounts for 33% of the total loss in a turbine stage; Denton [2].

However, the work presented here focuses on reducing classical secondary loss. This is associated with the loss produced by the low momentum fluid on the annulus walls which becomes overturned due to the influence of the pressure gradients created by the aerofoil as it turns the air through the blade row. This leads to the formation of passage vortices near the hub and casing.

As the flow impinges on the leading edge of the aerofoil, the radial variation in stagnation pressure creates flow along the leading edge of the aerofoil towards the end wall. When this flow reaches the end-wall, it then travels upstream along the annulus wall. Where the incoming boundary layer flow meets this flow, separation occurs and a horse shoe vortex forms around the leading edge of the aerofoil. The strength of this vortex is proportional to the thickness of the aerofoil leading edge and the variation in radial pressure gradient along the leading edge.

The cross passage pressure gradient produced by the aerofoil turning the flow drives the low momentum flow on the end wall from the pressure surface towards the suction surface. This flow meets the incoming boundary layer flow and a 3-D separation line is produced across the end wall. At the intersection of the separation line and the suction surface, a passage vortex is formed. This vortex runs along the suction surface and is continuously fed by the cross flow from the pressure surface. The strength of the end-wall flow is therefore a function of the cross passage pressure gradient which itself is proportional to the level of turning produced by the blade row. More detailed descriptions of the end-wall flows are provided by Hodson and Dominy [3] and Sieverding [4].

On a turbine rotor end wall, the incoming boundary layer is skewed in the opposite direction to the end-wall pressure gradient. This induces negative incidence on the aerofoil near the end wall which creates strong circumferential vorticity rotating in a direction which augments the secondary flows. This is in contrast to a compressor rotor, where the boundary layer is skewed in the same direction as the pressure gradient. In this case, positive incidence is induced on the blade row and the direction of the vorticity acts to oppose the secondary flows driven by the pressure gradient, thereby reducing the secondary loss. Therefore, the skewing of the boundary layer leads to a significant increase in the secondary loss of a turbine rotor; see Walsh and Gregory-Smith [5]. A summary of the entropy generation process within end-wall flow is given by Denton [2].

From a geometric point of view, for a given blade height and spacing, a longer chord length generates larger secondary flows on the end walls. Therefore, the secondary loss will be higher as a proportion of the overall loss. For this reason, high aspect ratio aerofoils are desirable in order to minimize secondary loss.

In summary, therefore, classical secondary loss in a turbine is

Contributed by the International Gas Turbine Institute and presented at the International Gas Turbine and Aeroengine Congress and Exhibition, New Orleans, Louisiana, June 4–7, 2001. Manuscript received by the IGTI, November 14, 2000. Paper No. 2001-GT-444. Review Chair: R. A. Natole.

 Copyright © 2003 by ASME

Downloaded 31 May 2010 to 171.66.16.27. Redistribution subject to ASME license or copyright; see http://www.asme.org/terms/Terms_Use.cfm

mainly a function of angle of turning, inlet relative stagnation pressure profile, aspect ratio, and leading edge thickness.

Previous Work

Early attempts to reduce secondary loss through end-wall profiling involved 2-D axisymmetric changes to the annulus wall. Geometries tested by Kopper and Milano [6], Atkins [7], and Dossena et al. [8] involved a strong contraction of the passage producing an increase in velocity ratio across the row. These geometries produced increases in loss near the profiled end-wall and reductions in loss near the unprofiled end wall. Although benefits were achieved, the adverse effects downstream cancelled out the benefit found in the upstream profiled blade row.

Three-dimensional nonaxisymmetric profiles have been tested by Morris and Hoare [9], Atkins [7], Hartland et al. [10]. Morris and Hoare applied profiling normal to the mid-passage streamline. Their design reduced the loss on the unprofiled side of the passage but led to higher loss on the profiled side of the passage. Atkins attempted to reduce the end-wall pressure gradient by applying a bump or trough near the aerofoil surfaces. The profiles tested resulted in an overall increase in loss relative to the axisymmetric case due to separations occurring near the profile. The blade wake also became strongly twisted.

Rose [11] attempted to use end-wall profiling to control the exit static pressure at the trailing edge platform. A sinusoidal profile was applied in the circumferential direction which was intended to average out the static pressure in order to reduce the peak pressure at the interplatform gap between the HP NGV and the HP rotor. By reducing the peak pressure, the turbine disk coolant leakage flow could be reduced. The geometry was tested by Hartland [10] and the profiling was shown to accurately control the static pressure in the circumferential direction. Following the success of this work, Rolls-Royce and Durham University began a series of tests to examine the use of nonaxisymmetric profiling within the passage to reduce secondary loss.

Hartland et al. [1] tested a nonaxisymmetric profile at Durham University designed to reduce secondary flows. The cascade is a low speed linear cascade operating at an exit Mach number of 0.1 with a Reynolds number of 400,000 and the geometry is representative of an HP rotor. The end-wall design consisted of a circumferential sinusoidal perturbation with its peak at the pressure surface near the leading edge of the aerofoil, Harvey et al. [12]. Further down the passage, another sinusoid of lower amplitude with its peak near the late suction surface is located. The end-wall design achieved a significant reduction in the strength of the cross passage pressure gradient early in the passage. The net reduction in mixed out secondary loss was 34%, which was accompanied by a reduction in the whirl angle deviation at cascade exit. A reduction in the overturning near the end wall was found to be due to a countervortex rotating in the opposite direction to and beneath the passage vortex. This vortex was due to the low pressures near the suction surface created by the convex curvature of the local profiling. The loss core of this countervortex was smaller than the passage vortex and led to increased loss near the end wall. The loss core of the passage vortex was found to be reduced relative to the axisymmetric case which was considered to be evidence of a reduction in the end wall flow swept into the passage vortex.

Following the success of research work at Durham it was decided to test the concept in engine representative conditions.

Design Methodology

The program used to generate the end-wall geometry is called FAITH (forward and inverse 3-D design) and a general description of this code is given by Shahpar and Lapworth [13].

The profiled end-wall shape is determined by six control stations which are fixed at specified axial distances along the mean camber line of the aerofoil. See Fig. 1 for a view of the control planes selected for the HP NGV design. At each station a sinusoidal shape may be generated in the circumferential direction. The height and phase angle of each wave are specified by the user. FAITH fits a b-spline in the axial direction through each control station. The final geometry is a surface fitted over the six b-splines. In order to limit the axial extents of the profiling, additional stations are placed upstream and downstream of the control stations.

FAITH offers the choice of four types of perturbations at each station, namely, 0th, 1st, 2nd and 3rd-order harmonics. A 0th harmonic implies an axisymmetric change in annulus shape which creates either a local raising or lowering of the annulus height. This produces a uniform change in cross passage area. A 1st harmonic perturbation implies a single sinusoid across the passage width, a 2nd harmonic perturbation implies two sinusoids across the passage, etc. The sinusoidal shape helps to conserve the cross passage area. Where combinations of harmonics are used at each station, a Fourier series expansion is used to combine their effects across the control station. In order to reduce the design space, only 0th and 1st-order harmonics are incorporated into the current design.

To begin the design process, a steady-state base case solution of the axisymmetric blade row is obtained. The code used for all nonlinear analysis is sz02 which is a finite volume 2nd-order accurate pressure correction solver based on the Moore's elliptic flow program (MEFP) algorithm; Moore [14]. The turbulence model employed is the Prandtl mixing length model. Sz02 is selected for its ability to model the end-wall geometry while providing a good simulation of the flow field.

Figures 2 and 3 present the base case meshes for the HP NGV and rotor for the Trent 500 model test rig. The mesh size used for the NGV is 150,000 and the Rotor uses 70,000 cells.

Having generated the Base Case solution, the next step is to create a matrix of perturbed geometries for the hub and casing which are used as a guide to determine the optimum phase of the perturbation for each control station. For each station, six sets of

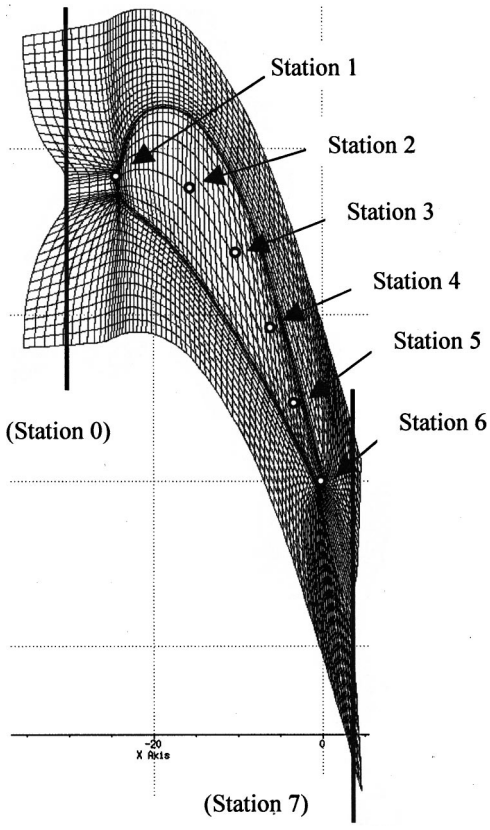

Fig. 1 Plot of control points along the mesh

Downloaded 31 May 2010 to 171.66.16.27. Redistribution subject to ASME license or copyright; see http://www.asme.org/terms/Terms_Use.cfm

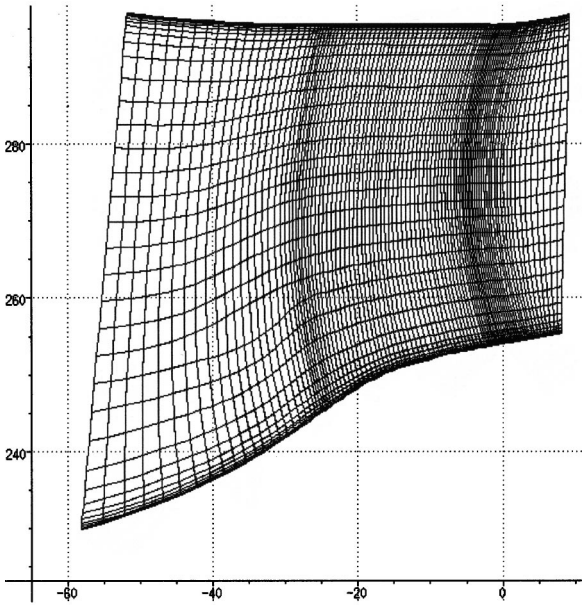

Fig. 2 HP NGV sz02 mesh

perturbation geometries are created which consist of two 0th Harmonic (positive and negative amplitude) and four 1st harmonic sinusoidal waves (0, 90, 180, 270 deg phase shifts). FAITH is used to generate all of the perturbation geometries and the associated files required to run each geometry within sz02. Sz02 is then used to create a nonlinear prediction of the flowfield for each perturbation. Therefore, a total of $6\times6\times2=72$ CFD runs are performed for each blade row.

A parameter typically used in secondary loss measurements is secondary kinetic energy (SKE), Gregory-Smith [15]. SKE is the energy of the flow normal to an ideal primary flow (possibly defined by an inviscid model). It is usually assumed to be dissipated in subsequent mixing and thus should be well correlated with the secondary loss. In a 2-D linear cascade it is straight forward to define the ideal flow direction across the flowfield. It is much harder for highly 3-D blading. In FAITH, this reference direction is taken to be the circumferentially averaged flow direction at each height. The main problem with this definition is that the aerofoil's potential flowfield, particularly around the leading and trailing edges, appears as regions of high SKE.

In order to focus on the SKE changes to the vortical components of the flow, the dot product of the SKE and helicity is used. Helicity is defined as the flux of streamwise vorticity. This has the effect of excluding the bulk of the changes of SKE associated with the potential flowfield. However, it does not exclude the changes due to the potential field in the regions of vortical flow. This contribution though, should be small compared with the changes due to the vortical flow. The dot product of SKE and helicity (SKEH) is therefore considered to be a more suitable design parameter than SKE.

From the results of experimental work by Hartland et al. [1], it is expected that a successful design should reduce the exit whirl angle deviations produced by the passage vortex. This is indicative of a weakening of the strength of the vortex, and therefore a reduction in secondary loss. Experimental research has shown that a successful end-wall design produces a reduction in SKE and whirl angle along with a reduction in pressure loss. CFD analysis of the geometry showed similar changes in the first two parameters; however, it did not show a corresponding improvement in pressure loss. The reason for this poor loss prediction is related to mesh size and the Code's inability to predict the mixing processes accurately enough. Thus, for this study, the main design objectives are to minimize SKEH and whirl angle deviations. Other parameters are monitored to avoid excessive increases in pressure loss, exit whirl angle, or Mach number.

Each of the perturbations are processed for SKEH and compared with the result for the base case. Reviewing the results of all 1st harmonic perturbations hub end-wall, the perturbations which produce the strongest reductions in SKEH are combined together to produce a preliminary end-wall design. A nonlinear prediction of the flow field is then produced by sz02 for the selected geometry.

The initial design is then optimized by adding or removing 1st harmonic terms at selected stations. Having selected an optimum configuration, the foregoing process is repeated for the 0th harmonic terms. The optimized 1st and 0th-harmonic designs are combined together. The 1st-harmonic terms of this combined design are then optimized for phase location by adjusting the phase angle of the sinusoid at each station starting with stations 1 through 6. The final step in the process is to adjust the amplitudes of the perturbations until an optimized design is achieved. This procedure is then repeated for the casing end wall, resulting in a final hub and casing profiled end-wall design.

NGV Results

The selected designs are based on the results of steady state numerical solutions obtained from sz02. A perspective view of the HP NGV profiled end-wall (PEW) design is shown in Fig. 4.

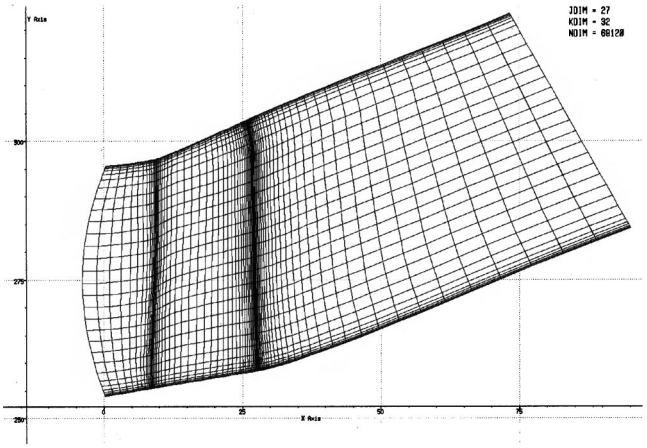

Fig. 3 HP Blade sz02 mesh

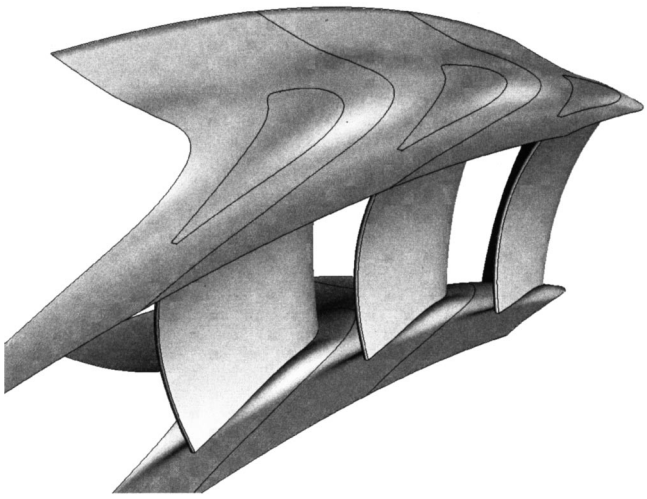

Fig. 4 HP NGV with profiled end wall

Downloaded 31 May 2010 to 171.66.16.27. Redistribution subject to ASME license or copyright; see http://www.asme.org/terms/Terms_Use.cfm

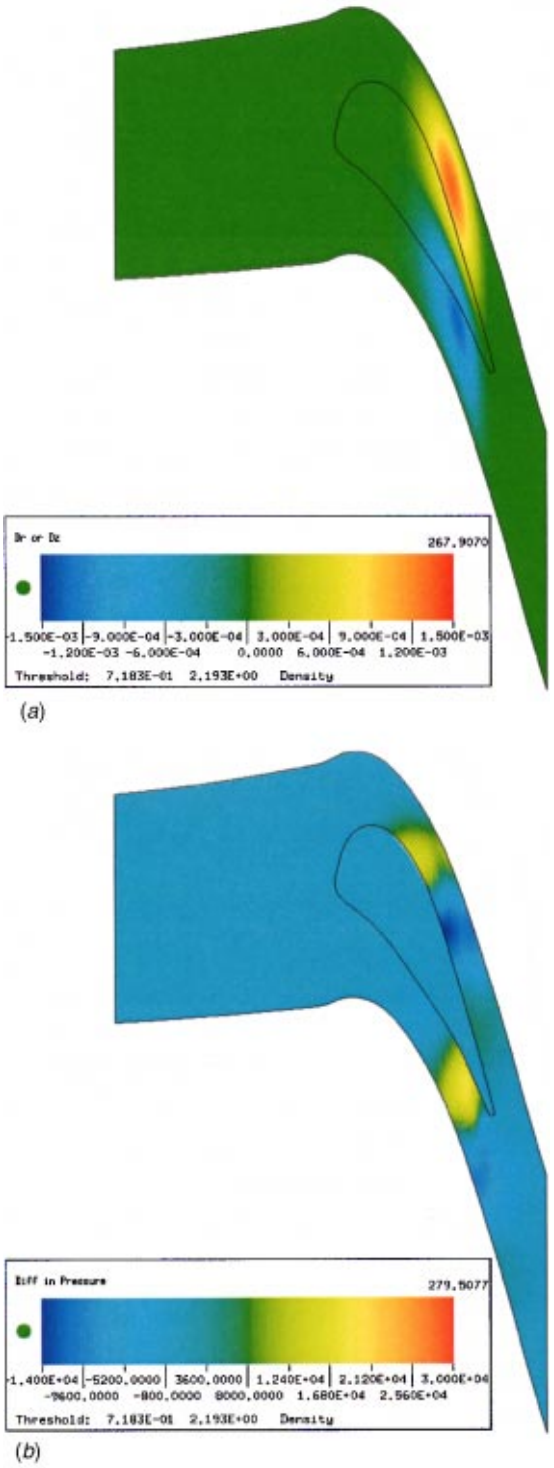

Fig. 5 NGV variation in hub (*a*) radial height (m), (*b*) surface static pressure (Pa)

The variation in radial height and surface static pressures are shown in Figs. 5(*a*) and (*b*), respectively, for the hub. These plots represent the difference between the axisymmetric and non-axisymmetric solutions. The radial variation in height is approximately −1.5 to +1.5 mm. The total wetted area of the profiled geometry is approximately +0.5% larger than the datum.

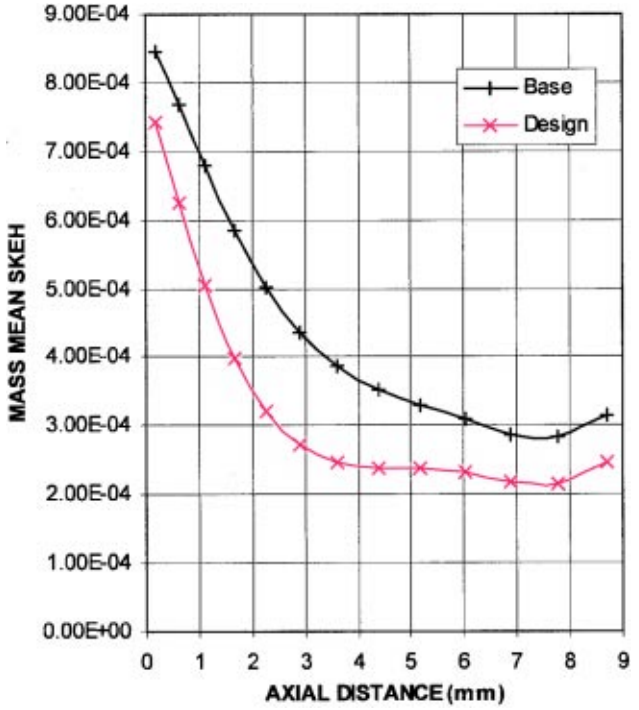

Fig. 6 Mass-averaged SKEH for NGV along axial direction; note: NGV trailing edge starts at axial position −2mm (not shown here)

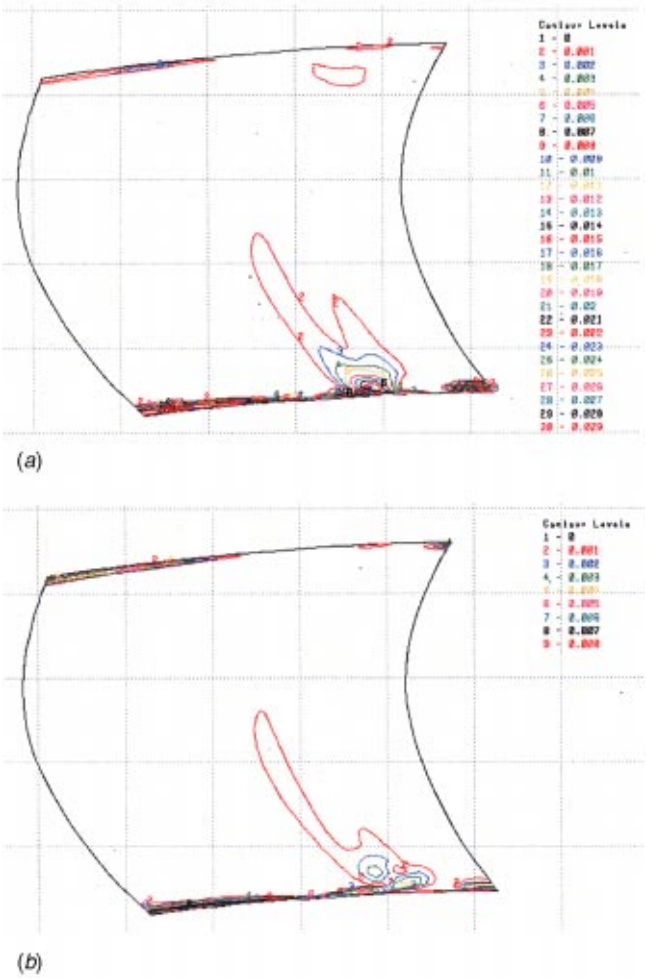

Fig. 7 Contours of SKEH at NGV exit—(*a*) base, (*b*) PEW design

Downloaded 31 May 2010 to 171.66.16.27. Redistribution subject to ASME license or copyright; see http://www.asme.org/terms/Terms_Use.cfm

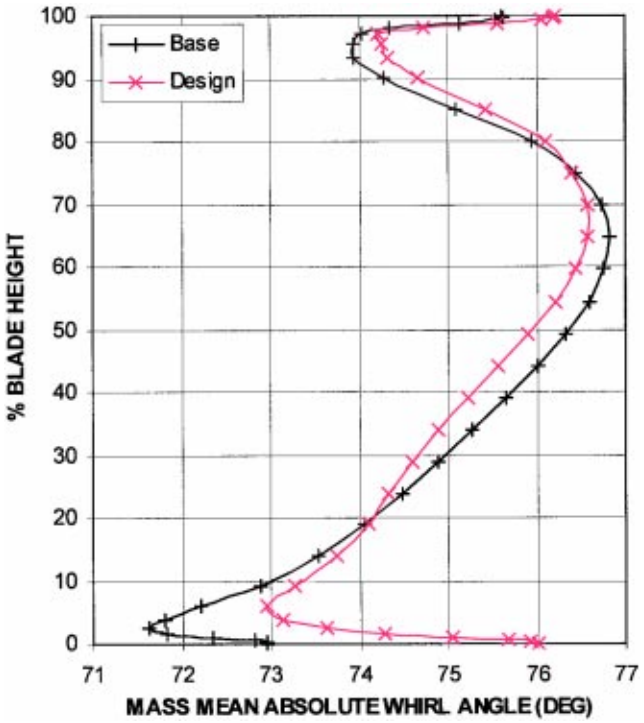

Fig. 8 Absolute whirl angle at NGV exit

The hub end-wall design results in an increased cross passage pressure gradient near the throat region followed by a reduction in the pressure gradient downstream of the throat.

The mass averaged values of SKEH are presented in Fig. 6 showing the average SKEH values from the trailing edge of the NGV to the leading edge of the HP blade. The plot shows the change relative to the base case. The net reduction in SKEH is taken to be 30% measured at a plane approximately half way from the trailing edge to the leading edge of the Rotor. Based on the results of experimental work of Hartland et al. [1], a reduction in SKEH is assumed to produce a proportional reduction in secondary loss. The improvement in stage efficiency due to the HP NGV is therefore estimated to be +0.24%.

Figure 7(*a*) is a plot of contours of SKEH for the base case at a plane approximately 20% Cax downstream of the trailing edge. The same plot is presented in Fig. 7(*b*) for the PEW case showing a strong reduction in the SKEH for the hub passage vortex.

The resulting absolute whirl angles at the NGV exit plane (20% Cax) are shown in Fig. 8 for the Base and end-wall designs. The latter produces a reduction in the whirl angle deviations over most of the span, but produces higher angles at the hub and casing. In the relative frame, the changes at mid-span lead to slightly increased negative incidence, while near the hub and casing the whirl angles lead to reduced negative incidence.

Figure 9 presents the isentropic Mach number distribution on the NGV hub. The profile exhibits a reduction in lift near the forward portion of the aerofoil and an increase of the lift near the rear portion of the aerofoil. This aft-loading of the aerofoil appears to be a common feature of all profiled end-wall designs to date.

The lower Mach numbers on the early suction surface results in a small reduction in profile loss which is offset to a degree by the increase in Mach number further downstream.

Rotor Results

A plot of the HP rotor PEW design is presented in Fig. 10. The variation of radial height and surface static pressures are shown in Figs. 11(*a*) and (*b*), respectively, for the hub end-wall design only. The end-wall height varies from +0.5 to −1.7 mm on the hub. The height on the casing end-wall design varies from +0.8 to −0.8 mm.

The most significant changes to the pressure field occur near the suction surface of the aerofoil where the Mach numbers are high. The cross passage gradient is reduced early in the passage followed by an increase in the pressure gradient further downstream producing an aft loading effect on the aerofoil.

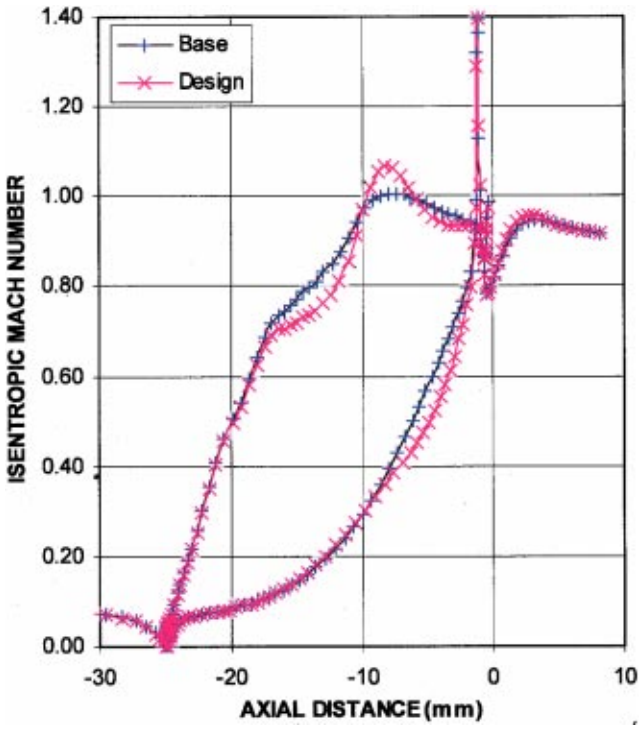

Fig. 9 NGV isentropic Mach no. at 10 percent height

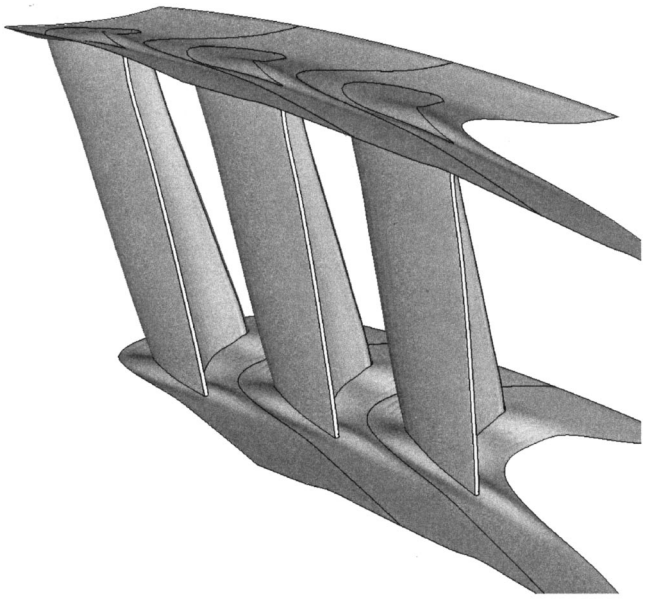

Fig. 10 HP rotor with profiled end walls

Downloaded 31 May 2010 to 171.66.16.27. Redistribution subject to ASME license or copyright; see http://www.asme.org/terms/Terms_Use.cfm

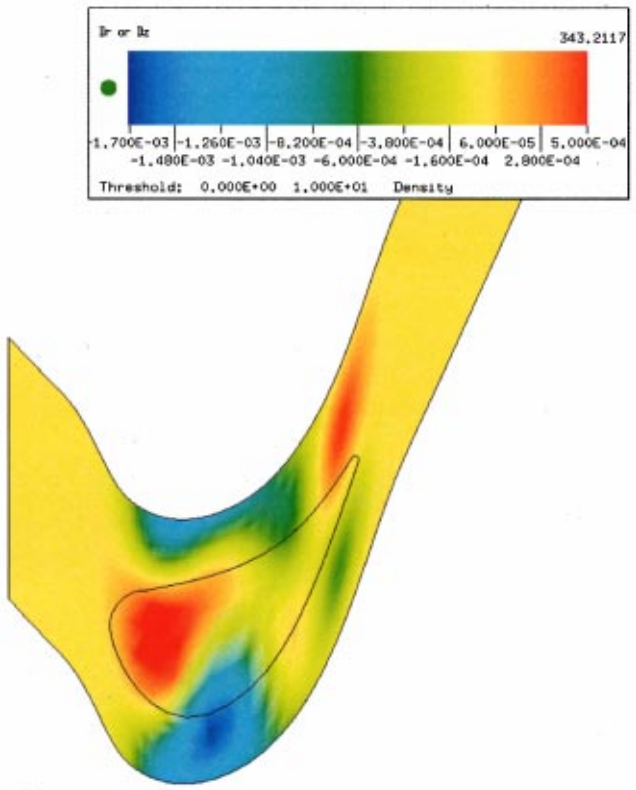

(*a*)

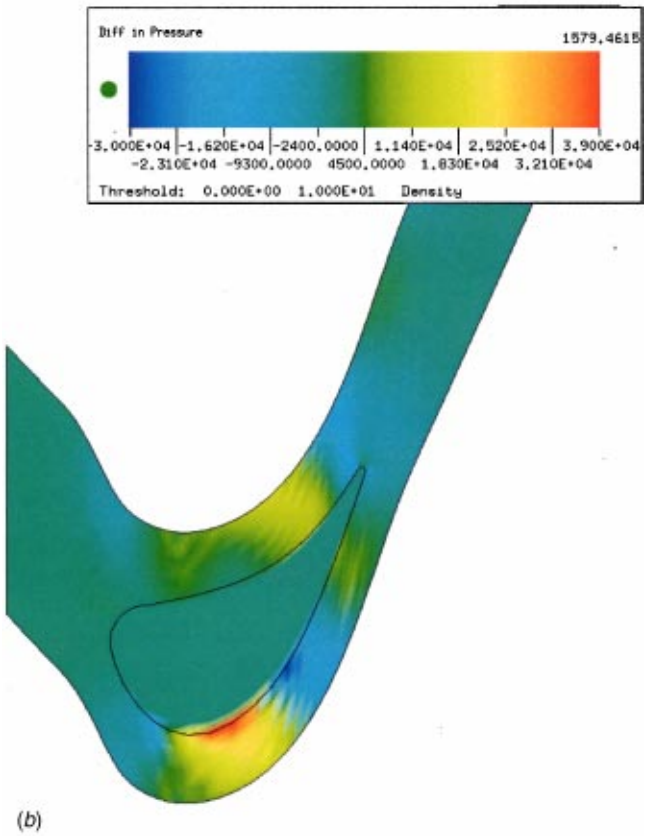

(*b*)

Fig. 11 Rotor hub variation in (*a*) radial height (m), (*b*) surface static pressure (Pa)

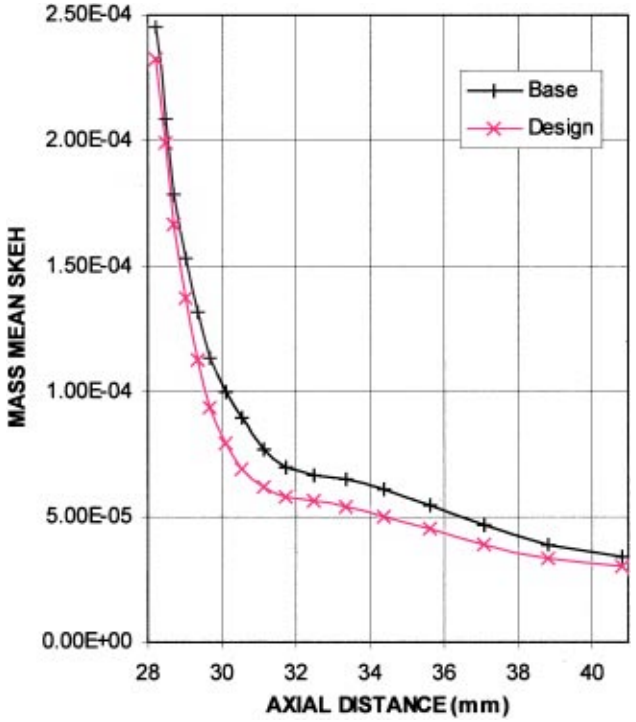

Fig. 12 HP rotor mass-averaged SKEH in axial direction; note: rotor trailing edge starts at axial position 28 mm

A plot of SKEH is presented in Fig. 12 showing the change in SKEH from the trailing edge of the rotor to the exit of the model. The average level of reduction is estimated to be 17%. This reduction in loss translates to an improvement in stage efficiency of +0.16%. The combined improvement (NGV + rotor) in stage efficiency for the turbine is therefore +0.4%.

Contours of SKEH at 20% Cax downstream of the trailing edge are shown in Figs. 13(*a*) and (*b*) for the base and design. In this case, significant reductions in the strength of the passage vortices near the hub and casing are visible indicating a reduction in the secondary flows.

The changes to the relative whirl angle are shown in Fig. 14 downstream of the rotor. The maximum reduction in whirl angle underturning near the hub is approximately 1 deg. The overturning has increased by 3 deg in the hub boundary layer and 1.5 deg in the casing boundary layer.

The isentropic Mach number at the hub is presented in Fig. 15. The distribution shows a strong reduction in lift early on in the passage and a large increase in lift in the later part of passage. The peak isentropic Mach number is 1.3. This high Mach number is caused by the convex curvature near the suction surface which causes the flow to accelerate. This feature is found to be strongly linked to the levels of SKEH reductions. The high Mach numbers are confined to a local area and there is no evidence of any flow separation downstream of the peak. Therefore, the increased Mach region is considered to be an acceptable design feature. At mid-height, there is no significant change to the lift distribution.

Conclusions

The addition of profiling to the end walls of the HP turbine is predicted to reduce secondary loss by 0.24% of stage efficiency for the NGV and by 0.16% for the rotor. The total improvement in stage efficiency for the HP turbine is therefore +0.4%.

Downloaded 31 May 2010 to 171.66.16.27. Redistribution subject to ASME license or copyright; see http://www.asme.org/terms/Terms_Use.cfm

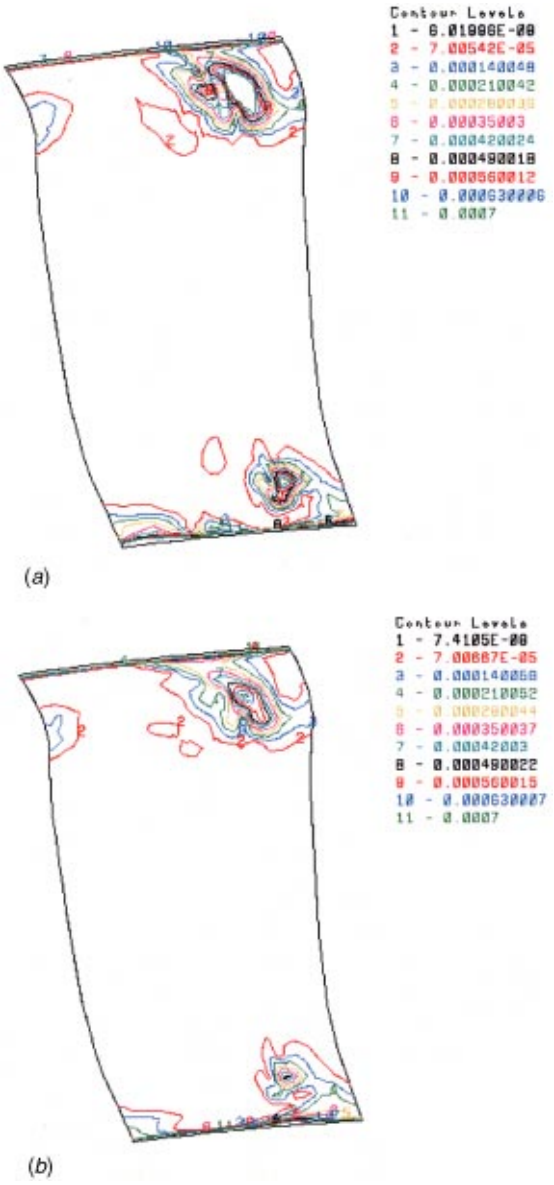

Fig. 13 Contours of SKEH at rotor exit—(*a*) base (*b*) PEW design

The whirl angle variations are reduced at exit of the NGV and Rotor. This allows for a more uniform flow distribution into the downstream blade row. However, the maximum overturning near the end-wall leads to higher exit whirl angles which increases the incidence angles on the roots of downstream blade row. The design criteria did not allow for a redesign of the aerofoil, which would be performed for a new engine design.

The lift distributions on the aerofoils near the end walls have become significantly aft loaded. This reduces aerofoil profile losses early in the passage but leads to increases in profile loss at the elevated Mach number regions. This effect is confined to 15% blade height nearest to the end walls.

The flow on the end wall appears to become more in-line with the primary flow direction suggesting a reduction in the secondary flow strength. As a consequence of this, it may be that some of the high loss fluid swept into the passage vortex remains on the end wall, which could explain the higher losses predicted on the end wall. Overall, the calculations of pressure loss show a small improvement for the NGV and a marginal increase in loss for the rotor.

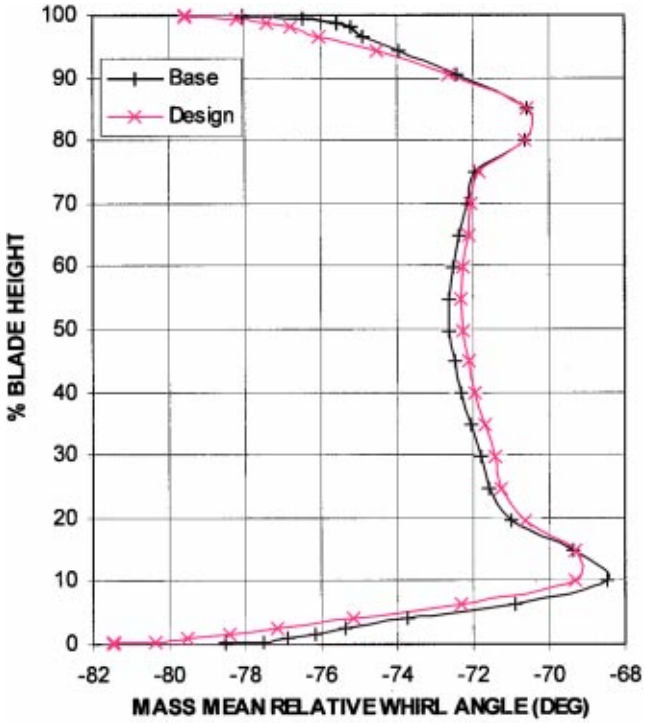

Fig. 14 Relative whirl angle at rotor exit

At present, the design process is performed through manual iteration. In order to reduce the design space, only designs comprising 0th and 1st-harmonic terms have been attempted. Therefore, it is intended to use a nonlinear optimization program to explore the possibilities offered by 2nd and 3rd-harmonic terms.

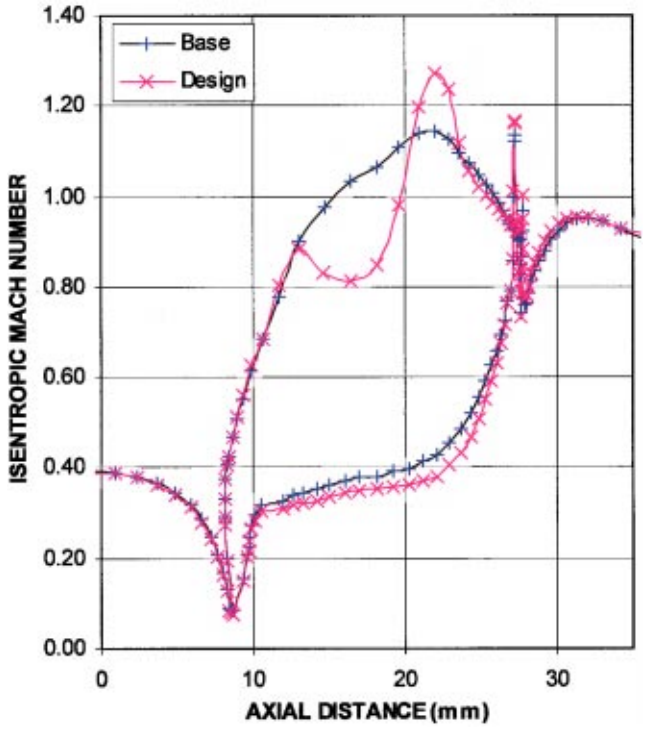

Fig. 15 HP rotor hub isentropic Mach no. (10% height)

Downloaded 31 May 2010 to 171.66.16.27. Redistribution subject to ASME license or copyright; see http://www.asme.org/terms/Terms_Use.cfm

Nomenclature

Cax = axial chord length
SKE = secondary kinetic energy
SKEH = secondary kinetic energy helicity
PEW = profiled end wall

References

[1] Hartland, J. C., Gregory-Smith, D. G., Harvey, N. W., and Rose, M. G., 1999, ''Non-Axisymmetric Turbine End Wall Design: Part II Experimental Validation,'' ASME 99-GT-338.
[2] Denton, J. D., 1993, ''Loss Mechanisms in Turbomachines,'' ASME 93-GT-435.
[3] Hodson, H. P., and Dominy, R. G., 1986, ''Three-Dimensional Flow in a Low Pressure Turbine Cascade at its Design Condition,'' ASME 86-GT-106.
[4] Sieverding, C. H., 1984, ''Recent Progress in the Understanding of Basic Aspects of Secondary Flow in Turbine Blade Passages,'' ASME 84-GT-78.
[5] Walsh, J. A., and Gregory-Smith, D. G., 1989, ''Inlet Skew and the Growth of Secondary Losses and Vorticity in a Turbine Cascade,'' ASME 89-GT-65.
[6] Kopper, F. C., Milano, R., and Vanco, M., 1980, ''An Experimental Investigation of Endwalls Profiling in a Turbine Vane Cascade,'' AIAA-80-1089.
[7] Atkins, M. J., 1987, ''Secondary Losses and End-Wall Profiling in a Turbine Cascade,'' I Mech. E C225/87, pp. 29–42.
[8] Dossena, V., Perdichizzi, A., and Savini, M., 1998, ''The Influence of Endwall Contouring on the Performance of a Turbine Nozzle Guide Vane,'' ASME 98-GT-71.
[9] Morris, A. W. H., and Hoare, R. G., 1975, ''Secondary Loss Measurements in a Cascade of Turbine Blades with Meridional Wall Profiling,'' ASME 75-WA/GT-13.
[10] Hartland, J. C., Gregory-Smith, D. G., and Rose, M. G., 1998, ''Non-Axisymmetric Endwall Profiling in a Turbine Cascade,'' ASME 98-GT-525.
[11] Rose, M. G., 1994, ''Non-Axisymmetric Endwall Profiling in the HP NGVs of an Axial Flow Gas Turbine,'' ASME 94-GT-249.
[12] Harvey, N. W., Rose, M. G., Taylor, M. D., Shahpar, S., Hartland, J., and Gregory-Smith, D. G., 1999, ''Non-Axisymmetric Turbine End Wall Design: Part I Three-Dimensional Linear Design System,'' ASME 99-GT-337.
[13] Shahpar, S., and Lapworth, B. L., 1998, ''A Forward and Inverse Three-Dimensional Linear Design System for Turbomachinery Applications,'' 4th ECCOMASS Computational Fluid Dynamics Conference, Athens, Sept. 7–11.
[14] Moore, J. G., 1985, ''Calculation of 3D Flow without Numerical Mixing,'' AGARD-LS-140 on 3D Computational Techniques Applied to Internal Flows in Propulsion Systems, pp. 8.1–8.15.
[15] Gregory-Smith, D., 1982, ''Secondary Flow and Losses in Axial Flow Turbines,'' ASME 82-GT-19.

Downloaded 31 May 2010 to 171.66.16.27. Redistribution subject to ASME license or copyright; see http://www.asme.org/terms/Terms_Use.cfm

O. Gentilhomme

N. J. Hills

A. B. Turner

Thermo-Fluid Mechanics Research Centre,
University of Sussex,
Brighton, East Sussex, BN1 9QT UK

J. W. Chew

Fluids Research Centre,
School of Engineering,
University of Surrey,
Guildford, Surrey, GU2 7XH UK

Measurement and Analysis of Ingestion Through a Turbine Rim Seal

Experimental measurements from a new single stage turbine are presented. The turbine has 26 vanes and 59 rotating blades with a design point stage expansion ratio of 2.5 and vane exit Mach number of 0.96. A variable sealing flow is supplied to the disk cavity upstream of the rotor and then enters the annulus through a simple axial clearance seal situated on the hub between the stator and rotor. Measurements at the annulus hub wall just downstream of the vanes show the degree of circumferential pressure variation. Further pressure measurements in the disk cavity indicate the strength of the swirling flow in the cavity, and show the effects of mainstream gas ingestion at low sealing flows. Ingestion is further quantified through seeding of the sealing air with nitrous oxide or carbon dioxide and measurement of gas concentrations in the cavity. Interpretation of the measurements is aided by steady and unsteady computational fluid dynamics solutions, and comparison with an elementary model of ingestion. [DOI: 10.1115/1.1556411]

1 Introduction

To avoid overheating of turbine discs, ingestion of hot turbine gas through turbine rim seals must be prevented or limited. This can be achieved by channeling cool, high-pressure air from the compressor to the turbine where it is ejected back into the main gas path through the rim seals. If sufficient sealing air is supplied, then inflow of hot gas through the rim seals will be completely suppressed. However, to minimize performance losses, the sealing flows generally need to be kept as low as possible. With the flows involved being complex and unsteady, the seal flows possibly having significant effects on blade passage aerodynamics and performance, and running seal clearances often subject to uncertainty, optimization of sealing flows presents a considerable challenge in turbomachinery design. While recent research has resulted in considerable progress in understanding these flows, significant questions and shortcomings in current predictive methods remain.

The importance of circumferential pressure gradients in the annulus flow for rim seal ingestion was noted by Campbell [1]. This was confirmed experimentally by several workers. For example, Abe et al. [2], Kobayashi et al. [3], Phadke and Owen [4], Dadkhah et al. [5], Hamabe and Ishida [6], and Chew et al. [7] have performed experiments with various asymmetries in the annulus caused by guide vanes or other stationary disturbances. The conclusion may be drawn from these results that, at engine conditions, circumferential pressure asymmetries are the primary cause of ingestion. Chew et al. reported both experimental and 3-D computational fluid dynamics (CFD) results and concluded that inertial effects associated with the swirl component of velocity had an important influence on the flow. The combined influence of pressure asymmetries due to stationary vanes and rotating blades was noted by Green and Turner [8] and Bohn et al. [9] who measured ingestion with both vanes and blades present. Bohn et al. also presented unsteady CFD solutions showing some qualitative agreement with their data. The need to develop further understanding of the combined effect of rotating and pressure asymmetries was apparent from this work.

Two very recent, concurrent, but independent, studies are also relevant to the present paper. Both Roy et al. [10] and Hills et al. [11] concluded that predictive methods for rim seal ingestion must take account of the unsteady nature of the flow. Roy et al. measured pressures and ingestion in a turbine rig. Based on their unsteady pressure measurements and the observation that steady CFD models did not correctly predict ingestion they concluded that the unsteadiness was playing an important part in the ingestion process. Hills et al. showed that an unsteady CFD model gave considerably better agreement with previously published experimental ingestion data than steady models. For the conditions considered it was shown that the circumferential pressure asymmetry due to rotating blades had a large influence on ingestion despite being considerably smaller than the pressure asymmetry due to the stationary vanes. This was explained by considering inertial effects on the flow and the fact that the swirl velocity of the air was much closer to the rotor speed than to that of the vanes. An elementary model, taking some account of these effects was also shown to capture the experimental trends.

In this paper experimental measurements of rim seal ingestion from a new single-stage turbine rig are presented and used to evaluate predictions using steady and unsteady CFD solutions for the main annulus flow and a more elementary model of rim seal ingestion. This level of modeling is considered practical for use within design time scales, yet offers significant advances over methods commonly used at present. The experimental rig and the measurements are described in the next section. The CFD studies are then presented and compared to measurements in Section 3. The ingestion model, which follows that presented by Hills et al., is given, and results compared with data in Section 4. The main conclusions from this study are then summarized in Section 5.

2 Experiments

2.1 Experimental Apparatus. The test facility consists of a complete axial turbine stage based on a modified Gnome helicopter engine (HP1200 power turbine module) enclosed in an annular channel through which the mainstream air flows. A close-up view of the rig is shown in Fig. 1.

The rotor-stator assembly is made up of titanium blisk with 59 twisted blades machined into its periphery and of 26 constant section aluminum nozzle guide vanes (NGVs). The exit angle of the NGVs is 70 deg and the radius of the disk is 152.8 mm. Both the NGV and rotor blade heights are 25 mm and the axial distance between the aerofoil rows is 13.2 mm. For the tests reported in this paper, the wheel-space width was 10 mm ($G=0.065$) and a simple axial clearance of 2 mm ($G_c=0.013$) with a radial extent

Contributed by the International Gas Turbine Institute and presented at the International Gas Turbine and Aeroengine Congress and Exhibition, Amsterdam, The Netherlands, June 3–6, 2002. Manuscript received by the IGTI January 25, 2002. Paper No. 2002-GT-30481. Review Chair: E. Benvenuti.

 Copyright © 2003 by ASME

Downloaded 31 May 2010 to 171.66.16.27. Redistribution subject to ASME license or copyright; see http://www.asme.org/terms/Terms_Use.cfm

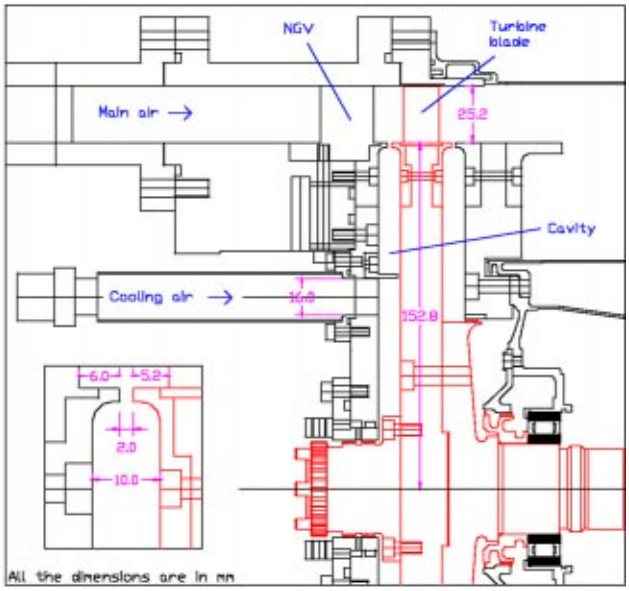

Fig. 1 Experimental rig

of 2 mm was fitted at the rim of the cavity. The stator and rotor faces are completely flat and the edge of the stator shroud is located 6 mm downstream of the NGV trailing edge.

Depending on the operating conditions tested, the annulus air is either supplied by a Rolls-Royce Dart centrifugal compressor capable of generating mass flow rates up to 10.5 kg/s at a pressure of 3.3 bar absolute (Turner et al. [12]) or a Keith Blackman compressor rated at 1.1 kg/s with 1.6 bar absolute. The turbine power (≈360 kW at the design point) is dissipated by a Heenan and Froude DPY590 water-cooled dynamometer connected to the rotor-stator system via a Gnome Main Reduction Gearbox (3.25:1). Figure 2 shows the turbine characteristic and the two operating conditions considered here (OC1 and OC2). Note that in this figure the mass flow was estimated from total and static pressure taps located upstream of the NGVs. This is because there is some uncertainty in the Venturi tube measurements at pressure ratios 1.6 and 2 due to an air leak. This did not affect conditions OC1 or OC2 and elsewhere in the paper the Venturi measurements have been used. Conditions OC1 and OC2 features are summarized in Table 1. Owing to the high heat dissipation by the dynamometer at the design point and the limited volume of water

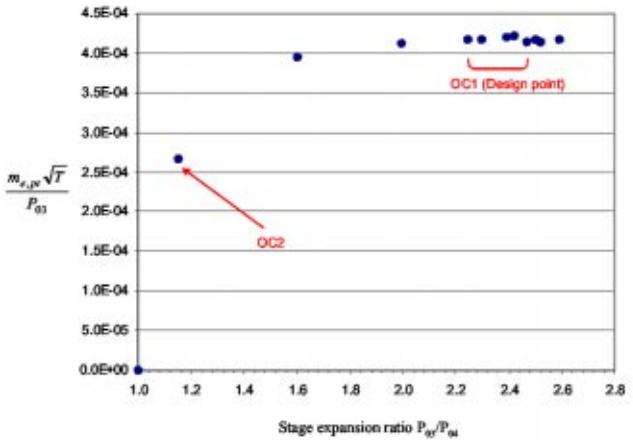

Fig. 2 Turbine characteristic

Table 1 Operating conditions investigated

	OC1	OC2
External flow		
NGV exit Mach no. M	0.963	0.390
Exit NGV Reynolds no. Re_z	6.23×10^5	1.77×10^5
Stage expansion ratio P_{03}/P_{04}	2.50	1.14
Disk		
Rotational speed Ω	13,500 rev/min	6,550 rev/min
Rotational Reynolds number Re_θ	2.83×10^6	9.04×10^5
Temperatures		
Annulus air	420 K	355 K
Cooling air	300 K	300 K
Cooling/annulus density ratio	1.41	1.2

available to cool it, more than one run was necessary to obtain a satisfactory range of sealing air conditions. This led to slightly different mainstream conditions at the design speed, hence the scattering of points at the turbine characteristic.

A separate source of air, either a hydrovane compressor (rated 0.1 m^3/s at 8 bar absolute) or a ZT250 type ATLAS COPCO compressor (up to 0.8 kg/s with a maximum outlet pressure of 7.5 bar absolute), provided the cooling air, which was admitted to the wheelspace cavity through 3 equi-spaced tubes of inside diameter 16 mm at a radius of 84.75 mm ($R=0.55$). Prior to its introduction into the cavity, the cooling flow is seeded with a tracing gas and the concentration is measured at four different radial positions on the stator surface ($R=0.4$, 0.71, 0.88, and 0.92) by means of a gas analyser. At OC1, the seeding gas employed was nitrous oxide (NO) whereas carbon dioxide (CO_2) was preferred at OC2, the sampled concentrations being measured with an IRGA 120 GP Instrumentation and a Leybold Heareus gas analyzers, respectively. The uncertainty of both systems is estimated to be +/−2%.

The circumferential variation of the static pressure in the mainstream flow is determined using 11 tappings in the annulus hub end wall drilled at 1.5-deg intervals over approximately 1.1 NGV pitch and located 1.5 mm downstream of the vanes. Pressures inside the wheel-space cavity are also measured by means of 12 static pressure taps equally distributed on two angular positions to check the flow axisymmetry. The taps are located at the radius ratios $R=0.4$, 0.71, 0.805, 0.88, 0.92, and 0.96 on the stator surface. These pressures are measured with a Scanivalve system.

2.2 Results. Figure 3 shows the circumferential variation of the annulus pressure measured downstream of the NGVs at the design point (OC1) for different seal-to-annulus velocity ratios U_m/U_e. The annular pressure coefficient C_{pa} is defined as the difference between the measured static pressure and the average of the measured static pressures nondimensionalized by the NGV exit dynamic head ($P_{03}-p_{\text{aver}}$). The maximum uncertainty of C_{pa} has been estimated to be 0.14% throughout all the experiments. In this figure are also included the guide vane profiles and the positions of the 11 pressure tappings. Note that the lines joining the data points in this figure are obtained from curve fits to the data. It can be seen that the nondimensionalized pressure profile is fairly independent of the quantity of cooling air introduced into the cavity. Thus as U_m/U_e increases, the pressure level in the annulus flow rises while the pressure asymmetry which is thought to be the dominant ingestion driving mechanism is only slightly affected. A comparison with the annulus pressure distribution obtained at OC2 for a velocity ratio of 0.048 is also provided. For both design and off-design operating conditions, the pressure asymmetry measured 1.5 mm downstream of the NGVs corresponds to about 20% of the dynamic head.

The effect of mainstream gas ingestion on the wheel-space pressure measurements can be observed in Fig. 4. In the upper part of the cavity where the tangential velocity of the rotating core $V_{\theta,\text{core}}$ is much higher than the radial component of velocity $V_{r,\text{core}}$, the radial momentum equation is reduced to

Downloaded 31 May 2010 to 171.66.16.27. Redistribution subject to ASME license or copyright; see http://www.asme.org/terms/Terms_Use.cfm

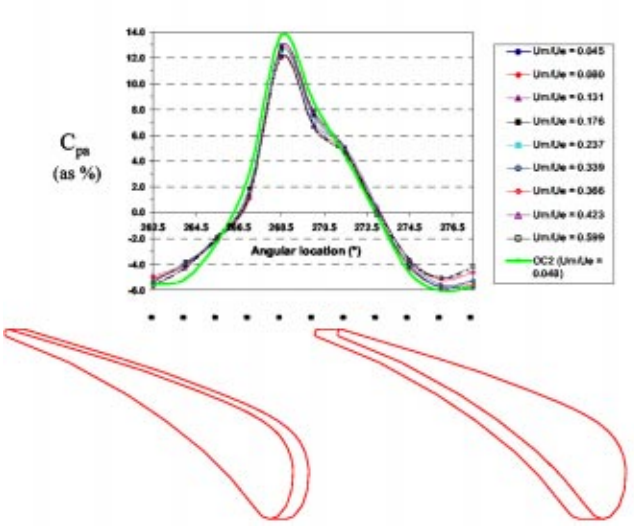

Fig. 3 Annulus pressure measurements

$$\frac{\partial p}{\partial r} = \frac{\partial V_{\phi,\text{core}}^2}{r} \tag{1}$$

Assuming $V_{\theta,\text{core}} = \beta \times \Omega r$, with β and density constant, the integration of Eq. (1) with respect to r gives

$$\frac{p_{R_2} - p_{R_1}}{\frac{1}{2}\rho\Omega^2 r_0^2} = \beta^2(R_2^2 - R_1^2) \tag{2}$$

where p_{R_1}, p_{R_2} denote the static pressures when $R = R_1$ and R_2 respectively. Using the pressure measurements in the cavity, it is then possible to estimate the core cavity swirl ratio. Note however that, since β may vary with radius, this method does involve some approximation. The results are shown in Fig. 4 for OC2. Here β is plotted against the non-dimensionalised flow parameter $\lambda\, R^{-2.6}$ $(= C_w\, \mathrm{Re}_\theta^{-0.8} R^{-2.6})$. When this parameter is equal to 0.22 the supplied sealing flow is equal to the free disk pumping flow as given by von Karman's [13] solution. A comparison has been made with the LDA measurements of Pincombe and El Oun

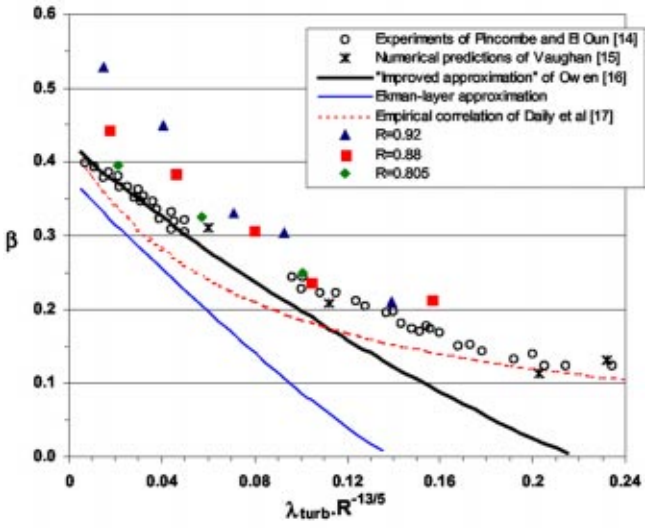

Fig. 4 Cavity swirl calculated from pressure measurements (OC2)

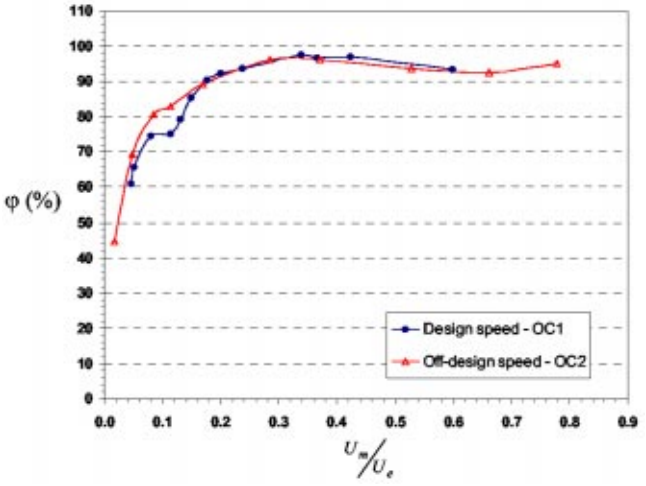

Fig. 5 Concentration measurements at $R = 0.92$

[14] and the numerical results of Vaughan [15] carried out with nonswirled axisymmetric external flow over the rotor-stator cavity.

As expected, the level of core rotation decreases with increasing values of the flow parameter λ. At low sealing flows, the tangential velocities calculated at the three radial locations $R = 0.92$, 0.88, and 0.805 are well above the data obtained by El Oun and Pincombe—sometimes even higher than the value $\beta = 0.426$ predicted with no throughflow. The agreement is better as the radial position R decreases. This behavior is a direct consequence of annulus flow ingestion affecting the cavity flow at low values of λ. Downstream of the NGVs, the annulus flow possesses a high tangential velocity $(V_\theta/\Omega r_o = 1.32)$ and with part of this flow being ingested through the rim seal clearance the swirl of the rotating core is increased. For the highest values of λ, where sealing flow rates are higher and ingestion is suppressed, the calculated swirl ratio is relatively insensitive to the considered radial position R and closer to the LDA measurements of El Oun and Pincombe.

Figure 5 shows the variation of sealing effectiveness φ against the velocity ratio U_m/U_e for the two operating points investigated OC1 and OC2. The percentage sealing effectiveness is defined as

$$\varphi = \frac{\eta_{R=0.92} - \eta_\infty}{\eta_c - \eta_\infty} \times 100 \tag{3}$$

where $\eta_{R=0.92}$, and η_c are, respectively, the gas concentrations of the air sampled at the location $R = 0.92$ on the stator surface in the cavity and of the cooling air. At OC2, since carbon dioxide is present in the ambient air (at a rate of about 300 ppm), it was necessary to introduce the parameter η_∞ in the expression of φ. This concentration was measured at the end of the tests. At OC1, η_∞ was zero. The variations of φ for OC1 and OC2 are in reasonably good agreement supporting the suggestion that the velocity ratio U_m/U_e is an appropriate correlating parameter. Use of the momentum ratio $(\rho_c U_m^2/(\rho_e U_e^2)$ does not improve the collapse of data, but this may be due to other differences between OC1 and OC2. Note that, for the same value of U_m/U_e, the coolant flow rates for the two operating conditions differ by a factor of more than two.

3 CFD Modeling

3.1 Description of the Model. CFD models for the flow in the main gas path annulus are described in this section. No account is taken of the sealing flows in these models, but the circumferential pressure asymmetries deduced from the CFD models will be used for the ingestion modelling in Section 4.

Downloaded 31 May 2010 to 171.66.16.27. Redistribution subject to ASME license or copyright; see http://www.asme.org/terms/Terms_Use.cfm

Table 2 Summary of CFD models

Model	Steady/unsteady	N deg vanes	N deg blades
1	Steady in stationary frame	1	0
2	Steady in rotating frame	0	1
3	Unsteady (sliding plane)	1	2

Three different models based on the experimental rig are used and their features are given in Table 2. Model 1 does not include the rotor blades and assumes a steady flow in the stationary frame. Model 2 does not include the NGVs and assumes a steady flow in the rotating frame. Model 3 represents the whole turbine stage and calculates the unsteady flow using a sliding interface between the stationary and rotating parts. Since the sliding mesh process requires that the two interface boundaries are based on the same geometry, 27 NGVs and 54 rotor blades (i.e., two blades per vane) are modelled as opposed to 26 NGVs and 59 blades in the experimental rig. The computational domain is represented in Fig. 6. (In all the models, the inlet and outlet was extended to avoid difficulties with spurious reflections from the boundaries.) Within Gambit [18], the mesh was generated on the hub end wall of the annulus channel using quadrilateral cells and then extended in the radial direction up to the tip end wall by projecting the mesh node patterns of the hub-end-wall through the volume. Boundary layers were previously applied to the solid surfaces using six rows of cells on the vane and three rows on the blade with a growth rate of 1.2. This resulted in about 436,000 cells for the model 1, 445,500 cells for model 2 and 636,500 for model 3.

The calculations were performed with Fluent 5.5 [19]. The governing equations (mass, momentum and energy) were solved using a segregated implicit solver and both the $k-\varepsilon$ (with a standard wall function treatment in the vicinity of the solid surfaces) and the Spalart-Allmaras turbulence models were tested. The models were run at the two operating conditions OC1 and OC2 previously described in this paper necessitating the use of the compressible ideal gas law for the fluid. At the inlet, the experimental mass flow (adjusted proportionally to the number of aerofoils present in the geometry) and the total temperature were specified while static pressure was specified at the outlet. For model 1, this pressure corresponds to the circumferential average of the pressure profile obtained experimentally 1.5 mm downstream of the NGV and was set in the CFD model at the hub of the annulus channel. The static pressure on the rest of the boundary was calculated assuming a radial equilibrium pressure distribution. For models 2 and 3, the pressure measured 40 mm downstream of the rotating blades on the outer casing of the annulus channel was used. For model 2, a flow angle corresponding to the exit angle of the NGV (=70 deg) was also specified at the inlet.

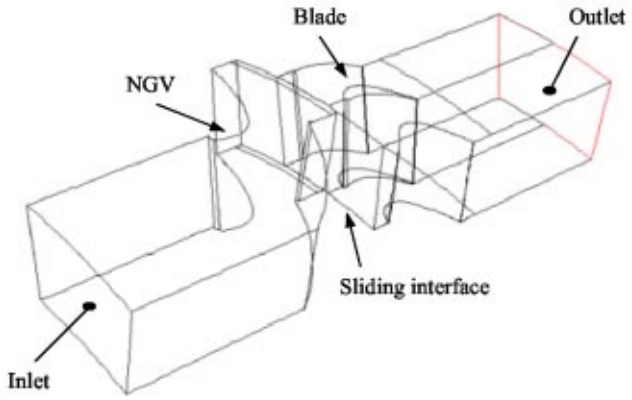

Fig. 6 Domain for the unsteady CFD model 3

Apart from the outlet of model 1, uniform boundary conditions were therefore assumed. The unsteady solution of model 3 was solved using time step sizes of 3 and 4 μs at OC1 and OC2, respectively. This led to a new rotor blade passing the NGV every 28 and 42 time steps.

The convergence of the steady solutions was checked by monitoring the conventional Fluent residuals of the continuity, momentum, energy and turbulence equations. For the unsteady model 3, this approach could be misleading, and thus it was preferred to monitor the mass flow difference between the inlet and outlet of the geometry. The unsteady calculation was judged to be close to convergence when the parameter showed an oscillatory behavior around 0 with the magnitude of the oscillations insignificant compared to the inlet mass flow.

3.2 CFD Results. Figures 7(*a*) and (*b*) show the circumferential variations of the annulus pressure at the design and off-design speed conditions OC1 and OC2, respectively. Both graphs show the pressure profiles measured 1.5 mm downstream of the NGV trailing edge and those obtained with the CFD models 1 and 3 at the same position. During the measurements, the quantity of cooling air introduced into the cavity was sufficiently small ($U_m/U_e=0.045$ at OC1 and 0.018 at OC2) to ensure that any effect of rim seal outflow on the mainstream pressure profile remains weak. The unsteady solution of model 3 was time-averaged over a period. The circumferential location was nondimensionalized using a fraction of the NGV pitch where the value 0 represents the trailing edge position.

Both at OC1 and OC2, the CFD models tend to overpredict the peak-to-peak amplitude of the measured pressure asymmetry though the agreement with the experiments is slightly improved when the Spalart-Allmaras turbulence model is used. This observation must be balanced by the fact that the pressure gradient might be underestimated due to the limited number of pressure taps in the rig. In addition, the experimental data are not perfectly periodic in the circumferential direction and the CFD models do not account for any effect of the ingestion and ejection of flow through the seal gap. Thus, some uncertainty surrounds the determination of the pressure asymmetry. It is also worth pointing out that there is no significant difference between model 1 (NGV only) and the time-average of model 3 (complete turbine stage).

Figure 8 gives the CFD-predicted axial decay of the circumferential pressure variation due to the NGVs at OC1 (using models 1 and 3 with a Spalart-Allmaras turbulence model). For the unsteady solution, the pressure profiles were time-averaged over a period. The circumferential pressure variation is plotted over a maximum 13.2-mm distance downstream of the NGVs because of the presence of the rotor blades. The position of the axial rim seal is also represented in the figure. Again, there is little difference between modeling the vane only or the whole turbine stage with the unsteady model giving a slightly faster decay of the NGV pressure asymmetry. The influence of the blades on the time-averaged pressure field appears to be limited to near the blade leading edge.

The pressure distributions obtained with model 1 at different axial positions downstream of the NGVs were Fourier-analyzed and expressed as

$$p_\theta = p_0 + \sum_k A_k \times \cos(\theta + B_k) \tag{4}$$

where p_θ is the static pressure at the angular location θ with A_k and B_k the amplitude and phase of the kth harmonic function. Axial decay of the 4 first harmonic components A_k is shown in Fig. 9. At the seal gap, results suggest that the first harmonic is likely to dominate the NGV pressure asymmetry. Also included in this figure is the potential flow approximation previously used by Chew et al. [7] and Hills et al. [20]. According to this analytical model, the first harmonic decays as e^{-kx} where

Downloaded 31 May 2010 to 171.66.16.27. Redistribution subject to ASME license or copyright; see http://www.asme.org/terms/Terms_Use.cfm

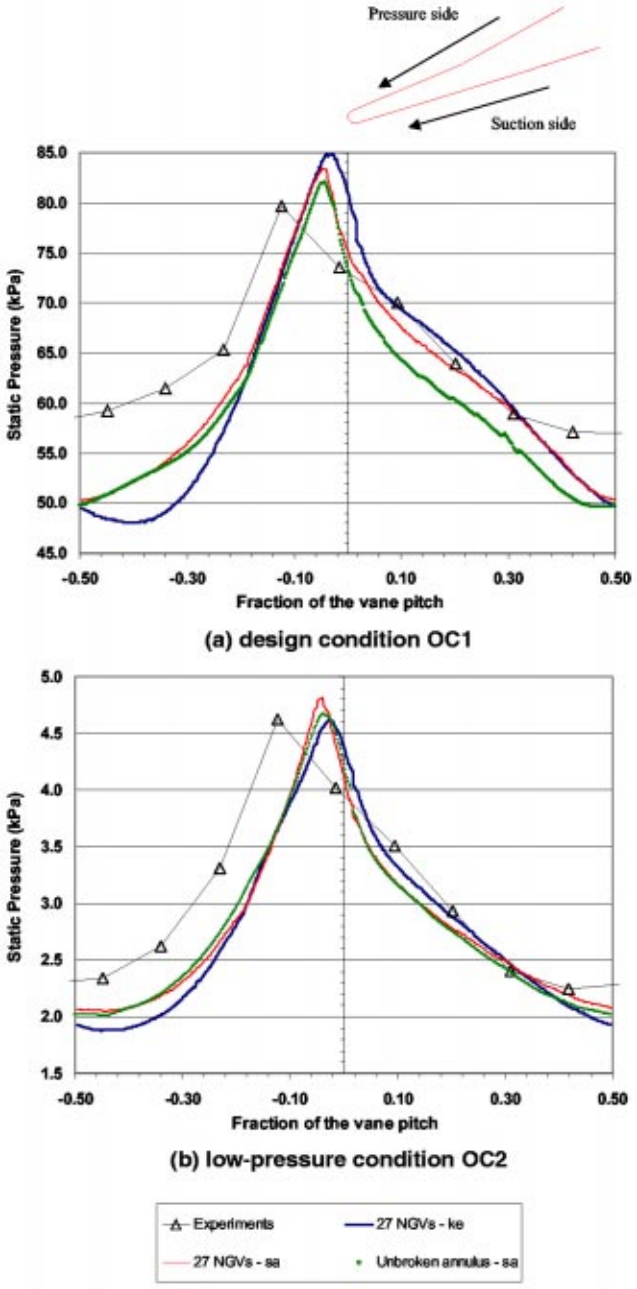

Fig. 7 Comparison with annulus pressure measurements (*ke*:*k*-ε turbulence model/sa:Spalart-Allmaras turbulence model)—(*a*) design condition OC1, (*b*) low-pressure condition OC2

$$k = \frac{N}{r}\frac{\sqrt{(1-M^2)}}{(1-M_z^2)} \tag{5}$$

N being the number of vanes (or blades), r the radius, M the Mach number (relative for the rotor) and M_z the Mach number based on the axial component of velocity. It can be seen that the potential flow approximation succeeds reasonably well in predicting the decline of the first harmonic given by the CFD calculations. It should also be noted that the pressure asymmetry is still significant at the leading edge of the rotor blades (13.2 mm downstream of the NGVs). Thus some effect of the NGV flow field on the blade flow can be expected.

Figures 10 and 11 focus on the pressure asymmetry generated by the rotor. Despite being much smaller than that produced by

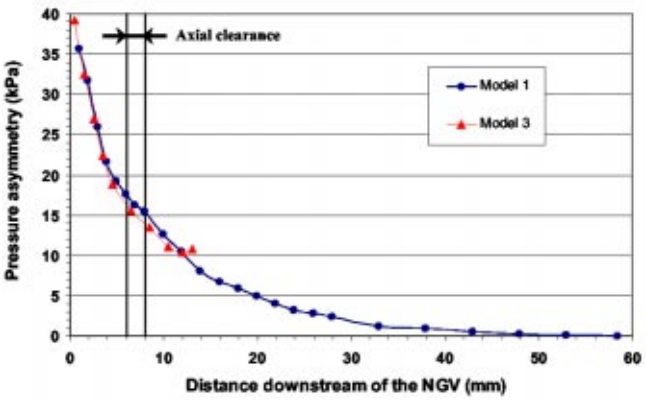

Fig. 8 Axial decay of the NGV pressure asymmetry at the design condition OC1 with the Spalart-Allmaras turbulence model

the NGV, the pressure gradient due to the rotating blades could have a significant effect on ingestion. Its axial decay upstream of the blade is shown in Fig. 10 at OC1 from the CFD models 2 and 3 (still using the Spalart-Allmaras turbulence model). For model 3, these results were obtained by averaging the time-dependent pressure profiles over a period in the rotating reference frame. The two models do not agree very well: the unsteady model results in an amplitude of the rotor pressure asymmetry twice as high as that

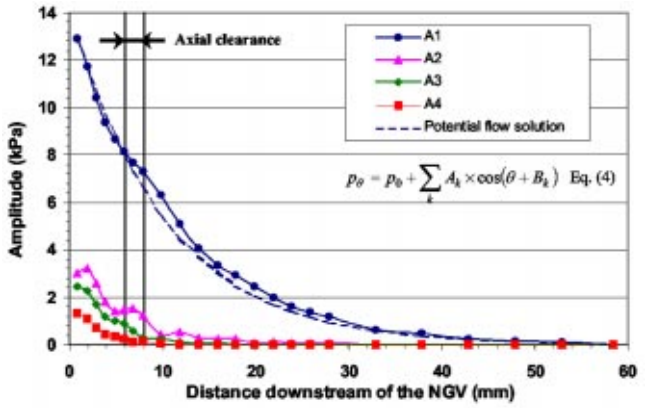

Fig. 9 Axial decay of harmonic components of the NGV pressure asymmetry at the design condition OC1 with the Spalart-Allmaras turbulence model

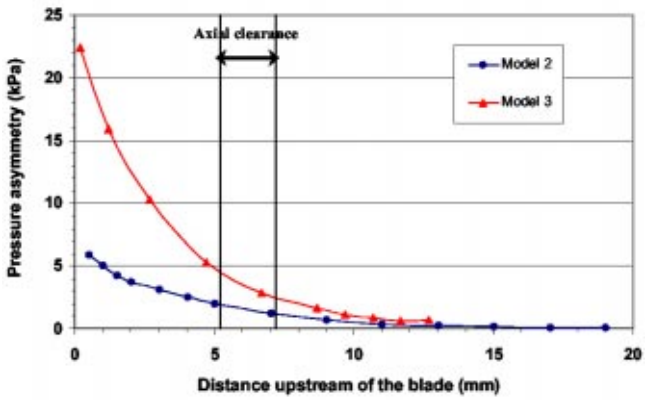

Fig. 10 Axial decay of the rotor pressure asymmetry at the design condition OC1 with the Spalart-Allmaras turbulence model

Downloaded 31 May 2010 to 171.66.16.27. Redistribution subject to ASME license or copyright; see http://www.asme.org/terms/Terms_Use.cfm

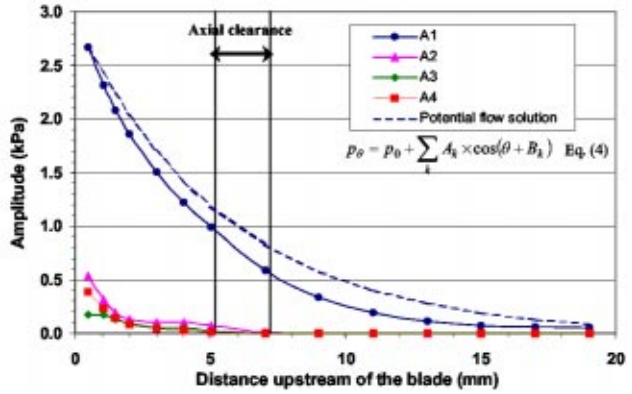

Fig. 11 Axial decay of harmonic components of the rotor pressure asymmetry at the design condition OC1 with the Spalart-Allmaras turbulence mode

given by the steady model 2. As previously noted, the pressure asymmetry due to the NGVs is still significant at the rotor blade leading edge, and the unsteady calculation confirms that this effects the rotor flow. The variations of the four first harmonic components A_k of the rotor pressure asymmetry from model 2 are given in Fig. 11. The axial decay of the first harmonic is also compared with the potential flow approximation given by Eq. (2). The potential flow looks to yield to a significant underprediction of the rotor pressure asymmetry decay.

4 Ingestion Modeling

The circumferential pressure asymmetries given by the CFD model in the previous section are now used in conjunction with the simple rim sealing model presented by Hills et al. [11]. Solutions for the simple model are obtained from a stand-alone computer program. The resulting predictions for sealing effectiveness for the present turbine are compared with the concentration measurements given in Section 2.

The simple model can be viewed as an extension of the widely used orifice model that estimates flow through the seal at each circumferential location using simple orifice theory. The extended model involves inclusion of some inertial effects and involves numerical solution of the following equation:

$$\rho l\left(\frac{\partial}{\partial t}+\frac{V_\theta}{r_o}\frac{\partial}{\partial \theta}\right)U+\frac{\rho U^2}{2}C_h\,\mathrm{sgn}(U)=\Delta p \tag{6}$$

Here C_h is a loss coefficient, l is an appropriate length scale (in the $r-z$ plane), r_o is the inner annulus wall radius which is taken to equal the seal radius, V_θ is the tangential velocity (assumed uniform), U is the mean velocity through the seal, and Δp is the pressure in the cavity minus the annulus pressure. Equation (6) is solved numerically for U with specified Δp, which in the present case is periodic in time. The numerical solution uses central differences for derivatives with respect to θ and first order implicit time stepping. Numerical experiments were performed to ensure that numerical errors were insignificant.

Mass flows into and out of the cavity are then calculated from the computed solutions for U, which requires specification of seal clearance (s_c) and discharge coefficient (C_d). An estimate of the sealing effectiveness is then given by

$$\Phi = m/(m+n_{\mathrm{in}}) \tag{7}$$

where m is the net mass flow rate through the seal and m_{in} is the ingestion flow rate. This estimate is based on a fully mixed assumption for the flow in the cavity. It does not fully account for the unsteady effects shown in previous CFD studies.

For the calculations described in the forthcoming, C_h was taken as 1 and discharge coefficients were obtained from the correlations given by Chew et al. [7]. These give the discharge coefficient as a function of the ratio of mean seal velocity to the axial component of the annulus velocity U_m/U_e. Following the practice of Hills et al., here l was set to $C_d \cdot s_c$ and V_θ was set to the estimated swirl velocity for the annulus flow above the seal. Sinusoidal variations of annulus static pressure are assumed with uniform and steady cavity pressure. The cavity pressure is varied to obtain results for a range of sealing mass flows. To show sensitivity, a second set of calculations is presented with V_θ set to half the value estimated for the annulus freestream.

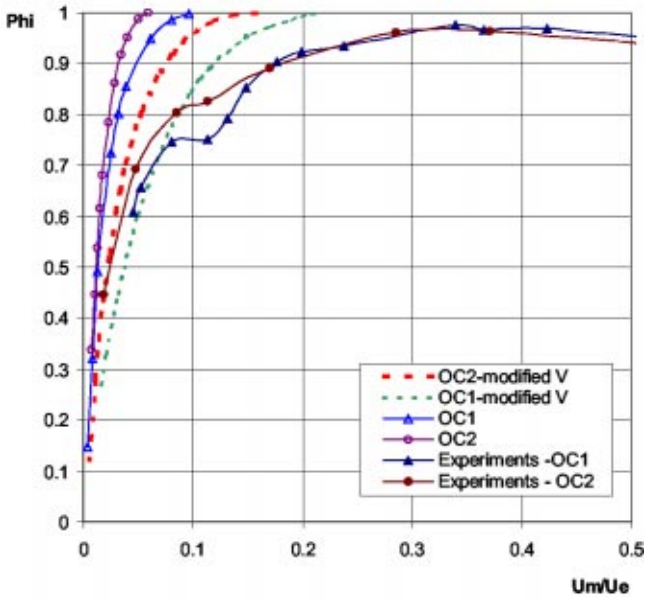

Fig. 12 Comparison of simple model for gas ingestion with measurements

Figure 12 shows a comparison of the simple model predictions with the experimental concentration measurements. For the model, pressure asymmetries for the NGVs and blades were estimated from the unsteady, stage CFD calculation. The measurements are presented as the sealing effectiveness estimated from the gas concentrations at $r/r_o=0.92$. It may be seen that the measurements generally show more ingestion than that calculated with the model, particularly at higher sealing flow rates. However, the degree of sensitivity to operating conditions is consistent with the experiments. These results agree with the trends found by Hills et al. [11] who showed a similar but less pronounced underprediction of ingestion for their configuration. Hills et al. also showed the importance of the parameters $\Delta p/\rho_c U_e^2$ and $N(s_c/r_o)\times(V_0/U_e)$ in the model. Estimating these for the rotor pressure asymmetry in Hills et al.'s configuration gives $\Delta p/\rho_e U_e^2 \approx 0.2$ and $N(s_c/r_o)(V_\theta/U_e)\approx 0.01$, while for the present configuration the corresponding values are 0.11 and 0.9 for OC1 and 0.13 and 0.5 for OC2. With this change in parameters the effects of the rotor pressure asymmetry would be expected to be considerably reduced for the present configuration. Although not shown on the figure, further results from the model for OC1 indicate that the influence of the rotor pressure asymmetry is rather small in this case. Further comparison with Hills et al.'s results shows that the model correctly predicts that the present configuration gives better sealing (for the same value of the velocity ratio), but overestimates this effect.

Considering these results and the uncertainties in both the model and the experimental conditions it was postulated that the simple model, with the initial choice of parameters overestimated the inertial effects represented by the first term in Eq. (6). This could be due to the effects of the hub boundary layer and/or the

Downloaded 31 May 2010 to 171.66.16.27. Redistribution subject to ASME license or copyright; see http://www.asme.org/terms/Terms_Use.cfm

lower value of tangential velocity of the sealing flow. Annulus flow entering the seal will come from the boundary layer on the stationary hub and may have a substantially lower tangential velocity than that estimated in the foregoing. The second set of results in Fig. 12 confirms the sensitivity to V_0. The differences between calculated and measured values are consistent with the swirl velocity of the seal flow decreasing as the sealing flow rate increases (and hence ingestion of highly swirling annulus gas reduces) It is expected that recalibration of the model could give considerably better agreement with the measurements. However, it should also be noted that both the present study and that of Hills et al. have considered only a simple axial seal. Calibration against data for other types of seal is also required.

5 Conclusions

Measurements showing ingestion of mainstream gas into a turbine disk cavity have been obtained for a single-stage turbine. Pressure measurements within the disc cavity show that for low sealing flows ingestion of the highly swirling annulus air leads to increased levels of swirl (and hence radial pressure gradients within the cavity). Gas concentration measurements also show ingestion of mainstream gas, and pressure measurements on the annulus hub show the circumferential pressure asymmetry just downstream of the NGVs. Comparison of the gas concentration measurements at two different operating points shows that the seal to annulus flow velocity ratio is a useful correlating parameter. These measurements will be useful in further evaluation of CFD and other models for rim sealing.

CFD studies of the annulus flow show fair agreement with the pressure measurements and estimates of the pressure asymmetry decay rates given by a linear potential flow solution. The pressure asymmetry at the seal due to the NGVs is only slightly affected by the presence of the rotor blades. However, the pressure asymmetry due to the rotor is very significantly modified by the potential field due to NGVs. The pressure asymmetry levels given by the CFD model were used in the simple ingestion model described by Hills et al. [11]. This model, using the same 'model constants' as Hills et al. significantly underestimated the ingestion levels for the present case. However, experimental trends are consistent with the measurements and recalibration of the model can be expected to give considerable improvement. The model shows strong sensitivity to the swirl velocity assumed for the seal flow.

Note that the present results should not be generalized to other turbine rim seals without careful consideration. Proximity of the seal to the vanes and blades will clearly have a significant effect, as will the number of blade and vanes. Rim seal geometry is also likely to be important. While Mach number effects appear relatively weak in the present case, the axial decay rate of the circumferential pressure asymmetries does vary with Mach number, and this could be more important in other circumstances. Clarification of these effects can be expected as further experimental and CFD results become available.

Acknowledgments

The authors wish to express their thanks to Rolls-Royce plc and Alstom for their support in the research work presented in this paper.

Nomenclature

c = vane chord
C_d = discharge coefficient
C_h = loss coefficient
C_{pa} = static pressure coefficient $=(p_\theta - p_{\text{aver}})/(P_{03} - p_{\text{aver}})$
C_w = nondimensional flow rate $=\text{m}/(\mu \text{r}_0)$
G = gap ratio $= s/r_0$
G_c = clearance ratio $= s_c/r_0$
k = axial decay coefficient
l = length scale for seal flow
m = mass flow rate
M = Mach no.
N = no. of vanes/blades
p = static pressure
P = total pressure
r = radius
r_0 = cavity outer radius
R = radius ratio $(=r/r_0)$
Re_z = vane exit Reynolds no. $=(\rho U_{\text{res}} c)/\mu$
Re_θ = rotational Reynolds no. $=(\rho \Omega r_0^2)/\mu$
s = cavity width
s_c = axial clearance
U = velocity
U_e = axial component of external flow
U_m = average velocity through seal gap $= m_c/(2\pi\rho s_c r_0)$
V_θ = swirl (or tangential velocity)
β = core-swirl ratio $= V_{\theta,\text{core}}/(\Omega r_0)$
Δp = pressure difference across seal
η_R = cavity concentration at R
η_c = coolant flow concentration
η_∞ = CO_2 concentration in the ambient air
λ = turbulent flow parameter $= C_w \text{Re}_0^{-4/5}$
φ = sealing effectiveness
ρ = density
Ω = rotational speed

Subscripts

03 = upstream of NGV
04 = downstream of rotor
aver = averaged downstream of NGV
c = coolant
e = external flow
res = resultant value
r, θ, z = radial, tangential, and axial directions

References

[1] Campbell, D. A., 1978, "Gas Turbine Disc Sealing System Design," Proc. Conf. on Seal Technology in Gas Turbine Engines, ASME Paper 91-GT-32; AGARD-CP-237.
[2] Abe, T., Kikuchi, J. and Takeuchi, H., 1979, "An Investigation of Turbine Disc Cooling," Paper GT30, 3rd CIMAC Congress, Vienna.
[3] Kobayashi, N., Matsumato, M., and Shizuya, M., 1984, "An Experimental Investigation of a Gas Turbine Disc Cooling System," ASME J. Eng. Gas Turbines Power, **106**, pp. 136–141.
[4] Phadke, U. P., and Owen, J. M., 1988, "Aerodynamic Aspects of the Rim Sealing of Gas Turbine Rotor-Stator Systems Parts 1–3," Int. J. Heat Fluid Flow, **9**, pp. 98–117.
[5] Dadkhah, S., Turner, A. B., and Chew, J. W., 1991, "Performance of Radial Clearance Rim Seals in Upstream and Downstream Rotor-Stator Wheelspaces," ASME Paper 91-GT-32; also ASME J. Turbomachinery, **114**, pp. 439–445.
[6] Hamabe, K., and Ishida, K., 1992, "Rim Seal Experiments and Analysis of a Rotor-Stator System With Non-Axisymmetric Main Flow," ASME Paper 92-GT-160.
[7] Chew, J. W., Green, T., and Turner, A. B., 1994, "Rim Sealing of Rotor-Stator Wheelspaces in the Presence of External Flow," ASME Paper 94-GT-126.
[8] Green, T., and Turner, A. B., 1992, "Ingestion Into the Upstream Wheelspace of an Axial Turbine Stage," ASME Paper 92-GT-303.
[9] Bohn, D., Rudzinsky, B., Surken, N., and Gartner, W., 2000, "Experimental and Numerical Investigation of the Influence of Rotor Blades on Hot Gas Ingestion Into the Upstream Cavity of an Axial Turbine Stage," ASME Paper 2000-GT-284.
[10] Roy, R. P., Xu, G., Feng, J., and Kang, S., 2001, "Pressure Field and Main Stream Gas Ingestion in a Rotor Stator Disc Cavity," ASME Paper 2001-GT-564.
[11] Hills, N. J., Chew, J. W. and Turner, A. B., 2001, "Computational and Mathematical Modelling of Turbine Rim Seal Ingestion," ASME Paper 2001-GT-204; also, to be published in ASME J. Turbomach.
[12] Turner, A. B., Davies, S. J., Childs, P. R. N., Harvey, C. J., and Millward, J. A., 2000, "Development of a Novel Gas Turbine Driven Centrifugal Compressor," Proc. Inst. Mech. Eng., **214**, Part A.
[13] Von Karman, T., 1921, "Uber Laminare und Turbulente Reibung," Z. Angew. Math. Mech., **1**, pp. 233–252.

Downloaded 31 May 2010 to 171.66.16.27. Redistribution subject to ASME license or copyright; see http://www.asme.org/terms/Terms_Use.cfm

[14] Pincombe, J. R. and El-Oun, Z., 1986, Unpublished work.
[15] Vaughan, C., 1987, ''A Numerical Investigation Into the Effect of an External Flow Field on the Sealing of a rotor-stator Cavity,'' Ph.D. thesis, University of Sussex, Brighton, England.
[16] Gambit 1, 1998, *Modeling Guide*, Fluent Inc.
[17] Fluent 5, 1998, *User's Guide*, Fluent Inc.
[18] Hills, N. J., Chew, J. W., Green, T., and Turner, A. B., 1997, ''Aerodynamics of Turbine Rim-Seal Ingestion.'' ASME Paper 97-GT-268.

Downloaded 31 May 2010 to 171.66.16.27. Redistribution subject to ASME license or copyright; see http://www.asme.org/terms/Terms_Use.cfm

An Investigation on Turbine Tip and Shroud Heat Transfer

Kam S. Chana
QinetiQ,
Cody Technology Park,
Farnborough Hants, GU14 OLX UK

Terry V. Jones
Department of Engineering Science,
University of Oxford,
Oxford, OX1 3PJ UK

Detailed experimental investigations have been performed to measure the heat transfer and static pressure distributions on the rotor tip and rotor casing of a gas turbine stage with a shroudless rotor blade. The turbine stage was a modern high pressure Rolls-Royce aero-engine design with stage pressure ratio of 3.2 and nozzle guide vane (ngv) Reynolds number of 2.54E6. Measurements have been taken with and without inlet temperature distortion to the stage. The measurements were taken in the QinetiQ Isentropic Light Piston Facility and aerodynamic and heat transfer measurements are presented from the rotor tip and casing region. A simple two-dimensional model is presented to estimate the heat transfer rate to the rotor tip and casing region as a function of Reynolds number along the gap. [DOI: 10.1115/1.1575253]

Introduction

As the general trend of increasing turbine pressure levels and loading continues, the heat load experienced by the rotor tip and stationary casing, above the rotor tip, is becoming increasingly important. The gas temperature at entry to the high-pressure (HP) turbine stage can be as high as 2100 K; the temperature seen by the rotor is lower as a result of the relative velocity. With blade metal temperatures limited at about 1100 K the nozzle guide vane (ngv) and rotor have to be cooled sufficiently to sustain this metal temperature. Hence, a major requirement and a problem area for turbine designers is the ability to adequately predict the surface heat transfer distribution, and thereby develop a cooling system to deal with the local thermal load. While many investigations have been carried out on turbine aerofoils the rotor tip and casing have been studied to a lesser extent. Hence, the rotor tip and casing still remains a problem area where frequent in-service repairs are necessary.

Tips of turbine blades rotating in close proximity to the stationary casing, experience a flow field that is highly unsteady and three-dimensional. Understanding the flow in this region is complicated by the presence of spanwise and circumferential pressure and temperature gradients. These are caused by the upstream blade row and nonuniform temperature profiles at inlet to the stage, generated by the combustion system. The latter occurs as a result of coolant being applied to the endwalls of the combustion chamber, dilution flows and the discrete fuel injection.

Clearance gaps in axial turbines are typically less than one percent of the blade height for large engines, increasing up to 1.5% or more for smaller engines with low aspect ratio blading (Metzger et al. [1]). The pressure differential between the pressure and suction surface of blades drives flow through the clearance gap. The flow in the vicinity of the pressure surface turns into the tip gap. Strong secondary flows can be expected to be present in the gas path as a whole, these cause very hot segments of the mainstream gas to flow into the clearance region, particularly over the central portion of the blade. As the flow emerges from the suction side of the clearance gap it rolls into a vortex when it encounters the cross flow. The leakage flow has a significant effect both on stage aerodynamic performance and on the heat transfer to the blade tip and casing.

A number of studies on the clearance gap flow field have been reported. The majority have concentrated on the aerodynamic aspects (Bindon, [2], Luo and Lakshminarayana [3]) with some focused on the leakage related convective heat transfer (Dunn et al. [4], Epstein et al. [5], Kumada et al. [6], Dunn and Halderman [7], Azad et al. [8], Ameri and Bunker [9], Bunker et al. [10].

The measurements by Dunn and Epstein are taken in short duration transient test facilities. Both of these studies have shown the casing and blade tips to experience large heat transfer rates. The chordwise variation of heat transfer rate was explained by a variation in the heat transfer coefficient and the driving temperature difference, although these effects were not separated. A model study by Mayle and Metzger [11] suggests that the high tip and casing heat transfer are caused by the presence of high driving temperatures with normal levels of heat transfer coefficient. This analysis was extended by Metzger and Rued [12] and suggests the sink like character of flow entering the clearance gap results in a very thin passage boundary layer; thus, the blade tip and casing are exposed to the full mainstream gas temperature. This indicated that the high levels of heat transfer are due mainly to high temperature leakage flow. More recently, Dunn [7] presented heat transfer results from a rotor tip with a recess. Measurements were obtained in the recess and on the lip of the blade tip. He found that the heat transfer values in the tip recess and on the lip were higher that those found on the blade stagnation point.

However, none of these investigations addresses the effects of nonuniform inlet temperature distortion on the heat transfer distribution at the rotor tip and casing, although Shang [13] reported measurements of heat transfer on the rotor blade surface in the presence of a spanwise temperature gradient. His studies showed that with a 12% radial temperature distortion factor (RTDF) the heat transfer levels towards the rotor tip increased by 20–30%.

The study reported here investigates the aerodynamics and heat transfer characteristics in the rotor tip and casing region with and without inlet temperature nonuniformity. Extensive measurements have been taken on a modern high-pressure turbine stage operated at realistic, nondimensional engine conditions as shown in Table 1.

Table 1 Turbine stage operating conditions

Parameter	
Mean inlet total pressure (bar)	4.6±1
Nominal mean inlet total temperature (K)	444±2
Ngv exit hub isentropic Mach number	1.034±1
Ngv exit casing isentropic Mach number	0.925±1
Rotor speed (rpm)	9500±1
Rotor exit hub static pressure (bar)	1.428±1
Rotor exit casing static pressure (bar)	1.435±1
Rotor relative inlet total pressure (bar)	2.707±1

Contributed by the International Gas Turbine Institute and presented at the International Gas Turbine and Aeroengine Congress and Exhibition, Amsterdam, The Netherlands, June 3–6, 2002. Manuscript received by the IGTI December 12, 2001. Paper No. 2002-GT-30554. Review Chair: E. Benvenuti.

 Copyright © 2003 by ASME

Downloaded 31 May 2010 to 171.66.16.27. Redistribution subject to ASME license or copyright; see http://www.asme.org/terms/Terms_Use.cfm

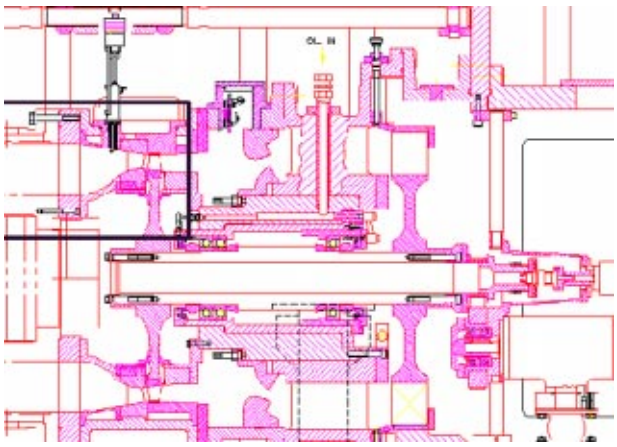

Fig. 1 The ILPF turbine module

Experimental Facility

The measurements have been taken using the Isentropic Light Piston Facility (ILPF), this is a short duration wind tunnel for testing full-sized high-pressure turbine stages. The main components are: i) the pump-tube containing a light-weight piston, ii) a fast acting valve, iii) the turbine stage, and iv) the turbo-brake. Prior to a run the piston is positioned at the end of the pump tube and the fast acting valve is closed. The pump-tube is then filled to a predetermined pressure, while the working section is evacuated, and the turbine assembly is spun up to the desired speed. To start a run, high-pressure air is introduced behind the piston causing it to move forward and compress the air between the piston and a fast-acting valve. This compression is nearly isentropic, thereby heating the test gas. When the desired pressure and temperature are reached, typically within one second, the fast acting valve is allowed to open, and a steady flow of air is passed through the turbine stage for approximately 500 ms.

The turbine module is shown in Fig. 1. A unique feature of this unit is the aerodynamic turbo-brake, which absorbs the energy produced by the turbine, so that the rotational speed is maintained nearly constant throughout the run. The ILPF is capable of matching all the nondimensional parameters relevant to turbine fluid mechanics and heat transfer for modern advanced gas-turbine engines.

The turbine investigated is the MT1 turbine which is an unshrouded, high-pressure research turbine relevant to future civil aircraft applications. The stage has 32 ngvs and 60 rotor blades.

The radial and circumferential non-dimensional temperature profiles generated at the ILPF inlet were matched with those found in a modern gas turbine engine. The profiles were generated in much the same way as in an engine, where the radial variation was achieved by blowing cooler air through the hub and casing walls. However, the circumferential variation was generated by injecting cooler air through turbulence rods upstream of the stage. The tunnel operating point was modified to achieve the required peak temperature.

Instrumentation

The time-averaged and time-varying static pressure was measured on the rotor casing using 57 flush-mounted pneumatic tappings and high-frequency response Kulite miniature pressure transducers. The Kulites were mounted in the same locations as the pneumatic tappings. The transducers were fitted in rows at an angle of 52 deg to the axial plane, approximately following the stagger angle of the rotor blade.

The time-averaged and time-varying heat transfer rate on the rotor casing wall was measured using 87 thin film gages. The gages were fitted in rows at an angle of 52 deg to the axial plane, approximately following the stagger angle of the rotor blade. The time-averaged and time-varying heat transfer rate on the rotor tip was measured using three thin film gages (Piccini et al. [14]).

Experimental Results

The tests with uniform and nonuniform temperatures at inlet to the stage were conducted at the same nominal design conditions. The area mean temperature in both cases was kept constant at 444 K and with the same rotational speed for the two tests, the mean corrected speed ($N/\sqrt{T}$) was the same. Hence, the radial and circumferential temperature profiles were adjusted to achieve this criterion. Particular attention was paid to ensure that the mean turbine inlet total pressure was not modified.

Figure 2 shows typical stage inlet total temperature traces, at midspan, verses time for the two inlet profiles OTDF1 and 2. These measurements are taken at the ngv leading edge and hence for OTDF2 the temperature is higher. Notably, the inlet temperature fluctuations on the trace from the nonuniform inlet temperature runs have increased markedly to those from the uniform inlet. It should be noted that this is not necessarily as a result of increased turbulence in the flow but as a result of cooler and warmer air mixing from different radial and circumferential positions caused by the turbulence.

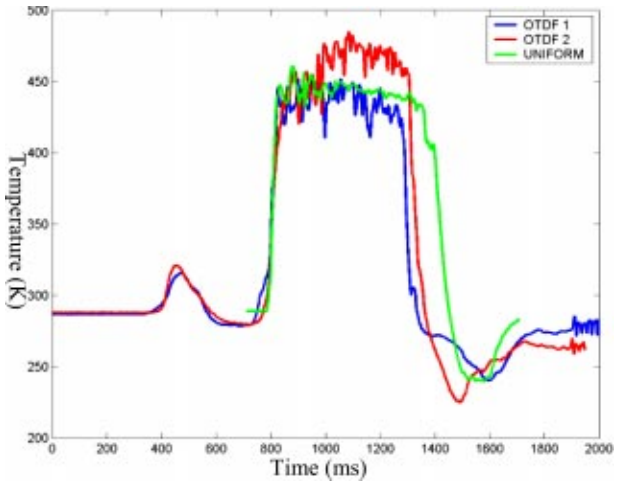

Fig. 2 Typical stage inlet total temperatures

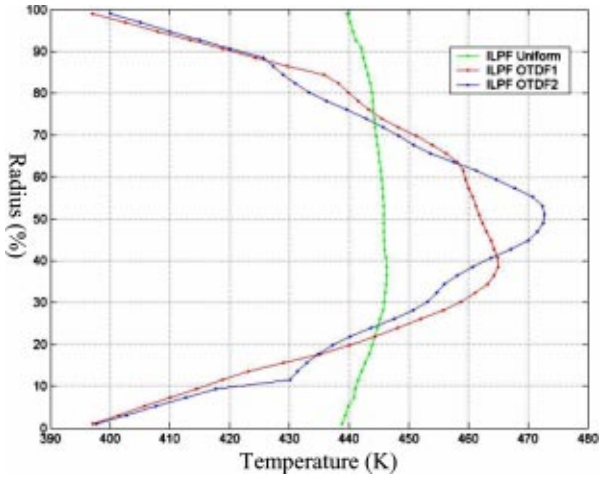

Fig. 3 Measured radial temperature profiles

Downloaded 31 May 2010 to 171.66.16.27. Redistribution subject to ASME license or copyright; see http://www.asme.org/terms/Terms_Use.cfm

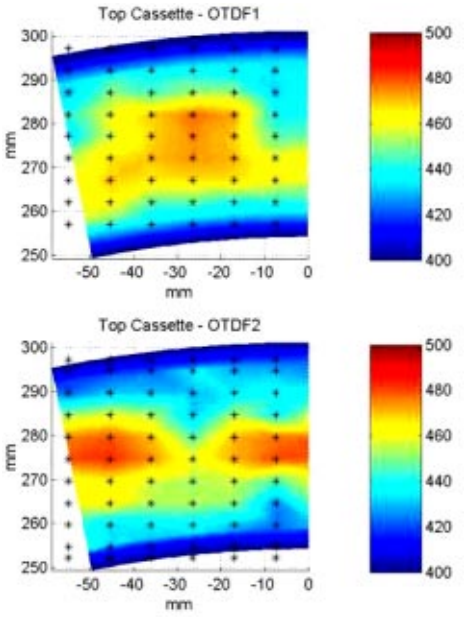

Fig. 4 Inlet temperature (K) for OTDF 1 and OTDF 2

Hence, there are larger temperature fluctuations present which would also be typical of an engine situation. The mean measured radial temperature profiles, circumferentially averaged, at inlet to the stage are given in Fig. 3.

Contour plots showing the measured inlet temperatures during the OTDF1 and OTDF2 tests are given in Fig. 4. The geometric leading edge of the ngvs coincide with the edges of the plot in this figure. Thus, OTDF1 has the ''hot spot'' at the center of the ngv passage whereas OTDF2 has the ''hot spot'' impinging on the ngv leading edge.

The measured rotor casing, time-averaged, static pressures are shown as a contour plot in Fig. 5. The positions of the tappings are marked as 'o'. The wall static pressure can be seen to fall by a factor of 2 in the axial plane through the blade passage, this reflects the supersonic design of the rotor blade. In the circumferential direction an effect of the ngvs can be seen by a variation in static pressure. Low patches of static pressure coincide with the predicted wake angle of the ngvs which are shown as dotted lines.

Figure 6 shows the unsteady rotor casing, static pressure for the uniform inlet temperature case. The data are plotted as individual time histories for one row of transducers (along the stagger angle) with the appropriate blade thickness shown. The blue and green vertical lines indicate the suction and pressure sides of the blade, whereas, the red line indicates the centerline of the transducer. For the last plot without these lines the blade does not cover the transducer. The solid lines are the measured static pressure and the dashed lines a TRANSCode CFD prediction. The calculation was performed for the rotor alone and contains no ngv secondary flow information or wake definition. Average inlet total pressure and a rotor hub exit static pressure were imposed as boundary conditions. These data have been ensemble averaged revolution-to-revolution over 120 rotor revolutions according to the following definition:

$$\tilde{P}(\tau) = \frac{1}{N}\sum_{n=1}^{N} P(n,\tau)$$

Pressure fluctuations within the time period of rotor passing reduce towards the trailing edge of the blade. The fluctuation levels over the early part of the blade are of the order of ± 0.5 bar.

For all axial locations a rapid pressure drop, starting just before the pressure side of the blade, across the rotor tip is seen. In the rotor passage the pressure decreases relatively slowly from pressure to suction surface.

In front of the suction surface a small peak in pressure can be seen. This feature becoming larger as we move from the leading edge to the trailing edge of the blade.

This is thought to be evidence of the tip leakage flow creating a vortex close to the suction surface. Over the blade chord the perturbations are lowest close to the rotor trailing edge. The perturbations increase to a maximum of approximately 0.6 bar by the midchord of the blade and remains at this maximum along most of the blade.

The comparison with the predicted static pressure is generally

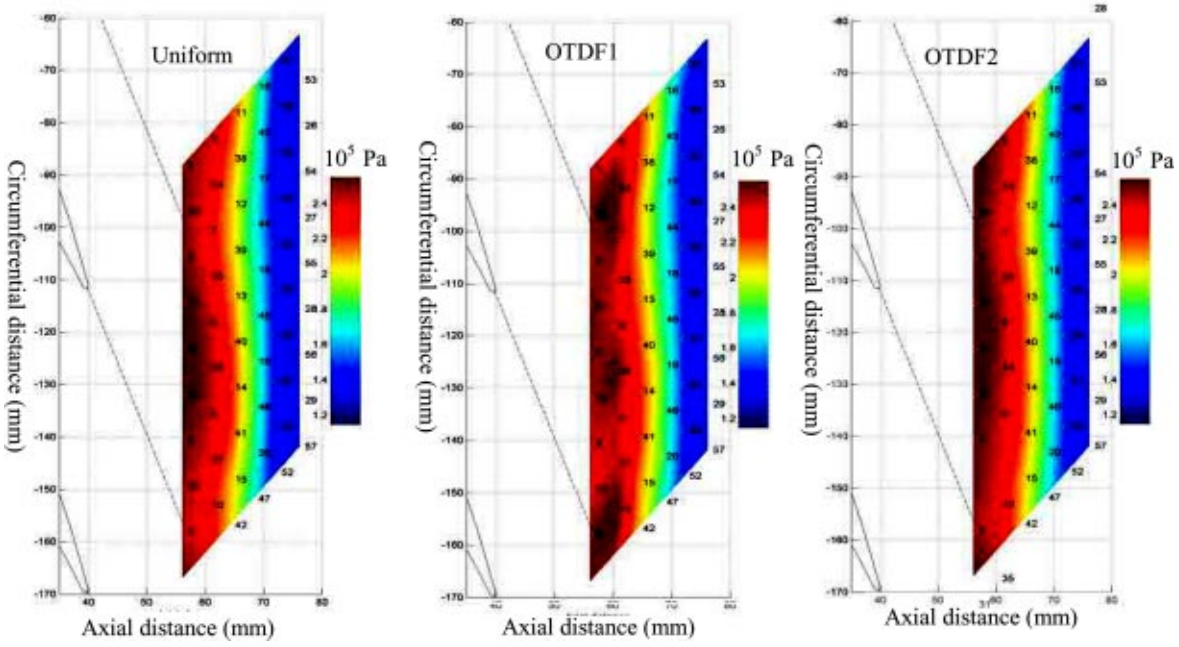

Fig. 5 Rotor casing static pressure (Pa)

Downloaded 31 May 2010 to 171.66.16.27. Redistribution subject to ASME license or copyright; see http://www.asme.org/terms/Terms_Use.cfm

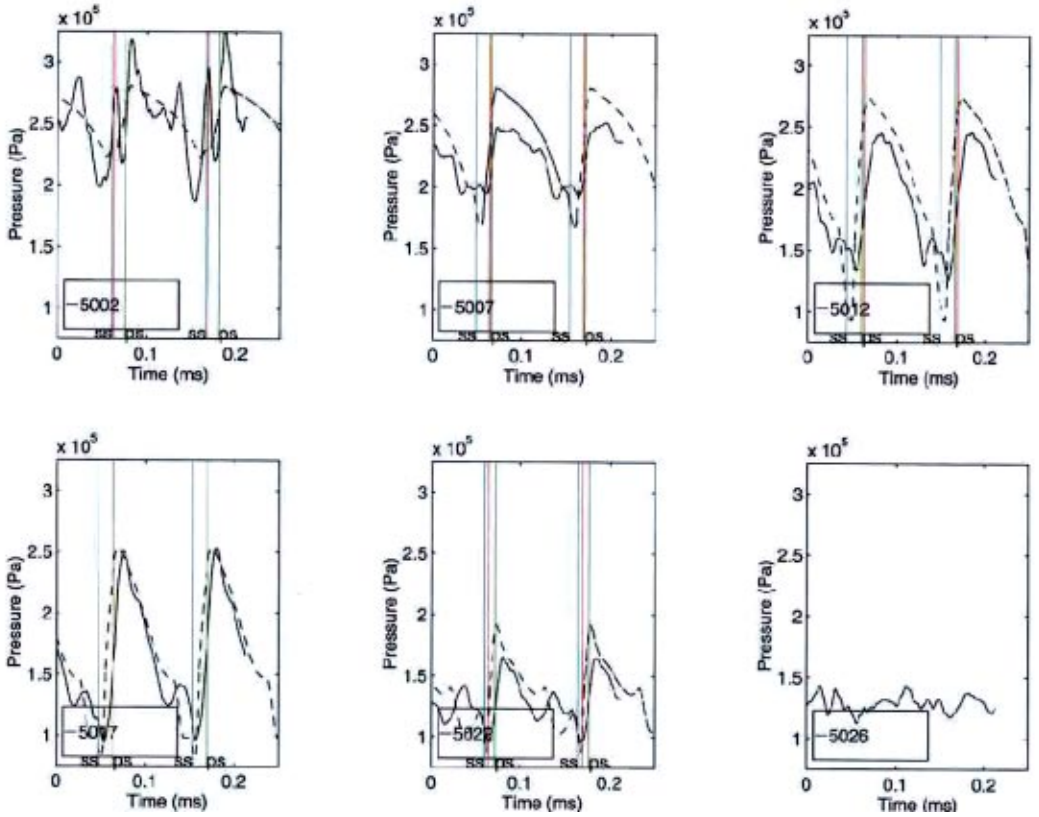

Fig. 6 Rotor casing static pressure time histories; blade surfaces and transducer positions indicated by vertical lines

good and improves towards the downstream part of the passage. This is most likely as a result of the CFD lacking in wake and interaction information from the ngvs.

Figures 7 and 8 show the complete rotor casing static pressure and the associated pressure random unsteadiness at specific times, for the uniform inlet temperature case. The random unsteadiness is calculated using the following definition:

$$\mathrm{Pr}(\tau)=\frac{1}{N}\sum_{n-1}^{N}\left|P(n,\tau)-\tilde{P}(\tau)\right|$$

The peak random unsteadiness time history shown in (Fig. 8) appears to move down the length of the turbine blade and repeat at the following blade.

The measured time-averaged heat transfer rate on the rotor casing has been used to compute the Nusselt number distribution. When calculating the Nusselt numbers for the ngv and rotor surface different driving temperatures are used. In the ngv case the stage inlet total temperature is used since the measurements are in the stationary frame of reference and the total temperature through the ngv is constant. For the rotor blade the measurements are in the relative frame of reference and hence, the rotor relative total temperature is used. With the rotor-casing wall the situation is more complex, the measurements are taken in the stationary frame of reference which results in a driving temperature reduction across the rotor row, due to the work extraction. The temperature across the MT1 rotor row reduces by about 100 K from the inlet to exit. Therefore to compute a relevant Nusselt number the local gas temperature (i.e., adiabatic wall temperature) is required.

The heat transfer rate and surface temperature history are both known and hence a plot of heat transfer rate against surface temperature was employed to find the adiabatic wall temperature. This adiabatic wall temperature from each thin film gage is thus used in the calculation of Nusselt numbers. Figure 9 shows the

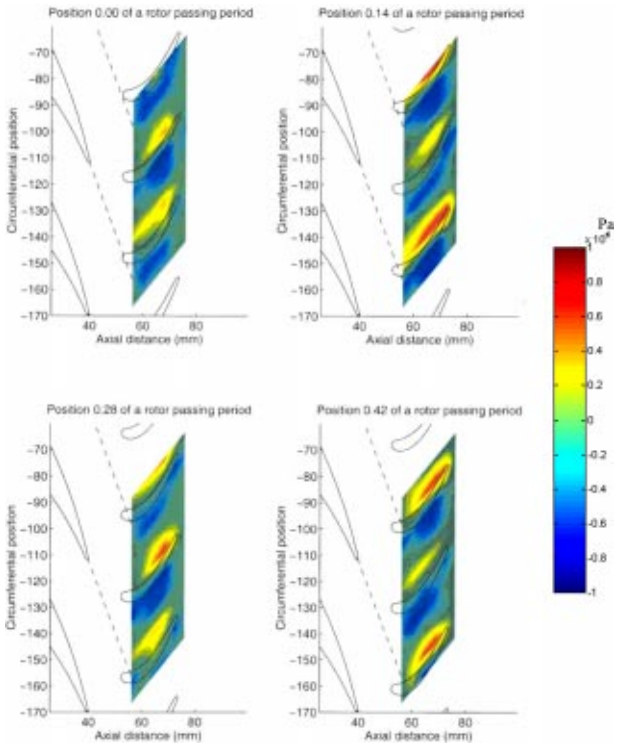

Fig. 7 Rotor casing instantaneous static pressure fluctuations (Pa)

Downloaded 31 May 2010 to 171.66.16.27. Redistribution subject to ASME license or copyright; see http://www.asme.org/terms/Terms_Use.cfm

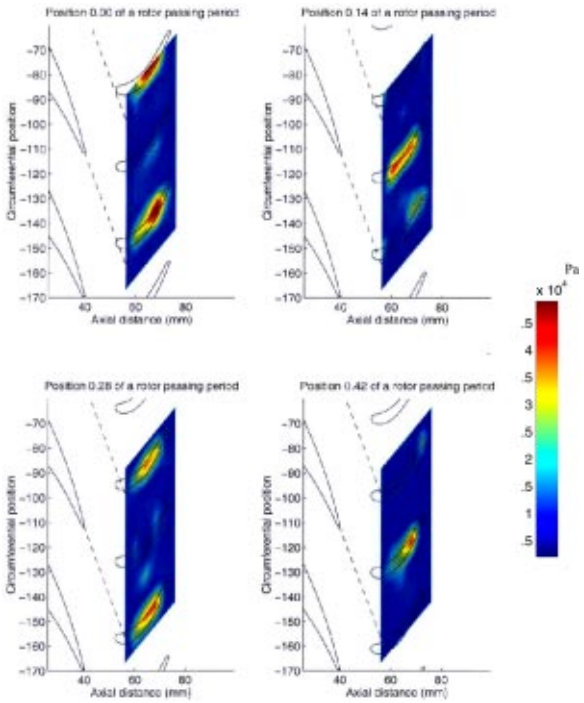

Fig. 8 Rotor casing instantaneous static pressure random unsteadiness

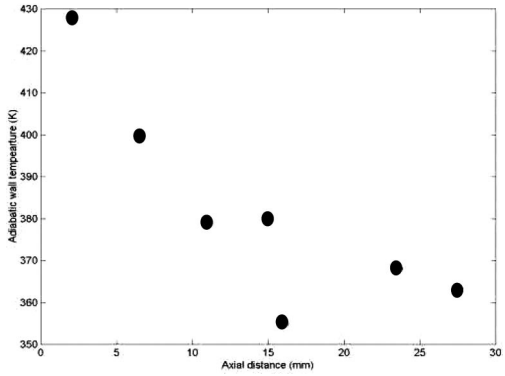

Fig. 9 Adiabatic wall temperature (K)

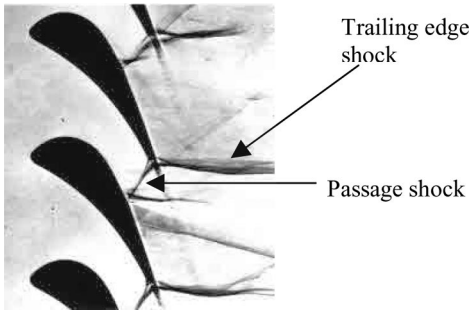

Fig. 11 Typical transonic NGV shock structure

adiabatic wall temperature for a row of gages through the rotor passage. The trace shows the temperature falling from around 430 K to about 360 K and more importantly it shows how the work extraction is distributed through the rotor passage.

The accuracy with which the adiabatic wall temperature is evaluated is assessed to be ±5 K. A contour plot of the Nusselt number for the whole endwall flow field measured is shown in Fig. 10 for the uniform, OTDF1 and OTDF2 inlet profiles. The Nusselt number is calculated using:

$$\mathrm{Nu}_c = \frac{q\bar{C}}{(T_{aw} - T_{\mathrm{wall}})k}$$

For the results with uniform inlet temperatures the Nusselt number distribution in the pitch wise direction varies by a factor of 2 with three regions of high Nusselt number.

Two of the high regions coincide with the trajectory of the predicted wake path. The third region is at about half an ngv pitch and the reasons for this are not obvious. Figure 11 gives a schlieren photograph of a cascade test showing the details of the shock structure formed for a transonic vane. Two shock waves can be seen within an ngv pitch. A trailing edge shock wave exists at the trailing edge of each ngv, extending downstream and is almost at 90 deg to the wake flow direction. The passage shock at the throat of the ngvs is reflected off the suction surface of the vane and follows an almost axial direction. When comparing the positions of these shock waves with the region of high Nusselt number, it becomes evident that the high Nusselt number regions coincide with the trailing edge shock waves and are not at the angle the wake flow takes. Furthermore, the third feature at mid passage can be explained by the reflected passage shock from the suction

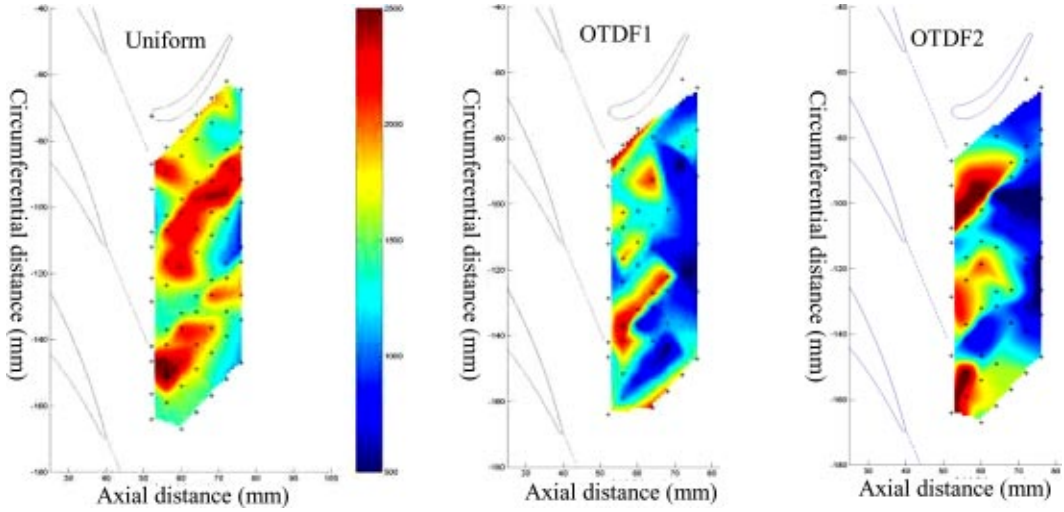

Fig. 10 Rotor casing Nusselt number based on rotor chord Nu_c

Downloaded 31 May 2010 to 171.66.16.27. Redistribution subject to ASME license or copyright; see http://www.asme.org/terms/Terms_Use.cfm

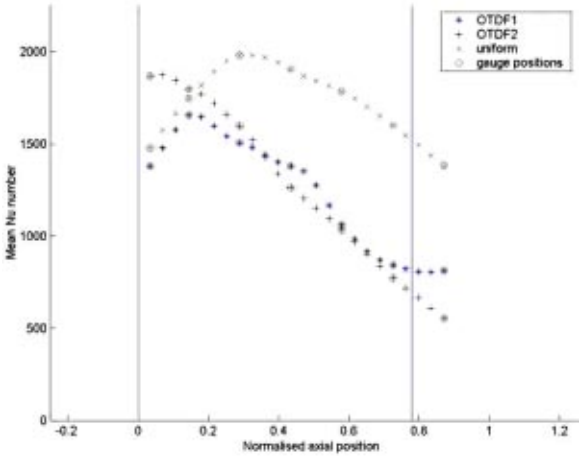

Fig. 12 Rotor casing Nusselt number Nu_c for conditions given in Table 1

side. The position and angle of the shock waves will vary with ngv passage, as each passage will have small manufacturing variations in throat size and trailing edge geometry. Hence, the regions of high Nusselt number may not necessarily be an ngv pitch apart. The shock location will also vary in an unsteady fashion as the rotor passes and modulates the ngv exit static pressure. This was seen earlier in the unsteady rotor casing pressure measurements (Fig. 8). Whilst the above hypothesis explains the reasons for the three regions of high Nusselt number, the steady-state measured and predicted ngv surface static pressure only show the presence

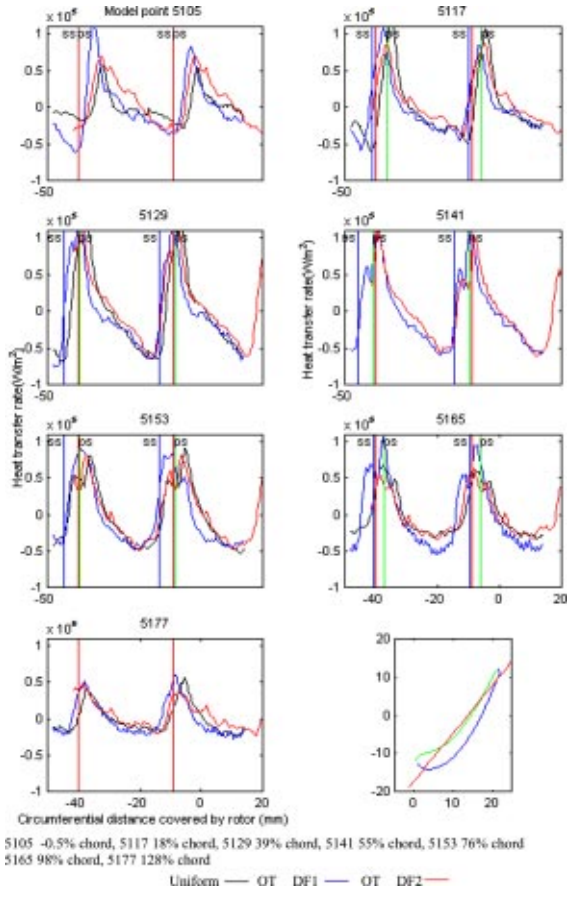

Fig. 13 Rotor casing heat transfer time histories

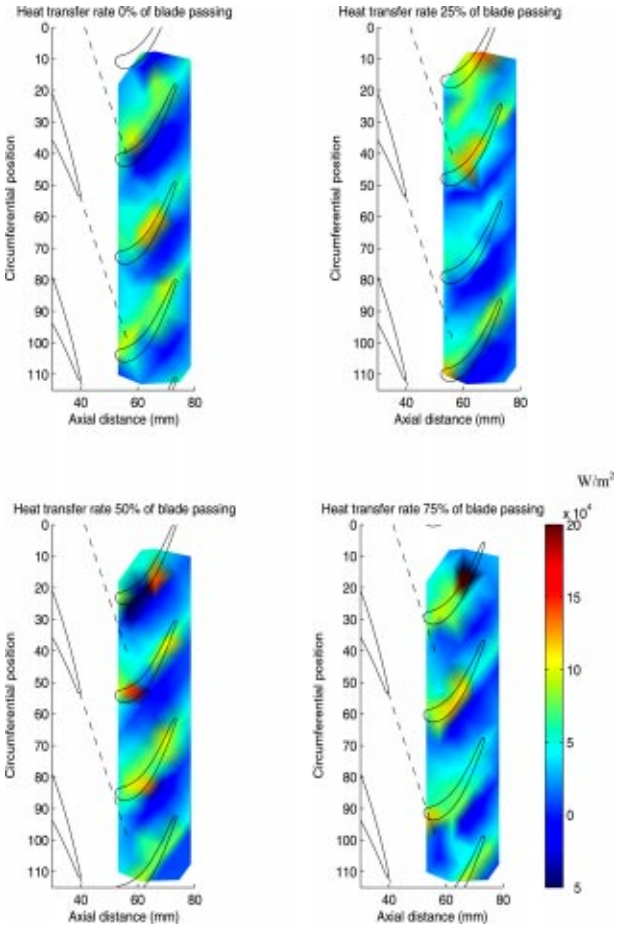

Fig. 14 Rotor casing instantaneous heat transfer rate fluctuations

of the passage shock wave. The trailing edge shock waves have not been measured or predicted thus far, however the rotor rotation causes the static pressure at exit to the ngv to fluctuate significantly. Hence, the trailing edge shock may only be present for short periods during the rotor passing period.

The OTDF1 results do not show three clear regions as with the uniform case. However, the OTDF2 results show three area of high heat transfer although they do not extend as far as the downstream part of the passage.

Figure 12 shows the casing data Nusselt number, circumferentially averaged to produce the axial variation. The uniform inlet temperature results show a Nusselt number around 1500 at the leading edge position of the rotor, peaking to a value of about 2000 at an axial location of around 30%. The Nusselt number then falls to a value of about 1400. The OTDF 1 results show similar results near the leading edge, but peak at about 1600 and then fall gradually to about 800. Whereas, the OTDF2 results show a higher value near the rotor leading edge position at around 1800 and fall gradually, in a similar way to the OTDF1 results.

Time-resolved heat transfer data were measured along rows which approximately follow the rotor stagger angle. These data have been ensemble-averaged similar to the rotor casing pressure measurements. Figure 13 shows heat transfer variations in time about the mean value over two rotor passings for a row of thin film gages. The blue and green vertical lines indicate the suction and pressure sides of the blades, whereas the red line indicates the centerline of the gage with the appropriate blade thickness. Gages that are not within the rotor passage have the red line to show the gage center line. Variations in heat transfer rate reduce towards the latter part of the blade. The peak-to-peak fluctuation levels are of

Downloaded 31 May 2010 to 171.66.16.27. Redistribution subject to ASME license or copyright; see http://www.asme.org/terms/Terms_Use.cfm

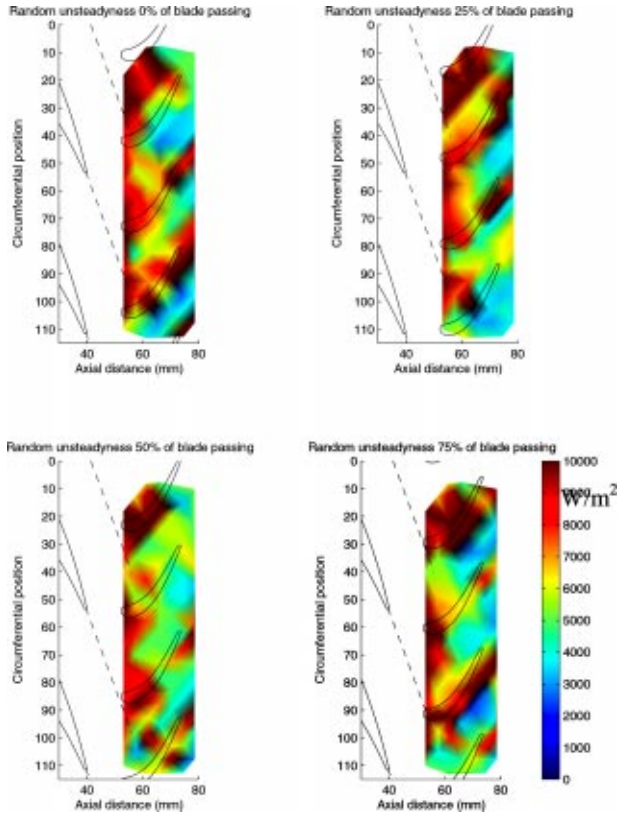

Fig. 15 Rotor casing heat transfer rate random unsteadiness

the order of 1.5E5 W/m^2. In all positions, except for the last gage which is after the blade, a rapid heat transfer rate drop can be seen taking place while the rotor tip passes, starting just before the pressure side of the blade. After reaching a minimum near the suction side the heat transfer rate increases as the pressure side approaches, reaching a peak just prior to the pressure side. As the blade tip passes over the third, fourth and fifth gages a small rise in heat transfer rate, which decreases after passing of the tip occurs. This feature becomes more evident on the fifth gage. This is thought to be caused by the tip leakage flow.

Overall, addition of RTDF/OTDF has not changed the shape or features of the heat transfer rate fluctuations significantly. However, the gage near the leading edge shows the peak heat transfer level to be higher.

Figures 14 and 15 show the overtip heat transfer rate distribution and the associated random unsteadiness distribution at various instantaneous time intervals for the uniform inlet case. The heat transfer rate is enhanced by the presence of the rotor blade at all time intervals with little effect from the ngv wake. The random unsteadiness given in Fig. 15 shows high unsteadiness in the earlier part of the rotor passage across the pitch. The remaining passage shows a lower level of unsteadiness.

The rotor tip time averaged Nusselt number is shown in Fig. 16. The levels are around 1000; this is similar to that measured on the rotor casing and rotor surface at 90% span. The OTDF1 results show a flatter distribution than the uniform results. Unfortunately, during the OTDF2 tests only one gage survived; however, this shows a higher level of Nusselt number than the uniform and OTDF1 case. A sample of time-resolved data for the rotor tip gages is shown in Fig. 17.

The heat transfer rate rises and falls very sharply at close to the ngv pitch period with fluctuations of $\pm$2E5 W/m^2. A smaller peak in between the larger ones is also evident on some parts of the data. The sharp rises and falls are thought to be caused by the shock structure discussed earlier.

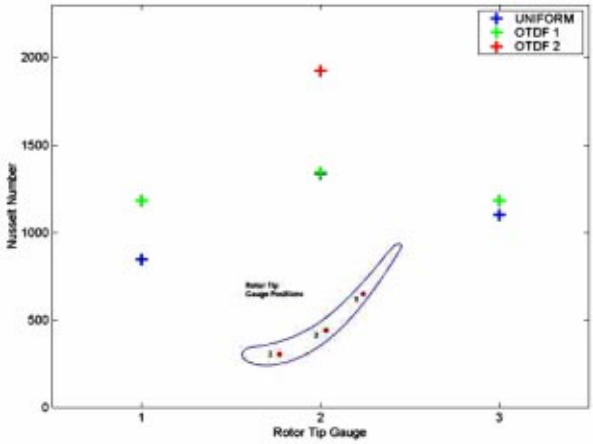

Fig. 16 Rotor tip Nusselt number Nu_c for conditions given in Table 1

Metzger et al. [1] presented a simple one-dimensional flow model to estimate the rotor tip heat transfer rates. A similar approach has been taken here to estimate heat transfer rate to the rotor tip and shroud. If we consider the simple tip model given in Fig. 18, calculations show that the flow over the tip is not fully developed. Hence, in the blade relative frame of reference the rotor tip can be treated as a flat plate Indeed this model will ignore the separation bubble on the leading edge of the tip although, Metzger did include an inlet shape correction to the heat transfer.

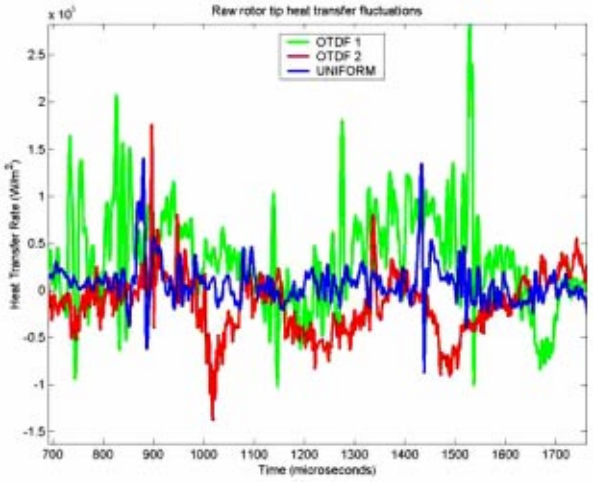

Fig. 17 Rotor tip unsteady heat transfer rate

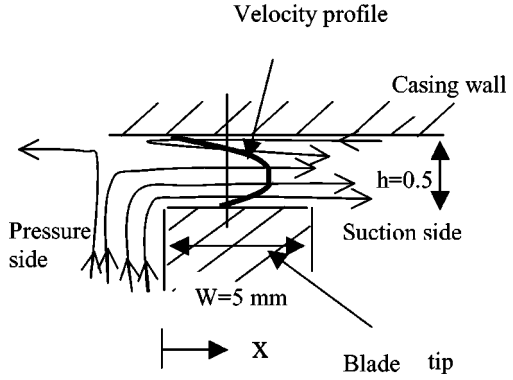

Fig. 18 Two-dimensional model of tip flow relative to the rotor

Downloaded 31 May 2010 to 171.66.16.27. Redistribution subject to ASME license or copyright; see http://www.asme.org/terms/Terms_Use.cfm

The following integral boundary layer correlation can be applied, starting at the leading edge of the blade tip at the pressure side:

$$\mathrm{Nu}_x = 0.0287 \ \mathrm{Pr}^{0.6} \mathrm{Re}_x^{4/5}$$

Re_x is based on the velocity of flow through the gap relative to the rotor. Evaluating this equation for a distance of 2.5 mm for the center of the blade tip yields a Nusselt number of about 1500. This is in reasonable agreement with the values for the uniform case in Fig. 17.

If we now consider the small part of the shroud, directly above the rotor blade tip, and assume that a stagnation point exists on it in line with the pressure side of the blade. Then, using a similar approach a flat plate turbulent boundary layer, calculation can be performed to evaluate the local heat transfer rate

$$\mathrm{Nu}_x = 0.0242 \ \mathrm{Pr}^{0.6} \mathrm{Re}_x^{4/5}$$

In this case, Re_x is based on the flow velocity through the gap relative to the casing. The gas temperature is the rotor relative temperature at this point. The local Nusselt number is evaluated to be approximately 2000, which is in reasonable agreement with the measured value.

Summary and Conclusions

The study investigated the rotor tip and shroud heat transfer and aerodynamics with and without inlet nonuniform temperatures. The detailed measurements provide a better understanding of the local heat transfer to the rotor tip and casing surfaces. When comparing the uniform case to OTDF1 and OTDF2 the heat transfer pattern was changed significantly. The overall heat load was reduced with inlet nonuniformity compared to a uniform inlet temperature. The OTDF1 and OTDF2 gave a similar overall thermal load. The unsteady heat transfer results showed little difference in form between the uniform and nonuniform cases. The highest heat transfer rate on the shroud was seen above the pressure side of the blade, this also showed the highest random unsteadiness marking the tip leakage region. The measured static pressures on the rotor casing provided complementary information on the flow field. The average static pressures showed very little difference between the uniform and nonuniform cases.

A simple one-dimensional boundary layer model has been used to estimate the heat transfer rates to the rotor tip and casing.

Acknowledgments

The assistance of S. J. Andeson, A. H. Mole, W. J. Cortbett, J. Hurrion and T. Patel in the acquisition of the data contained in this report is gratefully acknowledged. The work forms part of a Brite Euram Fourth Framework Programme TATEF, Contract No BRPR-CT97-0519.

Nomenclature

C = rotor tangential chord
K = thermal conductivity of air
N = total no. of revolutions
n = number of particular revolution
Nu_c = Nusselt no. based on true chord
Nu_x = Nusselt no. based on distance along tip gap from pressure surface, Fig. 18
$\tilde{P}(\tau)$ = time average signal, ensemble average
$P(n,\tau)$ = instantaneous signal
$\mathrm{Pr}(\tau)$ = random unsteadiness
Pr = Prandtl no.
q = measured heat transfer rate
Re_x = Reynolds no. based on distance x along tip gap from pressure surface, Fig. 18
T_{prel} = relative total temperature
T_{wall} = measured surface temperature
T_{aw} = adiabatic wall temperature
T_{coolant} = coolant temperature injected through casing, hub endwalls and turbulence rods
T_{mean} = mean temperature of flow
T_{radial} = radial temperature of flow circumferentially averaged
T_{local} = local temperature of flow
τ = time within each revolution
OTDF = overall temperature distortion factor $(T_{\mathrm{local}}-T_{\mathrm{mean}})/(T_{\mathrm{mean}}-T_{\mathrm{coolant}})$
RTDF = radial temperature distortion factor $(T_{\mathrm{radial}}-T_{\mathrm{mean}})/(T_{\mathrm{mean}}-T_{\mathrm{coolant}})$

References

[1] Metzger, D. E., Dunn, M. G., and Hah, C., 1991, "Turbine Tip and Shroud Heat Transfer," ASME J. Turbomach., **113**, pp. 502–507.
[2] Bindon, J. P., 1989, "The Measurement and Formation of Tip Clearance Loss," ASME J. Turbomach., **111**, pp. 257–263.
[3] Luo, J., and Lakshminarayana, B., 1997, "Three-Dimensional Navier-Stokes Analysis of Turbine Rotor and Tip Leakage Flowfield," ASME Int. Gas Turbine Conference 97-GT.
[4] Dunn, M. G., Rae, W. J., and Holt, J. L., 1984, "Measurements and Analysis of Heat FLux Data in a Turbine Stage: Part I—Description of Experimental Apparatus and Data Analysis," ASME J. Turbomach., **106**, pp. 229–240.
[5] Epstein, A. H., Guenette, G. R., Norton, R. J. G., and Yuzhang, C., 1985, "Time Resolved Measurements of a Turbine Rotor Stationary Tip Casing Pressure and Heat."
[6] Kumada, M., Iwata, S., Obata, M., and Watanabe, O., 1994, "Tip Clearance Effects on Heat Transfer and Flow Turbine," ASME J. Turbomach., **116**, pp. 39–44.
[7] Dunn, M. G., and Halderman, C. W., 2000 "Time-averaged Heat Flux for a Recessed Tip, Lip and Platform of a Transonic Turbine Blade," ASME 2000-GT-0197.
[8] Azad, G. S., Han, J., and Boyle, R. J., 2000, "Heat Transfer and Flow on the Squealer Tip of a Gas Turbine Blade," ASME 2000-GT-195.
[9] Ameri, A. A., and Bunker, R. S., 1999, "Heat Transfer and Flow on the First Stage Blade Tip of a Power Generation Gas Turbine: Part 2: Simulation Results," ASME 99-GT-283.
[10] Bunker, R. S., Baily, J. C., and Ameri, A. A., 1999, "Heat Transfer and Flow on the First Stage Blade Tip of a Power Generation Gas Turbine: Part 1: Experimental Results," ASME 99-GT-169.
[11] Mayle, R. E., and Metzger, D. E., 1982, "Heat Transfer at the Tip of Unshrouded Turbine Blade," Proceedings of the 7th Int. Heat Transfer Conference, Vol. 3, pp. 87–92.
[12] Metzger, D. E., and Rued, K., 1989, "The Influence of Turbine Clearance Gap Leakage on Flowpath Velocities and Heat Transfer, Part 1: Sink Flow Effects on Blade Pressure Sides," ASME J. Turbomach., **111**, pp. 284–292.
[13] Shang Tonghuo, 1995, "Influence of Inlet Temperature Distortion on Turbine Heat Transfer," Ph.D. thesis, Massachusetts Institute of Technology, Cambridge, MA.
[14] Piccini, E., Guo, S. M., and Jones, T. V., 2000, "The Development of a New Direct Heat Transfer Heat Flux Gage for Heat Transfer Facilities," Meas. Sci. Technol., **11**, pp. 342–349.

Downloaded 31 May 2010 to 171.66.16.27. Redistribution subject to ASME license or copyright; see http://www.asme.org/terms/Terms_Use.cfm

Local Mass/Heat Transfer on Turbine Blade Near-Tip Surfaces

P. Jin

R. J. Goldstein

Heat Transfer Laboratory,
Department of Mechanical Engineering,
University of Minnesota
Minneapolis, MN 55455

Local mass transfer measurements on a simulated high-pressure turbine blade are conducted in a linear cascade with tip clearance, using a naphthalene sublimation technique. The effects of tip clearance (0.86–6.90% of chord) are investigated at an exit Reynolds number of 5.8×10^5 and a low turbulence intensity of 0.2%. The effects of the exit Reynolds number ($4-7\times10^5$) and the turbulence intensity (0.2 and 12.0%) are also measured for the smallest tip clearance. The effect of tip clearance on the mass transfer on the pressure surface is limited to 10% of the blade height from the tip at smaller tip clearances. At the largest tip clearance high mass transfer rates are induced at 15% of curvilinear distance (S_p/C) by the strong acceleration of the fluid on the pressure side into the clearance. The effect of tip clearance on the mass transfer is not very evident on the suction surface for curvilinear distance of $S_s/C<0.21$. However, much higher mass transfer rates are caused downstream of $S_s/C\approx0.50$ by the tip leakage vortex at the smallest tip clearance, while at the largest tip clearance, the average mass transfer is lower than that with zero tip clearance, probably because the strong leakage vortex pushes the passage vortex away from the suction surface. High mainstream turbulence level (12.0%) increases the local mass transfer rates on the pressure surface, while a higher mainstream Reynolds number generates higher local mass transfer rates on both near-tip surfaces. [DOI: 10.1115/1.1554410]

Introduction

Tip leakage flow can have an important impact on the performance of a turbine system, in terms of aerodynamic losses and thermodynamic penalty. The leakage flow induced by the pressure difference between the pressure side and suction side of a blade increases the aerodynamic losses and inefficiency in the turbine, reducing the turbine blade forces and the work done in the stage. It is estimated that a 1% clearance of blade height can cause a 1–2% decrease in turbine stage efficiency [1]. In addition, the tip leakage flow and its interactions with the main passage flow and the secondary flows can increase the heat transfer on the turbine blade surface near the tip, leading to high surface temperatures in regions near the blade tip, diminishing the structural durability of the blades [2].

Experimental studies have been conducted to understand the tip leakage flow in turbine cascades, including flow visualization, and static pressure and loss coefficients measurement inside the tip clearance and blade passage in turbine cascades, such as Sjolander and Amrud [3], Moore and Tilton [4], Bindon [5], Yamamoto [6], and Kang and Hirsch [7].

Though effects of tip leakage flow on turbine blade heat transfer have been investigated, most studies were conducted on idealized experimental conditions (on a flat plate or in rectangular cavities). Not many detailed local heat transfer measurements on a turbine blade tip surface and the near-tip surfaces are available in the open literature.

The effect of leakage flow on turbine blade heat transfer was not emphasized until the paper of Mayle and Metzger [2]. Heat transfer experiments were conducted on a flat surface with a moving wall provided by the rim surface of a rotating disk. Their results were in good agreement with the Colburn equation. Chyu et al. [8] and Metzger et al. [9] experimentally investigated the mass/heat transfer process with turbulent flow over shrouded, rectangular cavities using naphthalene sublimation and a surface coating technique, respectively, to simulate the heat transfer at the tip region of grooved rotor blades.

The effects of sink flow on the blade pressure side, and source flow on the blade suction side on turbine blade heat transfer were studied by Metzger and Rued [10] and Rued and Metzger [11] in a water tunnel. The heat transfer measurements showed that the leakage generates large localized heat transfer rates near the gap due to the strong acceleration in the sink flow. Even higher local heat transfer rates are found in the source flow, though a different mechanism, the presence of a small but intensive vortex at the gap edge is involved.

Metzger et al. [12] proposed a simple model to describe the flow over an axial turbine blade tip and the adjacent stationary shroud using the Dittus-Boelter fully developed duct flow correlation together with an augmentation factor of 2.3 to account for the entry flow effect inside the tip. Film-cooled turbine blade tip heat transfer and effectiveness were investigated by Kim and Metzger [13] and Kim et al. [14] on a simulated blade tip surface downstream of a single line of film cooling injection sites using a transient thermal liquid crystal test technique.

Recently, Bunker et al. [15] investigated the heat transfer and flow on the first stage blade tip of a power generation gas turbine and provided full surface information on heat transfer coefficients with pressure distribution on the blade tip and shroud for sharp-edged and radius-edge clearances and at different free stream turbulence levels. The flow and heat transfer on the first stage blade tip of an aircraft gas turbine was studied by Teng et al. [16] and Azad et al. [17] using a transient liquid crystal technique.

In the present study, a naphthalene sublimation technique is utilized to measure the mass transfer coefficients from a high-pressure turbine blade near-tip surfaces in a linear cascade with tip clearance. Use of the heat/mass transfer analogy results provides information on the equivalent heat transfer situation.

Experimental Method and Apparatus

The naphthalene sublimation technique is a well-established method, which with the heat/mass transfer analogy enables us to obtain detailed local mass/heat transfer data on complex surfaces. The naphthalene sublimation method and the heat/mass transfer

Contributed by the International Gas Turbine Institute and presented at the International Gas Turbine and Aeroengine Congress and Exhibition, Amsterdam, The Netherlands, June 3–6, 2002. Manuscript received by the IGTI October 10, 2001. Paper No. 2002-GT-30556. Review Chair: E. Benvenuti.

 Copyright © 2003 by ASME

Downloaded 31 May 2010 to 171.66.16.27. Redistribution subject to ASME license or copyright; see http://www.asme.org/terms/Terms_Use.cfm

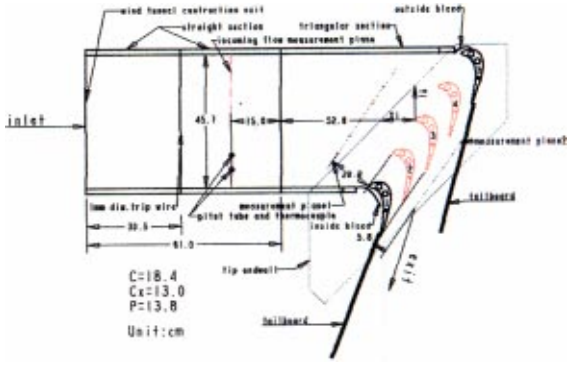

Fig. 1 Planview of the test section

analogy were reviewed by Goldstein and Cho [18]. Goldstein and Spores [19] used a local mass transfer technique to obtain much detail of the convection process for the secondary flows in a turbine cascade. Naphthalene sublimation technique was also used to investigate convective transport from a turbine blade in a linear cascade by Goldstein et al. [20] and Wang et al. [21], including the effects of high free stream turbulence level and length scale and mainstream Reynolds number.

To summarize, the naphthalene sublimation technique can be used to determine the convective component of mass transfer with the absence of wall conduction and radiation errors. A mass transfer problem can be converted to a heat transfer problem under the equivalent boundary conditions by the mass/heat transfer analogy. The mass transfer coefficient can be obtained from

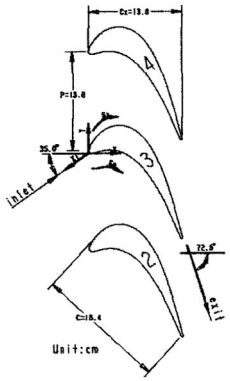

(*a*)

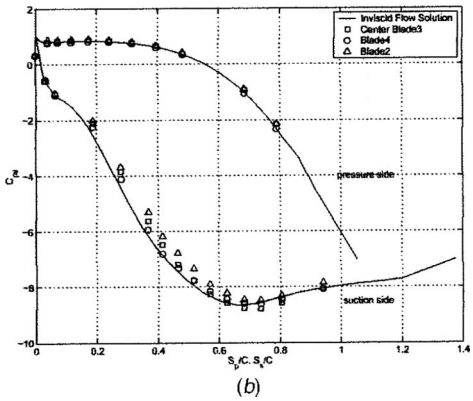

(*b*)

Fig. 2 Cascade blade geometry and balance test—(*a*) cascade blade geometry, (*b*) cascade blade balance test data

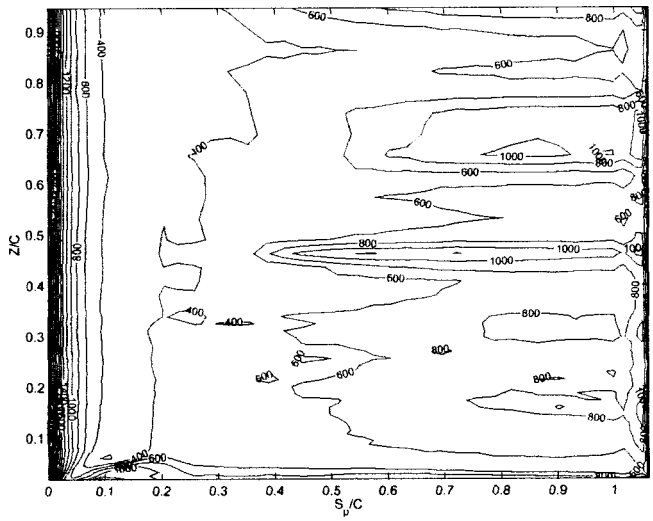

(*a*)

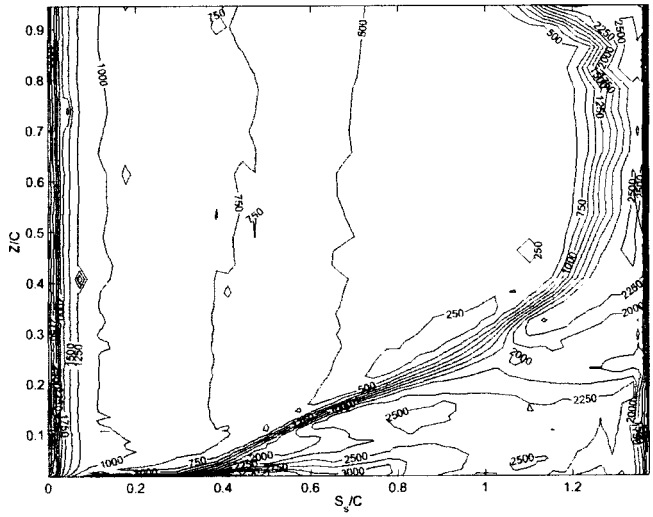

(*b*)

Fig. 3 Sh contour with zero tip clearance—(*a*) pressure surface, (*b*) suction surface

$$h_m = \frac{\dot{m}}{\rho_{v,w} - \rho_{v,\infty}} = \frac{\dot{m}}{\rho_{v,w}} \quad \text{since} \quad \rho_{v,\infty} = 0 \tag{1}$$

$$\dot{m} = \rho_s \frac{\delta y}{\delta \tau} \tag{2}$$

A dimensionless mass transfer coefficient, Sherwood number, similar to the heat transfer Nusselt number, is used for comparing results.

A multipurpose blowing-type wind tunnel in the Heat Transfer Laboratory at the University of Minnesota is employed in the study. Air drawn through a filter by a 22.4 kW blower arrives at the test section through a square contraction nozzle with an area ratio of 6.25 and an exit of 45.7×45.7 cm^2.

The test section as shown in Fig. 1 is connected to the exit of the contraction of the wind tunnel. The linear turbine cascade consists of five 45.7 cm long simulated high-pressure turbine rotor blades (aluminum) with central blade configuration. The top wall simulates the casing of the turbine. The space between the three middle blades and the tip-endwall forms the blade tip clearance, which can be varied by adding aluminum spacers with different thicknesses between the blades and the bottom wall. Tip clear-

Downloaded 31 May 2010 to 171.66.16.27. Redistribution subject to ASME license or copyright; see http://www.asme.org/terms/Terms_Use.cfm

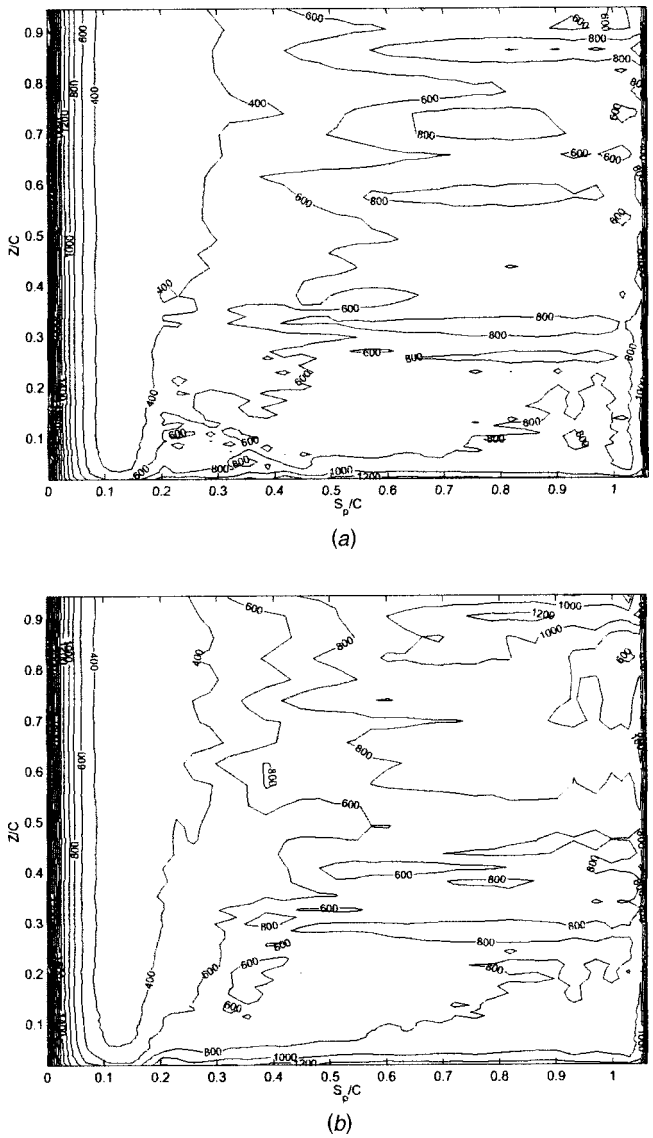

Fig. 4 Sh contour on the pressure surface—(*a*) $t/C=0.86\%$, (*b*) $t/C=1.72\%$

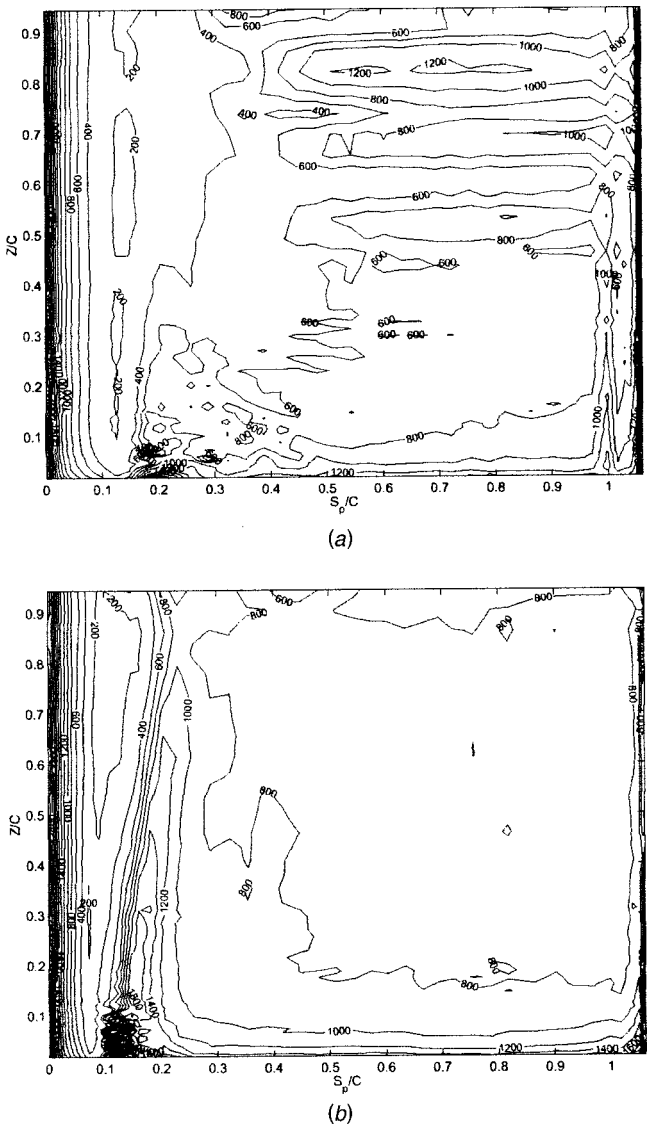

Fig. 5 Sh contour on the pressure surface—(*a*) $t/C=3.45\%$, (*b*) $t/C=6.90\%$

ances employed in this study are 0.86, 1.72, 3.45, and 6.90%C. The high-performance turbine blade profile and geometry data are shown in Fig. 2(*a*). The space between the bleeds and the outside blades as well as the orientation of the tailboards (Fig. 1) are adjustable to obtain periodic flows in the blade passages. The cascade balance is checked by comparing the static pressure obtained from a special pressure measurement blade at the positions of the three middle blades with data from an inviscid flow solution. The established periodic flows in the blade passages are shown in Fig. 2(*b*)

A specially designed mold and modified casting procedures are employed to obtain a naphthalene blade with smooth naphthalene-covered surfaces including the tip surface; particular care must be taken in controlling the temperature of the mold during casting. The T-type thermocouples used in the experiment for measuring the ambient, air flow, and naphthalene surface temperatures were previously calibrated and are integrated with a GPIB board enabled Linux workstation to collect the temperatures in the system during the experiment. The total pressure is measured with an impact tube inserted at the incoming flow measurement plane shown in Fig. 1. The dynamic pressure and static pressure are obtained with a micro-manometer and a manometer respectively. The depth change of the surfaces of the naphthalene blade during the test is measured with an automated four-axis data acquisition system developed in the Heat Transfer Laboratory at the University of Minnesota [18].

The uncertainty in naphthalene surface temperature measurement is 0.09% in absolute temperature with 95% confidence level. The uncertainty in mainstream velocity is 1.0%, and in the naphthalene sublimation depth measurement is 0.80%, which includes the error of repositioning of LVDT gage. The uncertainty in mass transfer coefficient and Sherwood number at 95% confidence level are 5.7 and 7.6%, respectively. The errors are mainly caused by the uncertainty in properties of naphthalene. The naphthalene loss due to natural convection is estimated and included in the foregoing uncertainty analysis. The experimental system and procedures are described in detail by Jin [22].

The turbulent boundary layer characteristics established downstream of the trip on the (blade-tip) endwall (in Fig. 1) are measured at three different locations on the measurement plane 1 ($X/C_x=-1.6$ and in Fig. 1) at a distance of one half pitch from each other on the tip endwall using a single-sensor hot wire probe. The integrated displacement thickness and shape factor near the leading edge of the test blade are 0.17 cm and 1.38 at a main-

Downloaded 31 May 2010 to 171.66.16.27. Redistribution subject to ASME license or copyright; see http://www.asme.org/terms/Terms_Use.cfm

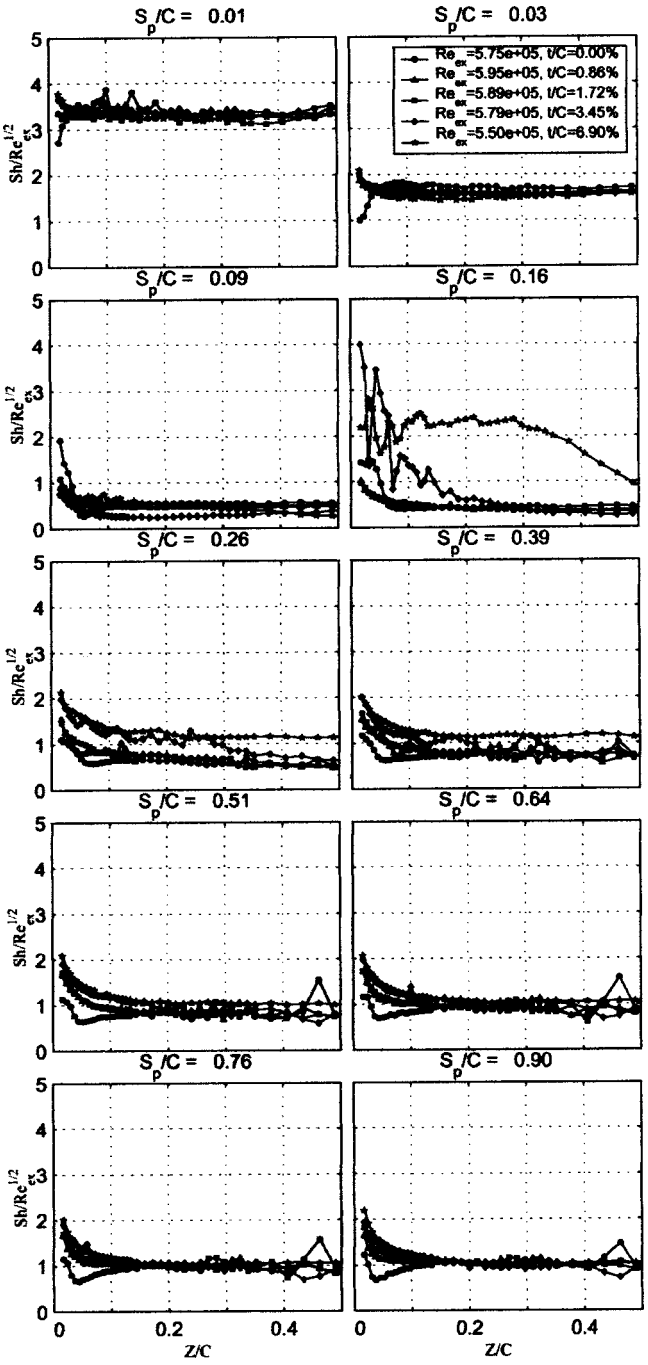

Fig. 6 $Sh/Re_{ex}^{1/2}$ on the pressure surface

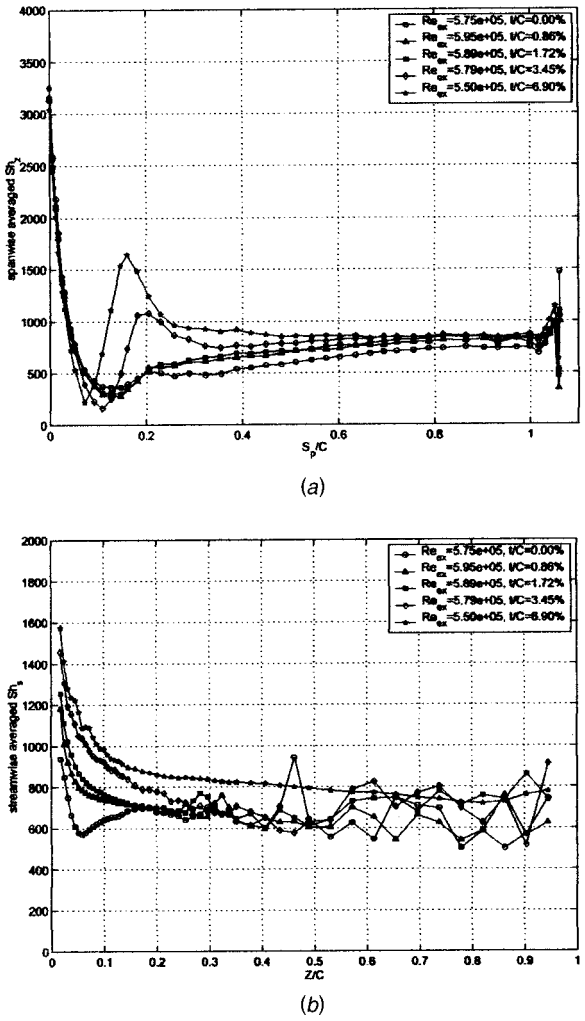

Fig. 7 Average Sh on the pressure surface—(*a*) spanwise average, (*b*) streamwise average

stream inlet velocity of 20 m/s and turbulence intensity of 0.2%, respectively, and the displacement thickness is typical of that in a gas turbine engine (1% of chord). For a typical sublimation depth of 60 μm, the effect of thinner naphthalene wall on boundary layer thickness (of order of 10 mm) can be neglected.

The mainstream turbulence characterization is also conducted at $X/C_x - 1.6$, but outside of boundary layer. A bar grid turbulence generator made from wood is placed 5 cm upstream of the trip wire. The data collected with the single hot wire sensor match well with the von Karman's correlation and power law (with an index of $-5/3$) for energy spectrum at relative high wave numbers, showing isotropic characteristics of the flow. A integral length scale of 2.7 cm is calculated from autocorrelations of local instantaneous velocity with mainstream turbulence intensity of 12%.

Experimental Results and Discussion

The results from the present study are presented for different tip clearances, Reynolds numbers, and turbulence intensities in this section. In all the figures, the blade tip has a coordinate of $Z/C = 0$.

Pressure Surface Near the Tip. Effects of zero tip clearance are shown in Fig. 3. Effects of tip clearance on the mass transfer on the pressure surface are shown in the contour plots of Figs. 4 and 5 at Reynolds number of about 5.8×10^5 and turbulence intensity of 0.2%. Similar to the results with no tip clearance (Fig. 3(*a*)), the nonuniform mass transfer rates appear on the pressure surface for all tip clearances except the largest one. However, the effect of corner vortices disappear near the tip edge. Instead, the relatively higher mass transfer region near the tip edge after $S_p/C > 0.15$ is caused by the leakage flow sucked into the tip clearance. This effect of acceleration is so strong that much higher and irregular mass transfer rates are induced at the two largest tip clearances at about $S_p/C = 0.15$ near the tip edge and extended further away from the tip in the span direction at $t/C - 6.90\%$. This strong acceleration apparently also reduces the nonuniform mass transfer rates on the pressure surface at the largest tip clearance, as shown in local and averaged Sh plots.

Downloaded 31 May 2010 to 171.66.16.27. Redistribution subject to ASME license or copyright; see http://www.asme.org/terms/Terms_Use.cfm

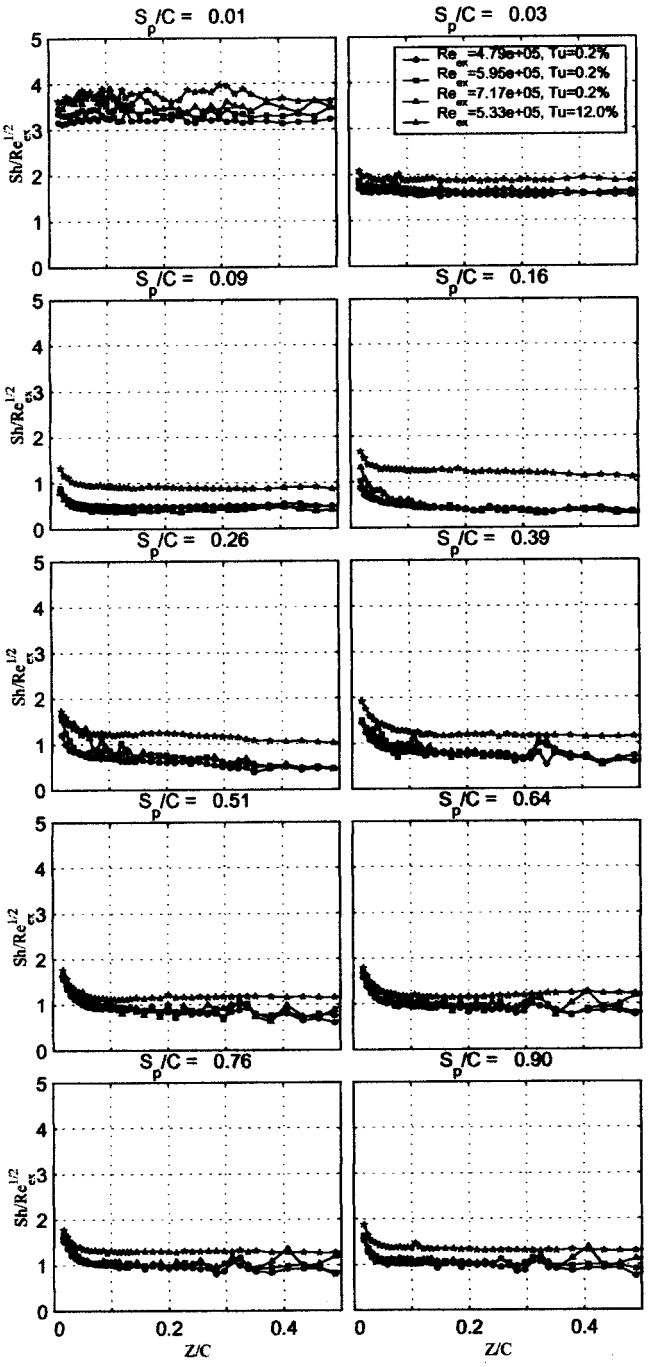

Fig. 8 Sh/$Re_{ex}^{1/2}$ on the pressure surface at $t/C=0.86\%$

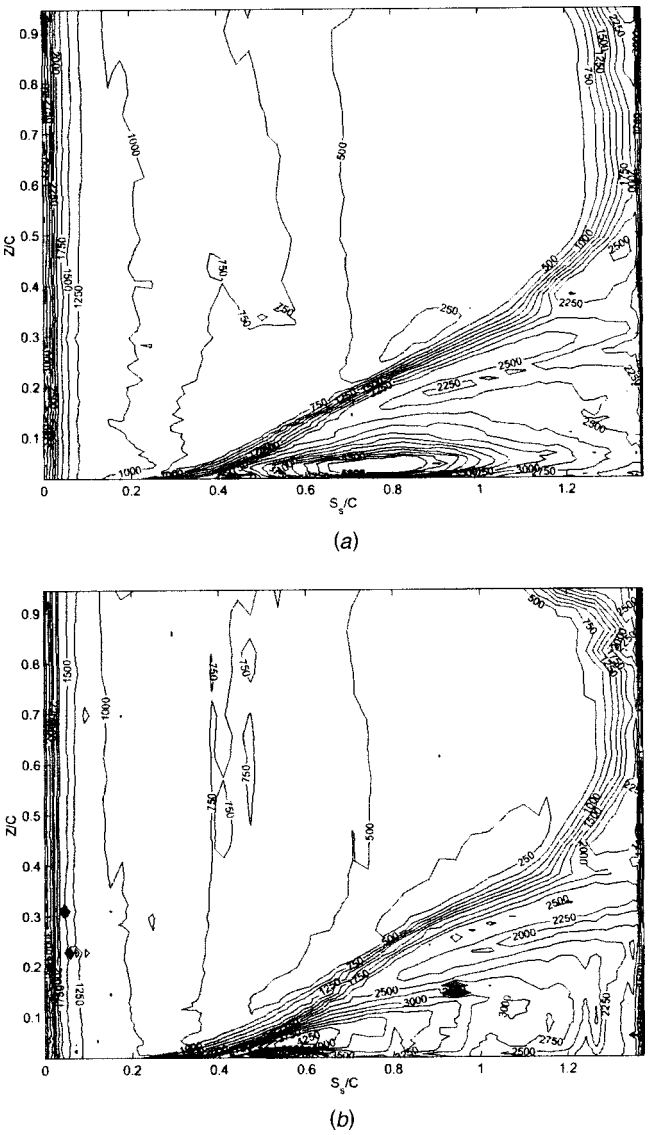

Fig. 9 Sh contour on the suction surface—(*a*) $t/C=0.86\%$, (*b*) $t/C=1.72\%$

Local $Sh/Re_{ex}^{1/2}$, calculated from the same set of data as the contour plots, at different S_p/C locations in the span direction starting from the tip are plotted in Fig. 6 for different tip clearances. The mass transfer near the tip on the pressure surface is quite different for the case with no tip clearance: the mass transfer is largest at the tip and decreases gradually in the span direction for all nonzero tip clearances (Fig. 6). However, the effect of different nonzero tip clearances on the mass transfer near the tip is not very strong upstream of $S_p/C=0.09$. Between $S_p/C=0.09$ and $S_p/C=0.51$, the two largest tip clearances result in much higher and irregular mass transfer rates near the tip than the two smaller tip clearances, which is not well understood at this publication since one expects the acceleration of leakage into the tip clearance is less strong for large tip clearances. Downstream of $S_p/C=0.51$, the mass transfer rates near the tip increase as tip clearance becomes larger and are much higher than the case with zero tip clearance, though the effect of tip clearance is limited to the region close to the tip edge and generally within $Z/C<0.15$. For $S_p/C>0.76$, the mass transfer curves tend to collapse to one after $Z/C=0.15$ disregarding the nonuniform mass transfer rates near $Z/C=0.4$. Generally, the effect of tip clearance is limited to $Z/C<0.1$ for the small tip clearances. The present results for the effect of tip leakage flow on the mass/heat transfer on the pressure surface differ from the results of Metzger and Rued's [10] sink flow measurements, which indicate higher heat transfer rates (up to 100% near the edge) to extend to 30% of the span for the small tip clearances. This may be caused by differences in experimental setup such as cascade flow versus gap flow, air versus water.

Spanwise and streamwise averaged Sh on the pressure surface are plotted in Fig. 7 for different tip clearances. From the top figure of Sh averaged over a span close to the blade chord, we observe that the effect of tip clearance is evident only for the two largest tip clearances around $S_p/C=0.2$. As suggested in the foregoing, this is caused by the highly accelerated suction flow at the larger tip clearances. In the bottom figure, the Sh numbers are averaged in the S_p direction. For zero tip clearance, the minimum

Downloaded 31 May 2010 to 171.66.16.27. Redistribution subject to ASME license or copyright; see http://www.asme.org/terms/Terms_Use.cfm

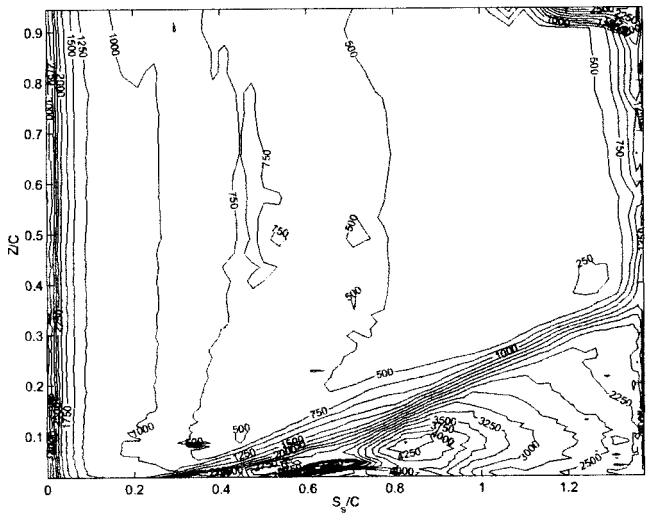

(*a*)

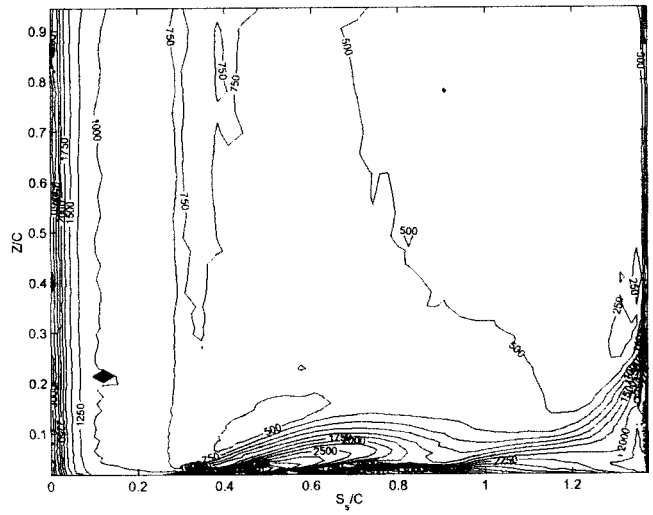

(*b*)

Fig. 10 Sh contour on the suction surface—(*a*) $t/c=3.45\%$, (*b*) $t/C=6.90\%$

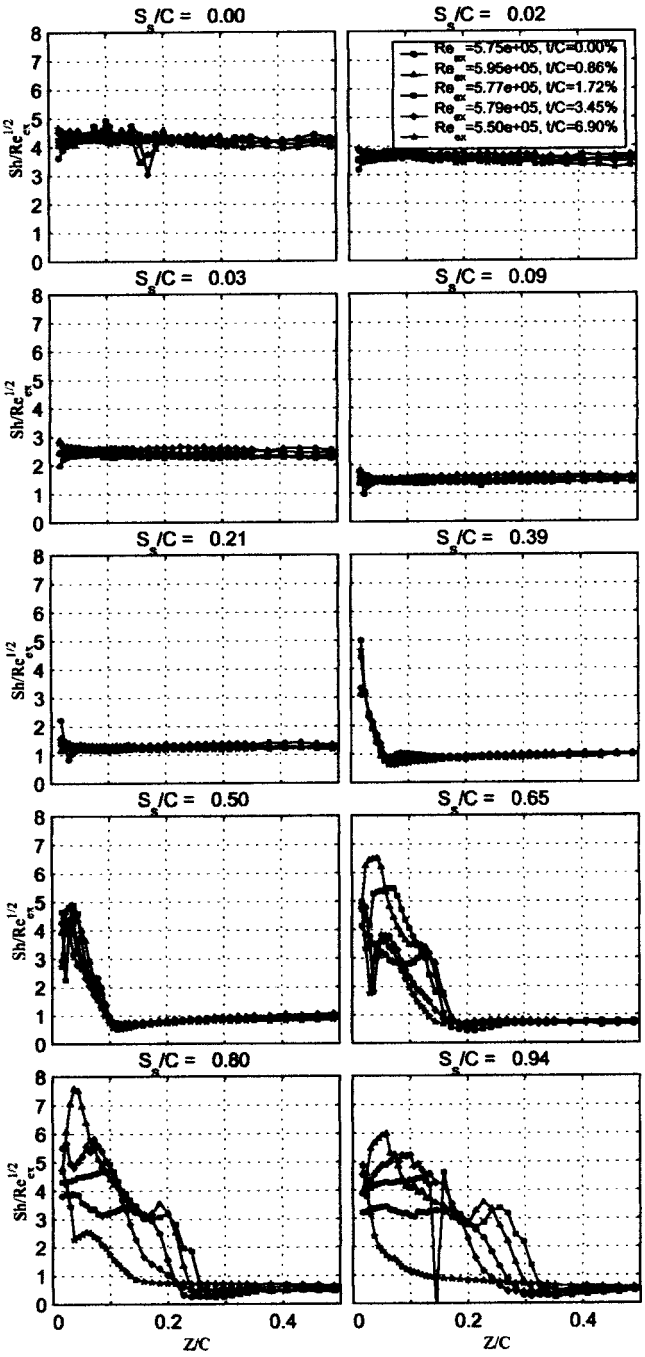

Fig. 11 $Sh/Re_{ex}^{1/2}$ on the suction surface

mass transfer rate around $Z/C=0.05$ is induced by the corner vortices, while the mass transfer rate increases monotonously toward the tip for all nonzero tip clearance cases. For the largest tip clearance of $6.90\%C$, the nonuniform Sh, associating with the Taylor-Gortler vortices [21] and existing for smaller tip clearance cases, disappears apparently due to the existence of highly accelerated suction flow on the pressure surface, disrupting the flow pattern of zero and smaller tip clearances.

At the tip clearance, $t/C=0.86\%$, the effects of mainstream Reynolds number and turbulence intensity on the mass transfer on the pressure surface are measured. Figure 8 plots the local mass transfer $Sh/Re_{ex}^{1/2}$ versus Z/C on the blade pressure surface. The high mainstream turbulence intensity level of 12% greatly enhances the mass transfer on the pressure surface, increasing the mass transfer rates by as much as 100% at $S_p/C=0.16$, which may be due to the fact that the flow on the pressure surface is no longer laminar. Mass transfer curves for different Reynolds numbers at low turbulence levels of 0.2% are very similar downstream of the leading edge, showing the laminar characteristic of the flow on the pressure surface, and with the nonuniformity occurring randomly. The effect of leakage flow drown into the tip clearance is again limited to $Z/C<0.1$ for all cases, causing at most a Sh two times as large as that near mid-span.

Suction Surface Near the Tip. In Figs. 9 and 10 the mass transfer on the suction surface in the form of contour plots for different tip clearances is shown for $Re=5.8\times10^5$ and turbulent intensity of 0.2%. The triangular region of high mass transfer caused by the secondary flows decreases in size as the tip clearance increases. At $t/C=0.86\%C$, the tip leakage vortex exiting from the suction side of the tip clearance produces a small high mass transfer zone centered around $S_s/C=0.7$ close to the tip edge. The effect of passage secondary flows still exists near the upper edge of the triangular region, which can be clearly identified for the case of zero tip clearance in Fig. 3(*b*). For t/C

Downloaded 31 May 2010 to 171.66.16.27. Redistribution subject to ASME license or copyright; see http://www.asme.org/terms/Terms_Use.cfm

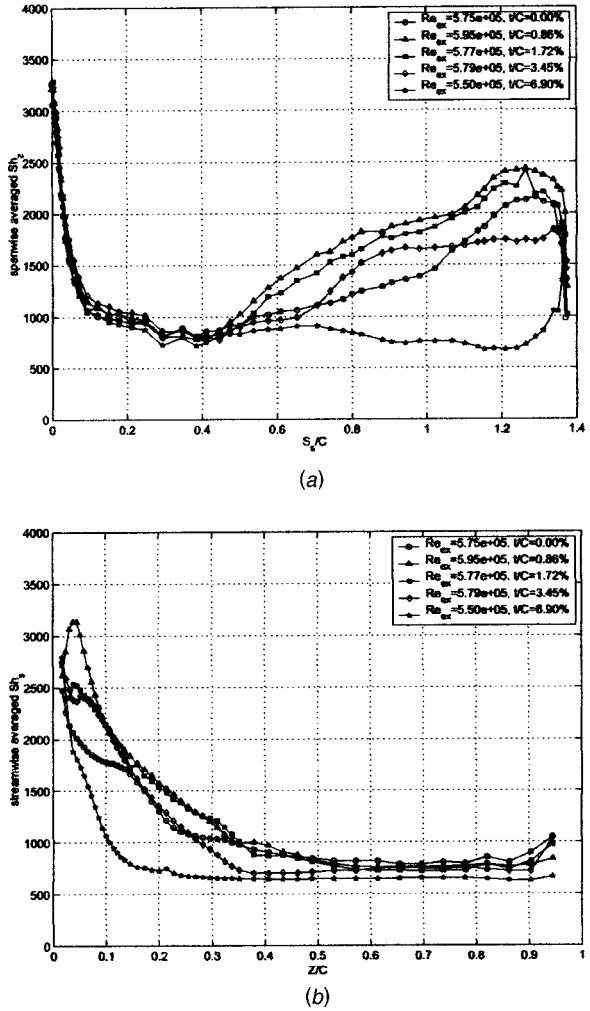

Fig. 12 Average Sh on the suction surface—(*a*) spanwise average, (*b*) streamwise average

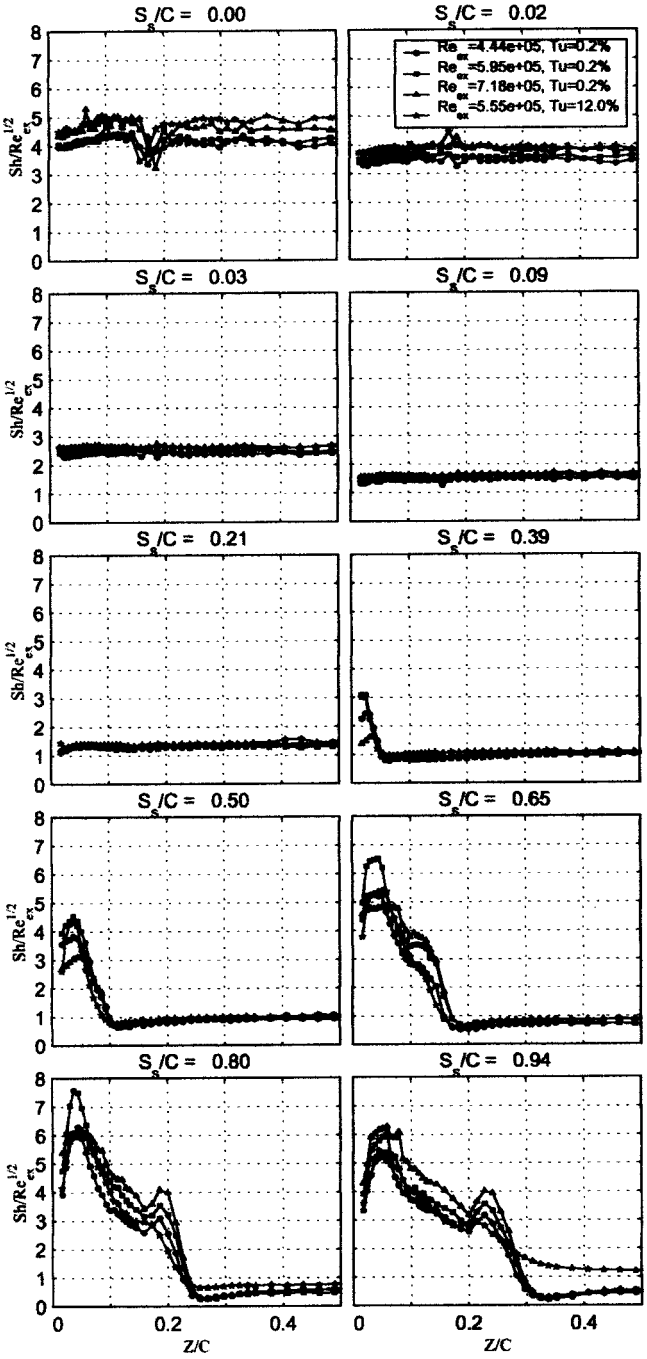

Fig. 13 $Sh/Re_{ex}^{1/2}$ on the suction surface at $t/C=0.86\%$

$=1.72\%$, the region affected by the tip leakage vortex extends both downstream and in the span direction with its peak at $S_s/C=0.5$ very close to the tip edge, while the region affected by the passage secondary flows becomes smaller, though still recognizable. At higher tip clearance, $3.45\%C$, the effect of secondary flows weakens and the smaller triangular region is mainly affected by the tip leakage vortex with two peaks of high mass transfer, probably indicating multiple tip leakage vortices. For the largest tip clearance, $t/C=6.90\%$, only the effect of tip leakage vortex can be seen and the high mass transfer region is no longer triangular in shape, due to the strong leakage vortex coming out of the clearance into the blade passage, pushing away the passage vortex and lowering the mass transfer rate near the tip [23].

Local value of $Sh/Re_{ex}^{1/2}$, calculated from the same data, at different S_s/C locations along the span are shown in Fig. 11 for different tip clearances, including the zero clearance case for comparison. The effect of tip clearance on the mass transfer on the suction surface is not evident and the mass transfer distributions near the tip edge are rather flat till $S_s/C=0.21$, though the values near the tip edge are still higher than those with zero tip clearance, indicating almost negligible leakage vortex near the leading edge of the blade. Downstream of S_s/C 0.50, the smaller tip clearance induces larger mass transfer rate near the tip. The peak near the tip edge is caused by the tip leakage flow reattaching on the surface. For the largest tip clearances the mass transfer rates are much lower after $S_s/C=0.80$ as the effect of secondary flows essentially disappears. The mass transfer data collapse (i.e., independent of Z) outside of the triangular region at these streamwise locations.

As for the pressure surface, spanwise and streamwise averaged value of Sh on the suction surface are plotted in Fig. 12 for different tip clearances. In Fig. 12(*a*), the effect of tip clearance is evident: the smaller the tip clearance (other than zero), the higher Sh for $S_s/C>0.5$ and the averaged Sh for the largest tip clearance is lower than that for zero tip clearance. The variation of Sh averaged in S_s direction versus Z/C in Fig. 12(*b*) shows a similar trend for all cases except the largest tip clearance with the peak Sh at smallest tip clearance of $0.86\%C$ caused by the tip leakage vortex.

At a tip clearance of $t/C=0.86\%$, the effects of mainstream Reynolds number and turbulence intensity on the mass transfer on

Downloaded 31 May 2010 to 171.66.16.27. Redistribution subject to ASME license or copyright; see http://www.asme.org/terms/Terms_Use.cfm

the suction surface are also investigated. The local mass transfer $Sh/Re_{ex}^{1/2}$ at different curvilinear locations is shown in Fig. 13. We see that near the leading edge ($S_s/C<0.09$), the Reynolds number has some effect on the mass transfer. Downstream of $S_{s1}C-0.09$, the curves at different Reynolds number collapse to one outside the triangular region. The $Sh/Re_{ex}^{1/2}$ data in the triangular region follow the same trend at different Reynolds numbers with low turbulence intensity of 0.2%: the first peak near the tip is caused by the leakage vortex reattachment, while the second peak is probably induced by the passage vortex separation from the surface, and the higher the Reynolds number, the higher the $Sh/Re_{ex}^{1/2}$ value. However, the effect of high mainstream turbulence level of 12% on the mass transfer rate is not important until S_s/C 0.94, where transition to turbulence begins.

Conclusions

In the present study, local mass transfer measurements from turbine blade near-tip surfaces is performed using the naphthalene sublimation technique. The experiments are conducted in a linear cascade consisting of five high-pressure turbine blades with central blade configuration. The blade Reynolds numbers are close to those in a gas turbine engine environment ($\delta_1/C=0.01$) with an exit Reynolds number of about 5.8×10^5. The effects of tip clearance (0.86–6.90%C), mainstream Reynolds number ($4-7\times10^5$) and turbulence intensity (0.2 and 12.0%) are investigated. The following conclusions can be made:

1. The effect of tip clearance on the mass transfer on the pressure surface is limited to $0.10C$ at smaller tip clearances. At the largest tip clearance high mass transfer rates are induced at $S_p\approx0.15C$ by the strong acceleration of flow into the clearance.
2. The effect of tip clearance on the mass transfer is not very evident for $S_s/C<0.21$ on the suction surface. However, much higher mass transfer rates are caused downstream of $S_s/C\approx0.5$ by the tip leakage vortex at the smallest tip clearance. At the largest tip clearance, the averaged mass transfer is lower than that of zero tip clearance, probably because the strong leakage vortex pushes the passage vortex away from the suction surface.
3. The mainstream turbulence level of 12.0% increases the local mass transfer rates on the pressure surface, while higher mainstream Reynolds number causes higher local mass transfer rates on both pressure and suction surfaces.

Acknowledgments

This research was supported by the U.S. Department of Energy-Federal Energy Technology Center through the AGTSR program.

Nomenclature

$\dot{m}$ = mass flux of sublimated naphthalene vapor
C = chord of blade, 18.4 cm in current study
C_{ps} = static pressure coefficient
C_x = axial chord of blade, 13.0 cm in current study
D_{naph} = naphthalene vapor diffusivity in air
H = height (span) of blade
h_m = mass transfer coefficient
P = pitch of blade, 13.8 cm in current study
Re_{ex} = exit Reynolds no. based on chord and exit velocity
S_p = curvilinear coordinate along pressure surface
S_s = curvilinear coordinate along suction surface
Sh = net mass transfer Sherwood no., $=h_mC/D_{\text{naph}}$
Sh_s = streamwise averaged Sh
Sh_z = spanwise averaged Sh from tip to $Z\approx C$ of naphthalene blade
t = blade tip clearance
Tu = inlet turbulence intensity
X = axial direction of cascade
Y = pitchwise direction of cascade
Z = spanwise direction of cascade starting from tip
$\delta\tau$ = net time duration in wind tunnel
δ_1 = boundary layer displacement thickness
δy = net naphthalene layer depth change due to turbulent convection
ρ_s = solid naphthalene density
$\rho_{v,\infty}$ = naphthalene vapor density in mainstream
$\rho_{v,w}$ = naphthalene vapor density at wall

References

[1] Booth, T. C., Dodge, P. R., and Hepworth, H. K., 1982. "Rotor-Tip Leakage: Part I-Basic Methodology." ASME J. Eng. Gas Turbines Power, **104**, pp. 154–161.
[2] Mayle, R. E., and Metzger, D. E., 1982. "Heat Transfer at the Tip of an Unshrouded Turbine Blade." *Proc., Seventh Int. Heat Transfer Conference*, **3**, pp. 87–92.
[3] Sjolander, S. A., and Amrud, K. K., 1987. "Effects of Tip Clearance on Blade Loading in a Planar Cascade of Turbine Blades." ASME J. Turbomach., **109**, pp. 237–245.
[4] Moore, J., and Tilton, J. S., 1988. "Tip Leakage Flow in a Linear Turbine Cascade." ASME J. Turbomach., **110**, pp. 18–26.
[5] Bindon, J. P., 1987. "Pressure Distributions in the Tip Clearance Region of an Unshrouded Axial Turbine as Affecting the Problem of Tip Burnout." ASME Paper 87-GT-230.
[6] Yamamoto, A., 1988. "Interaction Mechanisms between Tip Leakage Flow and the Passage Vortex in a Linear Turbine Rotor Cascade," ASME J. Turbomach., **110**, pp. 329–338.
[7] Kang, S., and Hirsch, C., 1993. "Experimental Study on the Three-Dimensional Flow within a Compressor Cascade with Tip Clearance: Part 1—Velocity and Pressure Fields." ASME J. Turbomach., **115**, pp. 435–443.
[8] Chyu, M. K., Moon, H. K., and Metzger, D. E., 1988. "Heat Transfer in the Tip Region of Grooved Turbine Blades." ASME Paper 88-GT-213.
[9] Metzger, D. E., Bunker, R. S., and Chyu, M. K., 1989. "Cavity Heat Transfer on a Transverse Groved Wall in a Narrow Flow Channel." ASME J. Heat Transfer, **111**, pp. 73–79.
[10] Metzger, D. E., and Rued, K., 1989. "Influence of Turbine Clearance Gap Leakage on Passage Velocity and Heat Transfer near Blade Tips. Part I. Sink Flow Effects on Blade Pressure Side." ASME J. Turbomach., **111**, pp. 284–292.
[11] Rued, K., and Metzger, D. E., 1989. "Influence of Turbine Clearance Gap Leakage on Passage Velocity and Heat Transfer near Blade Tips. Part II. Source Flow Effects on Blade Suction Sides." ASME J. Turbomach., **111**, pp. 293–300.
[12] Metzger, D. E., Dunn, M. G., and Hah, C., 1991. "Turbine Tip and Shroud Heat Transfer." ASME J. Turbomach., **113**, pp. 502–507.
[13] Kim, Y. W., and Metzger, D. E., 1995. "Heat Transfer and Effectiveness on Film Cooled Turbine Blade Tip Models." ASME J. Turbomach., **117**, pp. 12–21.
[14] Kim, Y. W., Downs, J. P., Soechting, F. O., Abdel-Messeh, W., Steuber, G. D., and Tanrikut, S., 1995. "Summary of the Cooled Turbine Blade Tip Heat Transfer and Film Effectiveness Investigations Performed by Dr. D. E. Metzger." ASME J. Turbomach., **117**, pp. 1–11.
[15] Bunker, R. S., Baily, J. C., and Ameri, A. A., 2000. "Heat Transfer and Flow on the First Stage Blade Tip of a Power Generation Gas Turbine: Part 1: Experimental Results." ASME J. Turbomach., **122**, pp. 263–271.
[16] Teng, S., Han, J.-C., and Azad, G. S., 2000. "Detailed Heat Transfer Coefficient Distribution on a Large-Gas Turbine Blade Tip." ISROMAC-8.
[17] Azad, G. S., Han, J.-C., Teng, S., and Boyle, R. J., 2000. "Heat Transfer and Pressure Distribution on a Gas Turbine Blade Tip." ASME J. Turbomach., **122**, pp. 717–724.
[18] Goldstein, R. J., and Cho, H. H., 1995. "A Review of Mass Transfer Measurements Using Naphthalene Sublimation." Exp. Therm. Fluid Sci., **8**, pp. 416–434.
[19] Goldstein, R. J., and Spores, R. A., 1988. "Turbulent Transport on the Endwall in the Region between Adjacent Turbine Blades." ASME J. Heat Transfer, **110**, pp. 862–869.
[20] Goldstein, R. J., Wang, H. P., and Jabbari, M. Y., 1995. "Influence of Secondary Flows Near the Endwall and Boundary Layer Disturbance on Convective Transport from a Turbine Blade." ASME J. Turbomach., **117**, pp. 657–665.
[21] Wang, H. P., Goldstein, R. J., and Olson, S. J., 1999. "Effect of High Free-Stream Turbulence with Large Length Scale on Blade Heat Mass Transfer." ASME J. Turbomach., **121**, pp. 217–224.
[22] Jin, P., 2000, "Local Measurement and Numerical Modeling of Mass/Heat Transfer From a Turbine Blade in a Linear Cascade With Tip Clearance," Ph.D. thesis, University of Minnesota, Minneapolis, MN.
[23] Jin, P., and Goldstein, R. J., 2000. "Visualization of Tip Leakage Flow in a Linear Turbine Cascade," *9th Int. Symposium on Flow Visualization*.

Downloaded 31 May 2010 to 171.66.16.27. Redistribution subject to ASME license or copyright; see http://www.asme.org/terms/Terms_Use.cfm

G. Vogel

A. B. A. Graf

Laboratoire de Thermique Appliquée et de Turbomachines (LTT),
EPFL,
1015 Lausanne, Switzerland

J. von Wolfersdorf

B. Weigand

Institut für Thermodynamik der Luft- und Raumfahrt,
Universität Stuttgart,
70569 Stuttgart, Germany

A Novel Transient Heater-Foil Technique for Liquid Crystal Experiments on Film-Cooled Surfaces

A novel transient measurement technique has been developed for determining the heat transfer characteristics in the presence of film cooling (heat transfer coefficient and adiabatic film-cooling effectiveness). The method is based on a transient heater foil technique, where a non-homogeneous surface heat flux is applied to the test surface. A regression analysis of multiple transient liquid crystal experiments is used to obtain the heat transfer characteristics. The method introduced here has the advantage that the (often not known) heat flux distribution at the surface is not needed for the analysis of the measured data. The method is used to study the influence of several heater foil configurations on a flat plate with film cooling, elucidating the effect of different thermal boundary conditions on film-cooling performance. The obtained data is also compared to results presented in literature and good agreement is found. [DOI: 10.1115/1.1578501]

1 Introduction

Efficient cooling methods are required in modern gas turbine designs due to excessive high turbine inlet temperatures introduced by the demand of high specific power and high cycle efficiency. Although the high temperature capabilities of the applied materials were improved over the last years, the thermal and stress environment are beyond the limit alloys can presently achieve. In order to protect the turbine blades from melting, the blades need extensive cooling. Usually a combination of internal convective cooling and external film cooling is employed. The cooling designs of these parts have to be highly efficient because a larger cooling mass flow rate degrades the thermal efficiency of the thermodynamic cycle of the gas turbine. This is especially true for the application of film cooling where a protective film of cold air is spread around the blade and large cooling mass flows are required. Because of the importance of film cooling for turbine blade design, this subject has been studied extensively over the past 35 yr (Goldstein [1,2], Leontiev [3]). Most of the studies concentrate on flat plate configurations with film injection through slots, cylindrical or shaped holes (Sinha et al. [4], Forth et al. [5]). When film cooling is considered on airfoil type flows (Ito et al. [6], Takeishi et al. [7], Drost [8]), numerical methods and correlations have been developed to predict the adiabatic film-cooling effectiveness and the increase in heat transfer coefficients. A large number of parameters influence the film cooling process such as cooling hole geometry, blowing and momentum flux ratio of the coolant and main stream turbulence effects. Several models can be found in literature (Crawford et al. [9], Weigand et al. [10], Garg [11]), albeit only for specific applications. In order to further develop the cooling schemes for gas turbine blades, high quality experimental data and the corresponding analytical and numerical methods are required.

Transient and steady-state heat transfer and film cooling effectiveness measurements using thermochromic liquid crystals (TLC) are very popular to obtain detailed full field surface information (Ireland et al. [12]). For film cooling measurements several techniques have been applied to determine the film cooling performance (adiabatic film-cooling effectiveness and increase in film cooling heat transfer coefficients) either by two separate experiments, or by a number of transient experiments. Two separate steady-state experiments were performed by Lutum et al. [13]. The increase in heat transfer coefficient due to film cooling was measured using a heater foil, the coolant temperature and the free stream temperature being equal. The adiabatic film-cooling effectiveness was additionally measured by using an adiabatic wall and by blowing with a different coolant temperature than the free stream temperature. The heater foil covered the region before and after the injection holes with some unheated region around the holes. Regression analysis on multiple transient liquid crystal measurements using rapidly changing free stream temperature, generally performed by the rapid insertion of a preconditioned model or by using heater grids in the main flow, or various coolant temperatures were reported by Reiss [14] and Dui et al. [15]. Transient heater-foil techniques with liquid crystal thermography were applied for heat transfer investigations by von Wolfersdorf et al. [16] and Turnbull et al. [17]. Since no film-cooling holes were considered, the full surface under investigation was covered with the heated layer. In case of film cooling, transient measurements using heater foils were applied for slots by Farmer et al. [18] and for a row of holes by Seager et al. [19], the heater-foil being then applied in the area behind the holes.

The aforementioned different heater-foil arrangements cause different thermal boundary conditions for the film cooling situation. Therefore, a new transient heater foil method was introduced by Vogel et al. [20], which is able to determine the film-cooling effectiveness and the heat transfer augmentation simultaneously even for nonuniform heat flux situations (e.g., film-cooling holes in the heater foil) using multiple transient experiments and regression analysis. The applicability of this method was shown for one film cooling experiments on a flat plate with cylindrical holes and two heater-configurations with longitudinal and transverse electrical current supply.

The objective of the present paper is to introduce a new transient heater foil method for liquid crystal experiments on film cooled surfaces. An analytical model and its numerical resolution are first derived. The experimental setup is then described as much as a measurement errors analysis. Furthermore, the present paper studies the influence of four different heater-foil configurations and therefore different thermal boundary conditions on the film

Contributed by the International Gas Turbine Institute and presented at the International Gas Turbine and Aeroengine Congress and Exhibition, Amsterdam, The Netherlands, June 3–6, 2002. Manuscript received by the IGTI October 10, 2001; revised manuscript received October 29, 2002. Paper No. 2002-GT-30552. Review Chair: E. Benvenuti.

Downloaded 31 May 2010 to 171.66.16.27. Redistribution subject to ASME license or copyright; see http://www.asme.org/terms/Terms_Use.cfm

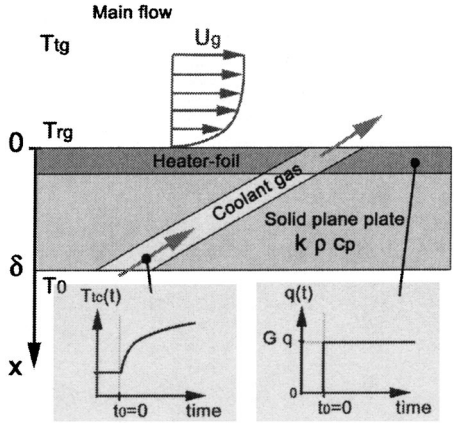

Fig. 1 Schema of the solid plane plate with the heater-foil, the coolant injection, cooling holes, the main gas flow, and some relevant physical quantities

cooling performance. This point is of major importance for the transfer of experimental data in literature to actual film cooling configurations in gas turbines.

2 Theoretical Investigation of the Measurement Technique

2.1 Model. Figure 1 gives an overview of the considered model. A coolant fluid is injected into the main flow of gas over a flat plate. The latter is covered by a thin heater foil. At $t=0$, the plate is suddenly exposed to a heat flux through the foil, causing a temperature change in the wall of the plate. The evolution of the temperature field in the plate is assumed to be one-dimensional and the heat diffusion conduction equation in the plate in the absence of heat sources can be written as

$$\frac{\partial T(x,t)}{\partial t}=\alpha\frac{\partial^2 T(x,t)}{\partial x^2},\quad \alpha=\frac{k}{\rho c_p} \tag{1}$$

The heater-foil is supposed to be infinitely thin compared to δ. Its effect is thus taken into account in the boundary conditions and not in the heat conduction equation itself. This same assumption allows the plate to be considered as homogenous.

The initial condition ($t=0$) is given by

$$T(x,0)=T_0 \tag{2}$$

whereas the boundary condition at the plate surface ($x=0$) is obtained using an energy balance

$$\dot{q}_W(t)=-k\frac{\partial T(0,t)}{\partial x}-h(T_{aw}(t)-T(0,t)) \tag{3}$$

where $T_{aw}(t)$ stands for the adiabatic wall temperature. This value can be replaced by the adiabatic film-cooling effectiveness, which is defined by

$$\eta=\frac{T_{aw}(t)-T_{rg}}{T_{tc}(t)-T_{tg}} \tag{4}$$

where T_{tg} and T_{rg} are determined using the flow conditions of the main stream of gas. Furthermore, it is assumed that the plate can be treated as half-infinite (Vogel et al. [21]), i.e., the measurement time is so short that a heat pulse generated at the upper surface ($x=0$) will not reach the lower one ($x=\delta$). This can be expressed by the condition

$$T(x\to\infty,t)=T_0 \tag{5}$$

Solving Eq. (4) for $T_{aw}(t)$ and substituting it into Eq. (3) yields

$$\dot{q}_W(t)=-k\frac{\partial T(0,t)}{\partial x}+h(T(0,t)-T_{rg})+h\,\eta(T_{tg}-T_{tc}(t)) \tag{6}$$

Equation (1) can be solved analytically under the conditions given by Eqs. (2), (5), and (6) using the Laplace transform technique as described by Carslaw et al. [22]. With $T^*(x,t)=T(x,t)-T_0$, the following transformed quantities are obtained:

$$\begin{cases}\hat{T}^*(x,s)=\sigma\exp\left(-\sqrt{\dfrac{s}{\alpha}}x\right)\\ \hat{q}_W(s)=-k\dfrac{\partial\hat{T}^*(0,s)}{\partial x}+h\hat{T}^*(0,s)+\dfrac{h(\eta T_{tg}+T_0-T_{rg})}{s}-h\,\eta\hat{T}_{tc}(s)\end{cases} \tag{7}$$

where σ is an integration constant. In order to determine the latter, the following assumptions are made: at $t=0$ a step in the surface heat flux is generated by the heater-foil and at the same time, a coolant gas is injected at a constant blowing ratio and with a given temperature evolution in time as defined in the following:
The coolant temperature is a function of time since the cooling fluid is transferred from the plenum chamber to the test section, this transfer being accompanied by a heat loss. The temperature rise of the coolant is assumed to follow an expression as:

$$T_{tc}(t)=a\exp(bt)+ct+d\sqrt{t} \tag{8}$$

where a, b, c, and d are constants fitted to the experimental profile of $T_{tc}(t)$. The surface heat flux follows a step function:

$$\begin{cases}\dot{q}_W(t\leqslant 0)=0\\ \dot{q}_W(t>0)=Gq\end{cases} \tag{9}$$

where G stands for the known gain with respect to an unknown reference heat flux q. Under the assumptions of Eqs. (8) and (9), the system of Eq. (7) has the following solution:

$$\hat{T}^*(x,s)=\left[\frac{Gq}{s}-\frac{h(\eta T_{tg}+T_0-T_{rg})}{s}+h\,\eta\left(\frac{a}{s-b}+\frac{c}{s^2}+\frac{\sqrt{\pi}d}{2\sqrt{s^3}}\right)\right]\frac{\exp\left(-\sqrt{\dfrac{s}{\alpha}}x\right)}{h+k\sqrt{\dfrac{s}{\alpha}}} \tag{10}$$

The inverse Laplace transform of the foregoing expression evaluated at $x=0$ yields for the wall temperature distribution

$$T_w(t)=A+\eta B+qC \tag{11}$$

where

Downloaded 31 May 2010 to 171.66.16.27. Redistribution subject to ASME license or copyright; see http://www.asme.org/terms/Terms_Use.cfm

$$A = T_0 + (T_{rg} - T_0)(1 - \exp(\beta^2)\operatorname{erfc}(\beta))$$

$$B = -T_{tg}(1 - \exp(\beta^2)\operatorname{erfc}(\beta)) + \frac{h}{k}\left[\frac{a\exp(bt)}{2}\mu - \frac{a\alpha}{\frac{h}{k}\alpha - \frac{kb}{h}}\exp(\beta^2)\operatorname{erfc}(\beta)\right]$$

$$-\frac{h}{k}\left[\frac{c}{\alpha\left(\frac{h}{k}\right)^3}\left(\exp(\beta^2)\operatorname{erfc}(\beta) - \sum_{r=0}^{2}\frac{(-\beta)^r}{\Gamma\left(\frac{r}{2}+1\right)}\right) - \frac{d\sqrt{\pi}}{2\sqrt{\alpha}\left(\frac{h}{k}\right)^2}\left(\exp(\beta^2)\operatorname{erfc}(\beta) - \sum_{r=0}^{1}\frac{(-\beta)^r}{\Gamma\left(\frac{r}{2}+1\right)}\right)\right]$$

$$C = \frac{G}{h}(1 - \exp(\beta^2)\operatorname{erfc}(\beta)) \tag{12}$$

with $\beta^2 = \alpha(h/k)^2 \; t \neq bt$ and:

$$\mu = \begin{cases} \dfrac{\sqrt{\alpha}}{\frac{h}{k}\sqrt{\alpha} + \sqrt{b}}\operatorname{erfc}(-\sqrt{bt}) + \dfrac{\sqrt{\alpha}}{\frac{h}{k}\sqrt{\alpha} - \sqrt{b}}\operatorname{erfc}(\sqrt{bt}) & \text{when } b \geqslant 0 \\ \dfrac{2\sqrt{\alpha}}{\left(\frac{h}{k}\right)^2\alpha + b}\left(\dfrac{h}{k}\sqrt{\alpha} + 2\sqrt{\dfrac{-b}{\pi}}\left(\displaystyle\int_0^{\sqrt{-bt}}\exp(t^2)dt\right)\right) & \text{when } b < 0 \end{cases} \tag{13}$$

When considering the case of no film cooling (i.e., $\eta = 0$) and a constant heat flux, the foregoing equations reduce to the expression given by von Wolfersdorf et al. [16].

2.2 Regression. All parameters in Eq. (11) are assumed to be known *a priori* or measured except for h, η, and q. These unknown quantities are determined below by a nonlinear least-square regression using the transient experimental data. The latter includes temperature-time data pairs which are given by the coating of narrow-band liquid crystals applied on the plate and can be written as $(T^i_{LC}, t^i_{LC})|^N_{i=1}$ where i indexes the $N \geqslant 3$ independent experiments such that

$$T_w(t^i_{LC}) = T^i_{LC}, \quad \forall i = 1,..,N \tag{14}$$

The foregoing holds locally since the value of q is inhomogeneous across the surface of the plate as it depends upon the influence of the cooling holes and upon the possible variation in thickness of the heater-foil. For $N = 3$, Eq. (14) yields exactly a solution triplet, if the latter exists. However, for $N > 3$, the problem is overdefined and an optimal solution, if it exists, has to be sought. This solution should fit best all the N equations together, without necessarily satisfying each of them exactly. The foregoing problem thus reduces to minimizing the following error function:

$$\varepsilon = \frac{1}{2}\|\vec{T}_w(t_{LC}) - \vec{T}_{LC}\|^2 = \frac{1}{2}\|\vec{A} + \eta\vec{B} + q\vec{C} - \vec{T}_{LC}\|^2 \tag{15}$$

where each component of a vector corresponds to a distinct experiment and where $\|\vec{x}\|^2 = \langle\vec{x}|\vec{x}\rangle$, $\langle .|. \rangle$ being the Euclidean scalar product for $\vec{x} \in \mathbb{R}^N$. The foregoing expression is minimal when:

$$\vec{\nabla}\varepsilon = 0 \Rightarrow \frac{\partial\varepsilon}{\partial\eta} = 0, \quad \frac{\partial\varepsilon}{\partial q} = 0, \quad \frac{\partial\varepsilon}{\partial h} = 0 \tag{16}$$

which is a necessary but nonsufficient condition.

In the context of Eq. (11), the above three-parameter optimization process may be reduced to a one-parameter one. For this, η is expressed as a function of the two remaining unknowns as

$$\frac{\partial\varepsilon}{\partial\eta} = 0 \Rightarrow \eta(h,q) = \frac{\langle\vec{T}_{LC} - q\vec{C} - \vec{A}|\vec{B}\rangle}{\|\vec{B}\|^2} \tag{17}$$

Subsequently q is determined with respect to h as follows:

$$\frac{\partial\varepsilon}{\partial q} = 0 \Rightarrow q(h) = \frac{\left\langle \vec{T}_{LC} - \vec{A} - \dfrac{\langle\vec{T}_{LC} - \vec{A}|\vec{B}\rangle}{\|\vec{B}\|^2}\vec{B} \,\middle|\, \vec{\omega}\right\rangle}{\|\vec{\omega}\|^2} \quad \text{where}$$

$$\vec{\omega} = \vec{C} - \frac{\langle\vec{C}|\vec{B}\rangle}{\|\vec{B}\|^2}\vec{B} \tag{18}$$

Equations (17) and (18) are inserted into Eq. (15), yielding an error function dependent solely upon h. This one-dimensional minimization may be done by classical methods of numerical analysis (Isaacson et al. [23]) such as the bisection rule. Once the optimal value of h is determined, the remaining unknowns are computed using Eqs. (18) and (17), respectively.

3 Validation Experiments

3.1 Test Facility. Experiments are carried out in an open low speed wind tunnel with a square cross section of 100 mm $\times$100 mm and a total length of 1500 mm. In order to have good optical access and low thermal conductivity, the walls of the channel are made out of 15-mm-thick Perspex. The air flow is generated by two electrical fans mounted in serie followed by a settling chamber and a convergent nozzle as represented in Fig. 2.

The flat plate test section is mounted into the bottom wall of the channel at 10 hydraulic diameters from the square channel inlet. The test section, 250 mm in length and a wall thickness of $\delta = 25$ mm, covers the complete width of the channel (100 mm). At the start of the test plate a small step is installed in order to guarantee a turbulent boundary layer of the main gas flow on the test section. The latter consists of a flat plate film-cooled by a row of five cylindrical holes of $D = 5\text{e}{-3}$ m diameter. This row of holes is located at 20 hole diameters from the end of the plate. The five holes are centered in the transversal (span-wise) direction of the squared channel with a pitch of $P/D = 3.5$. The axis of the holes is aligned to the channel flow direction with an exit angle of 30° to the surface of the flat plate. The ratio between the length of the hole L_d and its diameter D is $L_d/D > 3$.

Downloaded 31 May 2010 to 171.66.16.27. Redistribution subject to ASME license or copyright; see http://www.asme.org/terms/Terms_Use.cfm

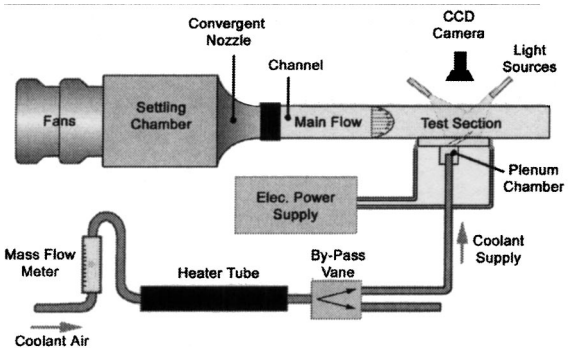

Fig. 2 Schematic drawing of the test facility and the devices present around the test section

The plenum chamber, containing the coolant and allowing its injection into the test section, is fixed to the bottom part of the test section. Coolant is supplied to the plenum chamber by an orifice located on the lateral right-hand side relative to the main flow direction in the channel. The coolant blowing ratio is adjusted and measured by a graduated glass flow meter. The temperature of the coolant is adjusted by an electrical heater tube mounted downstream of the glass flow meter. A by-pass vane mounted at the exit of the heater tube allows the preconditioning of the coolant flow before its injection into the plenum chamber where a thermocouple measures the coolant temperature during the experiments.

A nickel-chrome heater-foil of 20 μm thickness is glued onto the upper surface of the test section. The foil is connected to an electrical power supply through copper cables and bus bars. Thermocouples mounted slightly under the upper surface of the plate (for the sake of electrical insulation with the heater foil) and on its lower surface are used to monitor the homogeneity of the initial surface temperature and to verify the half infinite model assumption.

A black coating layer (Hallcrest BB-G1) followed by a thermochromic narrow band liquid crystals layer (Hallcrest BM/R36C1W) and a varnish protection layer (Hallcrest AQB-2) are applied on the heater foil. A thermocouple mounted (with a 3M Kapton tape) on top of these layers is used for the hue-temperature calibration of the liquid crystals. Cold light sources directed by optical fibers are used for the illumination of the test section. Hue value variations on the surface are recorded during the transient experiment by a 25 Hz color CCD camera mounted perpendicular to the test section and viewing through the upper channel wall. At any position on the plate, the time t_{LC} needed from the beginning of the transient experiment to reach a specific surface temperature T_{LC} is obtained by performing a data reduction of the hue video sequence (Vogel et al. [24]). An LED, mounted close to the test section and used to determine the beginning of the transient experiment on the video sequences, is triggered by the activation of the power supply connected to the heater-foil. The same trigger signal is also used to activate the bypass vane, hence synchronizing the coolant flow injection with the surface heat flux generation.

3.2 Test Cases for Validation. Experiments are performed in the above wind tunnel with an exit flow velocity of about $U_g = 22$ m/s and a total gas temperature of about $T_{tg} = 296$ K. Air is used as coolant and the film-cooling blowing ratio is set to BR $= 0.3$. The initial temperature of the test section is in the same range as the total gas temperature and a specific hue value of the narrow-band liquid crystals is calibrated for $T_{LC} = 309.2$ K. The coolant is preconditioned with temperatures varying from 298 to 323 K. The variable amount of heat flux applied during the N transient experiments is chosen in order to have a time event detection neither too short ($t_{LC} > 2$ s) because of the rapid evolution of T_w at the beginning of the transient test, nor too long ($t_{LC} < 1200$ s) in order to respect the half-infinite assumption. Numerical simulations of the temporal evolution of T_w were performed in order to assess the range of t_{LC} for the experiments. For every flat plate configuration, a total of nine experiments ($N = 9$) are performed, consisting of three different heat flux ratios combined with three different coolant temperature preconditioning. Four different heater-foil configurations as shown in Fig. 3 are investigated.

Case 1: Longitudinal Electrical Current. One pair of bus bars is connected perpendicular to the flow direction forcing a global

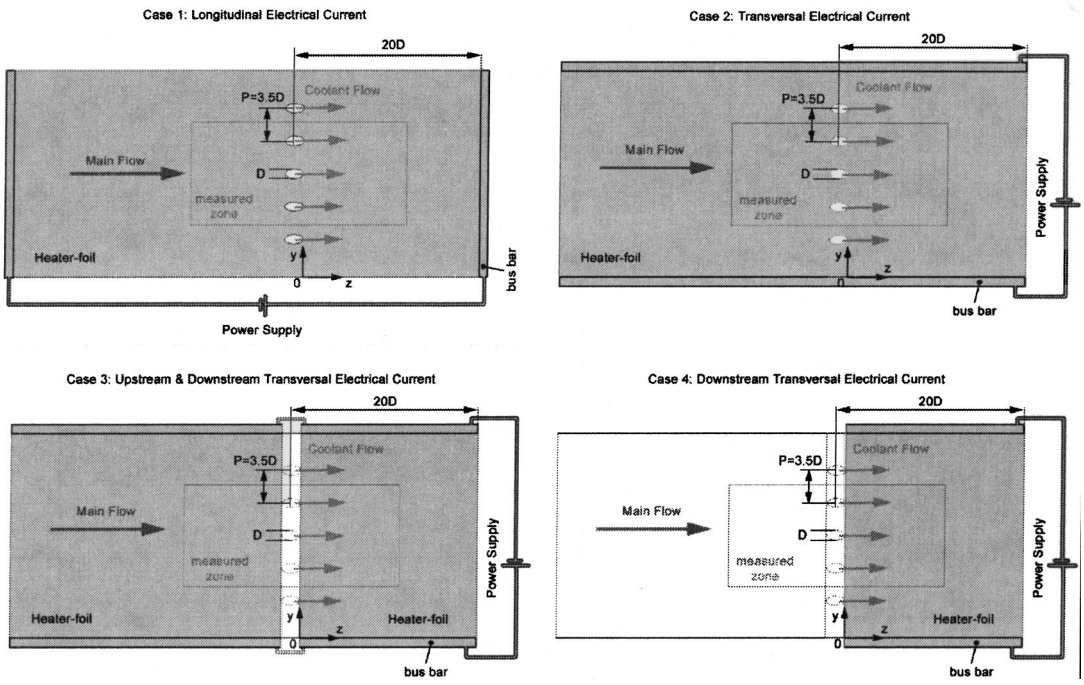

Fig. 3 Film-cooled flat plate heater-foils and bus bars configurations

Downloaded 31 May 2010 to 171.66.16.27. Redistribution subject to ASME license or copyright; see http://www.asme.org/terms/Terms_Use.cfm

longitudinal electrical current in the foil. This configuration generates a nonhomogeneous heat flux distribution with higher values in between the holes as a consequence of the reduced conductible surface (conservation of electric charge).

Case 2: Transversal Electrical Current. One pair of bus bars is connected parallel to the flow direction forcing a global transversal electrical current in the foil. This configuration also generates a nonhomogeneous heat flux distribution with lower values in between the holes.

Case 3: Upstream and Downstream Transversal Electrical Current. Two pairs of bus bars are connected parallel to the flow direction forcing a global transversal electrical current in two foils, one upstream and the other downstream of the row of cooling holes. This configuration generates two homogeneous heat fluxes, the latter being however different.

Case 4: Downstream Transversal Electrical Current. One pair of bus bars is connected parallel to the flow direction forcing a global transversal electrical current in the foil downstream of the row of cooling holes, generating thus a homogeneous heat flux.

Since the measurement technique proposed in this paper is developed for heater-foil experiments with an unknown surface heat flux distribution q, the first two cases provide a good illustration of its usefulness and general applicability, while the last two cases allow to determine the influence of the heater foil on the film-cooling measurements.

4 Measurement Errors

The approach used here for the measurement error analysis is similar to the one described by Kline et al. [25]. The values h, η and q are obtained from a regression analysis as described previously and have accordingly the dependencies (Eqs. (15), (17), and (18)) as

$$h=h(T_{LC}^i,t_{LC}^i,T_{tg}^i,T_{rg}^i,T_0^i,T_{tc}^i,G^i),\quad q=q(h),\quad \eta=\eta(h,q) \tag{19}$$

In the following, the absolute error Δx_j of the foregoing variables is considered identical across the different experiments. The following absolute errors can then be computed:

$$\Delta h=\sqrt{\sum_{i=1}^{N}\left[\left(\frac{\partial h}{\partial T_{LC}^i}\Delta T_{LC}\right)^2+\left(\frac{\partial h}{\partial t_{LC}^i}\Delta t_{LC}\right)^2+\left(\frac{\partial h}{\partial T_{tg}^i}\Delta T_{tg}\right)^2+\left(\frac{\partial h}{\partial T_{rg}^i}\Delta T_{rg}\right)^2+\left(\frac{\partial h}{\partial T_0^i}\Delta T_0\right)^2+\left(\frac{\partial h}{\partial T_{tc}^i}\Delta T_{tc}\right)^2+\left(\frac{\partial h}{\partial G^i}\Delta G\right)^2\right]}$$

$$\Delta q=\left|\frac{\partial q}{\partial h}\Delta h\right|\Delta\eta=\sqrt{\left(\frac{\partial \eta}{\partial h}\Delta h\right)^2+\left(\frac{\partial \eta}{\partial q}\Delta q\right)^2} \tag{20}$$

A centered scheme is used to approximate the foregoing partial derivatives as

$$\frac{\partial f}{\partial x_j}\approx\frac{f(x_1,\ldots,x_j+\Delta x_j,\ldots,x_J)-f(x_1,\ldots,x_j-\Delta x_j,\ldots,x_J)}{2\Delta x_j}=\frac{\tilde{f}(x_j)}{2\Delta x_j} \tag{21}$$

where x_j, $j=1\ldots J$, are the variables of a function f. The discretization step of the numerical scheme for a given variable is assumed to be identical to the absolute error of this variable and the following is then obtained:

$$\Delta h=\frac{1}{2}\sqrt{\sum_{i=1}^{N}\left[\tilde{h}(T_{LC}^i)^2+\tilde{h}(t_{LC}^i)^2+\tilde{h}(T_{tg}^i)^2+\tilde{h}(T_{rg}^i)^2+\tilde{h}(T_0^i)^2+\tilde{h}(T_{tc}^i)^2+\tilde{h}(G^i)^2\right]} \tag{22}$$

Subsequently, the errors for q and η become

$$\Delta q=\frac{1}{2}|\tilde{q}(h)|\quad \Delta\eta=\frac{1}{2}\sqrt{\tilde{\eta}(h)^2+\tilde{\eta}(q)^2} \tag{23}$$

A relative error of 1% on the heat flux ratio G is considered. For every temperature measurement, an absolute error of 0.1 K is taken into account. The time detection of the transient liquid crystal signal is based on an absolute error of 0.04 s corresponding to one frame of the video sequence. The error analysis is then based upon a total of nine tests resulting from a combination of three typical coolant gas variations T_{tc} combined with three typical heat flux ratios G.

For the representative result ($h=100$ W/m^{2}K^{-1}, $\eta=0.15$, and $q=1500$ W/m^2) of the four experimental cases introduced previously, this leads to a maximum relative error of $<15\%$ on h, of $<3\%$ on η and of $<5\%$ on q. For these conditions, an error analysis on the number of experiments taken into account for the regression shows that there may be an optimum number of coolant gas variations (Fig. 4). In all cases the errors decrease with an increasing number of experiments, albeit to different levels depending on the number of coolant gas variations used. The optimum appears to be for nine experiments issued from a combination of three different coolant gas variations with three different heat flux ratios. This combination of experiments is used for the four test cases presented in this paper.

In addition to the measurement errors, the initial temperature, the liquid crystal temperature, the coolant gas preconditioning levels, and the applied heat fluxes have to be chosen in accordance with the expected values of h, η, and q. This may be assessed using numerical simulations of the temporal evolution of T_w in order to have acceptable t_{LC} values during the experiments. Indeed, a too-fast transient liquid crystal signal leads to higher errors due to a limited time resolution for t_{LC}, and a too-slow transient signals leads also to higher errors as the half-infinite model assumption is no longer satisfied.

5 Results and Discussion

The results shown in the present chapter focus on the effect of different wall boundary conditions (see Fig. 3) on the film cooling performance on a flat plate. It can be seen that for cases 1 and 2, the heat flux distribution at the wall and therefore the wall boundary condition for the film cooling process is different. This is caused by the different connection of the power supply to the heater foil.

Downloaded 31 May 2010 to 171.66.16.27. Redistribution subject to ASME license or copyright; see http://www.asme.org/terms/Terms_Use.cfm

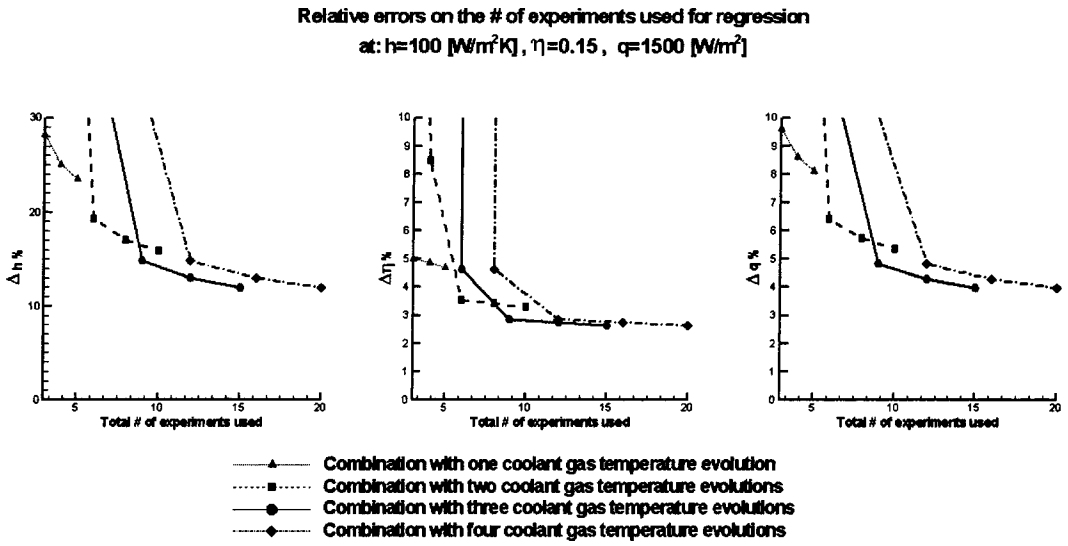

Fig. 4 Relative error evolution with the increase of the number of experiments used for the regression analysis

The reference heat flux q obtained by the regression is presented in its non-dimensional form $q/\overline{q}$ in Fig. 5. The effective surface heat flux generation applied during each experiment i is then the product of q by its gain factor G^i. For case 1, the local surface heat flux tends to increase in between the holes and decreases in the longitudinal prolongation of the holes. The opposite is true for case 2 where the local surface heat flux is low or close to zero in between the holes and increases in their longitudinal prolongation. This corresponds to the expected result when considering the local surface resistance of the foil and the path of the electrical current. The surface heat flux distributions in these two cases have been compared to numerical simulations done using a method described by Wiedner et al. [26]. It is only based on the heater-foil geometry with constant boundary conditions applied on

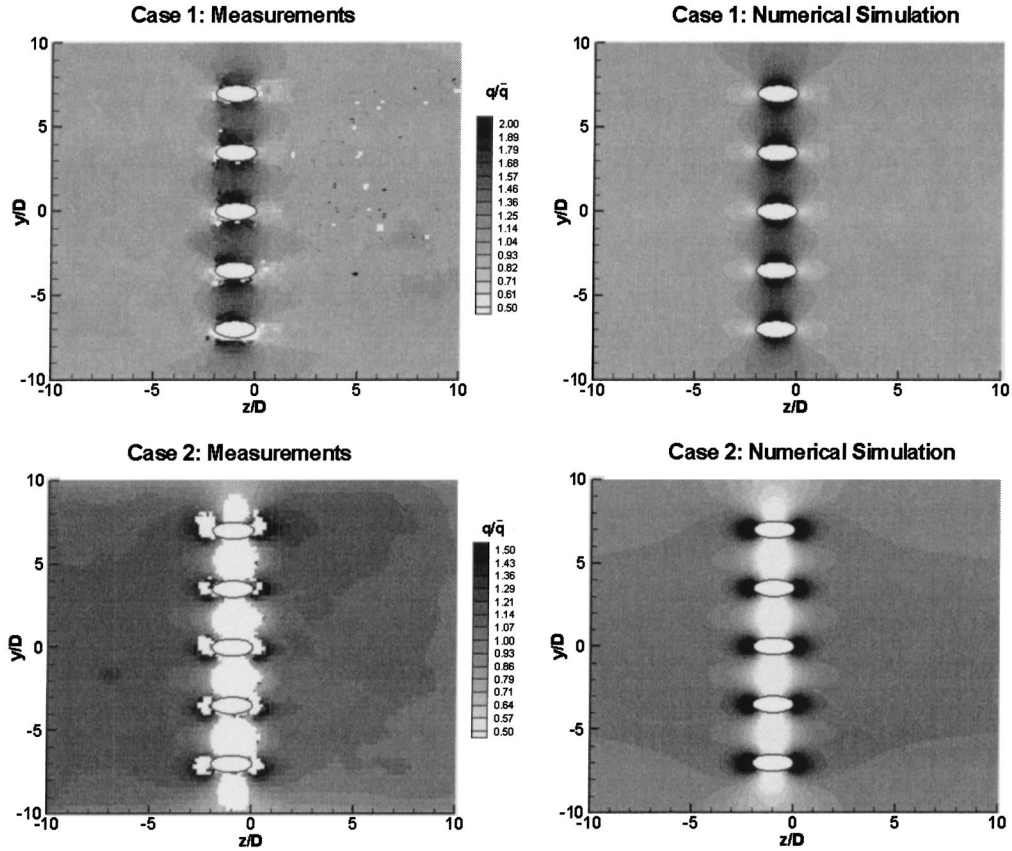

Fig. 5 From measurements derived (left) and calculated (right) dimensionless reference heat flux distribution for cases 1 and 2

Downloaded 31 May 2010 to 171.66.16.27. Redistribution subject to ASME license or copyright; see http://www.asme.org/terms/Terms_Use.cfm

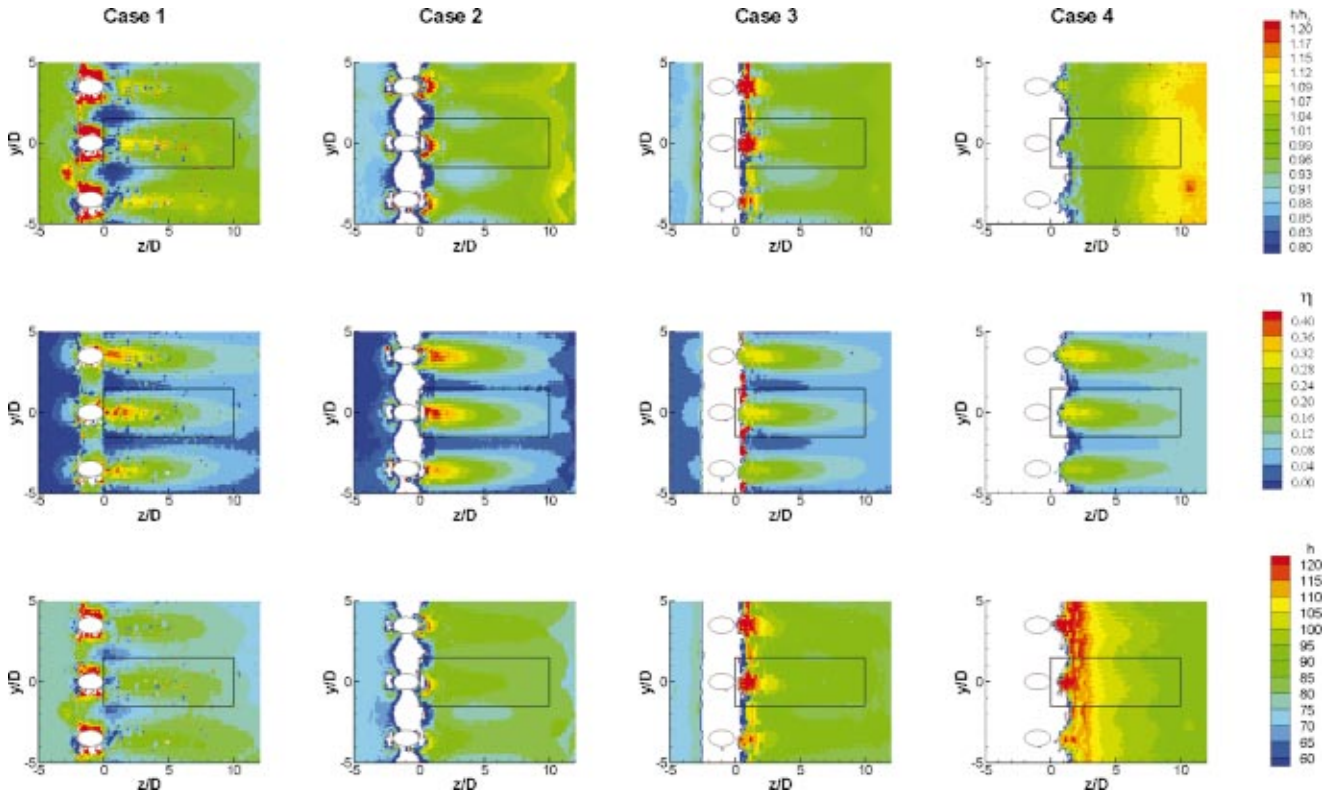

Fig. 6 Spatial distributions of heat transfer coefficients and adiabatic film cooling effectiveness

the bus bars location in order to simulate the electrical current. The resulting simulated heat flux distribution values are also shown in Fig. 5 and present excellent agreement with the experimental values. Hence, they validate the regression approach of multiple transient heater-foil experiments and the development of the new measurement technique described in the foregoing regarding the heat flux determination. Notice that with this measurement technique, the heat flux losses (electrical wiring, lateral conduction) are automatically accounted for without an explicit knowledge of them. These losses have been determined by assessing the difference between the power given by the power supply and the surface heat yielding a difference of ~25%. About 15% are due to the electrical wiring and 10% to lateral conduction effects.

Figure 6 shows the spatial distribution of the heat transfer coefficient and the film-cooling effectiveness for the four heater foil configurations. Additionally the figure shows the heat transfer coefficient ratio h/h_0, where the reference heat transfer coefficient h_0 is based on the value without blowing. If one focuses on the distribution of the heat transfer coefficients, one might see changes in the heat transfer distribution because of the changed thermal boundary conditions between the individual cases. If the near hole region is not taken into account (as there might be some heat conduction effects for $-2<z/D<1$), the difference between the heat transfer coefficients of case 1 and case 2 is quite small and can be generally neglected. This can be explained by the fact that the only difference for these two configurations is the different application of the power supply in order to produce the surface heat flux distribution, yielding a slight change in the thermal boundary layer. However, both configurations lead to the same starting point of the thermal boundary layer. Therefore, the total difference in heat transfer coefficient for a turbulent flowing fluid with a Prandtl number of around one (air) should not be too large. In contrast to these two cases, bigger differences in the heat transfer coefficients can be seen by comparing case 1 with case 3 or case 4. In case 4, the start of the thermal boundary layer is delayed to after the film cooling holes. This results in much higher heat transfer coefficients after the row of holes than in case 1. In case 3, the area between the film-cooling holes is not heated. Also this configuration shows differences in the heat transfer coefficient compared to case 1, the differences being mainly restricted to a near-hole area of about two to four hole diameters. This can be explained by the fact that the disruption in heat flux from the surface to the flow changes only locally the thermal boundary layer thickness for case 3. By relating the heat transfer coefficient to its value without blowing, it seems that smaller differences are present between the individual cases, the biggest differences appearing again between case 4 and the other cases. Focusing finally on the distribution of the adiabatic film-cooling effectiveness, one sees that only very small differences between the individual cases can be observed.

For nearly all design work for film-cooled gas turbine blades, laterally averaged values of the heat transfer coefficients and the film cooling effectiveness play a very important role. Therefore, the results have been laterally averaged for the rectangular area shown in the individual plots of Fig. 6, the results being displayed in Fig. 7. If one focuses on the distribution of the heat transfer coefficients, it is obvious that the heat transfer coefficients from case 4 show the largest deviation to all other cases. For the latter, the change in thermal boundary conditions on the heat transfer coefficients might be neglected. This is an important outcome of the present study, because there are several film-cooling studies known in literature which have used wall boundary conditions similar to case 3. However, the results for the heat transfer coefficients for case 4 show that care has to be taken in selecting appropriate thermal wall boundary conditions for film-cooling experiments. On the other hand, the lateral film-cooling effectiveness values show quite a good agreement for all different wall boundary conditions. Additionally, Fig. 7 shows for the film cooling effectiveness also values from a correlation given by Baldauf et al. [27] based on a large set of experimental data. As can be

Downloaded 31 May 2010 to 171.66.16.27. Redistribution subject to ASME license or copyright; see http://www.asme.org/terms/Terms_Use.cfm

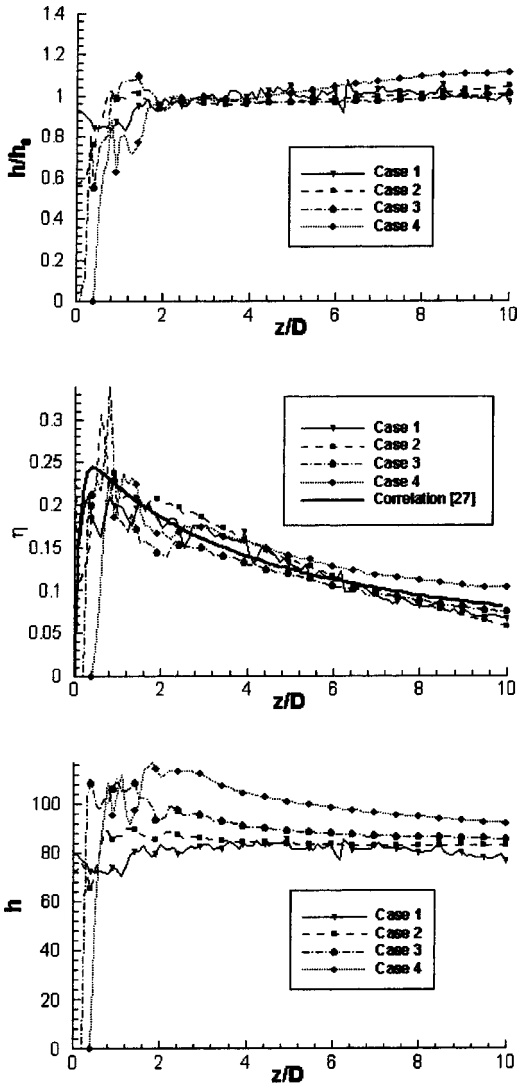

Fig. 7 Lateral-averaged values of the heat transfer coefficient and the adiabatic film-cooling effectiveness (derived from the data given in Fig. 6)

seen, the results obtained here are in good agreement with those found in literature, further validating the present measurement method.

6 Conclusions

The present paper introduces a novel method for determining the heat transfer coefficient and film-cooling effectiveness. This method is based on the liquid crystal technique applied on a heater-foil with film-cooling holes. The method does not need to take into account the surface heat flux distribution and is therefore independent from the power supply configuration and other factors like the variations in thickness and resistance of the heater foil.

In the present paper four different heater-foil configurations have been considered in order to study the influence of the thermal wall boundary conditions on the heat transfer performance of a film-cooled plate. It has been shown that care has to be taken when doing film-cooling experiments since there is a noticeable influence of the thermal wall boundary conditions on the heat transfer coefficients. The present method has been validated against data taken from literature and good agreement has been found.

Nomenclature

a,b,c,d = experimental interpolation parameters, (K, s^{-1}, Ks^{-1}, $Ks^{-1/2}$)
BR = blowing rate $(\rho_c U_c)/(\rho_g U_g)$, (-)
c_p = specific heat at constant pressure, $(J\,kg^{-1}\,K^{-1})$
D = hole diameter, (m)
G = gain factor or heat flux ratio
h = convective heat transfer coefficient, $(W\,m^{-2}\,K^{-1})$
h_0 = convective heat transfer coefficient without coolant injection, $(W\,m^{-2}\,K^{-1})$
k = thermal conductivity of the plate, $(W\,m^{-1}\,K^{-1})$
L_d = hole length, (m)
N = no. of experiments
P = pitch hole, (m)
q = reference wall heat flux, $(W\,m^{-2})$
$\overline{q}$ = average reference wall heat flux, $(W\,m^{-2})$
$\dot{q}_w$ = wall heat flux, $(W\,m^{-2})$
r = index of summation
s = Laplace variable corresponding to t, (s^{-1})
T = temperature, (K)
t = time, (s)
U = flow velocity, $(m\,s^{-1})$
x = axial coordinate, (m)
y = pitchwise coordinate, (m)
z = spanwise coordinate, (m)
α = thermal diffusivity, $(m^2\,s^{-1})$
δ = plate thickness, (m)
ε = error function
η = adiabatic film-cooling effectiveness
ρ = mass density of plate, $(kg\,m^{-3})$

Superscript

i = index of experiment

Subscripts

0 = initial condition
aw = adiabatic wall
c = for coolant gas
g = for main gas
LC = liquid crystals
rg = main gas recovery condition
tc = coolant gas total conditions
tg = main gas total conditions
w = wall $(x=0)$

Abbreviations

CCD = charge-coupled device
LED = light emitting diode

References

[1] Goldstein, R. J., 1971, "Film Cooling," *Advances in Heat Transfer*, eds., T. F. Irvine and J. P. Hartnett, Academic Press, New York, Vol. 7, pp. 321–379.
[2] VKI Lecture Series, 1982, "Film Cooling and Turbine Blade Heat Transfer," VKI-LS 82-02.
[3] Leontiev, A. I., 1999, "Heat and Mass Transfer Problems for Film Cooling," ASME J. Heat Transfer, **121**, pp. 509–527.
[4] Sinha, A. K., Bogard, D. G., and Crawford, M. E., 1990, "Film Cooling Effectiveness Downstream of a Single Row of Holes with Variable Density Ratio," 90-GT-43.
[5] Forth, C. J., Loftus, P. J., and Jones, T. V., 1980, "The Effect of Density Ratio on the Film Cooling of a Flat Plate," AGARD CP 390, Bergen.
[6] Ito, S., Goldstein, R. J., and Eckert, E. R. G., 1978, "Film Cooling of a Gas Turbine Blade," ASME J. Eng. Power, **100**, pp. 476–481.
[7] Takeishi, K., Aoki, S., Sato, T., and Tsukagoshi, K., 1992, "Film Cooling on a Gas Turbine Rotor Blade," ASME J. Turbomach., **114**, pp. 828–834.
[8] Drost, U., 1998, "An Experimental Investigation of Gas Turbine Airfoil Aero-Thermal Film Cooling Performance," thesis N°1817, EPF Lausanne, Switzerland.
[9] Crawford, M. E., 1986, "Simulation Codes for Calculation of Heat Transfer to Convectively Cooled Turbine Blades," VKI-LS, Convective Heat Transfer and Film Cooling in Turbomachinery.
[10] Weigand, B., Bonhoff, B., and Ferguson, J., 1997, "A Comparative Study Between 2D Boundary Layer Predictions and 3D Navier-Stokes Calculations

Downloaded 31 May 2010 to 171.66.16.27. Redistribution subject to ASME license or copyright; see http://www.asme.org/terms/Terms_Use.cfm

for a Film Cooled Vane,'' Proc., U.S. National Heat Transfer Conference, Baltimore, HTD 350, pp. 213–221.
[11] Garg, V. K., 1997, ''Comparison of Predicted and Experimental Heat Transfer on a Film-Cooled Rotating Blade using a Two-Equation Turbulence Model,'' 97-GT-220.
[12] Ireland, P. T., and Jones, T. V., 2000, ''Liquid Crystal Measurements of Heat Transfer and Surface Shear Stress,'' Meas. Sci. Technol., **11**, pp. 969–985.
[13] Lutum, E., von Wolfersdorf, J., Weigand, B., and Semmler, K., 2000, ''Film Cooling on a Convex Surface with Zero Pressure Gradient Flow,'' Int. J. Heat Mass Transfer, **43**, pp. 2973–2987.
[14] Reiss, H., 1998, ''The Transient Liquid Crystal Technique Employed for Sub- and Transonic Heat Transfer and Film Cooling Measurements in a Linear Cascade,'' 14th bi-annual symposium on Measurement Techniques in Transonic and Supersonic Flow in Cascades and Turbomachines.
[15] Dui, H., Han, J. C., and Ekkad, V., 1997, ''Detailed Film Cooling Measurements Over a Gas Turbine Blade Using a Transient Liquid Crystal Image Technique,'' HTD 350, National Heat Transfer Conference, **12**.
[16] von Wolfersdorf, J., Hoecker, R., and Sattelmayer, T., 1993, ''A Hybrid Transient Step-Heating Heat Transfer Measurement Technique Using Heater Foils and Liquid-Crystal Thermography,'' ASME J. Heat Transfer, **115**, pp. 319–324.
[17] Turnbull, W. N., and Oosthuizen, P. H., 1999, ''A New Experimental Technique for Measuring Surface Heat Transfer Coefficients Using Uncalibrated Liquid Crystals,'' ASME HTD-Vol. 364-4, pp. 121–126.
[18] Farmer, J. P., Seager, D. J., and Liburdy, J. A., 1997, ''The Effect of Shaping Inclined Slots on Film Cooling Effectiveness and Heat Transfer Coefficient,'' ASME 97-GT-339.
[19] Seager, D. J., and Liburdy, J. A., 1997, ''Experimental Investigation of the Effects of Compound-Angle Holes on Film Cooling Effectiveness and Heat Transfer Performance Using a Transient Liquid Crystal Thermometry Technique,'' *Optical Technology in Fluid, Thermal and Combustion Flow III*, SPIE, **3172**, pp. 173–182.
[20] Vogel, G., Graf, A., and Weigand, B., 2002, ''Film Cooling: A Comparative Study of Different Heater-Foil Configurations for Liquid Crystal Experiments,'' ASME GT-2002-30552.
[21] Vogel, G., and Weigand, B., 2001, ''A New Evaluation Method for Transient Liquid Crystal Experiments,'' NHTC01-1511, 35th ASME National Heat Transfer Conference, Anaheim, CA.
[22] Carslaw, H. S., and Jaeger, J. C., 1959, *Conduction of Heat in Solids*. Oxford University Press, London, Second Edition. Chapter XII and Appendices II & V.
[23] Isaacson, E., and Keller, H. B., 1966, *Analysis of Numerical Methods*, Dover Publications.
[24] Vogel, G., and Bölcs, A., 2000, ''A Novel Digital Image Processing System for the Transient Liquid Crystal Technique applied for Heat Transfer and Film Cooling Measurements,'' ICHMT Paper, Turbine 2000 Symposium, Cesme, Turkey.
[25] Kline, S. J., and McClintock, F. A., 1953, ''Describing Uncertainties in Single-Sample Experiments,'' J. Mech. Eng., Jan., pp. 3–8.
[26] Wiedner, B. G., and Camci, C., 1996, ''Determination of Convective Heat Flux on Steady-State Heat Transfer Surface With Arbitrarily Specified Boundaries,'' ASME J. Heat Transfer, **118**, pp. 850–856.
[27] Baldauf, S., Schulz, A., Wittig, S., and Schleurlen, M., 1997, ''An Overall Correlation of Film Cooling Effectiveness from One Row of Holes,'' 97-GT-79.

Downloaded 31 May 2010 to 171.66.16.27. Redistribution subject to ASME license or copyright; see http://www.asme.org/terms/Terms_Use.cfm

A Novel Transient Liquid Crystal Technique to Determine Heat Transfer Coefficient Distributions and Adiabatic Wall Temperature in a Three-Temperature Problem

Andrew C. Chambers
e-mail: Andrew.Chambers@eng.ox.ac.uk

David R. H. Gillespie

Peter T. Ireland

Department of Engineering Science,
University of Oxford,
Oxford, OX1 3PJ, UK

Geoffrey M. Dailey
e-mail: geoffrey.dailey@rolls-royce.com
Rolls-Royce CAEL,
Derby, UK

Transient liquid crystal techniques are widely used for experimental heat transfer measurements. In many instances it is necessary to model the heat transfer resulting from the temperature difference between a mixture of two gas streams and a solid surface. To nondimensionally characterize the heat transfer from scale models it is necessary to know both the heat transfer coefficient and adiabatic wall temperature of the model. Traditional techniques rely on deducing both parameters from a single test. This is a poorly conditioned problem. A novel strategy is proposed in which both parameters are deduced from a well-conditioned three-test strategy. The heat transfer coefficient is first calculated in a single test; the contribution from each driving gas stream is then deduced using additional tests. Analytical techniques are developed to deal with variations in the temperature profile and transient start time of each flow. The technique is applied to the analysis of the heat transfer within a low aspect ratio impingement channel with initial cross flow.
[DOI: 10.1115/1.1575252]

Keywords: Transient, Heat Transfer, Internal Cooling, Turbine

Introduction

Many modern turbine blades are cooled by passing air through the blade before bleeding it to the surface to form cooling films. In the steady state the heat transferred to a the blade surface must be transferred to the internal coolant flow. The heat removed is dependent on both the temperature of the flow and the heat transfer coefficient. Cooling by impingement channel is currently of particular interest as it provides heat transfer enhancement over a conventional passage while the continual injection of coolant gas keeps the driving gas temperature difference high maintaining locally high heat flux. Improvements in casting technology have increased the useful heat transfer area and the length of flow path of coolant while maintaining the robustness of impingement designs in comparison to film-cooling. Figure 1 shows typical cross sections through a turbine blade cooled using impingement channels integrally cast into the wall.

Frequently the experimental heat transfer data required for the design of such internal cooling systems are obtained from tests of large-scale Perspex models from which engine conditions can be determined through dimensional analysis. Many transient techniques are already used (Ireland et al. [1]), their advantage being that full-surface heat transfer coefficient distributions are obtained in a small number of tests. In the impingement configuration under current consideration, the impinging flow and the cross flow in the channel are likely to be of different temperatures. Thus, to correctly model the heat transfer process, the mixed bulk temperature, related to the source of the coolant flow, is required. This paper details the authors' development of general techniques to measure these parameters in a more robust manner than existing techniques allow.

Contributed by the International Gas Turbine Institute and presented at the International Gas Turbine and Aeroengine Congress and Exhibition, Amsterdam, The Netherlands, June 3–6, 2002. Manuscript received by the IGTI February 18, 2002. Paper No. 2002-GT-30532. Review Chair: E. Benvenuti.

Test Facility

Figure 2 shows the details of the impingement cooling channel geometry used in the current series of tests. The channel is constructed from perspex[1] and coated with a single narrowband thermochromic liquid crystal displaying peak intensity at 33.0°C. Cross flow is introduced at one end of the channel, while air impinges from a separate source through a single staggered row of 19 evenly spaced holes along the length of the channel, spacing $x/d=4.36$, $y/d=\pm 1.8$. The air exhausts at the far end of the channel to a vacuum pump. The total mass flow through the channel is controlled using a valve between the channel exit and the vacuum pump. A photograph of the impingement channel is also shown in Fig. 3 (no cross flow case). The proportion of cross flow is controlled by a variable speed blower. Independent heating of each gas stream is achieved by passing the air through two planar mesh heaters, Gillespie [2], powered from two 230V AC transformers. A timer that delays the power to the cross flow heater is used to ensure simultaneous arrival of both heated streams at the working section. A schematic is shown in Fig. 4. The transit delays within the channel itself are in the order of 0.1 seconds ensuring they have negligible effect on the experimental results. The apparatus is able to reproduce engine representative Reynolds numbers based on impingement hole diameter, $Re_{jet}=10000-35000$, and cross flow of up to 10% of the total mass flow rate.

Instrumentation

The heater mesh power is calculated from mesh voltage and current measurements made using a hand held clamp meter. Gas temperatures are based on these power measurements and verified using a series of gas thermocouples placed in the plenums upstream of the channel. Seven thermocouples equally distributed along the length of the impingement plenum allows monitoring of

[1]Perspex™—ICI Polymethylmethacrylate

 Copyright © 2003 by ASME

Downloaded 31 May 2010 to 171.66.16.27. Redistribution subject to ASME license or copyright; see http://www.asme.org/terms/Terms_Use.cfm

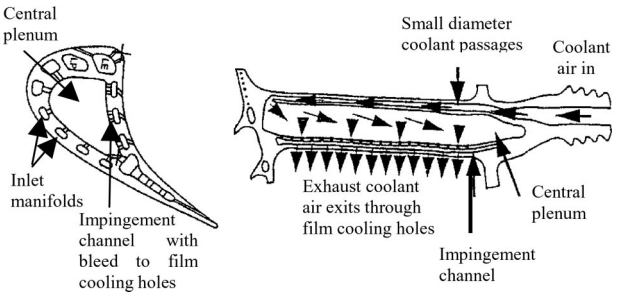

Fig. 1 Typical cross section of a turbine blade cooled by impingement channel

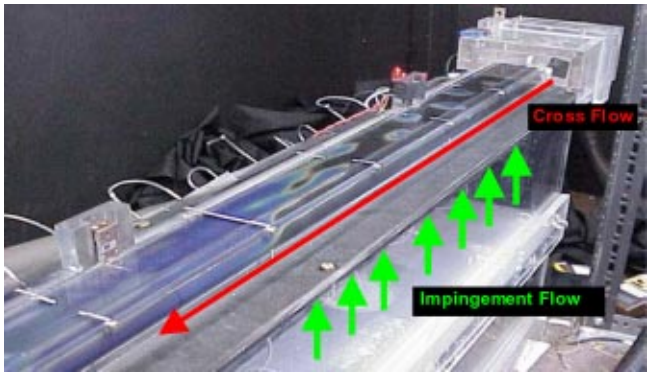

Fig. 3 Snapshot of a type A effectiveness test with only the impinging flow heated. Note the areas of no liquid crystal color play where cross flow is predominate.

temperature uniformity. Additional flow resistance was required to achieve a spanwise temperature uniformity of ±0.5°C. The thermocouples were logged using a PC. *Labview* software controls the data acquisition card and 16 temperature channels at a sample rate of 10 Hz are recorded in each test. Total mass flow rate and the cross flow mass flow rate are measured using BS ISO TR 15377 orifice meters. The color change in the liquid crystal is monitored using 2 PAL video cameras coupled to VHS recorders. Uniform lighting was provided along the length of the channel by a pair of fluorescent lights (color=''white'') offset on either side of the channel to prevent reflection.

Measurement Requirements

Flow introduced at the end of the passage and by impingement along the passage is of different temperatures both in the test rig and the engine. To scale results between the model and the engine, Nusselt number and impingement effectiveness are required. The Nusselt number is derived from the heat transfer coefficient based on local adiabatic wall temperature, while the effectiveness is the dimensionless adiabatic wall temperature. The effectiveness lies between 0 and 1: where 0 indicates that the local adiabatic wall temperature is the cross flow temperature and 1 that it is the impingement flow temperature.

$$\varepsilon = \frac{T_{\text{gas}} - T_{\text{cross}}}{T_{\text{imp}} - T_{\text{cross}}} \tag{1}$$

It should be possible to use established techniques to determine both the heat transfer coefficient and the effectiveness simultaneously from a single experiment provided that both gas streams are heated to different temperatures. If heated to the same temperature the determination of heat transfer coefficient becomes a well conditioned problem, but the effectiveness cannot be inferred.

Review of Existing Technology

Thermochromic liquid crystals have provided experimenters with the ability to measure entire surface temperature events almost noninvasively. Some of their first application to impingement cooling was by den Ouden and Hoogendoorn [3], who used a steady-state technique to measure impingement heat transfer from a fully developed turbulent jet not subject to cross flow. Subsequent developments of steady state techniques allowed the investigation of 3 temperature problems such as the influence of the impingement plate temperature on heat transfer to the impingement target plate, Lucas et al. [4], and in numerous studies of external film-cooling (e.g., Sargison et al. [5]). While the use of wide band liquid crystals, displaying color play over a range of up to 20°C, has increased the data available in each test, generally transient tests offer full surface data in a small number of tests for a set condition, and reduce errors introduced through lateral conduction in the model substrate and nonuniformity in the heating of the model surface.

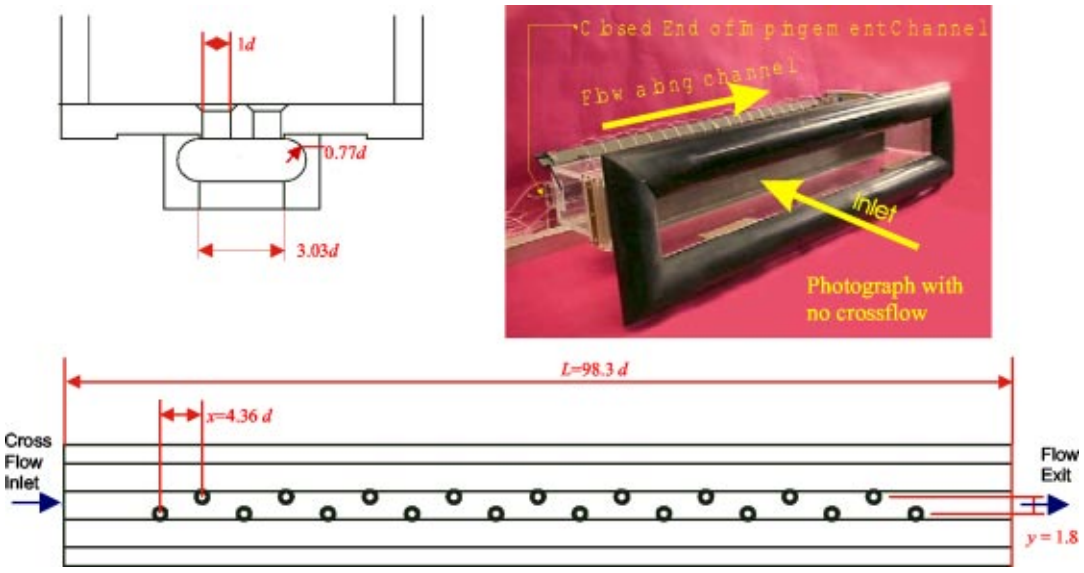

Fig. 2 Impingement channel geometry

Downloaded 31 May 2010 to 171.66.16.27. Redistribution subject to ASME license or copyright; see http://www.asme.org/terms/Terms_Use.cfm

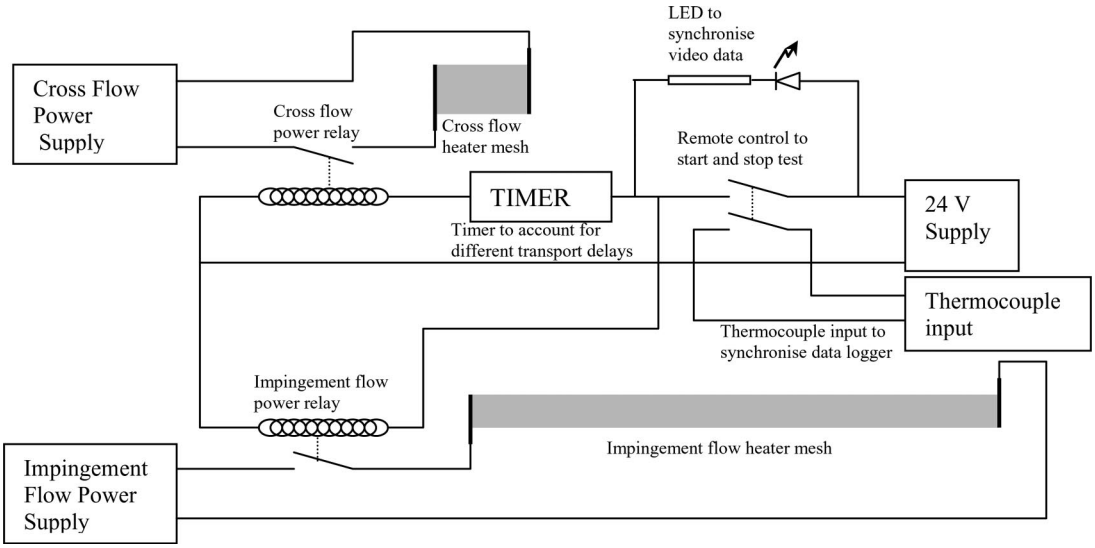

Fig. 4 Schematic of electrical system

Transient liquid crystal techniques for the measurement of heat transfer have been use since the 1980s. As the basic technique established by Ireland and Jones [6] is well known, only a brief description is given here. In the heat transfer experiments, scale models of engine components are manufactured from a poor thermal conductor such as perspex; a transparent plastic that allows excellent optical access. The liquid crystal coating (typically of thickness ~10 microns) is applied to the substrate using a small air brush and the optical response can be made insensitive to coating thickness. When a temperature transient is initiated in the flow, the model temperature starts to change. The liquid crystal color play at the surface is recorded, and these data yield the temperature history of the model surface, and hence the local heat transfer coefficient distribution. It is the ease with which the surface coating can be prepared, even if the model surface has compound curvature, which makes the method particularly suitable to the measurement of heat transfer coefficients on complex surfaces (Chyu et al. [7], Wang et al. [8], Gillespie et al. [9]). However, it should be noted that the liquid crystal is subject to a shift in the temperature calibrated color play, dependent on the relation between the angle of viewing and angle of illumination (Farina and Moffat [10]). This means that where the model cannot be taken through an *in-situ* isothermal calibration (Guo et al. [11]) it is desirable to use several narrow banded liquid crystals (color play $<1°C$) to obtain multiple temperature events based on relative intensity of illumination rather than a color index signal from a wide band crystal. Compared to infrared thermography or the use of multiple surface thermocouples, liquid crystals provides both a cheap and accurate way of attaining full surface temperature measurement. In the two temperature situation there has been much effort to increase the speed of data reduction. Of particular note is the work of Baughn et al. [12], and Turnbull and Oosthuizen [13] whose novel techniques involve subjecting the model to a periodically varying heat flux, and inferring the heat transfer coefficient from the attenuation of the signal and the phase delay in the corresponding local surface temperature response respectively.

Transient heat transfer techniques are not, however, without drawbacks. Of particular concern is the effect of the changing thermal boundary conditions, and the assumption of an isothermal wall temperature throughout the test. There are conditions in which the transient method and other methods will give dramatically different results, a good example of this being described by Butler and Baughn [14]. Tsang et al. [15] outlined a detailed procedure for assessing the effects of upstream wall temperature and the associated uncertainty in heat transfer coefficient measurements, while von Wolfersdorf et al. [16], proposed an analysis technique to account for these effects in long passages. When used in an investigation of impingement cooling these effects might be expected to change both the heat transfer coefficient and the local effectiveness measured. In fact, previous work has shown good agreement between impinging jet data under steady state and transient conditions, see Lucas et al. [4] *cf.* van Treuren et al. [17]. Similarly Son et al. [18] showed that transiently heated impingement flow and a pre-heated working section produced identical heat transfer coefficient measurements and equivalent adiabatic wall temperatures. Cho et al. [19] showed that at low $z/d(<4)$ there was little variation in the heat transfer from the jet to the plate, and that variations were dominated by the nozzle geometry, suggesting shearing flow rather than temperature gradients induce mixing between the shear and jet flows. This suggests that the effect of temperature induced addition flow mixing should be small in the current series of tests. This is further supported by the work of Florschuetz and Su [20] and Goldstein et al. [21] who investigated the effect of entrainment on a single jet in a series of steady state heated plate tests. They showed that the heat transfer coefficient obtained was independent of the relative magnitude of the jet temperature and the ambient temperature, when the adiabatic wall temperature is used as a reference temperature.

The transient liquid crystal technique has also been employed in three temperature problems to simultaneously obtain two unknown parameters over entire model surfaces in a single test. Here, two surface temperature events are required for solution. This may be straightforwardly implemented by applying a mixture of two or more narrowbanded liquid crystal to the model surface, however, this problem only remains well conditioned if at least one of the parameters varies over a fairly small range, and the liquid crystal color play temperature ranges are carefully chosen (Ireland and Jones [22]). The technique can be further extended using additional liquid crystals, but this may affect the quality of each of the color plays. Post processing of narrow band crystals, used where there is considerable surface curvature, may yield one temperature event for each liquid crystal used, linked to the maximum intensity seen. Alternatively, at each point the full intensity-time signature (Ling and Ireland [23]) may be compared to those predicted for all possible values of heat transfer coefficient and driving gas temperature to obtain a 'best fit' value. This approach provides many degrees of redundancy, and unlike wide band crystal techniques (Camci et al. [24], van Treuren et al. [25]) is not subject to problems of lighting and internal reflection.

Regardless of how the surface temperature history is recorded

Downloaded 31 May 2010 to 171.66.16.27. Redistribution subject to ASME license or copyright; see http://www.asme.org/terms/Terms_Use.cfm

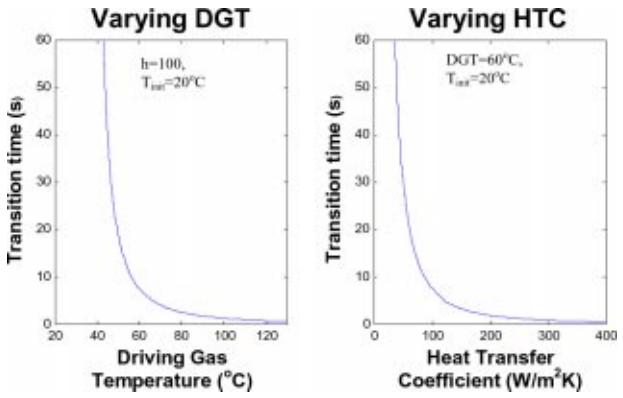

Fig. 5 Variation of liquid crystal transition times for the case of 1) fixed heat transfer coefficient with varying driving gas temperature, and 2) fixed driving gas temperature with varying heat transfer coefficient, respectively

there is a fundamental difficulty with the above techniques. Various combinations of heat transfer coefficient and driving gas temperature can produce very similar surface response profiles making the problem ill conditioned. Slight inaccuracies in measuring the experimental start time or the gas stream temperature can lead to large errors in both heat transfer coefficient and effectiveness measurement. Initial tests on the current impingement cooling configuration processed using the double crystal technique were not able to resolve data over the entire surface with sufficient accuracy. Vedula and Metzger [26] proposed a two test strategy for film-cooling configurations to allow the determination of both film-cooling effectiveness and heat transfer coefficient. The technique uses Duhamel's method to account for arbitrary inlet temperature profiles.

3-Test Technique—Introduction

A new technique has been developed that will allow both the effectiveness and heat transfer coefficient to be determined from a well-conditioned problem. For a single narrow band liquid crystal we know that the liquid crystal transition time is individually a strong function of either the heat transfer coefficient or the driving gas temperature providing the other parameter is known Fig. 5. This has led to the development of a 3-test technique; applicable to problems where there are two independently controlled temperature boundary conditions. Heated air passing through the impingement holes with the additional cross flow introduced at the upstream end of the channel is such a case. The technique involves combining the results from the three tests detailed below to determine both the heat transfer coefficient and the effectiveness.

Test name		Gas A	Gas B
Heat transfer coefficient test		Hot	Hot
Effectiveness tests	A	Hot	Cold
	B	Cold	Hot

When a heat transfer test is conducted, the liquid crystal on all of the test surface undergoes transition provided that the gas temperatures are correctly chosen for the expected heat transfer coefficient and the known liquid crystal transition temperature. Furthermore, the entire surface of interest should also undergo a crystal transition during either test A or B dependent on the local effectiveness, i.e., which flow is locally driving the heat transfer. The heat transfer coefficient and effectiveness may then be determined by comparing the transition times between the heat transfer coefficient test and either test A or B (referred to as the effectiveness tests). Using a combination of results from two separate tests allows a well conditioned solution of the 2-parameter problem. In the simplest case, where both gas streams are at the same temperature the heat transfer coefficient will be determined solely from the heat transfer coefficient test, the gas temperature being known. The effectiveness may then be determined from the second test, which is now well conditioned, as the heat transfer coefficient is known at all points on the surface. The analysis can also cater for complicated combinations of driving gas temperatures still solving the 2-parameter problem in a well-conditioned manner. Furthermore it has been possible to expand the analysis to take into account combinations of non-uniform temperature profiles. Thus, the technique can be applied to complex inlet temperature profiles. The use of hot pulses and ramps in temperature profile are being investigated by other workers at Oxford.

3-Test Strategy—Uniform Flow

The transient surface temperature response of a solid semi-infinite solid to a step change in driving gas temperature from T_0 to T_{gas} occurring at time $x=0$, $t=0$, (Carslaw and Jaeger [27]) is given by the equation.

$$\theta = 1 - e^{\beta^2}\,\text{erfc}(\beta) \tag{2}$$

where

$$\theta = \frac{T - T_0}{T_{gas} - T_0} \quad \text{and} \quad \beta = h\sqrt{\frac{t}{\rho c k}} \tag{3}$$

When this equation is used to analyze transient liquid crystal experiments the surface temperature of the substrate is known only at the crystal transition temperature, T_{crystal}, which occurs at time $=t$. If the starting temperature of the experiment, T_0, and the driving gas temperature, T_{gas}, are also known there is only 1 unknown, the heat transfer coefficient h, which may be solved directly. In a 3-temperature problem the local driving gas temperature is an additional unknown, but may be related to the temperature of the inlet gas streams using an effectiveness as described in Eq. (1). In the case of the test to determine the heat transfer coefficient when both streams are heated equation 2 may then be rewritten as:

$$\frac{T_{\text{crystal}} - T_{0h}}{(T_{\text{imp h}} - T_{0h})\varepsilon + (T_{\text{cross h}} - T_{0h})(1-\varepsilon)} = 1 - e^{h^2 \frac{t_h}{\rho c k}}\,\text{erfc}\left(h\sqrt{\frac{t_h}{\rho c k}}\right). \tag{4}$$

This equation becomes independent of ε if both flows are heated to the same temperature, allowing a simple solution for the heat transfer coefficient. This is often hard to achieve in practice during a transient test. Also, where the levels of heat transfer vary with effectiveness such as in the impingement channel described in this paper, it is advantageous to use different gas temperatures to achieve well conditioned crystal transition times. The surface response during each of the effectiveness tests where only the impingement flow and then the cross flow are heated may be expressed in a similar manner.

$$\frac{T_{\text{crystal}} - T_{0A}}{(T_{\text{imp}} - T_{0A})\varepsilon} = 1 - e^{h^2 \frac{t_A}{\rho c k}}\,\text{erfc}\left(h\sqrt{\frac{t_A}{\rho c k}}\right) \tag{5}$$

and

$$\frac{T_{\text{crystal}} - T_{0B}}{(T_{\text{cross}} - T_{0B})(\varepsilon - 1)} = 1 - e^{h^2 \frac{t_B}{\rho c k}}\,\text{erfc}\left(h\sqrt{\frac{t_B}{\rho c k}}\right). \tag{6}$$

As before these equations are functions of two unknowns, but both Eqs. (5) and (6) may be combined with Eq. (1) to remove the dependence on effectiveness

Downloaded 31 May 2010 to 171.66.16.27. Redistribution subject to ASME license or copyright; see http://www.asme.org/terms/Terms_Use.cfm

$$\frac{T_{\text{crystal}}-T_{0h}}{(T_{\text{imp}h}-T_{crossh})\left(\left(\frac{T_{\text{crystal}}-T_{0A}}{T_{\text{imp}}-T_{0A}}\right)\frac{1}{1-e^{h^2\frac{t_A}{\rho ck}}\text{erfc}\left(h\sqrt{\frac{t_A}{\rho ck}}\right)}\right)+(T_{\text{cross}h}-T_{0h})}=1-e^{h^2\frac{t_h}{\rho ck}}\text{erfc}\left(h\sqrt{\frac{t_h}{\rho ck}}\right) \tag{7}$$

and

$$\frac{T_{\text{crystal}}-T_{0h}}{(T_{\text{imp}h}-T_{\text{cross}h})\left(\left(\frac{T_{\text{crystal}}-T_{0B}}{T_{\text{cross}}-T'_{0B}}\right)\frac{1}{1-e^{h^2\frac{t_B}{\rho ck}}\text{erfc}\left(h\sqrt{\frac{t_B}{\rho ck}}\right)}+1\right)+(T_{\text{cross}h}-T_{0h})}=1-e^{h^2\frac{t_h}{\rho ck}}\text{erfc}\left(h\sqrt{\frac{t_h}{\rho ck}}\right) \tag{8}$$

respectively. Thence, for either combination of heat transfer test and effectiveness test a solution for the local value of h may then be obtained by solution of either Eq. (7) or (8). When this value of h is substituted back into any of Eqs. (4), (5), or (6), the solution yields the effectiveness, ε.

3-Test Strategy—Arbitrary Temperature Profiles

In many cases it is not possible to achieve a step change in the temperature as assumed above, and the analysis has been extended to take into account: heater mesh transients [2], variations in start times caused through varying transport delays and, an arbitrary inlet temperature profile.

The 1-D Fourier equation which is linear in temperature describes the semi-infinite substrate response during heat transfer tests; thus, the principle of superposition may be applied to model complex gas temperature profiles. The surface response to an incremental step change in temperature at a constant heat transfer coefficient is given by

$$\frac{\Delta T_{\text{surface},k}}{\Delta T_{\text{gas},k}}=1-e^{h^2\frac{t-t_k}{\rho ck}}\text{erfc}\left(h\sqrt{\frac{t-t_k}{\rho ck}}\right) \tag{9}$$

An arbitrary gas temperature profile may be approximated by a series of step changes in temperature at regular time interval

$$T_{\text{gas}}(\Delta t\times i)=\sum_{k=1}^{i}\Delta T_{\text{gas}\,k}, \tag{10}$$

where

$$\Delta T_{\text{gas},k}=T_{\text{gas}}(\Delta t\times k)-T_{\text{gas}}(\Delta t\times(k-1)). \tag{11}$$

The surface response of the substrate is then calculated through superposition.

$$T_{\text{surface}}(\Delta t\times i)=T_{\text{surface},0}+\sum_{k=1}^{i}\Delta T_{gas,k}\times\left(1-e^{h^2\frac{t-t_k}{\rho ck}}\text{erfc}\left(h\sqrt{\frac{t-t_k}{\rho ck}}\right)\right) \tag{12}$$

Now let us extend this technique to the current 3-test strategy. In the first test, the heat transfer test, the local driving gas temperature difference is a function of both effectiveness and the temperature profile of the individual gas streams.

$$\Delta T_{\text{gas}\,h,i}=\varepsilon\Delta T_{\text{gas imp}\,h,i}+(1-\varepsilon)\Delta T_{\text{gas cross}\,h,i} \tag{13}$$

In the subsequent effectiveness tests, where for each test only one gas stream is heated, the local driving gas temperature difference may be represented in a similar manner.

$$\Delta T_{\text{gas}\,A,i}=\varepsilon\Delta T_{\text{gas imp}\,A,i}, \quad (\Delta T_{\text{gas cross}\,A,i}=0) \tag{14}$$

and

$$\Delta T_{\text{gas}\,B,i}=(1-\varepsilon)\Delta T_{\text{gas cross}\,B,i}, \quad (\Delta T_{\text{gas imp}\,B,i}=0) \tag{15}$$

Solution of the 3-temperature problem is then obtained through the minimization of the functions below:

$$\left[T_{\text{crystal}}-T_{\text{surface},0}-\sum_{k=1}^{i}(\varepsilon\Delta T_{\text{gas imp}\,h,k}+(1-\varepsilon)\Delta T_{\text{gas cross}\,h,k})\times\left(1-e^{h^2\frac{t_h-t_k}{\rho ck}}\text{erfc}\left(h\sqrt{\frac{t_h-t_k}{\rho ck}}\right)\right)\right]^2+\left[T_{\text{crystal}}-T_{\text{surface},0}-\sum_{k=1}^{i}\varepsilon\Delta T_{\text{gas imp}\,A,k}\times\left(1-e^{h^2\frac{t_A-t_k}{\rho ck}}\text{erfc}\left(h\sqrt{\frac{t_A-t_k}{\rho ck}}\right)\right)\right]^2 \tag{16}$$

or

$$\left[T_{\text{crystal}}-T_{\text{surface},0}-\sum_{k=1}^{i}(\varepsilon\Delta T_{\text{gas imp}\,h,k}+(1-\varepsilon)\Delta T_{\text{gas cross}\,h,k})\times\left(1-e^{h^2\frac{t_h-t_k}{\rho ck}}\text{erfc}\left(h\sqrt{\frac{t_h-t_k}{\rho ck}}\right)\right)\right]^2+\left[T_{\text{crystal}}-T_{\text{surface}\,0}-\sum_{k=1}^{i}(1-\varepsilon)\Delta T_{\text{gas cross}\,B,k}\times\left(1-e^{h^2\frac{t-t_k}{\rho ck}}\text{erfc}\left(h\sqrt{\frac{t-t_k}{\rho ck}}\right)\right)\right]^2 \tag{17}$$

Each equation is a function of ε and h, and considerably greater computation is required for this solution as first, the equations need minimized with regards to both h and ε and second each trial solution require a sum of a series. Solution to the 3-temperature problem in this manner still produces well-conditioned results. In practice it was found that provided the crystal transition times were sufficiently greater than the experimental time constant both solutions produce almost identical results where start up transients are concerned.

Downloaded 31 May 2010 to 171.66.16.27. Redistribution subject to ASME license or copyright; see http://www.asme.org/terms/Terms_Use.cfm

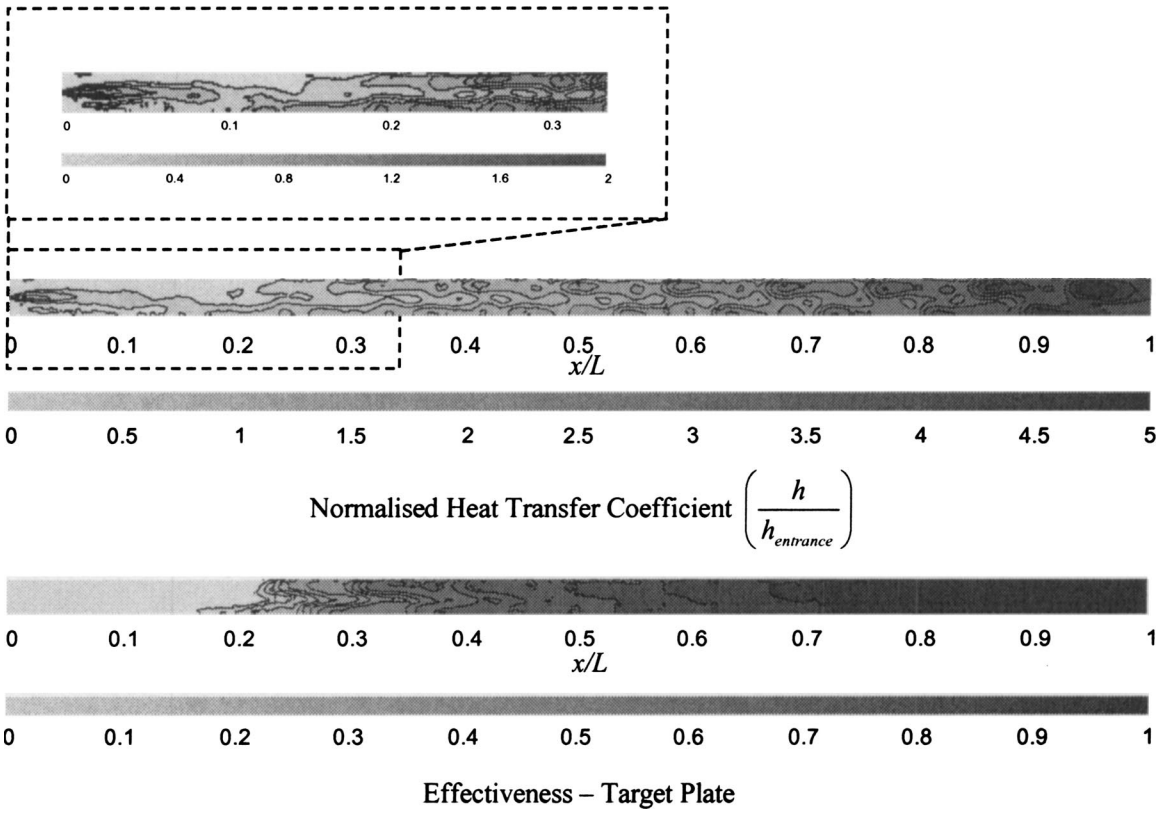

Fig. 6 Normalized heat transfer coefficient and effectiveness on the impingement target surface, $Re_{jet\ avg}$ = 20,000 and 5% initial cross flow

Experimental Results

Heat transfer tests were carried out in the impingement channel. Analysis employing the methods developed in the foregoing yielded both heat transfer coefficient and effectiveness. The results presented were carried out at a single average jet Reynolds number $Re_{jct\ avg} = 20{,}000$, with 5% of the total mass flow introduced as cross flow; and are shown in Figs. 6 and 7. Figure 6 shows data for the impingement target surface. The local heat transfer coefficient is presented normalized by the heat transfer coefficient at the entrance to the channel. The overall picture is of the heat transfer coefficient increasing by a factor of 4 moving from the inlet to the exit of the passage. At the entrance of the passage, $x/L = 0$, the heat transfer coefficient is dominated by the crossflow and there is no evidence of the impinging flow influencing the level of heat transfer coefficient, as indicated by the near zero value of effectiveness. The heat transfer coefficient distribution here is initially high away from the passage corners, dropping slightly moving into the tube. This is typical of the entry length of a rectangular tube. Interestingly the low effectiveness persists at higher values of x/L, and it not until $x/L \sim 0.35$, that the effectiveness reaches 50%. Further into the passage the impinging flow can be seen to locally increase the heat transfer co-

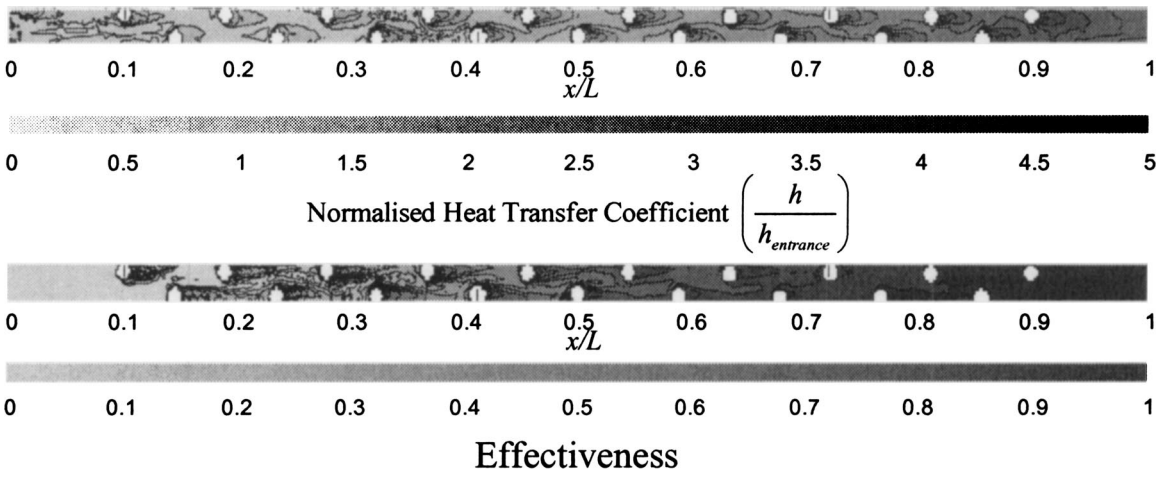

Fig. 7 Normalized heat transfer coefficient and effectiveness on the integrally cast impingement holed surface, $Re_{jet\ avg}$ = 20,000 and 5% initial cross flow

Downloaded 31 May 2010 to 171.66.16.27. Redistribution subject to ASME license or copyright; see http://www.asme.org/terms/Terms_Use.cfm

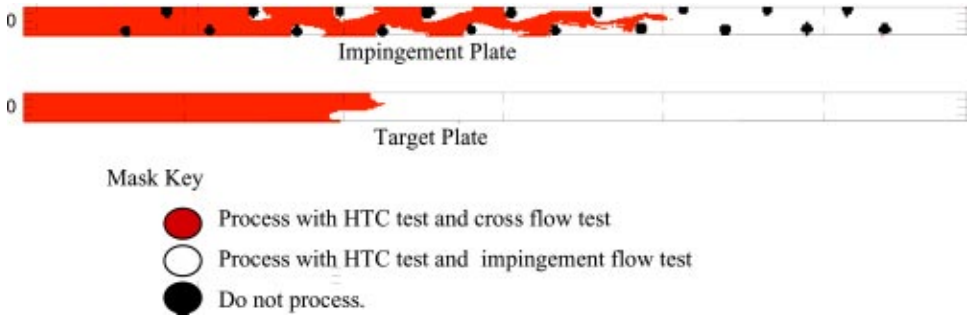

Fig. 8 Mask showing combination of tests used to calculate the heat transfer coefficient and effectiveness in different regions of the model

efficient. It is proposed that this is due to the local acceleration of the flow under, and around, the emerging jet. Clearly the jet does not reach the target surface, as the effectiveness does not reach unity here; this is thought to be due to the much higher cross flow induced in the long channel, compared to conventional impingement cooling configurations.

While the target surface conventionally is the only surface contributing to blade cooling, in the case of a cast passage of small aspect ratio, heat transfer on the holed impingement surface is also a major contributor to the overall heat transfer, and data on this surface are shown in Fig. 7. The same overall trend in the data is observed, but the most noticeable features are the enhancement of heat transfer coefficient and effectiveness downstream of each of the impingement holes. As previously observed ([18]), the impinging jets act as pedestals in the cross flow, while flow stripped from the edge of the jet causes the local sharp variation in effectiveness at the same position.

Figure 8 shows the method of solution used in different regions of the channel. Near to the entrance of the channel, the cross flow dominates, the effectiveness is low and the transition times from the heat transfer test is used in conjunction with effectiveness test B (cross flow heated) to determine the heat transfer parameters; far downstream effectiveness A (impingement flow heated) is used. Over a limited region in the center of the channel, results are available both from tests A and B. Fortunately, here the same heat transfer coefficient and effectiveness were found using either of the transition times. Indicating that the effect of changing momentum ratio between the 3 tests introduced negligible error as further discussed in the forthcoming.

Effect of Changes in the Momentum Ratio on the Observed Heat Transfer

Using a single species of gas for both the coolant flows, it is not possible to match the passage Reynolds number along with both momentum and mass flux ratios in all of the experiments performed using the 3-test strategy. Alternately, changing the temperature of the gas streams effects the flow density. In the current series of tests the passage Reynolds number was fixed. This approximately fixed the mass flux ratio, as Reynolds number is a weak function of temperature between 290 and 350 K.

$$\mathrm{Re}=\frac{\rho V d}{\mu}=\frac{4\dot{m}}{\pi d\mu}\approx \mathrm{const}\times\dot{m} \tag{18}$$

If the mass flux ratio and Reynolds number are maintained the effect is to cause a variation in the momentum flux ratio of up to 10%. While this could be overcome by the use of foreign gas injection, but this is undesirable as it would introduce additional experimental and analytical complexity. If a single fluid is used the momentum of each stream varies with the driving gas temperature.

$$\mathrm{Momemtum}=\rho V^2=\frac{1}{\rho}\left(\frac{\mu\,\mathrm{Re}}{d}\right)^2=\frac{\mu\,\mathrm{Re}}{d}\frac{RT}{p}=\mathrm{const}\times\mu T \tag{19}$$

The variation of momentum ratio introduced may be estimated for typical test conditions, as set out in Table 1.

It should be noted that if similar flow temperatures are used when carrying out the heat transfer coefficient test, the momentum ratio is correctly matched in this case. The error introduced into the measurement of the heat transfer coefficient is therefore minimal. In fact, where the regions of crystal transition during effectiveness tests A and B overlap (effectiveness=0.4–0.6) it is possible to assess the variation in the measured effectiveness. Typical variations of 4.7% were found and the maximum variation in effectiveness measured was 8.7%. This insensitivity of the impingement systems to variations in momentum ratio has previously been observed by other workers (Florschuetz et al. [28], etc.) who were able to make robust correlations of Nusselt number as a function of jet Reynolds number and the local jet to crossflow mass flux ratio.

Estimation of Experimental Error

An estimation of the experimental uncertainties associated with the 3-test technique has been made using the method of small perturbations described by (Moffat [29]). Calculations were performed to gage the effect of uncertainties in experimental parameters at test conditions typical to those found in the impingement channel. The effect of each type of measuring error is considered in isolation. It should however be noted that temperature errors are usually associated with a variation in the A/D board offset temperature, and driving temperature differences will on the whole remain error free. A typical experimental error has been estimated by considering the RMS sum of the component errors. The worst-case error is calculated as the sum of the component errors.

These errors are compared to the level expected if the same experiments had been performed using a single test, 2-crystal test technique [22]. The error analysis was performed using theoretical data for a typical heat transfer coefficient of 85 $\mathrm{Wm^{-2}K^{-1}}$ and an effectiveness of 0.5. A start temperature of 20°C was used for both cases in the comparison. A liquid crystal temperature of 33°C was

Table 1 Variation of impinging flow to cross flow momentum ratio when the mass flow ratio remains constant and the impingement and cross flow streams are independently heated

Test	Gas A	Gas B	Momentum ratio
Cold running	293	293	1
Gas A heated	323	293	1.08
Gas B heated	293	323	0.922
HTC test	323	323	1

Downloaded 31 May 2010 to 171.66.16.27. Redistribution subject to ASME license or copyright; see http://www.asme.org/terms/Terms_Use.cfm

Table 2 Contributors to uncertainties in heat transfer coefficient and effectiveness

Test Condition	Typical value	Typical error	3-test strategy htc error	3-test strategy Effectiveness error	2-crystal technique htc error	2-crystal technique Effectiveness error
Start temperature T_0, °C	20	0.5	5.88%	15.4%	6.53%	6.00%
Crystal temperature $T_{crystals}$, °C	33	0.3	4.03%	2.09%	10.15%	27.5%
Gas temperature T_{gas}, °C	50	0.5	1.47%	4.5%	2.15%	11.65%
Transition time t (s)	10	0.04	0.59%	2.5%	1.47%	3.75%
Perspex properties ($\sqrt{\rho ck}$)	569	29	5.00%	0%	5.88%	1.50%
RMS error			8.85%	16.37%	13.68%	30.73%
Maximum error			16.97%	24.49%	26.18%	50.40%

used during the error analysis for the 3-test technique, while typical liquid crystal temperatures of 30 and 35°C were used when assessing the single test strategy. Table 2 details the results. It is apparent from this error analysis that the 3-test technique offers much greater accuracy. It should be noted that experimenters using the single test strategy obtain much higher accuracy than the table suggests, because many of the errors occur in common mode and do not effect the overall accuracy. Also, the results of many experiments suggest that the uncertainty in the material properties of perspex, are much lower than that which can be quoted.

Summary and Conclusions

A technique has been developed to process transient heat transfer experiments where the heat transfer coefficient and local adiabatic wall temperature are unknown, and the adiabatic wall temperature lies between the temperatures of two incoming gas streams. The method of solution is more robust compared to traditional single test techniques as it largely uncouples the determination of heat transfer coefficient and effectiveness. Furthermore, regions of high and low effectiveness are determined from separate subsidiary tests. The authors have found that disadvantage of additional testing is far outweighed by the improved conditioning of the heat transfer problem, which allows highly automated data reduction. High quality data are produced in areas of both low and high effectiveness with uncertainties on a par with the best existing test strategies. An application of the technique to an impingement channel geometry produced effectiveness and heat transfer measurement of a much higher quality than could be attained using traditional techniques.

Acknowledgments

This work has been carried out with the support of Rolls-Royce plc., QinetiQ, DTI CARAD and MOD ARP26c, the continuance of which is greatly appreciated by the authors. The experimental apparatus was manufactured by Mr. Pat Timms.

Nomenclature

c = specific heat capacity, $JK^{-1}kg^{-1}$
c_p = specific heat capacity, $JK^{-1}kg^{-1}$
d = hole diameter, m
DGT = driving gas temperature, K
h, htc = heat transfer coefficient, $Wm^{-2}K^{-1}$
k = conductivity, $Wm^{-1}K^{-1}$
L = channel length, m
$\dot{m}$ = mass flow, $kg\,s^{-1}$
p = pressure, Pa
R = gas constant, $JK^{-1}kg^{-1}$
Re = Reynolds no.
t = time, s
T = temperature, K
V = velocity, ms^{-1}
x,y = distance, m
ε = effectiveness
ρ = density, $kg\,m^{-3}$
μ = viscosity, $Nm^2\,s^{-1}$

Subscripts

A = impingement test
B = cross flow test
cross = cross flow gas stream
gas = mixed bulk gas temperature
h = heat transfer coefficient test
i,k = sample
imp = impingement gas stream
jet = impinging jet
o = Initial condition
surface = surface

References

[1] Ireland, P. T., Neely, A. J., Gillespie, D. R. H., and Robertson, A. J., 1999, "Turbulent Heat Transfer Measurements Using Liquid Crystals," Int. J. Heat Fluid Flow, **20**, pp. 355–367.
[2] Gillespie, D. R. H., 1996, "Intricate Internal Cooling Systems for Gas Turbine Blading," D. Phil thesis, Oxford University Department of Engineering Science.
[3] den Ouden, C., and Hoogendoorn, C. J., 1974, "Local Convective Heat Transfer Coefficients for Jets Impinging on a Plate: Experiments Using a Liquid Crystal Technique," Proc. 5th Heat Transfer Conference, Vol. 5, New York, pp. 293–295.
[4] Lucas, M. G., Ireland, P. T., Wang, Z., and Jones, T. V., 1993, "Fundamental Studies of Impingement Cooling Thermal Boundary Conditions," AGARD CP-527, Paper No. 14.
[5] Sargison, J., E., Guo, S. M., Oldfield, M., L., G., Lock, G., D., and Rawlinson, A., J., 2001, "A Converging Slot-Hole Film-Cooling Geometry Part 1: Low-Speed Flat-Plate Heat Transfer and Loss," ASME Paper 2001-GT-0126.
[6] Ireland, P. T., and Jones, T. V., 1986, "Detailed Measurements of Heat Transfer on and Around a Pedestal in Fully-Developed Channel Flow," Proc., 8th Int. Heat Trans. Conf., San Francisco, pp. 975–986.
[7] Chyu, M. K., Ding, H., Downs, J. P., van Sutendael, A., and Soechting, F. S., 1997, "Determination of Local Heat Transfer Coefficient Based on Bulk Mean Temperature Using a Transient Liquid Crystals Technique," ASME Paper 97-GT-489.
[8] Wang, Z., Ireland, P. T., and Jones, T. V., 1995, "An Advanced Method of Processing Liquid-Crystal Video Signals from Transient Heat Transfer Experiments," ASME J. Turbomach., **117**(1), pp. 184–189.
[9] Gillespie, D. R. H., Ireland, P. T., and Dailey, G. M., 2000, "Detailed Flow and Heat Transfer Coefficient Measurements in a Model of an Internal Cooling Geometry Employing Orthogonal Intersecting Channels," ASME 2000-GT-653.
[10] Farina, D. J., and Moffat, R. J., 1994, "A System for Making Temperature Measurements Using Thermochromic Liquid Crystals," Stanford University, Department of Engineering, Report No. HMT-48.
[11] Guo, S. M., Lai, C. C., Jones, T. V., Oldfield, M. L. G., Lock, G. D., and Rawlinson, A. J., 2000, "Influence of Surface Roughness on Heat Transfer and Effectiveness for a Fully Film Cooled Nozzle Guide Vane Measured by Wide Band Liquid Crystals and Direct Heat Flux Gauges," ASME Paper 2000-GT-0204.
[12] Baughn, J. W., Mayhew, J. E., Anderson, M. R., and Butler, R. J., 1998, "A Periodic Transient Method Using Liquid Crystals for the Measurement of Local Heat Transfer Coefficients," ASME J. Heat Transfer, **120**, pp. 772–775.
[13] Turnbull, and Oosthuizen (1999), "Theoretical Evaluation of New Phase Delay Methods for Measuring Local Heat Transfer Coefficients," Trans Canadian Society Mechanical Engineering, Vol. 23, Issues 3–4, pp. 361–376.
[14] Butler, R. J., and Baughn, J. W., 1996, "The Effect of the Thermal Boundary Condition on Transient Method Heat Transfer Measurements on a Flat Plate With a Laminar Boundary Layer," ASME J. Heat Transfer, **118**, pp. 831–837.
[15] Tsang, C. L., Ireland, P. T., and Dailey, G. M., 2001, "Reduced Instrumentation Heat Transfer Testing of Model Turbine Blade Cooling Systems," Paper

Downloaded 31 May 2010 to 171.66.16.27. Redistribution subject to ASME license or copyright; see http://www.asme.org/terms/Terms_Use.cfm

16, RTA/AVT Symposium on Advanced Flow Management, Norway, May 7–11.
[16] von Wolfersdorf, J., Hoecker, R., and Hirsch, C., 1997, ''Data Reduction Procedure for Transient Heat Transfer Measurements in Long Internal Cooling Channels,'' 2nd Int. Symp. Turbulence, Heat and Mass Transfer.
[17] Van Treuren, K. W., Wang, Z., Ireland, P. T., and Jones, T. V., 1994, ''Detailed Measurements of Local Heat Transfer Coefficient and Adiabatic Wall Temperature Beneath an Array of Impinging Jets,'' ASME J. Turbomach., **116**, pp. 369–374.
[18] Son, C., Gillespie, D., Ireland, P., and Dailey, G. M., 2001, ''Heat Transfer and Flow Characteristics of an Engine Representative Impingement Cooling System,'' ASME J. Turbomach., **123**, pp. 154–160.
[19] Cho, H. H., Lee, C. H., and Kim, Y. S., 1998, ''Characteristics of Heat Transfer in Impinging Jets by Control of Vortex Pairing,'' ASME 98-GT-276.
[20] Florschuetz, L. W., and Su, C. C., 1987, ''Effects of Cross Flow Temperature on Heat Transfer Within an Array of Impinging Jets,'' ASME J. Heat Transfer, **109**, pp. 74–82.
[21] Goldstein, R. J., Sobolik, K. A., and Seoal, W. S., 1990, ''Effect of Entrainment on the Heat Transfer to a Heated Circular Air Jet Impinging on a Flat Surface,'' ASME J. Heat Transfer, **112**, pp. 608–611.
[22] Ireland, P. T., and Jones, T. V., 1987, ''Note on the Double Crystal Method of Measuring Heat Transfer Coefficient,'' OUEL Report 1710/87.
[23] Ling, J., and Ireland, P. T., ''Film Cooling Research For DLE Combustor Discharge Nozzles,'' OUEL Report 2244/01 (restricted).
[24] Camci, C., Kim, K., and Hippensteele, S. A., 1991, ''A New Hue Capturing Technique for the Quantitative Interpretation of Liquid Crystal Images Used in Convective Heat Transfer,'' ASME Paper 91-GT-122.
[25] Van Treuren, K. V., 1994, ''Impingement Flow Heat Transfer Measurement of Turbine Blades Using a Jet Array,'' D. Phil thesis, University of Oxford.
[26] Vedula, R. J., and Metzger, D. E., 1991, ''A Method for Simultaneous Determination of Local Effectiveness and Heat Transfer Distribution of Local Effectiveness and Heat Transfer Distributions in Three-Temperature Convection Situations,'' ASME 91-GT-345.
[27] Carslaw, H. S., and Jaeger, J. C., 1953, *Conduction of Heat in Solids*, OUP.
[28] Florschuetz, L. W., Metzger, D. E., and Truman, C. R., 1981, ''Jet Array Impingement with Crossflow Correlation of Streamwise Resolved Flow and Heat Transfer Distributions,'' NASA Contractor Report 3373.
[29] Moffat, R. J., 1982, ''Contributions to the Theory of Single Sample Uncertainty Analysis,'' ASME J. Fluids Eng., **104**, p. 250.

Downloaded 31 May 2010 to 171.66.16.27. Redistribution subject to ASME license or copyright; see http://www.asme.org/terms/Terms_Use.cfm

Effect of Internal Coolant Crossflow on the Effectiveness of Shaped Film-Cooling Holes

Michael Gritsch[1]
Achmed Schulz
Sigmar Wittig

Institut für Thermische Strömungsmaschinen,
Universität Karlsruhe (TH),
76128 Karlsruhe, Germany

Film-cooling was the subject of numerous studies during the past decades. However, the effect of flow conditions on the entry side of the film-cooling hole on film-cooling performance has surprisingly not received much attention. A stagnant plenum which is widely used in experimental and numerical studies to feed the holes is not necessarily a right means to re-present real engine conditions. For this reason, the present paper reports on an experimental study investigating the effect of a coolant crossflow feeding the holes that is oriented perpendicular to the hot gas flow direction to model a flow situation that is, for instance, of common use in modern turbine blades' cooling schemes. A comprehensive set of experiments was performed to evaluate the effect of perpendicular coolant supply direction on film-cooling effectiveness over a wide range of blowing ratios ($M=0.5 \ldots 2.0$) and coolant crossflow Mach numbers ($Ma_c=0 \ldots 0.6$). The coolant-to-hot gas density ratio, however, was kept constant at 1.85 which can be assumed to be representative for typical gas turbine applications. Three different hole geometries, including a cylindrical hole as well as two holes with expanded exits, were considered. Particularly, two-dimensional distributions of local film-cooling effectiveness acquired by means of an infrared camera system were used to give detailed insight into the governing flow phenomena. The results of the present investigation show that there is a profound effect of how the coolant is supplied to the hole on the film-cooling performance in the near hole region. Therefore, crossflow at the hole entry side has be taken into account when modeling film-cooling schemes of turbine bladings. [DOI: 10.1115/1.1580523]

Introduction

The continual increase of turbine inlet temperature requires the use of highly effective cooling schemes to keep thermal loads of turbine components at acceptable levels. The metal temperature of turbine airfoils can be reduced by means of film cooling where relatively cold compressor bleed air is injected through discrete holes in the airfoil's surface to build a protective film on the surface downstream of the ejection location.

Recently, film-cooling holes with expanded exits have received increasing attention since they are known to offer some advantages over standard cylindrical holes. Goldstein et al. [1] showed that cooling jets being ejected from laterally expanded holes provide a better lateral coverage of the surface and, therefore, increase film-cooling performance. Additionally, the jet-main flow interaction is reduced which results in lower heat transfer coefficients (Makki and Jakubowski [2]). The through-flow behavior of the hole which can be quantified by means of a discharge coefficient is profoundly altered as compared to cylindrical holes (Hay and Lampard [3], Gritsch et al. [4]).

In a previous study, Gritsch et al. [5,6] investigated the film-cooling effectiveness and the heat transfer coefficients downstream of a cylindrical, a laterally expanded, and a laterally forward expanded film-cooling hole. They found that both expanded holes offer significantly improved thermal protection of the blade surface as compared to the cylindrical hole. The laterally forward expanded hole, however, provides better lateral coverage at high blowing ratios than the laterally expanded hole. These findings were supported by flow field measurements of Thole et al. [7] who showed that for both expanded holes jet penetration as well as velocity gradients in the mixing region are significantly reduced.

Thus far, the effect of internal coolant supply crossflow on the cooling performance of the ejected jet has not been studied in detail. Most investigations were performed using a plenum feeding the film-cooling holes. However, a plenum is not necessarily a correct means of representing the internal coolant passage of an airfoil since high crossflow velocities can occur in the coolant supply channel. Additionally, the crossflow direction with respect to the main flow has to be taken into account. For modern multipass turbine blade cooling schemes, the coolant supply flow (radial flow direction) is typically directed perpendicular to the main flow (axial flow direction).

Discharge coefficient measurements performed by Hay et al. [8] and Gritsch et al. [9] showed that the throughflow characteristic of the hole is significantly altered when the coolant approach is perpendicular to the mainflow. Particularly, additional losses occur at the entrance of the film-cooling hole due to a strong turn of the flow entering the hole. Thole et al. [10] pointed out that coolant supply crossflow alters the flowfield inside a film-cooling hole substantially and, therefore, affects the film-cooling effectiveness distribution downstream of the ejection location, particularly for holes with expanded exits (Kohli and Thole [11,12]).

It is obvious from the literature that the effect of the coolant supply crossflow on the film-cooling effectiveness has not received much attention up to now. Therefore, the present investigation focuses on the effect of a coolant crossflow oriented perpendicular to the hot gas flow direction. Two-dimensional distributions of the film-cooling effectiveness in the near field of film-cooling holes with and without exit expansions are used for evaluation including a broad variation of the blowing ratio as well as the Mach number in the coolant supply passage in order to cover a wide range typical for real engine film-cooling applications.

[1]Present address: ALSTOM (Switzerland) Ltd, Gas Turbine Technology, 5405 Baden-Dattwil, Switzerland, e-mail: michael.gritsch@power.alstom.com

Contributed by the International Gas Turbine Institute and presented at the 33rd National Heat Transfer Conference, Albuquerque, NM, August 15–17, 1999. Manuscript received by the IGTI 1999; revised manuscript received March 4, 2003. Paper No. NHTC99-8. Associate Editor: R. Bunker.

 Copyright © 2003 by ASME

Downloaded 31 May 2010 to 171.66.16.27. Redistribution subject to ASME license or copyright; see http://www.asme.org/terms/Terms_Use.cfm

Table 1 Operating conditions of the film-cooling test rig

Internal temperature	T_{tc}	290 K
Blowing ratio	M	0.5 . . . 2
Temperature ratio	T_{tc}/T_{tm}	0.54
Internal Mach number	Ma_c	0, 0.3, 0.6
External Mach number	Ma_m	0.3
Internal Reynolds number	Re_{Dc}	up to $2.5 \cdot 10^5$
External Reynolds number	Re_{Dm}	$0.3 \cdot 10^5$
Boundary layer thickness	δ_{99}/D	0.5
External turbulence level	Tu_m	<2%
Internal turbulence level	Tu_c	1%

Experimental Apparatus and Measuring Technique

The present investigation was carried out in a continous flow wind tunnel supplied by a high-pressure, high-temperature (HPHT) test facility. The coolant-to-hot gas temperature ratio was 0.54 and kept constant for all test cases which can be assumed to be representative for typical gas turbine applications. The operating conditions are shown in Table 1. Further details of the test rig design and commisioning were given by Wittig et al. [13]. The film-cooling test rig consists of a primary loop representing the external hot gas flow and a secondary loop representing the internal coolant supply flow of an airfoil (Fig. 1).

Primary and Secondary Loop. Air is delivered to both loops by the compressor of the HPHT facility. Prior to being supplied to the primary loop the temperature of the air is raised by a heat exchanger to about 540 K. Hereafter the air passes a metering orifice and flow straigteners before entering the test section through a Laval nozzle. The mass flow rate and Mach number Ma_m in the primary loop are controlled by a valve upstream of the metering orifice. Flow for the secondary loop is also provided by the HPHT test facility. The coolant passes a metering orifice as well before it is delivered to the closed secondary loop. Under steady-state conditions, this mass flow rate entering the secondary loop is identical to the coolant mass flow rate ejected through the film cooling hole. In fact, it serves as a ''substitute'' for the film cooling hole bleed. The flow in the secondary loop is driven by an additional blower which is in charge of controlling the internal Mach number Ma_c.

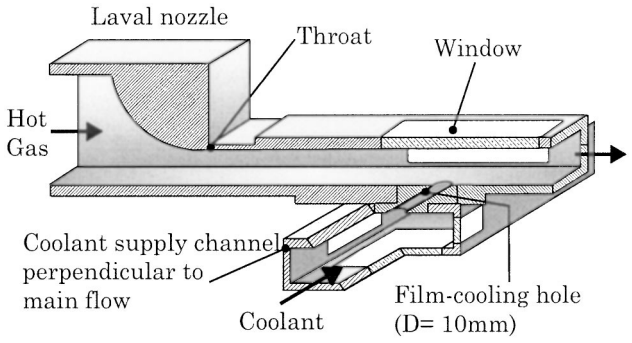

Fig. 1 Film-cooling test section

This specific setup has two main advantages. First, it allows to individually control the pressure—which determines the amount of coolant being ejected through the film-cooling hole and, hence, the blowing ratio M—and the Mach number Ma_c in the secondary loop. Therefore, all quantities that define a particular operating condition—Ma_m, Ma_c, and M can be set independently of each other. And second, the hole flow rate is obtained directly for all flow cases, independently of the crossflow rates. Very accurate measurements of the flow rate through the film-cooling hole were achieved [13] despite the fact that the film hole flow is in the range of only 1 . . . 9% of the internal crossflow rate.

The test section of the primary loop is 90 mm in width and 41 mm in height. The cross-sectional area of the secondary loop at the film-cooling hole location is 60 mm in width and 20 mm in height.

Previous investigations [5] have shown that—in particular for shaped holes—the impact of the external crossflow on film-cooling performance is much smaller than of the internal crossflow. Therefore, it was chosen to keep the external Mach number at $Ma_m = 0.3$ for all tests carried out during this study and to focus on the effect of internal crossflow on film-cooling performance.

For the present investigation, the orientation of the coolant supply passage with respect to the mainflow direction was set to be perpendicular to the external hot gas flow direction ($\beta = 90°$) in $+z$ direction. The present study is unique since it is the first time that the effect of a perpendicular coolant crossflow supply on film-cooling performance is investigated experimentally, for both cylindrical and shaped film-cooling holes. Three crossflow Mach numbers $Ma_c = 0$, 0.3, and 0.6 were considered providing a wide coverage of typical engine situations. Effectiveness distributions measured at plenum condition ($Ma_c = 0$) serve as a base for comparison and were taken from [5]. Note that $Ma_c = 0$ indicates that the blower in the secondary loop is turned off. In this case, the secondary loop acts as a plenum.

Film-Cooling Hole Geometries. All tests were carried out using single, scaled-up film-cooling holes with an inclination angle of $\alpha = 30$ deg. All holes were sharp edged and the interior surfaces were aerodynamically smooth. In total, three hole geometries (a cylindrical hole and two holes with an expanded exit portion) were tested (Fig. 2). The diameter of the cylindrical hole and the diameter of the cylindrical inlet section of the expanded holes was 10 mm. The length-to-diameter ratio L/D was 6 for all hole geometries. The lateral expansion angle of both expanded holes was 14 deg, resulting in a hole width of 30 mm at the hole exit. The forward expansion angle of the laid-back fan-shaped hole was 15 deg, resulting in a hole length of 40 mm at the hole

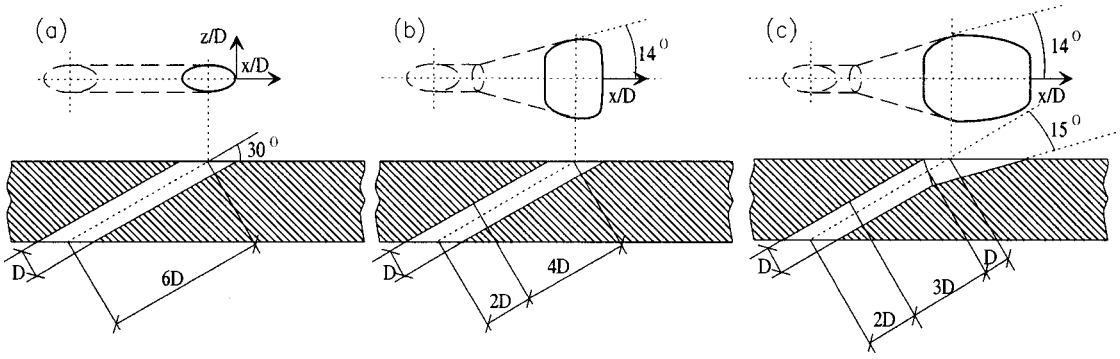

Fig. 2 (*a*) Cylindrical, (*b*) fan-shaped, and (*c*) laid-back fan-shaped film-cooling hole geometries

Downloaded 31 May 2010 to 171.66.16.27. Redistribution subject to ASME license or copyright; see http://www.asme.org/terms/Terms_Use.cfm

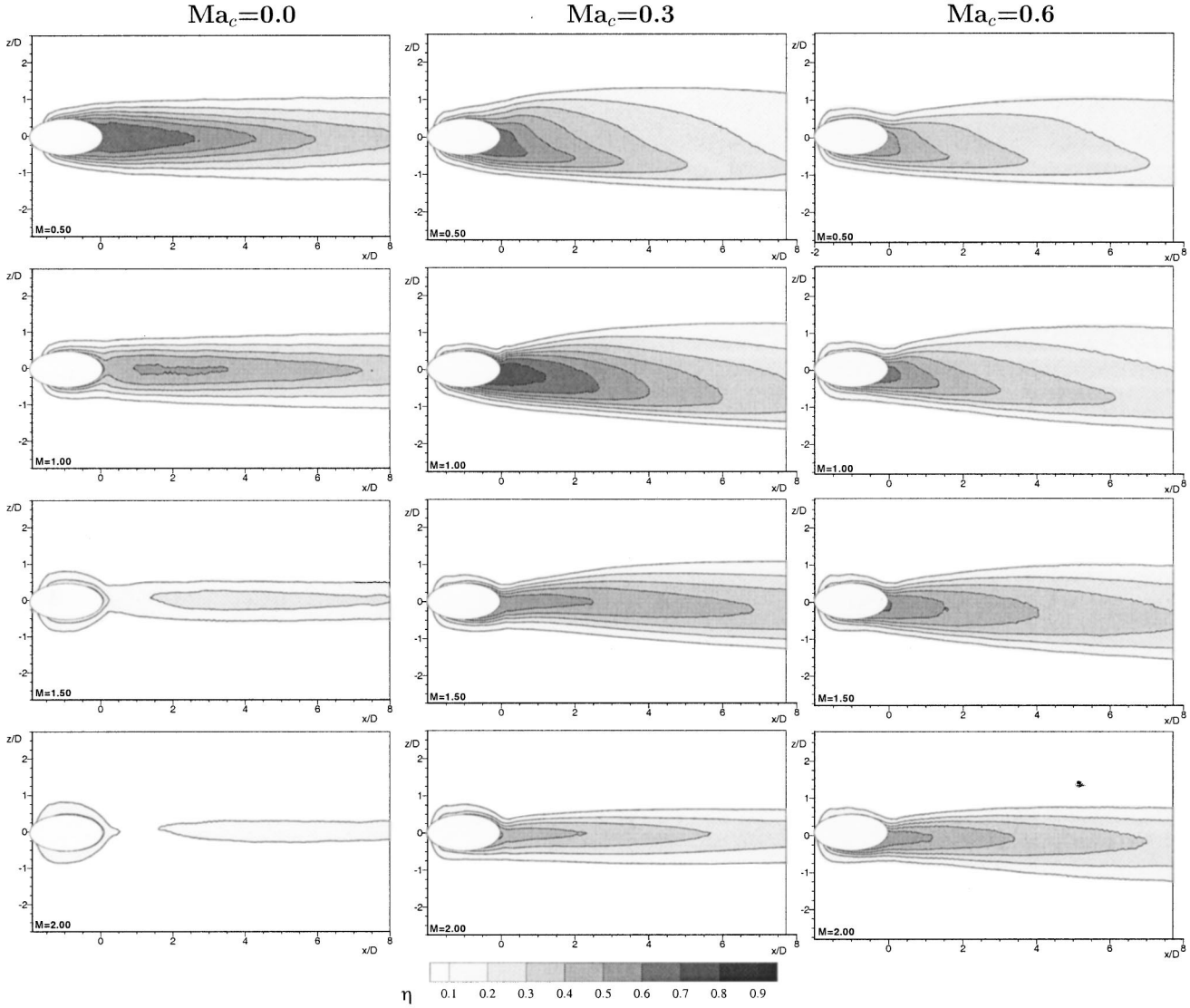

Fig. 3 Effect of internal coolant crossflow Mach number Ma$_c$ on the local film-cooling effectiveness distribution for the cylindrical hole

exit. The exit-to-entry area ratio of the fan-shaped and laid-back fan-shaped hole were 3.0 and 3.1, respectively (areas perpendicular to hole axis).

For both shaped holes, the calculation of the blowing ratio was based on the inlet cross-sectional area. Thus, the blowing ratio of the shaped holes can be directly compared to those of the cylindrical hole. This makes it convenient to evaluate the effect of hole geometry. In case of identical hot gas flow conditions same blowing ratio is synonymous with same amount of coolant ejected.

Adiabatic Wall Temperature Measurements. The test plate used for measuring adiabatic wall temperatures consisted of a semicrystalline high performance thermoplastic material (Tecapek) with a thermal conductivity of 0.2 W/mK and a maximum operating temperature of about 570 K. Surface temperatures were measured by means of a AGEMA 870 IR camera system which provided two-dimensional temperature distribution on the plate surface acquired through a sapphire window in the top wall of the mainflow channel. The image of the test plate surface was digitized into an array of 140×140 pixels with a spatial resolution of 0.8 mm×0.8 mm per pixel. The test plate surface was covered by black paint of a well-known emissivity of 0.95. The local film-cooling effectiveness was based on local wall temperatures, coolant supply total temperature $T_{t,c}$ (measured close to the inlet of the film-cooling hole), and the mainflow recovery temperature $T_{\mathrm{rec},m}$ as a reference temperature (measured upstream of the hole in a region not affected by the coolant ejection).

Fifteen thermocouples distributed on the plate surface were used for an in-situ calibration of the IR camera system in order to increase the accuracy of the temperature measurements (Martiny et al. [14]). The maximum deviation of the temperatures measured by means of the IR camera system from the temperatures of the surface thermocouples was less than 1.5 K. Other contributions to uncertainty were due to variations in blowing ratio (δM=2%), internal and external Mach number ($\delta\mathrm{Ma}_c=2\%$, $\delta\mathrm{Ma}_m=2.5\%$), and coolant to main flow temperature ratio ($\delta(T_c/T_m)=1.5\%$). Combining these uncertainties results in an average uncertainty of 2.5% in local and 2% in laterally and spatially averaged film-cooling effectiveness. The maximum uncertainty was calculated to be 8.5%.

Results and Discussion

Local Effectiveness Distribution. Figure 3 shows the local film-cooling effectiveness distributions for the cylindrical hole. It is obvious that for the case of perpendicular internal crossflow

Downloaded 31 May 2010 to 171.66.16.27. Redistribution subject to ASME license or copyright; see http://www.asme.org/terms/Terms_Use.cfm

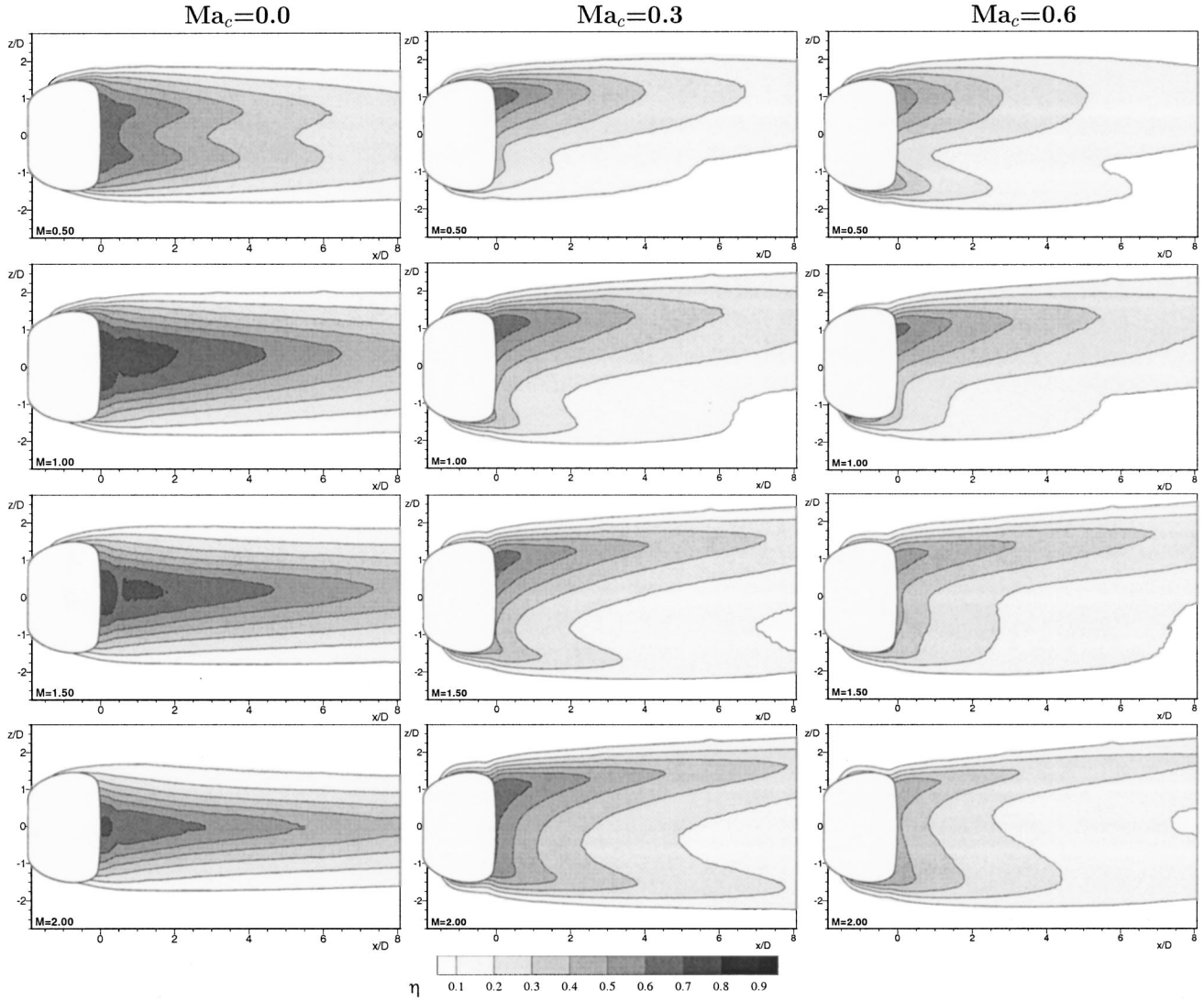

Fig. 4 Effect of internal coolant crossflow Mach number Ma$_c$ on the local film-cooling effectiveness distribution for the fan-shaped hole

($Ma_c = 0.3$ and 0.6) the coolant distribution on the surface downstream of the ejection location is not symmetric as it is for the plenum case but skewed in $-z$ direction, particularly at low blowing ratios. At low blowing ratios the lateral spreading as compared to the plenum case is increased while the effectiveness is reduced in the centerline portion.

At elevated blowing ratios the jet ejected at plenum condition is known to detach from the surface resulting in a rapid decrease of effectiveness. For both coolant crossflow cases ($Ma_c = 0.3$ and 0.6) local effectiveness decreases monotonously with streamwise distance indicating that even at highest blowing ratios no total jet detachment is present. Therefore, the performance of the cylindrical hole at high blowing ratios for the crossflow cases is improved as compared to the plenum case. This behavior is similar to what is found for compound angled cylindrical holes (e.g., Schmidt et al. [15]) where delayed jet detachment is observed at elevated blowing ratios as compared to hole ejecting in streamwise direction.

For the fan-shaped hole, the coolant distribution for both crossflow cases is even more skewed as compared to the cylindrical hole (Fig. 4). The lateral spreading of the jet is slightly increased as compared to the plenum case while the effectiveness in the centerline portion is profoundly decreased. Most of the coolant leaves the hole on the downstream $(+z)$ side of the hole. For some flow cases a second peak of the local effectiveness occurs on the upstream side $(-z)$ of the hole.

For the laid-back fan-shaped hole (Fig. 5), the behavior is very similar to the fan-shaped hole. However, for most flow cases considered the maximum local effectiveness occurs on the upstream side $(-z)$ of the hole. Only for the $Ma_c = 0.6$ case at very low blowing ratios the maximum is found on the downstream side of the hole. The slightly skewed distribution for plenum condition at a blowing ratio of $M = 0.5$ was already discussed by Gritsch et al. [5].

Relative Coolant Jet Position. It can be concluded from the previous figures that the relative jet position is affected by the internal crossflow Mach number as well as the blowing ratio. In order to trace the lateral displacement of the jet ejected from the hole the position of the local effectiveness maximum at a position three diameters downstream of the hole trailing edge $(x/D = 3)$ is plotted in Fig. 6.

For the cylindrical hole, the relative position of the local effectiveness maximum depends mainly on the blowing ratio. At low blowing ratios the maximum is found at $z/D = -0.7$ moving to the centerline $(z/D = 0)$ for elevated blowing ratios. For a coolant

Downloaded 31 May 2010 to 171.66.16.27. Redistribution subject to ASME license or copyright; see http://www.asme.org/terms/Terms_Use.cfm

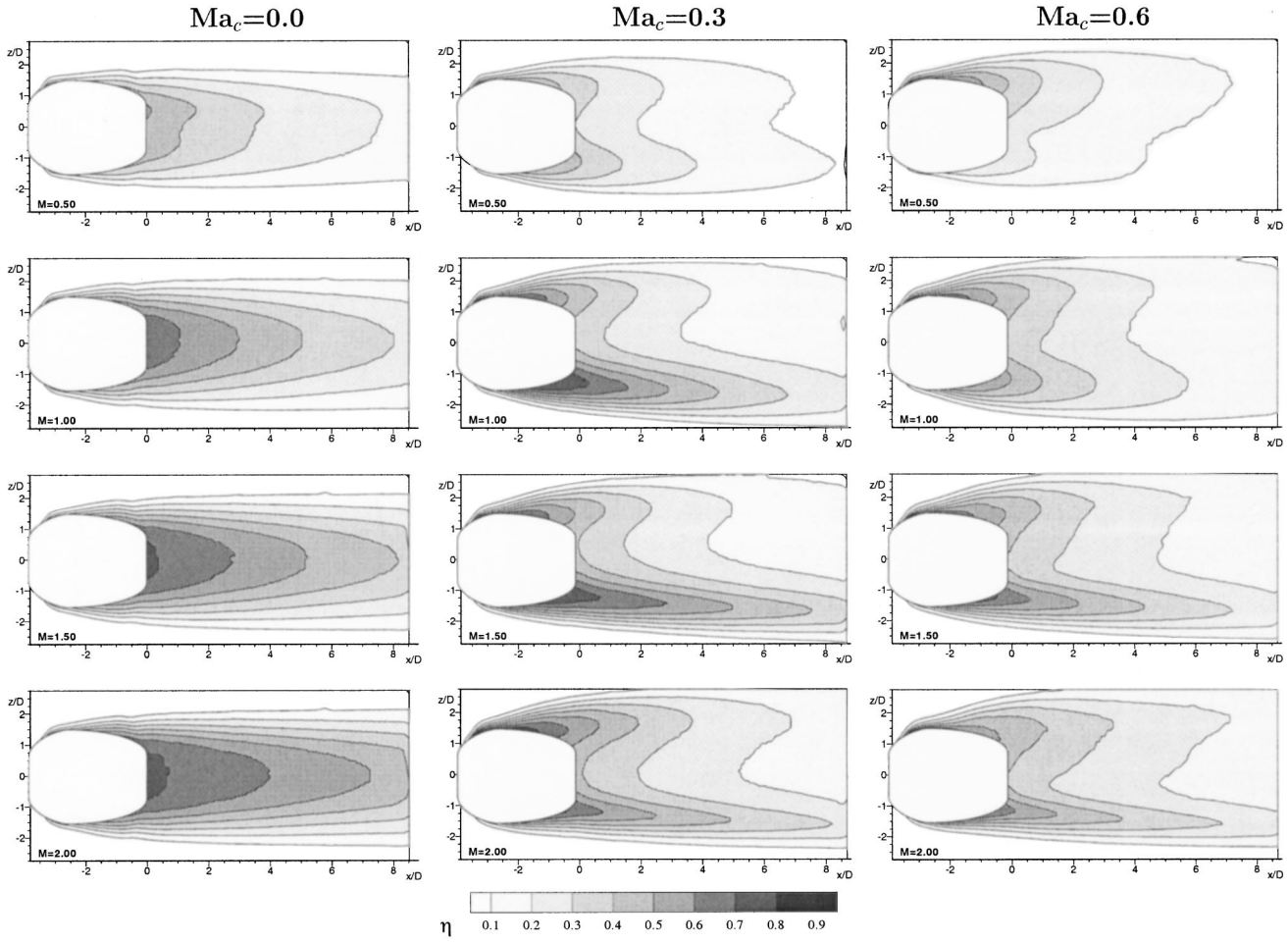

Fig. 5 Effect of internal coolant crossflow Mach number Ma$_c$ on local film-cooling effectiveness distribution for the laid-back fan-shaped hole

crossflow Mach number $Ma_c=0.6$, the position of the effectiveness maxima is in good agreement with the position for the $Ma_c=0.3$ case.

For both expanded holes, the lateral position of the effectiveness maximum is independent of the blowing ratio for a coolant crossflow Mach number $Ma_c=0.3$. For the fan-shaped hole the maximum is located on the downstream side ($z/D=+1.3$). For the laid-back fan-shaped hole, however, the maximum occurs on the upstream side of the hole ($z/D=-1.5$).

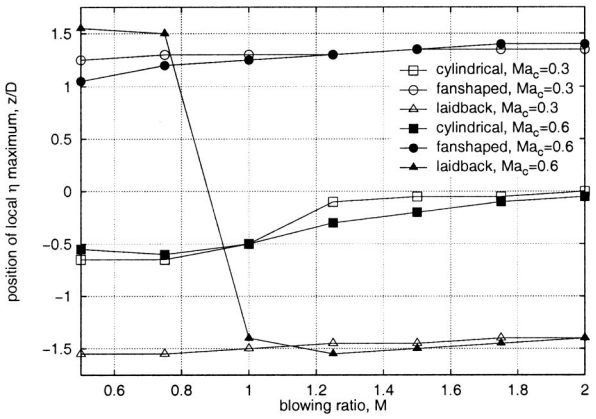

Fig. 6 Position of the local effectiveness maximum at $x/D=3$

At $Ma_c=0.6$ the position of the maximum for the fan-shaped hole slightly moves from $z/D=1$ at $M=0.5$ to $z/D=1.35$ at $M=2$. For the laid-back fan-shaped hole the position of the maximum is not located on the upstream, as it is for $Ma_c=0.3$, but on the downstream side at low blowing ratios. Increasing the blowing ratio the position of the maximum switches to the downstream side since the strength of the downstream ''leg'' decreases and of the upstream ''leg'' increases with blowing ratio. Note that for all cases investigated the relative jet position was steady, i.e. no oscillating from side to side occured. The split of the coolant jet into two ''legs'' after being ejected from the hole might be due to a breakdown of the single vortex in the diffuser portion of the hole, as discussed out by Kohli and Thole [12]. Their CFD results showed a similar coolant distribution with two separate ''legs'' occurs at the highest investigated coolant crossflow Reynolds number.

Laterally Averaged Effectiveness. To evaluate the effect of different lateral spreading of the coolant, local effectiveness will be presented laterally averaged over a pitch of $z/D=\pm 2.75$ which corresponds to the approximate maximum extent to which film coverage was observed for all cases.

For the cylindrical hole (Fig. 7), at low blowing ratios the decreased effectiveness in the centerline portion cannot be counterbalanced by the only slightly increased lateral spreading of the jet. Therefore, the laterally effectiveness for the crossflow cases is lower than for the plenum case. At elevated blowing ratios, however, jet detachment results in considerably lower effectiveness for the plenum case while for the crossflow cases the ejected jet

Downloaded 31 May 2010 to 171.66.16.27. Redistribution subject to ASME license or copyright; see http://www.asme.org/terms/Terms_Use.cfm

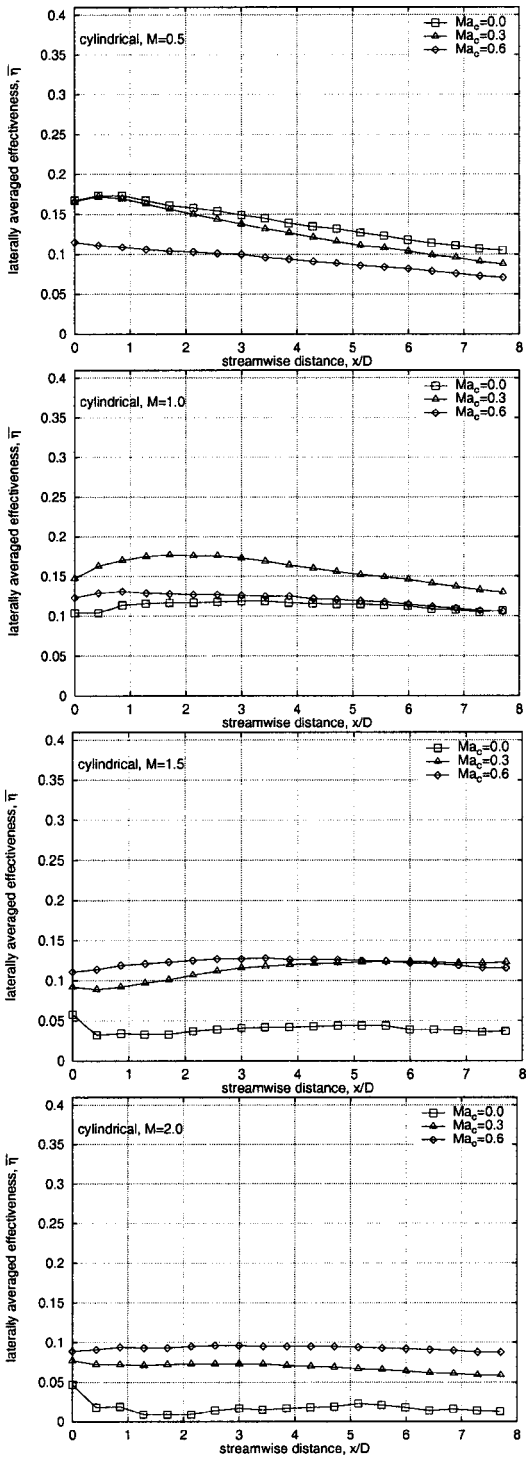

Fig. 7 Laterally averaged effectiveness for the cylindrical hole

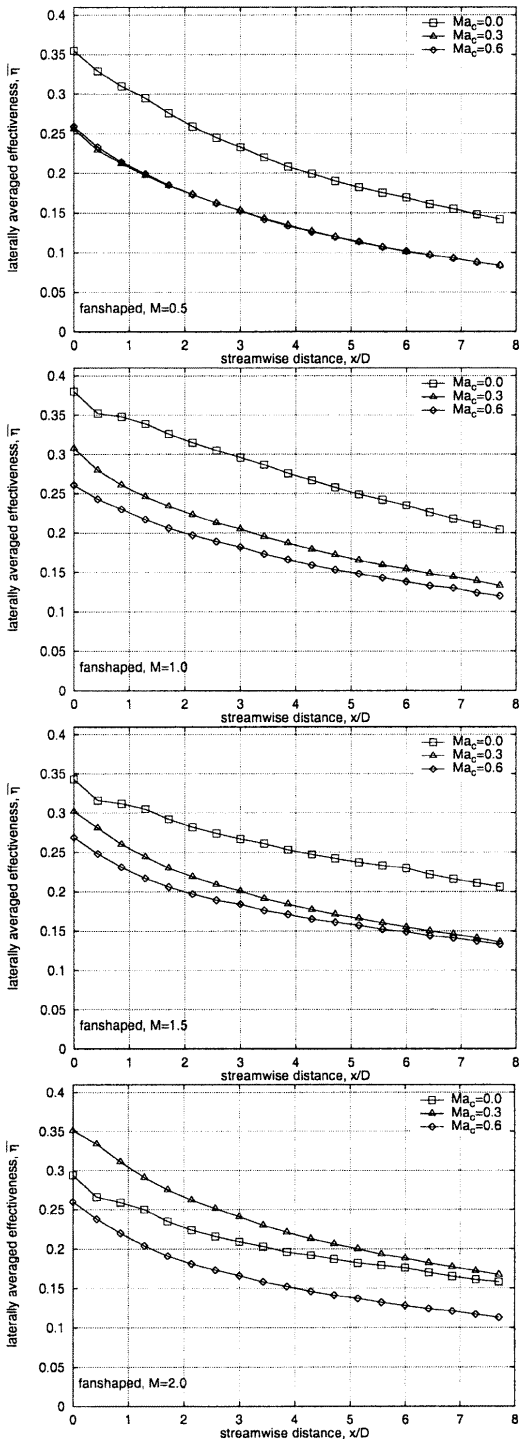

Fig. 8 Laterally averaged effectiveness for the fan-shaped hole

stays closer to the surface. Comparing the $Ma_c = 0.3$ and $Ma_c = 0.6$ cases, at low blowing ratios the laterally averaged effectiveness of the $Ma_c = 0.3$ is higher while at high blowing ratios it is higher for the $Ma_c = 0.6$ case.

For the fan-shaped hole (Fig. 8) at plenum condition, the jet detachment is not a big issue except for very high blowing ratios. Therefore, the unskewed coolant distribution for the plenum case provides higher effectiveness up to high blowing ratios. Only at a blowing ratio $M = 2.0$ the effectiveness of the $Ma_c = 0.3$ case is higher than for the plenum case.

For the laid-back fan-shaped hole (Fig. 9), the jet does not detach from the surface at all at plenum condition. Therefore, effectiveness of the plenum case is always higher than for the crossflow cases. Additionally, hot gas ingestion into the hole which reduces the cooling capability of the ejected jet seems to be an issue for the crossflow case according to a CFD study performed by Kohli and Thole [12].

Spatially Averaged Effectiveness. Spatially averaged film-cooling effectiveness was calculated by averaging local effectiveness of the surface downstream of injection location (x/D

Downloaded 31 May 2010 to 171.66.16.27. Redistribution subject to ASME license or copyright; see http://www.asme.org/terms/Terms_Use.cfm

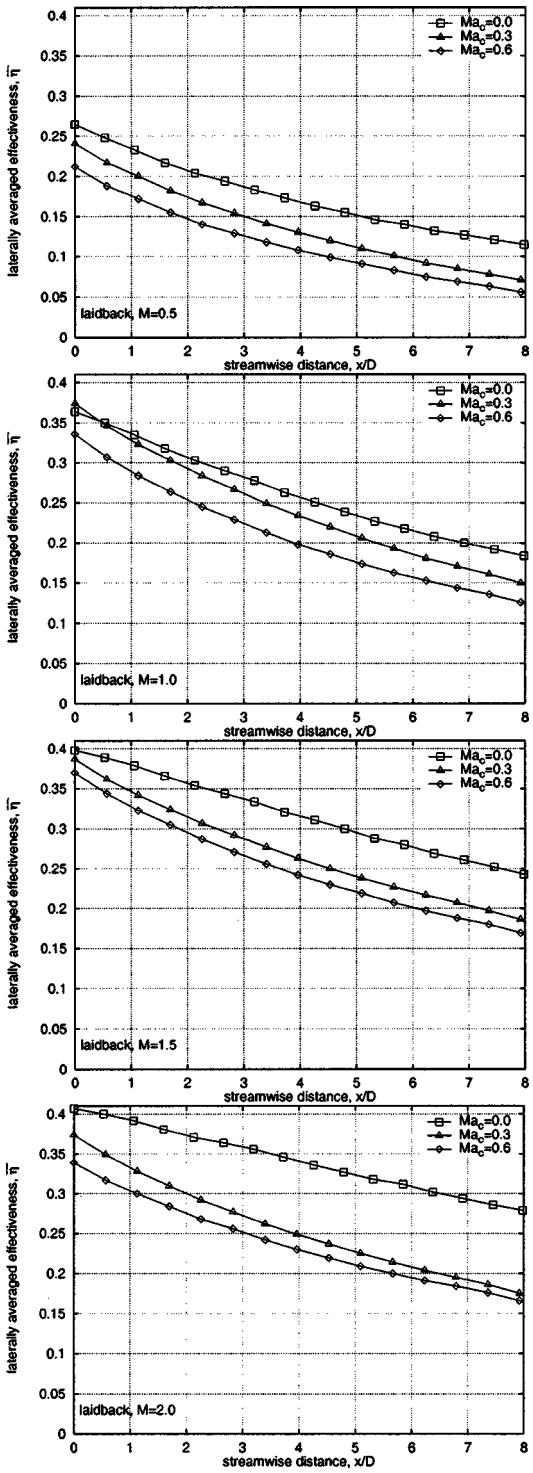

Fig. 9 Laterally averaged effectiveness for the laid-back hole

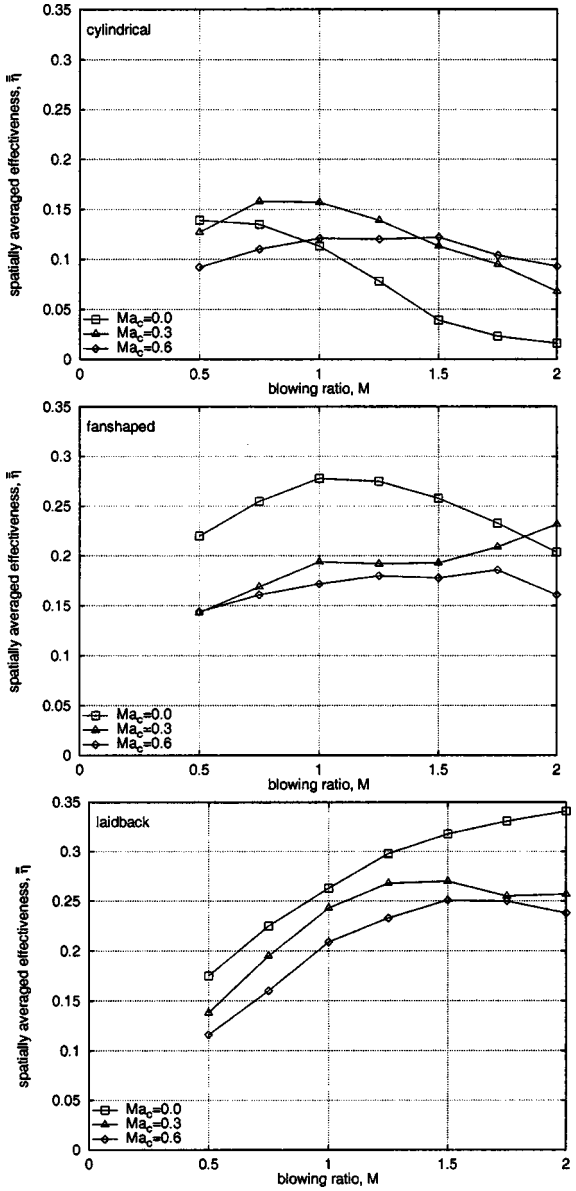

Fig. 10 Effect of the blowing ratio on the spatially averaged film-cooling effectiveness

$=0 \ldots 8$, $z/D=-2.75 \ldots 2.75$). These values were then plotted versus blowing ratio summarizing the results of the present investigation (Fig. 10).

For the cylindrical hole, three regimes were identified. At low blowing ratios ($M=0.5$) effectiveness is highest for the plenum case. Applying an internal coolant crossflow Mach number the maximum of the spatially averaged effectiveness occurs at higher blowing ratios since jet detachment is delayed with internal crossflow applied. At medium blowing ratios ($M=0.75 \ldots 1.25$) maximum effectiveness was found at $Ma_c=0.3$, while at high blowing ratios ($M \geqslant 1.5$) maximum effectiveness occurs at $Ma_c=0.6$.

For both shaped holes, the superiority of the plenum case holds for all blowing ratios considered except for the fan-shaped hole at $M=2.0$. Since jet detachment is not a major problem for the shaped holes, reduced spreading of the jets for the crossflow cases leads to lower spatially averaged film-cooling effectiveness as compared to the plenum case.

Conclusions

The present paper documents a unique study experimentally investigating the effect of a perpendicular coolant supply flow on film-cooling performance for different hole geometries. Three film-cooling hole geometries including a standard cylindrical hole and two hole with expanded exits were tested at an engine representative coolant-to-hot gas density ratio. Results showed that the film-cooling effectiveness in the near hole region can be altered

Downloaded 31 May 2010 to 171.66.16.27. Redistribution subject to ASME license or copyright; see http://www.asme.org/terms/Terms_Use.cfm

by over 100% for the crossflow cases as compared to the plenum case. Therefore, the coolant supply has to be taken into account when modeling film-cooling of a turbine blade.

The main finding of the present study is that the overall effect of an internal crossflow on film-cooling performance strongly depends on hole geometry and blowing ratio. For the cylindrical hole, film-cooling performance is improved as compared to the plenum case. Jet detachment is delayed and the jet is kept closer to the wall at elevated blowing ratios. Contrary to the cylindrical hole, film-cooling performance is reduced for both shaped holes with internal crossflow applied. The jet entering the diffuser section of the hole is highly disturbed causing a poor performance of the diffuser and leading to a less uniform cooling film.

Acknowledgment

This study was partly funded by the European Union within the Brite Euram program 'Investigation of the Aerodynamics and Cooling of Advanced Engine Turbine Components' under Contract AER2-CT92-0044.

Nomenclature

D = film-cooling hole diameter, m
L = film-cooling hole length, m
M = blowing ratio
Ma = Mach no.
Re_D = Reynolds no. based on hole diameter
T_t = total temperature, K
T_{rec} = recovery temperature, K
Tu = turbulence intensity
x = streamwise distance from downstream edge of film-cooling hole, m
z = lateral distance from centerline of film-cooling hole, m
α = angle of hole inclination, deg
β = angle of coolant supply channel orientation with respect to hot gas flow direction, deg
δ_{99} = boundary layer thickness, 99% point, m
η = local film-cooling effectiveness, $=(\mathrm{T}_{aw}-\mathrm{T}_{\mathrm{rec},m})/(\mathrm{T}_{t,c}-T_{\mathrm{rec},m})$

Subscripts

aw = adiabatic wall
c = internal flow conditions ('coolant')
m = external flow conditions ('mainflow')

Superscripts

$\bar{}$ = laterally averaged value
$\bar{\bar{}}$ = spatially averaged value

References

[1] Goldstein, R. J., Eckert, E. R. G., and Burggraf, F., 1974, "Effects of Hole Geometry and Density on Three-Dimensional Film Cooling," Int. J. Heat Mass Transfer, **17**, pp. 595–607.
[2] Makki, Y. H., and Jakubowski, G., 1986, "An Experimental Study of Film Cooling From Diffused Trapezoidal Shaped Holes," AIAA Paper 86-1326.
[3] Hay, N., and Lampard, D., 1995, "The Discharge Coefficient of Flared Film Cooling Holes," ASME Paper 95-GT-15.
[4] Gritsch, M., Schulz, A., and Wittig, S., 1998, "Discharge Coefficient Measurements of Film-Cooling Holes With Expanded Exits," ASME J. Turbomach., **120**, pp. 557–563.
[5] Gritsch, M., Schulz, A., and Wittig, S., 1998, "Adiabatic Wall Effectiveness Measurements of Film-Cooling Holes With Expanded Exits," ASME J. Turbomach., **120**, pp. 549–556.
[6] Gritsch, M., Schulz, A., and Wittig, S., 1998, "Heat Transfer Coefficient Measurements of Film-Cooling Holes With Expanded Exits," ASME Paper 98-GT-28.
[7] Thole, K. A., Gritsch, M., Schulz, A., and Wittig, S., 1998, "Flowfield Measurements for Film-Cooling Holes With Expanded Exits," ASME J. Turbomach., **120**, pp. 327–336.
[8] Hay, N., Lampard, D., and Benmansour, S., 1983, "Effect of Crossflows on the Discharge Coefficient of Film Cooling Holes," ASME J. Eng. Power, **105**, pp. 243–248.
[9] Gritsch, M., Saumweber, C., Schulz, A., Wittig, S., and Sharp, E., 2000, "Effect of Internal Coolant Crossflow Orientation on the Discharge Coefficient of Shaped Film Cooling Holes," ASME J. Turbomach., **122**, pp. 146–153.
[10] Thole, K. A., Gritsch, M., Schulz, A., and Wittig, S., 1997, "Effect of a Crossflow at the Entrance to a Film-Cooling Hole," ASME J. Fluids Eng., **119**, pp. 533–541.
[11] Kohli, A., and Thole, K. A., 1997, "A CFD Investigation on the Effects of Entrance Crossflow Directions to Film-Cooling Holes," Proc., 32nd National Heat Transfer Conference, Baltimore, MD, August 10–12.
[12] Kohli, A., and Thole, K. A., 1998, "Entrance Effects on Diffused Film-Cooling Holes," ASME Paper 98-GT-402.
[13] Wittig, S., Schulz, A., Gritsch, M., and Thole, K. A., 1996, "Transonic Film-Cooling Investigations: Effects of Hole Shapes and Orientations," ASME Paper 96-GT-222.
[14] Martiny, M., Schiele, R., Gritsch, M., Schulz, A., and Wittig, S., 1996, "In Situ Calibration for Quantitative Infrared Thermography," OIRT'96 Eurotherm Seminar No. 50, Stuttgart, Germany, September 2–5.
[15] Schmidt, D. L., Sen, B., and Bogard, D. G., 1996, "Film Cooling With Compound Angle Holes: Adiabatic Effectiveness," ASME J. Turbomach., **118**, pp. 807–813.

Downloaded 31 May 2010 to 171.66.16.27. Redistribution subject to ASME license or copyright; see http://www.asme.org/terms/Terms_Use.cfm

Heat Transfer in Rotating Rectangular Cooling Channels (AR=4) With Dimples

Todd S. Griffith

Luai Al-Hadhrami

Je-Chin Han

Turbine Heat Transfer Laboratory,
Department of Mechanical Engineering,
Texas A&M University,
College Station, TX 77843-3123

As the world of research seeks ways of improving the efficiency of turbomachinery, attention has recently focused on a relatively new type of internal cooling channel geometry, the dimple. Preliminary investigations have shown that the dimple enhances heat transfer with minimal pressure loss. An investigation into determining the effect of rotation on heat transfer in a rectangular channel (aspect ratio*=4:1) with dimples is detailed in this paper. The range of flow parameters includes Reynolds number (Re=5000–40000), rotation number (Ro=0.04–0.3) and inlet coolant-to-wall density ratio ($\Delta\rho/\rho$ =0.122). Two different surface configurations are explored, including a smooth duct and dimpled duct with dimple depth-to-print diameter (δ/D_p) ratio of 0.3. A dimple surface density of 10.9 dimples/in^2 was used for each of the principal surfaces (leading and trailing) with a total of 131 equally spaced hemispherical dimples per surface; the side surfaces are smooth. Two channel orientations of $\beta=90$ and 135 deg with respect to the plane of rotation are explored to determine channel orientation effect. Results show a definite channel orientation effect, with the trailing-edge channel enhancing heat transfer more than the orthogonal channel. Also, the dimpled channel behaves somewhat like a 45 deg angled rib channel, but with less spanwise variations in heat transfer.*
[DOI: 10.1115/1.1571850]

Keywords: Heat Transfer, Dimple, Channel, Rotating

Introduction

Extensive research efforts have recently focused on methods for reducing the consumption of non-renewable energy resources. The turbomachinery industry is one industry committed to improving the efficiency of its equipment. Gas turbines are used for a wide variety of applications including power generation, gas compression, and jet propulsion. The efficiency of a turbine can be increased by increasing the combustion temperature or decreasing the amount of compressor dilution air used to cool the extremely hot gas exiting the combustor. This poses a major problem in the hastened degradation of temperature sensitive components of the turbine, principally the turbine blades and vanes. To counter the high turbine inlet temperatures (1600–1800 K), the physics of turbulent heat transfer under rotation are investigated in a cooling model. Turbine blades incorporate internal cooling passages to extract the thermal energy absorbed from the hot combustion gases. This prolongs the life of the blade as well as allowing for increased combustion temperatures, which ultimately increases performance of the turbine.

A small amount of pressurized air is extracted from the compressor and injected into the turbine blades via the cooling air bypass. This relatively low enthalpy gas is forced through the internal cooling passages of the turbine blades, convectively extracting heat from the internal walls. For further thermal protection of the blade, a portion of the internal cooling air is ejected through tiny holes in the walls and tip of the blade, creating a cool film thermal boundary.

When considering the effects of rotation, certain flow phenomena are exhibited that are not observable in the stationary reference frame. Forces are generated under rotation, principally the Coriolis and buoyancy forces. These forces generate a secondary flow in the plane orthogonal to the mean flow direction. For radial outward flow, the Coriolis and buoyancy forces combine to shift the velocity profile toward the trailing surface. The coolant flow migrates along with the heat transfer augmentation toward the trailing surface. This rotationally induced migration of the cooler core flow results in the advantageous enhancement of heat transfer at the trailing surface, but it is typically balanced by the disadvantageous reduction in heat transfer from the leading surface. As with most temperature sensitive components, thermal failure in an isolated region is oftentimes just as problematic as failure of the entire component. This is why it is important to analyze the heat transfer phenomenon segment by segment along the length of the blade.

The aspect ratio of the channel also has a profound impact on the effect of rotation. Moving from the midchord to the trailing edge of the blade, the channels must become more rectangular as the blade becomes thinner. The orientation of a 4:1 aspect ratio cooling channel in a gas turbine blade is shown in Fig. 1. This thinning of the channel changes the effective secondary flow pattern from that of a square duct. For this reason, one cannot simply apply the knowledge of the rotationally induced flow patterns in a square channel to that of a rectangular channel. Therefore, an investigation of the rectangular channel is necessary to further understand the heat transfer characteristics of the internal cooling channels in a gas turbine blade.

To promote heat transfer in the internal cooling passages, various types of turbulators are used to trip the boundary layer. Ribs or ''trip-strips'' and pin-fins have been commonly used in gas turbines over the past decade. The dimple is a relatively new approach, investigated first by Schukin et al. [1]. When combining the effects of tripping the boundary layer (using ribs, pins, or dimples) and rotational forces (Coriolis and buoyancy), entirely different turbulence and flow phenomenon are achieved. Combining into this equation the various shapes and sizes of internal cooling channels, it is clear that there is no one single solution that can be applied universally in the field of turbine heat transfer. For this reason, an experimental investigation into each combination of the previously mentioned parameters is necessary.

Contributed by the International Gas Turbine Institute and presented at the International Gas Turbine and Aeroengine Congress and Exhibition, Amsterdam, The Netherlands, June 3–6, 2002. Manuscript received by the IGTI January 18, 2002. Paper No. 2002-GT-30220. Review Chair: E. Benvenuti.

 Copyright © 2003 by ASME

Downloaded 31 May 2010 to 171.66.16.27. Redistribution subject to ASME license or copyright; see http://www.asme.org/terms/Terms_Use.cfm

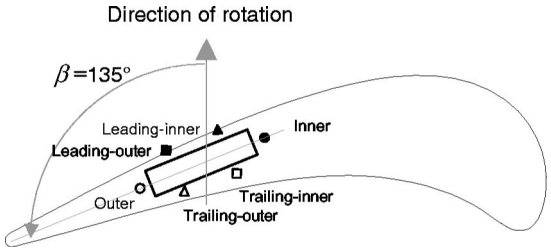

Fig. 1 Sketch illustrating orientation of a 4:1 aspect ratio channel in a gas turbine blade

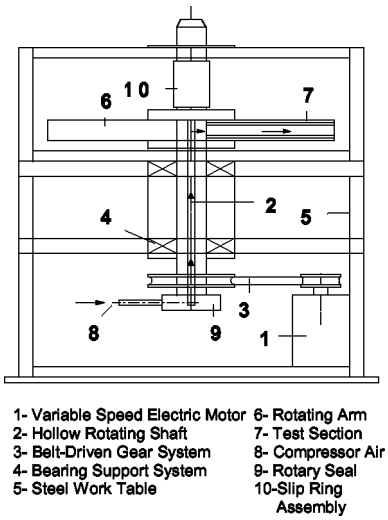

Fig. 2 Schematic of experimental rotating test rig

Numerous studies on turbulent flow and heat transfer in the cooling channels of a gas turbine blade have been performed in the past. Han and Park [2] published experimental investigations of the heat transfer phenomenon in a stationary rib roughened rectangular channel. Wagner et al. [3,4] conducted detailed experimental investigation to determine the effects of rotation, or more specifically the effects of Coriolis and buoyancy forces on the regionally averaged heat transfer distribution of a serpentine square channel with smooth walls. This study determined that in the first pass, the effect of rotation created a thinner boundary layer on the trailing surface and a thicker boundary layer on the leading surface.

Parsons et al. [5] studied the effects of channel orientation and wall heating condition on the regionally averaged heat transfer coefficients in a rotating two-pass square channel with ribbed walls. They discovered that the heat transfer enhancement for the constant wall heat flux boundary condition was more pronounced if the duct is twisted 45 deg to the plane of rotation when compared to a channel oriented orthogonal to the plane of rotation. Johnson et al. [6] determined that the model orientation with respect to the rotation plane greatly affected the heat transfer distribution.

Dutta and Han [7] investigated the regionally averaged heat transfer coefficients in a rotating two-pass square channel with three different model orientations. They found that the orientation of the channel with respect to the plane of rotation affected the heat transfer distribution. More specifically, they determined that orienting the channel at an angle with respect to the plane of rotation reduced the effect of rotation when compared to the orthogonal channel orientation.

Until recently, most of the experimental studies have explored only square ducts. However, it is quite common to find rectangular cooling passages, particularly toward the trailing edge of a gas turbine blade. Since the profile of a turbine blade is curved, the exclusive use of square channels is not practical. Past research focused mainly on the square channel; therefore, published data for a rectangular cooling channel is rare.

Willett and Bergles [8] performed a detailed investigation of the heat transfer in a narrow, 10:1 smooth rectangular channel oriented at 60 deg to the *r-z* plane. Most of their focus dealt with exploring the contribution of buoyancy forces under rotation. They found that the duct orientation induced a significant heat transfer gradient in the spanwise direction. It was also found that the normalized Nusselt number at the far-aft-end of the trailing side (or the trailing-outer equivalent in this paper) is a strong function of rotation number and buoyancy number.

Griffith et al. [9] studied the effects of rotation on a AR=4:1 rectangular channel with $\beta=90$ and 135 deg. They determined that the rib induced secondary flow dominated the rotation-induced vortices, particularly at lower rotation numbers. They also found that significant spanwise heat transfer gradients exist for both channel orientations.

Dimpled channel literature has surface quite recently. Ekkad et al. [10] used cylindrical dimples with several different depths to simulate the TBC spallation for flow over a flat plate. The paper also used other geometries such as square, rectangular, diamond, and elliptic shape of dimples. Azad et al. [11] Investigated a channel with cylindrical dimples on the target walls of impingement cooling, instead of the concave (hemispherical) dimples as in the current study.

Chyu et al. [12] investigated hemispheric and teardrop shaped concavities in a stationary channel using a liquid crystal technique. They found that the overall performance was nearly equal for the geometries, showing enhancement of approximately 2.5 times that of a smooth duct for the stationary case. Moon et al. [13] analyzed a stationary dimpled channel using a liquid crystal technique. They found that the heat transfer enhancement occurs mostly outside of dimples. They also found that the enhancement is reduced in the upstream portion of dimple and the enhancement is increased in the downstream portion (rim) of dimple. In addition, they determined that enhancement not a function of Reynolds number, and is typically constant at around 2.1. Mahmood et al. [14] investigated a stationary dimpled channel using infrared thermography and smoke-stream flow visualization. They found that a large upwash region occurs in the center of the dimple, and pairs of vortices are shed at the dimple diagonals. They also determined that the enhancement principally occurs on the plateau (or flat) surface. Zhou et al. [15] used the concave dimples on the leading and trailing surfaces of a rotating square channel.

For a more comprehensive compilation of turbine heat transfer research, please see the book by Han et al. [16] and review paper by Han and Dutta [17].

Considering that the effect of rotation has shown to significantly influence the heat transfer enhancement of a cooling channel, it is of interest to explore the rotational effects on the heat transfer in a dimpled channel. The following questions arise:

1. How does the spanwise heat transfer distribution vary within a dimpled, rotating, rectangular channel?
2. How does the dimpled channel compare to a smooth and ribbed channel?
3. What is the effect of the channel orientation with respect to the plane of rotation?
4. How do rotational forces quantitatively influence the heat transfer enhancement in a dimpled rectangular channel?

Answers to these questions are pursued in this paper.

Experimental Facility

The experimental test rig previously used by Dutta and Han [7] is utilized in this investigation (see Fig. 2). A variable frequency

Downloaded 31 May 2010 to 171.66.16.27. Redistribution subject to ASME license or copyright; see http://www.asme.org/terms/Terms_Use.cfm

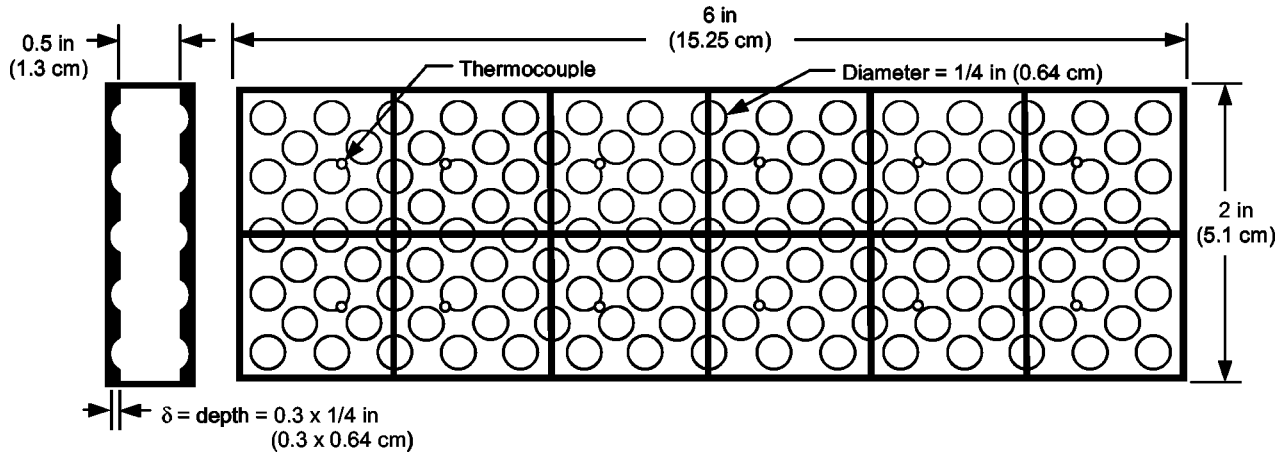

Fig. 3 Schematic of 4:1 dimpled test

motor is connected via a gear-and-belt mesh to a hollow, rotating shaft. This shaft runs from the base of the test rig to the work platform and is attached orthogonal to the hollow, rotating arm. The test section is inserted inside the hollow rotating arm, which rotates in a plane orthogonal to the rotating shaft. A hand held optical tachometer is used to determine the rotational velocity of the arm. Thermocouple and heater wires are connected to a 100-channel slip-ring assembly mounted to the rotating shaft. The output of the thermocouples is transferred to a data logger. Fuse-protected power input to the heaters from the variac transformers is also transmitted through the slip ring assembly. Cooling air is pumped from a steady flow compressor, through an ASME orifice flow meter, then through the hollow rotating shaft, turning 90 deg and passing into the rotating arm, then through the test section and is finally expelled into the atmosphere.

The test section is a 0.5-in. by 2-in. by 6-in.-long ($1.27\times5.08\times15.24$ cm) one-pass rectangular channel of aspect ratio 4:1 with a hydraulic diameter of $D=0.8$ in. Preceding the test section is an 8-in.-long (20.3-cm) smooth, unheated entrance length (same rectangular cross-section), sufficiently long enough to provide hydrodynamically fully developed flow at the entrance to the test section. The ratio of mean rotating radius to hydraulic diameter is $R/D=33$. The direction of airflow is radially outward from the axis of rotation. Two rows of copper plates are installed on both the leading and trailing surface to provide a grid for analysis of the spanwise variation in the regionally averaged heat transfer coefficient.

Figure 3 shows a detailed top view of the test section. The test section is divided into six cross-sections, each with six copper plates: two for the leading, two for the trailing, one for the outer and one for the inner surface. Moving along the direction of the flow (radially outward), there are six streamwise segments for a total of 36 copper plates in the entire test section. The channel length-to-hydraulic diameter ratio (L/D) is 7.5 with a ratio of 1.25 for each of the six cross section segments. Each plate is separated by a 0.0626-in. (0.159-cm) thin strip of nylon to prevent heat conduction between plates. This is important since the objective is to study the spatial distribution of heat transfer.

The copper plates are mounted in a nylon substrate, which comprises the bulk of the test section. Prefabricated flexible heaters are installed beneath the leading and trailing surfaces, two to each surface. The outer and inner walls (or side walls) are each heated by a wire-wound resistance heater, which is also installed beneath the copper plates. All heaters supply steady, uniform heat flux to the copper plates. Sufficient power is supplied in order to maintain a maximum wall temperature of nearly 340 K for the corresponding section. This corresponds to an inlet coolant-to-wall density (temperature) ratio $(\Delta\rho/\rho)_i$ of 0.122 for every test. Thermal conducting paste is applied between the heater and copper plates to promote heat transfer from the heater to the plate. Each 1/8-in. (0.318-cm) thick plate has a 1/16-in. (0.159-cm) deep blind hole drilled in the backside in which a copper-constantan thermocouple is installed 1/16 in. (0.159 cm) from the plate surface with thermal conducting glue.

Two different surface configurations (smooth and dimpled $\delta/D_p=0.3$) are studied as well as two different channel orientations with respect to the direction of rotation ($\beta=90$ and 135 deg). For the dimpled experiments, only the leading and trailing surfaces are dimpled with the side surfaces kept smooth. The dimples are machined using hemispherical end-mills. The experiments were conducted for Reynolds numbers of 5000, 10000, 20000, and 40000. The test section rotates at a constant speed of 550 rpm resulting in a range of rotation number (R_o) from approximately 0.04–0.3.

Data Reduction

This investigation focuses on detailing the regionally averaged heat transfer coefficient at various locations within the internal cooling channel. This heat transfer coefficient is determined by the net heat flux from the heated plate to the cooling air, the regionally averaged temperature of the plate, and the local bulk mean air temperature by the following:

$$h=q''_{\text{net}}/(T_w-T_{b,x}) \tag{1}$$

The net heat flux is calculated using the measured voltage and current supplied to the heater multiplied by the area fraction exposed to the respective plate minus the previously determined amount of heat losses due to external conduction, convection, and radiation energy escaping from the test section. This heat loss calibration is performed for both stationary and rotation experiments with a piece of insulation inserted inside the test section to inhibit natural convection. For this calibration, by knowing the amount of power supplied to the heater and measuring the temperature of the plate, it is possible to determine how much the heat is being lost into the environment using the conservation of energy principle. Equation 1 is used throughout the experiment, neglecting the change of area effect with the addition of dimples. That is, the heat transfer coefficient is calculated based on the projected area, neglecting the 19.3% increase in area due to the addition of dimples.

The regionally averaged wall temperature (T_w) is measured directly by the thermocouple installed in the back of each plate. The local bulk mean air temperature ($T_{b,x}$) is determined by a linear interpolation between the measured bulk air inlet and the average of two outlet temperatures (each installed at the midpoint

Downloaded 31 May 2010 to 171.66.16.27. Redistribution subject to ASME license or copyright; see http://www.asme.org/terms/Terms_Use.cfm

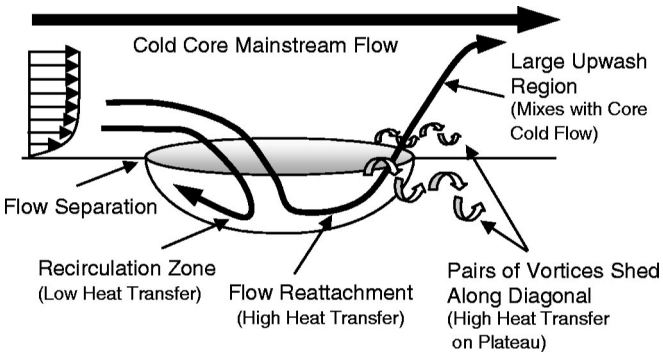

Fig. 4 Dimple induced secondary flow (conceptualization)

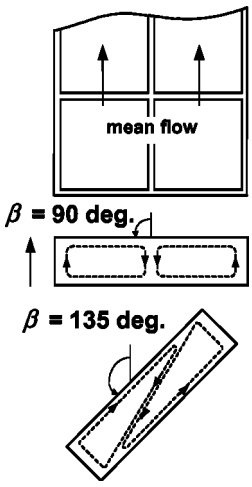

Fig. 5 Rotation-induced (Coriolis force) vortices in rectangular channel

of the two spanwise sections) due to the applicable constant heat flux assumption. Another method used to check the interpolation values is by performing an energy balance. It is reassuring to note that performing an energy balance to calculate the expected outlet temperature resulted in a close match to that of the average measured exit temperature value, typically to within 5%. Therefore the linear interpolation method is validated and is the method used in the calculation of the results presented in this paper. The energy balance equation is

$$T_{b,i} = T_{in} + \sum_i (q - q_{\text{loss}})/\dot{m}c_p, \quad i = 1,2 \ldots 6 \tag{2}$$

To provide a common reference for each analysis, a correlation is used comparing the Nusselt number for the specific duct case to that of fully developed flow through a smooth stationary pipe at the same Reynolds number. For this investigation, the Dittus-Boelter correlation for heating ($T_w > T_{bx}$) is used [18]

$$\frac{\text{Nu}}{\text{Nu}_o} = \frac{hD}{k_{\text{air}}} \frac{1}{(0.023\,\text{Re}^{0.8}\,\text{Pr}^{0.4})} \tag{3}$$

All air properties are taken based on the mean bulk air temperature with the Prandtl number (Pr) for air as 0.71.

Overall uncertainty for the regionally averaged heat transfer coefficient is predominantly dependent upon the difference between the wall temperature and the bulk air temperature, the net heat flux input and the ability to maintain a steady mass flow rate. As with most experiments, the uncertainty for this investigation decreases with the increasing magnitude of input parameters. For higher Reynolds numbers, the uncertainty has been determined to be nearly 7%. However, for lower Reynolds number (Re $=5000$), the uncertainty could be as much as 20%. The uncertainty analysis was performed using the Kline and McClintock [19] uncertainty analysis procedure.

Results And Discussion

The surface labeling scheme, seen in Fig. 1, will be used throughout this paper. The inner and outer surface side walls are named according to their location in the turbine blade. That is, the inner surface is closer to the mid-chord position of the blade (a relatively internal position), and the outer surface is closer to the trailing edge of the blade, and thus is closer to an external surface of the blade. The leading and trailing surfaces of the blade follow the conventional definitions of these surfaces, however each surface is subdivided into two surfaces in order to investigate the span-wise distribution of heat transfer along the major surfaces (leading and trailing). Therefore we have a total of six surfaces: leading-outer, leading-inner, trailing-outer, trailing-inner, outer, and inner. A brief discussion on the secondary flow pattern induced by a dimple is presented in the forthcoming.

Secondary Flow Behavior. Figure 4 shows a conceptualization of the secondary flow patterns over a dimpled surface. As the flow approaches the upstream portion of the dimple, flow separation occurs, and a recirculation zone appears in the upstream portion of the dimple resulting in mitigation of the heat transfer. As the flow reattaches at the downstream half of the dimple, an increase in the heat transfer enhancement occurs. Continuing in the streamwise direction, it has been shown that a large upwash region is produced by the dimple. This upward directed flow mixes to some degree with the cold core mainstream flow. Finally, pairs of vortices are shed along the dimple diagonals, enhancing the heat transfer on the flat portion of the surface. Considering the dimple induced secondary flows and superimposing the rotation induced secondary flow upon it, it is apparent that there is no primarily constructive combination of the two, as was shown in the case of a 45 deg angled-rib rotating channel investigated by Griffith et al. [9]. This complex combination of the dimple induced vortices in various directions with the rotation induced secondary flow does not generate any vision of a primary coherent flow structure, however the heat transfer enhancement is still increased at the trailing surface due to the thinning of the boundary layer under rotation.

Figure 5 shows a conceptualization of the secondary flow induced by rotating a smooth, rectangular channel. The Coriolis force induces two counter rotating vortices, which serve to push the colder fluid closer to the trailing surface. When the channel is twisted such that $\beta = 135$ deg, the linear distance of the Coriolis force main vector increases from a relatively small distance (as in the case of $\beta = 90$ deg to a much longer distance. The Coriolis vector now traverses the diagonal from the leading most corner to the trailing most corner of the twisted channel. This shifting of the rotation induced vortices serves to mix the flow more effectively.

Smooth Channel Results. Figures 6–8 contain the smooth duct data for three different channel configurations: stationary, rotation with $\beta = 90$ deg and rotation with $\beta = 135$ deg. Each case is subdivided into four experiments: (*a*) Re $=5000$, (*b*) Re $=10000$, (*c*) Re $=20000$, and (*d*) Re $=40000$. The corresponding rotation numbers for these cases are 0.305, 0.151, 0.075 and 0.038 respectively. Figure 6 contains data for the stationary cases. The initial decrease in the normalized Nusselt number plots is attributable to the entrance effect in thermally developing flow. The plots all approach a horizontal asymptote as the flow approached the thermally fully developed state.

Figure 7 shows the results for the rotation cases where the duct is oriented at $\beta = 90$ deg, that is, orthogonal to the plane of rotation. As was expected, the trailing surfaces exhibit higher heat

Downloaded 31 May 2010 to 171.66.16.27. Redistribution subject to ASME license or copyright; see http://www.asme.org/terms/Terms_Use.cfm

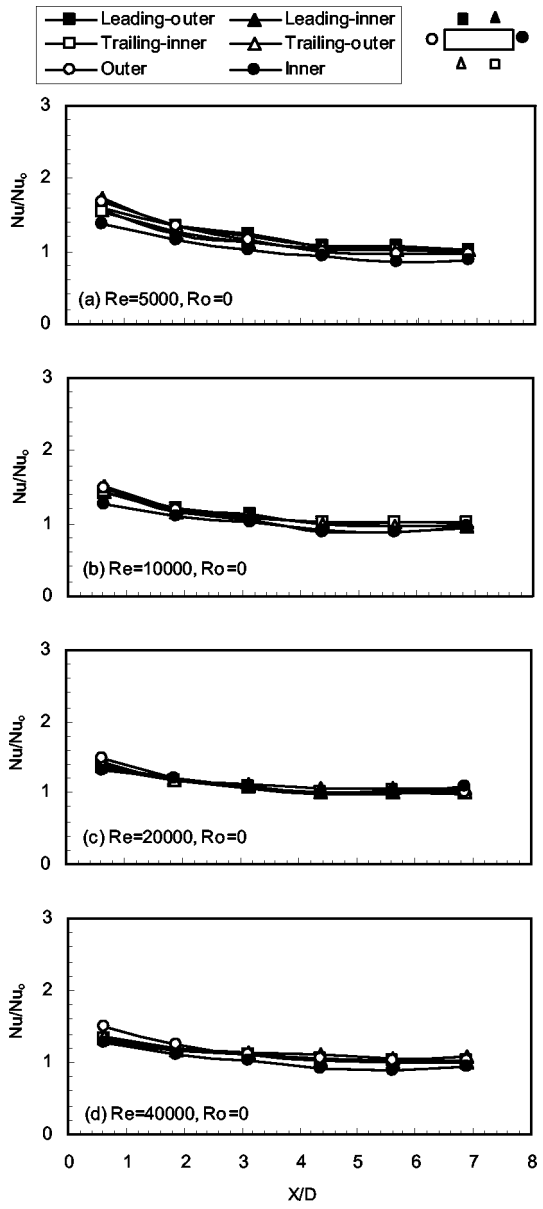

Fig. 6 Nusselt number ratio for stationary smooth case

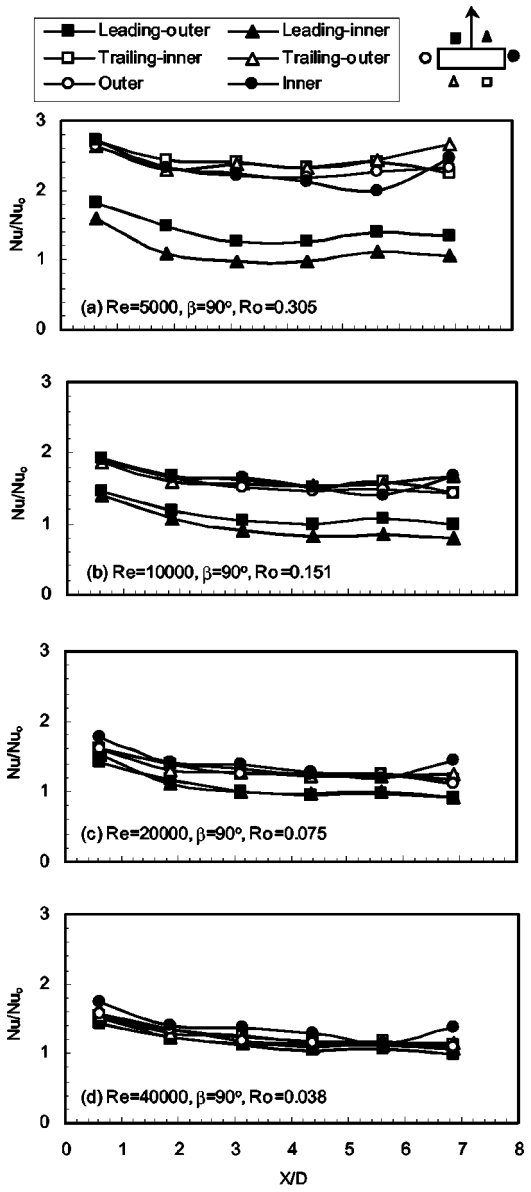

Fig. 7 Nusselt number ratio for rotation smooth case with β=90 deg

transfer enhancement than the leading surfaces due to the migration of the colder core fluid toward the trailing surface caused by the Coriolis rotational forces. At a duct angle of β=90 deg, the channel can be assumed to hold symmetry about the plane of rotation. This means that both of the leading surfaces (leading-outer and leading-inner) should have identical Nu plots, the trailing surfaces should exhibit identical behavior, and the two side surfaces should be equal. This is validated relatively well as seen in the figures, with a slight bias between the two trailing surfaces. An increase in the Reynolds number tends to suppress the effect of rotation. All six surfaces show very little streamwise variation in the Nu number plots. Both of the side surfaces (inner and outer) have a heat transfer enhancement nearly equal to the value of the two trailing surfaces.

Figure 8 presents the results of the smooth rotation case with the channel oriented at β=135 deg with respect to the plane of rotation. Figure 8*a* shows that at a low Reynolds number (high rotation number), there are distinguishable differences in the heat transfer trends among the various surfaces. It can be seen that the trailing-outer and outer surfaces exhibit the highest heat transfer enhancement of all of the surfaces in the duct. This is attributed to the fact that these two surfaces are the primary recipients of the shifting of the cooler core flow under rotation. This phenomenon is illustrated in Fig. 5 of the preceding section. After the flow impinges on the trailing-outer and outer surfaces, it passes along the leading and trailing surfaces to the inner surface, where the heat transfer coefficient is the lowest, and the secondary flow slows down dramatically. Then the flow cycles again, passing from the leading most corner diagonally across the channel toward the trailing most corner. At a high rotation number, the inner surface heat transfer follows a trend quite similar to the stationary cases. It appears that this inner surface is barely affected by rotation. Both of the trailing surfaces have higher heat transfer coefficients than the leading surfaces. A new and interesting finding is the substantial difference in the heat transfer coefficient between the two trailing surfaces. Furthermore, this span-wise difference does not come into effect until nearly half-way through the channel for high rotation numbers (R_o=0.305). It is also shown that the leading surface heat transfer increased when compared to the orthogonal channel. The overall increase in heat transfer from

Downloaded 31 May 2010 to 171.66.16.27. Redistribution subject to ASME license or copyright; see http://www.asme.org/terms/Terms_Use.cfm

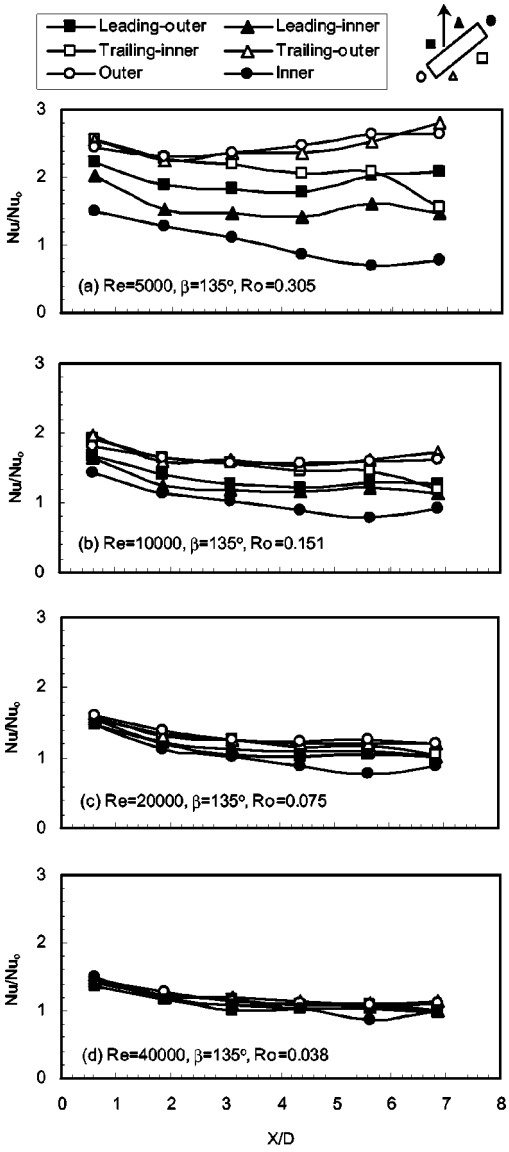

Fig. 8 Nusselt number ratio for rotation smooth case with β=135 deg

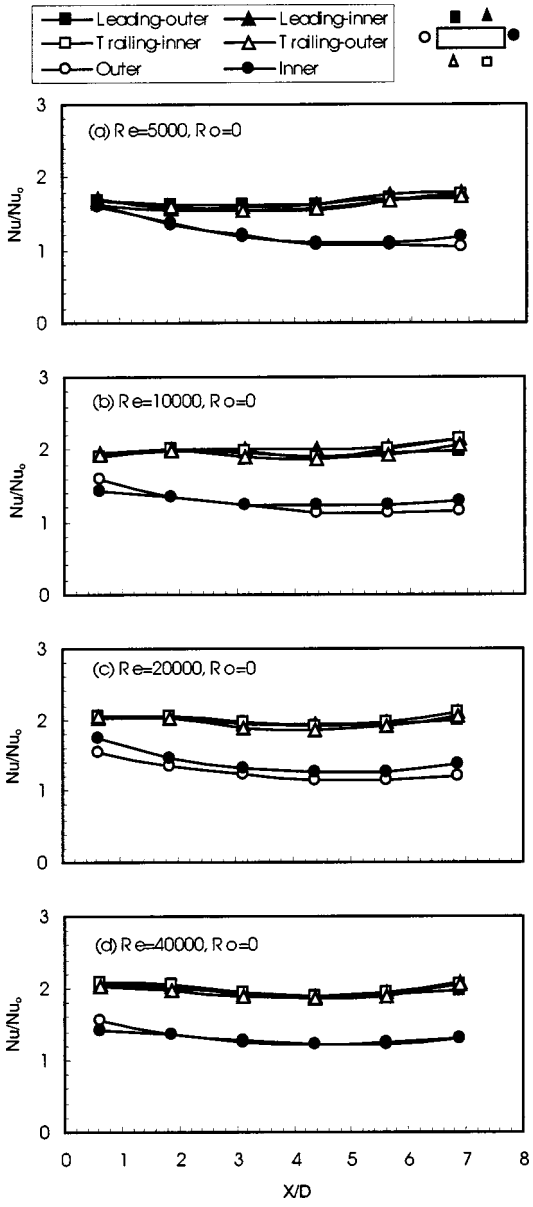

Fig. 9 Nusselt number ratio for stationary dimpled case

nearly all surfaces can be attributed to the fact that twisting the channel greatly increased the linear distance along which the main Coriolis force is directed (from leading most to trailing most corner) and provides an overall better mixing than the β=90 deg case. In the β=90 deg case, the principal Coriolis vector in the core region of the flow acts across only a short distance (the short width of the channel) and does not serve to mix the flow as well as the twisted channel.

One evident contrast of the results of the β=135 deg case (Fig. 8) compared to the β=90 deg (Fig. 7) case is apparent in the side surfaces. For the twisted channel, the trend of the outer surface increases while the inner surface trend decreases with X/D. Furthermore, the inner surface decreases in a similar way as seen in the stationary case. The outer surface, which trails after the inner surface, experiences a heat transfer enhancement of as much as three times that of the inner surface for the β=135 deg case. This is due to the shift of the primary Coriolis induced flow vector from the center of the trailing surface in the β=90 deg case to the trailing most corner in the β=135 deg case. This trailing most corner is adjacent to the outer surface, and therefore the outer surface benefits greatly in heat transfer enhancement due to the twisting of the duct. This is desirable since the outer surface of the β=135 deg case is closer to the trailing edge of the turbine blade, and thus is likely to experience a higher external heat flux than the inner surface. The inner surface interfaces with the side surface of the adjacent cooling passage, and therefore is less likely to be considered a critical surface.

Dimpled Channel Results. The data plots for the dimpled channel cases are presented in Figures 9–11. Figure 9 shows the stationary dimpled channel results. An enhancement of approximately 2.0 is produced by the dimpled surface. This is in close agreement with the results of Moon et al. [10]. The smooth side surfaces (inner and outer) appear to only benefit marginally from the mixing induced by the dimpled surfaces. It is shown that for Reynolds numbers 10000, 20000, and 40000, there appears to be almost no dependence upon Reynolds number. This observation was also made in the past by Moon et al. [10]. However, when the data for Re=5000 is considered, we see the emergence of Reynolds number dependence, with the enhancement decreasing with decreasing Reynolds number, but only at the lowest Re value.

Downloaded 31 May 2010 to 171.66.16.27. Redistribution subject to ASME license or copyright; see http://www.asme.org/terms/Terms_Use.cfm

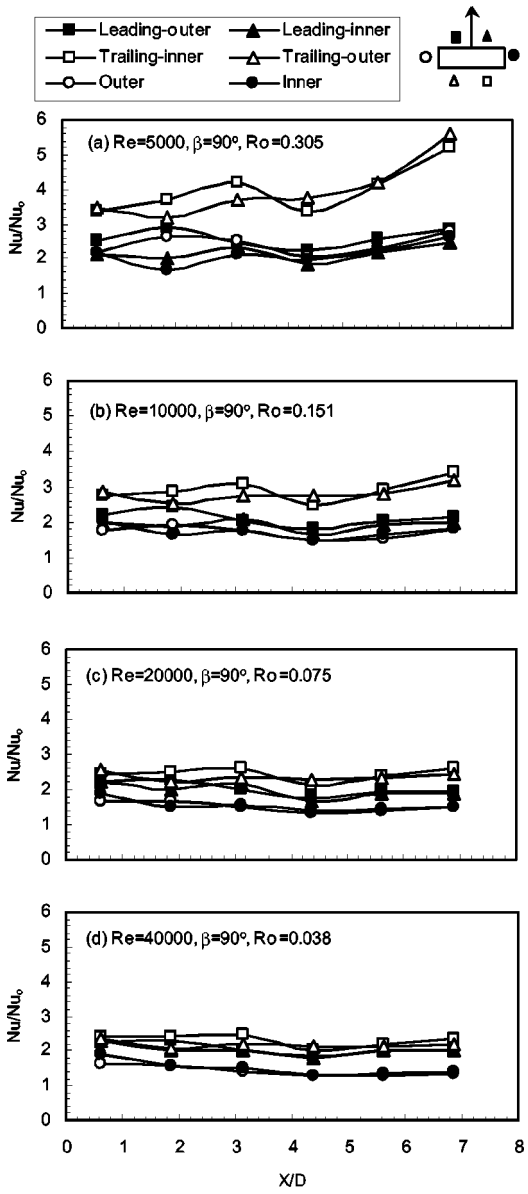

Fig. 10 Nusselt number ratio for rotation dimpled case with β=90 deg

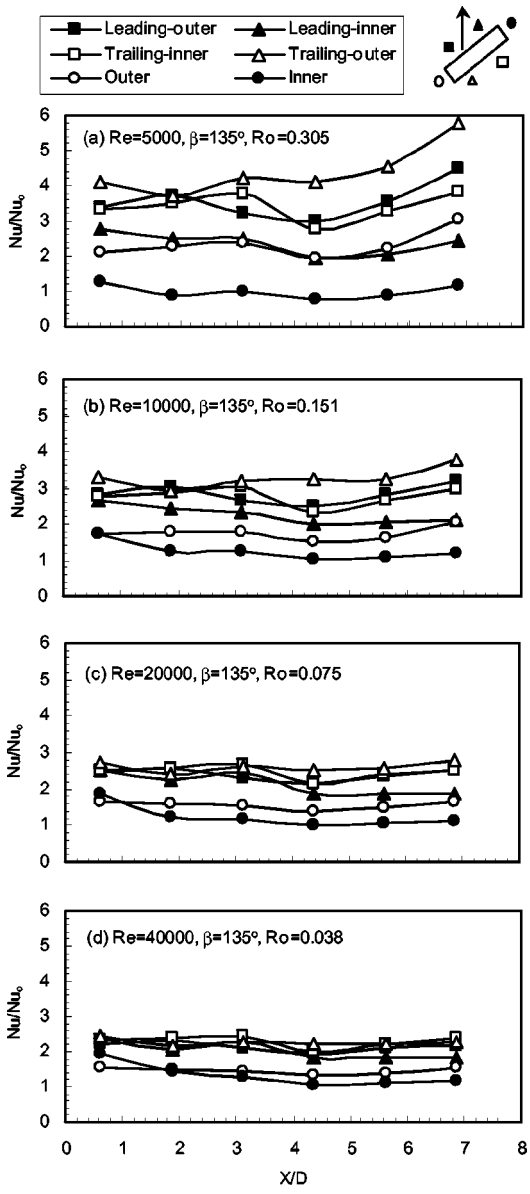

Fig. 11 Nusselt number ratio for rotation dimpled case with β=135 deg

Perhaps this is because the Reynolds number is much closer to the laminar-to-turbulent flow transition region of Re≅2300. Whatever the reason, such a low Reynolds number is not encountered in gas turbines, therefore consideration of this Reynolds number effect is only necessary for those wishing to consider the use of dimples for some other application outside of gas turbine heat transfer.

Figure 10 presents the data for the dimpled channel under rotation, orthogonal to the plane of rotation β=90 deg. It is apparent that there is a definite enhancement due to rotation for the trailing surfaces, which increases with increasing rotation number. Symmetry is achieved relatively well between the two spanwise segments of each dimpled surface, and symmetry between the two side surfaces. Also, the side surfaces experience enhancement equal to the leading surface. This is completely different than the smooth case, where the side surfaces were more equal to the trailing surface.

Figure 11 shows the results for the dimpled channel under rotation, twisted with respect to the plane of rotation (β=135 deg). The trailing-outer surface is enhanced more than the other surfaces, as it benefits from both the shifting of the cold flow toward the outer half of the channel, as well as the local mixing induced by the vortices shed by the dimples. In addition, the trailing-inner and leading-outer surfaces are enhanced (although to a lesser degree) by rotation. This occurs as the Coriolis vortex also serves to distribute some of the cold fluid in the core of the mainstream flow to the other surfaces, allowing the smaller scale dimple induced vortices to capture some of this cold fluid and pull it near to the wall. The outer surface is enhanced more than the inner surface due to the shifting of the majority of the colder flow toward the outer half of the twisted channel under rotation. This behavior was also seen in the smooth duct.

Streamwise Averaged Nusselt Number Ratio. Averaging the streamwise data for each surface provides a method of comparing the surfaces and the effect of rotation. Figures 12 and 13 presents the streamwise averaged data vs. Rotation number for the orthogonal and twisted channel. The solid line plots are for the dimpled channel and the dotted line plots are for the smooth channel.

Figure 12 presents the data for the orthogonal (β=90 deg)

Downloaded 31 May 2010 to 171.66.16.27. Redistribution subject to ASME license or copyright; see http://www.asme.org/terms/Terms_Use.cfm

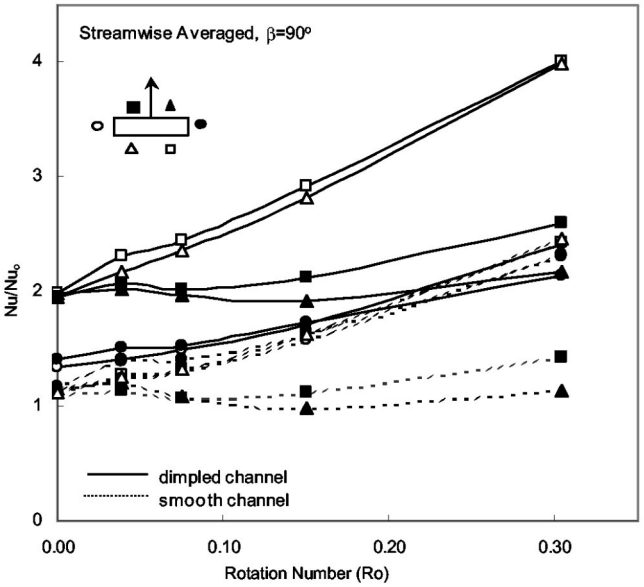

Fig. 12 Streamwise averaged Nusselt number ratio for dimpled and smooth channels with β=90 deg

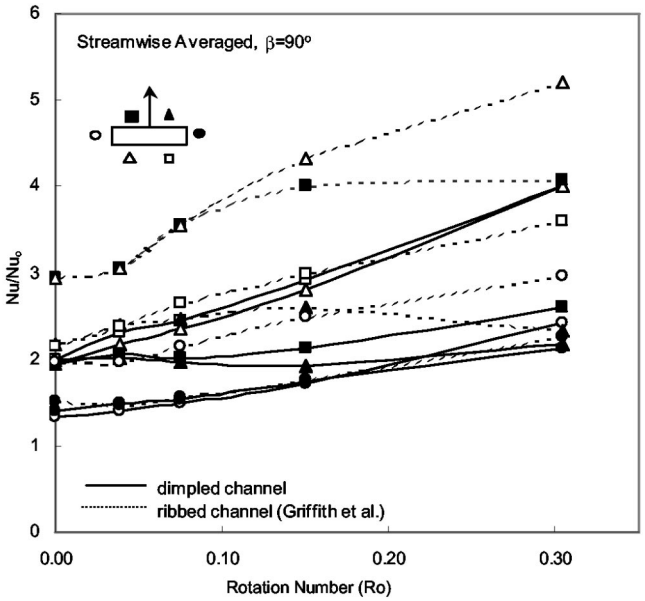

Fig. 14 Streamwise averaged Nusselt number ratio for dimpled and ribbed channels with β=90 deg

dimpled and smooth channel. From this plot, it can be seen that the dimpled trailing surfaces show greater dependence on rotation number than all other surfaces, with nearly 100% improvement in enhancement from the stationary to the highest rotation number case. The dimpled leading surfaces show very little dependence on rotation number due to the stable, thick boundary layer on the leading surface. The slight non-symmetry between the two leading surfaces is due to experimental uncertainty. A most interesting issue arises when comparing the side surfaces (inner and outer) of the dimpled channel to those of the smooth channel. It can be shown that while the side surfaces of the dimpled channel initially experience a higher enhancement without rotation, the smooth channel side surfaces show greater dependence on rotation than the dimpled channel side surfaces. This is possibly attributable to the disruption of the Coriolis vortices by the dimples. For the smooth surface, the Coriolis vortex passes from the center of the channel toward the side surfaces (see Fig. 5), where it enhances the heat transfer from the side surfaces. The secondary flow generated by the dimple has no single principal direction, and likely serves to reduce the intensity of the Coriolis vortices. Because of this, the effect of rotation is reduced for the side walls of the dimpled channel.

Figure 13 shows the streamwise averaged data versus Rotation number for the twisted (β=135 deg) dimpled and smooth channel. The dimpled trailing-outer surface shows the strongest dependence on rotation number and is clearly the primary recipient of enhancement for the twisted channel under rotation. In addition, the dimpled leading-outer and trailing-inner surfaces now show a moderate to high dependence on rotation number. This was also

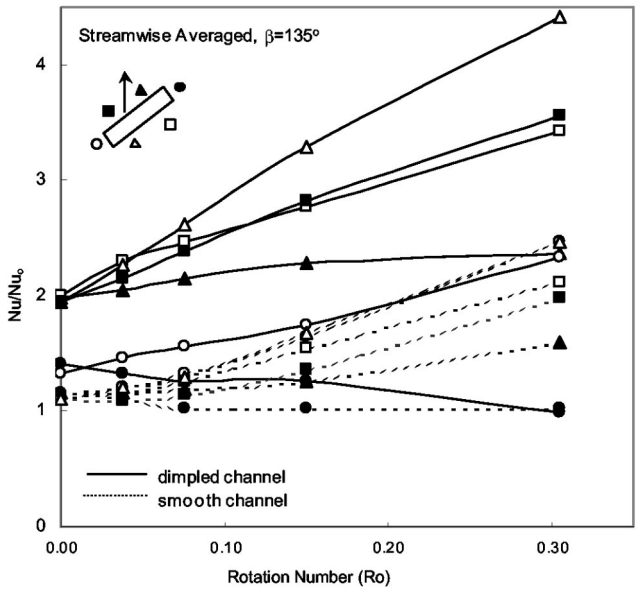

Fig. 13 Streamwise averaged Nusselt number ratio for dimpled and smooth channels with β=135 deg

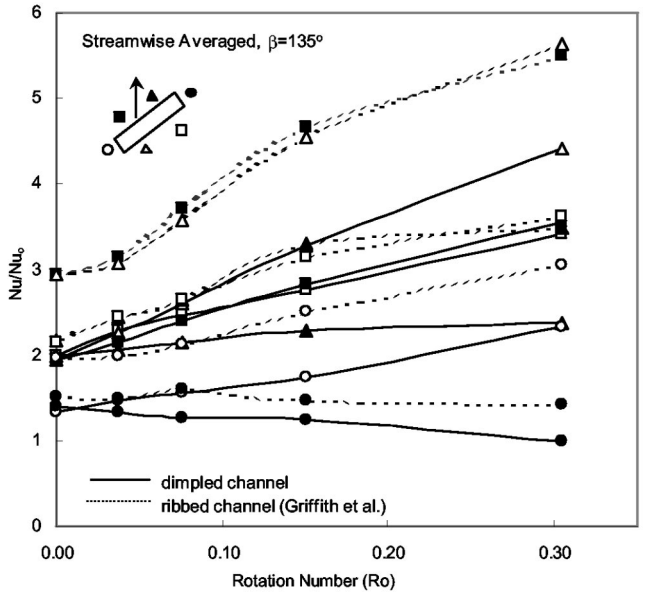

Fig. 15 Streamwise averaged Nusselt number ratio for dimpled and ribbed channels with β=135 deg

Downloaded 31 May 2010 to 171.66.16.27. Redistribution subject to ASME license or copyright; see http://www.asme.org/terms/Terms_Use.cfm

explained in the discussion of Fig. 11 where it was noted that the smaller scale vortices shed by the dimple are able to capture some of the lower enthalpy fluid, which is better distributed by the Coriolis vortices for the twisted channel. Again, it is noticed that the side surfaces of the twisted channel are enhanced less by rotation than those of the smooth duct due to the disruption of the Coriolis vortices by the vortices shed by the dimple.

Comparison of Dimpled and Ribbed Channel. Figures 14 and 15 compare the results of this investigation with the ribbed channel investigated by Griffith et al. [9]. We can see that the dimpled channel behaves similarly to the ribbed channel of the same geometrical and flow parameters. While the behavior under rotation is similar, it is noticed that the ribbed channel induces higher heat transfer enhancement when compared to the dimpled channel. This is evident even at the lowest rotation number, indicating that although the dimpled channel provides less enhancement at some surfaces, the behavior is very similar to that of the ribbed channel with increasing rotational effect. Some exceptions include the absence of spanwise variations for the orthogonal (β=90 deg) dimpled channel under rotation. Spanwise variations were quite significant in the case of the ribbed rotating channel due to the 45 deg rib-angle effect. Please note that past research has found that the ribbed channel creates greater pressure drop (friction penalty) than the dimpled channel.

Conclusions

1. Spanwise variations in heat transfer enhancement of the dimpled rotating rectangular channel exist only for the twisted (β=135 deg) orientation.
2. The effect of rotation exhibits similar trends for the dimpled and ribbed surface geometries, however the enhancement of the ribbed channel exceeds the enhancement of the dimpled channel for some surfaces. Both the dimpled and the ribbed channel provide advantageous enhancement compared to the smooth channel.
3. The twisted (β=135 deg) dimpled channel experiences greater overall enhancement than the orthogonal dimpled channel (β=90 deg).
4. For (β=90 deg), enhancement at the trailing surfaces increases by almost 100% from the stationary to highest rotation number case. Also, the leading surfaces show little dependence on rotation number. The side surfaces show slightly less dependence on rotation than those of a smooth duct.
5. For (β=135 deg), enhancement at the trailing-outer surface increases by more than 100% from the stationary to highest rotation number case. In addition, the trailing inner and leading outer surfaces experience nearly identical enhancement, increasing by more than 50% from the stationary to highest rotation number case. The outer surface increases by nearly 100% and the inner surface slightly decreases from the stationary to highest rotation number case.

Acknowledgments

The Advanced Gas Turbine Systems Research (AGTSR) program (project number SR-082) funded this experimental investigation under the supervision of the United States Department of Energy (DOE). The authors greatly appreciate the support of the AGTSR program and the DOE. Dr. H. K. Moon of Solar Turbines, Inc. and Dr. P. Ligrani of the University of Utah provided insight regarding the dimple concept. Without such support, this research would not have been possible.

Nomenclature

AR = aspect ratio
D = hydraulic diameter (m)
D_p = dimple print diameter (m)
L = length of duct (m)
Nu = regionally averaged Nusselt no., hD/k
Nu_o = Nusselt no. in fully developed turbulent nonrotating smooth tube flow
Pr = Prandtl no.
Q = heat transfer (W)
R = mean rotating radius (m)
Re = Reynolds no., $\rho VD/\mu$
R_o = rotation no., $\Omega D/V$
T_{bi} = inlet coolant bulk temperature (K)
T_{bx} = local coolant bulk temperature (K)
T_w = wall temperature (K)
V = bulk velocity in streamwise direction (m/s)
e = rib height (m)
h = heat transfer coefficient ($\mathrm{W/m^2\ K}$)
k = thermal conductivity of coolant (W/mK)
q''_{net} = net heat flux at wall based on projected area ($\mathrm{W/m^2}$)
β = angle of channel orientation
δ = dimple depth
Ω = rotational speed (rad/s)
ρ = density of coolant ($\mathrm{kg/m^3}$)
$\Delta\rho/\rho$ = inlet coolant-to-wall density ratio, $(T_w - T_{bi})/T_w$

References

[1] Schukin, A. V., Koslov, A. P., and Agachev, R. S., 1995, ''Study and Application of Hemispherical Cavities for Surface Heat Transfer Augmentation,'' ASME Paper No. 95-GT-59.
[2] Han, J. C., and Park, J. S., 1988, ''Developing Heat Transfer in Rectangular Channel With Rib Turbulators,'' Int. J. Heat Mass Transf., **31**(1), pp. 183–195.
[3] Wagner, J. H., Johnson, B. V., and Hajek, T. J., 1991, ''Heat Transfer in Rotating Passage With Smooth Walls and Radial Outward Flow,'' ASME J. Turbomach., **113**, pp. 42–51.
[4] Wagner, J. H., Johnson, B. V., and Kooper, F. C., 1991b, ''Heat Transfer in Rotating Serpentine Passage With Smooth Walls,'' ASME J. Turbomach., **113**(3), pp. 321–330.
[5] Parsons, J. A., Han, J. C., and Zhang, Y. M., 1995, ''Effects of Model Orientation and Wall Heating Condition on Local Heat Transfer in a Rotating Two-Pass Square Channel With Rib Turbulators,'' Int. J. Heat Mass Transf., **38**(7), pp. 1151–1159.
[6] Johnson, B. V., Wagner, J. H., Steuber, G. D., and Yeh, F. C., 1994, ''Heat Transfer in Rotating Serpentine Passage With Selected Model Orientations for Smooth or Skewed Trip Walls,'' ASME J. Turbomach., **116**, pp. 738–744.
[7] Dutta, S., and Han, J. C., 1996, ''Local Heat Transfer in Rotating Smooth and Ribbed Two-Pass Square Channels with Three Channel Orientations,'' ASME J. Heat Transfer, **118**, pp. 578–584.
[8] Willett, F. T., and Bergles, A. E., 2000, ''Heat Transfer in Rotating Narrow Rectangular Ducts with Heated Sides Oriented at 60deg to the R-Z Plane,'' ASME Paper No. 2000-GT-224.
[9] Griffith, T. S., Al-Hadhrami, L., and Han, J. C., 2002, ''Heat Transfer in Rotating Rectangular Cooling Channels (AR=4) With Angled Ribs,'' ASME J. Heat Transfer, **124**, pp. 617–625.
[10] Ekkad, S. V., and Han, J. C., 1996, ''Effect of Simulated TBC Spallation on Local Heat Transfer Coefficient Distributions Using a Transient Liquid Crystal Image Method,'' AIAA J. Thermophys. Heat Transfer, **10**(3), pp. 511–516.
[11] Azad, G. M. S., Huang, Y., and Han, J. C., 2000, ''Jet Impingement Heat Transfer on Dimpled Surfaces Using a Transient Liquid Crystal Technique,'' AIAA J. Thermophys. Heat Transfer, **14**(2), pp. 186–193.
[12] Chyu, M. K., Yu, Y., and Ding, H., Downs, J. P., Soechting, O. 1997, ''Concavity Enhanced Heat Transfer in an Internal Cooling Passage,'' ASME Paper No. 97-GT-437.
[13] Moon, H. K., O'Connell, T., Glezer, B., 1999, ''Channel Height Effect on Heat Transfer and Friction in a Dimpled Passage,'' ASME Paper No. 99-GT-163.
[14] Mahmood, G. I., Hill, M. L., Nelson, D. L., Ligrani, P. M., Moon, H.-K., and Glezer, B., 2001, ''Local Heat Transfer and Flow Structure on and Above a Dimpled Surface in a Channel,'' ASME J. Turbomach., **123**, pp. 115–123.
[15] Zhou, F., and Acharya, S., 2001, ''Mass/Heat Transfer in Dimpled Two-Pass Coolant Passages with Rotation,'' Heat Transfer in Gas Turbine Systems, ed., R. J. Goldstein, Ann. N.Y. Acad. Sci., **934**, pp. 424–431.
[16] Han, J. C., Dutta, S., and Ekkad, S. V., 2000. *Gas Turbine Heat Transfer and Cooling Technology*, Taylor and Francis, New York.
[17] Han, J. C., and Dutta, S., 2001, ''Recent Developments in Turbine Blade Internal Cooling,'' Heat Transfer in Gas Turbine Systems, ed., R. J. Goldstein, Ann. N.Y. Acad. Sci., **934**, pp. 162–178.
[18] Incropera, F. P., and DeWitt, D. P., 1996. *Fundamentals of Heat and Mass Transfer*, 4th ed. Wiley, New York.
[19] Kline, S. J., and McClintock, F. A., 1953, ''Describing Uncertainties in Single-Sample Experiments,'' Mech. Eng. (Am. Soc. Mech. Eng.), **75**.

Downloaded 31 May 2010 to 171.66.16.27. Redistribution subject to ASME license or copyright; see http://www.asme.org/terms/Terms_Use.cfm

Discussion: "Heat Transfer in Rotating Rectangular Cooling Channels (AR=4) With Dimples" (T. S. Griffith, L. Al. Hadhrami, and J.-C. Han., 2003, ASME J. Turbomach. 125, pp. 555–563)

P. Ligrani
Convective Heat Transfer Laboratory,
Department of Mechanical Engineering,
University of Utah, Salt Lake City, UT 84112-9208

As additional research efforts are conducted, the advantages of using arrays of dimples on the surfaces of internal passages are becoming more apparent. In particular, substantial heat transfer enhancements can be obtained with smaller pressure penalties than provided by other heat transfer augmentation devices, such as rib turbulators. As a result, dimpled surfaces for heat transfer augmentation are encountering wider use in different applications. The purpose of this comment is to point out additional features of the data presented in Fig. 9, which are obtained using a dimpled passage with no rotation.

1 Local and spatially-averaged Nusselt numbers increase as the ratio of dimple depth δ to dimple print diameter D_p increases, provided spherical indentation dimples are used and all other experimental parameters are held constant [20,21]. The δ/D_p ratio of the present study is 0.3. Results from other sources, obtained with no rotation, show that spatially averaged Nusselt number ratios range from 2.53 to 2.6 for $\delta/D_p=0.3$ [21], 2.41 to 2.47 for $\delta/D_p=0.28$ [12], and 2.08 to 2.25 for $\delta/D_p=0.19$ [13]. In each case, and in the present study, similar Reynolds numbers are used, and the ratio of channel height to dimple print diameter is 1 to 2. The spacing and arrangement of dimples on the test surface are the same in the present study as used by Burgess et al. [21], and very similar to the dimple spacings and arrangements used by Chyu et al. [12], and Moon et al. [13]. As the authors point out, spatially averaged Nusselt number data, presented as a ratio, are nearly independent of Reynolds number. Nusselt number ratio variations are also quite small at given Reynolds number as the ratio of channel height to dimple print diameter changes from 0.37 to 1.49 [13].

2 Nusselt number ratios, presented in Fig. 9, for no rotation, are about 2.0 for three of the Reynolds numbers investigated. This is lower than the expected value of 2.53–2.6 for the same δ/D_p. This appears to be tied to the limitations imposed by the rotating test rig, and the use of only one thermocouple to measure the "regionally averaged" surface temperature at one point on a surface segment with multiple dimples (Fig. 3). Large surface Nusselt number variations are present on dimpled surfaces in channels [12,13,20,21]. Accurate spatially averaged Nusselt numbers can only be obtained from spatially-averages of locally measured values over an area comprised of at least one complete period of dimple surface geometry [12,13,14,21].

3 The authors are congratulated for conducting difficult experiments in stationary and rotating environments where accurate heat transfer data are difficult to obtain.

References

[20] Gortyshov, Y. F., Popov, I. A., Amirkhanov, R. D., and Gulitsky, K. E., 1998, "Studies of Hydrodynamics and Heat Exchange in Channels with Various Types of Intensifiers," Heat Transfer, Proc., 11th IHTC, Vol. 6, pp. 83–88.

[21] Burgess, N. K., Oliveira, M. M., and Ligrani, P. M., 2003, "Nusselt Number Behavior on Deep Dimpled Surfaces Within a Channel," ASME J. Heat Transfer, **125**(1) pp. 11–18.

Closure to Discussion of "Heat Transfer in Rotating Rectangular Cooling Channels (AR=4) With Dimples" (2003, ASME J. Turbomach., 125, p. 564)

The authors appreciate Dr. Ligrani's comment on the paper. The discrepancy of heat transfer enhancement on the dimpled surface reported by different investigators might be due to the use of different measurement technique for the data taken and reduction. In addition to the aforementioned studies, for example, Zhou and Acharya [15] reported that the heat transfer enhancements of the dimpled surface for nonrotation could be about 1.5–2 times the smooth channel values for a dimple depth to print diameter ratio of 0.29 by using the naphthalene sublimation mass-transfer technique. Moon and Lau [22] showed that the dimpled surface heat transfer for nonrotation enhanced about 1.6–1.8 times the smooth-channel values for the dimple depth to print diameter ratios around 0.2–0.23 by using the standard aluminum plate with heaters and thermocouples. These heat transfer enhancement ratios are close to the present study's values for nonrotation by using the standard copper plate with heaters and thermocouples. But they are lower than the aforementioned values reported by Chyu et al. [12] using the transient liquid crystal technique, Moon et al. [13] using the transient liquid crystal technique, and Burgess et al. [21] using the IR camera technique. It is likely that using different measurement technique and data analysis could produce 10–20% different heat transfer enhancement values for turbulent channel flow through such a complex dimpled surface.

The present study used the traditional copper plate with heaters and thermocouples technique. The purpose was to obtain the regionally averaged heat transfer coefficient per copper plate. According to Fig. 3 in the paper, each copper plate is 2.54 cm by 2.54 cm facing to the cooling flow and with 0.3175-cm thickness. The estimated maximum Biot number of the copper plate is around 0.0022 for the highest heat transfer coefficient case at Re=40,000 of the present study. This means that the temperature gradient within the copper plate is small as expected by using this kind of standard measurement technique. On the other hand, in order to produce 20% heat-transfer coefficient's discrepancy in the copper plate, it requires 7°C of temperature gradient within each copper plate. This unlikely would happen in the present test condition ($Tw=67$°C, $Tb=32$°C). In addition, the high-conductivity copper plate with dimples represents the true span-averaged heat transfer coefficient including the potential end-wall effect from the channel smooth-side walls. For example, the potential smooth-side wall effect on the span-averaged heat transfer coefficient could not be included by viewing only the central 5-dimple area using the IR camera technique shown in Fig. 2 by Mahmood et al. [14]. The central 5-dimple area only might potentially produce higher heat transfer enhancement than the truly span-averaged values including the potential smooth end-wall effect.

To solve the issue, the authors plan to further investigate this topic. Again, the authors do appreciate Dr. Ligrani's insightful comment on the important dimple cooling technology for turbine blade cooling designs.

References

[22] Moon, S. W., and Lau, S. C., 2002, "Turbulent Heat Transfer Measurements on a Wall with Concave and Cylindrical Dimples in a Square Channel," ASME TURBO EXPO 2002, GT-2002-30208.

 Copyright © 2003 by ASME

Downloaded 31 May 2010 to 171.66.16.27. Redistribution subject to ASME license or copyright; see http://www.asme.org/terms/Terms_Use.cfm

Heat Transfer, Fluid Flow, and Pressure Measurements Inside a Rotating Two-Pass Duct With Detached 90-Deg Ribs

Tong-Miin Liou
College of Engineering,
Feng Chia University,
Taichung, Taiwan, ROC
e-mail: tmliou@pme.nthu.edu.tw

Meng-Yu Chen

Yu-Ming Wang

Department of Power Mechanical Engineering,
National Tsing Hua University,
Hsinchu, Taiwan, ROC
e-mail: d853708@oz.nthu.edu.tw

Transient thermochromic liquid crystal thermography, a laser-Doppler velocimeter, and pressure transducers have been used to measure the local heat transfer, velocity, and wall static-pressure distributions, respectively, in a rotating two-pass square duct with 90-deg ribs detached from the leading and trailing walls. The ribs were square in cross-section and their detached-distance/height ratio was 0.38. The rib-height/duct-height ratio and the pitch/rib-height ratio were 0.136 and 10, respectively. The duct Reynolds number was 1×10^4 and rotation number ranged from 0 to 0.2. Results are compared with attached rib cases in terms of regional averaged Nusselt number, transverse mean velocity component, pressure coefficient distributions and variation of friction factor with rotation number. The competition between convection effect of the wall jet and downwash effect of the rib-top separated shear layer on the heat transfer augmentation is addressed in detail. Discussion on local Nusselt number distribution, mean velocity components, and turbulent kinetic energy is included. Simple expressions are obtained to correlate friction factor with rotation number. Rib detachment is found to enhance heat transfer on the leading wall of the first outward pass and on the trailing wall of the second inward pass over as compared to the attached rib case. The trend is reversed on the other two walls. Nevertheless, detached ribs create more uniform heat transfer distributions on the leading and trailing walls than attached ribs. [DOI: 10.1115/1.1565086]

Introduction

When solid ribs are attached on duct walls, poor heat transfer occurs in the region immediately behind the 90° ribs for both rotating and stationary ducts. To reduce the local heat transfer decrement in the rearward concave corners of attached solid 90° ribs, detached solid ribs in non-rotating ducts have been proven effective [1,2]. This study further investigates if detached ribs positioned at a small distance from the walls have better thermal performance than attached ribs for a rotating duct.

Measuring fluid flow in a rotating coolant duct is challenging. Bons and Kerrebrock [3] investigated the internal flow of a single-pass square-sectioned smooth duct for rotating number Ro up to 0.2 using particle image velocimetry (PIV). Liou and Chen [4] focused on the serpentine coolant duct with square cross section and smooth walls to study the effect of 180° sharp turn on the fluid flow and heat transfer enhancement under rotation. Laser-Doppler velocimetry (LDV) measurements were performed for $Ro=0.08$. Servouze [5] presented three-dimensional LDV data in a rotating two-pass duct with a 180 deg sharp turn. Most of the data were obtained at $Ro=0.33$ and $Re=5\times10^3$ with some at $Ro=0.033$ and 0.066 and $Re=2.5\times10^4$. The relationship between the flow field and heat transfer enhancement in rotating smooth duct with a 180 deg sharp turn was systematically investigated by Chen and Liou [6] for $Re=1\times10^4$ and Ro ranged from 0 to 0.2. Their LDV measurements showed as Ro increased that both the skewness of streamwise mean velocity and the magnitude of secondary flow velocity increased linearly, and that turbulence intensity increased non-linearly. They concluded that the rotation-induced increases on the secondary-flow velocity and turbulent kinetic energy all contribute to the averaged heat transfer enhancement in the 180 deg sharp turn. Locally, however, the direction and strength of the secondary flow with respect to the wall are the most important fluid dynamic factors affecting the local heat transfer distributions in the turn region. All of the above fluid flow studies were for orthogonal duct rotation whereas the LDV measurements of Cheah et al. [7] were for a rotating duct with a duct axis parallel to the axis of rotating. Ribs are often arranged on the duct walls to augment heat transfer. Tse and Steuber [8] explored flow characteristics in a serpentine coolant duct with 45-deg ribs using LDV for orthogonal duct rotation. Recently, Liou et al. [9] studied the fluid flow in an orthogonally rotating two-pass square duct with in-line 90-deg ribs. Their LDV data were presented for rib height/hydraulic diameter and rib pitch/height of 0.136 and 10, respectively. The Reynolds number was fixed at 1×10^4 and Ro varied from 0 to 0.2. They found that the rotating ribbed duct flow produces higher $U_{\max}/U_b$ and $u'_{\max}/U_b$, stronger total averaged secondary flow, and higher heat transfer enhancement.

Numerical simulations most relevant to the present study are given below. Prakash and Zerkle [10] concluded that a low Reynolds number model and a Reynolds stress model, respectively, should be adopted to capture the practical aircraft gas turbine engine conditions and anisotropic turbulence effects. Iacovides and Raisee [11] assessed four turbulence models for predicting fluid flow and heat transfer characteristics in serpentine cooling ducts with 90° ribs. They found that the isotropic eddy viscosity model and the widely used wall function approach are unable to capture physically reasonable heat transfer and flow field features since the pressure of the turn and ribs usually generates flow separation and anisotropic turbulence. Jang et al. [12] computed flow and heat transfer in a rotating square duct with 45-deg ribs using a Reynolds stress turbulence model. Their results revealed that the 45-deg rib induced longitudinal vortices, rotating buoyancy, and Coriolis forces generate strong anisotropic turbulent stresses and

Contributed by the International Gas Turbine Institute and presented at the International Gas Turbine and Aeroengine Congress and Exhibition, Amsterdam, The Netherlands, June 3–6, 2002. Manuscript received by the IGTI January 17, 2002. Paper No. 2002-GT-30201. Review Chair: E. Benvenuti.

 Copyright © 2003 by ASME

Downloaded 31 May 2010 to 171.66.16.27. Redistribution subject to ASME license or copyright; see http://www.asme.org/terms/Terms_Use.cfm

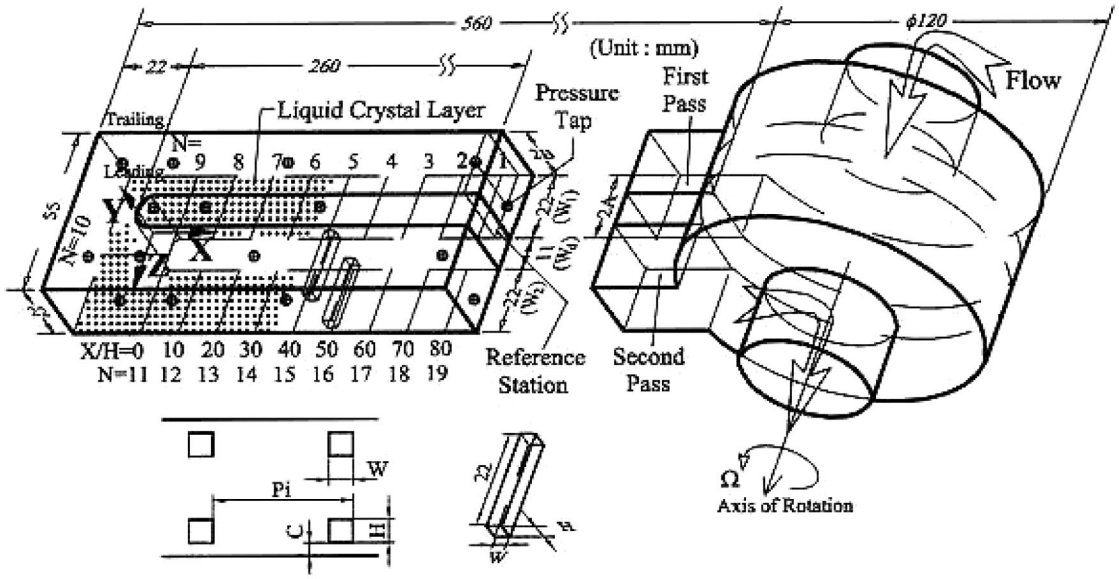

Fig. 1 Sketch of configuration, coordinate system, and dimensions of test section

heat fluxes. Obviously, the computational studies previously cited all suggest the necessity of detailed fluid flow measurements in an orthogonally rotating multi-pass ribbed duct with 180 deg sharp turning, especially under practical aircraft gas turbine engine conditions. Such flow field measurements are still lacking.

Heat transfer measurements in rotating serpentine ducts with 90-deg ribs are more abundant than the corresponding fluid flow measurements. Wagner et al. [13] performed such measurements using thermocouples on square ducts with staggered 90-deg ribs for $\mathrm{Re}=2.5\times10^3$ and Ro varying from 0 to 0.35. The H/D_H and Pi/H of ribs were respectively fixed at 0.1 and 10. They found that the maximum regionally averaged heat transfer coefficients augmented up to 4.5 times from the stationary fully developed circular tube values while the minimum heat transfer coefficients decreased to 50% of the stationary 90-deg ribbed wall results. Parsons et al. [14] performed thermocouple measurements to explore wall heating effect on heat transfer in a rotating two-pass square duct with in-line 90-deg ribs for Ro and Re varying from 0 to 0.35 and 2.5×10^3 to 2.5×10^4, respectively. It should be pointed out that although heat transfer results based on thermocouple readings have provided valuable information for reference, they gave actually regional averaged values instead of local values. In view of this fact, the transient thermochromic liquid crystal thermometry (TLCT) measurements were undertaken by Liou et al. [15] and Liou et al. [9] in rotating two-pass smooth duct and 90-deg ribbed duct, respectively. Nusselt number ratio mappings were provided on the leading and trailing walls to allow the relationships between the local fluid flow and heat transfer to be explored and established. Their results further showed that variations of regional and passage averaged Nusselt number ratios with Ro are in reasonable agreement between the TLCT and thermocouple results. They also found that for the Ro range examined ($\mathrm{Ro}=0\sim0.2$) the passage averaged Nusselt number ratios on the leading and trailing walls of the first and second passes can be correlated as linear functions of Ro.

As mentioned above, detached solid ribs in stationary coolant ducts have been proven effective in reducing heat transfer deterioration immediately behind attached ribs. However, owing to cross-stream secondary flow induced by rotation generated Coriolis and centrifugal forces, fluid flow and heat transfer distributions in rotating coolant ducts are different from those in nonrotating ducts. Hence, there is a need to explore whether the detached ribs can still enhance the heat transfer for rotating coolant ducts. TLCT and LDV will be applied to measure the local heat transfer and flow field distributions. Meanwhile, the coolant pressure losses will also be measured. The information gathered from the foregoing three measurements is believed to provide a useful reference in designing an efficient cooling system and validating the CFD codes.

Experimental Facility and Conditions

Test Section and Conditions. Figure 1 depicts the configuration, coordinate system, and dimensions of the test section made of acrylic sheets 20 mm thick for optical access. The hydraulic diameter of the square cross-sectional flow path was $D_H=22$ mm and the divider-wall thickness was $0.5\,D_H$. At the turn, the clearance between the tip of the divider wall and the duct outer wall was fixed at $1\,D_H$. The 90-deg transverse plexiglas ribs with a thermal conductivity 0.195 W/mK were detached from the leading and trailing walls and directly opposite (not staggered). The detached distance-to-rib height ratio (C/H) was 0.38. One pair of ribs was installed at the divider wall tip in the turn and 9 pairs of ribs in each pass.

The rib height-to-hydraulic diameter ratio (H/D_H) and the rib pitch-to-height ratio (Pi/H) were 0.136 and 10, respectively, in each pass. The Reynolds number, based on the bulk mean air velocity of 7.58 m/s and hydraulic diameter, was fixed at 1.0×10^4. The rotation number varied from 0 to 0.20 corresponding to rotational speeds from 0 to 660 rpm. Note that for comparison purposes the above conditions were selected from those reported by Liou et al. [9] for attached rib case. $C/H=0.38$ is the optimal rib-wall gap for the case of $\mathrm{Ro}=0$ [1,2].

The TLCT measurements were performed in the region 3.5 rib pitches upstream ($-7.3H<X<35H$, first outward pass) to 3.5 rib pitches downstream ($-7.3H<X<35H$, second inward pass) of the turn along the leading ($Y=-1$) and trailing ($Y^*=1$) walls (Fig. 1) while the LDV measurements were undertaken in the region 1.5 rib pitches upstream to 1.5 rib pitches downstream of the turn along the longitudinal central plane of each pass, i.e. $Z^*=\pm0.5$. At each X station the LDV measurements were made at 9 to 14 locations. The wall static pressures were measured at 16 locations indicated in Fig. 1 along the leading and trailing walls of the two-pass ducts with a 180-deg sharp turn. Both LDV and pressure loss measurements were performed without heater on.

Downloaded 31 May 2010 to 171.66.16.27. Redistribution subject to ASME license or copyright; see http://www.asme.org/terms/Terms_Use.cfm

1	Test Section	9	Down-Mixers
2	Timing Gear	10	RMR
3	Rotary Joint	11	Counter
4	Flowmeter	12	CCD & Lamp Facility
5	Encoder or Slip Ring	13	Power Supply
6	Traverse System	14	Data Recorder
7	Fiber Optic Probe	15	Video Capture & GPIB Interface
8	Photo Multipliers		

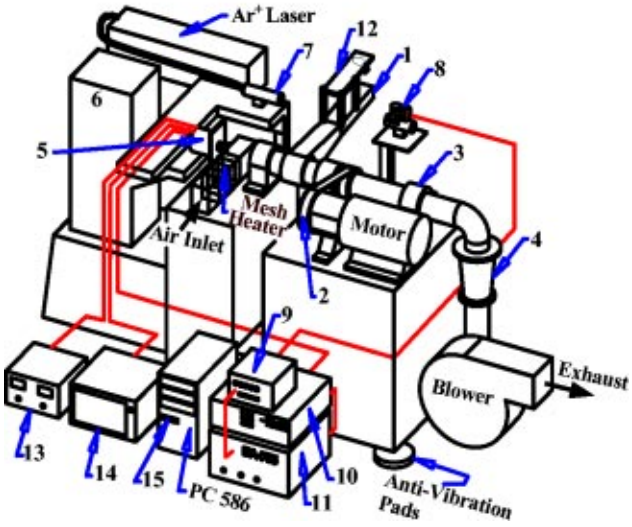

Fig. 2 Schematic drawing of LDV and TLCT facility

Experimental Facility. The experimental facility depicted in Fig. 2 consists of flow system and optical system. The inlet air was heated by a rapid-response mesh heater 100 mm long and flowed radially outward in the first pass. After making a 180-deg sharp turn, the hot air flowed radially inward in the second pass. The air cooled by the colder duct walls was sucked from the test section to ambient by a 2.2-KW turbo blower controlled by a frequency converter. During each test, the mesh heater was switched on to initiate the transient heat transfer rate measurements after the rotating duct flow had attained a steady state which allowed the development of the Coriolis forces in the test duct. By attaching white fluorescent lamps and a digital video camera to the rotating test section, the color change of the liquid crystal coating was recorded when the hot air passed through the test section. The main flow temperatures at the upstream and downstream locations of the test section were recorded using thermocouples and a recorder. The thermocouple junctions were about 0.15 mm in diameter. All the video and temperature data were fed to a PC via a slip ring. A microdifferential transducer (Kyowa PDL-40 GB) connected to 16 pressure taps on the leading and trailing walls (Fig. 1) measured the wall static pressures. The pressure transducer was located on the wall of hollow shaft (Fig. 1), i.e., at a radius of 60 mm. These signals were subsequently amplified and fed via the slip ring to the PC for storage. Note that the microdifferential pressure transducer was referenced to pressure tap located at the inlet reference station, $X^*=11.6$ or $X/H=85$ in Fig. 1. It uses a foil strain gage as its detector element and permits high precision measurement of very small differential pressure. Its accuracy was within $\pm 0.1\%$ of the 400 mmAq(3922 N/m^2) full-scale value.

The principles of TLCT and LDV have been described in detail in authors' previous studies [15,16] and [4,6], respectively. For TLCT, a one-dimensional transient heat conduction analysis was performed. The Duhamel's superposition theorem was adopted to approximate the time history of the main stream air temperature with a series of step functions.

Data Uncertainty

When the technique of TLCT is applied to measure the heat transfer distribution in a rotating duct, one must be cautious about the Nusselt number variation with varying buoyancy effect. Chang [17] and Chang and Morris [18] demonstrated that the effect of centrifugal buoyancy on heat transfer depends on the surface condition of heated wall. For a rotating duct fitted with 90 deg ribs, they found the variation of density ratio $\beta(T_w-T_b)$ from 0.055 to 0.221 caused about 15% Nusselt number variation when Ro and Re were, respectively, 0.2 and 8000. For a rotating smooth duct, the variation of $\beta(T_w-T_b)$ from 0.116 to 0.337 leads to about 50% Nusselt number variation when Ro and Re were 0.15 and 1.3×10^4, respectively. A much narrower range of density ratio, -0.058 to -0.050 (or buoyancy parameter, $\mathrm{Bu}=\beta(T_w-T_b)\times(\Omega D_H/U)(\Omega R/U)=-0.038$ to -0.031), at the inlet reference station for each single test was encountered in the present study with detached ribs and cold walls. This range of density ratio results in about 0.7% (based on ribbed duct [17,18]) to 1.8% (based on smooth duct [17,18]) of Nusselt number variation. Hence, the parameter range tested ($\mathrm{Ro}\leqslant 0.2$, $\mathrm{Re}=1\times10^4$, and $-0.058<\beta(T_w-T_b)<-0.050$) in the present study should not cause considerable buoyancy interaction when each single test was performed. However, the negative values of Bu indicate the buoyancy effect was reversed from the scenario of gas turbine rotor blade during each test. Thus, the present set of data acquired with cool walls and a warming flow is very pertinent, but may not have direct application to gas turbine designer. The most likely use of the data presented is to match these results with those from with computational runs with cooled walls at small Bu values. Once the computational code is verified by the present results, then possibly the computational code could be used to predict actual engine blades with hot walls.

As an indication of the force ratio between centrifugal buoyancy force and inertial force, the present buoyancy parameter in terms of Bu is in the range of -0.038 to -0.031. The test ranges of the buoyancy parameter performed by Wagner et al. [13], Chang and Morris [18], and Prakash and Zerklc [10] were 0.00 $\sim$0.85, 0.00$\sim$1.20, and 0.03$\sim$1.47 respectively. The range of centrifugal buoyancy forces examined by the present study is thus relatively small. As the centrifugal buoyancy effects could, respectively, cause about 30.3, 28.5, and 28.6% of heat transfer variations when the buoyancy parameters were 0.85 [13], 1.20 [18] , and 1.47 [10], it is unlikely that the considerable buoyancy interactions take place within the present test channel when the buoyancy parameters vary from -0.038 to -0.031. Also worth noting that, in order to cause reverse flow by the buoyancy force, the buoyancy parameter has to reach about 1.47 [10] which is far above the buoyancy forces examined by the present study. It is the engineering significance that the detached ribs can provide higher heat transfer coefficients over the attached ribs with rotation, which is one of the focuses for the present investigation. Moreover, a single test using the TLCT technique normally takes 30 $\sim$65 s to complete. This period of time is far less than the time span (at least 30 min) required for the test wall to respond to the changes in the flow and attain another steady state. The flow is affected by the variation of buoyancy force immediately after heater being turned on. In summary, within the parameter range examined by the present study, the heat transfer data generated shall be able to reflect the rotational effects due to negligible buoyancy variation during each single measurement.

The most proper uncertainty in obtaining heat transfer coefficient is estimated to be $\pm 10.0\%$ as a result of ± 1.8, ± 3.5, ± 5.0, ± 5.0, ± 5.5, ± 1.5, and $\pm 1.5\%$ uncertainty in buoyancy effect, time of color change, thermal diffusivity of wall, thermal conductivity of the wall, bulk mean temperature of main stream, green-

Downloaded 31 May 2010 to 171.66.16.27. Redistribution subject to ASME license or copyright; see http://www.asme.org/terms/Terms_Use.cfm

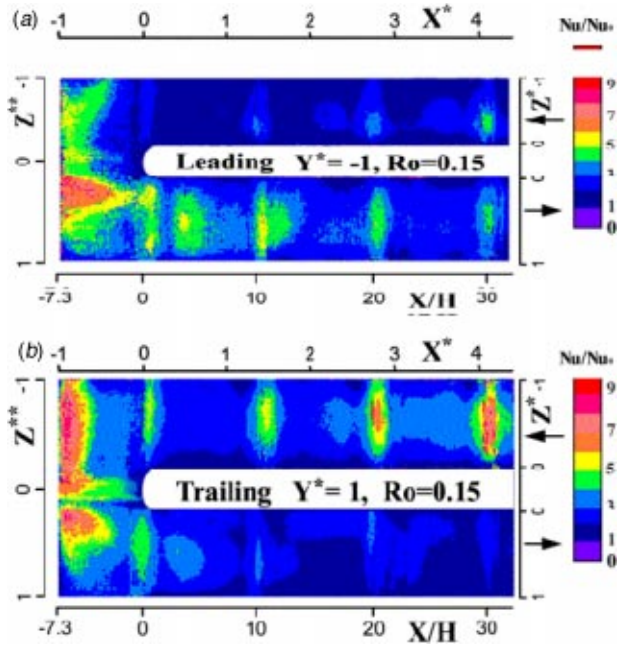

Fig. 3 Detailed local Nusselt number ratio distributions for the detached rib case at Ro=0.15 and Re=1×10^4 on (*a*) leading wall, and (*b*) trailing wall

point temperature, and initial temperature of the wall, respectively. Radiation is negligible since the entire walls of the channel are heated by the mainstream at fairly uniform temperature. The 20-mm test wall has a thermal penetration time 120 s, and is therefore sufficiently thick to meet the semi-infinite solid assumption required by the TLCT technique because the total time for each transient test is typically 30 to 65 s.

The statistical errors in the mean velocity and turbulence intensity are less than 1.8 and 3.1%, respectively, for a 95% confidence level. More detailed uncertainty estimates and velocity bias correlations are included in Liou et al. [4]. For the range of atomizer pressure settings, the saline solution was mixed producing particles from 0.5 to 1.2 μm. This particle diameter range is able to follow turbulence frequencies exceeding 1 KHz (Durst et al. [19]).

The uncertainties in the pressure loss measurements are ± 0.1, ± 0.5, and $\pm 0.1\%$ associated with the pressure transducer temperature effect on output, the slip ring noise, and the amplifier noise, respectively, which leads to a resultant uncertainty of $\pm 0.52\%$.

Results and Discussion

Local and Regional Averaged Heat Transfer. The results of the TLCT measurements are presented as Nu/Nu_0 contours on the leading and trailing walls for Ro=0.15 and Re=1.0×10^4 in Fig. 3. Owing to enhanced convective heat transfer by the wall jet emitting from the rib-wall gap, the poor heat transfer ($Nu/Nu_0 < 1$, purple color in Fig. 3) around the concave corner behind each attached rib reported previously ($C/H=0$, [1,9]) is now absent for the detached rib ($C/H=0.38$) in the entire coolant duct. Because the strength of the wall jet decays with increasing X/H in a pitch, it is expected that heat transfer augmentation by the wall jet will also decrease with increasing X/H. For the case of attached rib, however, the rib-top separated shear layer will curve downward and reattach onto the duct wall, typically $2H$ behind the rib, to disrupt the boundary layer and elevate the heat transfer. Hence, it is interesting to examine the competition between the wall jet and curved downward shear layer on the heat transfer enhancement. Figure 4 depicts such a comparison in terms of regional averaged

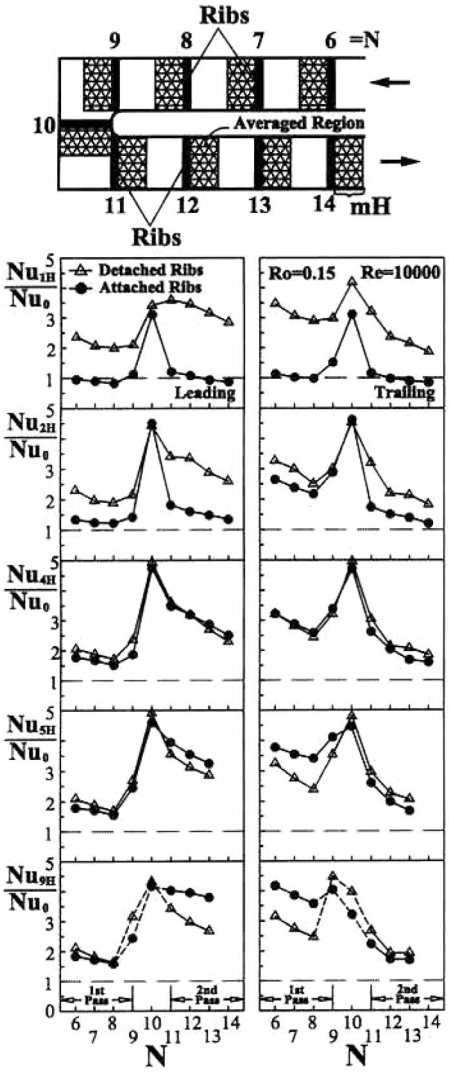

Fig. 4 Variation of regional averaged Nusselt number ratio Nu_{mH}/Nu_0 versus rib index *N* with step-increased region size

Nusselt number ratio [6,9] versus rib index N. In the plot Nu_{mH} ($m=1,2,\ldots,9$) denotes that the local Nu mapping shown in Fig. 3 is integrated and then averaged over the area (mH×channel width) behind each rib in a pitch. In other words, the region size for averaging Nu increases with increasing value of m from 1 to 9 in a pitch. It is seen from Fig. 4 that within the distance $1H$ behind the rib, Nu_{1H}/Nu_0 for detached ribs can be as high as 2 to 3.5 times that for attached ribs on the leading and trailing walls of both ducts.

The appearance of $Nu_{1H}/Nu_0<1$ for the attached rib case reflects the heat transfer deterioration due to the presence of separation bubble behind each rib, as mentioned before. Since the length of the separation bubble is typically less than $2H$, $Nu_{2H}/Nu_0>1$ to $Nu_{9H}/Nu_0>1$ hold in two passages. The detached ribs remain superior to the attached ribs until Nu_{4H}/Nu_0. For Nu_{4H}/Nu_0 the attached and detached ribs are comparable.

Although for Nu_{1H}/Nu_0 to Nu_{4H}/Nu_0 in Fig. 4 the wall jet originating from rib detachment is most prominent in heat transfer augmentation, the competing effect of flow reattachment strengthens with increasing region size (mH increasing) for averaging Nu. Along the leading wall of the first outward duct, the value of Nu_{mH}/Nu_0 remains about the same from Nu_{1H}/Nu_0 to Nu_{9H}/Nu_0 for the detached rib case but increases from Nu_{1H}/Nu_0 to Nu_{4H}/Nu_0 due to flow reattachment for the attached rib case. The

Downloaded 31 May 2010 to 171.66.16.27. Redistribution subject to ASME license or copyright; see http://www.asme.org/terms/Terms_Use.cfm

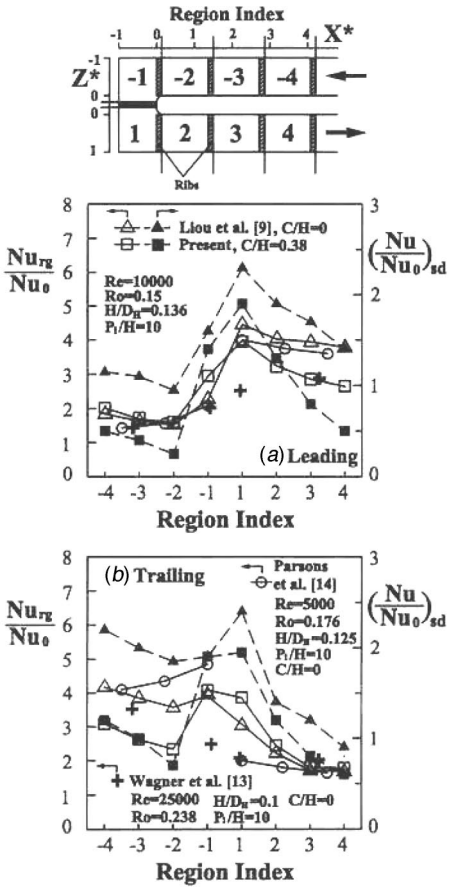

Fig. 5 Regional averaged Nusselt number ratio distributions measured by different researchers on (*a*) leading wall, and (*b*) trailing wall

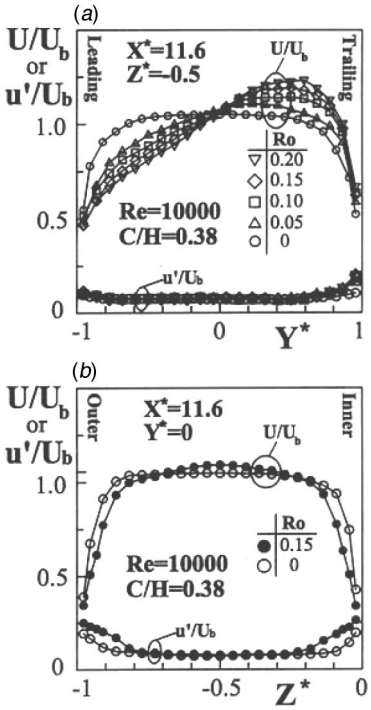

Fig. 6 Streamwise mean velocity and turbulence intensity profiles at inlet reference station $X^*=11.6$ (or $X/H=85$) of the first pass in (*a*) $Z^*=-0.5$, and (*b*) $Y^*=0$ planes

value of Nu_{4H}/Nu_0 to Nu_{9H}/Nu_0 for attached ribs stays at a level slightly below that of the detached rib case. A similar trend for Nu_{mH}/Nu_0 can also be observed along the trailing wall of the second inward duct. Consequently, in a rotating duct detached ribs can enhance the heat transfer on the leading wall of the first outward duct and trailing wall of the second inward duct as compared to corresponding attached rib results, as shown in Fig. 5 (open square versus open triangle, open circle [14], and cross [13]).

In the figure the x-axis parameter is replaced by the region index to facilitate the comparison with previously reported data taken by using thermocouples for $C/H=0$ [13,14]. As mentioned in the Introduction, the reported thermocouple measurements were mostly at one point or at most a few points per pitch, and thus provided actually regional averaged values instead of local values. Note that the Coriolis force is directed away from these two walls. In contrast, along the trailing wall of the first outward duct Fig. 4 shows that the Nu_{mH}/Nu_0 of the attached rib case rallies in the regions $2H$ to $4H$ downstream of the rib to overtake that of the detached rib case and quickly opens up a wide lead from Nu_{4H}/Nu_0 to Nu_{5H}/Nu_0. The lead is maintained to Nu_{9H}/Nu_0 immediately in front of the next rib. Similarly, along the leading wall of the second inward duct the Nu_{mH}/Nu_0 of the attached rib case comes from behind to beat that of the detached rib case. Thus, the heat transfer enhancement of the attached rib case should be larger than that of the detached rib case on the trailing wall of the first outward duct and leading wall of the second inward duct, as shown in Fig. 5 (open triangle, open circle, and cross versus open square). The fluid dynamics reason is that in addition to the flow reattachment of the rib-top separated shear layer, the Coriolis force is directed toward these two walls, all contributing to increase the transverse velocities of fresh core fluid (as will be evidenced later in Figs. 8 and 9) and, in turn, the heat transfer enhancement for the attached rib case. On the other hand, the spreading of wall jet for the detached rib case reduces the effects of flow reattachment and Coriolis force, resulting in smaller transverse velocities of fresh core fluid and lower heat transfer enhancement on the trailing wall of the first outward duct and leading wall of the second inward duct.

Mean Flow Pattern. The inlet reference station was selected at $X^*=11.6$ (or $X/H=85$) which is located at $5H$ distance upstream of the first rib pairs ($N=1$ in Fig. 1) in the first outward duct. Figure 6(*a*) shows the variation of streamwise mean X-component velocity and turbulence intensity profiles with Ro at inlet reference station in $Z^*=-0.5$ plane of the first outward duct. The U/U_b and u'/U_b profiles are rather symmetric for Ro $=0$. As Ro is increased from 0 to 0.2, the skewness of U/U_b and u'/U_b increases monotonically due to the increase of the Coriolis force directed toward the trailing wall ($Y^*=1$) and, in turn, the steeper mean velocity gradient near the trailing wall. The U and u' peaks can be as high as $1.24U_b$ and $0.2U_b$, respectively, for Ro$=0.2$. The uniform parts of u'/U_b profiles extend to (with respect to $Y^*=0$) 70% of the channel height and have values of $7.5\pm0.5\%$. For CFD reference, the boundary layer thickness defined at 95% U_{max} is $\delta_{95}/H=1.3/1.3,3.2/1.2,3.7/1.2,3.8/1.1,4.0/1.0$ along the leading/trailing wall for Ro$=0$, 0.05, 0.10, 0.15, and 0.2, respectively. The corresponding U/U_b and u'/U_b profiles in $Y^*=0$ plane are depicted in Fig. 6(*b*) for Ro$=0$ and 0.15. Because the span plane $Y^*=0$ is perpendicular to the Coriolis force, all the profiles are very symmetric to the central plane $Z^*=-0.5$. The peak U and u' respectively increase from $1.05U_b$ and $0.20U_b$ of Ro$=0$ to $1.10U_b$ and $0.25U_b$ of Ro$=0.15$. The boundary layer thickness is $\delta_{95}/H=1.0/1.0$ and $1.7/1.7$ along the inner/outer wall for Ro$=0$ and 0.15, respectively.

As the fluid flows over the first detached rib pair, the variations of U/U_b and u'/U_b profiles with Ro at the middle station between

Downloaded 31 May 2010 to 171.66.16.27. Redistribution subject to ASME license or copyright; see http://www.asme.org/terms/Terms_Use.cfm

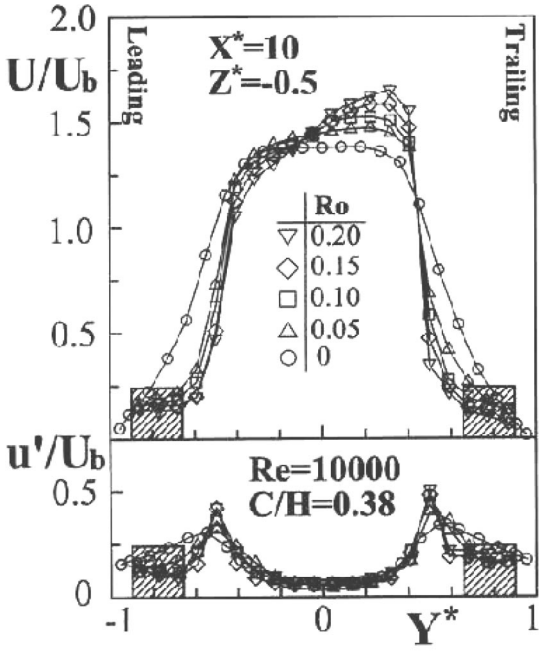

Fig. 7 Variation of streamwise mean velocity and turbulence intensity profiles with rotation number at $X^*=10$ in between $N=1$ and $N=2$ rib pairs of the first pass in $Z^*=-0.5$ plane

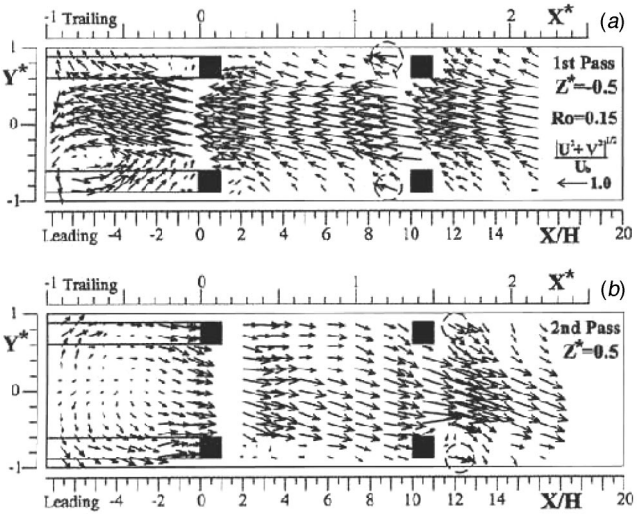

Fig. 8 Mean velocity vector plots around the turn for Ro $=0.15$ and Re$=1.0\times10^4$ in (*a*) first pass, and (*b*) second pass

N=1 and N=2 rib pairs are plotted in Fig. 7. The monotonic increase of skewness with Ro remains. One can see from comparing Fig. 7 with Fig. 6 that the presence of in-line ribs decreases the fluid flow velocity ratio for $|Y^*|>0.4$ due to the blockage of ribs but increases the fluid flow velocity ratio for $|Y^*|<0.4$ due to mass conservation. For the present detached rib duct rotating at Ro=0.2, the maximum U and u' are $1.65U_b$ and $0.51U_b$, respectively while $U_{\max}=1.49\,U_b$ and $u'_{\max}=0.48U_b$ for the attached rib duct at the same Ro [9]. It is obvious that rib detachment reduces the distance between the trailing and leading wall ribs and gives, therefore, higher $U_{\max}$ and mean velocity gradient (or higher $u'_{\max}$) than the attached rib case. Further downstream around the turn, the flow patterns in terms of the mean velocity vector plots in $Z^*=\pm0.5$ planes of the first and second passes are depicted in Figs. 8(*a*) and 8(*b*), respectively. The slant impingement of fluid flow on the trailing wall of the first pass and leading wall of the second pass directed by the Coriolis force is clearly revealed. The corresponding heat transfer on these two walls is shown in contour plots of $\mathrm{Nu/Nu_0}$ in Fig. 3. The edge of the wall jet is barely measured as indicated by the dashed circles in Fig. 8. Since the rib-wall gap is only 1.1 mm, measurements of a full profile of the wall jet were not attainable under rotating condition by using the present LDV system. The absence of main flow reattachment onto the leading and trailing walls is also obvious from Fig. 8. As a consequence, the heat transfer deterioration within the reattachment length behind each attached rib is absent for the detached rib case, providing a more uniform heat transfer distribution (or lower $(\mathrm{Nu/Nu_0})_{sd}$) in the whole coolant duct with detached ribs (solid square versus solid triangle in Fig. 5).

Inside the 180-deg sharp turn ($-1<X^*<0$ or $-7.3<X/H<0$) and in $Z^*=-0.5$ plane (Fig. 8(*a*)), the curvature and rotation make the flow pattern form a strongly skewed Dean-type vortex flow, degenerating into a single vortex located near the duct tip and leading wall. The velocity component normal to the leading or trailing wall plays an important role in augmenting heat transfer. Inside the turn ($-1<X^*<0$) on the first outward duct side, the near wall mean velocity vectors in the region ($Y^*=1$ and $-1<X^*<-0.5$) have larger Y-component and are directed toward the trailing wall ($Y^*=1$). The downwash effect markedly increases the heat transfer rate, as evidenced by the $\mathrm{Nu/Nu_0}$ contour in Fig. 3(*b*). In contrast, the near wall mean velocity vectors in the region ($Y^*=-1$ and $-0.5<X^*<0$) have larger *Y*-component but are directed away from the leading wall. The upwash effect contributes not much to the heat transfer enhancement. For $-1<X^*<-0.5$ on the leading wall, it is mainly the convective sweep of the X-component mean velocities dominates the heat transfer augmentation, except the narrow region ($Y^*=-1$ and $-1<X^*<-0.9$) acted on by down-wash. Thus, the heat transfer enhancement on the leading wall is less prominent than on the trailing wall, as shown in Figs. 3(*a*) and (*b*). Inside the turn ($-1<X^*<0$) on the second inward duct side, the mean velocity vectors have comparable normal and tangential components near the leading wall whereas the tangential components are larger near the trailing wall. Hence, one expects that heat transfer enhancement is higher on the leading wall than on the trailing wall, as can be seen from Figs. 3(*a*) and (*b*). As a whole, Figs. 3 and 5 show that heat transfer distributions inside the turn are less uniform than in the first and second passes.

Surface Heat Transfer and Fluid Flow. As mentioned in the preceding section, the magnitude and direction of the mean transverse velocity component *V* are most essential to the heat transfer enhancement on the leading and trailing walls. Figure 9 gives an example. Immediately before the turn, the fluid flow near the trailing wall between the 8th and 9th rib pairs (Fig. 1) for the attached rib case ($C/H=0$) has larger mean transverse velocity component produces a larger downwash effect than for the detached rib case ($C/H=0.38$), as depicted in Fig. 9(*a*). This observation illustrates why the $\mathrm{Nu}_{rg}/\mathrm{Nu_0}$ with region index -4 to -2 on the trailing wall attained by the attached rib case (empty triangle in Fig. 5(*b*)) are enhanced over the detached rib case (empty square in Fig. 5(*b*)).

Similarly, immediately downstream of the turn, Fig. 9(*b*) shows that the fluid flow near the leading wall between the 11th and 12th rib pairs for the attached rib case has larger $|V|/U_b$ in most part of the region than for the detached rib case. Thus, the regional averaged Nusselt number ratio is higher in region index 2 as indicated in Fig. 5(*a*). Similar trend is observed for $\mathrm{Nu}_{rg}/\mathrm{Nu_0}$ in the regions with region index from 3 to 4. As for the leading wall immediately before the turn and trailing wall immediately after the turn, higher values of $\mathrm{Nu}_{rg}/\mathrm{Nu_0}$ are found for the detached rib case, as shown

Downloaded 31 May 2010 to 171.66.16.27. Redistribution subject to ASME license or copyright; see http://www.asme.org/terms/Terms_Use.cfm

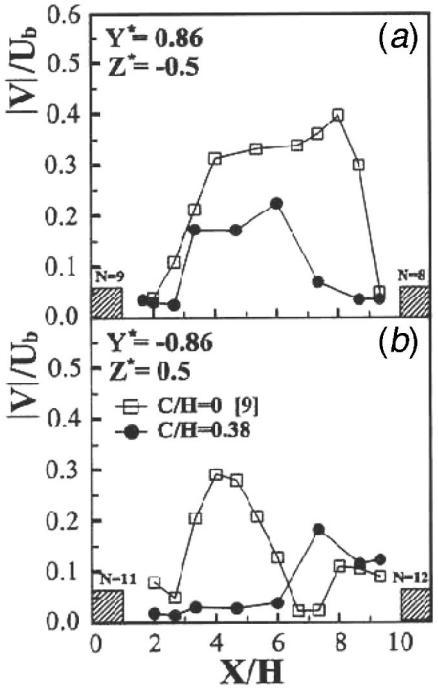

Fig. 9 Variation of the transverse mean velocity component with X/H: (a) immediately before the turn and near the trailing wall ($Y^*=1$), and (b) immediately behind the turn and near the leading wall ($Y^*=-1$)

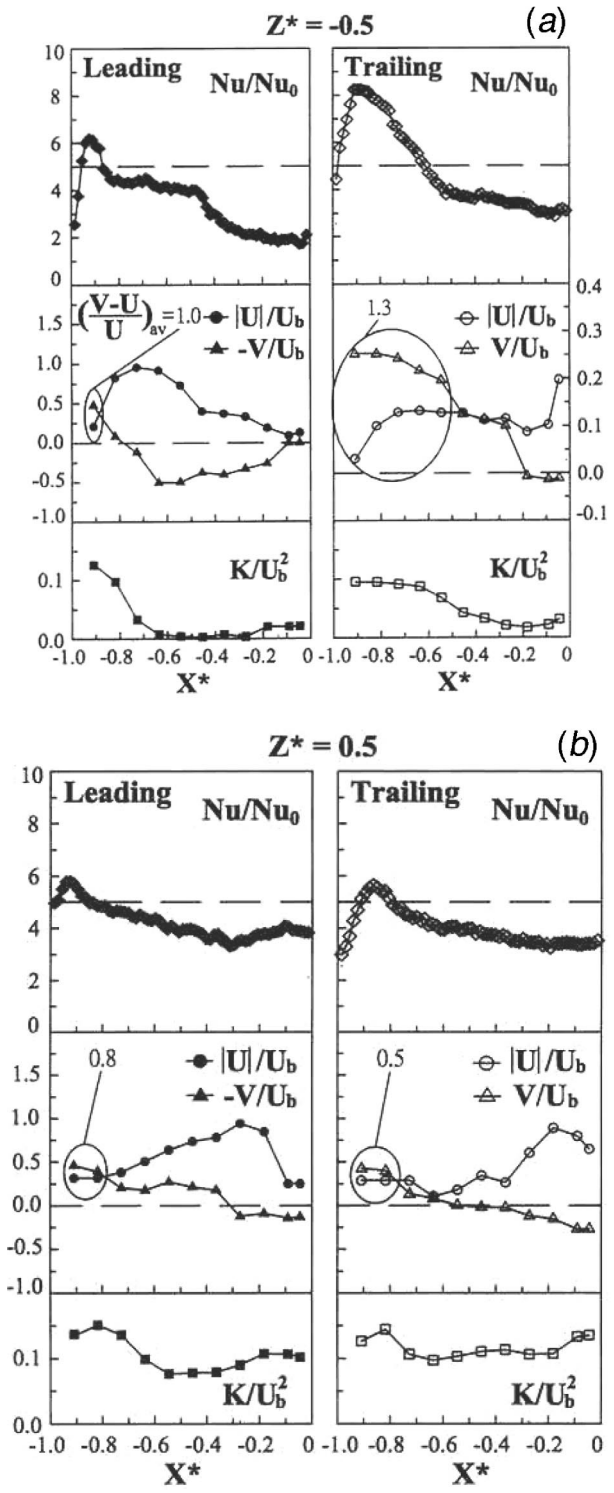

Fig. 10 Relations between mean velocity components, turbulent kinetic energy and surface heat transfer coefficient inside the turn on the leading and trailing walls in (a) $Z^*=-0.5$ plane, and (b) $Z^*=+0.5$ plane for $C/H=0.38$ and $Re=1.0\times10^4$

in Fig. 5 and pointed out previously. It is attributable to the net effect of the wall jet generated convective cooling versus the Coriolis force induced upwash.

It is also interesting to examine the relation between the local fluid dynamic parameters and local surface heat transfer coefficient distributions. Figure 10 shows measurements of X and Y mean velocity components (U/U_b, V/U_b) and turbulent kinetic energy K/U_b^2 along the lines at 1.5 mm away from the leading and trailing walls inside the turn in the longitudinal central planes $Z^*=\pm0.5$. First, the distributions of K/U_b^2 are generally correlated with those of Nu/Nu_0 within measurement uncertainties. In other words, turbulence enhances the heat transfer, as expected. Second, the distributions of Nu/Nu_0 on the trailing wall in $Z^*=-0.5$ plane and on the trailing wall in $Z^*=0.5$ plane toward which the Coriolis force is directed parallel those of V/U_b, as evidenced in Fig. 10. Third, if the attention is focused on the peak region of Nu/Nu_0 in Fig. 10, say the part above $Nu/Nu_0=5$, one finds that the magnitude of positive $[(V\text{-}U)/U]_{av}$ matches with the peak and size of $Nu/Nu_0>5$. Note that physically $(V\text{-}U)/U$ represents the competition between the downwash and convective velocity. $(V\text{-}U)/U>0$ means that the downwash velocity is larger then the convective velocity. Positive $[(V\text{-}U)/U]_{av}$ is the average value of all $(V\text{-}U)/U>0$.

Local Pressure Coefficient and Average Friction Factor. As pointed out by Han [20], to help in designing an efficient cooling system it is important to determine the associated coolant duct pressure losses. Nevertheless, this piece of information is scarce in open literature. Thus, the measured streamwise wall static pressure distributions along the leading and trailing wall for the detached and attached ribbed duct flows examined are plotted in Fig. 11. In general, for fluid flows through a curved duct the streamwise mean velocity displays acceleration near the outer wall for the front part of the turn, but for the latter part of the turn it is reversed. The aforementioned phenomena result from the influence of the streamwise pressure gradient. Prior to examining Fig. 11, note that the locations of pressure taps are depicted in Fig. 1 and that the two pressure taps inside the turn are nearer the outer wall.

It is seen from Fig. 11 that the streamwise pressure gradient is adverse over the leading and trailing walls for the front part of the turn, but for the later part of the turn is on the contrary. Upstream

Downloaded 31 May 2010 to 171.66.16.27. Redistribution subject to ASME license or copyright; see http://www.asme.org/terms/Terms_Use.cfm

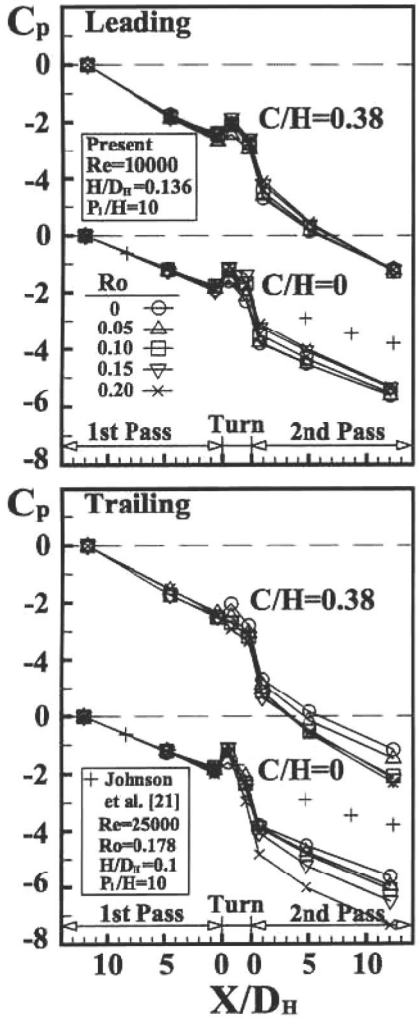

Fig. 11 Variation of dimensionless wall static pressure with X/D_H in detached and attached ribbed duct flows at various rotation number (+: measured along the outer and inner side walls of the first and second pass, respectively)

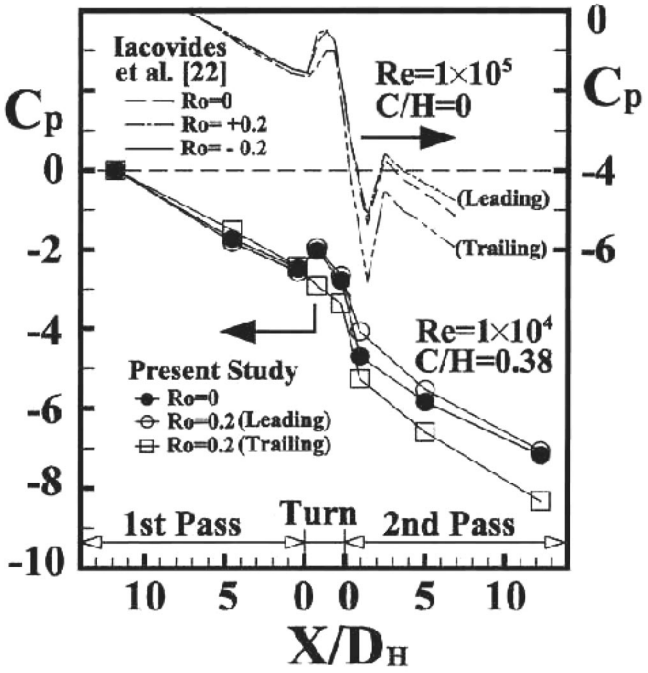

Fig. 12 Variation of dimensionless wall static pressure with X/D_H for orthogonal (present study) and parallel [22] rotations

of the turn in the first pass and downstream of the turn in the second pass, *Cp* decreases linearly with increasing X/D_H as that observed in a straight smooth duct.

For the detached rib case, one may note from Fig. 11 that for the front part of the turn on the trailing wall, the value of *Cp* decreases with increasing Ro or Coriolis force. The reason is as follows. As Ro is increased, the increasing Coriolis force restrains the wall jet from spreading out and, as a result, lowering the static pressure or *Cp* on the trailing wall. Owing to the absence of the wall jet for the attached rib case, the above trend is reversed, as shown in Fig. 11. The pressure loss results measured by Johnson et al. [21] in a rotating square duct ribbed by 90° attached semicircular ribs for $H/D_H=0.1$, $P_i/H=10$, Ro=0.178, and Re=2.5×10^4 are also included in Fig. 11 for comparison. It should be pointed out that their pressure taps were respectively arranged on the outer and inner side wall of the first outward and second inward duct. These side walls are smooth. Thus, their data (cross in Fig. 11) show a pressure loss smaller than the present case. Moreover, since the side wall is perpendicular to the Coriolis force, their data [21] (not included in Fig. 11) indicated an insensitivity to rotation rate for Ro$<$0.238 (or 550 rpm). It is also interesting to present a comparison of *Cp* data between the present orthogonal and previous parallel [22] rotations. As shown in Fig. 12, the results of two studies are in agreement in that the *Cp* distributions on the leading and trailing walls for Ro=0.2 are on the opposite sides of Ro=0 case and that upstream of the turn in the first outward duct frictional losses are insignificantly affected by rotation, at least for Ro$\leqslant$0.2. On the other hand, the results of two studies are different in that immediately after the turn there exists a sudden drop of *Cp* for the case of parallel rotation due to turn-induced flow separation [22], while it is absent for the present orthogonal rotation (also the data of Johnson et al. [21] in Fig. 11) due to the absence of turn induced flow separation [9].

Figure 13 depicts the rotation number dependence of average friction factor *f* in detached and attached ribbed duct flows. Previous results made by Iacovides et al. [22] in attached ribbed duct flow with different rotational mode, Reynolds number, and rib height are also included in Fig. 13 for comparison. The results show an increase of *f* with increasing Ro on the trailing wall but a decrease and a constant of *f* with increasing Ro on the leading wall for the attached and detached rib case, respectively. The above trend on the trailing wall is because of the decrease of *Cp* with increasing Ro on the trailing wall of the second inward duct, as shown in Figs. 11 and 12, away from which the Coriolis force is directed. In contrast, the decrease of *f* with increasing Ro on the leading wall of the attached rib case (Fig. 13) is due to the increase of *Cp* on the leading wall of second inward duct, as shown in Fig. 11, toward which the Coriolis force is directed. The reason for the Ro independence of *f* on the leading wall of the detached ribbed duct (Fig. 13) is that the presence of the wall jet balances the increase of *Cp* on the leading wall of second inward duct. Also, shown in Fig. 13 is that a small distance displacement of the ribs from the wall increases the friction loss approximately 1.1–1.3 times over that of the attached rib case under the same operating conditions. The reason is partly that the detached ribs have four wetted surfaces, whereas the attached ribs have three wetted surfaces. For engineering reference, the Ro dependences of *f* are expressed as compact correlations of linear increase or decrease in Fig. 13 for the range of parameters examined.

Thermal Performance and Heat Transfer Uniformity. From an engineering point of view, it is also useful to compare the thermal performance and heat transfer uniformity for each pass between the detached and attached rib cases. Table 1 summarizes

Downloaded 31 May 2010 to 171.66.16.27. Redistribution subject to ASME license or copyright; see http://www.asme.org/terms/Terms_Use.cfm

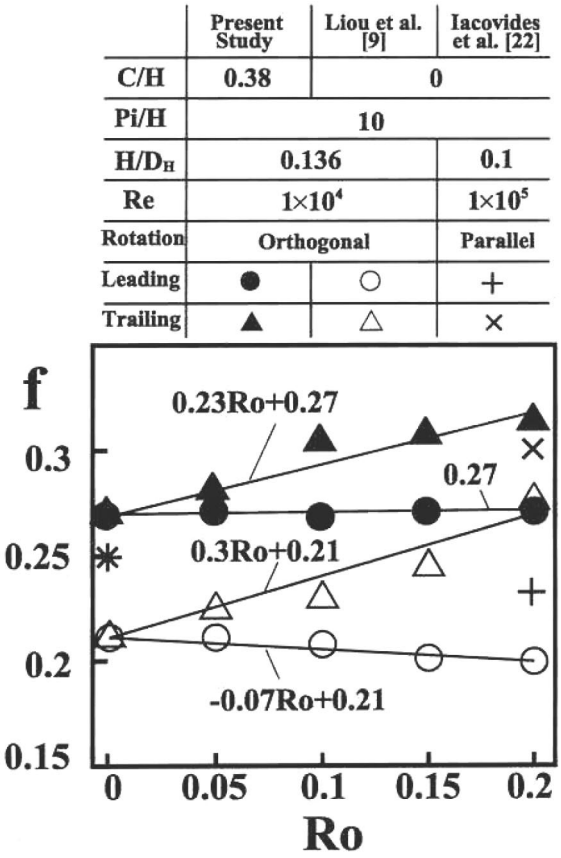

Fig. 13 Friction factor versus rotation number

such a comparison for Ro=0.15 and Re=1×10^4. Based on Fig. 5 and Table 1, the duct averaged Nusselt numbers for detached rib case on the leading wall of the first outward duct and trailing wall of the second inward duct under a constant flow rate/constant pumping work conditions are respectively 1.07/1.14 and 1.15/1.16 times those for the attached rib case ($(\mathrm{Nu}_p)_D/(\mathrm{Nu}_p)_A$ and $(\mathrm{Nu}_p^*)_D/(\mathrm{Nu}_p^*)_A$ in Table 1). Note that if the Reynolds number could be further raised, the above ratios would be even higher [2]. In contrast, $(\mathrm{Nu}_p)_D/(\mathrm{Nu}_p)_A/(\mathrm{Nu}_p^*)_D/(\mathrm{Nu}_p^*)_A$ are 0.77/0.72 and 0.75/0.64 on the trailing wall of the first pass and leading wall of the second pass, respectively. As for the heat transfer uniformity, Fig. 5 and the last column of Table 1 show that rib detachment provides much more uniform heat transfer distributions ($(\mathrm{Nu}_{sd})_D/(\mathrm{Nu}_{sd})_A=0.53\sim0.77$) on the leading and trailing walls of both the first and second passes than rib attachment.

Table 1 A list of regional averaged Nusselt number ratios and heat transfer uniformity in terms of standard deviation for Ro =0.15 and Re=1×10^4

	1st Pass		2nd Pass	
	Lea	Tra	Lea	Tra
$\left(\frac{\mathrm{Nu}_p}{\mathrm{Nu}_0}\right)_D$	2.02	3.01	3.00	2.44
$\left(\frac{\mathrm{Nu}_p}{\mathrm{Nu}_0}\right)_A$	1.89	3.93	4.02	2.13
$\frac{(\mathrm{Nu}_p)_D}{(\mathrm{Nu}_p)_A}$	1.07	0.77	0.75	1.15
$\frac{(\mathrm{Nu}_p^*)_D}{(\mathrm{Nu}_p)_A}$	1.14	0.72	0.64	1.16
$\left(\frac{\mathrm{Nu}}{\mathrm{Nu}_0}\right)_{sd,D}$	0.64	1.20	1.13	1.14
$\left(\frac{\mathrm{Nu}}{\mathrm{Nu}_0}\right)_{sd,A}$	1.20	1.99	1.83	1.48
$\frac{(\mathrm{Nu}_{sd})_D}{(\mathrm{Nu}_{sd})_A}$	0.53	0.60	0.62	0.77

Lea: leading, Tra: trailing, sd: standard deviation

Conclusions

The following main results are drawn from the data presented:

1. The regional averaged Nusselt number ratio indicates that the detached ribs remain superior to the attached ribs until 4 rib heights downstream of the rib for Ro=0.15 and Re=1×10^4. Within this effective distance, the wall jet emitting from the rib-wall gap dominates the heat transfer augmentation.
2. Surface heat transfer distributions inside the turn are found to be less uniform than in the first and second passes. In addition to the contribution of turbulent kinetic energy to the heat transfer enhancement, the parameter $((V\text{-}U)/U)_{\mathrm{av}}$ characterizing the competition between the downwash and convection effect is found to well correlate with peak region of surface local Nusselt number ratio distributions in the turn.
3. The pressure coefficient (C_p) distributions in the two-pass duct with 180 deg turn for the present detached rib case under orthogonal rotation are similar to those for the attached rib case under parallel rotation. The only exception is that immediately after the turn there exists a sudden drop of C_p for the latter due to the presence of turn induced flow separation whereas it is absent for the former due to the absence of turn induced flow separation.
4. For engineering reference, simple expressions are developed to linearly correlate the friction factor with rotation number for detached and attached rib cases.
5. Heat transfer uniformity is significantly improved, $(\mathrm{Nu}_{sd})_D/(\mathrm{Nu}_{sd})_A=0.5$ to 0.8, by detaching the rib array a small distance from the heat transfer wall.
6. Rib detachment enhances the heat transfer over rib attachment for surface heat transfer on the leading wall of the first pass and on the trailing wall of second pass. The trend is, however, reversed on the other two walls.

Acknowledgments

Support for this work was partially provided by the National Science Council of the Republic of China under contract NSC 90-2212-E-007-009-296J3.

Nomenclature

A = half-width of duct [m]
B = half-height of duct [m]
C = stand-off distance between rib and wall [m]
C_p = pressure coefficient, $(P-P_0)/0.5\rho U_b^2$
D_H = hydraulic diameter, $4AB/(A+B)$ [m]
f = friction factor, $(\Delta P/\Delta X)\cdot D_H/(\rho U_b^2/2)$
h = heat transfer coefficient [$\mathrm{Wm^{-2}K^{-1}}$]
H = rib height [m]
k = turbulent kinetic energy $(\overline{u^2}+\overline{v^2})/2$ [$\mathrm{m^2 s^{-2}}$]
k_a = thermal conductivity of air [$\mathrm{Wm^{-1}K^{-1}}$]
k_w = thermal conductivity of plexiglas wall, 0.19 [$\mathrm{Wm^{-1}K^{-1}}$]
Nu = local Nusselt no., $h\cdot D_H/k_a$
Nu_0 = Nusselt number in fully developed tube flow=$0.023\cdot \mathrm{Re}^{0.8}\cdot \mathrm{Pr}^{0.4}$
Nu_{mH} = regional averaged Nusselt with step-increased region size, $m=1$ to 9
Nu_p = pass averaged Nusselt no.

Downloaded 31 May 2010 to 171.66.16.27. Redistribution subject to ASME license or copyright; see http://www.asme.org/terms/Terms_Use.cfm

Nu_{rg} = regional averaged Nusselt no.
Nu_p = pass averaged Nusselt no. for constant pumping power
P_0 = pressure at $X/H=88$ in first pass [Nm^{-2}]
Pi = rib pitch [m]
Pr = Prandtl of air, $\rho C_p \nu / k_a$
Re = Reynolds, $U_b D_H / \nu$
Ro = rotation no., D_H / U_b
U = streamwise mean velocity [ms^{-1}]
U_b = duct bulk mean velocity [ms^{-1}]
u = streamwise velocity fluctuation [ms^{-1}]
u' = rms value of streamwise velocity fluctuation, $\sqrt{u^2}$ [ms^{-1}]
V = transverse mean velocity [ms^{-1}]
v = transverse velocity fluctuation [ms^{-1}]
v' = rms value of transverse velocity fluctuation, $\sqrt{v^2}$ [ms^{-1}]
W = rib width [m]
W_1 = width of first-pass duct, $2A$ [m]
W_2 = width of second-pass duct, $2A$ [m]
W_d = divider thickness [m]
W_d^* = dimensionless divider thickness, $W_d/(W_1+W_2)$
X = streamwise coordinate, Fig. 1 [m]
X^* = normalized streamwise coordinate, X/D_H
Y = transverse coordinate, Fig. 1 [m]
Y^* = normalized transverse coordinate, Y/B
Z = spanwise coordinate, Fig. 1 [m]
Z^*, Z^{**} = normalized spanwise coordinate,
(i) $X<0$, $Z^{**}=Z/(2A+W_d/2)$ (in the turn)
(ii) X 0,$Z<0$,$Z^*=(Z+W_d/2)/2A$ (in the first pass)
(iii) X 0,$Z>0$, $Z^*=(Z-W_d/2)/2A$ (in the second pass)
α_w = thermal diffusivity of wall [m^2/s]
β = thermal expansion coefficient [1/K]
ρ = air density [kg/m^3]
ν = kinematic viscosity [m^2/s]
Ω = rotating speed [rad s^{-1}]

Subscripts

A = attachment
b = bulk
D = detachment
max = maximum value
sd = standard deviation
w = wall

References

[1] Liou, T. M., Wang, W. B., and Chang, Y. J., 1995, "Holographic Interferometry Study of Spatially Periodic Heat Transfer in a Channel with Ribs Detached from One Wall," ASME J. Heat Transfer, **117**, pp. 32–39.
[2] Liou, T. M., and Wang, W. B., 1995, "Laser Holographic Interferometry Study of Developing Heat Transfer in a Duct with a Detached Rib Array," Int. J. Heat Mass Transf., **38**(1), pp. 91–100.
[3] Bons, J. P., and Kerrebrock, J. L., 1999, "Complementary Velocity and Heat Transfer Measurements in a Rotating Cooling Passage with Smooth Walls," ASME J. Turbomach., **121**(4), pp. 651–662.
[4] Liou, T. M., and Chen, C. C., 1999, "LDV Study of Developing Flows through a Smooth Duct with 180-Deg Straight-Corner Turn," ASME J. Turbomach., **121**, pp. 167–174.
[5] Servouze, Y., 1998, "3D Laser Anemometry in a Rotating Cooling Channel," ASME Paper No. 98-GT-123.
[6] Chen, C. C., and Liou, T. M., 2000, "Rotating Effect on Fluid Flow in a Smooth Duct with a 180-Deg Sharp Turn," The 45th ASME International Gas Turbine & Aeroengine Technical Congress, Munich, Germany. ASME Paper No. 2000-GT-228.
[7] Cheah, S. C., Iacovides, H., Jackson, D. C., Ji, H., and Launder, B. E., 1996, "LDA Investigation of the Flow Development through Rotating U-Ducts," ASME J. Turbomach., **118**, pp. 590–596.
[8] Tse, G. N., and Steuber, G. D., 1997, "Flow in a Rotating Square Serpentine Coolant Passage with Skewed Trips," ASME Paper No. 97-GT-529.
[9] Liou, T. M., Chen, M. Y., and Tsai, M. H., 2001, "Fluid Flow and Heat Transfer in a Rotating Two-Pass Square Duct with In-Line 90° Ribs," 46th ASME Int. Gas Turbine & Aeroengine Technical Congress, LA, ASME Paper No. 2001-GT-0185.
[10] Prakash, C., and Zerkle, R., 1995, "Prediction of Turbulent Flow and Heat Transfer in a Ribbed Rectangular Duct With and Without Rotation," ASME J. Turbomach., **177**, pp. 255–264.
[11] Iacovides, H., and Raisee, M., 1999, "Recent Progress in the Computation of Flow and Heat Transfer in Internal Cooling Passages of Turbine Blades," Int. J. Heat Fluid Flow, **20**, pp. 320–328.
[12] Jang, Y. J., Chen, H. C., and Han, J. C., 2000, "Flow and Heat Transfer in a Rotating Square Channel with 45° Angled Ribs by Reynolds Stress Turbulence Model," 45th ASME Int. Gas Turbine & Aeroengine Technical Congress, Munich, Germany, ASME paper No. 2000-GT-0229.
[13] Wagner, J. H., Johnson, B. V., Graziani, R. A., and Yeh, F. C., 1992, "Heat Transfer in Rotating Serpentine Passages with Trips Normal to the Flow," ASME J. Turbomach., **114**, pp. 847–857.
[14] Parsons, J. A., Han, J. C., and Zhang, Y. M., 1994, "Wall Heating Effect on Local Heat Transfer in a Rotating Two-Pass Square Channel with 90° Rib Turbulators," Int. J. Heat Mass Transf., **37**(9), pp. 1411–1420.
[15] Liou, T. M., Chen, C. C., and Chen, M. Y., 2001, "TLCT and LDV Measurements of Heat Transfer and Fluid Flow in a Rotating Sharp Turning Duct," Int. J. Heat Mass Transf., **44**(9), pp. 1777–1787.
[16] Liou, T. M., Chen, C. C., and Tsai, T. W., 2000, "Heat Transfer and Fluid Flow in a Square Duct with 12 Different Shaped Vortex Generators," ASME J. Heat Transfer, **122**, pp. 327–335.
[17] Chang, S. W., 1995, "An experimental study of heat transfer in the cooling passages of gas turbine rotor blades," Doctoral dissertation, Department of Mechanical Engineering, University of Wales, Swansea, UK.
[18] Chang, S. W., and Morris, W. D., 1998, "A comparative study of heat transfer between rotating circular smooth-walled and square rib-roughened ducts with cooling application for gas turbine rotor blade," JSME Int. J. Series B, **41**, pp. 302–315.
[19] Durst, F., Melling, A., and Whitelaw, J. H., 1976, *Principles and Practice of Laser-Doppler Anemometry*, Academic Press, New York, NY.
[20] Han, J. C., 2001, "Gas Turbine Heat Transfer and Cooling Technology," Proc. 35th National Heat Transfer Conference, Anaheim, CA.
[21] Johnson, B. V., Wagner, J. H., and Steuber, G. D., 1991, "Effects of Rotation on Coolant Passage Heat Transfer-Volume II Coolant Passages with Trips Normal and Skewed to the Flow," NASA Contractor Report 4396, pp. 103–108.
[22] Iacovides, H., Jackson, D. C., Ji, H., Kelemenis, G., Launder, B. E., and Nikas, K., 1996, "LDV Study of the Flow Development Through an Orthogonally Rotating U-Bend of Strong Curvature and Rib Roughened Walls," ASME Paper No. 96-GT-478.

Downloaded 31 May 2010 to 171.66.16.27. Redistribution subject to ASME license or copyright; see http://www.asme.org/terms/Terms_Use.cfm

Spatially Resolved Heat Transfer and Friction Factors in a Rectangular Channel With 45-Deg Angled Crossed-Rib Turbulators

P. M. Ligrani

G. I. Mahmood

Convective Heat Transfer Laboratory,
Department of Mechanical Engineering,
University of Utah,
Salt Lake City, UT 84112

Spatially resolved Nusselt numbers, spatially averaged Nusselt numbers, and friction factors are presented for a stationary channel with an aspect ratio of 4 and angled rib turbulators inclined at 45 deg with perpendicular orientations on two opposite surfaces. Results are given at different Reynolds numbers based on channel height from 10,000 to 83,700. The ratio of rib height to hydraulic diameter is .078, the rib pitch-to-height ratio is 10, and the blockage provided by the ribs is 25% of the channel cross-sectional area. Nusselt numbers are given both with and without three-dimensional conduction considered within the acrylic test surface. In both cases, spatially resolved local Nusselt numbers are highest on tops of the rib turbulators, with lower magnitudes on flat surfaces between the ribs, where regions of flow separation and shear layer reattachment have pronounced influences on local surface heat transfer behavior. The augmented local and spatially averaged Nusselt number ratios (rib turbulator Nusselt numbers normalized by values measured in a smooth channel) vary locally on the rib tops as Reynolds number increases. Nusselt number ratios decrease on the flat regions away from the ribs, especially at locations just downstream of the ribs, as Reynolds number increases. When adjusted to account for conduction along and within the test surface, Nusselt number ratios show different quantitative variations (with location along the test surface), compared to variations when no conduction is included. Changes include: (i) decreased local Nusselt number ratios along the central part of each rib top surface as heat transfer from the sides of each rib becomes larger, and (ii) Nusselt number ratio decreases near corners, where each rib joins the flat part of the test surface, especially on the downstream side of each rib. With no conduction along and within the test surface (and variable heat flux assumed into the air stream), globally-averaged Nusselt number ratios vary from 2.92 to 1.64 as Reynolds number increases from 10,000 to 83,700. Corresponding thermal performance parameters also decrease as Reynolds number increases over this range, with values in approximate agreement with data measured by other investigators in a square channel also with 45 deg oriented ribs. [DOI: 10.1115/1.1565353]

Introduction

Many techniques are used for enhancing convective heat transfer rates in gas turbine engine passages used for internal cooling of turbine airfoils and combustion chamber liners. These include rib turbulators, pin fins, jet impingement cooling, dimpled surfaces, surface roughness, surfaces with protrusions or other types of turbulence promoters, and swirl chambers. All of these devices act to increase secondary flows and turbulence levels to enhance mixing, in some cases, to form coherent fluid motions in the form of streamwise oriented vortices. Such vortices and secondary flows not only act to increase secondary advection of heat away from surfaces, but also to increase three-dimensional turbulence production by increasing shear and creating gradients of velocity over significant flow volumes. These then give larger magnitudes of turbulence transport over larger portions of the flow fields. The overall objective of each device is then significant enhancement of turbulence transport and convective heat transfer coefficients with minimal increases in pressure penalties. To determine the capabilities of these devices in accomplishing these tasks, spatially-resolved, spatially averaged, and globally averaged heat transfer coefficient data are needed, along with friction factors. The present paper presents such data for internal passages with ribs.

The earliest experimental studies of ribbed channels consider *single pass, stationary channels with no rotation*. Of these studies, Han et al. [1] address the effects of rib shape, angle of attack, and pitch-to-height ratio. According to the investigators, ribs with 45 deg inclinations produce better heat transfer performance than ribs with 90 deg orientations, when compared at the same friction power. Han and Park [2] vary the channel aspect ratio, and conclude that the best heat transfer performance is obtained using a square channel with a rib turbulator angle of attack from 30 to 45 deg. This range of angles of attack also yields the best heat transfer performance for rectangular channels.

Han et al. [3] indicate that best heat transfer enhancements in square channels are produced by V-shaped ribs with 45 deg and 60 deg arrangements, followed by 45 deg and 60 deg parallel ribs, which are followed by 45 deg and 60 deg crossed ribs. Han et al. [4] investigate wedge-shaped and delta-shaped turbulence promoters in square channels, and compare their performance with existing data for different types of rib turbulators. Delta-shaped ribs generally perform better than the wedge-shaped ribs, especially when the delta-shaped ribs on opposite walls are aligned, and arranged with a backward flow direction. The investigators also indicate that broken configurations of delta-shaped ribs and wedge-shaped ribs both give better performance than full-length configurations. Taslim et al. [5] provide additional evidence that

Contributed by the International Gas Turbine Institute and presented at the International Gas Turbine and Aeroengine Congress and Exhibition, Amsterdam, The Netherlands, June 3–6, 2002. Manuscript received by the IGTI October 24, 2001. Paper No. 2002-GT-30215. Review Chair: E. Benvenuti.

 Copyright © 2003 by ASME

Downloaded 31 May 2010 to 171.66.16.27. Redistribution subject to ASME license or copyright; see http://www.asme.org/terms/Terms_Use.cfm

45 deg ribs produce higher thermal performance parameters than 90 deg ribs. The authors also indicate that, of the configurations examined, the highest heat transfer enhancements and highest friction factors are produced by low-blockage ratio V-shaped ribs. In a later study, Taslim et al. [6] study twelve different geometries of ribs that are placed on all four walls of channels with both square and trapezoidal cross sections. Compared to channels with ribs on two walls, heat transfer coefficients and thermal performance parameters are enhanced.

More recent studies of *stationary channels with no rotation consider single pass and multi-pass channels*. Wang et al. [7] present heat transfer results from square ducts with 45 deg ribs. Thurman and Poinsatte [8] measure heat transfer and bulk air temperature in a three-pass duct with orthogonal ribs and bleed holes both located on one wall. According to the investigators, changing the locations of the ribs relative to the holes produces large changes to surface heat transfer coefficient distributions. Cho et al. [9] employ continuous and discrete, parallel and cross arrays of ribs in a single-pass square duct. Discrete ribs with gaps in between are found to produce more uniform heat transfer coefficient distributions than continuous ribs.

A number of other experimental and numerical studies also address the effects of rib turbulators on heat transfer in internal channels. Considered are single pass and multi-pass channels, square and rectangular channels, channels with and without rotation, and rotating channels with different orientations with respect to the axis of rotation. A review of these techniques, as well as other arrangements for internal passage cooling, is given by Ligrani et al. [10].

The present experimental study is conducted using a large-scale test section, without rotation, so that detailed, spatially resolved surface Nusselt numbers, and friction factors can be measured. A single-pass channel with aspect ratio of 4 is employed, which models internal cooling passages employed near the mid-chord and trailing edge regions of turbine airfoils used in gas turbine engines for utility power generation. The ribs are placed so that they are perpendicular to each other on the two widest, opposite walls of the channel with 45 deg angles with respect to the streamwise flow direction. Reynolds numbers, based on channel height, range from 10,000 to 83,700. Included are Nusselt number data obtained with and without analysis of conduction variations along and within the acrylic test surface. The one other study which uses a stationary, non rotating test section, similar rib geometry, and same channel aspect ratio [2], does not present spatially resolved surface heat transfer data. Two other studies with similar (but not exactly matching) rib turbulator geometry and non-rotating test sections, either use a square channel [5] or a channel with an aspect ratio of 20 [7]. Unlike the present investigation, none of these studies account for detailed conduction variations along and within the ribbed test surfaces employed.

The results given in the present paper are thus new and unique because of these differences, and because new spatially-resolved heat transfer and friction factor ratio data are presented and interrelated to each other, something which is impossible for experimental rotating ribbed channel studies [10]. Included in the present study for different channel Reynolds numbers are: (i) spatially resolved, spatially averaged, and globally averaged surface Nusselt number data assuming constant surface heat flux next to the air stream (with no conduction analyses applied to the ribbed test surface), (ii) spatially resolved, spatially averaged, and globally-averaged surface Nusselt number data for variable surface heat flux next to the air stream (determined from conduction analyses applied to the ribbed test surface), and (iii) friction factor data. Also discussed are the effects of thermal boundary layer development on Nusselt number ratios. These results are valuable because of the spatial resolution of the heat transfer data, and because conduction along and within the ribbed test surface is included in the analyses of the experimental results.

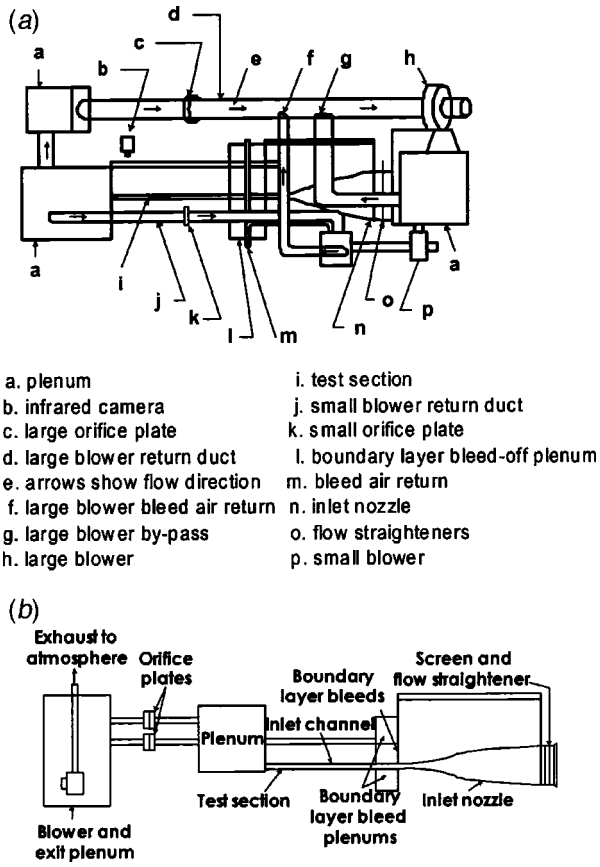

Fig. 1 Schematic diagrams of (*a*) the experimental apparatus used for heat transfer measurements, and (*b*) the experimental apparatus used for flow visualizations and measurements of flow structure

Experimental Apparatus and Procedures

The overall experimental apparatus (but not the test section) is similar to the one described by Mahmood et al. [11]. A brief description of this apparatus is also presented here.

Channel and Test Surface for Heat Transfer Measurements. A schematic of the facility used for heat transfer measurements is shown in Fig. 1(*a*). The air used within the facility is circulated in a closed-loop. The air mass flow rate from the test section is measured (upstream of the blower employed) using an ASME standard orifice plate and Validyne M10 digital pressure manometer. The blower then exits into a series of two plenums (0.9 m square and 0.75 m square). A Bonneville cross-flow heat exchanger is located between two of these plenums, and is cooled with liquid nitrogen at flow rate appropriate to give the desired air temperature at the exit of the heat exchanger. As the air exits the heat exchanger, it enters the second plenum, from which the air passes into a rectangular bell mouth inlet, followed by a honeycomb, two screens, and a two-dimensional nozzle with a contraction ratio of 5.6. This nozzles leads to a rectangular cross section, 411 mm by 103 mm inlet duct which is 1219 mm in length. This is equivalent to 7.4 hydraulic diameters (where hydraulic diameter is 164.7 mm). Two trips are employed on the top and bottom surfaces of the inlet duct, just upstream of the test section, which follows with the same cross section dimensions. It exits to another duct, and then to a 0.60 m square plenum, which is followed by two pipes, each containing an orifice plate, mentioned earlier.

Figure 2 gives the geometric details of the test surface, including rib turbulator geometry. A total of 13 ribs or rib segments are used on the top wall and on the bottom wall of the test section. As

Downloaded 31 May 2010 to 171.66.16.27. Redistribution subject to ASME license or copyright; see http://www.asme.org/terms/Terms_Use.cfm

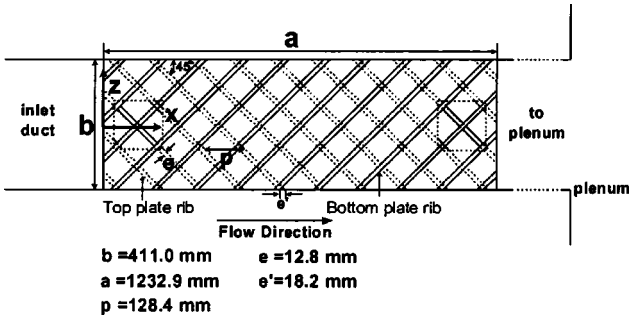

Fig. 2 Schematic diagram of the rib turbulator test surfaces, including coordinate system

mentioned, these are arranged with 45 deg angles with respect to the streamwise flow direction, such that the ribs on opposite walls of the channel are perpendicular to each other. Each rib has 12.8 mm height and square cross section. The ratio of rib height to hydraulic diameter is .078, the rib pitch-to-height ratio is 10, and the blockage provided by the ribs is 25% of the channel cross-sectional area. The top wall of the test section also has two cut-out regions (one at the upstream end and one at the downstream end) where a zinc-selenide window can be installed to allow the infrared camera to view a portion of the test surface on the bottom wall. When this window is not in use, inserts with ribs (which exactly match the adjacent rib turbulators on the top wall) are used in its place. Also identified in Fig. 2 is the test section coordinate system employed for the study. Note that the Y coordinate is directed normal to the bottom wall.

All exterior surfaces of the facility (between the heat exchanger and test section) are insulated with Styrofoam ($k=0.024$ W/mK), or 2 to 3 layers of 2.54 cm thick, Elastomer Products black neoprene foam insulation ($k=0.038$ W/mK) to minimize heat losses. Calibrated copper-constantan thermocouples are located between the three layers of insulation located all around the test section to determine conduction losses. Between the first layer and the 3.2-mm-thick acrylic test surfaces are custom-made Electrofilm etched-foil heaters (each encapsulated between two thin layers of Kapton) to provide a constant heat flux boundary condition on the test surface. The acrylic surfaces, which are adjacent to the airstream, contain 35 copper-constantan thermocouples, which are placed within the ribs as well as within flat portions of the test surfaces between the ribs. Each of these thermocouples is located 0.051 cm just below the surface to provide measurements of local surface temperatures, after correction for thermal contact resistance and temperature drop through the 0.051 cm thickness of acrylic. Acrylic is chosen because of its low thermal conductivity ($k=0.16$ W/mK at 20°C) to minimize streamwise and spanwise conduction along the test surfaces, and thus, minimize ''smearing'' of spatially varying temperature gradients along the test surfaces. Energy balances, performed on the heated test surfaces, then allow determination of local magnitudes of the convective heat flux.

The mixed-mean stagnation temperature of the air entering the test section is measured using five calibrated copper-constantan thermocouples spread across its cross section. To determine this temperature, thermocouple-measured temperatures are corrected for thermocouple wire conduction losses, channel velocity variations, as well as for the differences between stagnation and recovery temperature. All measurements are obtained when the test facility is at steady state.

Local Nusselt Number Measurement. To determine the surface heat flux (used to calculate heat transfer coefficients and local Nusselt numbers), the convective power levels provided by the etched foil heaters are divided by flat test surface areas. Spatially resolved temperature distributions along the bottom rib turbulator test surface are determined using infrared imaging in conjunction with thermocouples, energy balances, and in-situ calibration procedures [11,12]. To accomplish this, the infrared radiation emitted by the heated interior surface of the channel is captured using a VideoTherm 340 Infrared Imaging Camera, which operates at infrared wavelengths from 8 μm to 14 μm. Temperatures, measured using the calibrated, copper-constantan thermocouples distributed along the test surface adjacent to the flow, are used to perform the *in situ* calibrations simultaneously as the radiation contours from surface temperature variations are recorded.

This is accomplished as the camera views the test surface through a custom-made, zinc-selenide window (which transmits infrared wavelengths between 6 and 17 μm) located on the top wall of the test section. Eleven to thirteen thermocouple junction locations are usually present in the infrared field viewed by the camera. The exact spatial locations and pixel locations of these thermocouple junctions and the coordinates of a 12.7 cm by 12.7 cm field of view are known from calibration maps obtained prior to measurements.

Images from the infrared camera are recorded as 8-bit gray-scale images on commercial videotape using a Panasonic AG-1960 video recorder. Images are then digitized using NIH Image v1.60 software, operated on a Power Macintosh 7500 PC computer. Subsequent software is used to convert each of 256 possible gray scale values to local Nusselt number values at each pixel location using calibration data. Thermal conductivity in the Nusselt number is based on the average of the local wall temperature and the temperature of the air at the upstream inlet. Sargent et al. [12] and Mahmood et al. [11] provide additional details on the infrared imaging and measurement procedures.

Friction Factors. Wall static pressures are measured along the test section simultaneously as the heat transfer measurements are conducted, using 12 side wall pressure taps, located 25.4 mm apart near the downstream portion of the test section. These measurements are made in the test section with rib turbulators, as well as in a baseline test section with smooth surfaces on all four walls. Friction factors are then determined from streamwise pressure gradient magnitudes. In some cases, friction factors are measured using the facility shown in Fig. 1(*b*), which is ordinarily used for flow visualizations and measurements of flow structure. Pressures from the wall pressure taps are measured using Celesco LCVR pressure transducers. Signals from these transducers are processed using Celesco CD10D Carrier-Demodulators. Voltages from the Carrier-Demodulators are acquired using a Hewlett-Packard 44422A data acquisition card installed in a Hewlett-Packard 3497A data acquisition control unit, which is controlled by a Hewlett-Packard A4190A Series computer.

Uncertainty Estimates. Uncertainty estimates are based on 95% confidence levels, and determined using procedures described by Kline and McClintock [13] and Moffat [14]. Uncertainty of temperatures measured with thermocouples is 0.15°C. Spatial and temperature resolutions achieved with the infrared imaging are about 0.52 mm and 0.8°C, respectively. This magnitude of temperature resolution is due to uncertainty in determining the exact locations of thermocouples with respect to pixel values used for the in-situ calibrations. Local Nusselt number ratio uncertainty is then about ± 0.13 (for a ratio of 2.00), or about $\pm 6.5\%$. Reynolds number uncertainty is approximately $\pm 1.7\%$ for Re_H of 10,000. The uncertainties of local wall static pressure (relative to atmospheric pressure), and channel friction factors are ± 3.0 and $\pm 4.5\%$, respectively.

Conduction Analyses Within the Test Surface

Three-dimensional conduction along and within the test surface is determined using version 6.0 of the ANSYS numerical code. To accomplish this, a portion of the test surface, with one rib segment, is modeled using approximately 16,441 numeric node elements. In addition, a constant heat flux boundary condition (de-

Downloaded 31 May 2010 to 171.66.16.27. Redistribution subject to ASME license or copyright; see http://www.asme.org/terms/Terms_Use.cfm

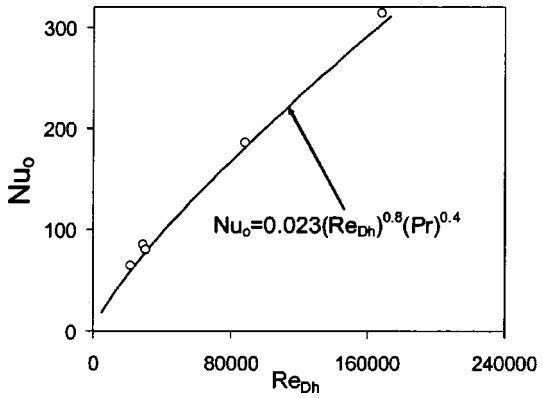

Fig. 3 Baseline Nusselt numbers, measured with smooth channel surfaces and constant heat flux boundary condition, as dependent upon Reynolds number based on hydraulic diameter

termined from values used in the experiments) is imposed on the back side of the 3.2-mm-thick acrylic test surface. Local surface temperatures, measured experimentally using infrared thermography, are used for the thermal boundary condition on portions of the test surface next to the air stream, including the top of the rib segment and the flat parts of the test surface around the rib. Temperatures are also imposed as the thermal boundary condition on the vertical parts of the rib segment, which are determined by interpolation of values measured at the edge of the rib top and at the corner (between each rib side and flat parts of the test surface). Except for small, local variations, this approach is validated by results presented by Metzger et al. [15].

Ordinarily, without the conduction analysis applied, the same heat flux produced by the etched-foil heater is assumed to leave the test surface next to the air stream at the rib top and along the flat parts of the test surface around the rib. This means that no heat is assumed to leave the vertical side walls of the rib, and that all of the thermal power into the test surface leaves entirely only from the horizontal surfaces next to the air stream. The ANSYS version 6.0 conduction analysis is used to determine the nonuniform variations of surface heat flux into the air stream, which are actually present, including along the vertical sides of the rib segment. As mentioned, this is accomplished using experimentally measured values as thermal boundary conditions around the numerical domain solved by the numerical code.

Experimental Results and Discussion

Baseline Nusselt Numbers. Baseline Nusselt numbers Nu_o, used to normalize the ribbed channel values, are measured in a smooth rectangular test section with smooth walls replacing the two ribbed test surfaces. Except for the absence of the ribs, all geometric characteristics of the channel are the same as when the ribbed test surfaces are installed. These measurements are made in the downstream portions of the test section where the channel flow is hydraulically and thermally fully developed. All Nu_o baseline values are obtained using a T_{oi}/T_w temperature ratio of 0.93 to 0.95. In addition, baseline measurements are conducted with all four surfaces wrapped with etched foil heaters to provide a heat flux boundary condition around the entire test section. The variation of baseline Nusselt numbers with Reynolds number Re_{Dh} is shown in Fig. 3. Here, values determined from an average of measurements made on the top and bottom walls, are presented. These values are in agreement with the Dittus-Boelter smooth circular tube [16] for $Re_{Dh}<180{,}000$.

Spatially Resolved Distributions of Local Nusselt Numbers. Figure 4 presents spatially resolved Nusselt number ratios, measured over about two periods of ribbed pattern, on the bottom test

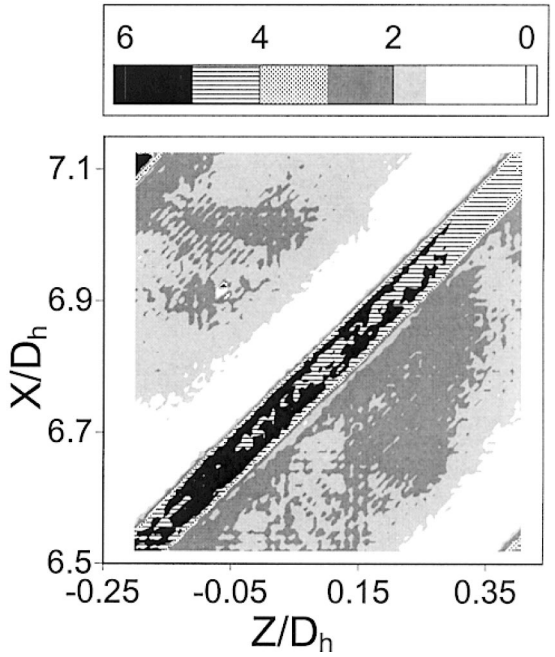

Fig. 4 Local Nusselt number ratio Nu/Nu$_o$ distribution along the rib turbulator test surface for Re$_H$=48,000 and T_{oi}/T_w =0.94, with constant surface heat flux and no surface conduction analysis applied

surface. The results are shown for $Re_H=48{,}000$ and $T_{oi}/T_w=0.94$, and are obtained with constant surface heat flux and no surface conduction analysis applied. In the figure, flow is directed from bottom to top in the increasing X/D_h direction. The darker diagonal regions show Nu/Nu_o values measured on the tops of the ribs. The data presented are time-averaged, determined from 25 instantaneous data sets acquired over a period of 25 s.

As indicated in Fig. 4, Nu/Nu_o ratios are relatively very high along the tops of the ribs. When compared along the rib tops, values are then highest near the upstream and downstream edges. As one moves from the rib in the streamwise or $+X/D_h$ direction, local Nu/Nu_o values initially decrease, and then are low relative to other locations on the test surface. This is due to a recirculating flow region just downstream of the rib, where the flow direction next to the surface is opposite to the bulk flow direction. Note that a shear layer forms between this recirculating flow region and the bulk flow located just above the rib. A region with relatively higher values of Nu/Nu_o then follows at slightly higher X/D_h (where $Nu/Nu_o>2.0$), which is due to reattachment of this shear layer which is initially formed above the recirculating flow region. With an additional increase in streamwise development, Nu/Nu_o values decrease slightly once again (and then sometimes increase locally) as a second 45 deg rib is approached. These are due to a smaller region of recirculating flow which forms just upstream of each rib turbulator. This pattern of flow and surface Nusselt number variations then repeats itself as additional ribs are encountered along the test surface. Other factors which affect the heat transfer augmenations are the skewing and three-dimensional nature of the boundary layer which develops due to the angled orientations of the ribs. Increased levels of three-dimensional turbulence production, turbulence transport, and the large-scale vortex pairs, which form in the channel, also make contributions [10].

The results presented in Fig. 4 for $Re_H=48{,}000$ are again given in Fig. 5, but with variable surface heat flux and surface conduction analysis applied. Comparison of these two figures thus provides information on the effects of three-dimensional conduction along and within the test surface. The results at this experimental condition are chosen to illustrate these effects, because the Reynolds number lies in the middle of the range of values investi-

Downloaded 31 May 2010 to 171.66.16.27. Redistribution subject to ASME license or copyright; see http://www.asme.org/terms/Terms_Use.cfm

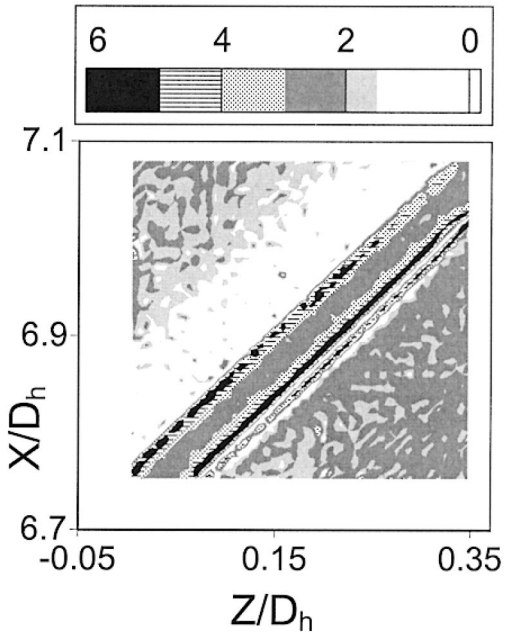

Fig. 5 Local Nusselt number ratio Nu/Nu_o distribution along the rib turbulator test surface for Re_H=48,000 and T_{oi}/T_w =0.94, for variable surface heat flux and surface conduction analysis applied

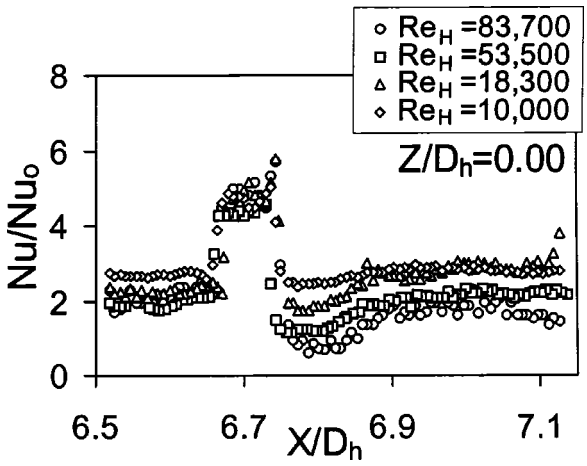

Fig. 6 Constant heat flux local Nusselt number ratios Nu/Nu_o along the rib turbulator test surface at Z/D_h=0.0 for different Reynolds numbers Re_H and T_{oi}/T_w of 0.93–0.95. No conduction analysis applied.

gated, and because variations due to conduction are similar to ones observed at other Reynolds numbers. Note that the results in the latter figure cover smaller ranges of X/D_h and Z/D_h values. A comparison of the data in Figs. 4 and 5 shows that Nu/Nu_o ratio changes due to three-dimensional conduction are present on the top of the rib segment and only on parts of the flat surface which are very near the rib. Such limited effects of three-dimensional conduction are due to the high-quality construction and performance of the heated test surface, within which, conduction is one-dimensional over most of its volume.

The Nu/Nu_o data in Fig. 4 are obtained by assuming that all of the heat flux into the rib segment leaves entirely from the top of the rib (with none leaving from the sides). When three-dimensional conduction is present and a portion of the heat transfer leaves the vertical sides of the rib, the surface Nu/Nu_o distribution in Fig. 5 is produced. As before, the darker diagonal regions with relatively high Nu/Nu_o ratios are again present along the tops of the ribs in this figure. Relative to constant heat flux values in Fig. 4, Nusselt number ratios in Fig. 5 are then lower in the middle part of the rib top, with higher Nu/Nu_o values near the upstream and downstream edges of the rib top. Nusselt number ratios on the flat surfaces just adjacent the ribs are also lowered (compared to constant heat flux values) along lines which are parallel to the rib segment.

The effects of Reynolds number on spatially resolved Nusselt number ratios (obtained with constant surface heat flux and no surface conduction analysis applied) are illustrated by the data presented in Figs. 6 and 7. The data presented in both figures at all Re_H are measured on the same part of the test surface. All of the results are also time-averaged using 25 instantaneous data sets. In the first of these figures, local Nu/Nu_o data are given as they vary with X/D_h for constant $Z/D_h=0$. In the second of these figures, Nu/Nu_o data are given as they vary with Z/D_h for constant $X/D_h=6.90$. These data are obtained from survey results (such as the ones shown in Fig. 4) at Re_H ranging from 10,000 to 83,700, and about constant temperature ratio T_{oi}/T_w of 0.93–0.95. In Fig. 6, local Nu/Nu_o values at $X/D_h=6.53$ to $X/D_h=6.67$ correspond to locations upstream of the central rib. $X/D_h=6.67$ to $X/D_h=6.75$ are then located on the rib, and $X/D_h=6.75$ to $X/D_h=7.14$ correspond to the flat surface downstream of the rib. In Fig. 7, $Z/D_h=-0.20$ to $Z/D_h=0.16$ and $Z/D_h=0.27$ to $Z/D_h=0.39$ correspond to spanwise locations on the flat portions of the surface between ribs, and $Z/D_h=0.16$ to $Z/D_h=0.27$ correspond to locations on the central rib.

Figures 6 and 7 both show that the highest Nusselt number ratio values are again present on the rib tops, especially near the edges, at all Reynolds numbers. Nu/Nu_o ratios also generally increase somewhat on the rib tops as Re_H increases. In contrast, Nusselt number ratios decrease on the flat regions away from the ribs, especially at locations just downstream of the ribs, as Re_H increases. Because of the normalization employed, this means that the observed Nusselt number Nu increases with Reynolds number are slower than baseline Nu_o increases with Re_H on flat regions, and more rapid on the ribs themselves. Such changes just downstream of the ribs are partially due to increases in the size and strength of the flow recirculation regions at these locations, and the shear layer associated with it, as the Reynolds number increases. Overall, this means that the effects of Reynolds number on Nu/Nu_o distributions are most prominent on the ribs, and on regions just downstream and parallel to ribs. For example, Fig. 6 shows that Nu/Nu_o values for Re_H=83,700 increase continually downstream of the rib as X/D_h increases up to 7.0. This initial increase due to shear layer re-attachment then becomes somewhat

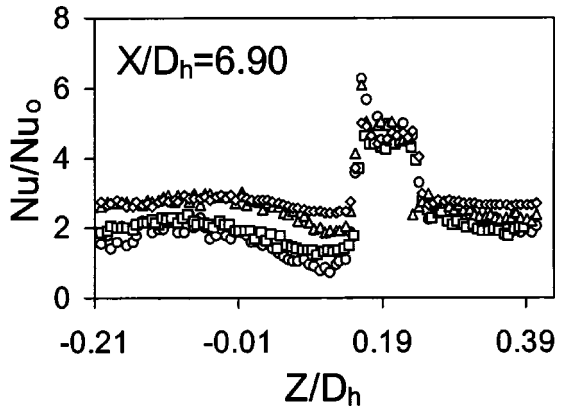

Fig. 7 Constant heat flux local Nusselt number ratios Nu/Nu_o along the rib turbulator test surface at X/D_h=6.90 for different Reynolds numbers Re_H and T_{oi}/T_w of 0.93–0.95. No conduction analysis applied. Symbols are defined in Fig. 6.

Downloaded 31 May 2010 to 171.66.16.27. Redistribution subject to ASME license or copyright; see http://www.asme.org/terms/Terms_Use.cfm

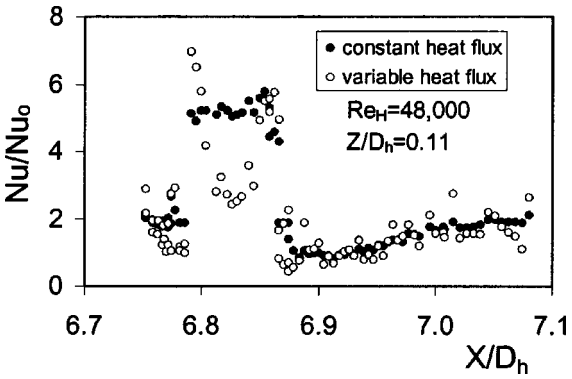

Fig. 8 Local Nusselt number ratios Nu/Nu_o along the rib turbulator test surface at $Z/D_h=0.11$ for a Reynolds number $Re_H=48{,}000$ and T_{oi}/T_w of 0.94. Data are given for constant surface heat flux (no surface conduction analysis) and for variable surface heat flux (with surface conduction analysis).

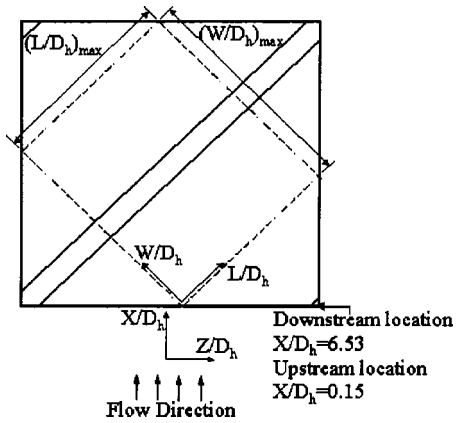

Fig. 10 Schematic diagram of a portion of the bottom rib turbulator test surface showing the orientations and layout of several rib turbulators, and the coordinates W/D_h and L/D_h, which are oriented perpendicular to and parallel to the rib turbulators, respectively

less as the Reynolds number decreases. Irrespective of the value of Reynolds number employed, the results in Figs. 6 and 7 show that Nu/Nu_o values are generally higher than 1.0 on most of the test surface, including the flat regions between the ribs.

The effects of three-dimensional conduction within and along the test surface are further illustrated by the results presented in Figs. 8 and 9. In both cases, local Nusselt number ratios Nu/Nu_o for constant surface heat flux (no surface conduction analysis) and for variable surface heat flux (with surface conduction analysis) are presented for a Reynolds number Re_H of 48,000 and T_{oi}/T_w of 0.94 In the first of these figures, local Nu/Nu_o data are given as they vary with X/D_h for constant $Z/D_h=0.11$. In the second of these figures, Nu/Nu_o data are given as they vary with Z/D_h for constant $X/D_h=6.90$. Both figures show variable heat flux Nu/Nu_o ratios which are significantly lower than constant heat flux values in the central part of the rib. As mentioned, this is partially due to heat transfer from the sides of the ribs, which also causes local Nu/Nu_o increases, determined with a variable heat flux thermal boundary condition, to be higher than values measured with constant heat flux, near the edges of the rib top. The only other variations of importance in Figs. 8 and 9 are located on the flat surfaces near the edges of the ribs, where variable flux values are sometimes locally lower than constant flux values over very small areas. The scatter of the variable flux data is due to the coarseness of the grid used on the thin part of the test surface, and the use of derivatives to compute surface heat flux magnitudes.

Spatially Averaged Nusselt Numbers. Spatially averaged Nusselt number ratios Nu/Nu_o, determined from local data (such as that shown in Fig. 4), are determined for the diagonal directions shown in Fig. 10. These diagonal directions are oriented parallel to and perpendicular to the direction of the ribs located along the bottom test surface. As shown in Fig. 10, W/D_h is then the diagonal directed normal to the ribs, and L/D_h is the diagonal directed parallel to the ribs. The origin of the L/D_h and W/D_h axes is positioned at $X/D_h=6.53$. $(W/D_h)_{max}$ then equals the spacing between adjacent ribs, or the rib pitch in the direction normal to the ribs. The resulting data are shown in Figs. 11–13. The first two of these figures are obtained with constant surface heat flux and no surface conduction analysis is applied. The conduction analysis is employed to obtain some of the results in the last of these figures, which are thus representative of a variable surface heat flux thermal boundary condition next to the air stream.

Figures 11 and 12 show data for Re_H from 10,000 to 83,700 at constant T_{oi}/T_w of 0.93–0.95. The $\overline{Nu}/Nu_o$ data in the first of these figures are averaged in the W/D_h direction, and shown as they vary with $(L/D_h)/(L/D_h)_{max}$. The data are approximately constant with L/D_h at each Reynolds number, Re_H. This is important because it means that the flow at each Reynolds number considered is thermally fully developed.

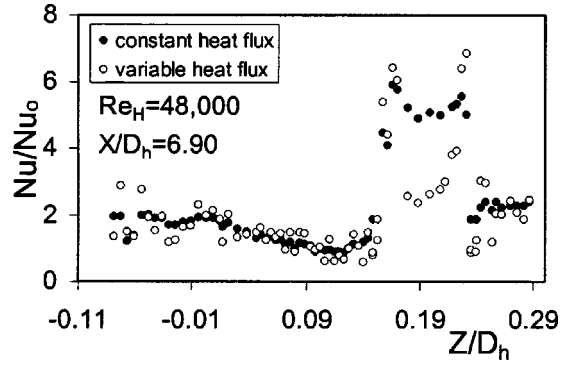

Fig. 9 Local Nusselt number ratios Nu/Nu_o along the rib turbulator test surface at $X/D_h=6.90$ for a Reynolds number $Re_H=48{,}000$ and T_{oi}/T_w of 0.94. Data are given for constant surface heat flux (no surface conduction analysis) and for variable surface heat flux (with surface conduction analysis).

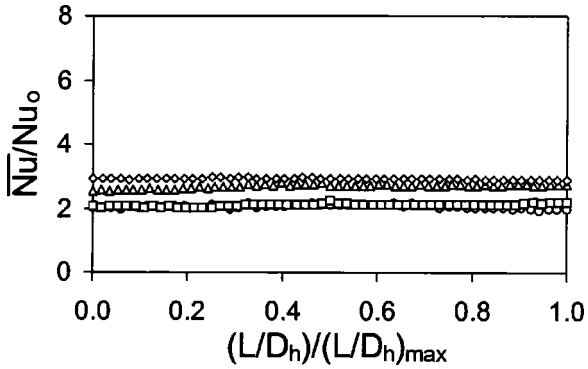

Fig. 11 Nusselt number ratios $\overline{Nu}/Nu_o$, for fully developed conditions measured at the downstream end of the test section and averaged in the W/D_h direction, as dependent upon the L/D_h coordinate for different Reynolds numbers and $T_{oi}/T_w=0.93-0.95$. Symbols are defined in Fig. 12. Surface heat flux is constant and no surface conduction analysis is applied.

Downloaded 31 May 2010 to 171.66.16.27. Redistribution subject to ASME license or copyright; see http://www.asme.org/terms/Terms_Use.cfm

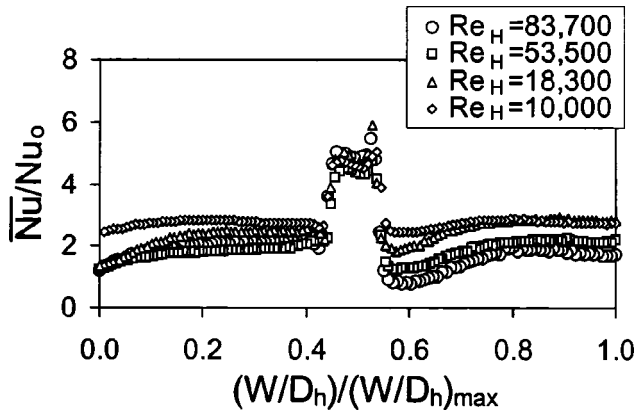

Fig. 12 Nusselt number ratios $\overline{Nu}/Nu_o$, for fully developed conditions measured at the downstream end of the test section and averaged in the L/D_h direction, as dependent upon the W/D_h coordinate for different Reynolds numbers and $T_{oi}/T_w = 0.93-0.95$. Surface heat flux is constant and no surface conduction analysis is applied.

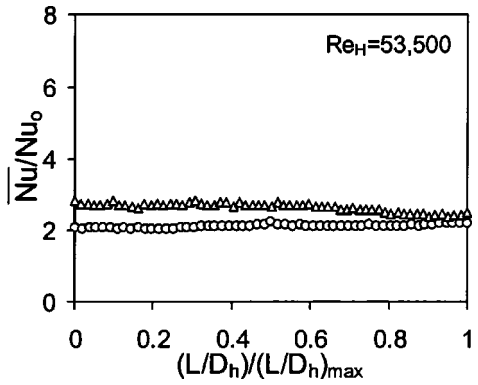

Fig. 14 Nusselt number ratios $\overline{Nu}/Nu_o$, for thermally developing flow measured at the upstream end of the test section and averaged in the W/D_h direction, as dependent upon the L/D_h coordinate for Re_H=53,500 and $T_{oi}/T_w = 0.93-0.95$.

The $\overline{Nu}/Nu_o$ distributions at each Re_H in Fig. 12 (averaged in the L/D_h direction and shown as they vary with W/D_h), then show important variations with $W/D_h/(W/D_h)_{max}$ because this coordinate is oriented perpendicular to the direction of the ribs. In some cases, these include $\overline{Nu}/Nu_o$ increases with Re_H at the top of the central rib. At larger $W/D_h/(W/D_h)_{max}>0.55$, which correspond to locations downstream of the central rib, $\overline{Nu}/Nu_o$ values then decrease substantially as Re_H increases. This is mostly due to increases in the strength and size of the flow recirculation region downstream of the rib, which occurs as the Reynolds number Re_H becomes larger, as mentioned.

The results in Fig. 13 are presented to illustrate the influences of three-dimensional conduction along the test surface on spatially averaged $\overline{Nu}/Nu_o$ values. These Nusselt number ratios are given for fully developed conditions because they are measured at the downstream end of the test section. Values are averaged in the L/D_h direction, and shown as they vary with the $W/D_h/(W/D_h)_{max}$ coordinate. The data are given for a Reynolds number number Re_H of 48,000 and T_{oi}/T_w of 0.94. The data are shown with and without the test surface conduction analysis applied (i.e., for variable and constant surface heat flux, respectively). Apparent in Fig. 13 are a number of important variations due to surface conduction, which are present along most of the extent of the rib. For example, variable flux $\overline{Nu}/Nu_o$ values are significantly lower than constant flux values along the rib top, except near the edges, where variable flux values are slightly higher. At $W/D_h/(W/D_h)_{max}>0.55$, which corresponds to locations downstream of the central rib, variable flux $\overline{Nu}/Nu_o$ values are lower than constant flux values over a very small region just next to the rib. The same situation is also present just upstream of the rib at $W/D_h/(W/D_h)_{max}<0.45$. This is important because it means that corners, where the ribs join the flat surrounding surface, are potential hot spots, especially when located just downstream of a rib near the largest flow recirculation zone.

Similar qualitative variations due to three-dimensional conduction are present for all of the data presented in Fig. 12 (for Re_H from 10,000 to 83,700), but are not shown. From a quantitative perspective, overall differences (with and without three-dimensional conduction considered) generally become larger as Re_H increases because of larger magnitudes of surface heat flux.

The $\overline{Nu}/Nu_o$ data presented in Figs. 14 and 15 are obtained for Re_H of about 53,500, and the same surface layout given in Fig. 10, except these data are obtained at a location farther upstream where the thermal boundary layers are still developing. In this case, the origin of the L/D_h and W/D_h coordinates is located at $X/D_h = 0.15$. In addition, surface heat flux is constant and no surface conduction analysis is applied to obtain the results in the two

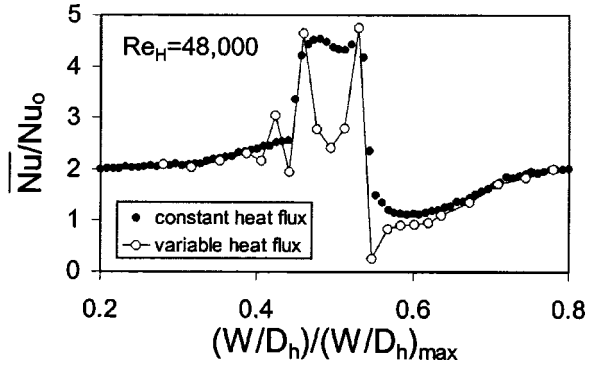

Fig. 13 Nusselt number ratios $\overline{Nu}/Nu_o$, for fully developed conditions measured at the downstream end of the test section and averaged in the L/D_h direction, as dependent upon the W/D_h coordinate for a Reynolds number Re_H=48,000 and T_{oi}/T_w of 0.94. Data are shown with and without conduction analysis applied (variable and constant surface heat flux respectively).

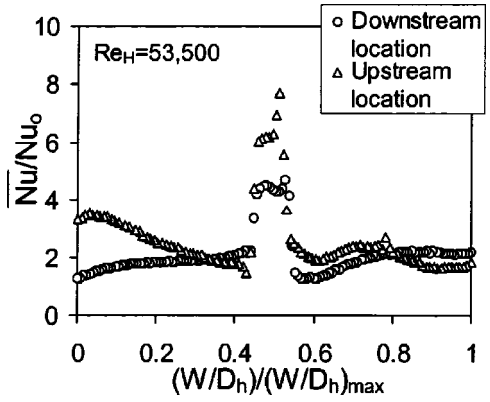

Fig. 15 Nusselt number ratios $\overline{Nu}/Nu_o$, for thermally developing flow measured at the upstream end of the test section and averaged in the L/D_h direction, as dependent upon the W/D_h coordinate for Re_H=53,500 and $T_{oi}/T_w = 0.93-0.95$. Surface heat flux is constant and no surface conduction analysis is applied.

Downloaded 31 May 2010 to 171.66.16.27. Redistribution subject to ASME license or copyright; see http://www.asme.org/terms/Terms_Use.cfm

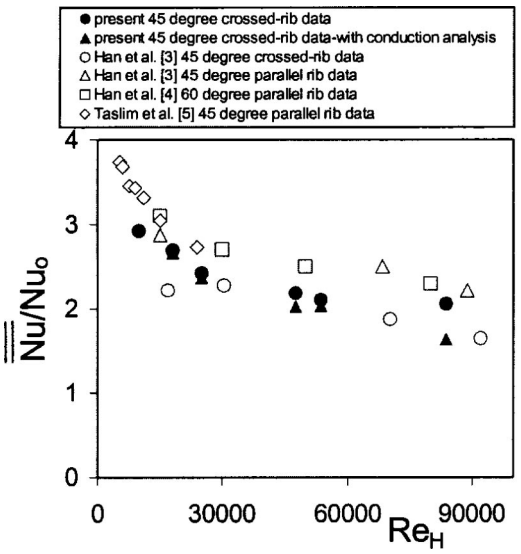

Fig. 16 Rib turbulator channel globally averaged Nusselt number ratios for fully developed flow, averaged over the surface area corresponding to one period of rib turbulator surface geometry. Comparisons with results from other investigations [3–5] are included.

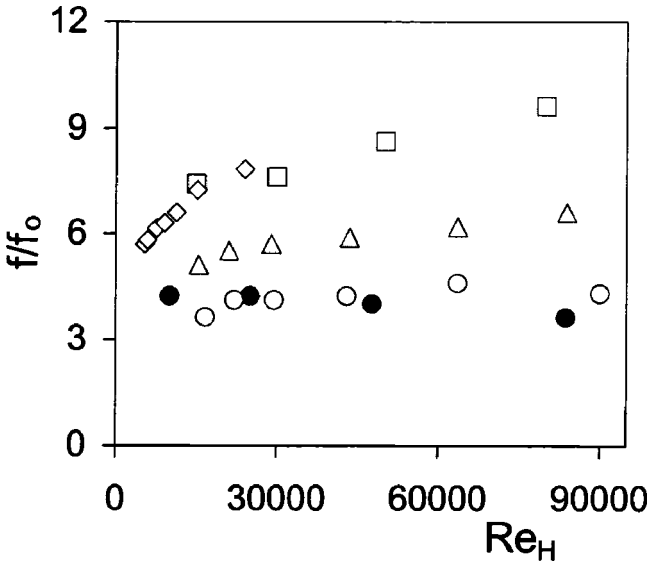

Fig. 17 Rib turbulator channel friction factor ratios f/f_o for fully developed flow conditions as dependent upon Reynolds number for $T_{oi}/T_w = 0.93-0.95$. Symbols are defined in Fig. 16. Comparisons with results from other investigations [3–5] are included.

figures. In Fig. 14, the $\overline{\mathrm{Nu}}/\mathrm{Nu}_o$ data measured upstream show significant variations with L/D_h, which confirms that the thermal boundary layers at this measurement location are not fully developed.

A similar conclusion is reached if the $\overline{\mathrm{Nu}}/\mathrm{Nu}_o$ data, given in Fig. 15 as dependent upon $W/D_h/(W/D_h)_{\max}$, are examined. For regions upstream of the rib ($W/D_h/(W/D_h)_{\max}<0.42$), on the rib ($0.42<W/D_h/(W/D_h)_{\max}<0.52$), and downstream of the rib ($W/D_h/(W/D_h)_{\max}>0.52$), the $\overline{\mathrm{Nu}}/\mathrm{Nu}_o$ values measured at the upstream channel locations are often higher than values measured at the downstream channel locations, when compared at the same $W/D_h/(W/D_h)_{\max}$. This is because of thinner, less-than-fully developed thermal boundary layers at the upstream location, which also cause $\overline{\mathrm{Nu}}/\mathrm{Nu}_o$ to decrease continually with streamwise development over each segment of the test surface.

Globally Averaged Nusselt Numbers and Friction Factors. Figures 16, 18, and 19 present globally averaged Nusselt number ratios for fully developed flow conditions, which are determined by averaging all the local data in the rectangular area enclosed by the lengths $(L/D_h)_{\max}$ and $(W/D_h)_{\max}$ shown in Fig. 10. Globally averaged Nusselt number ratios are thus determined from results like the ones in Figs. 11, 12, and 13. The data in Figs. 16–19 are given for Reynolds numbers Re_H from 10,000 to 83,700 and T_{oi}/T_w of 0.93–0.95. Results from Han et al. [3,4], and Taslim et al. [5] are included for comparison.

Recall that the present 45 deg square ribs are arranged so that they are perpendicular on opposite channel walls. They are installed in a channel with aspect ratio of 4, ratio of rib height to hydraulic diameter e/D_h of .078, rib pitch-to-height ratio p/e of 10, and ratio of rib blockage area to channel cross-sectional area $2e/H$ of 0.25 or 25%. The Han et al. [3] data used for comparison are obtained in a square channel with $e/D_h=.0625$, $p/e=10$, and $2e/H=.125$. These investigators consider nine different configurations of ribs placed on two opposite walls, including 90 deg ribs, 45 and 60 deg parallel ribs, 45 and 60 deg crossed-ribs, 45 and 60 deg V-shaped ribs, and 45 and 60 deg Λ-shaped ribs. The data used for comparison from Han et al. [4] are for square channels with 90 deg continuous ribs, 60 deg continuous ribs, and 60 deg broken ribs. In all cases, the ribs are parallel on opposite channel walls, e/D_h is .063, p/e is 10, and $2e/H$ is .126. The Taslim et al. [5] data used for comparison are also obtained in a square channel with $p/e=10$. For these data, $e/D_h=.083$, and $2e/H$ is .166. In addition, the 45 deg oriented ribs are arranged in the same direction on opposite channel walls, and placed at streamwise locations so that they are staggered with respect to each other.

Figure 16 shows that globally averaged Nusselt number ratios generally decrease as Re_H increases for all of the configurations. For the present rib-turbulator arrangement, globally averaged ratios (with no surface conduction analysis employed) vary from 2.92 to 2.06 as Re_H increases from 10,000 to 83,700. With surface conduction analysis, values range from 2.92 to 1.64 over the same range of Reynolds numbers. The present crossed-rib data are lower than the 45 and 60 deg parallel rib data from Han et al. [3,4] and the 45 deg parallel rib data from Taslim et al. [5] at most of the Reynolds numbers investigated. The present results, with surface conduction analysis applied, are in approximate agreement with the 45 deg crossed-rib data from Han et al. [3] for Re_H

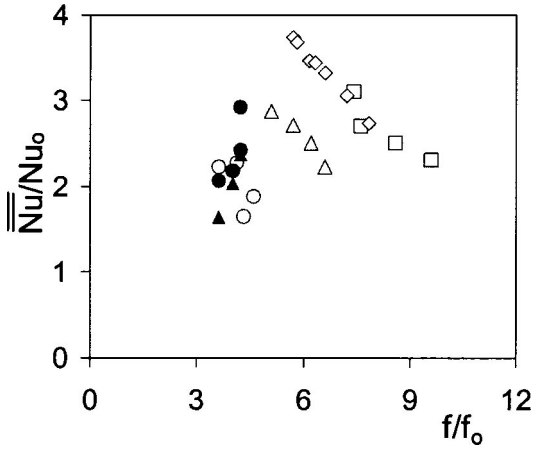

Fig. 18 Rib turbulator channel globally averaged Nusselt numbers for fully developed flow and $T_{oi}/T_w=0.93-0.95$ as dependent upon friction factor ratios, including comparisons with results from other investigations [3–5]. Symbols are defined in Fig. 16.

Downloaded 31 May 2010 to 171.66.16.27. Redistribution subject to ASME license or copyright; see http://www.asme.org/terms/Terms_Use.cfm

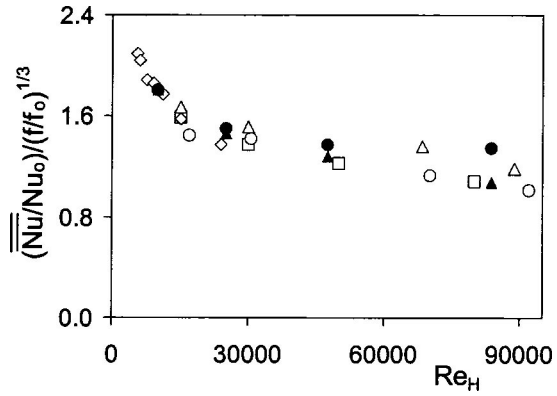

Fig. 19 Rib turbulator channel globally averaged performance parameters for fully developed flow and $T_{oi}/T_w = 0.93-0.95$ as dependent upon Reynolds number, including comparisons with results from other investigations [3–5]. Symbols defined in Fig. 16.

>17,000. Differences between these two data sets are due to different channel aspect ratios (1 and 4), different rib blockage percentages (12.5 and 25.0%), and because the Han et al. [3] results are based on measurements made at discrete locations, which can give differences when compared to data based on spatially-resolved measurements, such as the ones from the present study.

At most of the Reynolds numbers considered, the present data in Fig. 16, obtained with no conduction analysis applied, are generally higher than the data from the present study, which are obtained with conduction analysis. Differences between these two data sets become larger as the Reynolds number increases because of increasing amounts of heat flux into the test surface from the heater. Higher heat fluxes lead to larger heat flux variations along the test surface, especially on and in the near-vicinity of individual ribs. In both cases, the data points in Fig. 16 represent values which are globally averaged along the tops of the ribs and along the flat surfaces between the ribs (which means that the vertical rib sides are not included in the determination of globally averaged values). With no conduction analysis applied, the heat flux leaving the rib tops and the flat surfaces between the ribs is assumed to be constant, which means that all of the heat flux into the acrylic test surface leaves only at these locations (with none leaving from the vertical sides of the ribs). The conduction analysis is applied to the test surface to determine the nonuniform variations of surface heat flux which are present, including variations along the sides and tops of the ribs. Thus, the data obtained *with* the conduction analysis provide physically realistic *local Nusselt number values* for the tops of the ribs and the flat surfaces between the ribs. However, the *globally averaged Nusselt number data*, obtained with *no* conduction analysis applied, provide a more correct measure of the heat transfer augmentation capabilities of the rib turbulator test surface, because they more correctly account for the transfer of all of the thermal power which enters into the test surface.

Measured friction factor ratios in the rib-turbulator channel for Re_H of 10,000 to 83,700 at T_{oi}/T_w of 0.93–0.95 are shown as they depend upon Re_H in Fig. 17. These f/f_o data are also compared with results from Han et al. [3,4], and Taslim et al. [5]. The present data cover approximately the same range of values as the 45 deg crossed-rib data from Han et al. [3]. The present f/f_o data are then lower than the continuous, parallel rib data from Han et al. [3,4] and Taslim et al. [5] for all Reynolds numbers considered. Here, $2e/H$ also appears to have an important influence on f/f_o values, provided that continuous, parallel rib data are compared at about the same rib angle.

Globally averaged Nusselt number ratios and friction factor ratios from Figs. 16 and 17 are plotted together in Fig. 18 for Re_H from 10,000 to 83,700 and T_{oi}/T_w of 0.93–0.95. Here, globally averaged Nusselt number ratios generally decrease as f/f_o increases in almost all cases as channel and rib geometry are held constant. Overall, the best performance in the coordinates of Fig. 18 (as characterized by the highest Nusselt number ratios at the lowest f/f_o values) is produced by the 45 deg oriented, continuous, parallel ribs from Taslim et al. [5], followed by the 60 deg continuous, parallel ribs from Han et al. [4], the 45 deg continuous, parallel ribs from Han et al. [3], and then by the present 45 deg crossed-rib turbulators. The present crossed-rib data then cover a portion of the range of values associated with the 45 deg continuous, crossed-rib data from Han et al. [3].

Thermal Performance Parameters. These comparisons are further illustrated by the plot of thermal performance parameters as dependent upon Re_H in Fig. 19. This performance parameter is employed because it gives the ratio of heat transfer augmentation to friction augmentation, where each is given for the same ratio of mass flux in an internal passage with augmentation devices to mass flux in the internal channel with smooth surfaces [17].

Performance parameter magnitudes for the present study are determined from the data in Figs. 16–18, and decrease from 1.81 to 1.35 as Re_H increases from 10,000 to 83,700 in Fig. 19. With the conduction analysis employed, the present thermal performance values range from 1.81 to 1.07 over the same range of Reynolds numbers. Here, the best overall thermal performance is provided by the Taslim 45 deg continuous, parallel ribs at Re_H <12,000, and by the 45 deg continuous, parallel ribs from Han et al. [3] at higher Re_H. Our 45 deg crossed-rib performance parameters (obtained with no conduction analysis) are then in approximate agreement with the 45 deg continuous, parallel rib data from Han et al. [3] for most of the Re_H values considered. Performance parameter magnitudes from the present study (obtained *with* conduction analysis applied) are then lower than the parallel rib data sets, but in approximate agreement with the 45 deg crossed-rib data from Han et al. [3] when compared at the same Reynolds number.

Summary and Conclusions

Spatially resolved Nusselt numbers, spatially-averaged Nusselt numbers, and friction factors are presented for a stationary channel with an aspect ratio of 4 and angled rib turbulators inclined at 45 deg with perpendicular orientations on two opposite surfaces. Results are given at different Reynolds numbers based on channel height from 10,000 to 83,700, and ratios of air inlet stagnation temperature to surface temperature ranging from 0.93 to 0.95. The ratio of rib height to hydraulic diameter is .078, the rib pitch-to-height ratio is 10, and the blockage provided by the ribs is 25% of the channel cross-sectional area.

Nusselt numbers are given both with and without three-dimensional conduction considered along and within the acrylic test surface employed in the study. Without the conduction analysis, the heat flux from the horizontal parts of the test surface are assumed to be constant. However, regardless of whether or not the conduction analysis is applied, spatially-resolved, local Nusselt numbers, normalized by values measured in a smooth channel, are highest on tops of the rib turbulators. The resulting local and spatially averaged Nusselt number ratios vary locally on the rib tops as Reynolds number changes. Nusselt number ratios then decrease on the flat regions away from the ribs, especially at locations just downstream of the ribs, as Reynolds number increases. Such changes are partially due to increases in the size and strength of the flow recirculation region located downstream of the ribs, and the shear layer associated with it, as the Reynolds number increases. Other flow phenomena which affect Nusselt number augmentations are intense, highly unsteady secondary flows and vortex pairs, which act to increase secondary advection and turbulent transport over the entire channel cross section [10]. Because of such phenomena, local and spatially averaged Nusselt number ratios are generally much higher than 1.0 over most of the

Downloaded 31 May 2010 to 171.66.16.27. Redistribution subject to ASME license or copyright; see http://www.asme.org/terms/Terms_Use.cfm

ribbed test surface, including the flat regions between the ribs, irrespective of the value of Reynolds number employed.

When data are adjusted to account for three-dimensional conduction (and variable surface heat flux) along and within the test surface, Nusselt number ratios show different quantitative variations (with location along the test surface), compared to variations when no conduction is included. Changes include: (i) local and spatially-averaged Nusselt number ratios, obtained with variable surface heat flux, which are significantly lower than constant flux values along the rib top, except near the edges of rib tops, where variable flux values are slightly higher, and (ii) variable flux Nusselt number ratio decreases (relative to constant flux values) on the flat regions between the ribs, near corners where the ribs join the flat surrounding surface. This last characteristic is important because it means such corners are potential hot spots, especially when located just downstream of a rib near the largest flow recirculation zone.

Globally averaged Nusselt number ratios (obtained with conduction analysis applied to the data) vary from 2.92 to 1.64 as Reynolds number increases from 10,000 to 83,700. Thermal performance parameters also decrease somewhat as Reynolds number increases from 10,000 to 83,700, with values in approximate agreement with the 45 deg continuous rib data from other sources.

Acknowledgments

The work presented in this paper was sponsored by a AGTSR Advanced Gas Turbine Research Program research subcontract sponsored by the U.S. Department of Energy-National Energy Technology Laboratory through a cooperative agreement with the South Carolina Institute for Energy Studies at Clemson University. Mr. Eli Comeau, Mr. Arthur Fox, and Mr. Jacob Kingston helped in setting up the experimental apparatus employed in the investigation. Portions of the surface conduction analyses were set-up and conducted by Mr. David Kenney and Ms. Sarah Peddicord, under the partial direction of Professor Kuan Chen of the University of Utah. Mr. Se Youl Won aided in the analysis of the skin friction coefficients.

Nomenclature

a = streamwise extent of test surface
b = spanwise extent of test surface
b/H = channel aspect ratio
D_h = channel hydraulic diameter
e = rib turbulator width and height
e' = rib turbulator width in streamwise direction
f = friction factor
f_o = baseline friction factor in smooth channel with no rib turbulators
H = channel height
h = heat transfer coefficient based on flat projected area, $\dot{q}''/(T_w - T_m)$
k = thermal conductivity
L = coordinate in direction parallel to ribs
Nu = local Nusselt no., hD_h/k
Nu_o = baseline Nusselt no. in a smooth channel with no rib turbulators
p = streamwise pitch spacing of rib turbulators
Pr = Prandtl no.
$\dot{q}''$ = surface heat flux
Re_H = Reynolds no. based on channel height
Re_{Dh} = Reynolds no. based on hydraulic diameter
T = local static temperature
$\overline{U}$ = streamwise bulk velocity averaged over channel cross section
W = coordinate in direction normal to ribs
X = streamwise coordinate measured from test section inlet
Y = normal coordinate measured from test surface between ribs
Z = spanwise coordinate measured from test surface centerline

Subscripts

a = ambient value
i = test section inlet value
m = time-averaged, local mixed mean value
o = total or stagnation value
w = local wall value
max = maximum value

Superscripts

$-$ = spanwise or streamwise-averaged value
$=$ = globally averaged value

References

[1] Han, J. C., Glicksman, L. R., and Rohsenow, W. M., 1978, ''An Investigation of Heat Transfer and Friction For Rib-Roughened Surfaces,'' Int. J. Heat Mass Transf., **21**(7), pp. 1143–1156.
[2] Han, J. C., and Park, J. S., 1988, ''Developing Heat Transfer in Rectangular Channels With Rib Turbulators,'' Int. J. Heat Mass Transf., **31**(1), pp. 183–195.
[3] Han, J. C., Zhang, Y. M., and Lee, C. P., 1991, ''Augmented Heat Transfer in Square Channels With Parallel, Crossed, and V-Shaped Angled Ribs,'' ASME J. Heat Transfer, **113**, pp. 590–596.
[4] Han J. C., Huang J. J., and Lee C. P., 1993, ''Augmented Heat Transfer in Square Channels With Wedge-Shaped and Delta-Shaped Turbulence Promoters,'' *Enhanced Heat Transfer*, Vol. 1, No. 1, pp. 37–52.
[5] Taslim, M. E., Li, T., and Kercher, D. M., 1996, ''Experimental Heat Transfer and Friction in Channels Roughened With Angled, V-Shaped, and Discrete Ribs on Two Opposite Walls,'' ASME J. Turbomach., **118**, pp. 20–28.
[6] Taslim, M. E., Li, T., and Spring, S. D., 1998, ''Measurements of Heat Transfer Coefficients and Friction Factors in Passages Rib-Roughened On All Walls,'' ASME J. Turbomach., **120**, pp. 564–570.
[7] Wang, Z., Ireland, P. T., Kohler, S. T., and Chew, J. W., 1998, ''Heat Transfer Measurements to a Gas Turbine Cooling Passage With Inclined Ribs,'' ASME J. Turbomach., **120**, pp. 63–69.
[8] Thurman D., and Poinsatte P., 2000, ''Experimental Heat Transfer and Bulk Air Temperature Measurements for a Multipass Internal Cooling Model With Ribs and Bleed,'' ASME Paper No. 2000-GT-233.
[9] Cho H. H., Lee S. Y., and Wu S. J., 2001, ''The Combined Effects of Rib Arrangements and Discrete Ribs on Local Heat/Mass Transfer in a Square Duct,'' ASME Paper No. 2001-GT-175.
[10] Ligrani, P. M., Oliveira, M. M., and Blaskovich, T., 2003, ''Comparison of Heat Transfer Augmentation Techniques,'' AIAA J., **41**(3), pp. 337–362.
[11] Mahmood, G. I., Hill, M. L., Nelson, D. L., Ligrani, P. M., Moon, H.-K., and Glezer, B., 2001, ''Local Heat Transfer and Flow Structure On and Above a Dimpled Surface in a Channel,'' ASME J. Turbomach., **123**, pp. 115–123.
[12] Sargent, S. R., Hedlund, C. R., and Ligrani, P. M., 1998, ''An Infrared Thermography Imaging System For Convective Heat Transfer Measurements in Complex Flows,'' Meas. Sci. Technol., **9**(12), pp. 1974–1981.
[13] Kline, S. J., and McClintock, F. A., 1953, ''Describing Uncertainties in Single Sample Experiments,'' Mech. Eng. (Am. Soc. Mech. Eng.) **75**, pp. 3–8.
[14] Moffat, R. J., 1988, ''Describing the Uncertainties in Experimental Results,'' Exp. Therm. Fluid Sci., **1**(1), pp. 3–17.
[15] Metzger D. E., Chyu M.-K., and Bunker R. S., 1988, ''The Contribution of On-Rib Heat Transfer Coefficients to Total Heat Transfer From Rib-Roughened Surfaces,'' *Transport Phenomena in Rotating Machinery*, J. H. Kim ed., Hemisphere Publishing Co., Washington, DC.
[16] Lienhard J. H., 1987, *A Heat Transfer Textbook*, Second Edition, Prentice-Hall Inc., Englewood Cliffs, NJ.
[17] Gee, D. L., and Webb, R. L., 1980, ''Forced Convection Heat Transfer in Helically Rib-Roughened Tubes,'' Int. J. Heat Mass Transf., **23**, pp. 1127–1136.

Downloaded 31 May 2010 to 171.66.16.27. Redistribution subject to ASME license or copyright; see http://www.asme.org/terms/Terms_Use.cfm

Comparisons of High-Reynolds-Number EVM and DSM Models in the Prediction of Heat and Fluid Flow of Turbine Blade Cooling Passages

Yoji Okita
Aero-Engine and Space Operations,
Ishikawajima-Harima Heavy Industries (IHI),
Mizuho-Machi, Tokyo, 190-1297, Japan
email: youji_ookita@ihi.co.jp, web page:
http://www.ihi.co.jp

Hector Iacovides
Department of Mechanical, Aerospace and
Manufacturing Engineering,
University of Manchester Institute of Science and
Technology (UMIST),
Manchester, M60 1QD, U.K.
email: h.iacovides@umist.ac.uk, web page:
http://cfd.me.umist.ac.uk/tmcfd

This paper presents computations of flow and heat transfer through passages relevant to those used to internally cool gas-turbine blades, using high-Reynolds-number models of turbulence. Three types of internal flows are first examined, which between them contain all the main elements found in blade cooling passages; developing flow through a heated straight duct rotating orthogonally, repeating flow and heat transfer through a straight ribbed duct and flow and heat transfer through a round-ended U-bend of strong curvature square and of cross-section. Next, flows influenced by a combination of these elements are computed. The main objective is to establish how reliably, industry-standard high-Reynolds-number models can predict flow and wall-heat transfer in blade-cooling passages. Two high-Reynolds-number models have been used, the standard version of the high-Re k-ε (EVM) model and the basic high-Re model of stress transport (DSM). In all the cases the second-moment closure (DSM) consistently produced flow and thermal predictions that are closer to available measurements than those of the EVM model. Even the high-Re DSM predictions, however, are not in complete agreement with the experimental data. Comparisons with predictions of earlier studies that use low-Re models of turbulence show that at least some of the remaining differences between the current predictions and experimental data are due to the use of the wall-function approach.
[DOI: 10.1115/1.1580158]

Keywords: Eddy Viscosity Model, Differential Stress Model, Wall Function, Turbine Blade, Internal Cooling

1 Introduction

The internal cooling of gas-turbine blades is crucial in the drive for improvements in the efficiency and performance of gas-turbine engines. The development of more effective cooling systems will be greatly assisted by the availability of numerical flow solvers that can reliably predict convective heat transfer in the complex flow conditions encountered in blade-cooling passages. The flow complexity is caused by the presence of orthogonal rotation, surface rib-roughness and strong curvature. Reliable heat transfer predictions can only be produced if the effects of turbulence are correctly accounted for. Flow solvers used for the computation of such flows need to be able to resolve complex three-dimensional features of the mean motion with numerical accuracy and also to employ mathematical models of turbulence that reproduce the effects of separation, streamline curvature and rotation on the turbulence field.

The computation of flow and heat transfer through passages that are relevant to blade cooling applications has thus been the subject of numerous investigations. As far as the effects of orthogonal rotation are concerned, Prakash and Zerkle [1] have shown that computations based on the high-Reynolds-number k-ε model of turbulence qualitatively reproduce the enhancement of heat transfer along the trailing (pressure) side of a rotating duct (see Fig. 1) and the corresponding suppression of heat transfer along the leading (suction) side. When rotational buoyancy effects are important, the suppression of wall heat transfer along the suction side is under-estimated. In flows through U-bends of strong curvature, Besserman and Tanricut [2] and Xia and Taylor [3] carried out k-ε (effective viscosity) computations which suggested that the wall-functions are not appropriate. More recently, Rigby et al. [4] looked at flows through square-ended U-bends and show that the Wilcox [5] k-ω model of turbulence, that does not employ the wall-function strategy, produces reasonable Nusselt number predictions. When it comes to the effects of rib-roughness, most of the computational studies found in the open literature are still for two-dimensional flows. Three-dimensional studies include the work of Taylor et al. [6], who used finite element solver with a low-Re one-equation model to predict flow and heat transfer through ribbed rotating pipes. They compared their predicted distributions of wall temperature with experimentally determined variations and found that provided wall conduction effects are also included, good agreement can be achieved. Prakash and Zerkle's [7] high-Re k-ε computations of flow and heat transfer through ribbed ducts showed that this model is capable of reproducing the mean Nusselt number levels of experimental correlations. Another study that produced high-Re-model flow computations through ribbed passages is that of Bonhoff et al. [8], in which the commercial code FLUENT was used to predict the flow development through passages with ribs normal and also inclined to the flow direction. They showed that the effects of rib angle on the average Nusselt number and friction factor (obtained from experimental correlations) are well predicted by the high-Re second-moment closure and less well by the high-Re k-ε. Saidi and Sunden [9] have recently applied low-Re k-ε and explicit algebraic stress closures (EASM) to the computation of heat transfer through ribbed passages. Only minor differences were found between the local

Contributed by the International Gas Turbine Institute for publication in the JOURNAL OF TURBOMACHINERY. Manuscript received by the IGTI December 1, 2002; revised manuscript received March 5, 2003. Associate Editor: R. Bunker.

 Copyright © 2003 by ASME

Downloaded 31 May 2010 to 171.66.16.27. Redistribution subject to ASME license or copyright; see http://www.asme.org/terms/Terms_Use.cfm

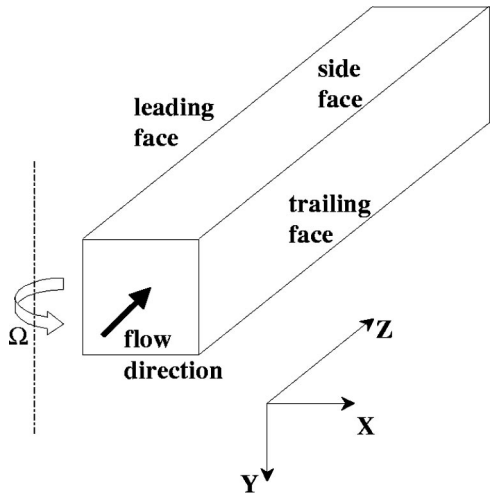

Fig. 1 Orthogonally rotating duct

Nusselt number predictions of the two different types of closures. Overall Nusselt number levels were well predicted, but the predicted increase in Nusselt number behind each rib was too high in comparison with the experimental data.

As the recent work of the UMIST group has shown (Iacovides and Raisee [10]), use of either low-Reynolds-number or zonal models, especially at second-moment level, can lead to satisfactory predictions in many flows relevant to blade-cooling applications. The use of low-Reynolds-number models is, however, prohibitively expensive in the industrial environment, where the flow is fully three-dimensional, the geometries are more complex, and the flow may also be time dependent. Hence, low-Re-model computations are out of question for some time to come, no matter what the advantages of low-Re models are. In this study therefore, the effectiveness of high-Reynolds-number models, with the conventional wall-function approach, in the computation of blade-cooling-related flows is further assessed. Three fundamental cases are first computed, all of them three-dimensional, which among them contain the three main elements that influence the flow development in blade cooling passages; orthogonal rotation, surface rib-roughness and strong curvature. The first case is that of developing and buoyancy-affected flow in a straight rotating duct with heated walls. The second case is that of repeating flow in a straight duct with square ribs on two opposite walls. The final case is that of flow through a U-bend of square cross section, whose curvature is strong enough to cause flow separation. Then two more cases are investigated to assess the combined effects of those three elements.

As earlier UMIST investigations have shown, Iacovides et al. [11], Bo et al. [12] and Iacovides and Raisee [10], the anisotropy of turbulence is also another important factor that needs to be taken into account in the computation of flows through blade-cooling passages. Computations are therefore carried out with two high-Reynolds-number models, the high-Reynolds-number k-ε effective-viscosity model (EVM) and also the basic form of the high-Reynolds-number differential stress model (DSM). The introduction of the DSM provides an opportunity to further assess the importance of the effects of turbulence anisotropy in blade-cooling flows.

2 Flow Equations

The flow equations are expressed here in the Cartesian tensor notation for a rotating coordinate system.

2.1 Mean Motion.

Continuity equation

$$\frac{\partial}{\partial x_i}(\rho U_i)=0 \tag{1}$$

Momentum transport equation

$$\frac{\partial}{\partial x_j}(\rho U_i U_j)=-\frac{\partial P}{\partial x_i}+\frac{\partial}{\partial x_j}\left[\mu\left(\frac{\partial U_i}{\partial x_j}+\frac{\partial U_j}{\partial x_i}\right)-\rho\overline{u_i u_j}\right] -2\rho\varepsilon_{ijp}\Omega_p U_j-\rho[\Omega_j X_j\Omega_i-\Omega_j X_i\Omega_j] \tag{2}$$

Enthalpy transport equation

$$\frac{\partial}{\partial x_j}(\rho U_j T)=\frac{\partial}{\partial x_j}\left(\frac{\mu}{\mathrm{Pr}}\frac{\partial T}{\partial x_j}-\rho\overline{u_j t}\right) \tag{3}$$

Ideal gas law

$$\rho=\frac{p}{RT} \tag{4}$$

2.2 Turbulent Flow Equations.

Effective Viscosity Model (EVM) [13]. The turbulent stresses are obtained through the effective viscosity approximation.

$$\overline{\rho u_i u_j}=\frac{2}{3}k\delta_{ij}-\mu_t\left(\frac{\partial U_i}{\partial x_j}+\frac{\partial U_j}{\partial x_i}\right),\quad \mu_t=\rho c_\mu\frac{k^2}{\varepsilon} \tag{5}$$

The turbulent viscosity depends on the turbulent kinetic energy and its dissipation rate which are in turn obtained through the solution of separate transport equations.

Similarly, the effective diffusivity approximation for turbulent heat fluxes

$$\rho\overline{u_i t}=-\frac{\mu_t}{\mathrm{Pr}_t}\frac{\partial T}{\partial x_i} \tag{6}$$

Transport equation for the turbulent kinetic energy

$$\frac{\partial}{\partial x_j}(\rho U_j k)=\frac{\partial}{\partial x_j}\left[\left(\mu+\frac{\mu_t}{\sigma_k}\right)\frac{\partial k}{\partial x_j}\right]+P_k-\rho\varepsilon \tag{7}$$

where P_k is the generation rate of turbulence obtained from

$$P_k=-\rho\overline{u_i u_j}\left(\frac{\partial U_i}{\partial x_j}\right) \tag{8}$$

Transport equation for the dissipation rate of turbulence

$$\frac{\partial}{\partial x_j}(\rho U_j\varepsilon)=\frac{\partial}{\partial x_j}\left[\left(\mu+\frac{\mu_t}{\sigma_\varepsilon}\right)\frac{\partial\varepsilon}{\partial x_j}\right]+c_{\varepsilon 1}\frac{\varepsilon}{k}P_k-\rho c_{\varepsilon 2}\frac{\varepsilon^2}{k} \tag{9}$$

Differential Stress Model (DSM) [14]. Here the turbulent stresses are obtained through the solution of six separate transport equations

$$C_{ij}=d_{ij}+P_{ij}+\phi_{ij}-\rho\varepsilon_{ij} \tag{10}$$

where

$$C_{ij}=\frac{\partial(\rho U_k\overline{u_i u_j})}{\partial x_k} \tag{11}$$

$$d_{ij}=\frac{\partial}{\partial x_k}\left[\left(\mu+\frac{\mu_t}{\sigma_k}\right)\frac{\partial\overline{u_i u_j}}{\partial x_k}\right] \tag{12}$$

$$P_{ij}=-\rho\left[\left\{\overline{u_i u_k}\frac{\partial u_j}{\partial x_k}+\overline{u_j u_k}\frac{\partial u_i}{\partial x_k}\right\}+\{2\Omega_p(\varepsilon_{ipq}\overline{u_q u_j}+\varepsilon_{jpq}\overline{u_q u_j})\} +\left\{\frac{c_T k}{T\varepsilon}\overline{u_i u_j}\left(\frac{\partial T}{\partial x_j}(\Omega_k X_k\Omega_j-\Omega_k\Omega_k X_j)+\frac{\partial T}{\partial x_i}(\Omega_k X_k\Omega_i -\Omega_k\Omega_k X_i)\right)\right\}\right] \tag{13}$$

Downloaded 31 May 2010 to 171.66.16.27. Redistribution subject to ASME license or copyright; see http://www.asme.org/terms/Terms_Use.cfm

$$\varepsilon_{ij}=\frac{2}{3}\delta_{ij}\varepsilon \tag{14}$$

$$\begin{aligned}\phi_{ij}&=\phi_{ij1}+\phi_{ij2}+\phi_{ijw}\\ \phi_{ij1}&=-\rho c_1\frac{\varepsilon}{k}\left(\overline{u_iu_j}-\frac{2}{3}\delta_{ij}k\right)\\ \phi_{ij2}&=-c_2\left(P_{ij}-\frac{2}{3}\delta_{ij}P_k\right)\end{aligned} \tag{15}$$

$$\begin{aligned}\phi_{ijw}=c_{1w}&\left(\overline{u_ku_m}n_kn_m\delta_{ij}-\frac{3}{2}\overline{u_iu_k}n_kn_j-\frac{3}{2}\overline{u_ku_j}n_kn_i\right)\frac{\rho k^{1/2}}{c_lx_n}\\ &+c_{2w}\left(\phi_{km2}n_kn_m\delta_{ij}-\frac{3}{2}\phi_{ik2}n_kn_j-\frac{3}{2}\phi_{kj2}n_kn_i\right)\frac{k^{3/2}}{c_l\varepsilon x_n}\end{aligned}$$

It is worth noting from the above equations that in a rotating frame of reference, rotation would exert a direct influence on the turbulence field, through the appearance of Coriolis-like contributions in the production rate term of the turbulent stresses, P_{ij}, and also in the redistribution term ϕ_{ij2}. Also note that, in order to decrease the size of the equations, the effective viscosity approximation is employed for the diffusion term, Eq. (12), in the present research. This is in common with the practice followed by Lin [15] and Lien [16].

The turbulent heat fluxes are now modeled through the generalized gradient diffusion hypothesis (GGDH)

$$\frac{\partial(\rho\overline{u_jt})}{\partial x_j}=\frac{\partial}{\partial x_j}\left[\left(\frac{\mu}{\mathrm{Pr}}\delta_{ij}+\rho c_T\overline{\overline{u_iu_j}\frac{k}{\varepsilon}}\right)\frac{\partial T}{\partial x_i}\right] \tag{16}$$

The empirical constants that appear in the equations have the following values, according to the proposals of Jones and Launder [13] for the EVM and Gibson and Launder [17] for the DSM. While the values were originally determined for ordinary attached boundary layers, they have been reported to behave favorably also in separated boundary layers and/or boundary layers under rotating effects [10,12].

$\mathcal{C}_\mu$	$\mathcal{C}_{\varepsilon1}$	$\mathcal{C}_{\varepsilon2}$	$\mathcal{C}_1$	$\mathcal{C}_2$	$\mathcal{C}_1^w$	$\mathcal{C}_2^w$	σ_k	σ_ε	Prt
0.09	1.44	1.92	1.8	0.6	0.5	0.3	1	1.3	0.9

Standard Wall Function (SWF). For both the foregoing models, which are based on the assumption that the flow is fully turbulent, the near-wall grid nodes are located far enough from the wall for the flow to be fully turbulent and the wall function strategy is used to represent the effects of near-wall turbulence.

The wall shear stress is obtained from the assumption that the near-wall velocity distribution follows the log-law:

$$\tau_w=\frac{\kappa c_\mu^{0.25}\rho k_P^{0.5}U_P}{\ln(Ec_\mu^{0.25}y_P^*)} \tag{17}$$

The dissipation rate at the near-wall node is prescribed through the local equilibrium assumption

$$\varepsilon_P=\frac{k_P^{1.5}}{c_ly_P} \tag{18}$$

For the k equation at the near-wall cells, as shown in the forthcoming, the average production rate over each cell is obtained through analytical integration of Eq. (8). The mean velocity distribution is assumed to be logarithmic, turbulent shear stress outside the viscous sublayer ($y_v^*>20$) is assumed to be constant (equal to the wall shear stress)

$$\overline{P_k}=\frac{1}{y_N}\int_{yv}^{yN}\frac{\tau_w^2}{\kappa c_\mu^{0.25}\rho k_P^{0.5}y}dy \tag{19}$$

The average dissipation rate over the near-wall cell is also obtained through analytical integration, by assuming that outside the viscous layer, as before, the variation of ε is obtained from the local equilibrium assumption and that within the viscous sub-layer ε is constant and equal to $2\nu k_P/y_v^2$

$$\overline{\varepsilon}=\frac{1}{y_N}\left[y_v\frac{2\nu k_P}{y_v^2}+\int_{yv}^{yN}\frac{k_P^{1.5}}{c_ly}dy\right] \tag{20}$$

For temperature at a near-wall cell is obtained from

$$T_P^+=\mathrm{Pr}_t\left[\frac{1}{\kappa}\ln\left(\frac{y_Pk_v^{0.5}\exp[\kappa c_\mu^{0.25}y_v^*]}{y_v^*\nu}\right)+y_v^*c_\mu^{0.25}\left(\frac{\mathrm{Pr}}{\mathrm{Pr}_t}-1\right)\right] \tag{21}$$

When the wall function is implemented in the DSM, two approaches have been tried, though most of the work presented here used the simpler one, DSM-WF1.

DSM-WF1. In this first approach, the k-equation in the EVM is solved rather than the equations for Reynolds stresses. In the near-wall local equilibrium shear flow, the transport of the Reynolds Stresses is assumed to be negligible. The stresses can then be related to the turbulence energy through

$$\overline{u_iu_j}=c_{ij}k \tag{22}$$

If the standard values for coefficients c_1, c_2, c_1^w, c_2^w are adopted, after some manipulations, c_{ij} are derived as follows:

$$\begin{aligned}&\overline{u'^2}=1.098k_P,\quad \overline{v'^2}=0.247k_P,\quad \overline{w'^2}=0.655k_P,\\ &\overline{uv'}=-0.255k_P\end{aligned} \tag{23}$$

(All the primed symbols mean values in the wall-oriented coordinate system.)

These near-wall values of the Reynolds stress components, specified in accordance with wall-oriented coordinates, are then transformed into the global Cartesian coordinates

$$\begin{aligned}\overline{u^2}&=t_1^2\overline{u'^2}+2t_1n_1\overline{uv'}+n_1^2\overline{v'^2}+m_1^2\overline{w'^2}\\ \overline{v^2}&=t_2^2\overline{u'^2}+2t_2n_2\overline{uv'}+n_2^2\overline{v'^2}+m_2^2\overline{w'^2}\\ \overline{w^2}&=t_3^2\overline{u'^2}+2t_3n_3\overline{uv'}+n_3^2\overline{v'^2}+m_3^2\overline{w'^2}\\ \overline{uv}&=t_1t_2\overline{u'^2}+(t_2n_1+t_1n_2)\overline{uv'}+n_1n_2\overline{v'^2}+m_1m_2\overline{w'^2}\\ \overline{uw}&=t_1t_3\overline{u'^2}+(t_3n_1+t_1n_3)\overline{uv'}+n_1n_3\overline{v'^2}+m_1m_3\overline{w'^2}\\ \overline{vw}&=t_2t_3\overline{u'^2}+(t_3n_2+t_2n_3)\overline{uv'}+n_2n_3\overline{v'^2}+m_2m_3\overline{w'^2}\end{aligned} \tag{24}$$

where t_i, m_i, n_i are coordinate transformation matrix components.

DSM-WF2. The coefficients in Eq. (23) in the DSM-WF1 are only valid for equilibrium conditions in the wall boundary layer and are not appropriate for general purposes. A more straightforward and physically more consistent approach involves solving simplified transport equations for the wall-oriented normal stress components directly

$$C'_{ij}-d'_{ij}=P'_{ij}+\phi'_{ij}-\rho\varepsilon'_{ij} \tag{25}$$

(All the primed terms in the equation mean the values in the wall-oriented coordinate system.)

Here, all the RHS source terms are evaluated using the cell center value except for P'_{ij}, ε'_{ij}. Averaging procedures for these are analogous to the EVM

$$\overline{P'_{11}}=\frac{1}{y_n}\int_{y_v}^{y_n}P'_{11}dy=\frac{2\tau_W^2}{\kappa c_\mu^{1/4}\rho k^{1/2}y_n}\ln\left(\frac{y_n}{y_v}\right) \tag{26}$$

$$\overline{P'_{22}}=0 \tag{27}$$

Downloaded 31 May 2010 to 171.66.16.27. Redistribution subject to ASME license or copyright; see http://www.asme.org/terms/Terms_Use.cfm

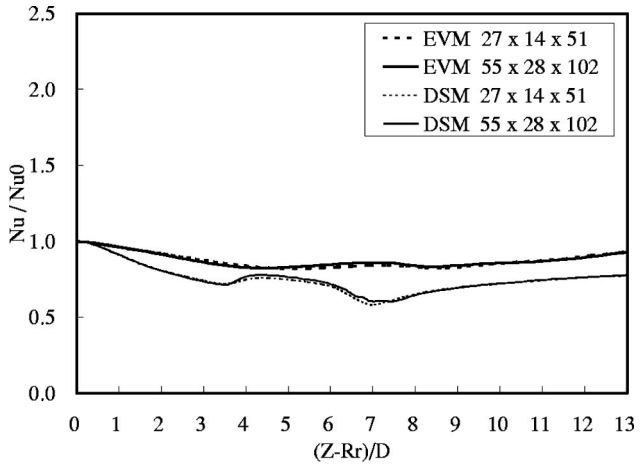

Fig. 2 Comparison of Nusselt number development along the leading face for the two grids

$$\overline{P}'_{33}=0 \tag{28}$$

$$\overline{\varepsilon}'_{ij}=\frac{2}{3}\delta'_{ij}\overline{\varepsilon}=\frac{2}{3}\delta'_{ij}\frac{1}{y_n}\left[\frac{2k^{3/2}}{y_v^*}+\frac{k^{3/2}}{c_l}\ln\left(\frac{y_n}{y_v}\right)\right] \tag{29}$$

The nonzero wall-oriented shear stress is set equal to the wall shear stress.

3 Numerical Aspects

A three-dimensional unstructured finite volume solver (Okita et al. [18]) was employed which solves for the Cartesian velocity components. It uses the pressure-correction, finite volume procedure (SIMPLE) and employs a collocated grid arrangement with mass flux modification [19]. In the case of the DSM, the apparent viscosity concept is used (see Appendix A for details). For the discretization of convective transport, a MUSCL scheme adapted for the unstructured grid is employed (see Appendix B).

4 Results and Discussion

4.1 Developing Buoyancy-Modified Flow in an Orthogonally Rotating Duct. The experimental study of Wagner et al. [20] (Fig. 1) was used for comparisons. Only the side-averaged heat transfer coefficients are available from this experiment. The Reynolds, rotation, and Rayleigh numbers are 25,000, 0.24 and 1.6×10^8, respectively. At the entry to the solution domain, fully developed stationary duct flow conditions were imposed, with a uniform temperature, a practice that Bo et al. [12] argue is the closest possible approximation of the experimental entry conditions. Constant wall temperature boundary conditions were employed. Only one-half of the duct was solved because of symmetry. The number of control-volume cells is $27\times14\times51$. A finer $55\times28\times102$ mesh was also tested for grid sensitivity comparisons. The streamwise development of Nusselt number obtained with the two grids are practically identical (Fig. 2). In this and the subsequent plots, the predicted and measured Nusselt numbers at each plane are normalized with the corresponding average Nusselt number Nu_0 for a stationary duct at the same length of thermal development. The converged solutions had near-wall mesh y^* values in the range $27<y^*<55$ for EVM and $18<y^*<64$ for DSM.

Figure 3 shows the mean flow development along the rotating duct. As expected, the Coriolis force generates a cross-duct secondary motion that along the side walls transports fluid from the trailing (pressure) to the leading (suction) side and then returns it to the trailing side through the duct center. The faster fluid is consequently convected to the trailing side, leaving the slower

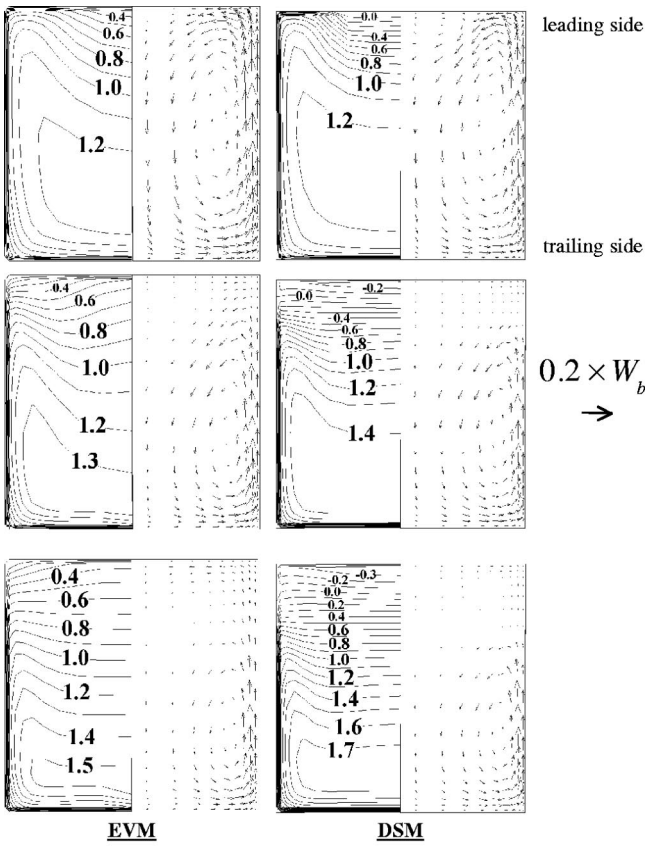

Fig. 3 Predicted mean flow development at Re=25,000, Ro =0.24, and Ra=1.6*10^8 (upper: *Z*/*D*=4 middle: *Z*/*D*=8 lower: *Z*/*D*=12)

fluid along the leading side. This in turn will increase the Nusselt number along the trailing and side walls and will cause a reduction along the leading side. Since at the duct entry the axial velocity has a symmetric distribution, as shown in the predictions of both models, initially the secondary motion is strong and as the flow field approaches its fully developed state it becomes weaker. Because the flow direction is away from the center of rotation (outward motion), the centrifugal force is expected to slow down the hotter and lighter near-wall fluid and accelerate the cooler fluid at the duct core. In the DSM computations, in which the direct effects of rotation on turbulence are also taken into account, rotational buoyancy causes flow reversal along the leading side, which gradually grows in the streamwise direction. The EVM computations do not show this feature. As a result, the DSM computations return a faster flow along the trailing side than the EVM model and a weaker secondary motion along the leading side.

Figure 4 shows the streamwise development of the side-averaged Nusselt number along the three different walls of the duct. While there are only small differences between the EVM and the DSM along the trailing and the side faces, where the DSM shows slightly better results, the DSM predictions show clear improvements along the leading face. In the experiment, the Nusselt number first falls, reaching a minimum level at about 8.5 diameters, and then gradually begins to rise, which is believed to be due to the buoyant effect [12]. Even though the DSM still fails to reproduce the correct level of this minimum it captures this behavior better than the EVM. The lower Nu levels returned by the DSM model along the leading side are consistent with the fact that the DSM predicts that the flow separates along this side of the rotating duct, while in the EVM computation it remains attached. These predictive differences must be attributed to more physically consistent representation of the effects of the more complex strain

Downloaded 31 May 2010 to 171.66.16.27. Redistribution subject to ASME license or copyright; see http://www.asme.org/terms/Terms_Use.cfm

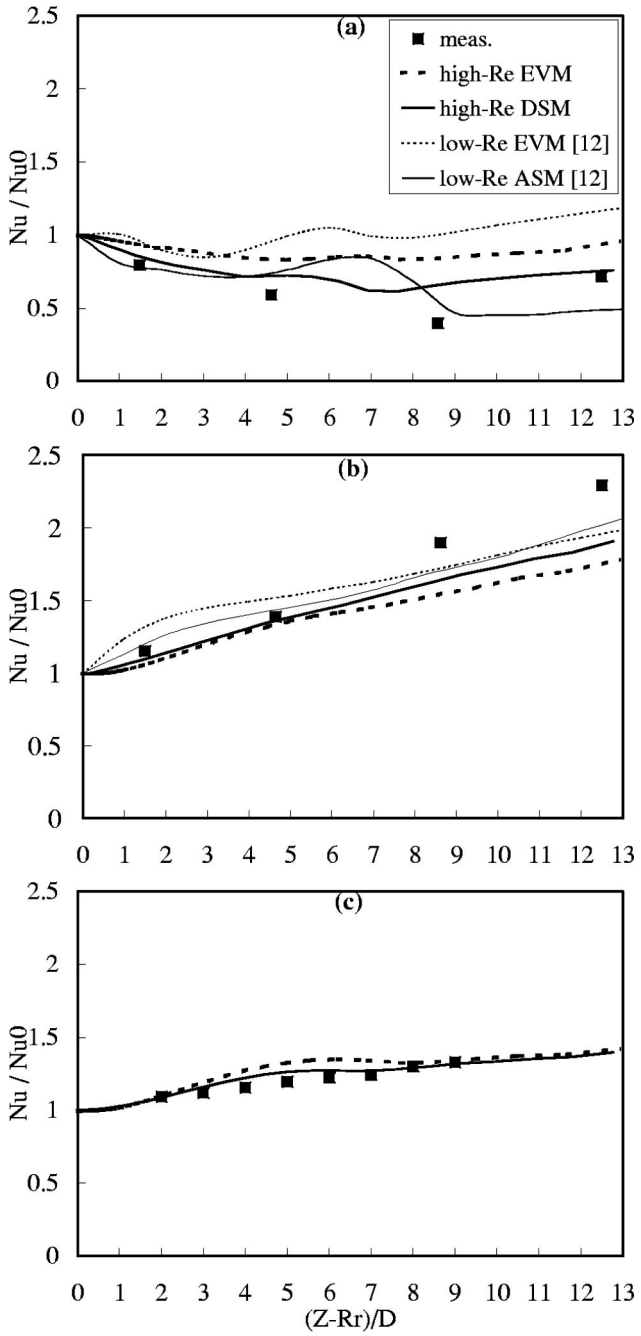

Fig. 4 Comparisons of the side-averaged Nusselt number development at Re=25,000, Ro=0.24, and Ra=1.6*10^8 ((*a*) leading face, (*b*) trailing face, (*c*) side face)

field in general and of rotation in particular on turbulence. As can be also seen in the figure, further improvements in the thermal predictions can be achieved by introducing a low-Re second-moment closure [12] along the trailing side. However, there is no clear advantage along the leading side.

4.2 Flow in a Three-Dimensional Rib-Roughened Passage. A straight duct with in-line ribs on opposite walls (Fig. 5) was examined (Baughn and Yan [21]). The Reynolds number, rib height to diameter ratio and the rib pitch to height ratio are 50,000, 0.0625, and 10, respectively. In the computation, constant wall heat flux thermal boundary condition was employed. After six or seven ribs, the flow and thermal fields are generally fully developed. So, using repeating flow boundary conditions, only

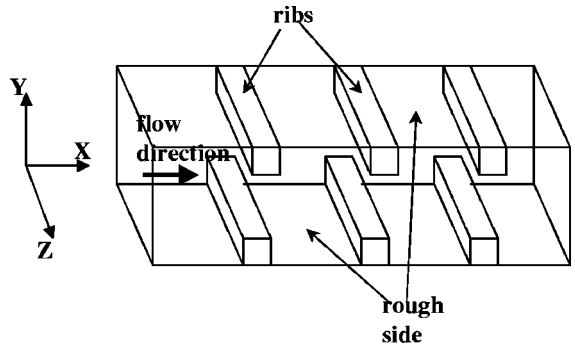

Fig. 5 Rib-roughened passage

one pitch of the rib-roughened passage was calculated. The repeating flow boundary conditions are imposed by first applying a bulk velocity correction at the exit plane, so as to maintain the specified flow rate, and then setting the entry conditions the same as those at the exit plane. For the temperature field, the temperature distribution at the entry plane is set equal to that at the exit plane, but with a bulk adjustment which maintains a constant temperature at a reference point, within the entry plane. The number of control-volume cells is 33×33×29. A finer 66×65×57 mesh was also tested for grid sensitivity comparisons. The streamwise profile of Nusselt number obtained with the two grids are practically identical (Fig. 6). The converged solutions had near-wall mesh y^* values in the range $18<y^*<108$ for EVM and $18<y^*<116$ for DSM.

Figure 7 shows the streamwise profiles of the local Nusselt number along the duct center-lines on the smooth side (marked with S) and on the rough side (R). On the rough side, the level of the Nusselt number is better reproduced by the DSM, which is still as much as 15% lower than the measured level. The stronger secondary motion, driven by the anisotropy of turbulence, returned by the DSM, discussed below, must be partly responsible for the higher heat transfer level. Figure 7 also shows that the EVM returns a faster recovery downstream of the rib, which is at variance with the experimental data, whereas the DSM shows better agreements. The slower recovery of the DSM-predicted Nusselt number after the rib indicates that the DSM predicts a longer separation after the rib than the EVM. A comparison between the distributions of the Nusselt number along the symmetry-plane, predicted in this study and those of Iacovides and Raisee [10], which employed low-Re models, shows that in

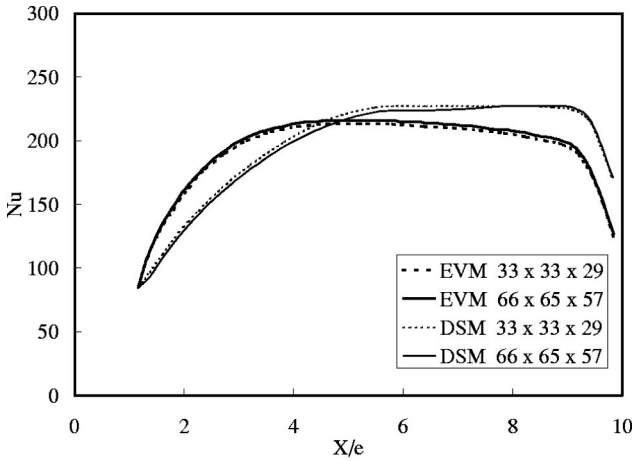

Fig. 6 Comparison of Nusselt number profile on the ribbed wall for the two grids

Downloaded 31 May 2010 to 171.66.16.27. Redistribution subject to ASME license or copyright; see http://www.asme.org/terms/Terms_Use.cfm

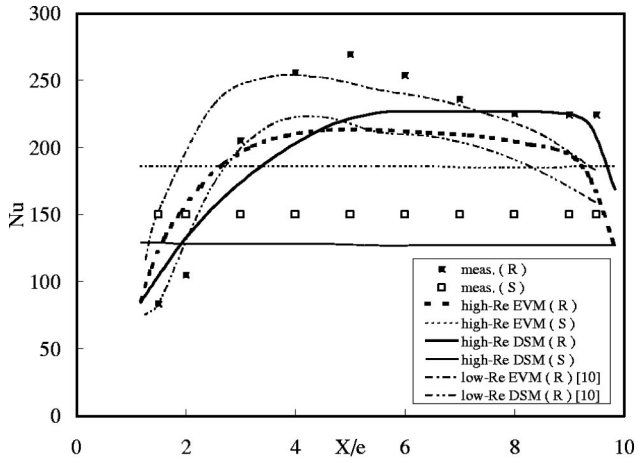

Fig. 7 Local Nusselt number comparisons along the center line of the ribbed and smooth walls, at Re=50,000

common with what is found in the high-Re-model predictions, the low-Re DSM also returns a more gradual rise in Nusselt number than the low-Re EVM, after each rib. Both the low-Re DSM and the low-Re EVM were able to return the high Nusselt number levels measured over the upstream half of the rib interval. Not surprisingly perhaps, the wall-function approach is less reliable in regions of flow separation.

Another predictive deficiency of the EVM, revealed in this figure, is that the streamwise-averaged Nusselt number on the smooth and rough sides are almost the same, which is contrary to the experimental data. Figure 8, in which the cross-duct vector plots and velocity contours at a plane half-way between the ribs are shown, might explain the reason. In the case of the DSM, the strong turbulence-driven secondary motions, shift the fluid from the smooth walls to the duct core and then directs it towards the top and bottom ribbed walls of the duct. As a result of this process the boundary layer on the smooth wall becomes much thicker. The EVM completely misses these important turbulence-driven flow features, which results in the aforementioned incorrect heat transfer distributions.

Comparison between the predicted contours of the local Nusselt number along the ribbed and smooth walls and those measured, shown in Figs. 9–11, also show that the DSM reproduced the experimental distribution more faithfully. The EVM model returns a faster recovery downstream of the rib and returns generally lower Nu levels over the entire ribbed wall, which is not in accord with the experimental data. Along the smooth wall the EVM produces very high Nu levels over the central region, while the lower values returned by the DSM are in closer agreement with the experimental data. Both EVM and DSM fail to return the dip found in the corner region, upstream of the rib. It also should be noted that both calculations cannot capture the heat transfer enhancement in the region close to the rib on the smooth wall.

4.3 Flow Through Sharp U-Bends. The flow and heat transfer through the round-ended sharp U-bend of square cross section (Fig. 12) was the third of the ''basic cases'' examined. For experimental data, Iacovides et al. [22] and Li [23] presented very detailed data not only for heat transfer but also for velocity and some of the turbulent quantities. The Reynolds number and the bend-curvature-to-duct-diameter ratio are 95,000 and 0.65, respectively. Again, only one-half of the duct needs to be considered for the solution domain assuming the symmetry. Hydrodynamically and thermally fully developed flow is set at the inlet of the domain which is located three duct diameters upstream of the bend. A uniform heat flux is applied at the duct inner and outer walls, while the side-wall is thermally insulated. The number of

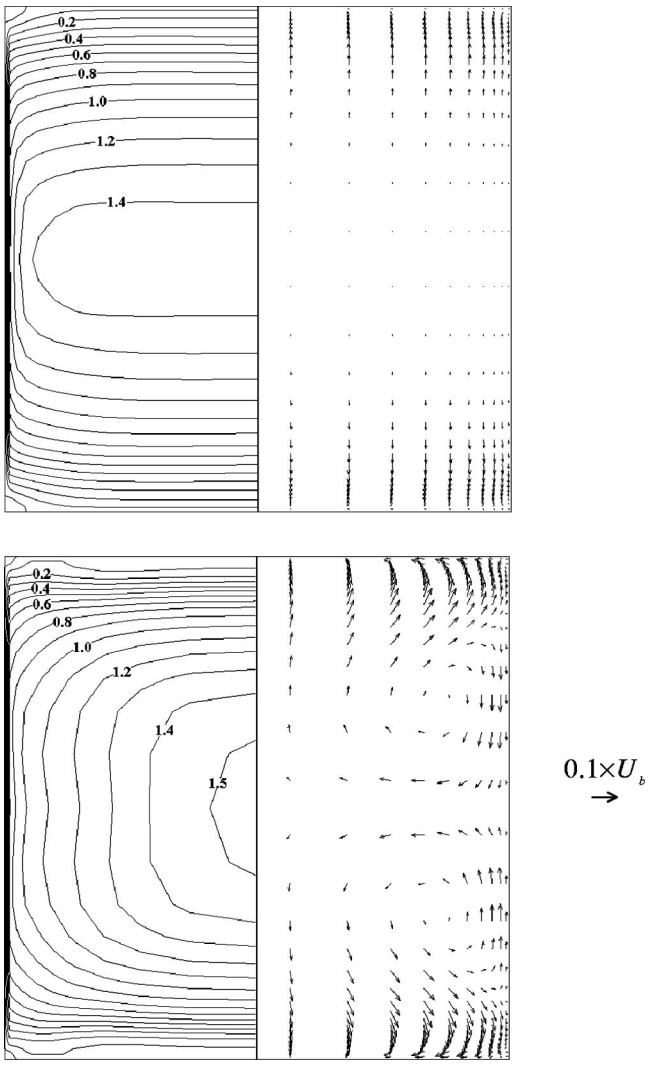

Fig. 8 Predicted flow field across the duct, half-way between the in-line ribs, at Re=50,000 (top: EVM, bottom: DSM)

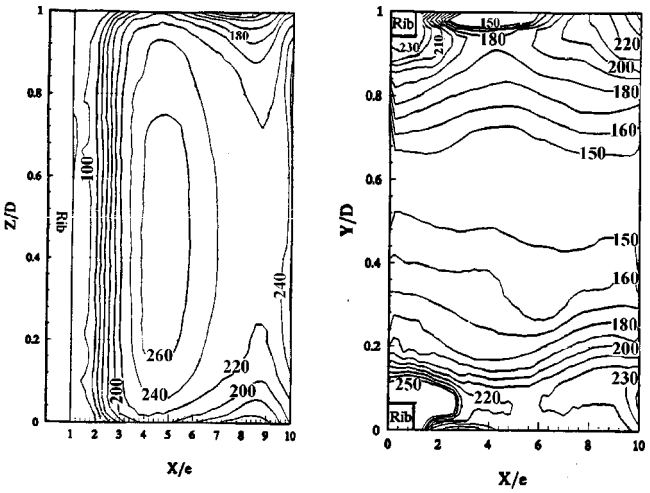

Fig. 9 Measured contours of Nusselt number at Re=50,000, Baughn and Yan [21] (left: rough surface, right: smooth surface)

Downloaded 31 May 2010 to 171.66.16.27. Redistribution subject to ASME license or copyright; see http://www.asme.org/terms/Terms_Use.cfm

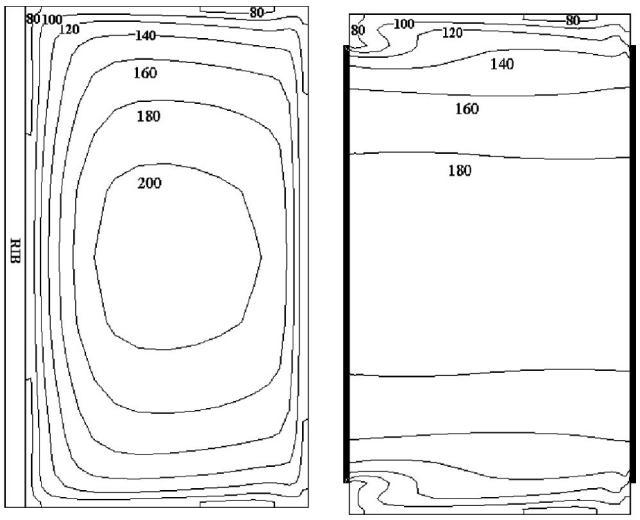

Fig. 10 Predicted contours of Nusselt number at Re=50,000 with EVM (left: rough surface, right: smooth surface)

control-volume cells is 25×13×61. A finer 49×26×122 mesh was also tested for grid sensitivity comparisons. The streamwise distributions of the Nusselt number obtained with the two grids are practically identical (Fig. 13). The converged solutions had near-wall mesh y^* values in the range $22<y^*<96$ for EVM and $21<y^*<98$ for DSM.

Figure 14 shows the streamwise distributions of the side-averaged Nusselt number on the inner and the outer walls of the bend. The higher measured levels of the heat transfer in the upstream section suggest that the flow might not have been fully

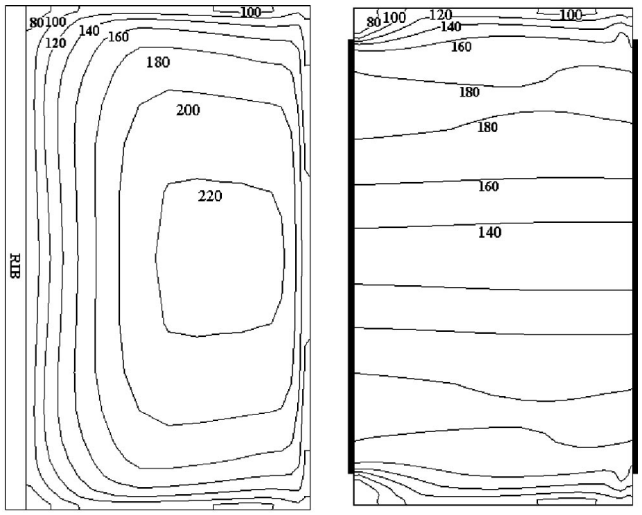

Fig. 11 Predicted contours of Nusselt number at Re=50,000 with DSM (left: rough surface, right: smooth surface)

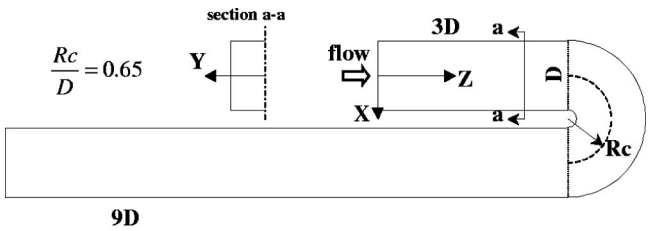

Fig. 12 Flow through sharp U-bends

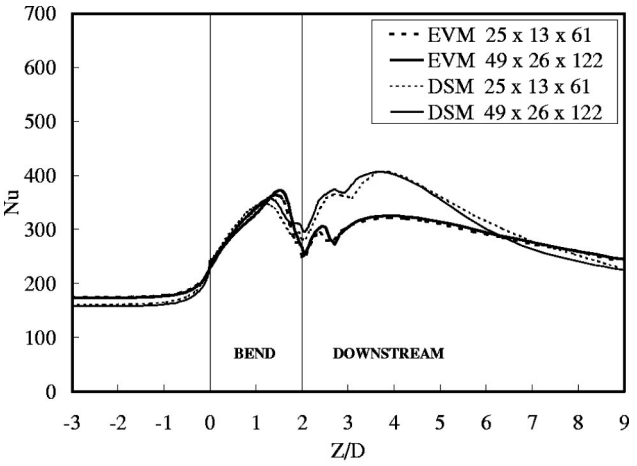

Fig. 13 Comparison of Nusselt number profile on the inner wall for the two grids

developed (at least thermally) at entry. Along the inner wall, for which experimental data within the bend are not available, the predictive improvements in the downstream region that result with the introduction of the DSM in place of the EVM are striking. The DSM clearly captures the heat transfer enhancement due to the flow reattachment after the large separation due to the strong curvature on the inner side, though it still under estimates its peak value by 15%. Along the outer wall, the EVM now substantially overpredicts the heat transfer level and it also misses the location

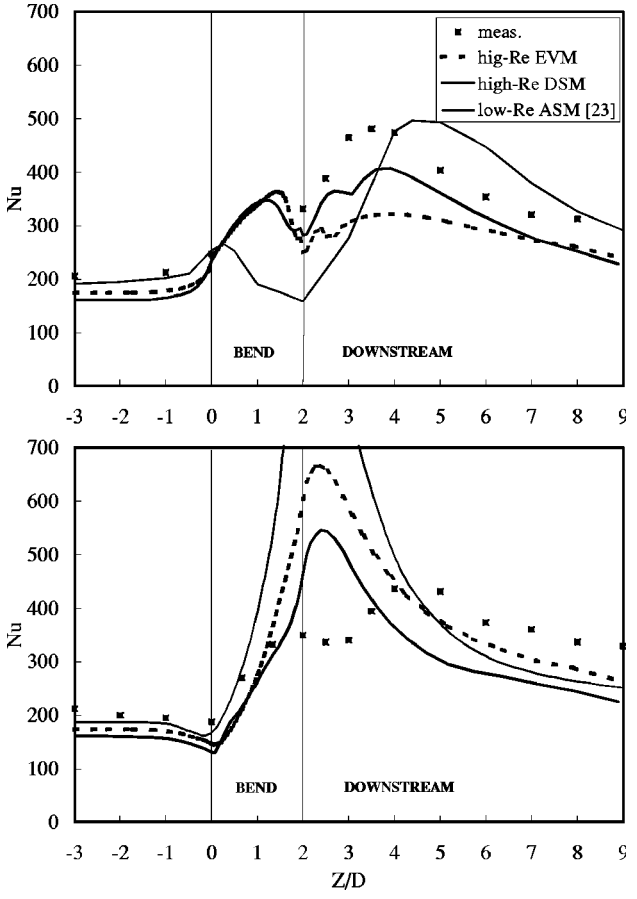

Fig. 14 Axial variation of side-averaged Nusselt number of the U-bend at Re=95,000 (top: inner wall, bottom: outer wall)

Downloaded 31 May 2010 to 171.66.16.27. Redistribution subject to ASME license or copyright; see http://www.asme.org/terms/Terms_Use.cfm

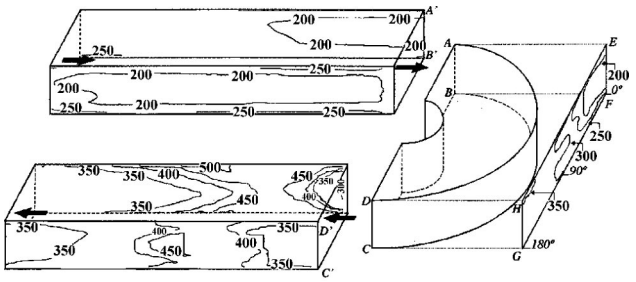

Fig. 15 Measured Nusselt number contours for the U-bend at Re=95,000, Iacovides et al. [22]

of the peak, which is predicted just at the exit of the bend, whereas the peak is located four to five diameters downstream. The DSM considerably remedies this over-shoot. The results with a low-Re ASM [23] are also shown in Fig. 14. Along the inner wall, it returns a very slow recovery after the bend exit. As a result, the maximum Nu levels predicted by the low-Re downstream of the bend, while similar to those measured, occur one or two diameters further downstream. Along the outer wall, Nu levels are considerably overpredicted by the low-Re DSM, over the second half of the bend and the first three downstream diameters. Comparisons of the local Nusselt number contours, downstream of the bend, are shown in Figs. 15 and 16. Along the inner wall, the DSM is able to reproduce the measured distribution of the local Nusselt number and in particular the fact that the maximum Nusselt number levels are not on the symmetry line, but close to the corners with the side wall. Along the outer wall, both models predict that the maximum Nusselt number levels are now on the symmetry line, but, as also indicated by the side-averaged Nusselt

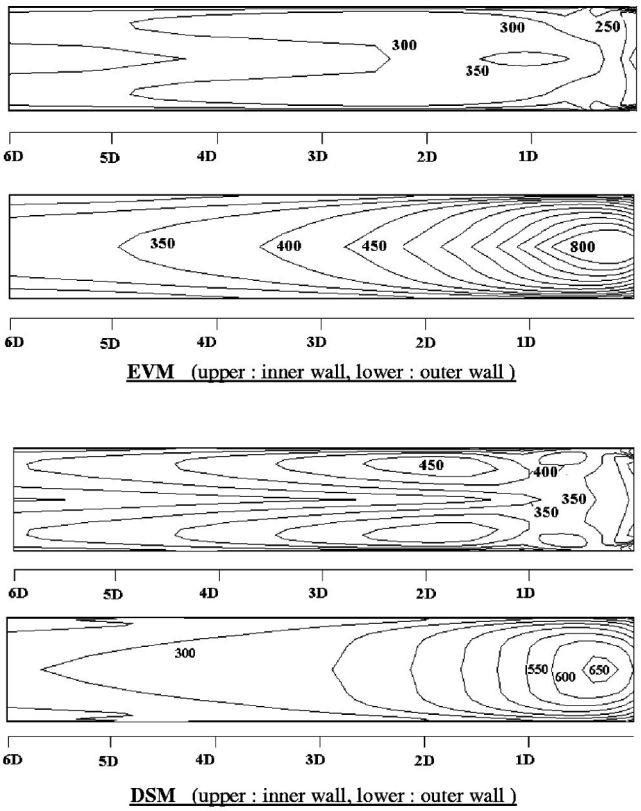

Fig. 16 Calculated Nusselt number contours for the U-bend at Re=95,000

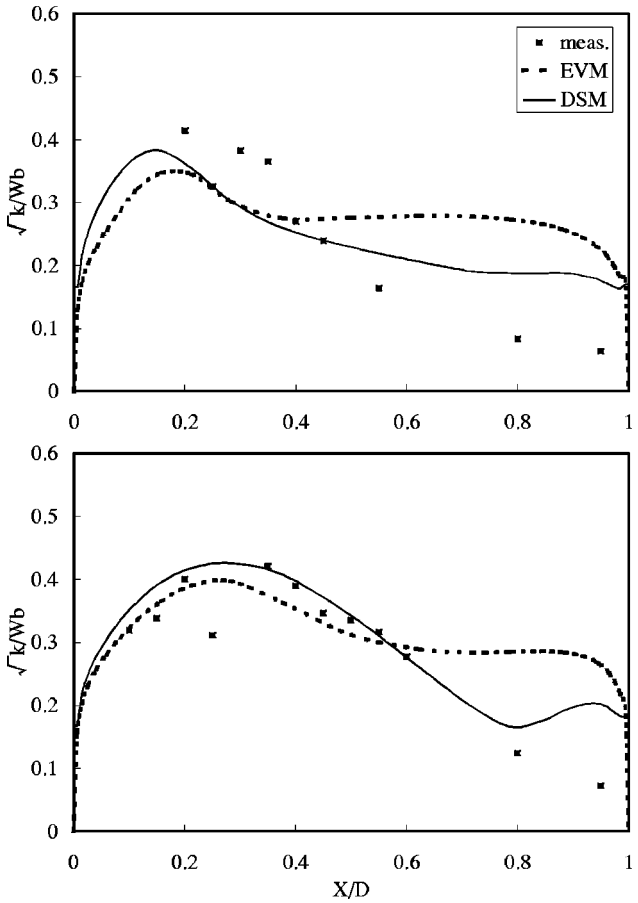

Fig. 17 Comparison of turbulent intensity profiles at Z/D=3 (top: 2Y/D=0.8, bottom: 2Y/D=0.4)

number comparisons, they occur immediately after the bend exit and not three diameters downstream, as found in the measurements.

As shown in the Fig. 17, where the turbulent intensities are plotted across the duct at two different traverse lines, downstream of the bend $(Z/D=3)$, the turbulence level decreases considerably in the outer half of the cross section, where the flow remains attached after the bend exit. The DSM captures this trend more closely than the EVM, which leads to the prediction of more reasonable levels of heat transfer. Nevertheless, the turbulence and also the heat transfer levels near the outer wall are still overpredicted even with the DSM. A possible explanation is the difficulty in capturing so-called relaminarization. The acceleration of fluid near the outer wall produces local thickening of the viscous sublayer, which in turn leads to a reduction of turbulence generation. Li [23] also showed the same trend even with a more sophisticated near-wall treatment (one, or two-equation model with the low-Re number modification). So another novel near-wall model dealing with the viscous layer thickening, under these three-dimensional flow conditions, may need to be developed in the future.

4.4 The Effects of Near-Wall Treatment in DSM With WFs. So far in this paper, DSM results have only been presented with the local equilibrium-based wall function approach, DSM-WF1. For flows in near local-equilibrium conditions, one can expect that both DSM-WF1 and -WF2 may behave in nearly the same manner. DSM-WF2 is expected to work better in separated flows. So, both approaches were tested in the flow through sharp U-bends discussed in Section 4.3.

Downloaded 31 May 2010 to 171.66.16.27. Redistribution subject to ASME license or copyright; see http://www.asme.org/terms/Terms_Use.cfm

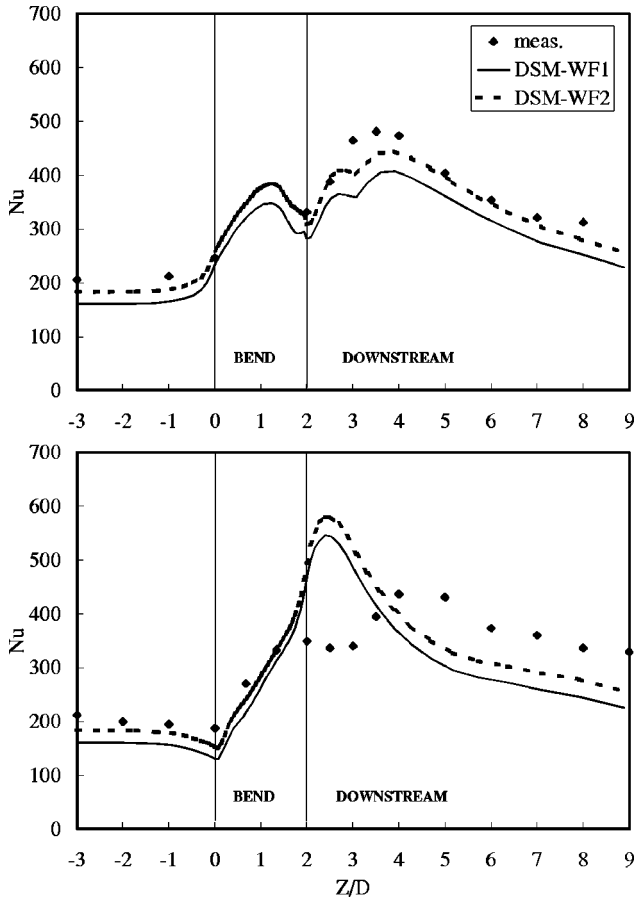

Fig. 18 Effects of wall treatment in DSM on the side-averaged Nusselt number (top: inner wall, bottom: outer wall)

Figure 18 compares the Nusselt number with both WFs in the same manner as in Fig. 14. The introduction of the more elaborate wall function, WF2, increases the Nusselt number levels returned by the DSM, bringing an overall improvement in the DSM heat transfer predictions, especially along the inner wall, where the flow separates at the bend exit. It is also notable that the introduction of WF2 also corrects the tendency of DSM-WF1 to underpredict wall heat transfer in the straight section upstream of the bend entry. While WF2 fails to improve the Nusselt number levels returned by the DSM along the outer wall at the bend exit, where the boundary layer is strongly accelerated, comparisons with the corresponding EVM predictions, shown in Fig. 14, shows that the heat transfer predictions of DSM-WF2 are in better overall agreement with the measurements than those of DSM-WF1 and also superior to those of the EVM, over the entire flow domain.

The local Nusselt number contours with DSM-WF2 are shown in Fig. 19. Comparison with Fig. 16 shows that the distribution along both walls is similar to that predicted by the simpler wall-function. The actual Nu levels predicted by DSM-WF2 along the inner wall are however higher than the corresponding DSM-WF1 levels, which, as already noted, is in closer accord with the data.

One uncertainty still present in the DSM-WF2 is the treatment of the pressure-strain terms in the near-wall cell, which at present are based on cell center values. Use of cell-average values may provide a more consistent alternative. The pressure-strain terms contain products of stresses and strains, and the variation of the former across the sublayer is both uncertain and highly influential to the averaging process.

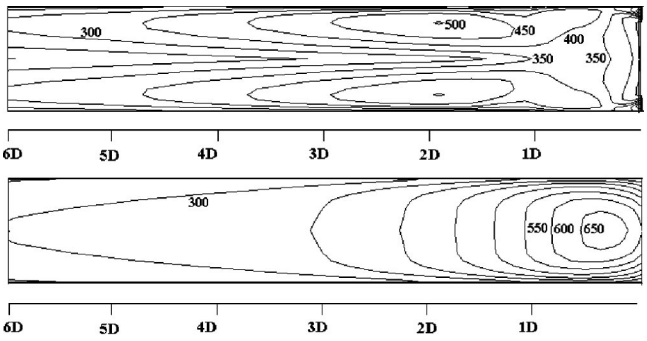

Fig. 19 Calculated Nusselt number contours for the U-bend at Re=95,000, with DSM-WF2 (upper: inner wall, lower: outer wall)

4.5 Combined Effects of the Three Key Elements. Finally, two further cases are examined which include more than one of the three key elements that appeared separately in the flows examined so far.

Rotating Smooth U-Bend. This case has been experimentally studied by Iacovides et al. [24]. As shown in Fig. 20 it involves flow through a square-ended U-bend with smooth walls, which can rotate orthogonally about an axis normal to that of the bend curvature and whose two flat walls (leading and trailing under rotation) were heated under conditions of constant wall heat flux. The Reynolds and rotation numbers are 30,000 and 0.2, respectively. The working fluid in the experiment was water, Pr=5.9. Measured Nusselt number contours for stationary and rotating

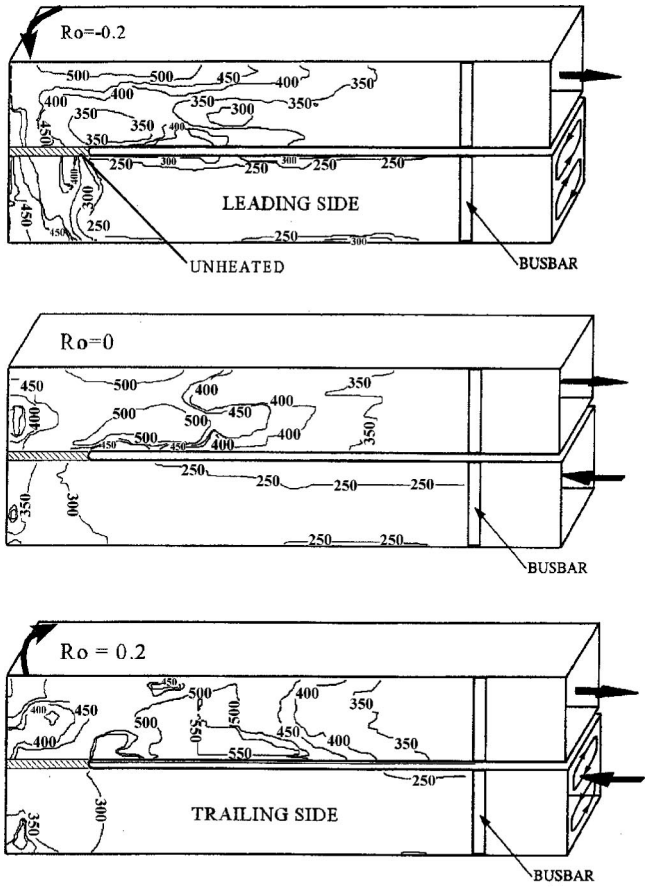

Fig. 20 Measured Nusselt number contours for the rotating U-bend at Re=30,000 and Pr=5.9 [24]

Downloaded 31 May 2010 to 171.66.16.27. Redistribution subject to ASME license or copyright; see http://www.asme.org/terms/Terms_Use.cfm

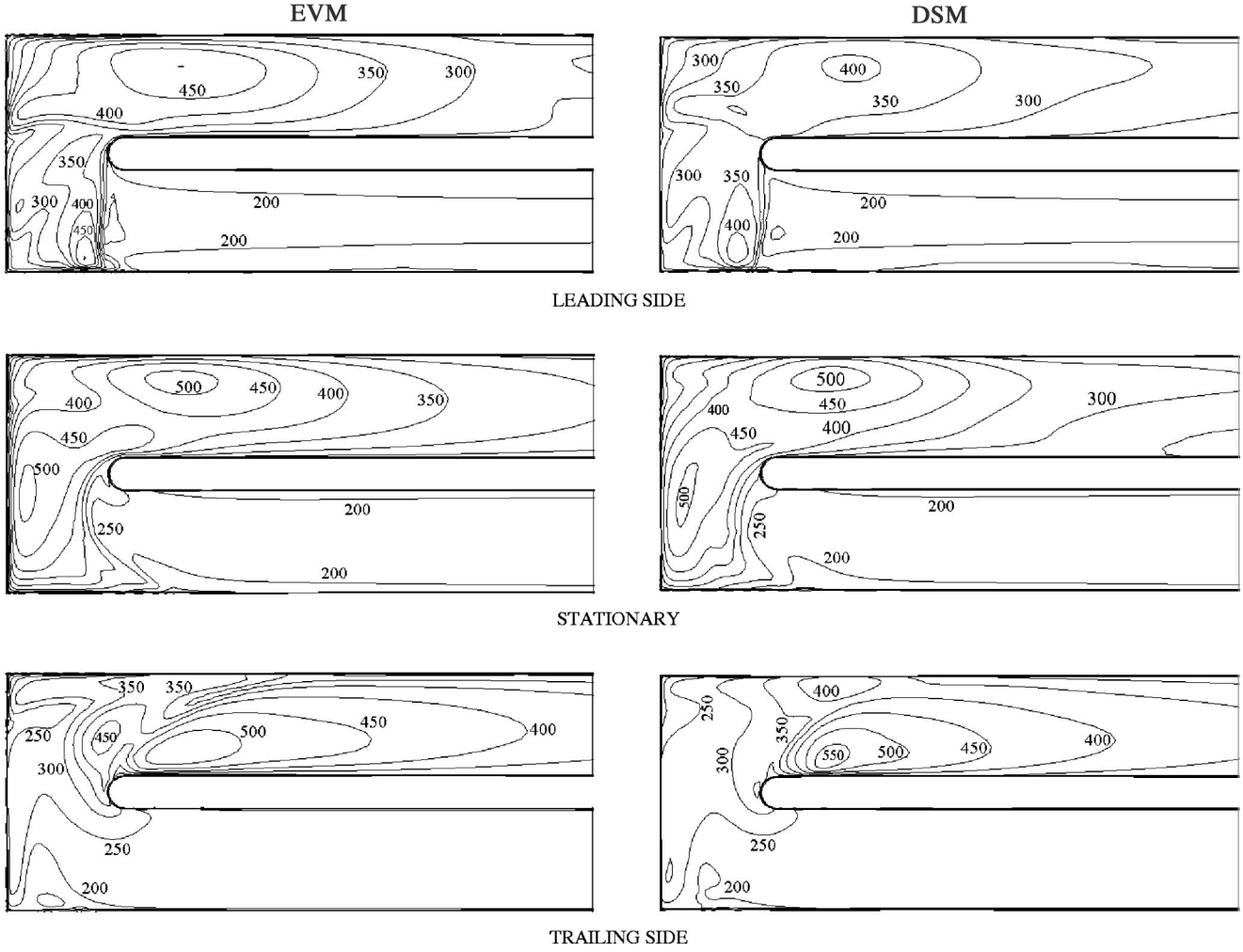

Fig. 21 Calculated Nusselt number contours for the rotating U-bend at Re=30,000 and Pr=5.9

conditions are displayed in Fig. 20. Corresponding computation results with EVM and DSM are shown in Fig. 21.

Under the stationary conditions, measured Nusselt numbers rise within the U-bend, especially along the corner with the end-wall, which is probably due to higher turbulence levels cause by flow impingement and also flow separation along the corner between the upstream outer wall and the end wall. Both EVM and DSM reproduce this trend, while they overestimate the level. At the bend exit two region of high Nu levels appear, one along the corner with the downstream inner wall and one along the corner with the downstream outer wall. After the first downstream diameter, these high-Nusselt-number levels gradually reduce. Both calculations reproduce the enhancement along the corner with the outer wall, just downstream of the bend exit, and the gradual recovery further downstream, but fail return the high levels along the corner with the inner wall.

Under rotating conditions, along the leading side, there is an abrupt rise in heat transfer at the bend entry observed in the measured data, which are consistent with the presence of a strong vortex that was found in the accompanying LDA measurements [24] and flow visualisations. This sharp increase in Nusselt number and also the particularly high levels near the outer wall, at the bend entry, are well captured in the EVM and DSM calculations. The second peak near the inner wall just after the bend entry is not, however, reproduced. Over the second half of the bend and downstream of the bend exit, where the vortex is observed to turn away from the leading side and as shown by the LDA data the flow remains attached [24], the high levels of heat transfer near the inner wall are suppressed. The measurements show that the higher heat transfer regions are now along the outer wall. The DSM predicts this trend even more faithfully than the EVM.

Along the trailing side, over the first half of the bend, the increase in the measured Nusselt number is not as strong as that observed either on the leading side, or even for the stationary case. Both predictions are consistent with this trend. After the bend exit, the measurements show that there is a sizeable high Nusselt number region, which starts along the corner with the inner wall and extends over most of the surface, while there is only a very small high Nu region near the outer wall. This thermal behavior is consistent with the large separation bubble that, according to the LDA data [24], is formed along the corner between the trailing side and the inner wall. Both computations reproduce the extended high-Nu region near the inner wall, though with both models it is predicted to start about half a diameter further upstream than in the measurements. Moreover the DSM predictions also return the small high Nu region near the outer wall, after the bend exit.

It thus appears that the two high-Re models tested reproduce most of the effects on wall heat transfer, due to the combined presence of strong curvature and orthogonal rotation. The DSM thermal predictions are in some places closer to the data, but agreement is by no means complete.

Downloaded 31 May 2010 to 171.66.16.27. Redistribution subject to ASME license or copyright; see http://www.asme.org/terms/Terms_Use.cfm

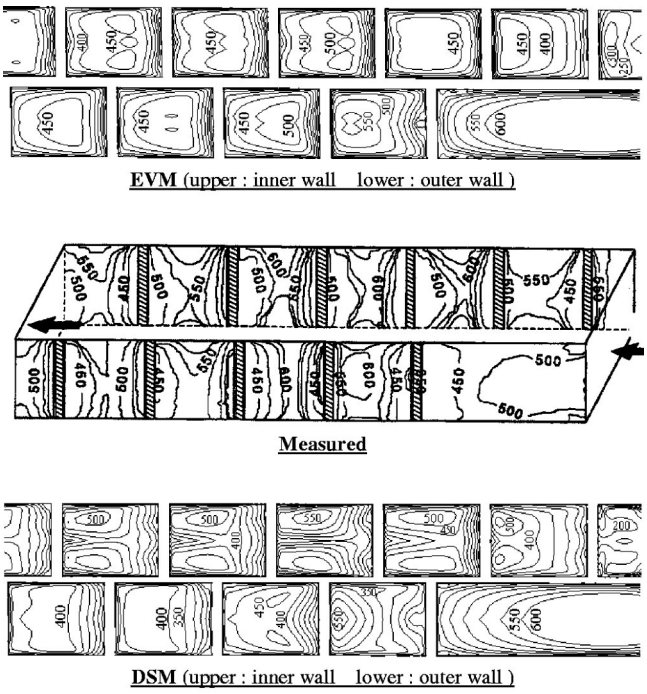

Fig. 22 Comparison of Nusselt number contours for the ribbed U-bend at Re=95,000 [22]

Rib-Roughened Duct With U-Bend. The case of flow in a nonrotating ribbed duct with a sharp U-bend [22] has been included in order to examine the effectiveness of the high-Re models in flows influenced by both strong curvature and rib-roughness. The flow conditions and the model geometry are identical to the smooth U-bend in Section 4.3, but with ribs on opposite walls in a staggered arrangement. Measured Nusselt number contours of only the region downstream of the bend exit, where the flow is most complex, are displayed in Fig. 22. In the figure, the corresponding numerical results are also shown.

Along the outer wall, the measured data shows that downstream of the bend, Nu levels fall after the first diameter, where the flow along the outer wall starts to decelerate. Over the first downstream rib interval, where, according to LDA measurements [22], a large separation bubble is present, the Nusselt number rises to levels higher than those encountered upstream of the bend. Heat transfer coefficients gradually fall over the subsequent rib intervals, tending towards the levels measured in the upstream section. Both predictions overestimate the heat transfer levels at the bend exit by about 20%, but, encouragingly, the DSM reproduces the fall in Nu after the first diameter more faithfully than the EVM. The high rise over the first rib interval and the gradual decrease over subsequent intervals are well captured by both the EVM and DSM.

Along the inner wall, over the first downstream rib interval, which is partially within the region of the bend-induced flow separation, measured heat transfer levels are especially high at the corner regions. Over the several subsequent rib intervals, the measured Nusselt number rises even further, to levels higher than those along the outer downstream wall. Further downstream, heat transfer coefficients begin to fall towards those of the upstream sections. The high levels in the corner regions over the first downstream interval are clearly captured with the DSM, while they are completely missed by the EVM. The DSM also captures more faithfully the further enhancement in wall heat transfer over the subsequent intervals. The EVM, on the other hand, clearly underpredicts the measured Nusselt number levels over this region.

These comparisons suggest that there are clear advantages in using a second-moment closure for the prediction of convective heat transfer in internal flows that are simultaneously influenced by strong curvature and surface rib-roughness. It is encouraging to see that the high-Re version of the DSM model reproduces most of the features present in the thermal measurements.

5 Conclusions

The comparisons presented here establish how effective high-Reynolds-number models are in computations of complex, three-dimensional flows that are relevant to blade-cooling applications. The cases considered contain among them the three important features encountered in blade-cooling passages, namely rotation, rib-roughness, and strong curvature. While agreement with experimental data cannot be said to be complete, the second-moment closure consistently produced more realistic flow and heat transfer predictions than the widely used effective-viscosity model. This confirms the findings of earlier studies by the UMIST group, that in complex flows with streamline curvature, flow separation and also in flows affected by Coriolis forces and rotational buoyancy, the anisotropy of the turbulence field strongly influences the flow and thermal development.

At least some of the remaining differences, between the predictions and the experimental data are caused by the use of the wall-function approach. While, as shown both here and in other studies the predictions can in many cases be improved to some extent through the introduction of low-Reynolds number models, this approach would be prohibitively expensive in industry, where the flow geometries tend to be more complex and flows are sometimes time-dependent. The development of more refined wall functions [25,26] may be a more promising route to follow.

Acknowledgments

The authors would like to express their thanks to the New Energy and Industrial Technology Development Organization (NEDO) and the Ministry of Economy, Trade and Industry (METI), who gave them the opportunity to conduct "Research and Development of Environmentally Compatible Propulsion System for Next-Generation Supersonic Transport (ESPR) project."

Nomenclature

C_{ij} = convection term in $\overline{u_i u_j}$ equation

$c_1, c_2, c_{\varepsilon 1}, c_{\varepsilon 2}, c_T, c_1^w, c_2^w, \sigma_k, \sigma_\varepsilon, c_\mu, c_l$ = turbulence modeling constants

D = duct hydraulic diameter

d_{ij} = diffusion term in $\overline{u_i u_j}$ equation

E = constant in logarithmic velocity profile

e = rib height

k = turbulent kinetic energy

Nu = Nusselt no.$=q_w D/(\lambda(T_w - T_b))$

P = pressure

P_{ij} = generation rate of turbulent stress

P_k = generation rate of turbulence energy

Pr = molecular Prandtl no.

Pr_t = turbulent Prandtl no.

R = gas constant

r = distance from center of rotation

Ra = Rayleigh no.$=\Omega^2 r D^3 (T_w - T_b)\mathrm{Pr}/(\nu^2 T_b)$

Re = Reynolds no.$=U_b D/\nu$

Ro = rotation no.$=\Omega D/U_b$

Rr = root radius

T = mean temperature

t = fluctuating temperature

U_i, U, V, W = Cartesian mean velocity components

u_i = Cartesian fluctuating velocity components

$\overline{u_i u_j}, \overline{u^2}, \overline{v^2}, \overline{w^2}, \overline{uv}, \overline{uw}, \overline{vw}$ = components of Reynolds stress tensor

y^* = nondimensional wall distance$=y k^{0.5}/\nu$

Downloaded 31 May 2010 to 171.66.16.27. Redistribution subject to ASME license or copyright; see http://www.asme.org/terms/Terms_Use.cfm

δ_{ij} = Kronecker delta
ε = dissipation rate of turbulence energy
ε_{ij} = rate of turbulence dissipation tensor
ε_{ijp} = third-order alternating tensor
ϕ_{ij} = pressure-strain correlation term
κ = constant in logarithmic velocity profile
λ = thermal conductivity
μ = dynamic viscosity
μ_t = turbulent dynamic viscosity
ν = kinematic viscosity
ρ = density
τ = shear stress
Ω = angular velocity

Subscripts

b = bulk values
N = levels prevailing at outer edge of near-wall cell
v = values at outer edge of viscous sublayer
w = wall values

Appendix A

Apparent Viscosity in the DSM. As far as the momentum equations are concerned, the diffusion terms, unlike those in the EVM models, do not have any contributions from turbulence. Instead, the Reynolds stress gradient terms are directly loaded into the source terms. As a result, the solution procedure may be quite unstable. To overcome this problem, the concept of apparent viscosity has been applied to the momentum equations. To highlight this method, the momentum equations, with the source terms neglected, are written as

$$\frac{\partial(U_iU_j)}{\partial x_j}=\frac{\partial}{\partial x_j}\left(\nu\frac{\partial U_i}{\partial x_j}\right)-\frac{\partial}{\partial x_j}(\overline{u_iu_j})$$

The foregoing equation set can also be rewritten as

$$\frac{\partial(U_iU_j)}{\partial x_j}=\frac{\partial}{\partial x_j}\left(\langle\nu+\nu_a\rangle\frac{\partial U_i}{\partial x_j}\right)+\frac{\partial}{\partial x_j}\left(-\nu_a\frac{\partial U_i}{\partial x_j}-\overline{u_iu_j}\right)$$

here ν_a is the apparent viscosity, whose contribution to the diffusion term must be cancelled out in the residual stress term, the second term in the RHS. There are several ways to determine ν_a in practice. The authors found that, in the present study, the use of the turbulent viscosity was effective enough, namely

$$\nu_a=c_\mu k^2/\varepsilon$$

Appendix B

Muscl Scheme. In the two-dimensional case (Fig. 23), the variable at the interface between the adjacent control volumes is evaluated as

$$\phi_e=\phi_P+\lambda_e^E\,sign(\Delta\phi_e)\max[0,\min\langle|\Delta\phi_e|,\mathrm{sign}(\Delta\phi_e)\times((\phi_E-\phi_P))\rangle]$$

where

$$\lambda_e^E=\frac{\overline{Pe}}{\overline{Pe}+\overline{eE}}$$

($\overline{Pe}$ and $\overline{eE}$ are distances between P and e, e and E, respectively.)

$$\Delta\phi_e=r_{PE,j}\left.\frac{\partial\phi}{\partial x_j}\right|_P$$

($r_{PE,j}$ denotes the components of the vector directed from the centroid of the upwind cell P to the centroid of the downstream cell E.)

For $\partial\phi/\partial x_j|_P$, any kind of gradient reconstruction method can be used. Green's theorem is utilized in the current work. While the foregoing formulation is for a positive velocity only (Fig. 23), the derivation of a negative velocity case is straightforward.

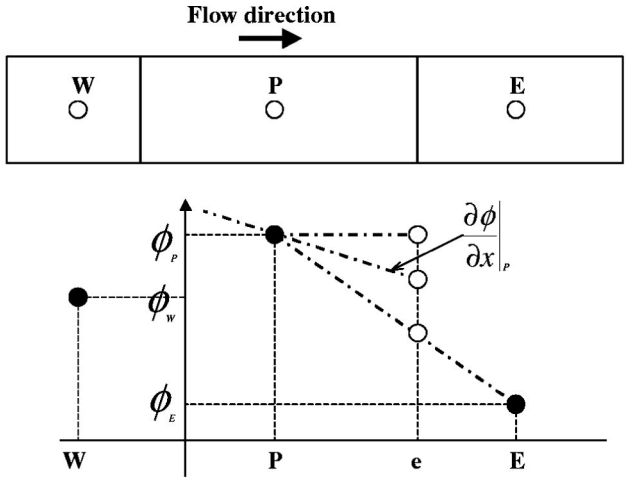

Fig. 23 MUSCL discretization of convective variables at the cell interface

References

[1] Prakash, C., and Zerkle, R., 1992, "Prediction of Turbulent Flow and Heat Transfer in a Radially Rotating Square Duct.," ASME J. Turbomach., **114**, pp. 835–846.
[2] Besserman, D. L., and Tanricut, S., 1991, "Comparison of Heat Transfer Measurements With Computations for Turbulent Flow Around 180° Bend," ASME Paper No. 91-GT-2, International Gas Turbine and Aero Congress, Orlando, FL.
[3] Xia, J. Y., and Taylor, C., 1993, "The Prediction of Turbulent Flow and Heat Transfer in a Tight Sectioned 180° Bend," Proc., 8th Int Conference Numerical Methods in Laminar and Turbulent Flows, Swansea, Wales.
[4] Rigby, D. L., Ameri, A. A., and Steinhorsson, E., 1996, "An Internal Passage Heat Transfer Prediction Using Multi-Block Grids and a k-Omega Turbulence Model," ASME Paper No 96-GT-188, International Gas Turbine and Aero Congress, Birmingham, UK.
[5] Wilcox, D. C., 1994, "A Simulation of Transition With a Two-Equation Turbulence Model," AIAA J., **23**(2), pp. 247–255.
[6] Taylor, C., Xia, J. Y., Medwell, J. O., and Morris, W. D., 1991, "A Numerical Simulation of Three-Dimensional Turbulent Flow and Heat Transfer Within a Multi-Rib Cylindrical Duct," ASME Paper No 89-GT-8, International Gas Turbine and Aero Congress, Brussels, Belgium.
[7] Prakash, C., and Zerkle, R., 1995, "Prediction of Turbulent Flow and Heat Transfer in a Ribbed Rectangular Duct With and Without Rotation," ASME J. Turbomach., **117**, pp. 255–264.
[8] Bonhoff, B., Parneix, S., Leusch, J., Johnson, B. V., Schabacker, J., and Bolcs, A., 1998, "Experimental and Numerical Study of Developed Flow and Heat Transfer in Coolant Channels With 45 and 90° Ribs," 2nd EF Conference on Turbulent Heat Transfer, Manchester, UK.
[9] Saidi, A., and Sunden, B., 2000, "Numerical Simulation of Turbulent Convective Heat Transfer in Square Ribbed Ducts," Numer. Heat Transfer, Part A, **38**, pp. 67–68.
[10] Iacovides, H., and Raisee, M., 1998, "Recent Progress in the Computation of Flow and Heat Transfer in Internal Cooling Passages of Turbine Blades," 2nd Int. Conf. Turbulent Heat Transfer, Manchester, UK.
[11] Iacovides, H., Launder, B. E., and Li, H.-Y., 1995, "The Computation of Flow Development Through Stationary and Rotating U-Bends of Strong Curvature," Int. J. Heat Fluid Flow, **17**, pp. 22–33.
[12] Bo, T., Iacovides, H., and Launder, B. E., 1995, "Developing Buoyancy-Modified Turbulent Flow in Ducts Rotating in Orthogonal Mode," ASME J. Turbomach., **117**, pp. 474–483.
[13] Jones, W. P., and Launder, B. E., 1972, "The Prediction of Laminarization With a Two-Equation Model of Turbulence," Int. J. Heat Mass Transfer, **15**, pp. 301–314.
[14] Launder, B. E., Reece, G. J., and Rodi, W., 1975, "Progress in the Development of a Reynolds Stress Turbulence Closure," J. Fluid Mech., **68**, pp. 537–566.
[15] Lin, C. A., 1991, "Computation of Three-Dimensional Jet-Injection Processes With Second-Moment Closures," Ph.D. thesis, Faculty of Technology, University of Manchester.
[16] Lien, F.-S., 1992, "Computation Modeling of 3D Flow in Complex Ducts and Passages.," Ph.D. thesis, Faculty of Technology, University of Manchester.
[17] Gibson, M. M., and Launder, B. E., 1978, "Ground Effects on Pressure Fluid Fluctuations in Atmospheric Boundary Layers," J. Fluid Mech., **86**, pp. 491–511.

Downloaded 31 May 2010 to 171.66.16.27. Redistribution subject to ASME license or copyright; see http://www.asme.org/terms/Terms_Use.cfm

[18] Okita, Y., Kodama, H., and Yamawaki, S., 1997, ''Numerical Simulation of Flow and Heat Transfer in 3D Complicated Geometries Using Unstructured Grids,'' AIAA-97-1948.
[19] Rhie, C. M., and Chow, W. L., 1983, ''Numerical Study of the Turbulent Flow Past and Airfoil With Trailing Edge Separation,'' AIAA J., **21**, pp. 1525–1532.
[20] Wagner, J. H., Johnson, B. V., and Hajek, T. J., 1991, ''Heat Transfer in Rotating Passages With Smooth Walls and Radial Outward Flow,'' ASME J. Turbomach., **113**, pp. 42–51.
[21] Baughn, J. W., and Yan, X., 1992, ''Local Heat Transfer Measurements in Square Ducts With Transverse Ribs,'' ASME National Heat Transfer Conf.
[22] Iacovides, H., Jackson, D. C., Kelemenis, G., and Launder, B. E., 2000, ''The Measurement of Local Wall Heat Transfer in Stationary U-Ducts of Strong Curvature, With Smooth and Rib-Roughened Walls,'' ASME J. Turbomach., **122**, pp. 386–392.
[23] Li, H., 1995, ''The Computation of 3D-Turbulent Flows in Curved and Rotating Ducts,'' Ph.D. thesis, UMIST.
[24] Iacovides, H., Jackson, D. C., Kelemenis, G., Launder, B. E., and Yuan, Y. M., 1999, ''Experiments on Local Heat Transfer in a Rotating Square-Ended U-Bend,'' Int. J. Heat Fluid Flow, **20**, pp. 302–310.
[25] Craft, T. J., Gerasimov, A. V., Iacovides, H., and Launder, B. E., 2002, ''Progress in the Generalization of Wall-Function Treatments,'' Int. J. Heat Fluid Flow, **23**, pp. 148–160.
[26] Craft, T. J., Gant, S. E., Iacovides, H., and Launder, B. E., 2001, ''Development and Application of a New Wall Function for Complex Turbulent Flows,'' ECCOMAS CFD Conference, Swansea, UK.

Downloaded 31 May 2010 to 171.66.16.27. Redistribution subject to ASME license or copyright; see http://www.asme.org/terms/Terms_Use.cfm

A Unified Approach for Designing a Radial Flow Gas Turbine

M. S. Y. Ebaid

F. S. Bhinder

G. H. Khdairi

King Abdulah II Design & Development Bureau, Amman 11195, Jordan

Radial flow turbo machines have been used for a long time in a variety of applications such as turbochargers, cryogenics, auxiliary power units, and air conditioning of aircraft cabins. Hence numerous papers have been written on the design and performance of these machines. The only justification for yet another paper is that it would describe a unified approach for designing a single stage inward flow radial turbine comprising a rotor and the casing. The current turbine is designed to drive a direct-coupled permanent magnet high-speed alternator running at 60000 rpm and developing a maximum of 60 kW electrical power. The freedom of choice of the tip diameter and the tip width of the rotor that would be necessary for optimum isentropic efficiency of the turbine stage was restricted by the specified rotational speed and power output. Hence, an optimization procedure was developed to determine the principal dimension of the rotor. The mean relative velocity in the rotor passages in the direction of the flow would be accelerated but flow velocity on the blade surfaces experiences a significant space rate of deceleration. The rate of deceleration can be controlled by means of a proper choice of the axial length of the rotor. A prescribed mean stream velocity distribution procedure was used to spread the rate of deceleration of the mean flow velocity along the meridional length of the flow passages. The nozzle-less volute casing was designed to satisfy the mass flow rate, energy and angular momentum equations simultaneously. This paper describes the work undertaken to design both the rotor and the casing. The work was motivated by the growing interest in developing gas turbine based hybrid power plant for road vehicles. The authors believe that the paper would lead to a stimulating discussion. [DOI: 10.1115/1.1574824]

Introduction

Inward flow radial turbines have established their place in industrial applications, especially in the field of small turbomachinery because of their simplicity, reliability, low emissions, multi-fuel capabilities and fast response. These attractive features have made them ideal prime movers for many applications, particularly for producing small electrical power, typically in the range of 10–100 kW.

Research programmes regarding the design of these machines have been cited in the open literature. For the rotor design, both Von der Nuell [1] and Balje [2,3] suggested that the choice of the principal dimensions might be based on specific speed and specific diameter. Rohlik [4] developed a relationship between specific speed and a number of important design ratio. He argued that for the same specific speed, it was possible to produce a large number of rotor shapes by choosing different combination of these ratios. Therefore, the problem was to determine specific speed that would result in maximum efficiency.

Wallace et al. [5] used one-dimensional analysis together with empirical loss models to determine the principal dimensions of the rotor. Further studies on one-dimensional design analysis procedures have been described also by other authors, Rodgers [6], Whitfield and Baines [7], and Wasserbauer and Glassman [8]. The common features of these studies are that the user has to specify the geometry of the turbine, together with any assumptions about losses from which to calculate efficiency values. Since most of the turbine geometry is likely to be undefined and many different assumptions about losses are possible, a large combinations are possible and must be investigated. This is time consuming therefore, there is a great incentive to reduce the time taken and the number of cases to be investigated. Whitfield [9] proposed a method based on maximizing efficiency by minimizing the energy losses of the fluid which are considered to be a function of the square of the velocity and expressed at inlet and outlet conditions in terms of Mach numbers. The procedure is largely nondimensional and it is based on an initial power ratio and an estimate of the total to static efficiency. The later in particular can cause problems, because the designer has still to decide on the likely magnitude of the efficiency that can be achieved.

In recent years, a number of computer aided design procedures have been developed for turbine rotors. Benson and Fisher [10] and Baines et al. [11] in their work assumed a preliminary shape, which would be improved progressively through analysis. This work is an indirect mode and the main draw back of this approach is that a decision on whether or not a particular step produces a satisfactory result tends to be made quite arbitrarily. Furthermore, it is not a simple matter to determine what changes in the geometry would produce the desired results.

The turbine casing design is often based on the assumptions of an adiabatic incompressible flow, together with a free vortex distribution about the rotor. The passage design is specified in terms of area to radius ratio at the centroid as described by Bhinder [12], Chapple et al. [13], Hussian et al. [14]. Whitfield and Noor [15] extended the work further by considering the flow to be viscous and compressible.

From the foregoing introduction, several limitations to these procedures can be identified which deserve attention:

1. Most of the design methodologies were based on iterative procedures involving successive modifications to the hub, shroud and blade profiles to arrive at an acceptable and efficient design.
2. For a given set of performance requirements such as power output, pressure ratio, and rotational speed or mass flow parameter, several rotor shapes may be drawn which would appear to meet the specifications. The choice of optimum shape is by no means simple.
3. The choice of number of rotor blades was based on empirical formulas given in the open literature and the choice of axial length was made arbitrarily based on known engineering practice.

Contributed by the International Gas Turbine Institute and presented at the International Gas Turbine and Aeroengine Congress and Exhibition, Amsterdam, The Netherlands, June 3–6, 2002. Manuscript received by the IGTI January 25, 2002; revised manuscript received January 6, 2003. Paper No. 2002-GT-30578. Review Chair: E. Benvenuti.

 Copyright © 2003 by ASME

Downloaded 31 May 2010 to 171.66.16.27. Redistribution subject to ASME license or copyright; see http://www.asme.org/terms/Terms_Use.cfm

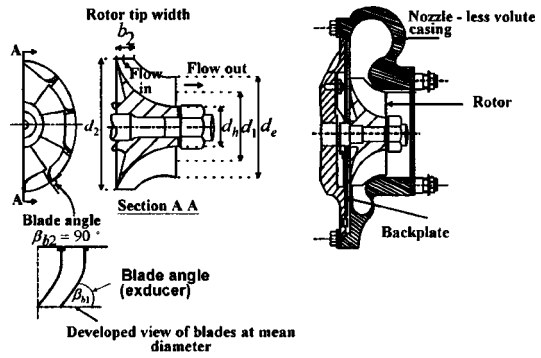

Fig. 1 The geometrical shape and the principal dimensions of the IFR gas turbine

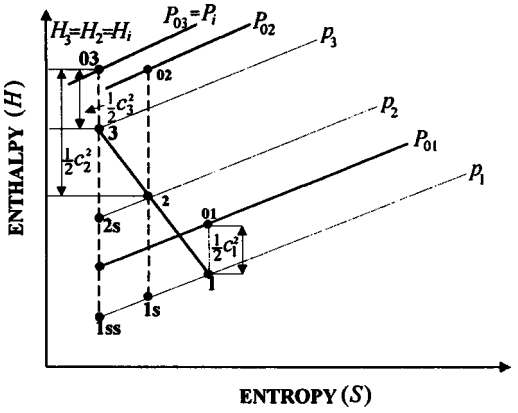

Fig. 3 Enthalpy—entropy diagram for a turbine stage

4. Papers describing the whole design of the rotor and the casing were scarce for a specific rotational speed and power intended for the current design.

This paper provides a unified approach for designing radial flow gas turbines, which, it is claimed, does not suffer from the above limitations.

Proposed Design Procedure

The design procedure of an inward flow radial (IFR) turbine was divided into the following two stages:

1. The design of the turbine rotor for which the design methodology consists of two main procedures: firstly, the determination of the optimum principal dimensions and number of blades of the turbine rotor; secondly, the optimization of axial length and passage geometry for a prescribed or assumed mean-stream velocity.
2. The design of the nozzle-less volute casing for which the mass flow rate, energy and angular momentum equations must be satisfied simultaneously.

Rotor Design

The Choice of the Principal Dimensions of the Rotor. The geometrical shape of a typical IFR turbine rotor is shown in Fig. 1. The inlet and outlet velocity diagrams and the thermodynamics of the expansion process are illustrated in Figs. 2 and 3, respectively.

The momentum, continuity and energy equations can be combined to produce the following principal equations:

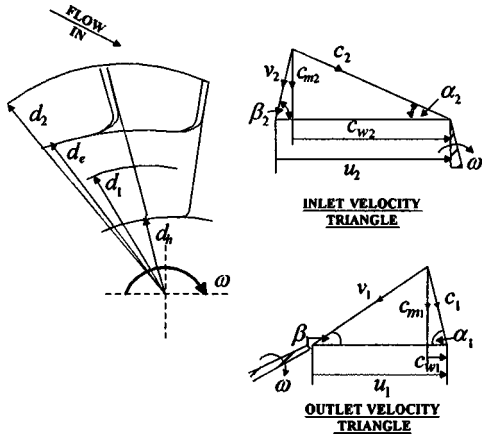

Fig. 2 Velocity triangles of an inward flow radial gas turbine

Speed parameter

$$\frac{d_2 N}{\sqrt{C_p T_i}} = \left(\frac{60\sqrt{2}}{\pi}\right)\cdot\left(\frac{u_2}{c_s}\right)\cdot\left[\sqrt{1-\left(\frac{P_e}{P_i}\right)^{\gamma-1/\gamma}}\right] \tag{1}$$

Absoluter flow angle at rotor inlet

$$\cos\alpha_2 = \left(\frac{c_{w2}}{u_2}\right)\cdot\left(\frac{\pi}{60}\right)\cdot\left(\frac{d_2 N}{\sqrt{C_p T_i}}\right)\cdot\left(\sqrt{\frac{1+\frac{\gamma-1}{2}M_2^2}{(\gamma-1)M_2^2}}\right) \tag{2}$$

Blade width to tip diameter ratio

$$\left(\frac{b_2}{d_2}\right) = \frac{\dot{m}\sqrt{C_p T_i}}{d_2^2 P_i}\left[\frac{1}{\pi B_{f_2}\left(\frac{\sqrt{\gamma-1}}{\gamma}\right)}\right]\left[\frac{\left(1+\frac{\gamma-1}{2}M_2^2\right)^{\gamma+1/2(\gamma-1)}}{M_2\sin\alpha_2}\right] \tag{3}$$

Mass flow parameter

$$\frac{\dot{m}\sqrt{C_p T_i}}{d_2^2 P_i} = \left(\frac{P_e}{P_i}\right)\cdot\left[\frac{1}{\left\{1-\eta_{tt}\left(1-\left(\frac{P_e}{P_i}\right)^{\gamma-1/\gamma}\right)\right\}}\right]^{1/2} \times\left[B_f\left(\frac{\pi}{4}\right)\left(\frac{\gamma}{\sqrt{\gamma-1}}\right)\cdot\left(\left(\frac{d_e}{d_2}\right)^2-\left(\frac{d_h}{d_2}\right)^2\right)\right] \times\left[\frac{M_{er}\sin\beta_e}{\left(1+\left(\frac{\gamma-1}{2}\right)(M_{er}\sin\beta_e)^2\right)^{\gamma+1/2(\gamma-1)}}\right] \tag{4}$$

$$B_{f_2} = 1-\frac{1}{\pi}\left[n\left(\frac{\overline{t_2}}{d_2}\right)\right] \tag{5}$$

$$B_{f_1} = \frac{2}{\pi}\frac{n(\overline{t_1}/d_2)}{[(d_e/d_2)+(d_h/d_2)]} \tag{6}$$

For a given set of design conditions as listed in Table 1, the optimum principal dimensions of the rotor were found by solving equations (1) to (6) within the specified ranges of the constraints variables. The solution can be obtained by using a suitable optimization algorithm. The authors used the algorithms OPRQP developed by Biggs [16,17]. The general mathematical representation of the algorithm can be described as:

$$\text{Minimize } F(\overline{x}), \quad \text{where } \overline{x}=[x_1,\ldots x_n]^t$$

$$\text{Subject to: } g_i(\overline{x})=0 \quad i=1,\ldots q$$

$$g_j(\overline{x})\geq 0 \quad j=q+1,\ldots m$$

Downloaded 31 May 2010 to 171.66.16.27. Redistribution subject to ASME license or copyright; see http://www.asme.org/terms/Terms_Use.cfm

Table 1 Input data at design point

Design variable	Design value
Mass flow, $\dot{m}$	0.572
Pressure ratio, P_i/P_e	3.6
Inlet stagnation temperature, T_i	1000 K
Rotational speed, N	60,000 rpm
Total to total efficiency, η_{tt}	0.87
Average blade thickness at rotor inlet, $\overline{t_2}$	2.5 mm
Average blade thickness at rotor outlet, t_1	1.5 mm

where $F(\overline{x})$ represents the objective function, in this case is the inlet tip diameter d_2 and the functions $g_i(\overline{x})$ and $g_j(\overline{x})$ are sets of equality and inequality constraints, respectively. Providing details of the optimization program used are beyond the scope of this paper, but may be found in references [16,17].

Optimization Results

The optimization program was run for a number of blades ranging from 12 to 20. The number of blades was specified within this range in accordance with the assumed efficiency η_{tt}, blockage B_f and blade loading factor c_{w2}/u_2.

The results indicated clearly that the optimum number of blades lies in the range between 12 and 20. Consequently, any blade number in this range would be acceptable provided it satisfies the other design criteria and specifications set by the designer. The design velocity diagrams based on optimization technique and the complete design data are shown in Fig. 4 and Tables 2 and 3, respectively.

Optimization of Passage Geometry and the Choice of Axial Length. The choice of a suitable axial length is almost a prerequisite for completely defining the passage geometry. The effect of the axial length on velocity distribution is shown qualitatively in Fig. 5. It can be seen that the shortest channel length of rotor (A) should produce minimum friction loss, but the flow would separate due to high deceleration rate in the exducer section. In contrast, rotor (C), which has the longest channel, would be expected to produce highest friction loss, but flow separation would be delayed due to the gradual deceleration rate in the exducer. Following this, a prescribed mean stream velocity distribution approach was used to optimize the passage geometry and the axial length of the rotor.

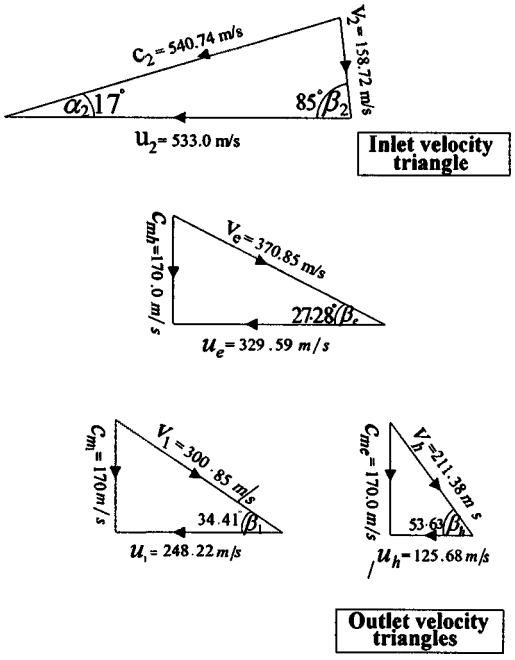

Fig. 4 Velocity triangle based on numerical optimization program

Table 2 Design data (1) for the turbine rotor based on numerical optimization

Flow velocities at rotor inlet (m/s)	Flow velocities at rotor exit (m/s)
$c_2=538.82$	$c_1=186.77$
$v_2=158.13$	$c_{w2}=0.0$
$c_{m2}=157.34$	$c_h=186.77$
$c_{w2}=515.11$	$c_e=186.77$
	$v_1=346.77$
	$v_h=267.32$
	$v_e=411.39$
Rotor speed at rotor inlet and exit (m/s)	Performance parameters
$u_2=531.24$	$\dot{m}=0.574$
$u_1=292.18$	$S_P=0.157$
$u_h=191.25$	$S_T=0.24$
$u_e=366.55$	$\eta_{tt}=0.87$
	$R=0.56$
	$c_{m1}/u_2=0.32$
	$N_s=0.56$

The relative velocity vector $\overline{V}$ at any point inside the turbine rotor passage, as shown in Fig. 6, can be resolved into three basic components along the axial, radial and tangential directions, $\overline{V_z}$, $\overline{V_r}\overline{V_w}$, ... Here $\overline{V_m}$ is the velocity vector along the mean streamline in the hub-to-shroud plane, hence:

$$\overline{V}=\overline{V_z}+\overline{V_r}+\overline{V_w} \tag{7}$$

The boundary values of the components of the relative velocity are known from the inlet and outlet velocity triangles, which resulted from the previous optimization, as shown in Fig. 6.

At rotor inlet: $V_z=0$, $V_r=(V_r)_{\max}$, and $V_w=(1-\psi)U_2$

At rotor outlet: $V_z=(V_z)_{\max}$, $V_r=0$, and $V_w=V_z\sin\beta_1$

The angles shown in Fig. 6 can be expressed in terms of the velocities as follows:

$$\beta=\sin^{-1}\sqrt{1-V_m^2/V},\quad \tan\theta=\frac{V_z}{V_w}\quad \text{and}\quad \cos\alpha=\frac{V_z}{V_w}$$

Table 3 Design data (2) for the turbine rotor based on numerical optimization

Design specifications	Geometrical dimensions (cm)
$W_{net}=60$ kW	$d_2=16.91$
$N=60000$ rpm	$b_2=0.87$
$P_i/P_e=4.0$	$t_2=0.25$
$T_i=1000$ K	$d_1=9.30$
$u_2/c_S=0.67$	$d_h=6.09$
	$d_e=11.67$
	$t_1=0.15$
Flow angles at rotor inlet and exit (deg)	Mach numbers at rotor inlet and exit
$\alpha_2=17.0$	$M_2=0.93$
$\beta_2=84.2$	$M_1=0.35$
$\alpha_1=90$	$M_{hr}=0.50$
$\alpha_h=90$	$M_{1r}=0.65$
$\alpha_e=90$	$M_{er}=0.8$
$\beta_h=44.32$	
$\beta_1=32.59$	
$\beta_e=27.0$	

Downloaded 31 May 2010 to 171.66.16.27. Redistribution subject to ASME license or copyright; see http://www.asme.org/terms/Terms_Use.cfm

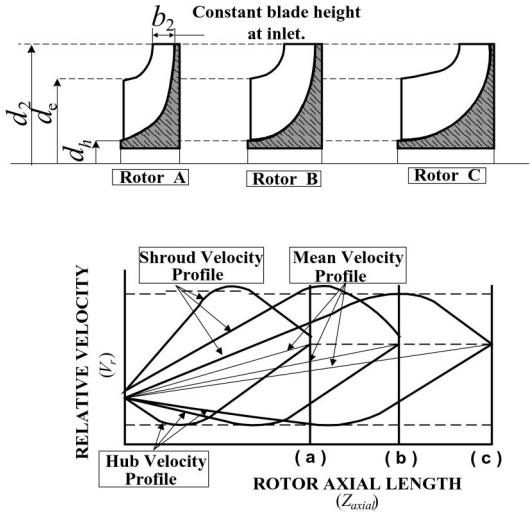

Fig. 5 Qualitative description of the effect of axial length on velocity distribution

By combining the foregoing relationships, the angles (α, β, and θ) are related to each other by the following relationship:

$$\tan \beta = \tan \theta \cos \alpha \tag{8}$$

The spatial description of the mean streamline can be found iteratively by assuming a starting value for the meridional length z_m, and the distributions of the relative velocity vector.

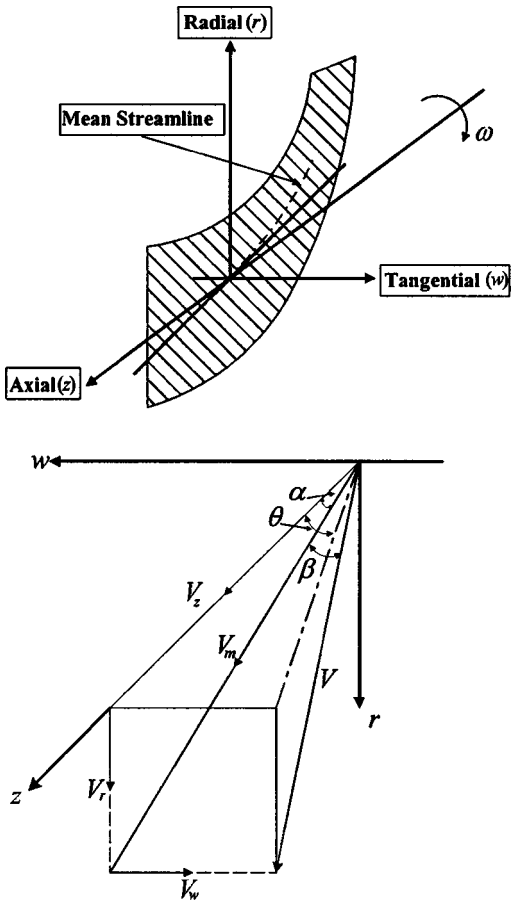

Fig. 6 Notation for the relative velocity vector and its components

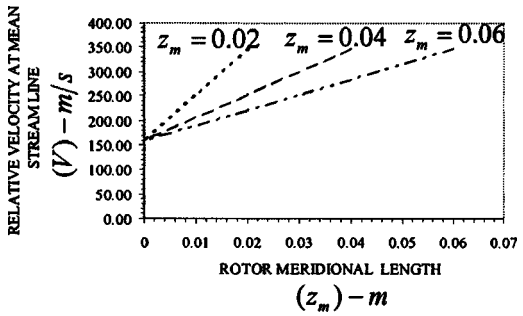

Fig. 7 Assumed variation of the relative velocity vector at various meridional lengths for the same boundary conditions

Figure 7 shows three meridional lengths 0.02, 0.04, and 0.06 of the turbine rotor. Figure 8 describes the velocity components V_r, V_z and V_w for one assumed value of Z. At the start, all these figures are based on the assumption that the variation of the relative velocity vector (V) is linear.

A computer program was written to perform the iterative calculations to check this linear relationship variation of relative velocity vector along the mean streamline. The output results are plotted in Fig. 9 and a flow chart based on this program is shown in Fig. 10.

The next step was to optimize the axial length (Z) by minimizing the loss of stagnation pressure in the flow channels. For this purpose, the losses were expressed as functions of the resultant velocity (V), the length of the channel, and the radius of curvature r_c.

Several models are available in Dallenbach [18] and Rodgers [19] which take account of the losses. These loss models were adopted for the turbine rotor. A detailed review of these loss models is outside the scope of this paper, but it should be mentioned that any loss models might be integrated into the program as subroutine. A computer program was written to optimize the axial length and the flow passage based on the relations listed here.

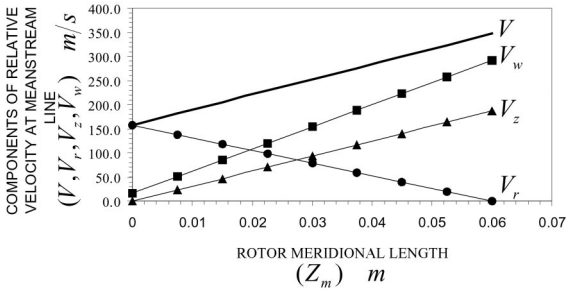

Fig. 8 Assumed linear relationship of relative velocity vector and its components for an assumed $Z = 0.06$ m

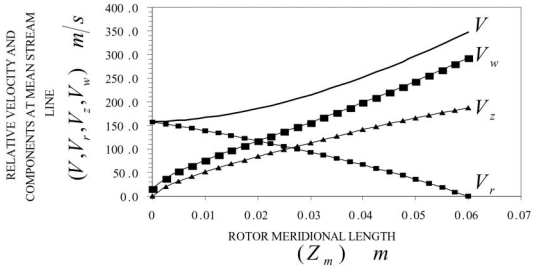

Fig. 9 Prescribed relative velocity distribution along mean streamline for an assumed meridianal length of 0.06 m

Downloaded 31 May 2010 to 171.66.16.27. Redistribution subject to ASME license or copyright; see http://www.asme.org/terms/Terms_Use.cfm

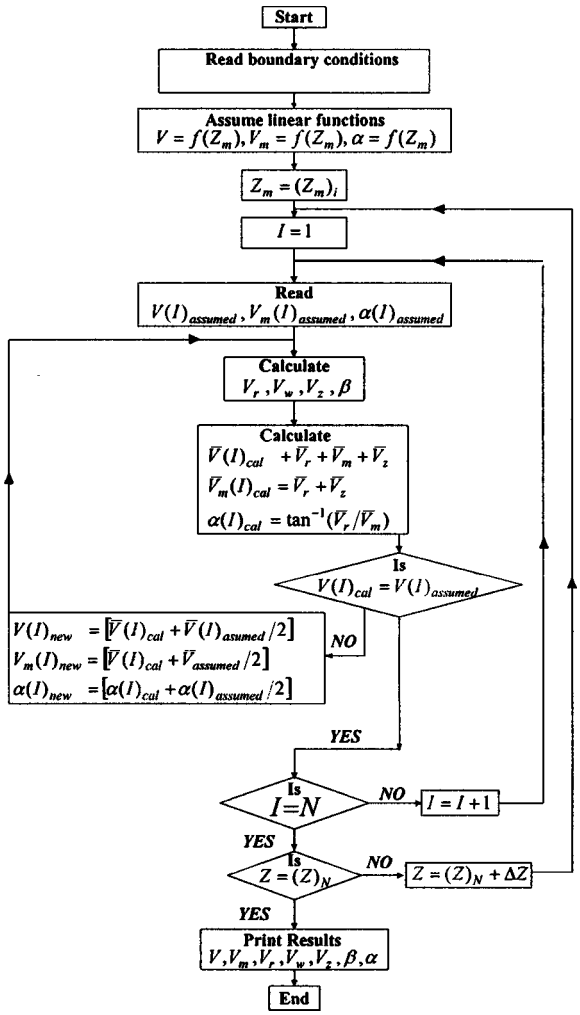

Fig. 10 Flow chart for relative velocity vector variation along mean streamline

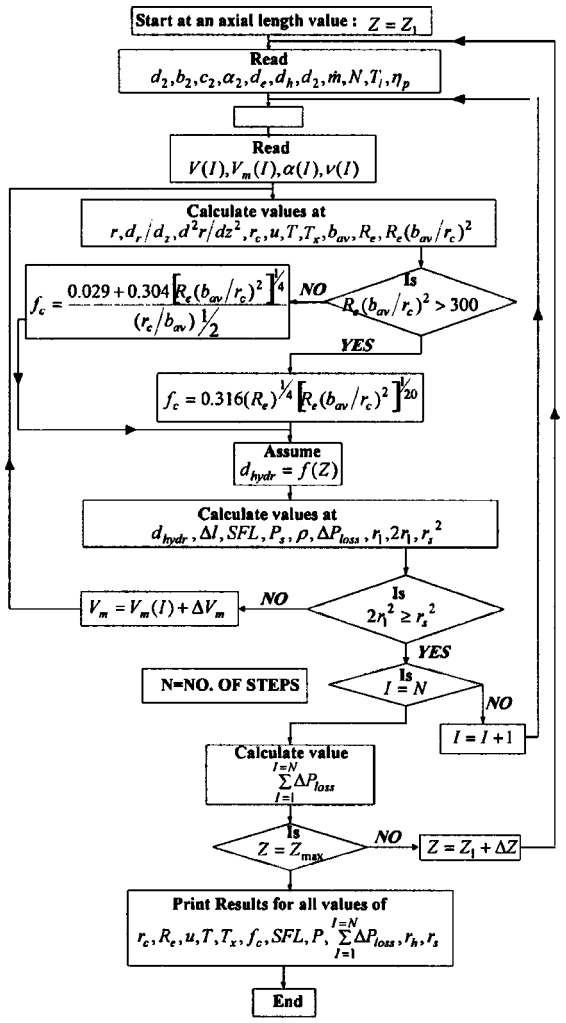

Fig. 11 Flow chart for the design of the flow passage and the optimization of the meridional length

Here the radius r of the mean streamline in the meridional plane can be represented using Lame's ovals relationship as

$$r = (r - r_2)\left[1 - \left(\frac{z_m - z_{m1}}{z_{m2} - z_{m1}}\right)^3\right]^{1/2} + r_2 \tag{9}$$

The first and second derivatives of dr/dz are given in Eqs. (10) and (11), respectively

$$\frac{dr}{dz} = -\left[\frac{3}{2}\right]\left(\frac{r_1 - r_2}{z_{m2} - z_{m1}}\right)\frac{l}{j}\left(\frac{z_m - z_{m1}}{z_{m2} - z_{m1}}\right)^2\left(\frac{r - r_2}{r_1 - r_2}\right)^{-1} \tag{10}$$

$$\frac{d^2r}{dz_m^2} = \left[\frac{dr}{dz_m}\right]\left[\left(\frac{2}{z_m - z_{m1}}\right) + \left(\frac{-1}{r - r_2}\right)\left(\frac{dr}{dz_m}\right)\right] \tag{11}$$

The length of the streamline is given by

$$L = \int_{z_{m1}}^{z_{m2}}\left(1 + \frac{dr}{dz_m}\right)dz_m \tag{12}$$

The temperature at any section inside the passage

$$\frac{T_x}{T_i} = 1 + \frac{1}{2}\left(\frac{u_x^2 - 2c_{wi}u_i}{C_p T_i}\right) \tag{13}$$

The pressure at any section inside the passage

$$\frac{P_x}{\phi P_i} = \left(\frac{T_x}{T_i}\right)_s^{r/r-1} \tag{14}$$

The density at any section inside the passage

$$\rho_x = \left(1 - \frac{v_x^2}{2C_p T_x}\right)^{1/r-1}\left(\frac{P_x}{RT_x}\right) \tag{15}$$

The shroud contours at any section inside the passage

$$r_{sx} = \sqrt{(r_{rms}^2)_x + \frac{1}{2}\frac{\dot{m}\cos\alpha_x}{\pi\rho_x v_{mx} B_{fx}}} \tag{16}$$

The hub contours at any section inside the passage

$$r_{hx} = \sqrt{(2r_{rms}^2)_x - r_{sx}^2} \tag{17}$$

It can be seen from Eqs. (16) and (17) that they can be used to calculate the shroud and the hub contours at any section inside the blade passage, hence the final shape of the blade passage can be defined.

A flow diagram for optimizing the axial length of the turbine rotor and the optimized design of the flow passage are shown in Fig. 11. The output results are plotted as shown in Fig. 12. The plot of the stagnation pressure loss vs. the meridional length indicates that the minimum losses of stagnation pressure occurs when the meridional length equal to 40.0 mm. The final design drawings are shown in Figs. 13–15, respectively.

Downloaded 31 May 2010 to 171.66.16.27. Redistribution subject to ASME license or copyright; see http://www.asme.org/terms/Terms_Use.cfm

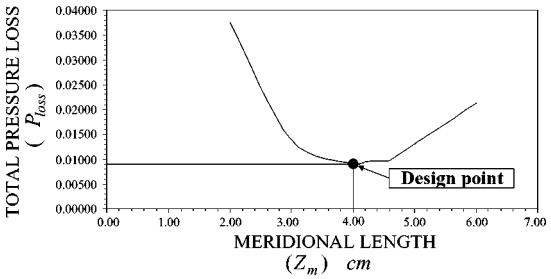

Fig. 12 Total pressure loss vs. meridional length

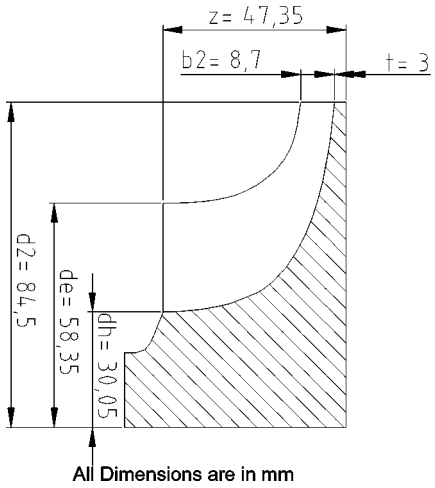

Fig. 13 Meridional section of the turbine rotor

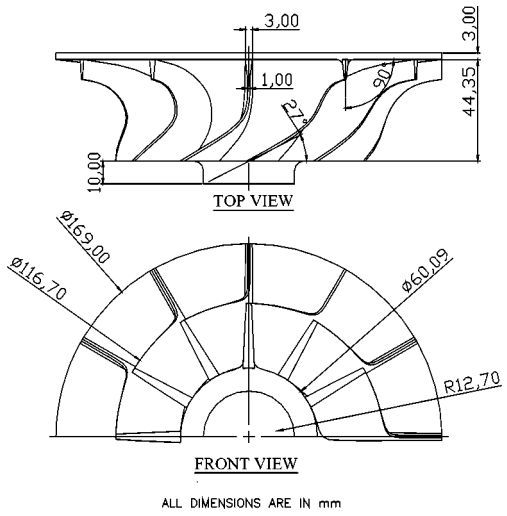

Fig. 14 Multiple views of the turbine rotor

Nozzleless Casing Design

The design objectives of the casing are:

1. Accelerate the working fluid to the leading edge of the rotor and generate the desired rotor inlet conditions in terms of the magnitude and direction of the absolute velocity vector.
2. Distribute the working fluid uniformly around the rotor periphery.
3. Achieve these requirements as efficiently as possible that is with minimum loss in stagnation pressure.

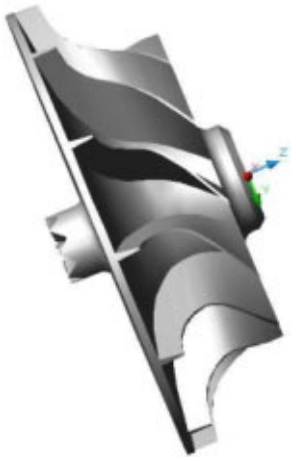

Fig. 15 Solid model of the turbine rotor

The required inlet conditions must be derived from the desired turbine performance, e.g., the desired rotational speed and power output. The nozzleless volute must be designed to provide these rotor inlet conditions peripherally uniform. The preliminary design of the volute is often based on the assumptions of an isentropic flow, together with a free vortex distribution about the rotor.

The passage design is often specified in the form of the variation, with azimuth angle, of cross-sectional area, casing width or parameter $A_\varphi/\overline{r}_\varphi$. The desired rotor inlet condition is one of a uniform distribution of angular momentum about the rotor periphery, whilst the volute inlet conditions at the tongue are those of a fully developed turbulent flow.

Theory of Volute Design Procedure

Assumptions. The following assumptions were used in the design procedure:

1. Steady, one-dimensional, isentropic flow, constant angular momentum, energy and linear distribution of mass along the volute length.
2. Vortex motion is fully established before the commencement of any outer flow from the volute in the radial direction. This is a necessary condition for the flow angles α_2 and β_2 to be independent of the azimuth angle and the flow into the rotor to be uniform.
3. The flow near the outer wall profile is assumed to follow the same contour as the outer profile of the casing, the boundary layer thickness being negligible.

A diagrammatic sketch of a centripetal turbine fitted with a nozzleless casing is shown in Fig. 16.

Principal Design Variables of the Nozzleless Volute Casing.

1. Volute Parameters
   i. The cross-sectional area A_φ of the volute and the variation of this area as a function of the azimuth angle φ.
   ii. The radial distance of the centriod $\overline{r}_\varphi$ of the cross-sectional area from the axis of rotation.
   iii. The shape of the volute cross-section.
2. Rotor Parameters
   i. Rotor tip diameter d_2 and blade width b_2.
   ii. Effective peripheral flow area A_2 or the number of blades and blade thickness at d_2.
3. Operating Conditions
   i. Rotational speed, N
   ii. Mass flow rate, $\dot{m}$
   iii. Stagnation temperature, T_i and stagnation pressure P_i of the working gas at the entry flange of the turbine.

Downloaded 31 May 2010 to 171.66.16.27. Redistribution subject to ASME license or copyright; see http://www.asme.org/terms/Terms_Use.cfm

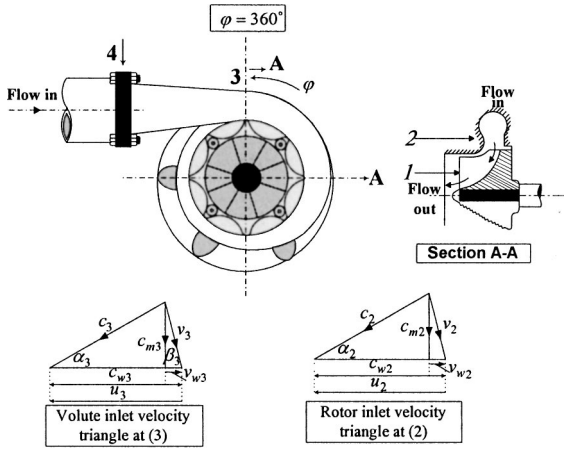

Fig. 16 IFR turbine fitted with a single nozzleless volute casing

Design Method. The design method employed in the current work is described hereafter.

The frame size and weight of the turbine is often an important design consideration and it is essential that the overall size be minimized. The design procedure first assesses the overall size in terms of the volute radius ratio $\bar{r}_3/r_2$, and area ratio A_3/A_2 and consider the parameters, which must be varied in order to adjust the overall size.

Using the equations of mass flow, energy and angular momentum and based on the assumption of free vortex relationship, the following expression defining the interconnection of the design parameters of the casing:

$$\frac{A_\varphi}{\bar{r}_\varphi} = (B_{f_2})(\tan\alpha_2)\left(\frac{\varphi}{360}\right)\left(\frac{A_2}{r_2}\right) \times \left[\frac{1-\left(\frac{\pi}{\sqrt{2}}\cdot\frac{d_2N}{\sqrt{C_pT_i}}\cdot\frac{\sin\beta_2}{\sin(\alpha_2+\beta_2)}\right)^2}{1-\left(\frac{\pi}{\sqrt{2}}\cdot\frac{r_2}{\bar{r}_\varphi}\cdot\frac{d_2N}{\sqrt{C_pT_i}}\cdot\frac{\sin\beta_2\cos\alpha_2}{\sin(\alpha_2+\beta_2)}\right)^2}\right]^{1/\gamma-1} \quad (18)$$

where B_{f_2} is the blockage factor corresponding to rotor entry and is given as:

$$B_{f_2} = \frac{\text{Total flow area of the passage}}{\text{Peripheral area}}$$

$$B_{f_2} = \frac{\text{Peripheral flow area—Blockage due to blades}}{\text{Peripheral area}} \quad (19)$$

$$B_{f_2} = 1-\left(\frac{n_b t_2 b_2}{\pi d_2 b_2}\right)$$

where n_b is the number of blades, and t_2 is the thickness of inlet rotor blades.

Equation (18) represents a fundamental design formula linking the main design parameter $A_\varphi/\bar{r}_\varphi$ of the volute with relevant principal dimensions of the rotor and the operating conditions as follows:

$$\frac{A_\varphi}{\bar{r}_\varphi} = f\left[\left(\frac{\dot{m}\sqrt{T_i}}{A_2P_i}\right),\left(\frac{b_2}{d_2}\right),(\alpha_2),(\varphi),(N)\right]$$

i.e. $A_\varphi/\bar{r}_\varphi = f(A_2, d_2, b_2, \alpha_2)$—these variables represent rotor parameters.

And $A_\varphi/\bar{r}_\varphi = f(\dot{m}, P_i, T_i, N, \alpha_2)$—these variables represent operating conditions.

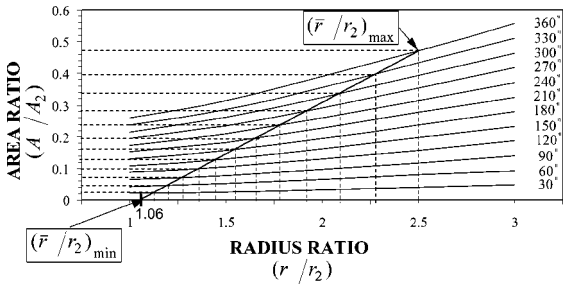

Fig. 17 Relationship between area ratio, radius ratio and azimuth angle $\beta_2 = 85$ deg

The losses may be included in Eq. (18). However experiments have shown [20,21] that, in general, stator losses are a small fraction of the overall losses, therefore the assumption of isentropic flow, at least for design calculations, is unlikely to introduce serious errors.

Figures 17–19 show graphically the plots of A_φ/A_2 versus $\bar{r}_\varphi/r_2$ for azimuth angles φ ranging from 0 *to* 360 deg and different relative flow angle β_2. The plotted graphs are based on the design parameters depicted in Table 4. The trend of the lines in these plots is similar for different values of inlet relative flow angle β_2.

The choice of $(\bar{r}_\varphi/r_2)_{\min}$ and $(\bar{r}_\varphi/r_2)_{\max}$ would normally dictated by the tip diameter of the rotor and the allowable overall dimensions of the volute casing. The initial design values were chosen to be 1.06 and 2.5, respectively.

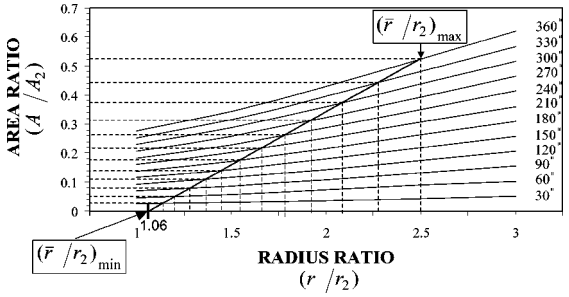

Fig. 18 Relationship between area ratio, radius ratio and azimuth angle for $\beta_2 = 73$ deg

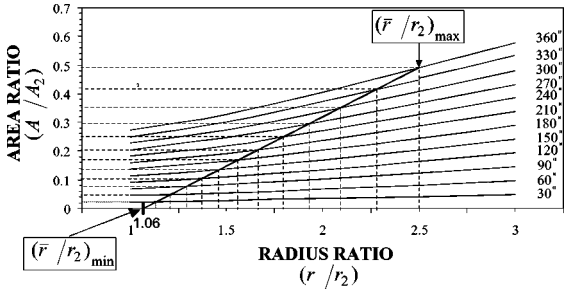

Fig. 19 Relationship between area ratio, radius ratio and azimuth angle for $\beta_2 = 90$ deg

Downloaded 31 May 2010 to 171.66.16.27. Redistribution subject to ASME license or copyright; see http://www.asme.org/terms/Terms_Use.cfm

Table 4 Constant design parameters

Design parameter	Values
Speed parameter, $d_2N/\sqrt{C_pT_i}$	0.157
Inlet absolute flow angle, α_2	17 deg
Inlet relative flow angle, β_2	73, 85, 90 deg
Blockage factor, B_{f_2}	0.93

Therefore, the corresponding pairs of values of the dimensionless parameters A_φ/A_2 and $\bar{r}_\varphi/r_2$ can be directly read from such a plot by joining $(\bar{r}_\varphi/r_2)_{\min}$ and $(\bar{r}_\varphi/r_2)_{\max}$ by a straight line as shown in Figs. 18–20.

Since $(A_\varphi/\bar{r}_\varphi) \propto [(A_\varphi/A_2) \div (\bar{r}_\varphi/r_2)]$

$$\text{then} \left(\frac{A_\varphi}{\bar{r}_\varphi}\right) = K\left(\frac{A_\varphi}{A_2}\right)\left(\frac{r_2}{\bar{r}_\varphi}\right)$$

where $K = A_2/r_2$ to satisfy the expression above. The final design graph of $A_\varphi/\bar{r}_\varphi$ versus φ can be obtained from the corresponding values of A_φ/A_2, $\bar{r}_\varphi/r_2$ and φ which can be read either from Figs. 17–19. Such a graph is shown in Fig. 20.

It should be noted that the shape of the graph above depends on the shape of the line joining the minimum and maximum values of $(\bar{r}_\varphi/r_2)$ chosen by the designer. Once the shape of cross section, i.e., $b = f(r)$ has been decided, in the current work, a circular cross section was chosen, its dimensions can be found from the following equation:

$$\left(\frac{A_\varphi}{r_\varphi}\right) = \int_{r_2}^{r_1} \left(\frac{b}{r}\right)_x \cdot dr \tag{20}$$

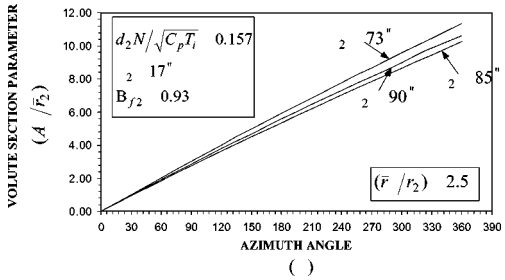

Fig. 20 Design graph for nozzle-less volute casing for various incidence angles

Table 5 Design values of turbine nozzleless casing

Position of points	Azimuth angle (degree)	Radius of centroid (mm)	Elevation-z- (mm)	Radius of casing cross section (mm)
1	0	85.65	−53	3.00
2	30	90.26	−51.53	4.47
3	60	94.87	−50.93	5.07
4	90	99.49	−48.23	7.77
5	120	104.10	−44.62	11.38
6	150	108.71	−40.6	15.40
7	180	113.32	−36.27	19.73
8	210	117.94	−31.67	24.29
9	240	122.55	−26.91	29.09
10	270	127.16	−21.89	34.11
11	300	131.77	−16.64	39.36
12	330	136.39	−11.16	44.84
13	360	141.00	−5.43	50.57
14	383	144.54	−5.43	50.57

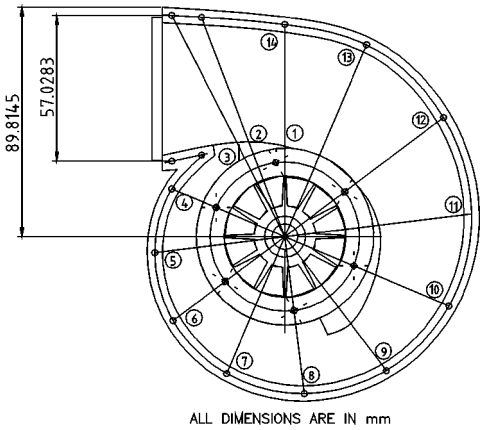

Fig. 21 Front view of the nozzleless casing

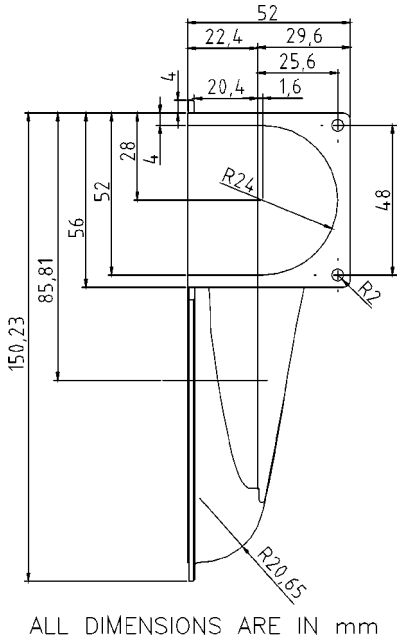

Fig. 22 Side view of the of the nozzleless casing

The final design dimensions and drawings for the nozzleless casing are shown in Table 5 and in Figs. 21 and 22.

The final design of the IFR turbine assembly is shown in Fig. 23. This assembly has been processed for manufacturing so that it can be tested experimentally for performance and efficiency.

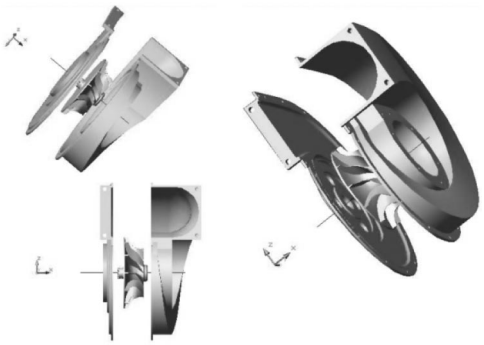

Fig. 23 Solid model of the IFR turbine assembly

Downloaded 31 May 2010 to 171.66.16.27. Redistribution subject to ASME license or copyright; see http://www.asme.org/terms/Terms_Use.cfm

Concluding Remarks

1. A unified approach for designing a single stage inward flow radial turbine comprising a rotor and a nozzle-less casing has been described. The radial turbine has been designed to drive a direc-coupled permanent magnet high-speed alternator running at 60,000 rpm and developing 60 kW electrical power.

2. A computer program was developed to find the optimum choice of the principal dimensions of the rotor and the number of blades.

3. The theory of the prescribed mean stream velocity distribution was used to find the optimum axial length and optimizing the blade passage.

4. A procedure for designing the nozzle-less casing was given based on the equations of mass flow rate, energy and angular momentum. The flow is assumed to be isentropic and satisfies the free vortex relationship.

Acknowledgments

The authors wish to thank king Abdullah II Design & Development Bureau for their endless support and encouragements. Also, would like to thank the University of Hertfordshire for their cooperation and help throughout this research program.

Nomenclature

A = area normal to mean flow direction (m^2)
b = blade width (m)
B_f = blockage factor
C = absolute flow velocity of gas (m/s)
C_p = specific heat capacity at constant pressure for gas (kJ/kgK)
d = diameter (m)
f_c = friction factor
M = absolute Mach no.
M_r = relative Mach no.
$\dot{m}$ = mass flow rate (kg/s)
N = rotational speed (rpm)
N_s = specific speed
n_b = no. of blades
P = stagnation pressure (N/m^2, bar)
R = degree of reaction
R_e = Reynolds no.
r_c = radius of curvature (m)
S_p = speed parameter
S_T = specific torque
T = stagnation temperature (K)
t = blade thickness (m)
u = rotor tip velocity (m/s)
v = relative velocity (m/s)
W = work output (kJ)
z = axial length (m)
α = absolute flow angle relative to axial direction (deg), angle between meridional streamline and axis
β = relative flow angle relative to axial direction (deg), angle between relative velocity vector and meridional plane
β_b = blade angle
θ = relative angular coordinate
γ = ratio of specific heats
η = efficiency of process
ρ = gas density (kg/m^3)
ψ = blade loading
ϕ = pressure loss coefficient
φ = centroid
ω = angular velocity (rad/s).
Δ = small increment of

Subscripts

0 = stagnation conditions
3 = turbine station
2 = rotor inlet station
1 = rotor outlet station at mean
a = air
av = average
c = compressor
e = exit condition, exducer
h = hub
i = inlet condition
m = mean
s = spouting velocity, shroud
SFL = skin friction loss
t = turbine
tt = total to total
w = tangential direction
rms = root mean square
r = radial direction
x = any station inside rotor passage

References

[1] Von Der Nuell, 1951, ''Single Stage Radial Turbines for Gaseous Substances With High Rotative and Low Specific Speed,'' ASME Paper 51-f-16, Fall meeting, Minneapolis, Sept.
[2] Balje, O. E., 1951, ''A Contribution to the Problem of Designing Radial Turbomachines,'' ASME Paper 51-F-12, Fall meeting, Minneapolis, Sept.
[3] Balje, O. E., 1960, ''A Study of Design Criteria and Matching of Turbomachines. Part A-Similarity Relations and Design Criteria of Turbines,'' ASME Paper No. 60-Wa-230 winter annual meeting. New York, Nov–Dec.
[4] Rohlik, H. E., 1970, ''Analytical Determination of Radial Inflow Turbine Design Geometry for Maximum Efficiency,'' NASA Tech. Memo., TN D 4384, Oct.
[5] Wallace, F. J., Baines, N. C., and Whitfield, A., 1976, ''A Unified Approach to One Dimensional Analysis and Design of Radial and Mixed Flow Turbines,'' ASME Paper No. 76-GT-100, Mar.
[6] Rodgers, C., 1987, ''Small High Pressure Ratio Radial Turbine Technology,'' VKI Lectures Series 1987-07.
[7] Whitfield, A., and Baines, N. C., 1990, *Design of Radial Turbomachines*, Longman Scientific and Technical.
[8] Wasserbauer, C. A., and Glassman, A. J., 1975, ''Fortran Program for Predicting of-Design Performance of Radial Inflow Turbines,'' NASA Tech. Memo, TND-8063.
[9] Whitfield, A., 1990, ''The Preliminary Design of Radial Inflow Turbines,'' Trans. ASME, Jan., pp. 50–57.
[10] Benson, R. S., and Fisher, U., 1978, ''A Proposal Scheme for Computer Aiaded Design and Manufacture of Radial Turbine Rotors,'' ASME Paper No. 78-GT-156.
[11] Baines, N. C., Wallace, F. J. and Whitfield, A., 1978, ''Computer Aided Design of Mixed Flow Turbines for Turbochargers,'' ASME Paper No. 78-GT-191.
[12] Bhinder, F. S., 1969, ''Investigation of Flow in the Nozzle-Less Spiral Casing of a Radial Inward Flow Gas Turbine,'' I Mech E Conf. Publ., **184**, Pt. 3G(II), pp. 66–77.
[13] Chapple, P. M., Flynn, P. F., and Mulloy, J. M., 1980, ''Aerodynamic Design of Fixed and Variable Geometry Nozzle-Less Casings,'' ASME J. Eng. Power, **102**, pp. 141–147.
[14] Hussian, M., Ilyas, M., and Bhinder, F. S., 1982, ''A Contribution to Designing a Nozzle-Less Volute Casing for the Inward Flow Radial Turbine,'' I Mech E Conf. Publ., No. C35/82.
[15] Whitfield, A., and Noor, A. B., 1991, *A Non-Dimensional Conceptual Design Procedure for the Vaneless Volute of Radial Inflow Turbines*. ASME.
[16] Biggs, M. C., 1982, ''Recursive Quadratic Programming Methods for Nonlinear Constraints,'' Powel, M. J. C., ed., *Nonlinear Optimization*, Academic Press, London, pp. 213–221.
[17] Biggs, M. C., 1999, ''Further Methods for Nonlinear Optimization,'' Mathematics Division, University of Hertfordshire.
[18] Dallenbach, C. et al., 1956, ''Study of Supersonic Radial Compressors for Refrigeration and Pressurization,'' WADC Technical Report 55–257, A.S.T.I.A Document No. AD110467, Dec.
[19] Rodgers, C., 1978, ''A Diffusion Factor Correlation for Centrifugal Impeller Stalling,'' ASME J. Eng. Power, **Oct. 100**.
[20] Hiett, G. F., and Johnston, I. H., 1964, ''Experiments Concerning the Aerodynamic Performance of Inward Radial Flow Turbine,'' I Mech E Conf. Publ., **178**, Pt. 31(II).
[21] Benson, R. S., 1966, ''An Analysis to the Losses in a Radial Gas Turbine,'' I Mech E Conf. Publ., **Apr**.

Downloaded 31 May 2010 to 171.66.16.27. Redistribution subject to ASME license or copyright; see http://www.asme.org/terms/Terms_Use.cfm